

Dissertation
submitted to the
Combined Faculty of Mathematics, Engineering and Natural Sciences
of Heidelberg University, Germany
for the degree of
Doctor of Natural Sciences

Put forward by
Caroline Sophie Gieser
born in: Heidelberg, Germany
Oral examination: 13.07.2022

Physical and chemical properties during high-mass star formation

Referees:

Prof. Dr. Henrik Beuther

Prof. Dr. Cornelis Dullemond

Abstract

This thesis is dedicated to the characterization of the physical and chemical properties in high-mass star-forming regions. I use interferometric observations at 1 and 3 mm wavelengths with the NOthern Extended Millimeter Array (NOEMA) and Atacama Large Millimeter/submillimeter Array (ALMA) of a sample of high-mass star-forming regions at different evolutionary stages ranging from infrared dark clouds, high-mass protostellar objects, hot molecular cores, to ultra-compact HII regions.

At angular resolutions $\lesssim 1''$, the physical and chemical properties of individual fragmented cores can be studied on scales < 0.1 pc using both continuum and molecular line emission. Molecule properties, for example, the column density and rotation temperature, are derived using the eXtended CASA Line Analysis Software Suite (XCLASS) of species such as SO, OCS, SiO, H₂CO, CH₃CN, and CH₃OH. I determine for a statistical sample of cores radial temperature and density profiles ($T \sim r^{-q}$ and $n \sim r^{-p}$, respectively), masses M , and molecular column densities N . Chemical timescales τ_{chem} are estimated using the physical-chemical model Multi Stage Cloud code (MUSCLE).

There is a high degree of fragmentation in the regions and the spatial morphology of the continuum emission is diverse, where in some regions there is a single isolated core, while in other regions, for example, filamentary structures that have many embedded cores are found. The molecular content of individual cores have local chemical variations and with MUSCLE this chemical differentiation can be explained by the cores being at slightly different evolutionary stages. By combining the results of the in total 31 high-mass star-forming regions that were observed with either NOEMA or ALMA at high angular resolution and that were analyzed within this thesis, evolutionary trends of the physical core properties are found. The temperature profile q steepens from $q \approx 0.1$ to $q \approx 0.7$ and the density profile p_1 on clump scales (0.1 – 1 pc) flattens from $p_1 \approx 2.2$ to $p_1 \approx 1.2$ with time as the cores evolve. No evolutionary trend is found for the density profile p_2 on core scales (< 0.1 pc), with $p_2 \approx 2$, indicating that all of the analyzed cores are collapsing to form (high-mass) stars. These results provide invaluable observational constraints to test theoretical formation models of high-mass stars.

Zusammenfassung

Diese Doktorarbeit befasst sich mit der Charakterisierung der physikalischen und chemischen Eigenschaften in massereichen Sternentstehungsgebieten. Ich verwende hierfür interferometrische Beobachtungen bei Wellenlängen von 1 und 3 mm mit dem Northern Extended Millimeter Array (NOEMA) und dem Atacama Large Millimeter/submillimeter Array (ALMA) von einem Sample an massereichen Sternentstehungsgebieten, die sich in verschiedenen evolutionären Stadien befinden, von Infrarot-Dunkelwolken, massereichen protostellaren Objekten, heißen molekularen Kernen, bis hin zu ultra-kompakten HII Regionen.

Bei Winkelauflösungen von $\lesssim 1''$ ist es möglich die physikalischen und chemischen Eigenschaften von einzelnen fragmentierten Kernen auf Skalen < 0.1 pc anhand der Emission des Kontinuums und der Moleküllinien zu untersuchen. Molekulare Eigenschaften, wie die Säulendichte und Rotationstemperatur, werden mit der eXtended CASA Line Analysis Software Suite (XCLASS), zum Beispiel von SO, OCS, SiO, H₂CO, CH₃CN, und CH₃OH, hergeleitet. Für ein statistisches Sample von Kernen bestimme ich radiale Temperatur- und Dichteprofile ($T \sim r^{-q}$ und $n \sim r^{-p}$), Massen M , und molekulare Säulendichten N . Chemische Zeitskalen τ_{chem} werden mit dem physikalisch-chemischen Modell Multi Stage Cloud code (MUSCLE) abgeschätzt.

Es gibt einen hohen Grad an Fragmentation in den Regionen und die räumliche Morphologie der Kontinuumsmission ist vielfältig. Während in einigen Regionen ein einzelner isolierter Kern vorhanden ist, gibt es in anderen Regionen beispielsweise filamentäre Strukturen, in welchen viele Kerne eingebettet sind. Die molekulare Zusammensetzung der einzelnen Kerne zeigen lokale chemische Variationen und mithilfe von MUSCLE können diese chemischen Unterschiede dadurch erklärt werden, dass sich die Kerne in geringfügig verschiedenen evolutionären Stadien befinden. Durch die Vereinigung der Ergebnisse der insgesamt 31 massereichen Sternentstehungsgebieten, die entweder mit NOEMA oder ALMA bei einer hohen Auflösung beobachtet wurden und die in dieser Doktorarbeit analysiert wurden, können evolutionäre Entwicklungen der physikalischen Eigenschaften festgestellt werden. Das Temperaturprofil q wird steiler von $q \approx 0.1$ zu $q \approx 0.7$ und das Dichteprofil p_1 auf Klumpskalen (0.1 – 1 pc) wird flacher von $p_1 \approx 2.2$ zu $p_1 \approx 1.2$ während sich der Kern mit der Zeit entwickelt. Keine zeitlichen Veränderungen können für das Dichteprofil p_2 auf Kernskalen (< 0.1 pc) gefunden werden, mit $p_2 \approx 2$, was darauf hinweist, dass alle analysierten Kerne kollabieren und sich (massereiche) Sterne bilden. Diese Ergebnisse basierend auf den interferometrischen Beobachtungen liefern wertvolle Grundlagen, um theoretische Modelle der Entstehung von massereichen Sternen zu testen.

Contents

1	Introduction	1
1.1	The interstellar medium	1
1.2	High-mass star formation	2
1.3	Astrochemistry	5
1.3.1	Reaction types	6
1.3.2	Chemical kinetics	7
1.3.3	Physical-chemical modeling	8
1.4	Radio astronomy	9
1.4.1	Single-dish telescopes	10
1.4.2	Interferometry	11
1.5	Radiative transfer	16
1.5.1	Continuum emission	18
1.5.2	Spectral line emission	19
1.6	Scientific motivation and outline of this thesis	24
2	Physical and chemical structure of high-mass star-forming regions: Unraveling chemical complexity with the NOEMA large program CORE	27
2.1	Context	27
2.2	Observations	27
2.2.1	Sample	28
2.2.2	NOEMA	29
2.2.3	IRAM 30m telescope	29
2.2.4	Self-calibration	29
2.2.5	Data products and public release	33
2.3	Physical structure	33
2.3.1	Continuum emission	34
2.3.2	Temperature structure	35
2.3.3	Density structure	42
2.4	Molecular gas content	47
2.4.1	Molecular hydrogen and core mass estimate	47
2.4.2	Spectral line modeling with XCLASS	48
2.5	Physical-chemical modeling of the cores	51
2.5.1	MUSCLE setup	51
2.5.2	Chemical timescales	55
2.6	Discussion	56
2.6.1	Physical structure of high-mass star-forming cores	56
2.6.2	Mass-to-luminosity ratio as a tracer of evolutionary trends	59
2.6.3	Correlations between chemical species	60
2.6.4	Comparison of physical and chemical timescales	62
2.7	Summary and conclusions	64

3	Clustered star formation at early evolutionary stages: Physical and chemical analysis of two young star-forming regions	67
3.1	Context	67
3.2	Sample	68
3.3	Observations	70
3.3.1	CORE-extension data	70
3.3.2	Archival data	72
3.4	Continuum	75
3.4.1	Fragmentation properties	75
3.4.2	Radial density profiles	80
3.4.3	Spectral energy distribution	82
3.5	Spectral line emission	88
3.5.1	Molecular outflows	88
3.5.2	Spatial morphology and correlations	90
3.5.3	Kinematic properties	97
3.5.4	Formaldehyde distribution	98
3.5.5	Radial temperature profiles	100
3.5.6	Molecular column densities	102
3.6	Physical-chemical modeling	103
3.6.1	Model setup	104
3.6.2	Chemical timescales	105
3.7	Discussion	106
3.7.1	Core properties	107
3.7.2	Dynamics in ISOSS J23053+5953	113
3.8	Summary and conclusions	115
4	Unveiling the physical properties during high-mass star formation with ALMA from infrared dark clouds to ultra-compact H_{II} regions	117
4.1	Context	117
4.2	Sample	118
4.3	Observations	121
4.3.1	ALMA	122
4.3.2	Archival data	125
4.4	Continuum	126
4.4.1	Fragmentation	126
4.4.2	Free-free emission	129
4.5	Temperature structure	131
4.5.1	HCN-to-HNC intensity ratio	134
4.5.2	Methyl cyanide	134
4.5.3	Radial temperature profiles	138
4.6	Density profiles	141
4.6.1	Source subtraction	141
4.6.2	Visibility profiles	141
4.7	Molecular hydrogen column density and mass estimates	145
4.8	Discussion	146
4.8.1	Evolutionary trends of the clump properties	146
4.8.2	Evolutionary trends on core scales	148
4.9	Summary and conclusions	152

5 Summary and outlook	155
5.1 Summary of this thesis	155
5.2 Outlook	157
Bibliography	163
List of Figures	173
List of Tables	177
A Supplementary material for Chapter 2	179
A.1 Position properties	179
A.2 Spectral line properties	185
A.3 Temperature maps	186
A.4 Abundance histograms	193
A.5 Column density results	194
A.6 Spectra	209
A.7 Model results	239
B Supplementary material for Chapter 3	241
B.1 Moment maps	241
B.2 Molecular column densities derived with XCLASS	251
B.3 MUSCLE results	257
C Supplementary material for Chapter 4	261
C.1 Summary of the ALMA observations	261
C.2 Overview of the sample	263
C.3 Source properties	274
C.4 Integrated intensity maps	282
Acknowledgements	283

Chapter 1

Introduction

For many decades, star formation (SF) has been subject to extensive observational and theoretical studies. Observations toward the Galactic plane revealed that stars form in dense molecular clouds (e.g., Solomon et al. 1979; Dame et al. 2001) and early star formation models by Larson (1969) and Shu (1977) considered the collapse of an isothermal gas sphere into a low-mass star. However, more sophisticated physical models are required to describe efficient gas accretion onto a high-mass protostar such as an accretion disk and outflow (e.g., McKee & Ostriker 2007; Krumholz et al. 2009; Kölligan & Kuiper 2018; Rosen et al. 2020; Zhao et al. 2020), as otherwise the radiation pressure halts further accretion (Wolfire & Cassinelli 1987). Within our own Galaxy, individual star-forming regions (SFRs) can be resolved down to individual protostars (e.g., Tobin et al. 2016), but with today's technological advances, sensitive instruments at large telescopes allow us to even study individual molecular clouds in nearby galaxies (e.g., Leroy et al. 2021).

Stars form in the coldest and densest parts in molecular clouds located in the interstellar medium whose properties are introduced in Sect. 1.1. Final stellar masses range from $\approx 0.1 M_{\odot}$ (at lower masses hydrogen fusion cannot take place) to a few $100 M_{\odot}$ (Crowther et al. 2016) and according to the observed initial mass function (IMF, e.g., Kroupa 2001) low-mass stars are much more common than high-mass stars ($M_{\star} \geq 8 M_{\odot}$). Between $2 M_{\odot}$ and $55 M_{\odot}$, the luminosity scales as $L \sim M^{3.5}$ (Kuiper 1938), therefore the luminosity of one high-mass star easily outshines the luminosity of many low-mass stars. Even though massive stars are less prevalent, throughout their lifetimes several feedback mechanisms - including stellar winds (e.g., Meynet et al. 1994; Gatto et al. 2017), outflows (e.g., Beuther et al. 2002b; Kölligan & Kuiper 2018), and supernova explosions (e.g., McKee & Ostriker 1977; Girichidis et al. 2016) - shape not only the surrounding molecular cloud, but can impact the entire host galaxy.

It is therefore important to understand the physical and chemical processes occurring during high-mass star formation introduced in Sect. 1.2. The physical properties can be probed by molecules and their formation and destruction mechanisms in the interstellar medium are explained in Sect. 1.3. The early stages of the formation of massive stars can best be probed with observations at mm wavelengths since protostars are still deeply embedded in their parental molecular cloud with a high extinction at optical and infrared (IR) wavelengths. An introduction to radio single dish telescopes and interferometry is given in Sect. 1.4. The electromagnetic radiation received and measured with instruments at telescopes is based on the principle of radiative transfer that is explained in Sect. 1.5. The aim of this thesis is given in Sect. 1.6.

1.1 The interstellar medium

The space between stars in a galaxy is not completely empty and is referred to as the interstellar medium (ISM) containing a mixture of gas, dust, and cosmic rays (CRs). In addition, the ISM

is filled with electromagnetic radiation from, for example, (proto)stars, dust grains (Sect. 1.5.1), atomic and molecular lines (Sect. 1.5.2), and the cosmic microwave background (CMB).

The physical properties of the ISM span a wide range in density and temperature and can be divided into several phases from a diffuse hot ionized medium ($n < 1 \text{ cm}^{-3}$ and $T > 10^5 \text{ K}$, e.g., Nava et al. 2019) to cold and dense molecular clouds ($n > 10^4 \text{ cm}^{-3}$ and $T < 20 \text{ K}$, e.g., Rathborne et al. 2006). The different phases can have sharp discrete boundaries, but in other cases one phase continuously transitions into another phase. In the cold atomic phase (cold neutral medium, CNM) the densities are on the order of 10 cm^{-3} and the temperature is $\approx 100 \text{ K}$, with hydrogen being mostly in atomic and neutral form (H I). Out of the atomic gas, molecular clouds form (e.g., Tielens 2005; Syed et al. 2020) with densities that can reach $> 10^4 \text{ cm}^{-3}$ and the gas can cool down below 20 K , with hydrogen being mostly in molecular form, H_2 . In the ISM, heating mechanisms are stellar radiation, CRs, collisions, photoelectrons, and shocks, while cooling occurs via atomic and molecular line (e.g., C I and CO) emission (summarized, e.g., in Table 1.3 in Draine 2011, for different phases of the ISM). Cosmic rays consisting of energetic relativistic electrons and ions can enter deep into the densest regions of molecular clouds and are an important ionization source (e.g., Padovani et al. 2009).

About 1% of the mass in the ISM is confined to dust grains (Draine 2011) that are mainly produced in the envelope of evolved asymptotic giant branch and red giant stars (e.g., Zuckerman & Dyck 1986; Ferrarotti & Gail 2006; Nanni et al. 2013). In the cooling envelope of these stars, molecules containing refractory atoms such as silicon (Si) and titanium (Ti) react with oxygen (O) to SiO and TiO, form crystalline structures, and eventually the dust particles are released into the ISM by stellar winds. In addition to silicates, carbon compounds are also abundant in the form of polycyclic aromatic hydrocarbons (PAHs, Allamandola et al. 1985, 1989; Tielens 2008). The sizes of dust grains span a wide range from $\approx 0.01 \mu\text{m}$ to $1 \mu\text{m}$ (e.g., Mathis et al. 1977; Weingartner & Draine 2001). Dust grains are also relevant for planet formation as they can coagulate in protoplanetary disks (e.g., Dullemond & Dominik 2005; Okuzumi et al. 2012).

1.2 High-mass star formation

By definition, the stellar mass M_\star of a high-mass star is at least $8 M_\odot$, that is the minimum required mass to end up in a core collapse supernova with a remnant neutron star or stellar black hole (e.g., Heger et al. 2003). Massive stars are luminous ($L > 10^3 L_\odot$) objects with a high flux of ultraviolet (UV) photons with effective temperatures $T_{\text{eff}} > 10^4 \text{ K}$ (Eq. 1.42). At the end of their lifetimes they explode in energetic core collapse supernovae enriching the ISM with heavy elements (e.g., Woosley & Janka 2005), thus, they have a strong influence on the properties of not only their nearby environment, but also on the whole host galaxy itself and consequential star formation epochs. It is therefore important to understand how massive stars form.

The characterization of high-mass star-forming regions (HMSFRs) is, even within our own Galaxy, a challenging task from an observational perspective, since massive stars are less common, located at typical distances $> 1 \text{ kpc}$ and their evolution is much faster compared to their low-mass analogues. High-mass star formation (HMSF) has therefore become an active field of modern astrophysics. With sensitive radio single-dish telescopes and interferometers, we can peek through the dense gas into the optically thin regime at mm wavelengths and analyze the properties of individual fragmented objects.

Star formation is a hierarchical process from cloud ($> 1 \text{ pc}$), clump ($0.1 - 1 \text{ pc}$), to core ($< 0.1 \text{ pc}$) scales (e.g., Beuther et al. 2007a; Zhang et al. 2009; Roman-Duval et al. 2010).

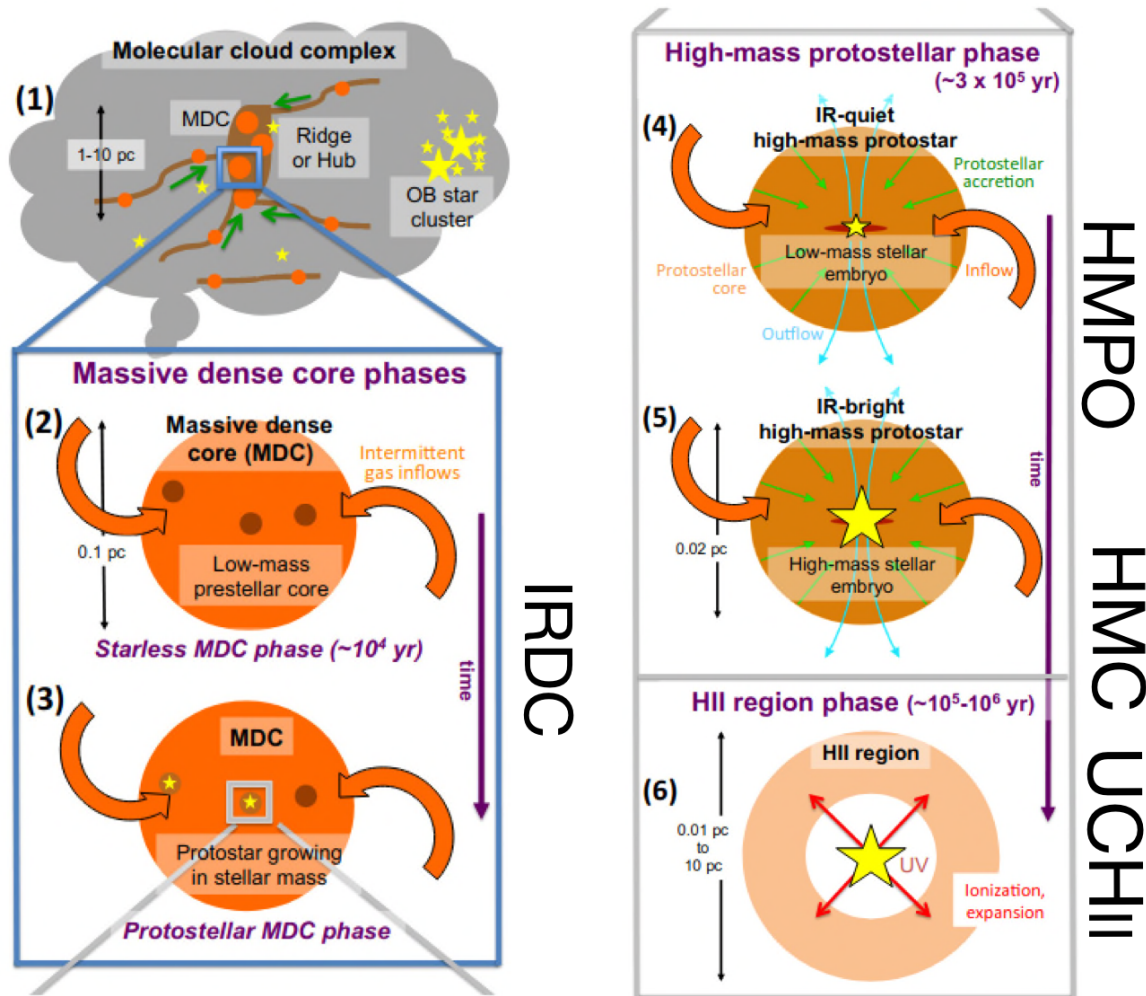


FIGURE 1.1: High-mass star formation scenario proposed by Motte et al. (2018) and evolutionary stages (figure taken and adapted from Tigé et al. 2017).

Molecular clouds appear as filamentary structures with “hubs” in which multiple filaments converge (e.g., Myers 2009; Schneider et al. 2012; André et al. 2014; Kumar et al. 2020; Hacar et al. 2022). Dedicated reviews regarding observational and theoretical aspects of HMSF can be found, for example, in Beuther et al. (2007a), Bonnell (2007), Zinnecker & Yorke (2007), Smith et al. (2009), Tan et al. (2014), Krumholz (2015), Schilke (2015), Motte et al. (2018), and Rosen et al. (2020).

Massive stars form in the densest regions of molecular clouds with typical formation time scales on the order of 10^5 yr (McKee & Tan 2002, 2003; Mottram et al. 2011a; Kuiper & Hosokawa 2018). The evolutionary stages of high-mass protostars can be categorized into four different stages based on observed properties that are further explained in the following:

- infrared dark cloud (IRDC)
- high-mass protostellar object (HMPO)
- hot molecular core (HMC)
- ultra-compact HII (UCHII) region

Considering the underlying physical properties during HMSF (e.g., Beuther et al. 2007a; Zinnecker & Yorke 2007; Gerner et al. 2014), these evolutionary stages can be related to the high-mass star formation scenario proposed by Motte et al. (2018) that is sketched in Fig. 1.1.

Due to their high extinctions at near-infrared (NIR) and mid-infrared (MIR) wavelengths, IRDCs were initially identified as absorption features against the bright Galactic MIR background, while at far-infrared (FIR) wavelengths they appear in emission (e.g., Rathborne et al. 2006; Henning et al. 2010). IRDCs with sizes of 1 – 10 pc have a typical density of $n \gtrsim 10^4 \text{ cm}^{-3}$ and temperature of $T < 20 \text{ K}$, and are the birth places of stars (e.g., Carey et al. 1998; Pillai et al. 2006a; Rathborne et al. 2006; Zhang et al. 2015). In local high-density regions, star formation with MIR-bright protostellar cores takes place, while in other parts of the cloud prestellar cores can be found that are only detected at FIR and mm wavelengths. In this stage, low- and intermediate-mass protostars and potentially high-mass starless cores exist (Motte et al. 2018).

Dense cores that undergo gravitational collapse can harbor high-mass protostars that have high luminosities, $L > 10^3 L_{\odot}$, and high accretion rates, $\dot{M} \gtrsim 10^{-4} M_{\odot} \text{ yr}^{-1}$, inferred from large bipolar molecular outflows (e.g., Beuther et al. 2002b; Duarte-Cabral et al. 2013) and are referred to as HMPOs (e.g., Beuther et al. 2002a; Williams et al. 2004; Motte et al. 2007; Beuther et al. 2010). The temperature in the envelope increases due to the central heating of the protostar and since outflows are commonly observed, disks should be present as well, but due to their small sizes ($\lesssim 1000 \text{ au}$) they remain challenging to observe (e.g., Sánchez-Monge et al. 2013a; Beltrán & de Wit 2016), while they are commonly found around low-mass protostars (e.g., ALMA Partnership et al. 2015; Andrews et al. 2018; Avenhaus et al. 2018; Öberg et al. 2021). HMPOs are bright at mm wavelengths, but have no or only weak emission at cm wavelengths.

As the protostar heats up the envelope to $\geq 100 \text{ K}$, molecules that have resided and/or formed on dust grains evaporate into the gas-phase (Sect. 1.3) revealing line rich emission spectra, being classified as HMCs or “hot cores” (Cesaroni et al. 1997; Osorio et al. 1999; Belloche et al. 2013; Sánchez-Monge et al. 2017; Beltrán et al. 2018). In HMCs, complex organic molecules (COMs, consisting six or more atoms, following the definition by Herbst & van Dishoeck 2009) are very abundant, for example, methanol (CH_3OH), acetone (CH_3COCH_3), methyl formate (CH_3OCHO), and ethyl cyanide ($\text{CH}_3\text{CH}_2\text{CN}$) as revealed by spectral line surveys (e.g., Belloche et al. 2013). Due to the ionizing radiation of the protostar, in the central region of the HMC, a hyper-compact (HC) HII region might already be present.

The strong protostellar radiation causes an expansion and further ionization of the surrounding envelope that is eventually disrupted revealing the massive star. The region is then classified to be a UCHII region (e.g., Wood & Churchwell 1989; Hatchell et al. 1998; Garay & Lizano 1999; Kurtz et al. 2000; Churchwell 2002; Palau et al. 2007; Qin et al. 2008; Sánchez-Monge et al. 2013b; Klaassen et al. 2018). UCHII regions can be studied at cm wavelengths due to free-free emission from scattered electrons (Churchwell 2002; Peters et al. 2010) and show diverse spatial morphologies from compact cores to cometary halos (Churchwell 2002). Typical sizes of UCHII regions are $R < 0.1 \text{ pc}$, while HCHII regions are even more compact with $R < 0.01 \text{ pc}$. At NIR and MIR wavelengths, the massive star might be detectable depending on the extinction in the cloud.

The formation of massive stars has not only been subject of extensive observational studies. Early star formation models by Larson (1969) and Shu (1977) considered the collapse of an isothermal sphere forming low-mass stars between 1 – 5 M_{\odot} . This picture is too simplistic in order to explain the formation of massive stars since the high luminosity would halt the spherical accretion process (Wolfire & Cassinelli 1987). Therefore, several theoretical models were developed over the last decades to explain HMSF that are introduced in the following.

The turbulent core model proposes that HMSF is a scaled-up version of low-mass star formation (e.g., Lizano & Shu 1989; Myers & Fuller 1992; McLaughlin & Pudritz 1996; McKee & Tan 2002; Tan et al. 2014). The cores are supported by magnetic fields and turbulence that allow high accretion rates to overcome the feedback caused by the radiation pressure. In these

models, one massive star or a bound multiple system forms out of a single core.

The competitive accretion model considers large scale accretion flows due to converging flows and/or gravity onto an initially low-mass protostar (e.g., Bonnell et al. 2001; Bonnell 2007). Out of a clump, a cluster of stars forms with stars toward the gravitational center having higher accretion rates and therefore higher stellar masses. Embedded, initially low-mass, cores continuously accrete the surrounding material growing into high-mass cores. The global hierarchical collapse scenario considers a hierarchical SF process from clouds, to filaments, to clumps, to core scales with non-thermal motions due to turbulence and infall (e.g., Vázquez-Semadeni et al. 2009, 2019).

The four evolutionary stages are not sharp transitions and within a single HMSFR, protostars at different evolutionary stages can be present. The extreme physical conditions in HMSFRs lead to intense feedback that can eventually disrupt molecular clouds and stop further star formation. However, beforehand HMSFRs provide the perfect environment for the formation of large molecules and in the next section it is explained how molecules are able to assemble despite the relatively low densities in the ISM.

1.3 Astrochemistry

The existence of a large number of molecules in space has been doubted for a long time (Swings & Rosenfeld 1937): due to the low densities and due to the fact that molecules should be rapidly destroyed by the interstellar radiation field (ISRF), only a few small molecules, such as CH, OH, NH, CN, and C₂, could persist in such an environment. The first detected molecules were CH (Adams 1941), CH⁺ (Douglas & Herzberg 1941), and CN (Adams 1941). In the 20th century, radio telescopes opened a new window to astronomical observations, revealing that in fact a large variety of molecules exists in space, such as OH (Weinreb et al. 1963), NH₃ (Cheung et al. 1968), H₂O (Cheung et al. 1969), H₂CO (Snyder et al. 1969), CO (Wilson et al. 1970), and H₂ (Carruthers 1970). To date, about 250 molecules have confirmed detections in space (McGuire 2018; Guelin & Cernicharo 2022).

Molecules can be identified through their observed rotational and vibrational states (Sect. 1.5.2). This requires precise reference measurements in the laboratory. In addition, in order to understand the formation and destruction mechanisms of molecules, experiments and theoretical calculations and models are required. Thus, astrochemistry is an interdisciplinary field in modern astrophysics.

The most abundant molecule in the ISM is molecular hydrogen, H₂, but since it does not have a dipole moment, it does not have rotational dipole transitions that are easily excited for other molecules even at low temperatures (Sect. 1.5.2). Quadrupole transitions of H₂ in the infrared are only excited at higher temperatures. The second most abundant molecule is CO, which can be easily excited even in low-temperature regions toward IRDCs and thus has become a common tracer of the molecular gas (e.g., Dame et al. 2001; Bolatto et al. 2013). Millimeter and submillimeter observations reveal that a variety of molecules are present in star-forming regions, consisting of atoms such as hydrogen (H), carbon (C), nitrogen (N), oxygen (O), sulfur (S), silicon (Si), and phosphor (P). Molecules detected in SFRs can be saturated (e.g., CH₃OH) or unsaturated (e.g., HC₃N), ionized (e.g., HCO⁺), cyclic (e.g., c-C₃H₂), and in the form of radicals (e.g., CN). In addition to the main species, less abundant isotopologues are also found (e.g., ¹³C, ¹⁸O, ³⁴S).

1.3.1 Reaction types

In the ISM, the formation of molecules is a complex process depending not only on the local density and temperature, but also on the radiation field and cosmic ray flux. Chemical reactions can occur either in the gas-phase or on the surfaces and in the icy mantles of dust grains (e.g., Garrod & Herbst 2006; Garrod et al. 2008; Pilling 2013).

Gas-phase reactions

Due to low densities in the ISM, if collisions between atoms and molecules occur, predominantly two-body collisions are relevant in the gas-phase. Collisions can not only put atoms or molecules into an excited state, but a chemical reactions can follow after a collision depending on the energy and geometry of the reactants. Photons, γ , and CR particles, CR, can also participate in reactions. Depending on the type of the reactants and products, different gas-phase reaction mechanisms can occur, with an example reaction given in the following:

- Neutral-neutral: $\text{CN} + \text{HCO} \rightarrow \text{HCN} + \text{CO}$ (Smith et al. 2004)
- Ion-neutral: $\text{H}_3^+ + \text{CO} \rightarrow \text{HCO}^+ + \text{H}_2$ (Huntress & Anicich 1976)
- Associative detachment: $\text{H} + \text{H}^- \rightarrow \text{H}_2 + \text{e}^-$ (Bieniek & Dalgarno 1979)
- Charge transfer: $\text{H}^+ + \text{HCN} \rightarrow \text{HCN}^+ + \text{H}$ (McElroy et al. 2013)
- Mutual neutralization: $\text{C}^- + \text{HCO}^+ \rightarrow \text{C} + \text{HCO}$ (McElroy et al. 2013)
- Dissociative recombination: $\text{NH}_4^+ + \text{e}^- \rightarrow \text{NH}_3 + \text{H}$ (Herbst 1978)
- Cosmic rays: $\text{H}_2 + \text{CR} \rightarrow \text{H} + \text{H} + \text{CR}$ (Padovani et al. 2018)
- Collisional dissociation: $\text{H} + \text{H}_2\text{O} + \gamma \rightarrow \text{OH}^* + 2 \text{H}$ (Gwinn et al. 1973)

The * marks an excited state, where excess energy is removed through, for example, rotational and vibrational levels (Sect. 1.5.2).

Photochemistry

Interaction with photons, γ , of the ISRF can also trigger reactions:

- Photodissociation: $\text{CH}_3\text{OH} + \gamma \rightarrow \text{OH} + \text{CH}_3$ (Pilling et al. 2007)
- Radiative association: $\text{H}_2\text{COH}^+ + \text{H}_2\text{CO} \rightarrow \text{H}_2\text{COHOCH}_2^+ + \gamma$ (Horn et al. 2004)
- Radiative electron attachment: $\text{C}_4 + \text{e}^- \rightarrow \text{C}_4^- + \gamma$ (Terzieva & Herbst 2000)
- Radiative recombination: $\text{H}_2\text{CO}^+ + \text{e}^- \rightarrow \text{H}_2\text{CO} + \gamma$ (McElroy et al. 2013)

Grain surface reactions

Early chemical models could not reproduce the observed abundances of COMs in HMCs based on pure gas-phase models. It was then proposed that large molecules can form via hydrogenation on the surface of dust grains (e.g., Tielens & Hagen 1982; Charnley et al. 1992; Hasegawa et al. 1992). Another important molecule that can only efficiently form on grains is H_2 (e.g., Le Boulot et al. 2012). Small atoms and molecules (such as H and CO) can stick to the grains in potential minima (binding sites) via weak van-der-Waals forces (physisorption) or via chemical bonds (chemisorption). Even at low temperatures of ≈ 10 K, hydrogen can move on the surface (thermal hopping) or tunnel through energy barriers as sketched in Fig. 1.2. In case molecules or atoms are located in the binding site, a chemical reaction can occur (Herbst & van Dishoeck

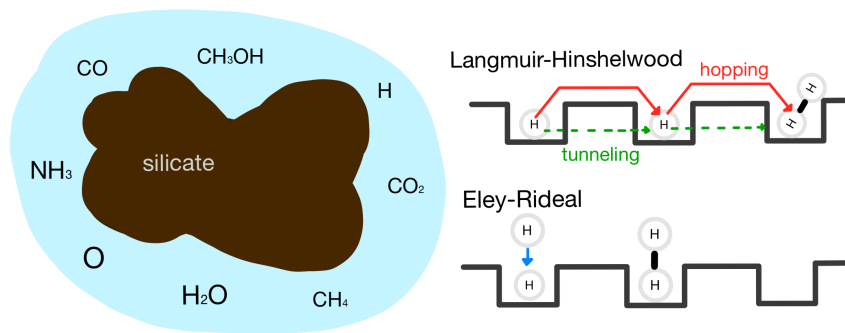


FIGURE 1.2: Sketch of a dust particle with an icy mantle (*left panel*) and grain surface reaction mechanisms (*right panel*). The dust particle consists of silicates and the icy mantle is composed of molecules such as H₂O, CO₂, and NH₃. On the grain surface, binding sites for atoms and molecules enable chemical reactions by either tunneling or thermal hopping (Langmuir-Hinshelwood mechanism) or by collisions with particles from the gas-phase (Eley-Rideal mechanism).

2009) and the dust grain can absorb excess energy. The two main mechanisms considering reactions on dust grains (Herbst & van Dishoeck 2009) are:

- Langmuir-Hinshelwood: $O_{(\text{grain})} + H_{(\text{grain})} \rightarrow OH_{(\text{grain})}$ (Bergeron et al. 2008)
- Eley-Rideal: $H_{(\text{grain})} + H_{(\text{gas})} \rightarrow H_{2(\text{grain})}$ (Le Boulot et al. 2012)

In the cold ISM, icy mantles form on dust grains with species such as CO, CO₂, H₂O, and NH₃ (Fig. 1.2). Large molecules can form on dust grains via consecutive hydrogenation (e.g., Watanabe & Kouchi 2002), for example, CH₃OH:

- hydrogenation: $CO \xrightarrow{+H} HCO \xrightarrow{+H} H_2CO \xrightarrow{+H} H_2COH \xrightarrow{+H} CH_3OH$

Methanol is then the starting point to form even more complex species such as CH₃OCHO, CH₃COCH₃, CH₃OCH₃ that are commonly detected in HMCs (e.g., Belloche et al. 2013). Molecules that formed and resided on dust grains can evaporate into the gas-phase once the temperature increases (Herbst & van Dishoeck 2009) or due to shocks (e.g., Csengeri et al. 2019). Gas-phase species can be studied best at FIR and mm wavelengths, while the composition of the ices are analyzed with observations at NIR and MIR wavelengths (e.g., Perotti et al. 2020, 2021).

1.3.2 Chemical kinetics

Considering a reaction of a two-body collision $A + B \rightarrow C + D$, the time evolution of the concentration of species A can be described by the reaction rates $k_{r,1}$ and $k_{r,2}$ destroying and forming A, respectively:

$$\frac{d[A]}{dt} = -k_{r,1}[A][B] + k_{r,2}[C][D], \quad (1.1)$$

with $[X]$ denoting the concentration of species X. The Arrhenius equation is an empirical relation describing the dependence of the reaction rate on the temperature T ,

$$k_r(T) \sim \exp\left(\frac{E_a}{RT}\right), \quad (1.2)$$

with activation energy E_a required to overcome the energy barrier in the chemical reaction and gas constant R .

In the laboratory, reaction rates are typically measured at room temperature and therefore are usually extrapolated to low temperatures according to Eq. (1.2). Most of the reactions in the ISM are exothermic, meaning that some energy is required for the reaction to occur. However, at low temperature, other effects might result in an enhanced reaction rate, for example, deuterium (D) fractionation is very efficient at low temperatures toward IRDCs where the process becomes endothermic, meaning that energy is released after the reaction. The D-bond is slightly stronger than the H-bond causing an increase of the D/H ratio in prestellar cores ($D/H > 0.2$, e.g., Caselli et al. 2002) compared to the average value of the ISM ($D/H \approx 1.5 \times 10^{-5}$, Oliveira et al. 2003).

1.3.3 Physical-chemical modeling

A large variety of atoms and molecules are found in the ISM and in order to understand the observed molecular abundances, a chemical network is required that considers all important chemical reactions to form and destroy a certain species. Depending on the molecular complexity, chemical networks can contain thousands of reactions including hundreds of species taking into account the different reaction types (Sect. 1.3.1). To follow the evolution of the abundances, a set of coupled differential equations in the form of Eq. (1.1) has to be solved. In common astronomical chemical models, the reaction rate of two-body collisions is estimated by the Arrhenius equation (Eq. 1.2) in a parametric form:

$$k_r(T) = \alpha \left(\frac{T}{300 \text{ K}} \right)^\beta \exp\left(-\frac{\gamma}{T}\right) \quad (1.3)$$

with α , β , and γ measured either in laboratory experiments or inferred from theoretical quantum calculations. The most important databases regarding astrochemically relevant reactions are the Ohio State University (OSU) database (Prasad & Huntress 1980), the University of Manchester Institute of Science and Technology (UMIST) database for astrochemistry (McElroy et al. 2013), and the KInetic Database for Astrochemistry (KIDA, Wakelam et al. 2012, 2015).

In this thesis, I use the physical-chemical model MUlti Stage CLOUD code (MUSCLE) to model the time evolution of chemical abundances. MUSCLE was developed for a study of 59 HMSFRs that were observed with single-dish telescopes from 1 to 3 mm wavelengths (Gerner et al. 2014, 2015). The sample covers all four evolutionary stages introduced in Sect. 1.2. Molecular column densities (Sect. 1.5.2) of, for example, HCN, C_2H , N_2H^+ , HNC, CH_3OH , and CH_3CN (Gerner et al. 2014) and deuterated molecules, for example, DCO^+ , DCN, DNC, and N_2D^+ (Gerner et al. 2015) were derived. The column densities were averaged for each of the four evolutionary stages in order to create template column densities from IRDC to UCHII regions.

The physical structure of the model is described by static, spherically symmetric density and temperature power-law profiles beyond an inner radius r_{in} up to an outer radius r_{out} and a constant inner region,

$$n(r) = n_{in} \quad (\text{if } r < r_{in}) \quad (1.4)$$

$$n(r) = n_{in} \left(\frac{r}{r_{in}} \right)^{-p} \quad (\text{if } r \geq r_{in}) \quad (1.5)$$

$$T(r) = T_{in} \quad (\text{if } r < r_{in}) \quad (1.6)$$

$$T(r) = T_{in} \left(\frac{r}{r_{in}} \right)^{-q} \quad (\text{if } r \geq r_{in}), \quad (1.7)$$

with density and temperature power-law index p and q , respectively. The physical structure is described by, in total, 40 radial grid points. The model core is embedded in material with a visual extinction $A_V = 10^{\text{mag}}$ at the outer radius effectively shielding the core from external FUV radiation.

The time-dependent chemical network **ALCHEMIC** (Semenov et al. 2010) runs on top of the physical structure and calculates radial abundance profiles as a function of time. The chemical network includes in total 1 260 species and 38 500 reactions (Gerner et al. 2015) with a sophisticated deuterium network by Albertsson et al. (2013), and both gas-phase reactions, as well as grain surface reactions. The chemical code runs in user-defined time steps and at each time step the radial abundance profiles are converted into beam convolved column densities N_{mod} . With a χ^2 analysis, the modeled and observed column densities are compared considering a factor of ten in the uncertainty of N_{mod} . In the studies by Gerner et al. (2014, 2015) a chemical timescale τ_{chem} was estimated and template abundances were created for each evolutionary stage. A more detailed overview of the model parameters used in this thesis and results from the Gerner et al. (2014, 2015) studies are presented in Table 2.4.

1.4 Radio astronomy

TABLE 1.1: Examples of radio single-dish telescopes and interferometers being currently in operation.

Radio regime	
	Single-dish telescopes
submm	Atacama Pathfinder EXperiment (APEX)
mm	IRAM 30m telescope, James Clerk Maxwell Telescope (JCMT)
cm	Effelsberg 100m telescope, Green Bank Telescope (GBT), Five hundred meter Aperture Spherical Telescope (FAST)
	Interferometers
submm	SubMillimeter Array (SMA)
mm	Atacama Large Millimeter/submillimeter Array (ALMA), NOthern Extended Millimeter Array (NOEMA)
cm	Australia Telescope Compact Array (ATCA), Very Large Array (VLA), MeerKAT (“More” Karoo Array Telescope), Square Kilometre Array (SKA), LOW Frequency ARray (LOFAR)

Since HMSFRs are deeply embedded within their parental molecular cloud with a high extinction in the optical and infrared regime, they are best studied at FIR and radio wavelengths, where the emission is optically thin. The radio window in the electromagnetic spectrum ranges from wavelengths of ≈ 0.3 mm (1 THz) up to ≈ 10 m (30 MHz). At shorter wavelengths, H_2O and O_2 bands in the troposphere of the Earth’s atmosphere absorb incoming radiation, and at larger wavelengths extraterrestrial radio waves are reflected by the ionosphere of the Earth’s atmosphere. However, within the radio window, ground-based observations can be carried out and since the Sun is not radio-bright, observations can in principle be carried out day and night, which is a great advantage compared to optical ground-based telescopes.

The radio window is further divided into submm, mm and cm regimes. At (sub)mm wavelengths, water vapor in the atmosphere can limit observations with radio telescopes, therefore, they are typically located in dry places (with low precipitable water vapor, PWV) and at high altitudes. A list of single-dish telescopes and interferometers currently operating at radio wavelengths is shown in Table 1.1. In this section the background how the incoming radiation of

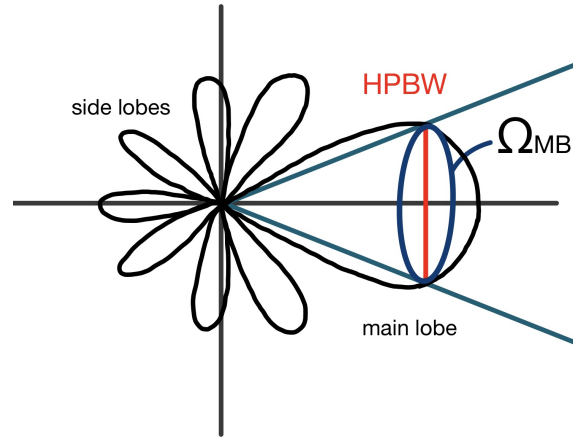


FIGURE 1.3: Antenna radiation pattern. The single-dish beam Ω_{MB} is defined by the half power beam width (HPBW) of the main lobe.

radio sources can be measured is explained using radio telescopes (Sect. 1.4.1) and interferometers (Sect. 1.4.2), while in the next section (Sect. 1.5) the underlying radiative transfer equations are derived.

1.4.1 Single-dish telescopes

Compared to optical telescopes, at (sub)mm wavelengths single-dish telescopes require a large diameter D in order to achieve high angular resolutions, since $\theta_{\text{tel}} \sim \frac{\lambda}{D}$ (Thompson et al. 2001; Wilson et al. 2009). The intensity of astronomical radio sources can be measured at radio telescopes as the incoming electromagnetic radiation induces a voltage U at the antenna that can be measured and processed with receiver instruments. A detailed description of the theoretical and technical background of signal processing can be found, for example, in Thompson et al. (2001) and Wilson et al. (2009).

The beam solid angle Ω_{A} is the normalized power pattern P_{n} integrated over the whole sphere ($4\pi \hat{=} 1$ sr):

$$\Omega_{\text{A}} = \int_0^{2\pi} \int_0^{\pi} P_{\text{n}}(\theta, \phi) \sin(\theta) d\theta d\phi. \quad (1.8)$$

However, a telescope beam is not equally sensitive to all directions of θ and ϕ , but dominated by the power received in the so-called main lobe as sketched in Fig. 1.3. It is therefore convenient to define the main beam solid angle Ω_{MB} as

$$\Omega_{\text{MB}} = \int_{\text{main lobe}} P_{\text{n}}(\theta, \phi) d\Omega_{\text{main lobe}}. \quad (1.9)$$

The main beam efficiency η_{B} , with

$$\eta_{\text{B}} = \frac{\Omega_{\text{MB}}}{\Omega_{\text{A}}} \quad (1.10)$$

is the fraction of the power that is received in the main lobe. The telescope beam size θ_{tel} is typically expressed as the half power beam width (HPBW) of the main lobe (Fig. 1.3). The output of a receiver is the system temperature T_{sys} , that is the sum of the sky T_{sky} , receiver cabin T_{ground} , and receiver T_{rx} contributions:

$$T_{\text{sys}} = T_{\text{sky}} + T_{\text{ground}} + T_{\text{rx}} \quad (1.11)$$

and the system noise σ_{sys} is proportional to the system temperature, integration time t_{int} , and frequency resolution $\delta\nu$,

$$\sigma_{\text{sys}} \sim \frac{T_{\text{sys}}}{\sqrt{\delta\nu t_{\text{int}}}}. \quad (1.12)$$

In order to extract the source signal, one can use the *chopper wheel* method (Penzias & Burrus 1973) to calibrate observations. With this method, a hot load (ambient load at room temperature T_{amb}) and a cold load (toward the sky T_{sky}) measurement are taken before the telescope is pointed at the target source:

$$U_{\text{hot load}} = G(T_{\text{amb}} + T_{\text{rx}}) \quad (1.13)$$

$$U_{\text{cold load}} = G(F_{\text{eff}}T_{\text{sky}} + (1 - F_{\text{eff}})T_{\text{ground}} + T_{\text{rx}}) \quad (1.14)$$

$$= G(F_{\text{eff}}T_{\text{amb}}(1 - e^{-\tau_{\nu}^{\text{atm}}}) + (1 - F_{\text{eff}})T_{\text{amb}} + T_{\text{rx}}), \quad (1.15)$$

with system gain G , forward efficiency F_{eff} , atmospheric absorption τ_{ν}^{atm} and assuming that the temperature T_{amb} is the same in the receiver cabin and in the atmosphere (Downes 1989). Hot and cold load measurements are carried out every time before the source is observed due to fast changes in the atmosphere at (sub)mm wavelengths. The difference between the hot and cold load, U_{cal} , is

$$U_{\text{cal}} = U_{\text{hot load}} - U_{\text{cold load}} = GF_{\text{eff}}T_{\text{amb}}e^{-\tau_{\nu}^{\text{atm}}}. \quad (1.16)$$

The source signal is

$$U_{\text{source}} = GT'_{\text{A}}e^{-\tau_{\nu}^{\text{atm}}}, \quad (1.17)$$

and in terms of T'_{A} , that is the source antenna temperature outside of Earth's atmosphere,

$$T'_{\text{A}} = \frac{U_{\text{source}}}{U_{\text{cal}}}F_{\text{eff}}T_{\text{amb}}. \quad (1.18)$$

The corrected antenna temperature T_{A}^* is defined as

$$T_{\text{A}}^* = \frac{T'_{\text{A}}}{F_{\text{eff}}} = \frac{U_{\text{source}}}{U_{\text{cal}}}T_{\text{amb}}, \quad (1.19)$$

and the main beam temperature T_{MB} is defined as

$$T_{\text{MB}} = \frac{F_{\text{eff}}}{B_{\text{eff}}}T_{\text{A}}^* = \frac{T_{\text{A}}^*}{\eta_{\text{MB}}}, \quad (1.20)$$

with beam efficiency B_{eff} that takes into account the finite size of the source. Typical values for the IRAM 30m telescope at 230 GHz are $\theta_{\text{tel}}=10.''5$, $F_{\text{eff}}=0.92$, and $B_{\text{eff}}=0.59$ ¹.

1.4.2 Interferometry

At radio wavelengths, single-dish telescopes do not provide sufficient angular resolution to resolve core scales (<0.1 pc) in HMSFRs which are typically located at distances >1 kpc. Thus, radio interferometry has been used for decades now to study star-forming regions at high angular resolutions. Currently, the most powerful interferometers are the SMA, ALMA, NOEMA, VLA, ATCA, and MeerKAT (Table 1.1).

In the following, for simplicity, the concept of an interferometer is explained based on an interferometer consisting of two antennas. However, in reality, modern interferometers consist

¹<https://publicwiki.iram.es/Iram30mEfficiencies>

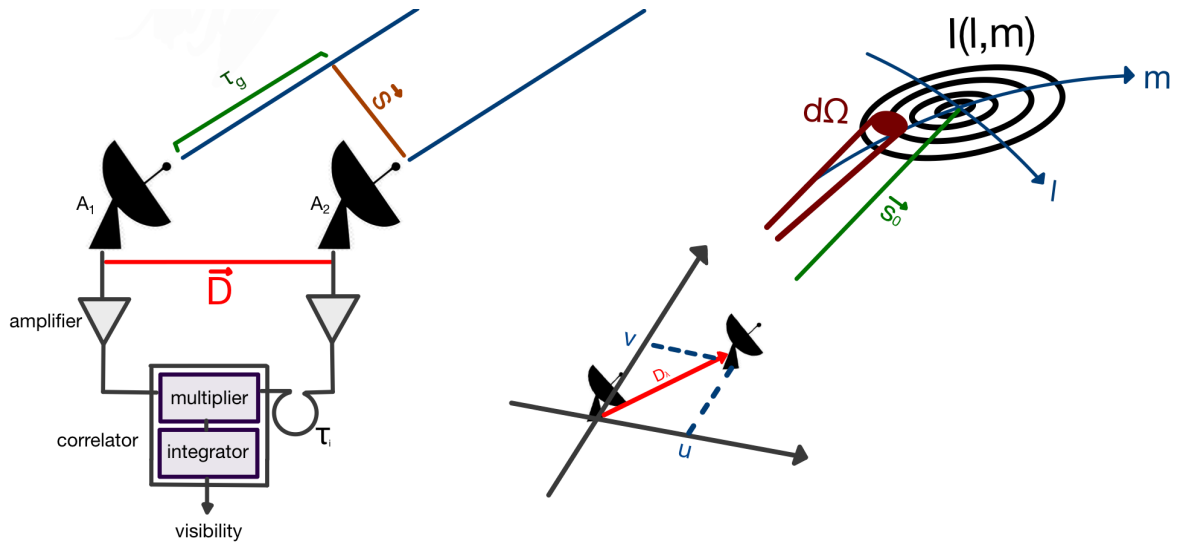


FIGURE 1.4: Principle of a two antenna interferometer. The *left panel* shows two antennas, A_1 and A_2 , with separation \vec{D} . The incoming radiation is combined in the correlator producing the measured visibility. The *right panel* shows the coordinate system of the antenna baselines (u, v) and the sky coordinates (l, m) of a source with intensity distribution $I(l, m)$. The interferometer covers an area $d\Omega$ of the source. The phase center \vec{s}_0 is set such that the phase is zero at the center of the source.

of a large number of antennas (e.g., 8 in the SMA, 12 in NOEMA, 66 in ALMA). The basic concept of interferometry is that two telescopes with diameter d and separation $D \gg d$ can act as a single-dish telescope with angular resolution, $\theta_{\text{tel}} \sim \frac{\lambda}{D}$ (Thompson et al. 2001; Wilson et al. 2009).

In Fig. 1.4 an interferometer consisting of two antennas, A_1 and A_2 , and separation \vec{D} is sketched. The electromagnetic field E at frequency ν of a radio source produces the following voltages as function of time t at the antennas

$$U_1 \sim E e^{2\pi i \nu t} \quad (1.21)$$

$$U_2 \sim E e^{2\pi i \nu (t - \tau_g)}, \quad (1.22)$$

with the geometric delay $\tau_g = \frac{\vec{D} \cdot \vec{s}}{c}$ (left panel in Fig. 1.4). The signals are combined in the correlator, where the signals are multiplied and integrated, resulting in the correlation (or response) function R :

$$R(\tau_g) \sim \frac{1}{2T} \int_{-T}^T U_1 U_2 dt \sim \frac{E^2}{2T} \int_{-T}^T e^{2\pi i \nu t} e^{2\pi i \nu (t - \tau_g)} dt. \quad (1.23)$$

Since the geometric delay τ_g varies as the Earth rotates, the correlation function $R(\tau_g)$ measures the interferences fringes as a function of time. The image center of the source can be set such that the phase is zero at the phase reference position \vec{s}_0 (right panel in Fig. 1.4),

$$\vec{s} = \vec{s}_0 + \vec{\sigma} \quad (1.24)$$

A source with intensity distribution I_ν (Sect. 1.5) produces the power P at the antenna at bandwidth $\Delta\nu$ and beam solid angle $d\Omega$,

$$P = \frac{1}{2} \Delta\nu \int_{\Omega} A(\vec{\sigma}) I_\nu(\vec{\sigma}) d\Omega, \quad (1.25)$$

with antenna reception pattern $A(\vec{\sigma})$ that is the effective collecting area. The total delay is the

difference between the geometric and instrumental delay $\tau = \tau_g - \tau_i$ (Fig. 1.4). The total response function as a function of baseline measured in wavelengths, $\vec{D}_\lambda = \frac{\vec{D}}{\lambda}$, is

$$R(\vec{s}_0, \vec{D}_\lambda) = \Delta\nu \int_{\Omega} A(\vec{\sigma}) I_\nu(\vec{\sigma}) \cos[2\pi \vec{D}_\lambda \cdot (\vec{s}_0 + \vec{\sigma})] d\Omega, \quad (1.26)$$

and the complex visibility with amplitude $|V|$ and phase ϕ_V is defined as,

$$V = |V|e^{i\phi_V} = \int_{\Omega} A_N(\vec{\sigma}) I_\nu(\vec{\sigma}) e^{-2\pi i \vec{D}_\lambda \cdot \vec{\sigma}} d\Omega, \quad (1.27)$$

with normalized antenna reception pattern $A_N(\vec{\sigma}) = \frac{A(\vec{\sigma})}{A(\vec{s}_0)}$. The correlator output is

$$R(\vec{s}_0, \vec{D}_\lambda) = A_0 \Delta\nu |V| \cos(2\pi \vec{D}_\lambda \cdot \vec{s}_0 - \phi_V). \quad (1.28)$$

The cross-correlation (denoted by a \star) of the visibilities V_1 and V_2 measured at the two antennas corresponds to

$$r(\tau) = V_1(t) \star V_2(t) = \lim_{T \rightarrow \infty} \frac{1}{2T} \int_{-T}^T V_1(t) V_2^*(t - \tau) dt. \quad (1.29)$$

Instead of the Cartesian coordinate system, the coordinates are expressed in the (u, v, w) plane (u and v directed into the East and North, respectively), which is a projection onto the celestial hemisphere with coordinates l and m (right panel in Fig. 1.4):

$$\vec{D}_\lambda \cdot \vec{s}_0 = w \quad (1.30)$$

$$\vec{D}_\lambda \cdot \vec{s} = ul + vm + w \sqrt{1 - l^2 - m^2} \quad (1.31)$$

$$d\Omega = \frac{dldm}{\sqrt{1 - l^2 - m^2}}. \quad (1.32)$$

With $w \approx 0$, the visibility $V(u, v)$ and intensity $I(l, m)$ are related by a Fourier transformation:

$$V(u, v) = \int \int \frac{A_N(l, m) I(l, m)}{\sqrt{1 - l^2 - m^2}} e^{-2\pi i (ul + vm)} dldm \quad (1.33)$$

$$I(l, m) = \frac{\sqrt{1 - l^2 - m^2}}{A_N(l, m)} \int \int V(u, v) e^{2\pi i (ul + vm)} dudv \quad (1.34)$$

The combination of the electromagnetic fields at various antennas must be executed coherently, and for this heterodyne receivers are used: a local oscillator is needed for the down conversion of the signal as sketched in Fig. 1.5. The sky frequency ν_{sky} is shifted to a lower frequency, the intermediate frequency ν_{IF} , which allows the system to better transmit the measurements preserving the phase. Using aperture synthesis, the underlying intensity distribution $I(l, m)$ is derived from the measured visibilities $V(u, v)$ by a Fourier transform (Eq. 1.34).

Before the intensity distribution can be constructed from the interferometric observations, the measured visibilities \widetilde{V} have to be calibrated first. The true visibility of a baseline connecting antenna i and j , V_{ij} , is

$$\widetilde{V}_{ij}(t) = g_i(t) g_j^*(t) V_{ij} + \epsilon_{ij}(t) \quad (1.35)$$

with complex antenna gain $g_i = a_i e^{i\phi_i}$ and noise term ϵ_{ij} . The bandpass of the receiver, that is the spectral response, is corrected by observing a bright quasar, typically in the beginning of

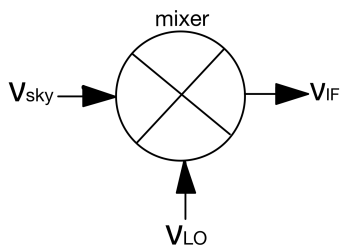


FIGURE 1.5: Principle of a mixer and local oscillator that is used to convert the sky frequency ν_{sky} down to the intermediate frequency ν_{IF} using the local oscillator frequency ν_{LO} .

the observations. The phase and amplitude are corrected using calibrator sources (bright unresolved quasars with known position) that should be close to the target source and are frequently observed (typically every few minutes at mm wavelengths) in order to correct for rapid changes in the atmosphere. The absolute flux calibration is achieved with bright stars that have known fluxes due to frequent monitoring and whose time variations can be modeled. For example, MWC 349 and LkH α 101 are commonly used as flux calibrators for NOEMA observations.

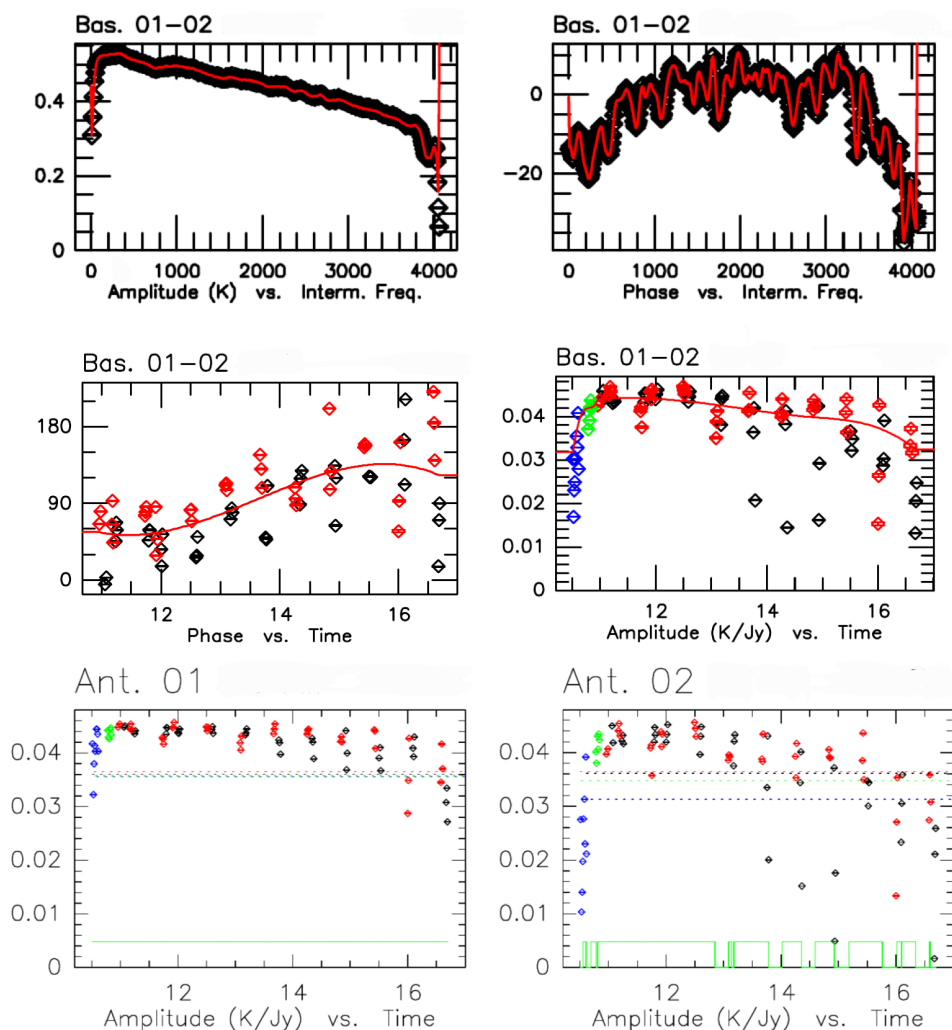


FIGURE 1.6: NOEMA calibration of the receiver bandpass (*top panels*), amplitude and phase (*middle panels*), and flux calibration (*bottom panels*). The calibrators are 3C84 (bandpass), 2146+608 and J0011+707 (phase and amplitude), and MWC349 (flux). These NOEMA observations are part of the CORE+ program (Sect. 5.2).

As an example, the calibration steps are presented in Fig. 1.6 for a NOEMA track of antenna 1 and 2 (and corresponding baseline 01-02) of the CORE+ observing program (Sect. 5.2). In reality, the calibration is carried out for 11 antennas and a total of 55 baselines. The calibrator sources are 3C84 (bandpass), 2146+608 and J0011+707 (phase and amplitude), and MWC349 (flux). As a function of time, the amplitude and phases change significantly. It can be seen in Fig. 1.6 that at the end of the track the weather conditions worsened causing a decrease of the amplitudes and an increase of the scatter in the flux calibration.

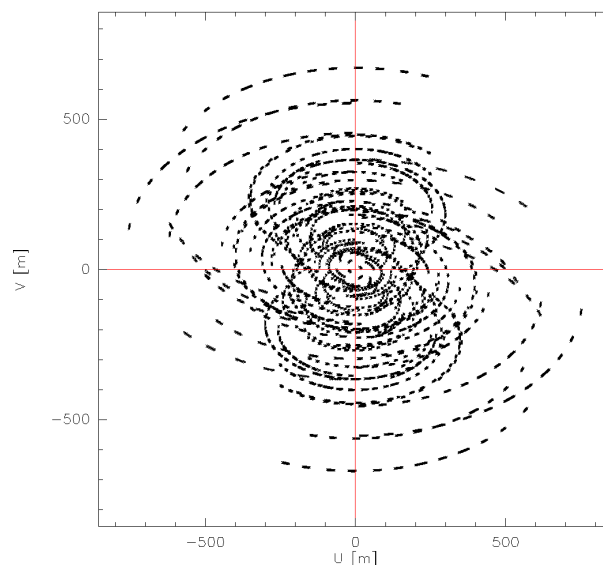


FIGURE 1.7: Example of a NOEMA uv coverage. The longest baseline is ≈ 800 m. The minimum spacing of two antennas is limited by their diameters and thus, there are no uv points in the center.

To construct the intensity distribution $I(l,m)$ of a source, the calibrated visibilities $V(u,v)$ are Fourier transformed according to Eq. (1.34). Since the uv plane is not fully sampled (an example uv coverage of NOEMA is shown in Fig. 1.7), the empty uv points have to be filled, that is carried out using aperture synthesis. In radio astronomy, the CLEAN algorithm “Högbom” developed by Högbom (1974) is the most commonly applied method. It is therefore said that, when deconvolving the visibilities to the image plane, the data are “CLEANed”.

First, the “dirty” image is constructed by convolving the visibilities with the synthesized beam (point spread function). The visibilities are typically weighted by their noise, $w \sim \frac{1}{\sigma^2}$. With natural weighting, all visibilities have the same weight resulting in a relatively large synthesized beam. With robust (or Briggs) weighting (Briggs 1995), the S/N of individual visibilities are considered that enables higher weightings of the longer baselines, resulting in a smaller synthesized beam and therefore a higher angular resolution.

The CLEAN algorithm assumes that the measured visibilities are caused by a number of point sources and searches for the peak intensity in the “dirty” image that is then subtracted leaving a residual image. In a next iteration, the residual image is again examined for the highest intensity. The iterations proceed until a user-defined stopping criterion. This can be the number of iterations, an absolute intensity threshold (e.g., three times the expected noise), or a fractional intensity threshold (e.g., 1% of the peak intensity).

Several improvements of the CLEAN algorithm exist. The Clark algorithm was developed to increase the speed of CLEANing large images (Clark 1980). For sources with extended emission, the CLEAN algorithm causes artifacts that can be improved using the SDI (Steer, Dewdney, Ito) algorithm (Steer et al. 1984).

The point-source sensitivity of interferometric observations (in comparison to a single-dish telescope, Eq. 1.12) is

$$\sigma_{\text{sys}} = \frac{JT_{\text{sys}}}{\eta_{\text{atm}} \sqrt{N_{\text{ant}}(N_{\text{ant}} - 1)} \delta_{\nu} t_{\text{int}}}, \quad (1.36)$$

with antenna efficiency J in Jy K^{-1} , atmospheric phase noise η_{atm} , and number of antennas N_{ant} .

Since atmospheric conditions at mm wavelengths are not ideal and can cause a high phase noise that can not be corrected by the phase calibrators alone, the self-calibration method can be applied that uses the target source itself as a calibrator. Self-calibration can be implemented for both phase and amplitude, and in the following, the focus is on phase self-calibration that is applied in this thesis for NOEMA (Sect. 2.2.4) and ALMA observations (Sect. 4.3.1). Self-calibration is possible since the number of baselines, $N_{\text{base}} = \frac{(N_{\text{ant}}-1)N_{\text{ant}}}{2}$, is larger than the number of antennas, but for the phase calibration only $N_{\text{ant}} - 1$ measurements are required. The complex gains of the antennas (Eq. 1.35) can be improved with self-calibration when the signal-to-noise ratio, S/N , is high (typically >15).

In a first step, a model of the source has to be constructed by a shallow CLEAN of the data, that contains enough iterations to cover the source structure, but is shallow enough that noise artifacts are not included in the model. Otherwise, self-calibration can cause an enhancement of noise artifacts resulting in artificial sources. The observed visibilities are divided by the model visibilities according to Eq. (1.35) in order to compute the antenna gains. In order to increase the S/N , the model visibilities can be time-averaged. The observed visibilities are then corrected by the new antenna gains. This process can then be iterated with a more complex source structure and decreasing time average, until in principle the thermal noise threshold is reached.

1.5 Radiative transfer

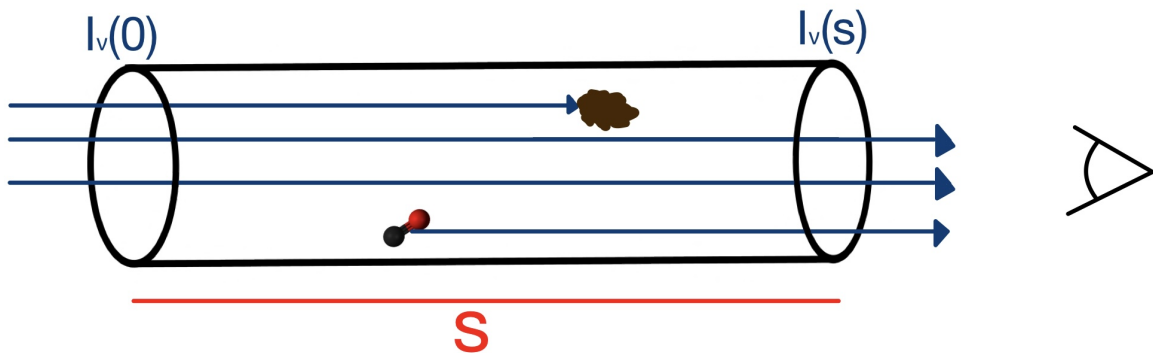


FIGURE 1.8: Sketch of radiative transfer through a medium with length s . The incoming intensity I is partially absorbed by a dust particle. In addition, molecular line radiation is emitted.

In radio astronomical observations, the (specific) intensity² I_{ν} is measured - the power per area, frequency, and solid angle - that is independent of the source distance d and has units of

²In other physics fields the specific intensity corresponds to the specific radiance.

$\text{W m}^{-2} \text{Hz}^{-1} \text{sr}^{-1}$. The flux density F_ν is the intensity integrated over the source solid angle Ω_S ,

$$F_\nu = \int_{\Omega_S} I_\nu d\Omega_S, \quad (1.37)$$

measured in units of $\text{W m}^{-2} \text{Hz}^{-1}$. Since the flux densities are very low toward astronomical radio sources, the unit Jansky (Jy) is used, with 1 Jy corresponding to $10^{-26} \text{W m}^{-2} \text{Hz}^{-1}$. In mm interferometry, the common unit of the intensity I_ν is not Jy sr^{-1} , but Jy beam^{-1} . The conversion between steradian (sr) and arcsecond (") is $1 \text{sr} = 1 \text{rad}^2 = \left(\frac{360^\circ}{2\pi}\right)^2 = \left(\frac{360 \times (60 \times 60)''}{2\pi}\right)^2 = (206265'')^2$. For example, a synthesized beam with major and minor axis $\theta_{\text{maj}} \times \theta_{\text{min}}$ of $5'' \times 3''$ covers an area of $3.5 \times 10^{-10} \text{sr beam}^{-1}$.

As radiation of a source moves through a medium along the line of sight s (Fig. 1.8), absorption and emission processes can take place that are described by the equation of radiative transfer,

$$\frac{dI_\nu}{ds} = -\kappa_\nu I_\nu + \epsilon_\nu, \quad (1.38)$$

with the frequency-dependent absorption and emission coefficients κ_ν and ϵ_ν , respectively. The optical depth τ_ν describes the attenuation along the line of sight s ,

$$d\tau_\nu = -\kappa_\nu ds, \quad (1.39)$$

and the source function S_ν is defined as

$$S_\nu = \frac{\epsilon_\nu}{\kappa_\nu}. \quad (1.40)$$

Using Eq. (1.39) and Eq. (1.40), the radiative transfer equation (Eq. 1.38) can be written as

$$\frac{dI_\nu}{d\tau} = I_\nu + S_\nu \quad (1.41)$$

In thermodynamic equilibrium the intensity of an ideal black body ($\frac{dI_\nu}{ds} = 0$) with temperature T is given by Planck's law,

$$I_\nu = B_\nu(T) = \frac{\epsilon_\nu}{\kappa_\nu} = \frac{2h\nu^3}{c^2} \frac{1}{\exp\left(\frac{h\nu}{k_B T}\right) - 1}. \quad (1.42)$$

At radio frequencies, $h\nu \ll k_B T$ holds, so the Planck function B_ν (Eq. 1.42) can be approximated by

$$B_\nu(T) \simeq \frac{2\nu^2}{c^2} k_B T \quad (\text{if } h\nu \ll k_B T), \quad (1.43)$$

which is the Rayleigh-Jeans law. The brightness temperature T_B is defined from Eq. (1.43),

$$T_B = \frac{c^2}{2k_B \nu^2} I_\nu, \quad (1.44)$$

corresponding to the thermodynamic temperature T , if the radio source can be approximated by a black body and $h\nu \ll k_B T$ holds. For example, the brightness temperature of the CMB (Fig. 1.9) with $T_{\text{CMB}} = 2.73 \text{K}$ (e.g., de Bernardis et al. 2000) is

$$T_B^{\text{CMB}} = T_B(T_{\text{CMB}}, \nu) = \frac{c^2}{2k_B \nu^2} B_\nu(T_{\text{CMB}}). \quad (1.45)$$

In the following, the basic equations are derived and how continuum and line radiation can be used to determine physical parameters such as mass M , temperature T , or molecular column density N .

1.5.1 Continuum emission

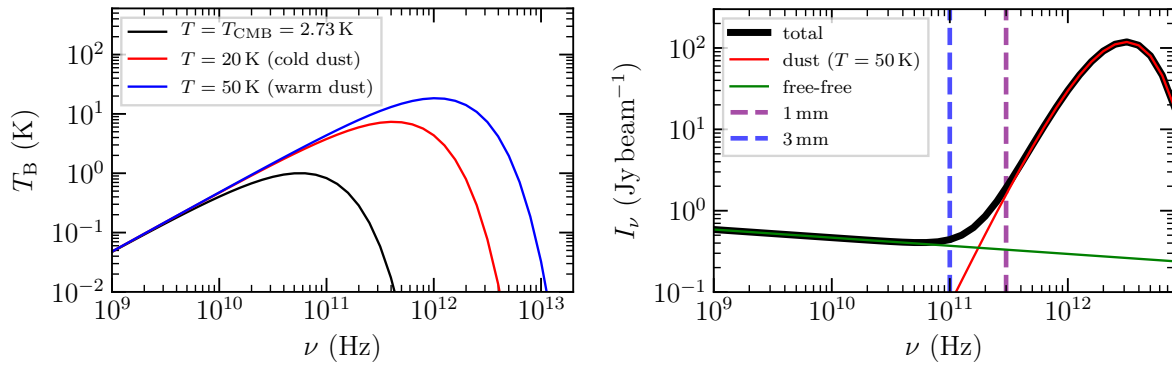


FIGURE 1.9: Spectral energy distribution of black body and free-free components. The *left panel* shows the spectral energy distribution of a black body in units of brightness temperature (Eq. 1.42) of the CMB (black, $T = 2.73$ K), and cold (red, $T = 20$ K) and warm (blue, $T = 50$ K) dust. The *right panel* shows the total spectral energy distribution (black) of a combination of a warm dust (red, $T = 50$ K, Eq. 1.42) and an optically thin free-free component (green, Eq. 1.50) for a $1.''5 \times 1.''5$ beam. The blue and purple dashed vertical lines indicate a wavelength of 3 mm and 1 mm, respectively.

Toward HMSFRs, there are two major continuum sources in the mm regime (Fig. 1.9). The first and dominant continuum contribution is the thermal emission of dust. Secondly, in regions containing evolved protostars (e.g., HMCs and UCHII regions, Sect. 1.2) there can be a significant contribution of free-free emission from scattered electrons.

Dust emission

At mm wavelengths, cold dust emission dominates the spectral energy distribution (SED) of the cold ISM. The dust emission can be approximated by a black body (Eq. 1.42) with dust temperature T and assuming a homogeneous medium with constant source function S_ν the radiative transfer equation (Eq. 1.41) is solved by

$$I_\nu = B_\nu(T)(1 - e^{-\tau_\nu^{\text{cont}}}). \quad (1.46)$$

The continuum optical depth τ_ν^{cont} can be estimated by rearranging Eq. (1.46),

$$\tau_\nu^{\text{cont}} = -\ln\left(1 - \frac{I_\nu}{B_\nu(T)}\right). \quad (1.47)$$

Following the calculations by Hildebrand (1983), in the optical thin limit ($\tau_\nu^{\text{cont}} \ll 1$), the measured intensity I_ν and flux density F_ν (Eq. 1.37) of dust continuum emission can be used to derive the molecular hydrogen column density $N(\text{H}_2)$,

$$N(\text{H}_2) = \int n(\text{H}_2) ds = \frac{I_\nu \eta}{\mu m_{\text{H}} \Omega_{\text{A}} \kappa_\nu B_\nu(T)}, \quad (1.48)$$

and mass M

$$M = \frac{F_\nu \eta d^2}{\kappa_\nu B_\nu(T)}, \quad (1.49)$$

with H_2 number density $n(\text{H}_2)$, gas-to-dust mass ratio η , mean molecular weight μ , hydrogen mass m_{H} , beam solid angle Ω_{A} assuming a Gaussian telescope beam θ_{tel} , dust absorption coefficient κ_ν , and distance d . Typical values toward HMSFRs are $\eta = 150$ (Draine 2011; Giannetti et al. 2017), $\mu = 2.8$ (Kauffmann et al. 2008), and $\kappa_\nu = 0.9 \text{ g cm}^{-2}$ at 1.3 mm (Ossenkopf & Henning 1994).

Free-free emission

Protostellar radiation can be high enough to ionize the surrounding material, with ionized hydrogen, denoted as HII , present. This can be observed by hydrogen recombination lines, as well as free-free emission that is strong in the cm regime. For example, UCHII regions are studied best at radio wavelengths through their strong free-free emission (e.g., Churchwell 2002). The free-free flux density F_{ff} at high frequencies (right panel in Fig. 1.9) is described by

$$\frac{F_{\text{ff},\nu_1}}{F_{\text{ff},\nu_2}} = \left(\frac{\nu_1}{\nu_2}\right)^{-0.1}, \quad (1.50)$$

with $\nu_1 > \nu_2$ (Condon & Ransom 2016).

For sources that have a non-negligible free-free contribution at mm wavelengths at frequency ν_1 , the free-free flux density has to be subtracted from the measured mm flux density when estimating the molecular hydrogen column density and mass according to Eqs. (1.48) and (1.49), respectively. This can be done, for example, by extrapolating the measured cm emission at frequency ν_2 to mm wavelengths according to Eq. (1.50),

$$F_{\text{dust},\nu_1} = F_{\nu_1} - F_{\text{ff},\nu_1} = F_{\nu_1} - F_{\text{ff},\nu_2} \left(\frac{\nu_1}{\nu_2}\right)^{-0.1}. \quad (1.51)$$

1.5.2 Spectral line emission

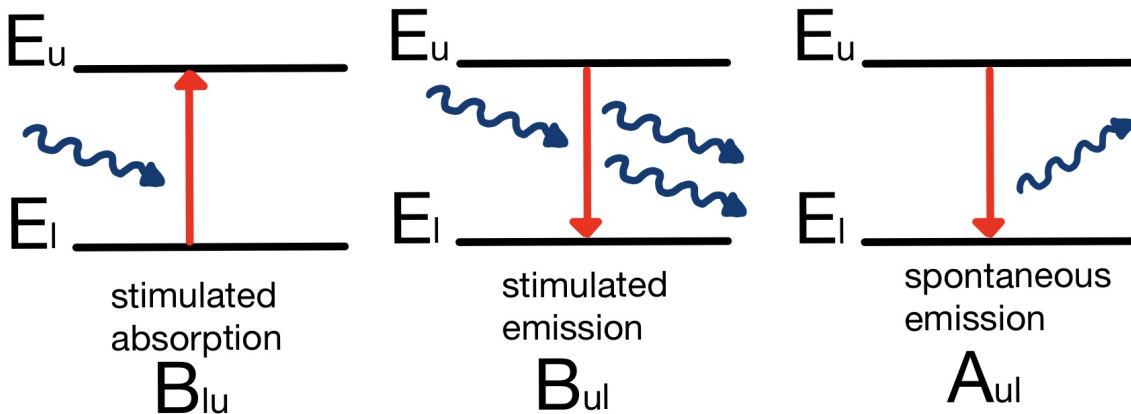


FIGURE 1.10: Emission and absorption processes in atoms and molecules.

In atoms and molecules, emission and absorption processes, considering a lower and upper state l and u , respectively, are described by Einstein coefficients B_{lu} , B_{ul} , and A_{ul} (Fig. 1.10):

a change of state can occur due to stimulated absorption B_{lu} and emission B_{ul} , and due to spontaneous emission A_{ul} , given by

$$A_{ul} = \frac{2h\nu_{ul}^3}{c^2} B_{ul} \quad (1.52)$$

$$B_{ul} = \frac{g_l}{g_u} B_{lu}. \quad (1.53)$$

A photon can only be emitted or absorbed at the corresponding frequency of the energy difference E_{ul} between the two states,

$$E_{ul} = E_u - E_l = h\nu_{ul}. \quad (1.54)$$

The emission and absorption coefficients required to solve the radiative transfer equation (Eq. 1.38) are defined as

$$\epsilon_\nu = \frac{h\nu}{4\pi} n_u A_{ul} \quad (1.55)$$

$$\kappa_\nu = \frac{h\nu}{4\pi} (n_l B_{lu} - n_u B_{ul}) \quad (1.56)$$

Depending on the energy E_{ul} of an incoming photon, a molecule can be electronically, vibrationally, or rotationally excited. Typically, electronic transitions occur at optical, vibrational levels in the IR, and rotational levels can be observed at radio wavelengths. Since HMSFRs are embedded in dense molecular clouds, predominantly vibrational and rotational levels are observed in the FIR and mm regime.

Rotational levels

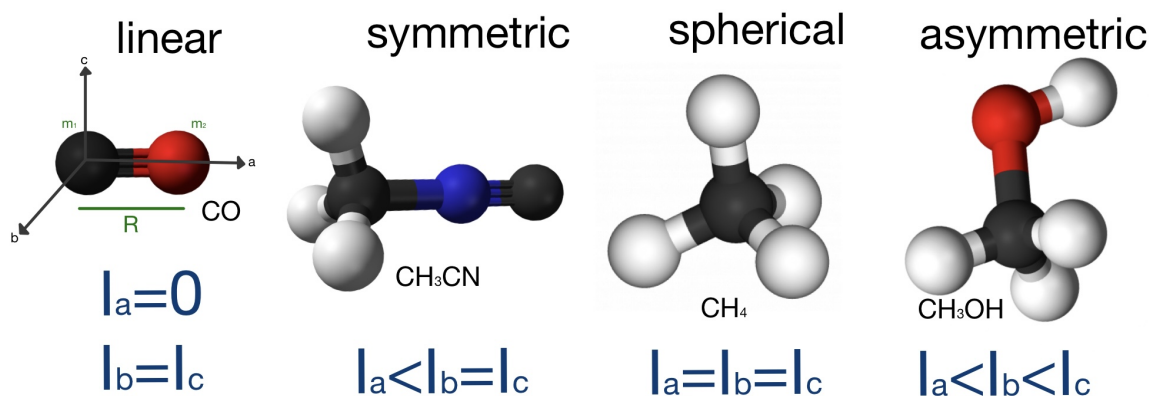


FIGURE 1.11: Molecule types and moment of inertia axes depending on the symmetry.

Under the assumption that molecules are rigid rotators, the moment of inertia I can be described by three principal axes, I_a , I_b , and I_c , with the convention that $I_c \geq I_b \geq I_a$ (left panel in Fig. 1.11). The moment of inertia is calculated by

$$I = \sum_i m_i x_i^2. \quad (1.57)$$

For example, a diatomic molecule with masses m_1 and m_2 and separation R , the moment of inertia is $I_c = I_b = I = m_{\text{eff}} R^2$ with reduced mass $m_{\text{eff}} = \frac{m_1 m_2}{m_1 + m_2}$ (left panel in Fig. 1.11).

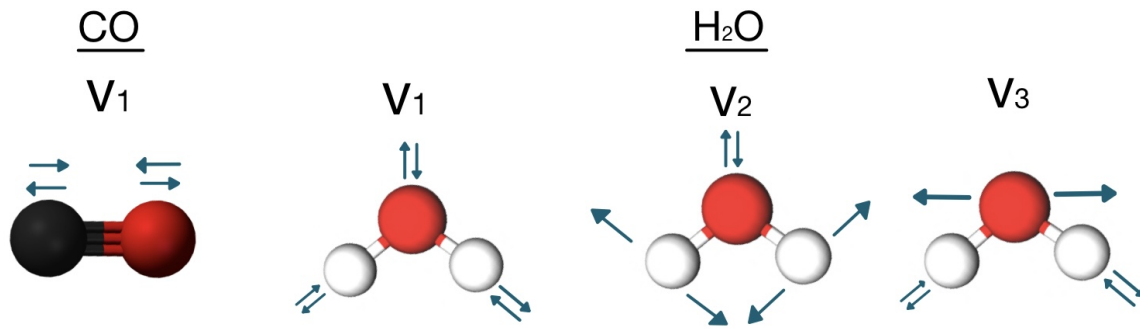


FIGURE 1.12: Vibrational modes of carbon monoxide and water.

Depending on the geometry of a molecule, different types exist as sketched in Fig. 1.11:

- linear molecule: $I_c = I_b, I_a = 0$ (e.g., CO, OCS)
- symmetric molecule: $I_c = I_b, I_a \neq 0$ (e.g., NH₃, CH₃CN)
- spherical molecule: $I_c = I_b = I_a$ (e.g., CH₄)
- asymmetric molecule: $I_c \neq I_b \neq I_a$ (e.g., H₂CO, CH₃OH)

The discrete rotational energy levels of linear ($I = I_c = I_b$) and spherical ($I = I_c = I_b = I_a$) molecules are described by the total angular momentum quantum number J ($J = 0, 1, 2, \dots$):

$$E_{\text{rot}}(J) = \frac{\hbar^2}{2I} J(J+1) = hBJ(J+1) \quad (\text{linear and spherical molecules}) \quad (1.58)$$

with rotational constant $B = \frac{\hbar}{4\pi I}$. For symmetric molecules, the rotational levels depend on the J and K quantum numbers ($J = 0, 1, 2, \dots$ and $K = 0, \pm 1, \dots, \pm J$):

$$E_{\text{rot}}(J, K) = hBJ(J+1) - (A - B)K^2 \quad (\text{symmetric molecules}) \quad (1.59)$$

with rotational constants $B = \frac{\hbar}{4\pi I_b}$ and $A = \frac{\hbar}{4\pi I_a}$. At $K \approx J$ the molecule rotates around the molecular axis, while at $K = 0$ the molecule rotates perpendicular to the molecular axis. For asymmetric molecules, three quantum numbers are required in order to calculate the rotational energy levels, given by J , K_a , and K_b . K_a and K_b is the projected angular momentum to the a and b axis, respectively (Fig. 1.11). Transitions of molecules are therefore given by, for example, CO $J^u - J^l = 2 - 1$, CH₃CN $(J_K)^u - (J_K)^l = 12_1 - 11_1$, and H₂CO $(J_{K_a, K_a})^u - (J_{K_a, K_a})^l = 3_{0,3} - 2_{0,2}$.

Vibrational levels

In molecules, groups or atoms can move or “vibrate” with respect to the remaining parts. The vibrational energy levels of a molecule can be approximated by a harmonic oscillator with quantum number v ($v = 1, 2, \dots$):

$$E_{\text{vib}}(v) = \left(v + \frac{1}{2}\right) \hbar\omega, \quad (1.60)$$

with $\omega = \sqrt{\frac{k_f}{m_{\text{eff}}}}$ (with force constant k_f and reduced mass m_{eff}). The larger a molecule, the more vibrational modes exist. For example, a diatomic molecule (e.g., CO) has one mode of

vibration and triatomic molecules such as water have three vibrational modes as sketched in Fig. 1.12.

For linear molecules, such as HC₃N, the transitions of a vibrational mode can further split up depending on the parity of the wave function (Herzberg 1942). The levels of this l -type doubling are referred to as e and f levels (Bizzocchi et al. 2017). For example, the $J = 24 - 23$ transition of the C-CN bending mode $\nu_7 = 1$ of HC₃N splits up to a $l = 1e$ and $l = 1f$ level.

Nuclear spin

All symmetric molecules with a non-zero proton nuclear spin S , have different isomers, for example, for H₂ and H₂CO, there exists an ortho (parallel spin) and para (antiparallel spin) isomer: o-H₂/p-H₂ and o-H₂CO/p-H₂CO. For CH₃OH different isomers depending on the proton spin states of the three hydrogen atoms in the methyl (CH₃) group are denoted as A (parallel spin) or E (anti-parallel spin).

Torsion

Molecules can have internal rotation of functional groups rotating within the molecule. For example, in CH₃OH, the CH₃ group can rotate with respect to the OH-group. This is called torsion or internal rotation. These transitions are labeled as ν_t .

Spectral line modeling with XCLASS

Molecular line emission of the rotational and vibrational states can be used to quantify the molecular content and trace the underlying physical conditions, such as the temperature, in the ISM. In order to model the spectral line emission, one has to not only consider the theoretical background of line emission explained in this section, but also the observations have to be taken into account (e.g., the telescope beam).

In this thesis, spectral line emission is modeled using the eXtended CASA Line Analysis Software Suite (XCLASS, Möller et al. 2017)³ solving the one-dimensional (1D) radiative transfer equation for an isothermal source under local thermal equilibrium (LTE) conditions, meaning that all transitions of one species are described by the same excitation temperature T_{ex} (also referred to as T_{rot} when rotational transitions are considered).

The solution of the radiative transfer equation $T_{\text{B}}(\nu)$ is derived for a molecule with one emission component. Since in this thesis, continuum and spectral line data products are analyzed separately, any continuum contributions (e.g., dust) are neglected in the following derivations. The population levels of a species in the lower and upper states are given by the Boltzmann distribution,

$$\frac{n_u}{n_l} = \frac{g_u}{g_l} \exp\left(-\frac{E_u - E_l}{k_{\text{B}} T_{\text{ex}}}\right), \quad (1.61)$$

where g_l and g_u are degeneracy factors. An energy level is degenerate when multiple states share the same energy level, for rotational levels $g_J = 2J + 1$ and for vibrational levels $g_v = 1$. The column density of a molecule in the upper level u is given by

$$N_u = \int n_u ds. \quad (1.62)$$

³<https://xclass.astro.uni-koeln.de/>

The partition function Q describes the statistical properties in thermodynamic equilibrium as a function of T_{ex} summed over all states i ,

$$Q(T_{\text{ex}}) = \sum_{i=0}^{\text{inf}} g_i e^{\frac{E_i}{k_{\text{B}} T_{\text{ex}}}}. \quad (1.63)$$

Combining Eqs. (1.61), (1.62), and (1.63), the total column density N is the sum of the column density in all states,

$$N = \sum_{i=0}^{\text{inf}} N_i = \frac{N_{\text{u}}}{g_{\text{u}}} e^{\frac{E_{\text{u}}}{k_{\text{B}} T_{\text{ex}}}} Q(T_{\text{ex}}). \quad (1.64)$$

In LTE conditions and neglecting any background contribution (e.g., from the CMB) and assuming a constant source function along the line of sight, the solution to the radiative transfer equation (Eq. 1.38) is

$$I_{\nu} = S_{\nu} (1 - e^{-\tau_{\nu}^{\text{line}}}), \quad (1.65)$$

Under real observation conditions, the emission component might stem from a smaller area than the telescope beam. The measured intensity in Eq. (1.65) is therefore corrected by the beam filling factor η_{fill} :

$$I_{\nu} = \eta_{\text{fill}} S_{\nu} (1 - e^{-\tau_{\nu}^{\text{line}}}). \quad (1.66)$$

The beam filling factor η_{fill} for a Gaussian emission profile of a source θ_{source} and a Gaussian telescope beam θ_{tel} is

$$\eta_{\text{fill}} = \frac{\theta_{\text{source}}^2}{\theta_{\text{source}}^2 + \theta_{\text{tel}}^2}. \quad (1.67)$$

A detailed derivation of Eq. (1.67) can be found in Appendix B.2 in Möller et al. (2017). For astronomical sources, the beam filling factor is usually not known. However, it can be estimated based on the typical scales of the source, for example, COM emission of a compact HMC is not resolved in single-dish observations ($\eta_{\text{fill}} < 1$), but might be resolved with interferometers ($\eta_{\text{fill}} \approx 1$). For each transition t of a molecule, a Gaussian line profile $\phi^t(\nu)$ is described by

$$\phi^t(\nu) = \frac{1}{\sqrt{2\pi}\sigma^t} e^{-\frac{[\nu - (\nu^t + \Delta\nu_{\text{off}}^t)]^2}{2(\sigma^t)^2}}, \quad (1.68)$$

with standard deviation σ^t and transition frequency $\nu^t = \nu_{\text{ul}}$ (Eq. 1.54). $\Delta\nu_{\text{off}}^t$ is the frequency offset from the rest-frequency of the transition, taking into account that the molecular line emission stems from the source velocity, and is calculated considering v_{LSR} and any additional molecule-specific velocity offset v_{off} ,

$$\Delta\nu_{\text{off}}^t = \frac{v_{\text{off}} + v_{\text{LSR}}}{c} \nu^t. \quad (1.69)$$

The standard deviation σ^t is related to the line full width half maximum (FWHM), $\Delta\nu$, by

$$\sigma^t = \frac{\Delta\nu}{2\sqrt{2\ln(2)}} \frac{\nu^t + \Delta\nu_{\text{off}}^t}{c}. \quad (1.70)$$

Taking Eqs. (1.68) and (1.64) into account (a detailed derivation is given in Appendix B.3 in Möller et al. 2017), the line optical depth τ_ν^{line} considering all transitions t is given by

$$\tau_\nu^{\text{line}} = \sum_t \frac{c^2}{8\pi\nu^2} A_{\text{ul}}^t N \frac{g_{\text{u}}^t e^{-\frac{E_1^t}{k_{\text{B}} T_{\text{ex}}}}}{Q(T_{\text{ex}})} \left(1 - e^{-\frac{h\nu^t}{k_{\text{B}} T_{\text{ex}}}}\right) \phi^t(\nu) \quad (1.71)$$

With the source function in the form

$$S_\nu = T_{\text{B}}(T_{\text{ex}}, \nu) = \frac{c^2}{2k_{\text{B}}\nu^2} B_\nu(T_{\text{ex}}) \quad (1.72)$$

the spectral line emission in terms of brightness temperature (Eq. 1.44) is described as

$$T_{\text{B}}(\nu) = \eta_{\text{fill}} S_\nu (1 - e^{-\tau_\nu^{\text{line}}}). \quad (1.73)$$

Due to a finite channel width with frequency resolution $\delta\nu$ in real observations, the final modeled spectrum is averaged along one channel:

$$T_{\text{B}}(\nu) = \frac{1}{\delta\nu} \int_{\nu - \frac{\delta\nu}{2}}^{\nu + \frac{\delta\nu}{2}} T_{\text{B}}(\nu') d\nu' \quad (1.74)$$

With XCLASS, the spectral line emission of one emission component of a molecule is modeled combining Eqs. (1.68), (1.71), (1.72), and (1.73). There are in total five molecule-specific parameters tied to the local conditions of the source: θ_{source} , T_{ex} , N , $\Delta\nu$, and ν_{off} .

For each molecule, the properties of the line transitions (ν^t , A_{ul}^t , g_{u}^t , E_1^t , and Q) are taken from the Cologne Database for Molecular Spectroscopy (CDMS, Müller et al. 2005) and the Jet Propulsion Laboratory (JPL, Pickett et al. 1998), using the Virtual Atomic and Molecular Data Centre (VAMDC, Endres et al. 2016).

In XCLASS it is possible to choose a variety of algorithms that can also be combined in an algorithm chain in order to find the best-fit parameters by minimizing the χ^2 value between the modeled and observed spectrum with the implemented model optimizer package MAGIX (Möller et al. 2013). In this work, I adopt an algorithm chain with the Genetic algorithm (Herrera et al. 1998, 2005) and the Levenberg-Marquardt method (Marquardt 1963) optimizing toward global and local minima, respectively. Uncertainties of the fit parameters are estimated with the Markov chain Monte Carlo (MCMC) emcee package (Foreman-Mackey et al. 2013) that is implemented in MAGIX.

1.6 Scientific motivation and outline of this thesis

One of the central questions in high-mass star formation and astrochemistry is what the physical and chemical properties are at the earliest phases of star formation on core scales (<0.1 pc) and how they evolve over time. The diverse morphologies observed in HMSFRs require a statistical study of the underlying physical and chemical processes from the largest cloud to the smallest core scales to test various formation models. To investigate this topic, the characterization of the core scales is achieved by interferometric mm observations at high angular resolution of HMSFRs over all evolutionary stages. With continuum and spectral line data, the dust and chemical properties can be analyzed.

While in the past, many sample studies on the larger cloud and clump scales toward HMSFRs have been carried out, it is now possible with interferometers such as NOEMA and ALMA

to observe a large number of HMSFRs at small core scales requiring sub-arcsecond resolutions. A study based on a homogeneous data set and analysis allows us to perform a statistical analysis of the core properties considering physical aspects (such as the temperature and density) and chemical characteristics (molecular abundances).

In Chapter 2, we characterize the physical and chemical properties of 22 cores that are observed within the NOEMA large program CORE (Beuther et al. 2018a). The CORE sample consists of 18 HMSFRs that show a large diversity of fragmentation properties with multiple fragmented cores present in some of the regions, while in others, the dust continuum emission is dominated by a single isolated core. The observed physical-chemical properties are combined in MUSCLE in order to estimate a chemical timescale of each core to investigate potential age differences between and within the regions.

To complement the CORE sample with cores at earlier evolutionary stages, we observed two young and cold HMSFRs (CORE-extension) with NOEMA in the same spectral setup as CORE that is presented in Chapter 3. The derived physical and chemical properties are compared to the CORE sample to investigate possible evolutionary trends. The spatial morphology of the molecular emission is investigated using integrated intensity maps and the histogram of oriented gradients (HOG) method. The latter allows a velocity-resolved analysis of potential correlations between two species. The clustered nature of the two regions is investigated with archival Spitzer and Herschel observations at MIR and FIR wavelengths.

Our physical-chemical model MUSCLE is based on the chemical study by Gerner et al. (2014, 2015) that was based on low-resolution single-dish observations where multiple cores at different evolutionary stages can be present within one beam. To resolve the corresponding substructures at core scales, we revisited a sub-sample of 11 regions with ALMA at 3 mm wavelengths in order to perform a more detailed characterization of the fragmentation and physical properties that is presented in Chapter 4. The 11 regions cover all evolutionary stages (Sect. 1.2) from IRDC to UCH_{II} regions and thus evolutionary trends of the properties are investigated.

The results and conclusions of this thesis are summarized in Chapter 5. An outlook with follow-up studies and observations based on the findings in this thesis are further presented.

Chapter 2

Physical and chemical structure of high-mass star-forming regions: Unraveling chemical complexity with the NOEMA large program CORE

This chapter is based on Gieser et al. (2021), published in Astronomy & Astrophysics, 648, A66. I led this study under the supervision of Henrik Beuther and in close collaboration with Dmitry Semenov. The calibration and imaging of the NOEMA and IRAM 30m observations was performed by Henrik Beuther, Aida Ahmadi, and Joseph Mottram. I self-calibrated the NOEMA data in close collaboration with the GILDAS team at IRAM Grenoble and I reimaged the self-calibrated NOEMA+IRAM 30m data. I performed the analysis of the continuum and spectral line data, radiative transfer modeling with XCLASS (Möller et al. 2017) and physical-chemical modeling with MUSCLE. The initial chemical conditions from the Gerner et al. (2014, 2015) study with MUSCLE were provided by Dmitry Semenov. The text in the publication was written by me, I created the figures and all 32 co-authors provided comments for the manuscript.

2.1 Context

Current star formation research centers the characterization of the physical and chemical properties of massive stars, which are in the process of formation, at the spatial resolution of individual high-mass cores. We use sub-arcsecond resolution ($\sim 0.''4$) observations with NOEMA at 1.37 mm (Sect. 2.2) to study the dust emission and molecular gas of 18 high-mass star-forming regions that are part of the NOEMA large program CORE. The regions have distances in the range of 0.7 – 5.5 kpc, corresponding to spatial scales down to 300 – 2 300 au that are resolved by our observations. We combined the derived physical and chemical properties of individual cores in these regions to estimate their chemical timescales with MUSCLE (Sect. 1.3.3). The temperature structures of these regions are determined by fitting the H_2CO and CH_3CN line emission. The density profiles are inferred from the 1.37 mm continuum visibilities. The column densities of 11 different species are determined by fitting the emission lines with XCLASS (Sect. 1.5.2). This allows us to study the physical as well as the chemical properties of fragmented cores in a statistical sample.

2.2 Observations

The NOEMA large program “Fragmentation and disk formation during high-mass star formation - CORE” is a high angular resolution survey ($\sim 0.''4$ at 1.37 mm) designed to study the

TABLE 2.1: Overview of the CORE sample. The isotopic ratios are taken from Wilson & Rood (1994).

Region	Coordinates		Gal.			Isotopic Ratios		
	α	δ	Dist.	Dist.	Velocity	$^{12}\text{C}/^{13}\text{C}$	$^{32}\text{S}/^{34}\text{S}$	$^{16}\text{O}/^{18}\text{O}$
	J(2000)	J(2000)	(kpc)	(kpc)	(km s^{-1})			
IRAS 23033	23:05:25.00	+60:08:15.5	4.3	10.4	-53.1	86	22	649
IRAS 23151	23:17:21.01	+59:28:47.5	3.3	9.8	-54.4	81	22	613
IRAS 23385	23:40:54.40	+61:10:28.0	4.9	11.1	-50.2	91	22	690
AFGL 2591	20:29:24.86	+40:11:19.4	3.3	8.2	-5.5	69	22	519
CepA HW2	22:56:17.98	+62:01:49.5	0.7	8.4	-10.0	71	22	531
G084.9505	20:55:32.47	+44:06:10.1	5.5	9.4	-34.6	78	22	590
G094.6028	21:39:58.25	+50:14:20.9	4.0	9.3	+29.0	77	22	584
G100.38	22:16:10.35	+52:21:34.7	3.5	9.4	-37.6	78	22	590
G108.75	22:58:47.25	+58:45:01.6	4.3	10.3	-51.5	85	22	643
G138.2957	03:01:31.32	+60:29:13.2	2.9	10.5	-37.5	86	22	654
G139.9091	03:07:24.52	+58:30:48.3	3.2	10.8	-40.5	89	22	672
G075.78	20:21:44.03	+37:26:37.7	3.8	8.1	-8.0	68	22	513
IRAS 21078	21:09:21.64	+52:22:37.5	1.5	8.3	-6.1	70	22	525
NGC7538 IRS9	23:14:01.68	+61:27:19.1	2.7	9.5	-57.0	79	22	596
S106	20:27:26.77	+37:22:47.7	1.3	7.9	-1.0	67	22	502
S87 IRS1	19:46:20.14	+24:35:29.0	2.2	7.3	+22.0	62	22	466
W3 H2O	02:27:04.60	+61:52:24.7	2.0	9.6	-48.5	80	22	602
W3 IRS4	02:25:31.22	+62:06:21.0	2.0	9.6	-42.8	80	22	602

fragmentation, kinematic, and chemical properties of a homogeneous sample of 20 HMSFRs. The observations consist of spectral line and continuum data in Band 3 (1 mm). An overview of the project and results of the analysis of the dust continuum and fragmentation properties are presented in Beuther et al. (2018a).

2.2.1 Sample

The sample of the CORE project consists of well-studied HMSFRs on the northern hemisphere. They were selected based on high bolometric luminosities ($L > 10^4 L_{\odot}$) and relatively close distances ($d < 6$ kpc), allowing us to study the evolution at early stages of HMSF in the HMPO-HMC stage. An overview of the properties of the regions is shown in Table 2.1 in this work and additional properties, such as the luminosity L and mass M , are listed in Table 1 in Beuther et al. (2018a). With declinations higher than $+20^{\circ}$, most of the regions are difficult or impossible to observe with ALMA and, therefore, can only be studied with NOEMA at a high angular resolution ($< 1''$) at mm wavelengths. The angular resolution for all regions is homogeneous ($\sim 0.''4$), but the resolved linear spatial scales vary from 300 au to 2 300 au, as the regions are located at distances between 0.7 kpc and 5.5 kpc.

The regions show a large diversity of fragmentation properties (Beuther et al. 2018a): while some regions contain mainly a single isolated core (e.g., AFGL 2591), other regions fragment into up to 20 cores (e.g., IRAS 21078). Individual case-studies were carried out on some of the regions, for instance, the kinematic properties of W3 H2O (Ahmadi et al. 2018), IRAS 23385 (Cesaroni et al. 2019), IRAS 23033 (Bosco et al. 2019), W3 IRS4 (Mottram et al. 2020), and IRAS 21078 (Moscadelli et al. 2021); the chemical composition of the pilot regions NGC7538 S and NGC7538 IRS1 (Feng et al. 2016), and AFGL 2591 (Gieser et al. 2019).

A multi-wavelength modeling study of AFGL 2591 is presented in Olguin et al. (2020). In Ahmadi et al. (in preparation) the kinematic analysis of the complete CORE sample will be covered, while in this study, we focus on the physical structure (temperature and density) and chemical composition of the molecular gas. We do not include the pilot regions NGC7538 S and NGC7538 IRS1 presented in Beuther et al. (2018a) in our analysis, as it is only for the remaining 18 regions, we have a homogeneous multi-configuration NOEMA data set. The pilot studies have no corresponding D array observations, and thus, less uv -coverage, so these could not be accurately compared. However, a detailed individual chemical analysis of the pilot regions is already presented in Feng et al. (2016).

2.2.2 NOEMA

The sample was observed from 2014 to 2017 in the A (extended), the old B or new C (intermediate), and D (compact) array configurations. Two regions were observed at a time in track-sharing pairs to reduce calibration time. Spectral line data were obtained with the broadband WideX correlator at a rest-frequency range of 217.2 – 220.8 GHz, with a spectral resolution of $\sim 2.7 \text{ km s}^{-1}$. In addition, eight narrow-band units were placed within this frequency range in order to obtain high spectral resolution data ($\sim 0.4 \text{ km s}^{-1}$) of kinematically interesting lines such as CH_3CN (a summary of the high spectral resolution units is summarized in Table 2 and 3 in Ahmadi et al. 2018). The interferometric data were calibrated with the CLIC package in GILDAS¹. The 1.37 mm continuum data were extracted from the broadband WideX data by carefully selecting line-free channels in each region.

2.2.3 IRAM 30m telescope

Interferometers spatially filter the extended emission (Sect. 1.4.2). The shortest baseline of the NOEMA array is $\sim 20 \text{ m}$, thus spatial scales larger than $16''$ are not recovered by the interferometric observations at 1.37 mm. All CORE regions were therefore observed with the IRAM 30m telescope using the Eight MIXer Receiver (EMIR, Carter et al. 2012) in order to recover the missing flux in the spectral line data due to spatial filtering.

EMIR has four basebands and each have a width of $\sim 4 \text{ GHz}$ and a spectral resolution of 200 kHz corresponding to $\sim 0.3 \text{ km s}^{-1}$ at 1.37 mm). The lower inner baseband (LI) of the EMIR spectral setup covers the same spectral range as the NOEMA observations with the broadband WideX correlator. The half power beam width (HPBW) of the IRAM 30m telescope is $11.''8$ at 1.37 mm. For a detailed description of the IRAM 30m data calibration we refer to Appendix A in Mottram et al. (2020). The continuum data have no complementary single-dish observations, so here spatial filtering can remain an issue as discussed in Beuther et al. (2018a).

2.2.4 Self-calibration

The majority of the continuum data have a high signal-to-noise ratio (S/N) in the GILDAS standard calibrated data (see Table 2.2). However, the phase noise can be high due to an unstable atmosphere during the observations that causes the flux to be scattered around the source. This issue can be improved by applying phase self-calibration to the interferometric data (e.g., Pearson & Readhead 1984; Radcliffe et al. 2016, also Sect. 1.4.2).

The CORE continuum data presented in Beuther et al. (2018a) were successfully phase self-calibrated using the Common Astronomy Software Applications package (CASA) through

¹<https://www.iram.fr/IRAMFR/GILDAS/>

an iterative masking of the source. However, at that time, it was not possible to apply the self-calibration solution to the spectral line data. The CASA phase self-calibration of the continuum data was performed by applying an interactive mask in each self-calibration loop starting with the strongest structures first and proceeding with the weaker structures (Beuther et al. 2018a). Depending on the S/N of the region, we used solution intervals of 220, 100, or 45 s.

We now used the self-calibration tool in GILDAS to phase self-calibrate the continuum as well as the spectral line data of the CORE project to provide homogeneously calibrated data products of the full CORE observations. The crucial point of phase self-calibration is to start with a good enough spatial model of the source. The `selfcal` procedure of the GILDAS/MAPPING package uses as a source model the first CLEAN components n_{CLEAN} found during a previous step of deconvolution. The basic idea is that the first CLEAN components deliver a model of the source with a high S/N whose spatial structure is not much affected by flux scattering. The number of CLEAN components n_{CLEAN} must be large enough to get a fair representation of the source structure and small enough to avoid deconvolving scattered flux that would be confused with noise. The visibilities are usually averaged in time to increase their S/N during the first self-calibration iteration and this averaging time is progressively lowered to the minimum possible integration time in the following iterations. In practice, we started by deconvolving the continuum source with an absolute flux stopping criterion set to three times the continuum noise. This gives a number of CLEAN iterations, n_{iter} , which we used to iterate the self-calibration three times, increasing n_{CLEAN} from $n_{\text{iter}}/4$, to $n_{\text{iter}}/2$, and to n_{iter} , and decreasing the averaging time from 200 s, to 100 s, and to 45 s. Only visibilities with a $S/N > 6$ were self-calibrated, but the remaining visibilities were kept in the proceeding CLEANing of the data in order to avoid losing visibilities of the longest baselines, which would decrease the angular resolution. With this method, simple structures, as well as regions with a complicated morphology, can all be successfully phase self-calibrated. As the continuum data has the highest sensitivity, we used the solution from the continuum self-calibration and applied the gain solution to the broadband and narrow-band spectral line data using the `UV_CAL` task.

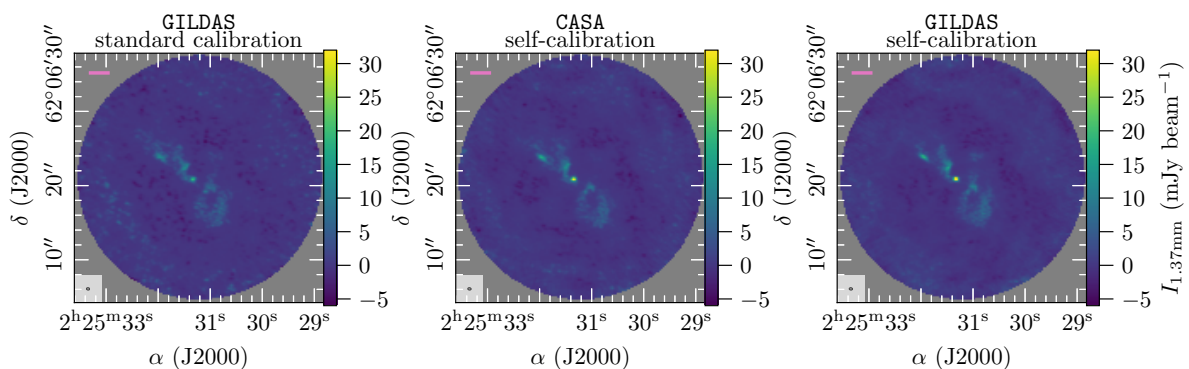


FIGURE 2.1: Comparison of GILDAS standard calibrated (*left panel*), CASA self-calibrated (*middle panel*), and GILDAS self-calibrated (*right panel*) W3 IRS4 continuum data. In each panel, the beam size is shown in the bottom left corner and the pink bar in the top left corner indicates a linear spatial scale of 5 000 au.

An example of how self-calibration is increasing the quality of the continuum data is shown in Fig. 2.1 for W3 IRS4, which has a complex morphology in the continuum data. While the GILDAS standard calibrated data already reveals the complex structure of the region, the noise is high throughout the primary beam with many negative features. Applying the CASA and GILDAS self-calibration significantly lowers the noise and increases the peak intensity. The continuum noise σ_{cont} and peak intensity I_{peak} are summarized for all regions in Table 2.2. The mean continuum noise, σ_{cont} , is $0.74 \text{ mJy beam}^{-1}$ in the standard calibrated data, while for the CASA

and GILDAS self-calibrated data, the mean noise, σ_{cont} , is lowered by $\sim 25\%$ to $0.53 \text{ mJy beam}^{-1}$ and $0.56 \text{ mJy beam}^{-1}$, respectively. In general, σ_{cont} is higher toward the bright continuum sources S106, CepA HW2, and W3 H2O. The mean S/N of the GILDAS standard calibrated continuum data is 74, while for the CASA and GILDAS self-calibrated continuum data, the mean S/N is improved by a factor of two to 130 and 132, respectively.

Even though both CASA and GILDAS self-calibration methods improve the data quality, due to the different techniques to define a source model (interactive masking and defining number of CLEAN components, respectively), there are differences in the resulting images. In Fig. 2.1, a faint structure toward the NW of the continuum peak is seen in the GILDAS standard calibrated and self-calibrated image, but it is not recovered in the CASA self-calibrated image. Comparing the self-calibration results (Table 2.2), the peak intensities are higher in the GILDAS self-calibrated data, while a lower noise is achieved in the CASA self-calibrated data. For very faint structures and a complex source morphology, a careful interpretation of the self-calibrated data is recommended, but overall all the main features are recovered with both self-calibration methods.

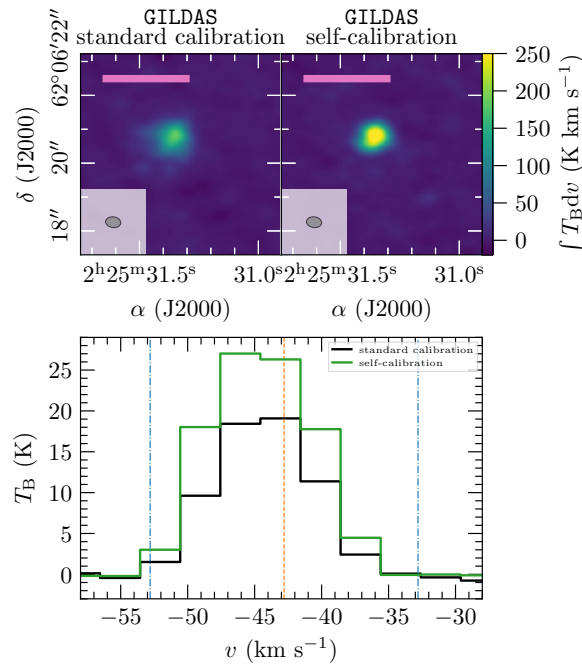


FIGURE 2.2: *Top panel:* Comparison of GILDAS standard calibration (*left panel*) and GILDAS self-calibration (*right panel*) of the W3 IRS4 broadband spectral line data zoomed in toward the position of the continuum peak. The integrated intensity of the $\text{CH}_3\text{CN } 12_3 - 11_3$ transition is shown in color. In each panel, the beam size is shown in the bottom left corner and the pink bar in the top left corner indicates a linear spatial scale of 5 000 au. *Bottom panel:* $\text{CH}_3\text{CN } 12_3 - 11_3$ spectrum at the position of the W3 IRS4 continuum peak of the GILDAS standard calibrated data (black) and of the GILDAS self-calibrated data (green). The dashed orange line shows the systemic velocity of the region v_{LSR} and the dash-dotted blue lines show the lower and upper velocity limits ($v_{\text{LSR}} \pm 10 \text{ km s}^{-1}$) used for the integrated intensity map shown in the top panel.

A comparison between the standard and self-calibrated broadband spectral line data is shown in Fig. 2.2 for the $\text{CH}_3\text{CN } 12_3 - 11_3$ transition around the location of the 1.37 mm continuum peak in the W3 IRS4 region. The emission is less fuzzy and more compact in the self-calibrated data product. On individual spectra, self-calibration provides a significant increase of the line intensity which has a big impact, for example, when deriving column densities (Sect. 2.4.2).

TABLE 2.2: Overview of the CORE data products. The noise of the continuum data σ_{cont} is computed in a $3.''5 \times 3.''5$ rectangle in an emission-free region. The average map noise of the merged (combined NOEMA + IRAM 30m) spectral line data $\sigma_{\text{line,map}}$ is computed in a line-free range from a rest-frequency of 219.00 GHz to 219.13 GHz with a channel width of 3 km s^{-1} (2.2 MHz) within the full primary beam.

Region	Synthesized Beam				GILDAS		CASA		GILDAS		
	Continuum Data		Merged Line Data		Standard Calibration		Self-calibration		Self-calibration		
	$\theta_{\text{maj}} \times \theta_{\text{min}}$ ($'' \times ''$)	PA ($^\circ$)	$\theta_{\text{maj}} \times \theta_{\text{min}}$ ($'' \times ''$)	PA ($^\circ$)	σ_{cont} (mJy beam^{-1})	I_{peak}	σ_{cont} (mJy beam^{-1})	I_{peak}	σ_{cont} (mJy beam^{-1})	I_{peak}	$\sigma_{\text{line,map}}$ (K)
IRAS 23033	0.45×0.37	47	0.43×0.43	96	0.50	28.21	0.43	38.76	0.53	38.13	0.40
IRAS 23151	0.45×0.37	50	0.47×0.38	54	0.26	26.41	0.26	32.65	0.25	33.78	0.48
IRAS 23385	0.48×0.43	58	0.49×0.44	55	0.29	14.61	0.16	18.03	0.16	17.84	0.30
AFGL 2591	0.47×0.36	65	0.48×0.37	65	0.53	56.31	0.50	87.33	0.51	85.10	0.65
CepA HW2	0.42×0.41	41	0.44×0.39	80	3.72	239.93	2.39	441.07	2.43	448.50	0.68
G084.9505	0.43×0.38	69	0.44×0.39	72	0.10	4.37	0.08	6.28	0.08	5.19	0.28
G094.6028	0.41×0.39	77	0.41×0.38	85	0.15	10.24	0.15	13.65	0.13	12.84	0.36
G100.38	0.49×0.33	56	0.49×0.34	55	0.07	6.35	0.05	8.51	0.06	7.28	0.25
G108.75	0.50×0.44	49	0.51×0.44	49	0.17	10.53	0.12	14.75	0.13	16.08	0.27
G138.2957	0.50×0.41	60	0.51×0.41	59	0.16	6.28	0.16	6.15	0.10	6.28	0.33
G139.9091	0.51×0.40	56	0.52×0.41	56	0.18	9.23	0.20	13.84	0.15	13.49	0.34
G075.78	0.48×0.37	60	0.49×0.37	60	0.47	46.31	0.38	64.50	0.38	71.67	0.58
IRAS 21078	0.48×0.33	41	0.48×0.33	41	0.41	26.76	0.44	34.64	0.44	36.69	0.41
NGC7538 IRS9	0.44×0.38	80	0.44×0.38	80	0.32	29.14	0.19	41.28	0.21	46.09	0.42
S106	0.47×0.34	47	0.48×0.34	47	0.88	77.41	0.96	136.00	1.20	150.47	0.35
S87 IRS1	0.54×0.35	37	0.55×0.36	37	0.12	19.42	0.17	33.35	0.18	37.37	0.44
W3 H2O	0.43×0.32	86	0.45×0.32	86	4.28	279.11	2.54	449.84	2.82	456.29	0.74
W3 IRS4	0.45×0.32	82	0.46×0.32	83	0.69	21.73	0.42	39.34	0.33	51.50	0.72

2.2.5 Data products and public release

With the GILDAS/MAPPING package we perform the data merging of the self-calibrated interferometric with the single-dish data and the consecutive imaging. The WideX and the corresponding EMIR spectral-line data are smoothed to a common spectral resolution of 3.0 km s^{-1} . The narrow-band and the corresponding EMIR spectral line data are smoothed to a common spectral resolution of 0.5 km s^{-1} . In order to merge the NOEMA and IRAM 30m data, the task UV_SHORT converts the short spacings into a pseudo uv -table and combines them with the NOEMA data.

The deconvolution of the NOEMA continuum, NOEMA spectral line and merged (combined NOEMA + IRAM 30m) spectral line data is performed in GILDAS/MAPPING using the Clark CLEAN algorithm (Clark 1980) and adopting three different weightings: robust weighting with a robust parameter of 0.1 ($\theta \sim 0.''4$); a robust parameter of 1.0 ($\theta \sim 0.''6$); and natural weighting ($\theta \sim 1.''0$). The stopping criterion for the continuum and broadband spectral line data is set to $f_{\text{res}} = 0.01$, which corresponds to a minimum fraction of 1% of the peak intensity in the dirty image. The stopping criterion for the narrow-band spectral line data is either $n_{\text{iter}} = 5000$ (maximum number of iterations) or $a_{\text{res}} = 0.01$, which corresponds to a maximum intensity of 10 mJy beam^{-1} in the residual image.

Molecules such as CO isotopologues and SO may have extended emission in the merged data products (Mottram et al. 2020). As the Clark algorithm assumes emission from point sources, the CLEANed map may have point-like artifacts. The SDI algorithm (Steer et al. 1984) may improve the CLEANed image in such cases. A comparison between the Clark and SDI algorithms for imaging of the W3 IRS4 region is presented in Mottram et al. (2020). Final data products of the merged broadband spectral line data of molecular lines with potential large scale emission ($^{13}\text{CO } 2-1$, $\text{SO } 6_5-5_4$, $\text{H}_2\text{CO } 3_{0,3}-2_{0,2}$, $\text{H}_2\text{CO } 3_{2,2}-2_{2,1}$, $\text{H}_2\text{CO } 3_{2,1}-2_{2,0}$) CLEANed using the SDI algorithm with robust weighting (robust parameter of 3, $\theta \sim 0.''6$), with a stopping criterion of $n_{\text{iter}} = 25000$ are provided as well. Primary beam correction is applied to all continuum and spectral line data products.

In this study, we use the primary beam corrected NOEMA-only continuum and merged (NOEMA + IRAM 30m) broadband spectral line data. Both data products are imaged with the Clark algorithm and a robust parameter of 0.1, resulting in the highest angular resolution ($\theta \sim 0.''4$). Table 2.2 summarizes the properties of the standard and self-calibrated data products for all regions, including the synthesized beam (major axis θ_{maj} , minor axis θ_{min} , and position angle PA), noise of the continuum data σ_{cont} , continuum peak intensity I_{peak} , and noise in the merged (NOEMA + IRAM 30m) spectral line data $\sigma_{\text{line,map}}$. The mean map noise of the merged spectral line data is 0.44 K .

2.3 Physical structure

The linear spatial resolution of the CORE sample ranges from $300\text{--}2300 \text{ au}$. At this spatial resolution, it is not possible to resolve potential disks surrounding the protostars, but these can be studied and characterized through a kinematic analysis of the line profiles (Ahmadi et al. 2019). However, we do resolve the gas and dust envelopes around individual cores which can be approximated as spherically symmetric objects for which the radial temperature profile $T(r)$ and radial density profile $n(r)$ of the envelope gas can be described by power-laws (e.g., van der Tak et al. 2000; Beuther et al. 2002a; Palau et al. 2014):

$$T(r) = T_{\text{in}} \times \left(\frac{r}{r_{\text{in}}} \right)^{-q}, \quad (2.1)$$

$$n(r) = n_{\text{in}} \times \left(\frac{r}{r_{\text{in}}} \right)^{-p}, \quad (2.2)$$

with $T_{\text{in}} = T(r_{\text{in}})$ and $n_{\text{in}} = n(r_{\text{in}})$ at an arbitrary radius r_{in} . The temperature power-law index q and density power-law index p of the core envelopes are important properties of HMSFRs. By studying these quantities with observations, theoretical analytical models on how massive stars form can be constrained.

2.3.1 Continuum emission

A detailed analysis of the continuum data is given in Beuther et al. (2018a). The updated GILDAS self-calibrated continuum data are presented in contours in Fig. 2.3. While the sample was selected to be largely homogeneous in luminosity, at an angular resolution of $\sim 0.''4$, a variety of structures can be identified. While some regions appear as isolated single objects (IRAS 23151, AFGL 2591), others show spatially separated cores (IRAS 23033, G108.75, G139.9091, S106, CepA HW2, W3 H2O). There are regions in which fragmentation is observed within an embedded envelope (IRAS 23385, IRAS 21078). Many of the regions have a complex morphology such as filamentary structures and extended envelopes (G084.9505, G094.6028, G100.38, G138.2957, G75.78, NGC7538 IRS9, S87 IRS1, W3 IRS4).

In this study, we aim to analyze the physical properties and chemical variation across the regions, therefore, we selected a number of positions throughout the different regions. Deriving the column density of all detected species in every single spectrum in each region is computationally expensive and we restrict this method to the analysis of the H_2CO and CH_3CN temperature maps (Sect. 2.3.2). In order to study the cores and envelopes around forming protostars, we selected positions which have a clear spherically symmetric core-like morphology in the 1.37 mm continuum data which is the case for most regions toward the continuum peak position, but also multiple spherically symmetric objects within a region can be identified (e.g., toward IRAS 23033). In addition, we select positions in the extended envelopes to study potential differences in the chemical abundances. The in total 120 selected positions are summarized in Table A.1 and marked in Fig. 2.3. The nomenclature of each position is denoted by the region name and increasing number with decreasing 1.37 mm continuum intensity. For each region, position 1 is toward the 1.37 mm continuum emission peak.

In order to estimate the H_2 column density (Sect. 2.4.1), we require for all positions to be detected in the 1.37 mm continuum ($I_{1.37\text{mm}} \geq 5\sigma_{\text{cont}}$). The number of selected positions is higher toward regions with extended envelopes and complex morphologies (e.g., IRAS 21078 and G138.2957) compared to compact regions (e.g., G139.9091 and S106). In this study, we define (in Sect. 2.3.2) a ‘‘core’’ as an object that shows a radially decreasing temperature profile along at least the width of two beams. In Sect. 2.5, we apply a 1D physical-chemical model to these defined cores using the observed temperature and density structure analyzed in Sect. 2.3.2 and Sect. 2.3.3, respectively, and observed molecular column densities (Sect. 2.4). These positions are labeled as ‘‘C’’ (core) in Table A.1. The remaining positions are locations in the dust envelope and environment around the cores. There are a few positions with a clear spherically symmetric core morphology in the dust emission, but no temperature profile can be derived (e.g., position 1 in S106). Cores with unresolved radial temperature profiles are also not included in this approach. In total we select 120 positions including 22 core positions. The broadband spectra of the 120 positions are shown in Fig. A.3. Table A.1 lists the noise of the broadband spectrum extracted from these positions and the systemic velocity v_{LSR} determined from the C^{18}O 2 – 1 line (Sect. 2.4.2), which may differ from the average region v_{LSR} (listed in Table 2.1) due to velocity gradients within the region. In contrast to this core definition, in the analysis by Beuther et al. (2018a), ‘‘cores’’ are defined as fragmented objects with emission

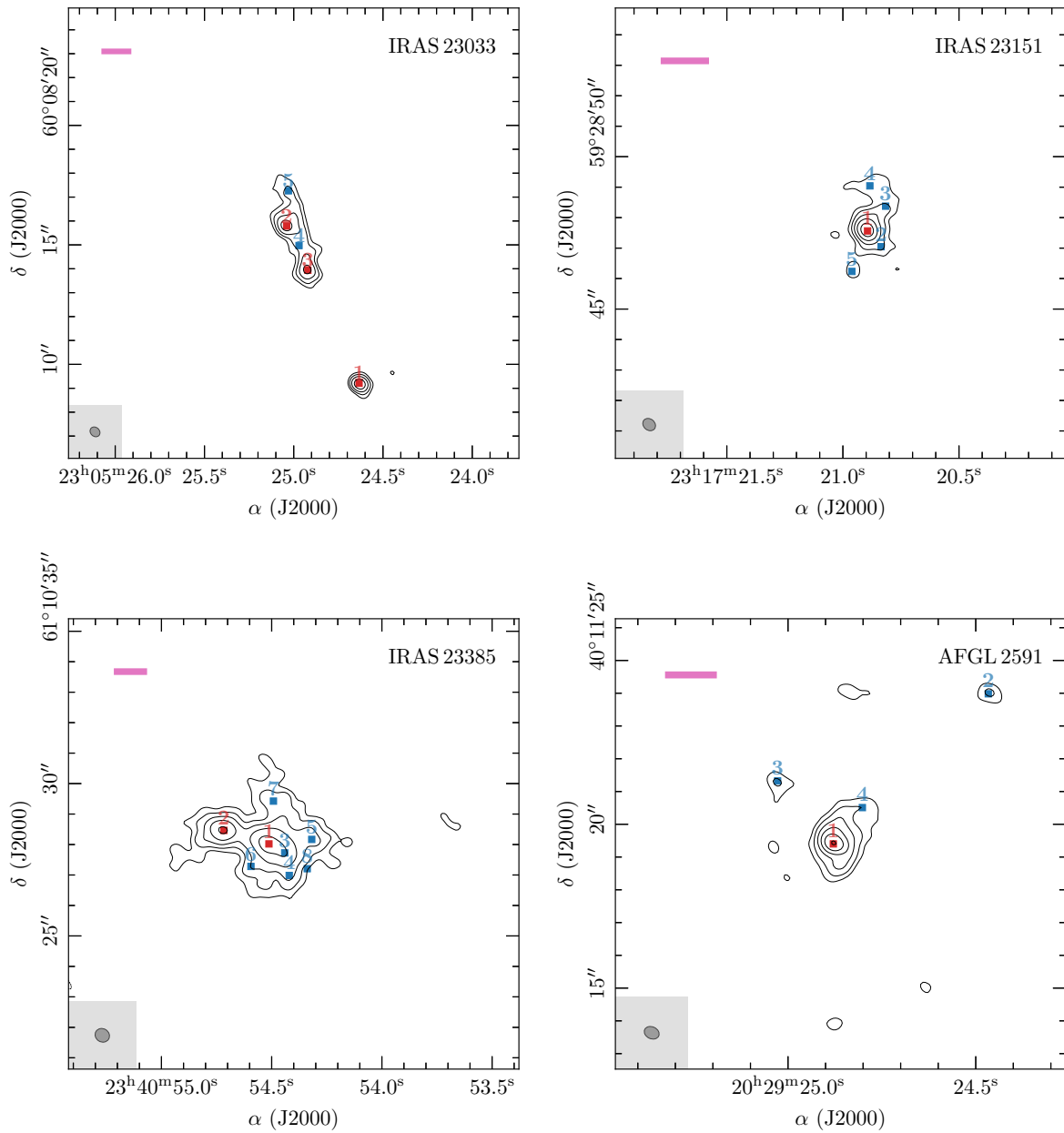


FIGURE 2.3: 1.37 mm continuum emission of the CORE regions. The selected positions analyzed in this work (summarized in Table A.1) are marked and labeled in red (core positions) and blue (all remaining positions). The dashed black contours show the $-5\sigma_{\text{cont}}$ emission and the solid black contours start at $5\sigma_{\text{cont}}$ with contour steps increasing by a factor of 2 (e.g., $-5, 5, 10, 20, 40, 80, \dots \sigma_{\text{cont}}$; see Table 2.2 for values of σ_{cont} for each region). In each panel, the beam size is shown in the bottom left corner and the pink bar in the top left corner indicates a linear spatial scale of 5000 au. The field of view in each region is adjusted to only show the area with significant emission ($\geq 5\sigma_{\text{cont}}$), and for regions with wide-spread emission, the primary beam is indicated by a black circle.

$\geq 10\sigma_{\text{cont}}$ using the `clumpfind` algorithm (Williams et al. 1994) and, thus, more cores are found in their analysis.

2.3.2 Temperature structure

To reliably determine the rotation temperature, T_{rot} , it is required to observe multiple transitions of a molecule. We use formaldehyde (H_2CO) and methyl cyanide (CH_3CN) as thermometers to

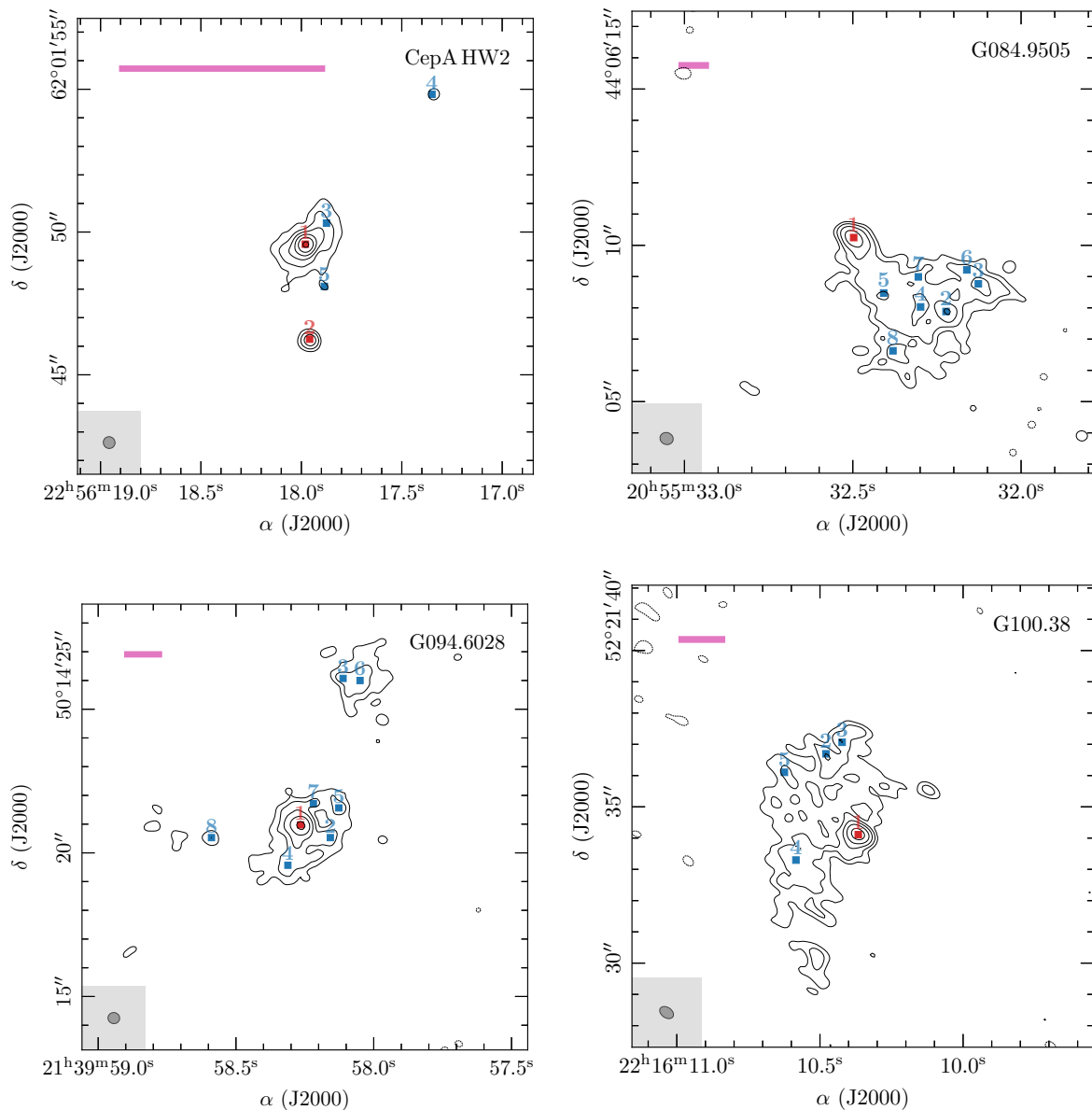


FIGURE 2.3 (cont.): 1.37 mm continuum emission of the CORE regions. The selected positions analyzed in this work (summarized in Table A.1) are marked and labeled in red (core positions) and blue (all remaining positions). The dashed black contours show the $-5\sigma_{\text{cont}}$ emission and the solid black contours start at $5\sigma_{\text{cont}}$ with contour steps increasing by a factor of two (e.g., $-5, 5, 10, 20, 40, 80, \dots, \sigma_{\text{cont}}$, see Table 2.2 for values of σ_{cont} for each region). In each panel, the beam size is shown in the bottom left corner and the pink bar in the top left corner indicates a linear spatial scale of 5 000 au. The field of view in each region is adjusted to only show the area with significant emission ($\geq 5\sigma_{\text{cont}}$). For regions with wide-spread emission, the primary beam is indicated by a black circle.

determine the temperature structure of the regions, as both have multiple strong and optically thin lines in our spectral setup. The spectral line properties of these molecules are listed in Table A.2.

We model the spectral line emission of these molecules using XCLASS (Möller et al. 2017) as introduced in Sect. 1.5.2. With XCLASS, molecular lines can be modeled and fitted by solving the 1D radiative transfer equation (Eq. 1.73). In the calculation of the Gaussian line profiles (Eq. 1.68) optical depth effects are included (Eq. 1.71).

The broadband spectral setup includes three strong formaldehyde lines, two of which have

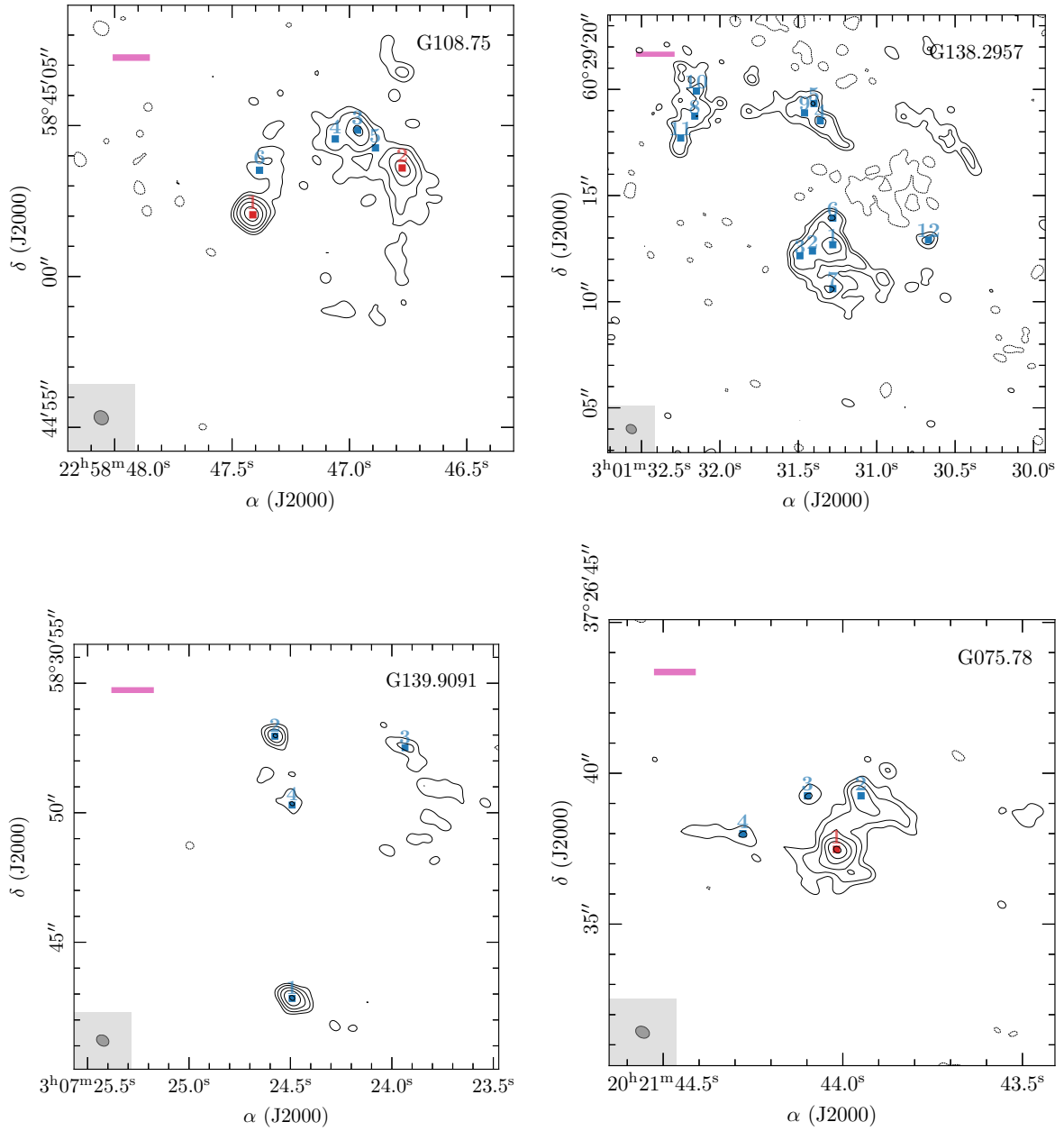


FIGURE 2.3 (cont.): 1.37 mm continuum emission of the CORE regions. The selected positions analyzed in this work (summarized in Table A.1) are marked and labeled in red (core positions) and blue (all remaining positions). The dashed black contours show the $-5\sigma_{\text{cont}}$ emission and the solid black contours start at $5\sigma_{\text{cont}}$ with contour steps increasing by a factor of 2 (e.g., $-5, 5, 10, 20, 40, 80, \dots\sigma_{\text{cont}}$; see Table 2.2 for values of σ_{cont} for each region). In each panel, the beam size is shown in the bottom left corner and the pink bar in the top left corner indicates a linear spatial scale of 5000 au. The field of view in each region is adjusted to only show the area with significant emission ($\geq 5\sigma_{\text{cont}}$). For regions with wide-spread emission, the primary beam is indicated by a black circle.

the same upper energy level, and one weak transition from the H_2^{13}CO isotopologue. The H_2CO and H_2^{13}CO lines are fitted simultaneously in XCLASS using an isotopic ratio calculated from Wilson & Rood (1994): $^{12}\text{C}/^{13}\text{C} \approx 7.5 \times d_{\text{gal}} + 7.6$. The $^{12}\text{C}/^{13}\text{C}$ ratio is listed in Table 2.1 for each region. While formaldehyde is a good low-temperature gas tracer at $T_{\text{kin}} < 100$ K (Mangum & Wootten 1993), at high densities and temperatures, the $3_{0,3} - 2_{0,2}$ transition is optically thick and a reliable temperature can no longer be derived from the line ratios with this

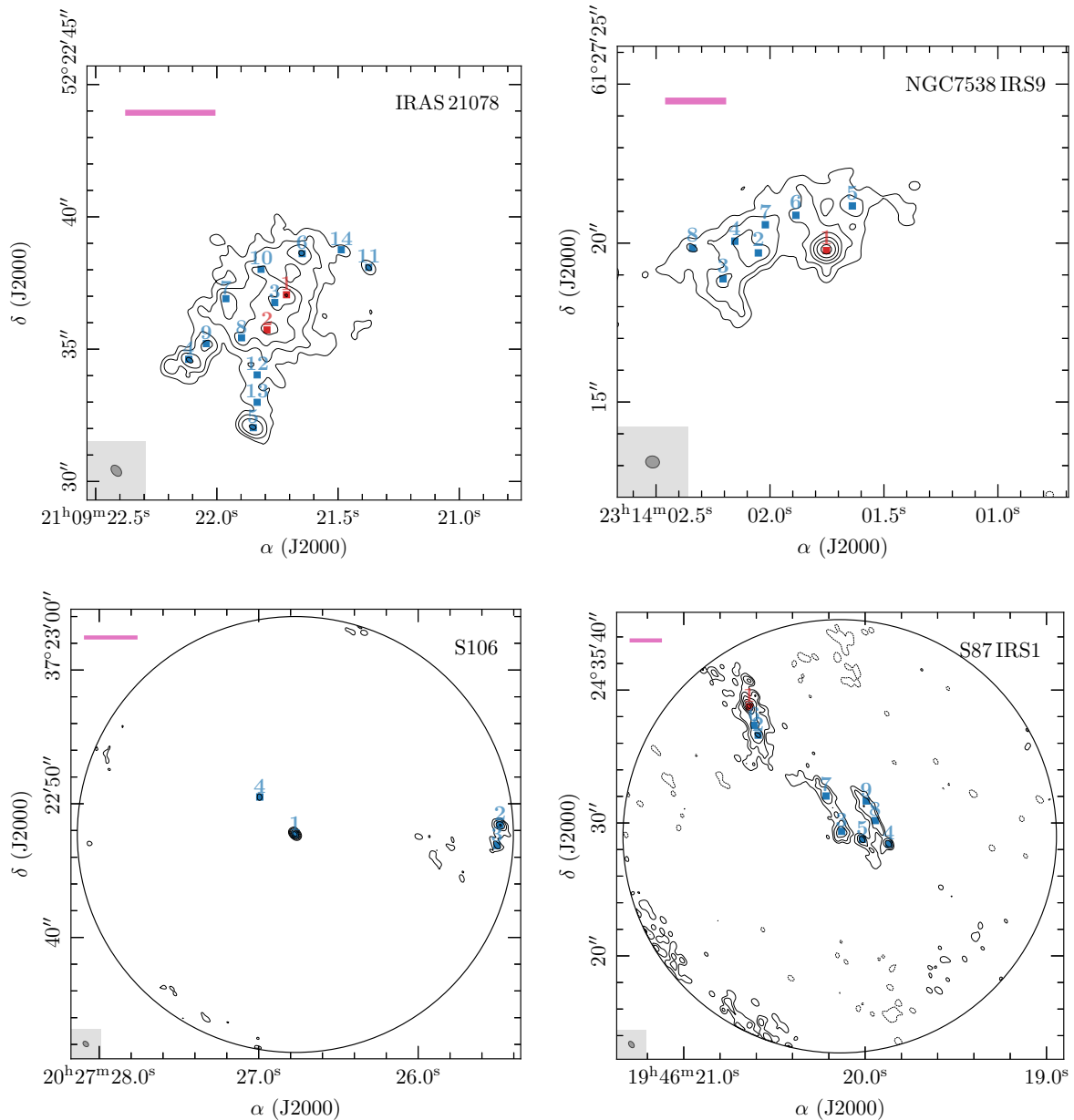


FIGURE 2.3 (cont.): 1.37 mm continuum emission of the CORE regions. The selected positions analyzed in this work (summarized in Table A.1) are marked and labeled in red (core positions) and blue (all remaining positions). The dashed black contours show the $-5\sigma_{\text{cont}}$ emission and the solid black contours start at $5\sigma_{\text{cont}}$ with contour steps increasing by a factor of 2 (e.g., $-5, 5, 10, 20, 40, 80, \dots \sigma_{\text{cont}}$; see Table 2.2 for values of σ_{cont} for each region). In each panel, the beam size is shown in the bottom left corner and the pink bar in the top left corner indicates a linear spatial scale of 5000 au. The field of view in each region is adjusted to only show the area with significant emission ($\geq 5\sigma_{\text{cont}}$). For regions with wide-spread emission, the primary beam is indicated by a black circle.

method (Rodón et al. 2012; Gieser et al. 2019). To determine temperatures at higher densities, we use nine methyl cyanide lines ($J = 12 - 11$ and $K = 0 - 8$, $E_u/k_B = 69 - 526$ K). In addition, seven lines of the $\text{CH}_3^{13}\text{CN}$ isotopologue are fitted simultaneously ($J = 12 - 11$ and $K = 0 - 6$, $E_u/k_B = 69 - 326$ K). A detailed discussion of the line optical depth is given in Sect. 2.4.2.

In XCLASS, each molecule can be described by a number of emission and absorption components. The fit parameter set of each component consists of the source size θ_{source} , the rotation

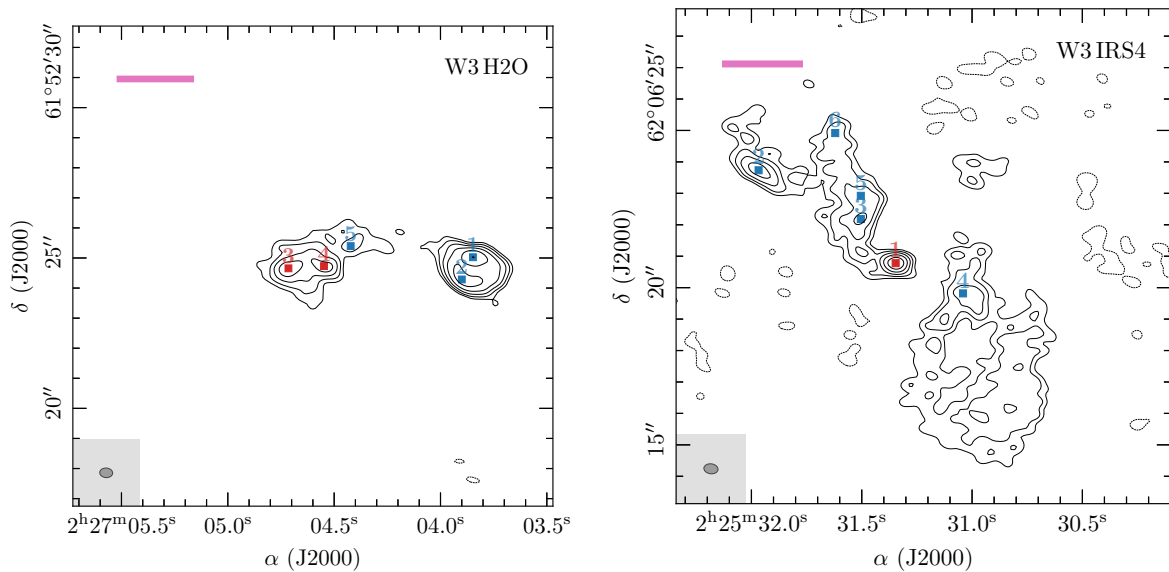


FIGURE 2.3 (cont.): 1.37 mm continuum emission of the CORE regions. The selected positions analyzed in this work (summarized in Table A.1) are marked and labeled in red (core positions) and blue (all remaining positions). The dashed black contours show the $-5\sigma_{\text{cont}}$ emission and the solid black contours start at $5\sigma_{\text{cont}}$ with contour steps increasing by a factor of 2 (e.g., $-5, 5, 10, 20, 40, 80, \dots \sigma_{\text{cont}}$; see Table 2.2 for values of σ_{cont} for each region). In each panel, the beam size is shown in the bottom left corner and the pink bar in the top left corner indicates a linear spatial scale of 5000 au. The field of view in each region is adjusted to only show the area with significant emission ($\geq 5\sigma_{\text{cont}}$). For regions with wide-spread emission, the primary beam is indicated by a black circle.

temperature T_{rot} , the column density N , the line width Δv , and the velocity offset from the systemic velocity v_{off} . It is possible to choose a variety of algorithms that can also be combined in an algorithm chain in order to find the best-fit parameters by minimizing the χ^2 value. We adopted an algorithm chain with the Genetic and the Levenberg-Marquardt (LM) methods optimizing toward global and local minima, respectively.

For each region, we use the `myXCLASSMapFit` function to fit the H_2CO and CH_3CN lines in each pixel within the primary beam. All lines with a peak intensity $> 10\sigma_{\text{line,map}}$ are fitted with one emission component. We chose a high threshold of $10\sigma_{\text{line,map}}$ so multiple transitions have a high S/N to accurately determine the rotation temperature. Only a single value can be set as the threshold in the `myXCLASSMapFit` function, therefore, toward the edges of the primary beam, the temperature estimates are less reliable due to an increase in the noise.

Under the assumption of local thermal equilibrium (LTE), the kinetic temperature of the gas can be estimated from the rotation temperature $T_{\text{kin}} \approx T_{\text{rot}}$. As HMSFRs have high densities $n > 10^5 \text{ cm}^{-3}$ toward the locations of the protostars, LTE can be assumed here (Mangum & Shirley 2015). The critical densities, $n_{\text{crit}} = \frac{A_{\text{ul}}}{C_{\text{ul}}}$, for the CH_3CN and H_2CO lines are $\sim 4 \times 10^6 \text{ cm}^{-3}$ and $\sim 3 \times 10^6 \text{ cm}^{-3}$, respectively (A_{ul} is the Einstein A coefficient and C_{ul} is the collisional rate coefficient). Here, we use C_{ul} measured at 140 K taken from the Leiden Atomic and Molecular Database (LAMDA, Schöier et al. 2005). The H_2CO and CH_3CN temperature maps of each region are shown in Fig. A.1. The H_2CO lines trace the extended low temperature gas at 10 – 100 K. The CH_3CN maps mostly show spatially compact emission tracing the higher temperature gas at > 100 K.

For each selected position (Table A.1), we extract the H_2CO and CH_3CN radial temperature profile which are binned in steps of half a beam (Δr). In each bin, the uncertainties are computed from the standard deviation of the mean. After a first visual inspection of all radial profiles of

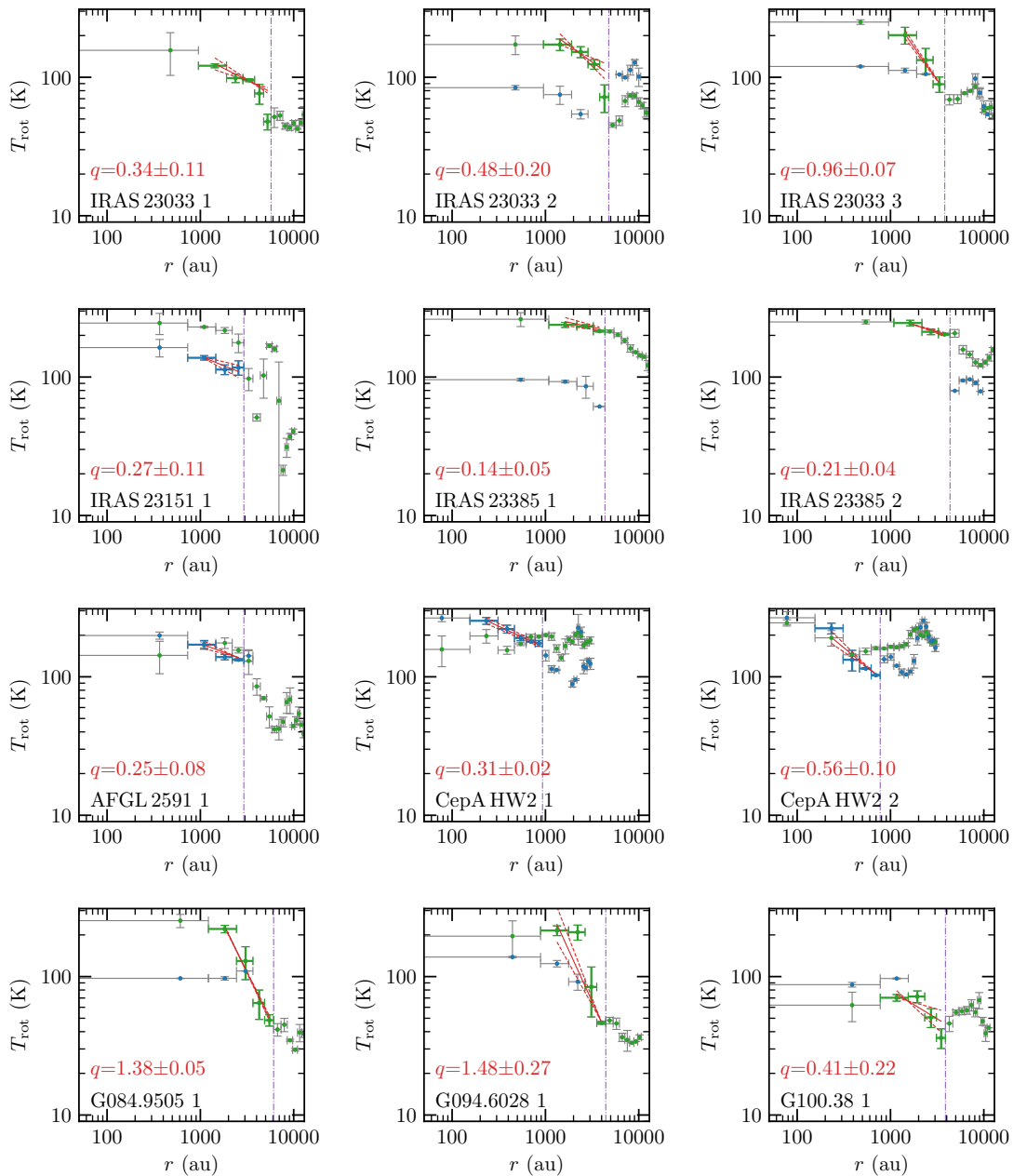


FIGURE 2.4: Radial temperature profiles of the 22 cores. Each panel shows the binned radial temperature profile derived from the H_2CO (green) and CH_3CN (blue) temperature maps shown in Fig. A.1. The data points used for the radial profile fit are shown by corresponding colored errorbars, the data points excluded from the fit are indicated by grey errorbars. The outer radius of the temperature fit is shown by the vertical purple dash-dotted line. The inner unresolved region is shown as a grey-shaded area. The linear fit and the $\pm 1\sigma$ uncertainty are shown by the solid and dashed red lines, respectively.

the 120 positions, we select all positions with a radially decreasing temperature profile along at least two beams in at least one temperature tracer. With this method, we are able to extract in total 22 positions, which we define as “cores.” The radial temperature profiles of the cores are shown in Fig. 2.4. In cases where both temperature tracers are detected toward the central core (e.g., IRAS 23033 2), the observed H_2CO temperature profile has significantly higher values when compared to CH_3CN . As discussed previously, this is due to the high optical depth in these dense regions causing the fit algorithm to converge toward high temperatures. The line optical depth is discussed further in Sect. 2.4.2.

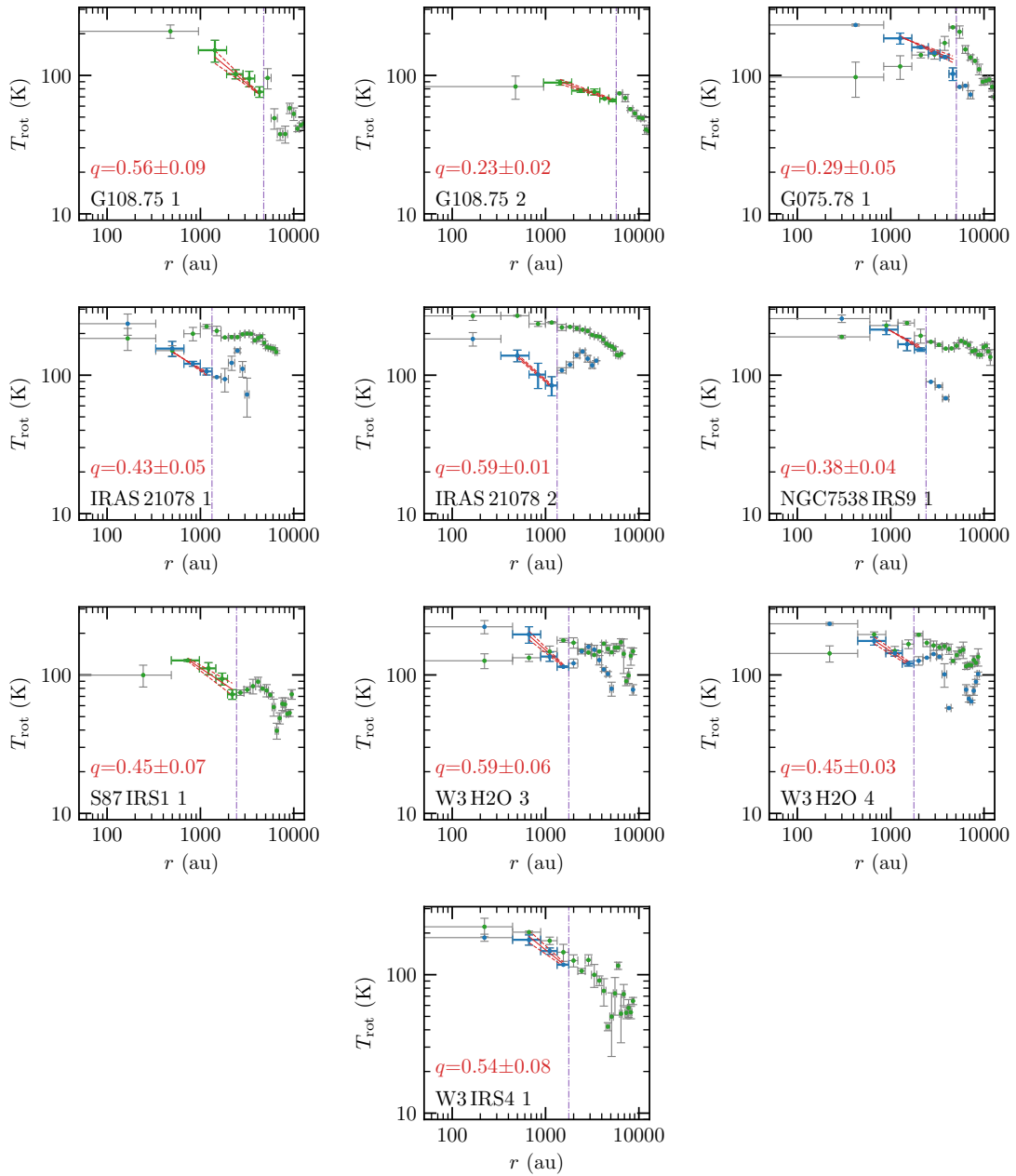


FIGURE 2.4 (cont.): Radial temperature profiles of the 22 cores. Each panel shows the binned radial temperature profile derived from the H_2CO (green) and CH_3CN (blue) temperature maps shown in Fig. A.1. The data points used for the radial profile fit are shown by corresponding colored errorbars, the data points excluded from the fit are indicated by grey errorbars. The outer radius of the temperature fit is shown by the vertical purple dash-dotted line. The inner unresolved region is shown as a grey-shaded area. The linear fit and the $\pm 1\sigma$ uncertainty are shown by the solid and dashed red lines, respectively.

We fit the profiles with a power-law according to Eq. (2.1) using the minimum χ^2 method to derive the temperature power-law index q . We used the CH_3CN temperature profile for the fit if it is detected along at least two beams and the H_2CO temperature profile otherwise. The inner radius is the temperature at a radius of half the beam size $r_{\text{in}} = \Delta r$. The outer radius r_{out} is chosen as a local minimum, when $T_{\text{rot}}(r_{\text{out}}) < T_{\text{rot}}(r_{\text{out}} + \Delta r)$ and $T_{\text{rot}}(r_{\text{out}}) < T_{\text{rot}}(r_{\text{out}} + 2\Delta r)$. In cases where the outer radii of nearby cores overlapped or the 2D temperature distribution would become highly asymmetric, we reduced the outer radius. The outer radii are also marked in Fig. 2.4 and Fig. A.1. The fit results for q , r_{in} , r_{out} , and $T_{\text{kin}}(r_{\text{in}})$ are summarized in Table 2.3

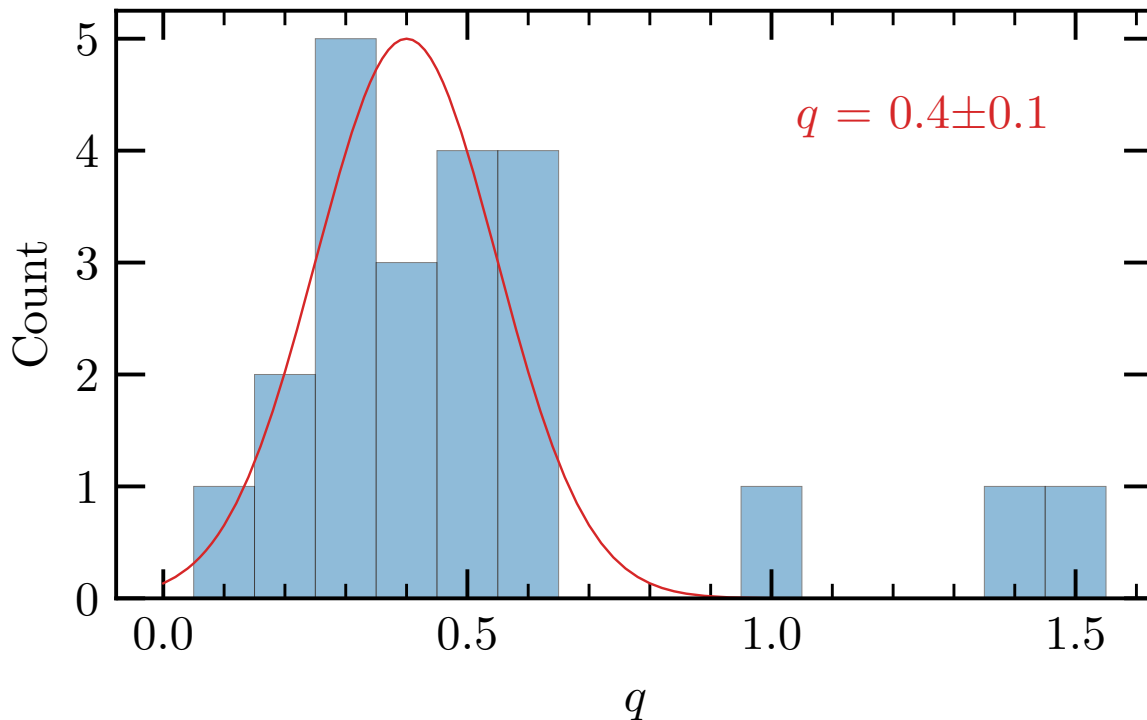


FIGURE 2.5: Histogram of the temperature power-law index q . The red line shows a Gaussian fit to the data points for $q = 0.1 - 0.6$.

for each core.

A histogram of the temperature power-law index q is shown in Fig. 2.5. Most of the data points are distributed between 0.1 and 0.6, but three outliers are located at $q > 0.9$. A Gaussian fit to the data with $q = 0.1 - 0.6$ yields an average value of $q = 0.4 \pm 0.1$, which is in very good agreement with theoretical predictions (Emerson 1988; Osorio et al. 1999; van der Tak et al. 2000) and observations (e.g., Palau et al. 2014, 2021). The issue of optical depth of the H_2CO lines and CH_3CN being only detected toward the densest parts result in the high uncertainties and spread in q . We observe a broad range of q with shallow profiles ($q = 0.1$) up to steep profiles ($q = 1.5$). In order to study if q is constant for all high-mass cores or if the range of q is real, observations of more cores are required. Osorio et al. (1999) and van der Tak et al. (2000) suggest steeper values for q on scales < 2000 au. In addition, the temperature maps and radial profiles are 2D projected, whereas the real 3D profile may be more complicated.

2.3.3 Density structure

In contrast to the merged (NOEMA + IRAM 30m) spectral line data, the 1.37 mm continuum NOEMA data suffer from missing flux due to the lack of short-spacing information. Therefore, it is difficult to reliably derive radial intensity profiles in the final images that are required to determine the density structure. This issue can be minimized by analyzing instead the complex visibilities of the 1.37 mm continuum data in the uv -plane (Adams 1991; Looney et al. 2003; Beuther et al. 2007b; Zhang et al. 2009). Assuming spherical symmetry, the power-law index of the complex visibility profile α is related to the density power-law index of the radial density distribution p by (Looney et al. 2003):

$$\alpha = p + q - 3. \quad (2.3)$$

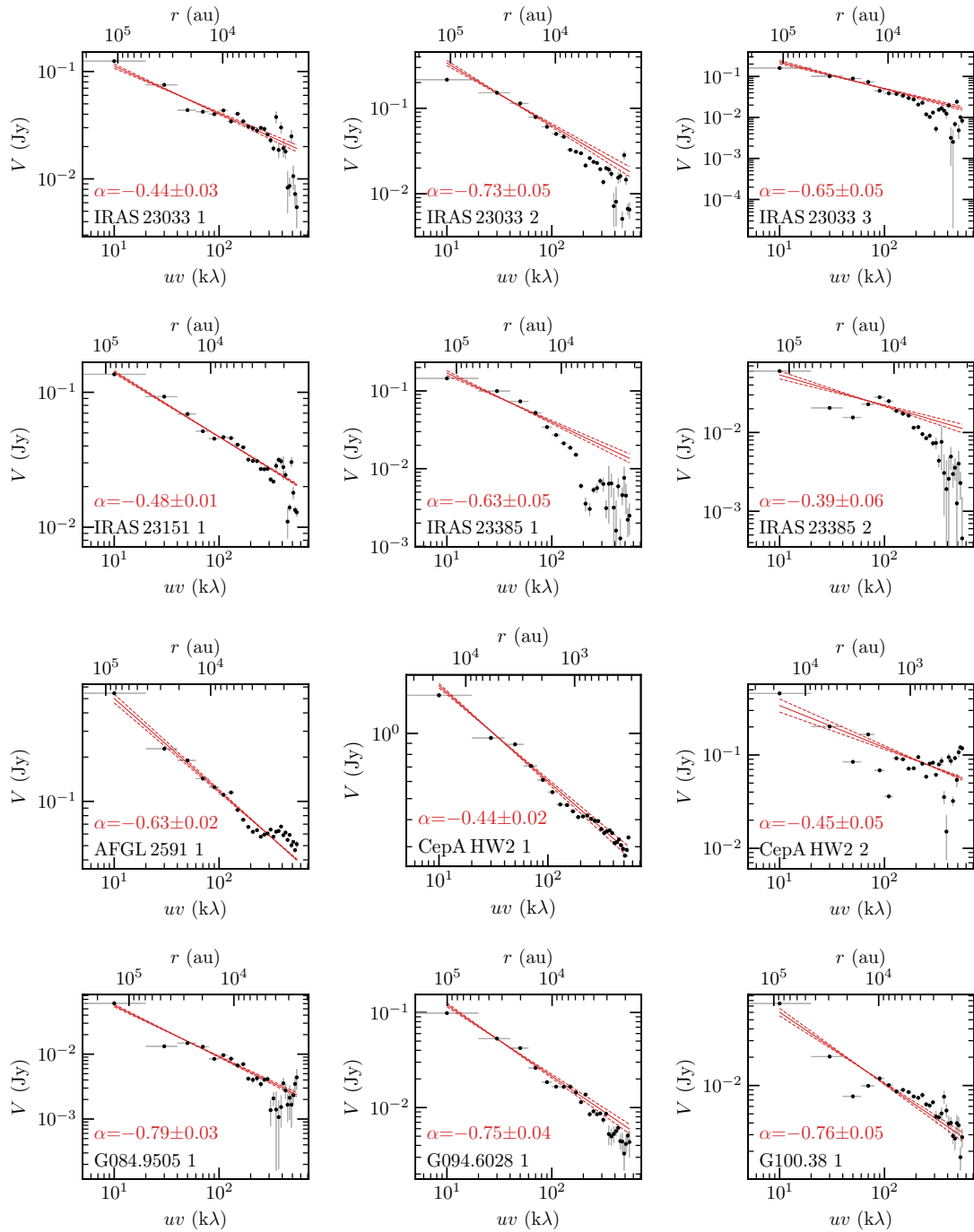


FIGURE 2.6: Radial 1.37 mm continuum visibility profiles of the 22 cores. The black data points show the radial profile of the averaged complex visibilities of the 1.37 mm continuum as a function of uv distance (bottom x-axis) and of the corresponding linear scale (top x-axis). The linear fit and the $\pm 1\sigma$ uncertainties are indicated by the solid and dashed red line, respectively.

For each core position, the phase center is shifted to this location. The remaining cores within a region are fitted as a point source + circular Gaussian (to account both for the compact and the extended emission) and subtracted using the UV_FIT task in GILDAS. With this approach, the blending of nearby cores in the visibility profiles within a single region can be minimized. The azimuthally averaged complex visibilities, computed using the UVAMP task in MIRIAD (Sault et al. 1995), are binned in steps of 20 kλ. The radial visibility profiles are shown in Fig. 2.6. The NOEMA baselines range from $\sim 20 - 800$ m corresponding to spatial scales of

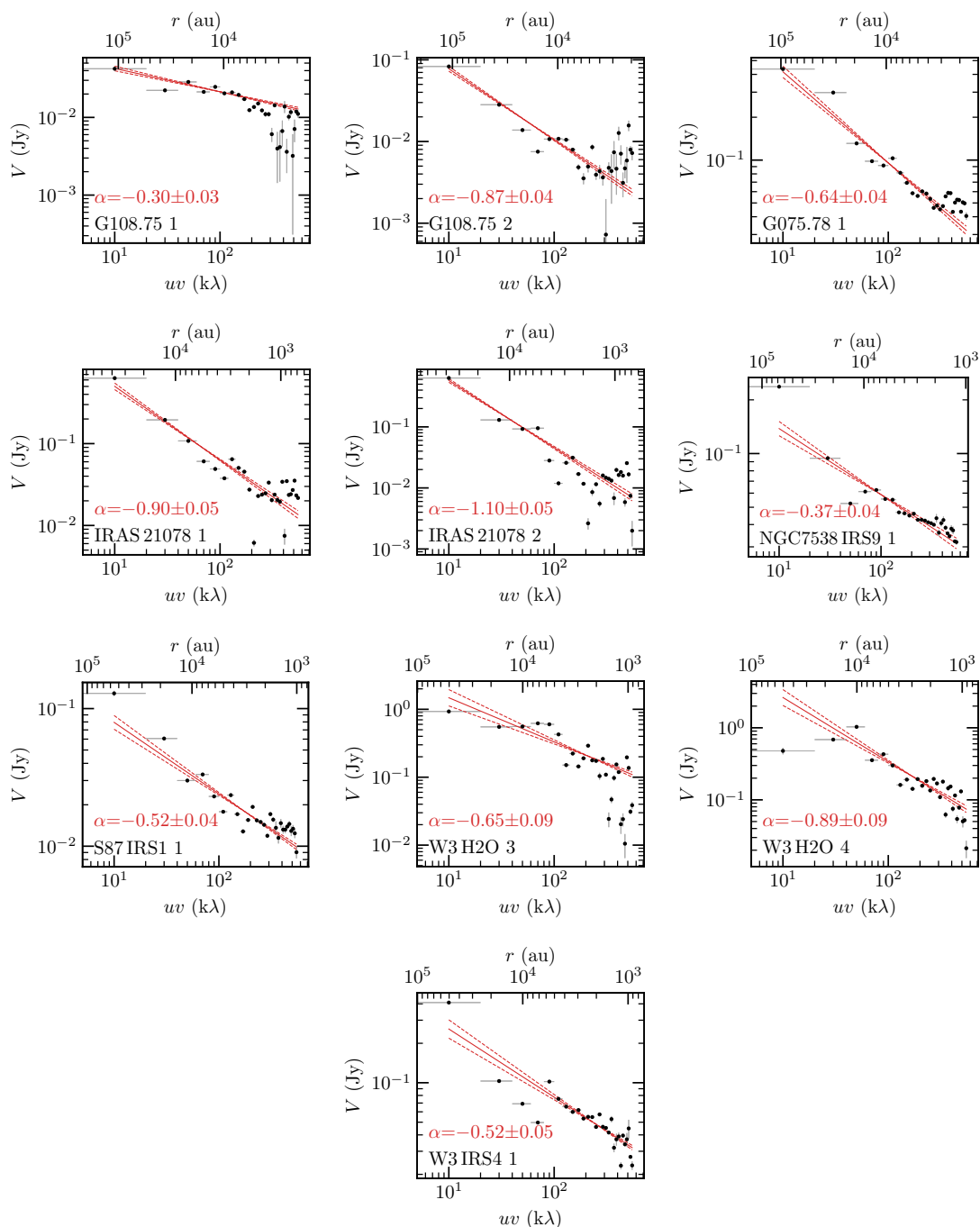


FIGURE 2.6 (cont.): Radial 1.37 mm continuum visibility profiles of the 22 cores. The black data points show the radial profile of the averaged complex visibilities of the 1.37 mm continuum as a function of uv distance (bottom x-axis) and of the corresponding linear scale (top x-axis). The linear fit and the $\pm 1\sigma$ uncertainties are indicated by the solid and dashed red line, respectively.

$\sim 10^3 - 10^5$ au at distances of a few kpc. We apply a power-law fit to the data in order to derive the visibility power-law index α . The density power-law index p is calculated according to Eq. (2.3), taking into account the temperature power-law index q derived in Sect. 2.3.2. The results for α and p for all cores are summarized in Table 2.3.

Most of the visibility profiles (Fig. 2.6) can be described by a single power-law. The higher scatter at large uv distances is due to the fact that less visibility measurements are available at long baselines. For IRAS 23385, the visibility profiles of core 1 and 2 do not follow a simple

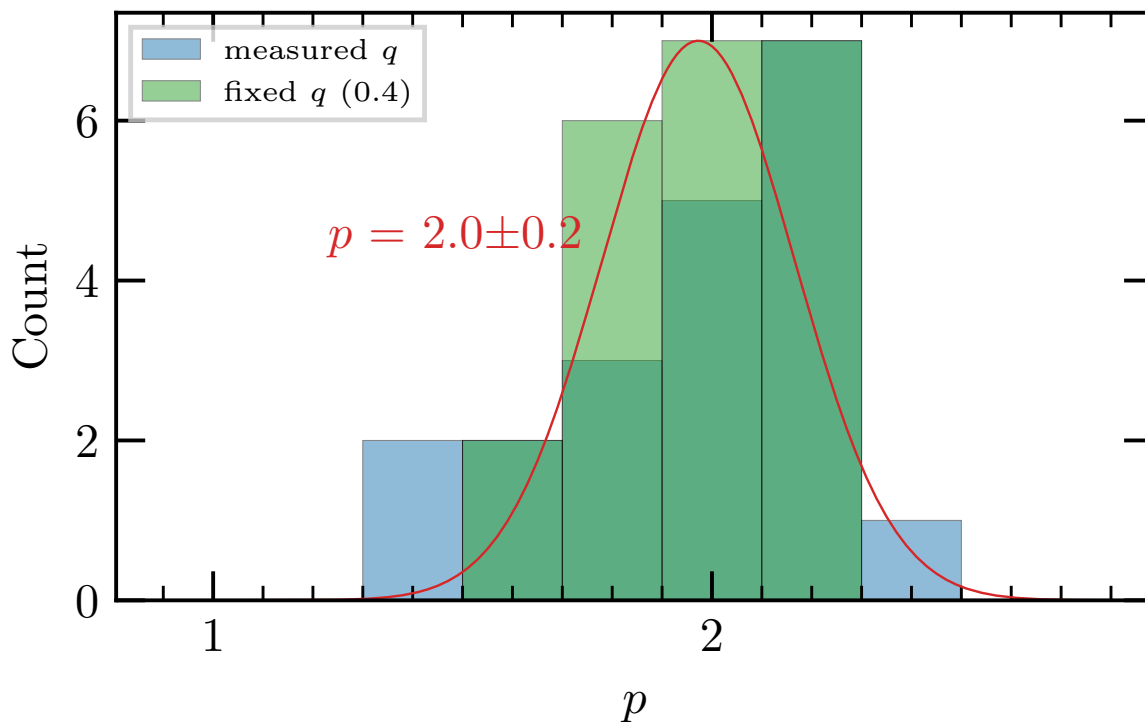


FIGURE 2.7: Histogram of the density power-law index p . The density power-law index derived with the measured values of q for each core are shown in blue. In green, the results for p calculated with a fixed temperature index ($q = 0.4$) for all cores are shown. The red line shows a Gaussian fit to the green histogram.

power-law. Toward smaller spatial scales ($< 10^4$ au), the profiles are steeper. This could be due to the fact that even though the contribution of nearby cores is minimized by subtracting a point source + circular Gaussian, in the case of IRAS 23385, it is not possible to clearly distinguish the contribution of both cores, which are embedded within a common dust envelope.

The histogram of the density index p is shown in Fig. 2.7. Using the observationally derived values of q , the power-law index ranges from 1.4 – 2.4. Fixing the temperature power-law index q to the mean value of 0.4 and calculating p with the results from the uv -analysis, the distribution of p gets narrower, peaking at $p = 2.0 - 2.1$. A Gaussian fit to this distribution yields a mean of $p = 2.0 \pm 0.2$. The results of the derived physical structure of these 22 cores are discussed in detail in Sect. 2.6.1.

TABLE 2.3: Physical structure (Sect. 2.3) and chemical timescales (Sect. 2.5) of the cores in the CORE sample. The density power-law index p is calculated according to Eq. (2.3). The core mass M_{core} is calculated according to Eq. (1.49). The estimate of the chemical timescale τ_{chem} is explained in detail in Sect. 2.5.2. Fit results for r_{in} , r_{out} , $T_{\text{kin}}(r_{\text{in}})$, and q derived from either the H_2CO or CH_3CN radial temperature profiles (Fig. 2.4) are indicated by either a \dagger or $*$, respectively.

Region + Number	r_{in} (au)	r_{out} (au)	$T_{\text{kin}}(r_{\text{in}})$ (K)	q	α	p	M_{core} (M_{\odot})	τ_{chem} (yr)
IRAS 23033 1	1 837	5 720	114.9 \pm 8.2	0.34 \pm 0.11 \dagger	-0.44 \pm 0.03	2.22 \pm 0.11	6.06 \pm 1.29	3.4(4)–9.8(4)
IRAS 23033 2	1 837	4 767	167.2 \pm 6.6	0.48 \pm 0.20 \dagger	-0.73 \pm 0.05	1.79 \pm 0.21	7.81 \pm 1.59	1.8(4)
IRAS 23033 3	1 837	3 813	160.8 \pm 8.0	0.96 \pm 0.07 \dagger	-0.65 \pm 0.05	1.39 \pm 0.09	5.22 \pm 1.08	1.9(4)
IRAS 23151 1	1 392	2 926	129.2 \pm 4.7	0.27 \pm 0.11 $*$	-0.48 \pm 0.01	2.25 \pm 0.11	3.28 \pm 0.67	1.9(4)–8.4(4)
IRAS 23385 1	2 299	4 345	239.5 \pm 12.1	0.14 \pm 0.05 \dagger	-0.63 \pm 0.05	2.23 \pm 0.07	4.43 \pm 0.92	4.9(4)
IRAS 23385 2	2 299	4 345	226.0 \pm 2.3	0.21 \pm 0.04 \dagger	-0.39 \pm 0.06	2.40 \pm 0.07	2.30 \pm 0.46	9.5(4)
AFGL 2591 1	1 394	2 926	159.9 \pm 6.8	0.25 \pm 0.08 $*$	-0.63 \pm 0.02	2.12 \pm 0.08	7.43 \pm 1.52	8.4(4)
CepA HW2 1	289	931	238.2 \pm 11.4	0.31 \pm 0.02 $*$	-0.44 \pm 0.02	2.25 \pm 0.03	1.24 \pm 0.26	8.4(4)
CepA HW2 2	289	776	170.5 \pm 13.3	0.56 \pm 0.10 $*$	-0.45 \pm 0.05	1.99 \pm 0.11	0.28 \pm 0.06	1.9(4)–8.8(4)
G084.9505 1	2 273	6 097	169.0 \pm 0.8	1.38 \pm 0.05 \dagger	-0.79 \pm 0.03	0.83 \pm 0.06	1.67 \pm 0.33	1.7(4)
G094.6028 1	1 584	4 434	183.8 \pm 45.4	1.48 \pm 0.27 \dagger	-0.75 \pm 0.04	0.77 \pm 0.27	2.35 \pm 0.76	5.7(4)–8.4(4)
G100.38 1	1 452	3 880	68.2 \pm 0.7	0.41 \pm 0.22 \dagger	-0.76 \pm 0.05	1.83 \pm 0.23	1.85 \pm 0.37	8.4(4)
G108.75 1	2 044	4 767	111.2 \pm 8.2	0.56 \pm 0.09 \dagger	-0.30 \pm 0.03	2.14 \pm 0.09	2.58 \pm 0.55	2.0(4)
G108.75 2	2 044	5 720	82.9 \pm 2.6	0.23 \pm 0.02 \dagger	-0.87 \pm 0.04	1.90 \pm 0.04	3.73 \pm 0.76	1.1(5)
G075.78 1	1 642	5 055	176.8 \pm 0.3	0.29 \pm 0.05 $*$	-0.64 \pm 0.04	2.07 \pm 0.06	9.21 \pm 1.84	8.4(4)
IRAS 21078 1	612	1 330	135.5 \pm 0.2	0.43 \pm 0.05 $*$	-0.90 \pm 0.05	1.67 \pm 0.07	1.60 \pm 0.32	5.5(4)–9.2(4)
IRAS 21078 2	612	1 330	121.9 \pm 3.4	0.59 \pm 0.01 $*$	-1.10 \pm 0.05	1.31 \pm 0.05	1.70 \pm 0.34	4.9(4)
NGC7538 IRS9 1	1 114	2 394	200.5 \pm 0.9	0.38 \pm 0.04 $*$	-0.37 \pm 0.04	2.25 \pm 0.06	1.60 \pm 0.32	8.4(4)
S87 IRS1 1	1 005	2 439	112.0 \pm 5.2	0.45 \pm 0.07 \dagger	-0.52 \pm 0.04	2.03 \pm 0.08	2.15 \pm 0.44	5.9(4)
W3 H2O 3	770	1 774	176.6 \pm 10.9	0.59 \pm 0.06 $*$	-0.65 \pm 0.09	1.76 \pm 0.11	11.61 \pm 2.44	8.4(4)
W3 H2O 4	770	1 774	166.4 \pm 9.0	0.45 \pm 0.03 $*$	-0.89 \pm 0.09	1.66 \pm 0.09	11.22 \pm 2.33	8.6(4)
W3 IRS4 1	780	1 774	173.0 \pm 15.4	0.54 \pm 0.08 $*$	-0.52 \pm 0.05	1.94 \pm 0.09	1.14 \pm 0.25	2.0(4)–8.6(4)

Notes. a(b) = $a \times 10^b$.

2.4 Molecular gas content

In this section, we analyze the chemical content of the molecular gas toward the 18 CORE HMS-FRs by studying the molecular column densities derived toward the 120 positions. The column density of molecular hydrogen $N(\text{H}_2)$ is derived from the 1.37 mm dust continuum emission (Sect. 2.4.1). In addition, molecular column densities are derived from the merged spectral line data with XCLASS by fitting the emission lines assuming LTE conditions (Sect 2.4.2). Spectra extracted toward the selected positions are shown in Fig. A.3. In total, we consider 11 species among a total of 16 isotopologues that are commonly detected within the 4 GHz spectral bandwidth of the broadband WideX correlator: ^{13}CO , C^{18}O , SO , OCS , SO_2 , DCN , H_2CO , HNCO , HC_3N , CH_3OH , CH_3CN . A spectral resolution of 3 km s^{-1} is not sufficient to study the line widths and kinematic properties in detail, but sufficient to derive molecular column densities, N .

2.4.1 Molecular hydrogen and core mass estimate

The beam-convolved molecular hydrogen column density $N(\text{H}_2)$ toward all 120 positions and mass calculation of the 22 cores M_{core} can be derived according to Eqs. (1.48) and (1.49), respectively, from the continuum intensity I_ν assuming that the emission is optically thin (Hildebrand 1983). We assume a gas-to-dust mass ratio $\eta = 150$ ($\eta = \frac{M_{\text{gas}}}{M_{\text{H}}} / \frac{M_{\text{dust}}}{M_{\text{H}}}$, with $\frac{M_{\text{gas}}}{M_{\text{H}}} = 1.4$ and $\frac{M_{\text{dust}}}{M_{\text{H}}} = 0.0091$; see Table 1.4 and 23.1 in Draine 2011, respectively), mean molecular weight $\mu = 2.8$ (Kauffmann et al. 2008), and dust opacity $\kappa_\nu = 0.9 \text{ cm}^2 \text{ g}^{-1}$ for dust grains with a thin icy mantle at a gas density of 10^6 cm^{-3} at 1.3 mm (Ossenkopf & Henning 1994).

We use T_{kin} for the temperature, T , in the Planck function taken from the thermometers H_2CO and CH_3CN , assuming LTE conditions ($T_{\text{kin}} \approx T_{\text{rot}}$). If the spectrum is extracted from a core position, T_{kin} is taken from the radial temperature fit described in Sect. 2.3.2 with $T = T_{\text{kin}}(r_{\text{in}})$ (see Table 2.3). If the spectrum is extracted from a position not corresponding to a core, the kinetic temperature is computed from $T_{\text{rot}}(\text{CH}_3\text{CN})$ if detected or from $T_{\text{rot}}(\text{H}_2\text{CO})$ otherwise. If there is no temperature tracer detected toward the position, we adopt a lower limit of $T_{\text{kin}} = 20 \pm 10 \text{ K}$, as the lowest derived rotation temperatures range between 10–30 K (Table A.1). In order to validate that the assumption of optically thin dust emission is valid, the continuum optical depth, τ_ν^{cont} , is computed for each position according to Eq. (1.47).

The kinetic temperature, T_{kin} , molecular hydrogen column density, $N(\text{H}_2)$, and continuum optical depth, τ_ν^{cont} , are listed in Table A.1 for all 120 positions. The uncertainties of $N(\text{H}_2)$ and M_{core} are calculated based on the assumption of Gaussian error propagation and include the uncertainty of the continuum intensity, with an estimated 20% flux calibration uncertainty (Beuther et al. 2018a) and uncertainty of the derived rotation temperature, ΔT_{kin} (listed in Table A.1). The optical depth, τ_ν^{cont} , is $\ll 1$ toward most positions, so optically thin dust emission can be assumed here and the H_2 column density and core mass calculation provide reliable results. The only exceptions with $\tau_\nu^{\text{cont}} > 1$ are positions 1 and 2 of the W3 H₂O region, which corresponds to the W3 OH UCHII region (see also Ahmadi et al. 2018). The molecular hydrogen column density $N(\text{H}_2)$ has a mean value of $1.5 \times 10^{24} \text{ cm}^{-2}$, ranging from $2.7 \times 10^{22} \text{ cm}^{-2}$ up to $2.8 \times 10^{25} \text{ cm}^{-2}$. The core masses, M_{core} , are listed in Table 2.3. We find a mean core mass of $4.1 M_\odot$ in a range between $0.3 M_\odot$ and $11.6 M_\odot$. As discussed previously, due to missing short-spacing information, both $N(\text{H}_2)$ and M_{core} should be considered as lower limits. However, the high core masses indicate that they are harboring protostars that will eventually end up as massive stars.

2.4.2 Spectral line modeling with XCLASS

We use the spectral line data of the CORE project to derive molecular column densities of 11 different species using the XCLASS software. A description of the XCLASS software is presented in Sect. 2.3.2. Using the `myXCLASSFit` function, individual spectra are fitted species by species with one emission component to derive the molecular column density, N .

A spectrum is extracted from the merged spectral line data for each position listed in Table A.1. The noise σ_{line} in each spectrum is computed in a line-free range from 219.00 GHz to 219.13 GHz. Compared to the average map noise $\sigma_{\text{line, map}}$ listed in Table 2.1, the noise in each spectrum σ_{line} may have higher or lower noise values since the noise distribution is not uniform within the primary beam. The systemic velocity v_{LSR} is determined by fitting the $\text{C}^{18}\text{O } 2 - 1$ transition and may differ from the global v_{LSR} listed in Table 2.1 due to velocity gradients in the region, hence, it allows us to employ a narrow parameter range for v_{off} and so fitting strong nearby emission lines is avoided. The systemic velocity v_{LSR} and noise σ_{line} are listed in Table A.1 for each position.

All molecules and their corresponding transitions that are fitted with XCLASS are listed in Table A.2. Lines which are blended with transitions of other detected species (at a resolution of 3 km s^{-1}) are also listed, but excluded from the fit. For most molecules, only the rotational ground-state level $v = 0$ are detected in our spectral setup. For SO_2 and HC_3N vibrationally excited levels ($v_x > 0$) are present and for CH_3OH torsionally excited lines are detected ($v_t = 1$). The following species for which we observe multiple isotopologues are fitted simultaneously: OCS and O^{13}CS ; SO_2 and $^{34}\text{SO}_2$; H_2CO , and H_2^{13}CO ; HC_3N and HCC^{13}CN ; CH_3CN and $\text{CH}_3^{13}\text{CN}$. The isotopologue ratios are summarized in Table 2.1 and are calculated either from Wilson & Rood (1994) ($^{12}\text{C}/^{13}\text{C} \approx 7.5 \times d_{\text{gal}} + 7.6$) or taken from references within ($^{32}\text{S}/^{34}\text{S} \approx 22$). The uncertainties of these isotopic ratios are high due to a large scatter of the data points. However, we do not observe a sufficient number of strong isotopic lines to measure it more precisely. We did not fit ^{13}CO and C^{18}O simultaneously because the $^{13}\text{CO } 2 - 1$ line has a high optical depth (see Table A.2).

We use an algorithm chain with the Genetic and Levenberg-Marquardt (LM) methods and to estimate the uncertainties of the fit parameters, we used the MCMC error estimation algorithm afterward. The following criteria are applied to the fitted model spectrum and column density, $N_{-\Delta N_{\text{low}}}^{+\Delta N_{\text{upp}}}$, of each species in order to determine and exclude bad fits:

- model spectra with a peak intensity $< 3\sigma_{\text{line}}$
- the upper error of the column density ΔN_{upp} is converging toward high values ($\Delta N_{\text{upp}} > 10 \times N$)
- the lower error of the column density is not constrained $\Delta N_{\text{low}} = 0 \text{ cm}^{-2}$

With these three criteria, weak and unresolved lines are automatically discarded and we consider the best-fit value of N only as an upper limit.

The column densities, N , for all species fitted with XCLASS and their uncertainties derived with the MCMC error estimation algorithm are summarized in Tables A.3 and A.4 for all positions. Histograms of the logarithmic column density distributions including $N(\text{H}_2)$ are shown in Fig. 2.8, with the mean and standard variation of the column density noted in each panel (upper limits are not included). The logarithmic bin width is set to 0.5. Separate histograms of the core and non-core populations are shown in the same panels. However, as discussed in Sect. 2.2, for the spectral line data, we have short-spacing information, while we do not have this for the continuum data, hence we systematically underestimate the H_2 column density.

There are species with a distribution having a clear column density peak (e.g., H_2 , ^{13}CO , C^{18}O , SO , DCN , H_2CO , HNCO). Other species have a double-peaked distribution with a

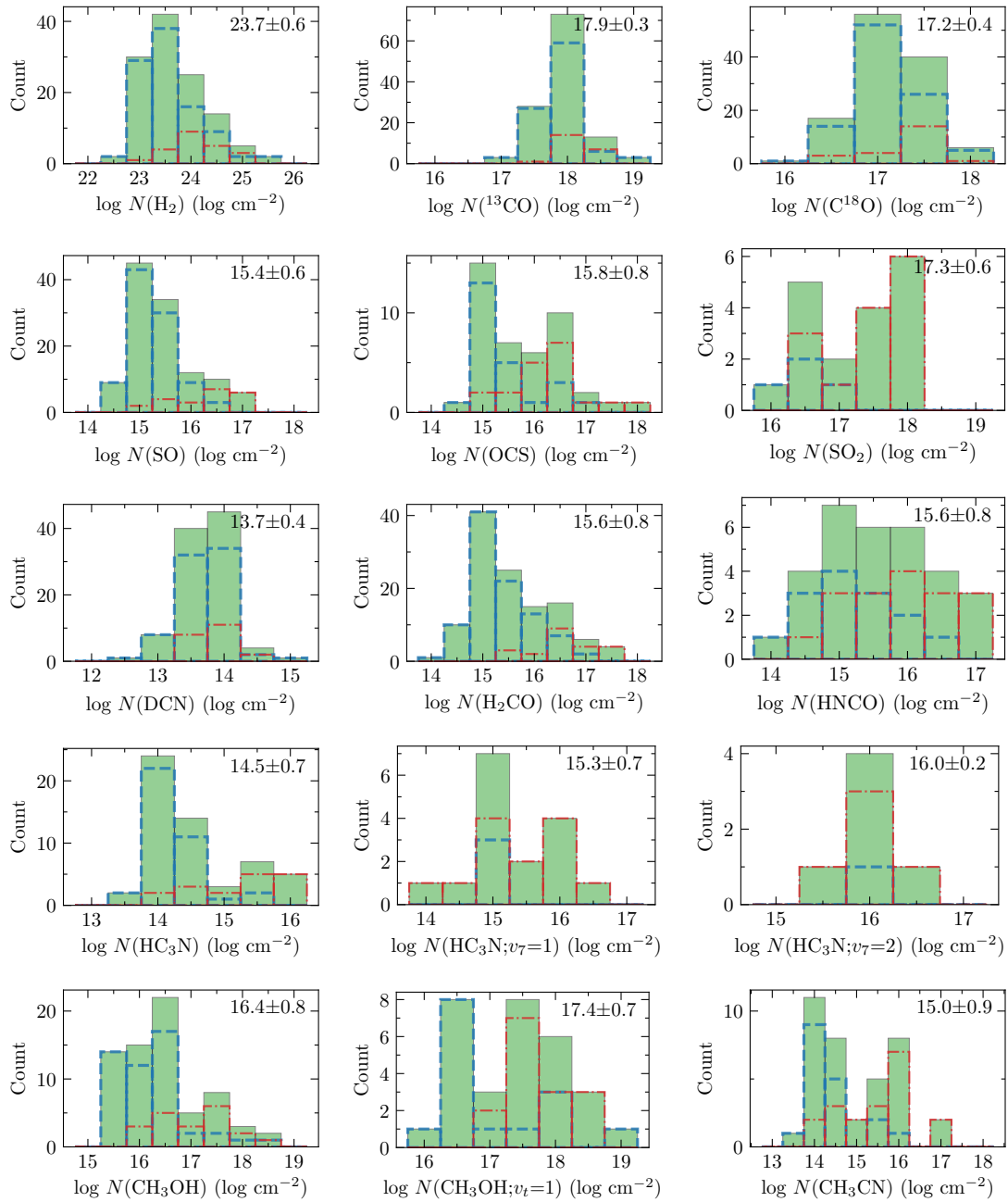


FIGURE 2.8: Column density histograms. The molecular hydrogen (H_2) column density is derived from the 1.37 mm continuum emission (Sect. 2.4.1) and the remaining molecular column densities are derived with XCLASS (Sect. 2.4.2). Column density histograms of all 120 positions are shown in green bars (upper limits are not included). Separate column density histograms of the core and the remaining positions are indicated by the dash-dotted red and dashed blue lines, respectively.

clear separation between the core and the remaining positions (e.g., OCS, HC_3N , CH_3OH , $\text{CH}_3\text{OH};v_1=1$, and CH_3CN). In these cases, the column density is enhanced by a factor of $\sim 10 - 100$ toward the core positions. There are not enough data points for the SO_2 , $\text{HC}_3\text{N};v_7=1$, $\text{HC}_3\text{N};v_7=2$ to draw any conclusions about the distribution, however, they are detected mostly in the densest regions toward core positions. In general, high column densities are found toward core positions and low column densities are found toward the remaining positions.

To account for the fact that toward the core positions the column density is expected to be higher in a higher density region, we show relative abundance $N(\text{X})/N(\text{C}^{18}\text{O})$ histograms in

Fig. A.2 (upper limits are not included). Assuming that both species trace the same emission region, the relative abundances are independent of the absolute column density value, which differ from region to region and from core to core. Normalized to $N(\text{C}^{18}\text{O})$, most species have a single-peaked distribution. Exceptions are OCS, HNC, HC_3N , CH_3OH , and CH_3CN with double-peaked distributions indicating that high temperature gas-phase chemistry has a big impact on these N-bearing molecules by increasing their abundances. However, in general there is still a clear difference between core positions (high abundance) and non-core positions (low abundance). The fact that larger molecules have a clearer distinction between the core and non-core positions, while for simpler species it is less obvious (e.g., ^{13}CO and DCN), hints that the emission of COMs is associated with the cores while simple molecules are abundant in the envelope as well. The difference of the core and the remaining positions indicates that the high densities and possible energetic processes around the protostars have a strong impact on the molecular abundances in the gas-phase (e.g., through protostellar outflows, shocks, disk accretion, and strong radiation from the protostars). Correlations of the derived column densities are discussed in Sect. 2.6.3.

Observed and XCLASS modeled spectra are shown in Fig. A.3 for all positions. The computed optical depth for all fitted lines as a function of rest-frequency is shown as well. Even though the sample was selected to be at a similar evolutionary stage (HMPO/HMC), the number of emission lines in the observed spectra vary from region to region, but also within a region. Typical hot core spectra are observed for the positions AFGL 2591 1, CepA HW2 1, G75.78 1, W3 H2O 1, and W3 H2O 2. Many weak emission features are detected in the spectra at a $\sim 2-3\sigma_{\text{line}}$ level originating from COMs. These COM emission features are difficult to fit as the transitions are weak, have similar upper energy levels E_u/k_B , and are blended at a spectral resolution of 3 km s^{-1} , so they were excluded from this analysis. A detailed study of the integrated line emission (including line stacking of weak COM emission lines) are subject to a future study. Fewer species are detected in spectra toward the non-core positions. In contrast to the line-rich sources, there are several sources that show only a handful of emission lines mainly from CO-isotopologues, SO, and H_2CO even toward the continuum peak positions. The line-poor regions are G139.9091, G138.2957, S87 IRS1, and S106. In the case of IRAS 23033, core 1 has a line-poor spectrum, whereas for core 2 and 3, which are embedded in a common envelope, significantly more emission lines are detected. These cores either could be at different evolutionary stages or they are embedded in an inhomogeneous local radiation field. The former can be investigated by applying a chemical model to the observed column densities and by estimating the chemical timescales of the regions. We investigate this possibility in Sect. 2.5.

The mean and maximum line optical depth, $\tau_{\text{mean}}^{\text{line}}$ and $\tau_{\text{max}}^{\text{line}}$, computed for each fitted transition with XCLASS are summarized in Table A.2. The ^{13}CO 2 – 1 transition has the highest mean optical depth with $\tau_{\text{mean}}^{\text{line}} = 1.5$, but for most other species and transitions, the mean line optical depth is < 1 , so the column density and temperature determination should be reliable, especially when multiple transitions of a molecule are fitted simultaneously. The mean optical depth of the H_2CO $3_{0,3} - 2_{0,2}$ transition is a factor of four higher than the remaining two transitions. When the $3_{0,3} - 2_{0,2}$ transition is optically thick, temperature estimates depending on the line ratios are difficult to determine with the remaining two optically thin lines as they have similar upper energy levels (68 K). In 23 out of the 118 spectra where H_2CO was detected and fitted with XCLASS, the calculated optical depth of the $3_{0,3} - 2_{0,2}$ transition is $\tau^{\text{line}} > 1$.

2.5 Physical-chemical modeling of the cores

The continuum data of the CORE sample show a large diversity in fragmentation properties (Beuther et al. 2018a) and our analysis (Sect. 2.4) demonstrates that the composition of the molecular gas varies within as well as between the regions: some have a rich plethora of molecular lines, while others have line-poor spectra. This diversity of physical and chemical properties could be explained by a number of reasons. Magnetic fields or different initial density structures could explain the variety in fragmentation properties (Beuther et al. 2018a). Different initial conditions in, for instance, the large scale kinematics and mass distribution might also have an effect on the molecular abundances. To investigate whether the observed variation of the physical and chemical properties of the cores may be due to the fact that they are at slightly different evolutionary stages, we model the chemical evolution of the 22 cores in the following.

2.5.1 MUSCLE setup

We apply a physical-chemical model (Sect. 1.3.3) to the physical properties and molecular column densities of each core determined from the CORE 1 mm observations in order to estimate chemical timescales. MUSCLE (MULTI Stage CLOUD code) has previously been successfully applied to the CORE pilot regions NGC7538 S and NGC7538 IRS1 (Feng et al. 2016) as well as the CORE region AFGL 2591 (Gieser et al. 2019). The model consists of a spherically symmetric physical structure. The temperature and density profiles of the cores are described by power-laws up to the outer radius, r_{out} , with index q and p (see Eqs. 2.1 and 2.2, respectively). At an inner radius, r_{in} , and further in, the density and temperature reach a constant value. We adopt 40 logarithmic grid points for the radial profiles.

On top of this static physical structure, the time-dependent gas-grain chemical network ALCHEMIC (Semenov et al. 2010) computes the abundances of hundreds of atomic and molecular species using thousands of reactions. A detailed description of MUSCLE can be found in Gerner et al. (2014, 2015). We adopt most of the model parameters from the AFGL 2591 case study described in Gieser et al. (2019), which yielded a good estimate of the chemical timescale of this hot core compared to literature estimates. A summary of the input parameters is listed in Table 2.4. In contrast to the AFGL 2591 case-study, we use a higher value for the cosmic ionization rate ζ_{CR} based on a study of multiple HMSFRs by Indriolo et al. (2015). These authors find that ζ_{CR} is constant at a Galactic radius > 5 kpc and with all the CORE regions at Galactic distances > 7 kpc (Table 2.1), we use a constant value of $1.8 \times 10^{-16} \text{ s}^{-1}$. By setting the extinction at r_{out} to $A_{\text{v}} = 10^{\text{mag}}$, the core is shielded from the interstellar radiation field.

For each of the 22 cores, we run a physical-chemical model with MUSCLE. The input are the H_2 column density (Sect. 2.4.1) and all molecular column densities derived with XCLASS (Sect. 2.4.2). The CO column density $N(\text{CO})$ is calculated from $N(\text{C}^{18}\text{O})$ as C^{18}O is less optically thick than ^{13}CO (Table A.2) and, hence, more reliably fitted in XCLASS. For each region, we calculate the $^{16}\text{O}/^{18}\text{O}$ isotopic ratio according to Wilson & Rood (1994): $^{16}\text{O}/^{18}\text{O} \approx 58.8d_{\text{gal}} + 37.1$. The $^{16}\text{O}/^{18}\text{O}$ ratio is listed in Table 2.1 for each region. For HC_3N and CH_3OH , we compute the mean column density of the rotational ground state and vibrationally or torsionally excited states for the MUSCLE input. Molecular column densities, for which only upper limits could be determined, are also set as upper limits in MUSCLE. We set the temperature structure of the model core to the observed temperature profile (Sect. 2.3.2) and use the density power-law index derived from the continuum visibility analysis (Sect. 2.3.3).

Two undetermined model parameters remain. We do not know, for one, how evolved the cores are, described by the chemical timescale, τ_{chem} , and second, what the initial chemical composition of the parental molecular cloud/clump was. Due to the fact that the CORE regions

TABLE 2.4: MUSCLE input parameters.

Parameter	Value
Radiation field:	
CR ionization rate ζ_{CR}	$1.8 \times 10^{-16} \text{ s}^{-1}$ (Indriolo et al. 2015)
Extinction A_{v} at r_{out}	10^{mag}
UV photodesorption yield	1×10^{-5} (Cruz-Diaz et al. 2016; Bertin et al. 2016)
Grain properties:	
Grain radius r_{g}	$0.1 \mu\text{m}$ (Gerin 2013)
Dust density ρ_{d}	3 g cm^{-3} (Gerin 2013)
Gas-to-dust mass ratio η	150 (Draine 2011)
Surface diffusivity $E_{\text{Diff}}/E_{\text{Bind}}$	0.4 (Cuppen et al. 2017)
Mantle composition	olivine (Gerin 2013)
Initial Chemical Abundances	
HMPO model	
best-fit IRDC stage (Table A.4 in Gerner et al. 2015)	
Inner radius r_{in}	12 700 au
Outer radius r_{out}	0.5 pc
Temperature T_{in} at r_{in}	11.3 K
Temperature power-law index q	0.0 (isothermal)
Density n_{in} at r_{in}	$1.4 \times 10^5 \text{ cm}^{-3}$
Density power-law index p	1.5
Stage lifetime τ_{IRDC}	16 500 yr
HMC model	
best-fit HMPO stage (Table A.5 in Gerner et al. 2015)	
Inner radius r_{in}	103 au
Outer radius r_{out}	0.5 pc
Temperature T_{in} at r_{in}	75.8 K
Temperature power-law index q	0.4
Density n_{in} at r_{in}	$1.5 \times 10^9 \text{ cm}^{-3}$
Density power-law index p	1.8
Stage lifetime τ_{HMPO}	32 000 yr
UCHII model	
best-fit HMC stage (Table A.6 in Gerner et al. 2015)	
Inner radius r_{in}	1 140 au
Outer radius r_{out}	0.5 pc
Temperature T_{in} at r_{in}	162.9 K
Temperature power-law index q	0.4
Density n_{in} at r_{in}	$1.3 \times 10^8 \text{ cm}^{-3}$
Density power-law index p	2.0
Stage lifetime τ_{HMC}	35 000 yr

are far more evolved than typical cold IRDCs and the physical structure of each model stage is static, we have to have a sensible initial condition for the chemical composition. The initial conditions we apply are based on a study of 59 HMSFRs using single-dish observations (Gerner et al. 2014, 2015). These HMSFRs were classified according to their evolutionary stage (IRDCs, HMPOs, HMCs, and UCHII regions) and a template was created from the average column densities for each evolutionary stage. The four template stages were modeled using MUSCLE to create average abundances for all molecular and atomic species and to estimate a mean chemical timescale of each evolutionary stage. The physical properties of their template IRDC, HMPO, and HMC model are summarized in Table 2.4. Following the convention by Gerner et al. (2014, 2015), the chemical timescale τ_{chem} is 0 yr when the gas density reaches 10^4 cm^{-3} .

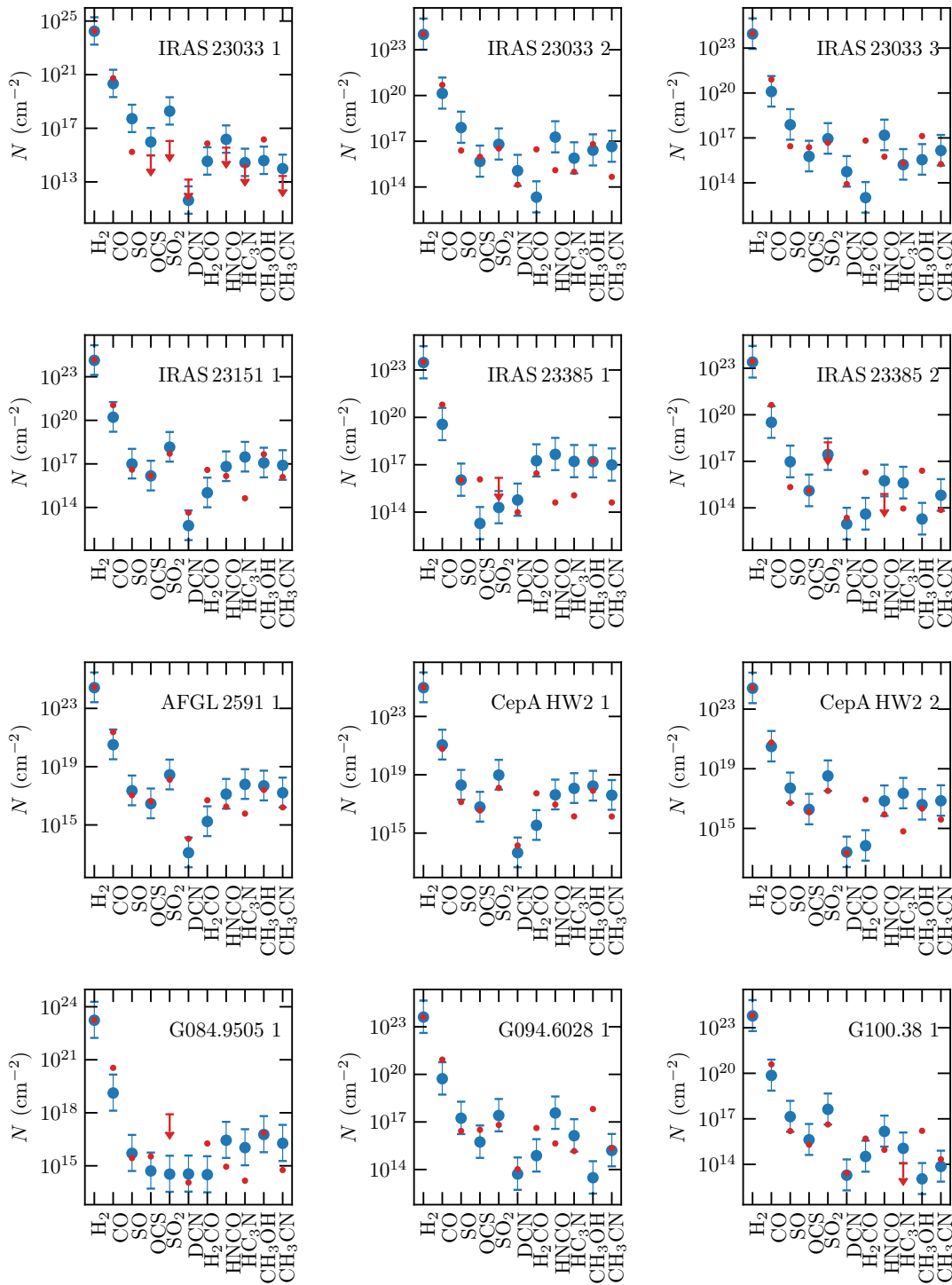


FIGURE 2.9: Comparison of the observed and modeled column densities of the 22 cores shown in red and blue, respectively. Upper limits are indicated by an arrow.

Based on the temperature profiles of the 22 cores, we can assume that they lie somewhere between the HMPO and early UCH_{II} stage, since the average temperatures around cores are too high to be classified as IRDCs ($T \sim 20$ K). There are a few known UCH_{II} regions with strong free-free emission at cm wavelengths resolved in the CORE data. In W3 H2O, the Western part (around position 1 and 2 in Fig. 2.3) is the UCH_{II} region W3 OH. In W3 IRS4, the Southern ring-like structure is a UCH_{II} region as well (Mottram et al. 2020). However, for the W3 OH UCH_{II} region we do not find a clear radial decreasing temperature profile and toward the W3 IRS4

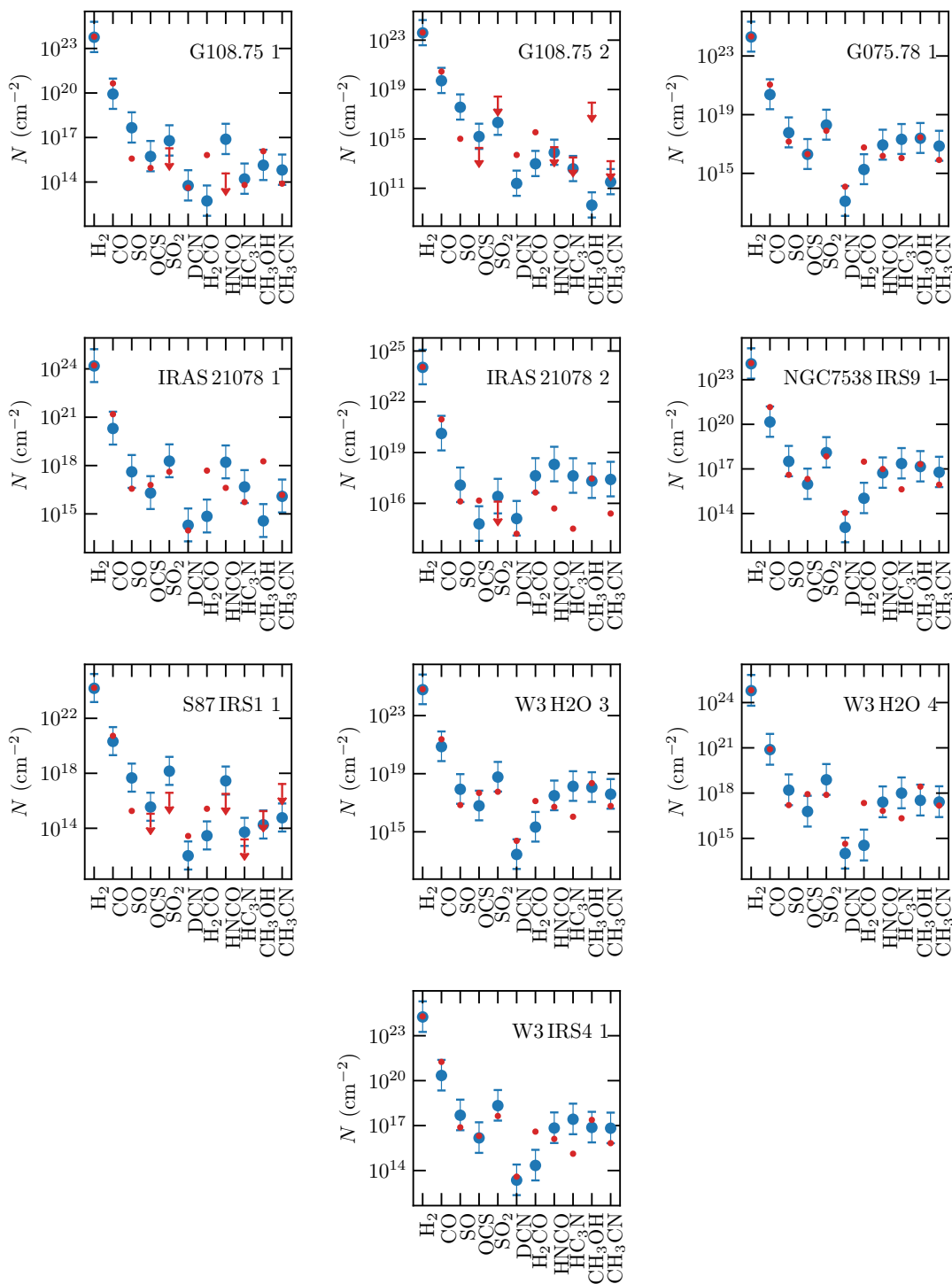


FIGURE 2.9 (cont.): Comparison of the observed and modeled column densities of the 22 cores shown in red and blue, respectively. Upper limits are indicated by an arrow.

UCHII region no H₂CO or CH₃CN line emission is detected at a $10\sigma_{\text{line, map}}$ level to estimate the kinetic temperature. The S106 region is a UCHII as well, for which we do not detect neither H₂CO nor CH₃CN emission around the compact core. This already suggests that toward this later stage, the molecular richness in these regions is decreased.

To test which initial chemical conditions (see Table 2.4) fit best to the observed molecular column densities, we model each of the 22 cores with initial abundances after an initial IRDC phase (referred to as the HMPO model), after an initial HMPO phase (referred to as the HMC

model), and after an initial HMC phase (referred to as the UCH_{II} model). While most cores are unlikely to have formed a strong UCH_{II} region yet, we include the UCH_{II} model, as the observations in Gerner et al. (2014, 2015) have large beam sizes (11'' and 29''), and UCH_{II} regions may have contamination from less evolved line-rich objects, which are blended into the single-pointing spectra. It is not our aim to classify the cores into these evolutionary stages, but to find sensible initial chemical conditions as an input for our physical-chemical modeling. For example, an evolved HMC that is more evolved than the template HMC from Gerner et al. (2015) would best be described best by the UCH_{II} model in our nomenclature.

For each model, the chemical evolution, τ_{model} , runs up to 100 000 yr in 100 logarithmic time steps. In each time step, the computed radial abundance profiles are converted into beam-convolved column densities with the beam size fixed to the mean synthesized beam of the observations. The best-fit model is determined by a minimum χ^2 analysis by comparing the modeled and observed column densities in each time step and for all three adopted initial condition models. Applying this physical-chemical model allows us to estimate the chemical timescale.

2.5.2 Chemical timescales

The best-fit chemical timescale τ_{chem} , χ^2 , and percentage of well-modeled molecules are summarized in Table A.5 for each initial abundance model and core. Gerner et al. (2014) estimated that chemical timescales are uncertain by a factor of between two and three and that the modeled column densities are uncertain by a factor of ten. But this depends on the number of modeled molecules, but also cores embedded in complex dynamic environments are harder to fit with our model. The chemical timescale τ_{chem} is the sum of the time of the initial abundance model and τ_{model} :

- HMPO model: $\tau_{\text{chem}} = \tau_{\text{IRDC}} + \tau_{\text{model}}$
- HMC model: $\tau_{\text{chem}} = \tau_{\text{IRDC}} + \tau_{\text{HMPO}} + \tau_{\text{model}}$
- UCH_{II} model: $\tau_{\text{chem}} = \tau_{\text{IRDC}} + \tau_{\text{HMPO}} + \tau_{\text{HMC}} + \tau_{\text{model}}$

For some cores, multiple initial condition models have a similarly low χ^2 (e.g., the HMPO and UCH_{II} model for core 1 in IRAS 23033). In these cases, we cannot constrain the chemical timescale well. Comparing the lowest χ^2 model with the remaining initial condition models, if the χ^2 difference is less than 5%, only chemical timescale ranges spanning over these models are further considered. Table 2.3 shows the chemical timescale τ_{chem} for models with a clear lowest χ^2 initial condition model or a time range in chemical timescale for cores with multiple best-fit initial condition models. The estimated chemical timescales τ_{chem} of the cores vary between $\sim 20\,000$ – $100\,000$ yr within the CORE sample with a mean of $\sim 60\,000$ yr. The youngest core being G084.9505 1 and the oldest core being G108.75 2.

A comparison of the best-fit modeled and observed column densities for all cores is shown in Fig. 2.9. For most cores, the model underestimates the H₂CO and CH₃OH column densities as compared to the observed values. This can be explained by the fact that the quasi-static model does not sufficiently take into account the warm-up stage from 30 – 80 K where surface chemistry on the dust grains plays an important role and where these two molecules are formed by subsequent hydrogenation of CO (Sect. 1.3). These discrepancies between modeled and observed H₂CO and CH₃OH column densities have already been noticed by Gerner et al. (2014) in their template HMPO stage modeled with MUSCLE. They explain that this is due to the fact that the formation route of H₂CO consists of grain-surface as well as gas-phase chemistry which are both time-dependent and not correctly implemented in the chemical models. This results in the over and underproduction of these species, which is also the case in our modeling results, shown in Fig. 2.9.

Large discrepancies between the modeled and observed column density exist also for the SO molecule for which the model overproduces the SO column density by a factor > 10 for many cores (e.g., IRAS 23033 core 1, 2, and 3). This overproduction in SO is seen in all three initial condition models, but in most cases, other modeled S-bearing species (OCS and SO₂) are modeled well. The applied initial chemical conditions based on the Gerner et al. (2015) models also included S-bearing species (SO, CS, and OCS). Their initial IRDC stage model started with elemental abundances and only H₂ in molecular form taken from the low metals set of Lee et al. (1998). But in order to fit the IRDC phase accurately, Gerner et al. (2015) had to increase the initial elemental S abundance from 8×10^{-8} to 8×10^{-7} (w.r.t. H). However, an overproduction of SO is also seen in their best-fit HMPO, HMC and UCH_{II} models. This might be connected to a poorly understood chemistry of the reactive SO molecule, as also in their models the remaining S-bearing species can be reproduced properly. In addition, as only one SO transition is covered in our spectral setup, which can typically be optically thick (Table A.2 and Fig. A.3), we may underestimate the observed SO column density. This might partially explain the differences between the modeled and observed SO column density.

With multiple cores resolved within a region, it is possible to study how the chemical timescale τ_{chem} varies across small spatial scales. In the IRAS 23033 region, core 1 seems to be more evolved ($\sim 30\,000 - 100\,000$ yr), even though the spectrum is line-poor (see Fig. A.3) compared to the spectra of core 2 and 3 which are embedded in a common envelope (see Fig. 2.3) and for which we estimate similar chemical timescales of $\sim 20\,000$ yr. Core 1 and 2 in CepA HW2 have a chemical timescale of $\sim 80\,000$ yr and $\sim 20\,000 - 90\,000$ yr, respectively. The cores are very close ($\sim 2\,300$ au), but within our sensitivity limit, these cores are not embedded in a common envelope, but have very steep density profiles ($p \gtrsim 2$). In IRAS 21078, core 1 and 2 have a chemical timescale of $\sim 60\,000 - 90\,000$ yr and $\sim 50\,000$ yr, respectively, suggesting a small age gradient. The cores are embedded within a common envelope and have small projected separations. Core 3 and 4 in W3 H2O have a chemical timescale of $\sim 90\,000$ yr and $\sim 20\,000 - 90\,000$ yr, respectively. In the IRAS 23385 region, core 1 is younger ($\sim 50\,000$ yr), while core 2 is estimated to be much older ($\sim 100\,000$ yr). In G108.75 a large difference between the chemical timescales of core 1 ($\sim 20\,000$ yr) and core 2 ($\sim 110\,000$ yr) is estimated. The cores have a separation of $\sim 20\,000$ au, but have the same systemic velocity (Table A.1). A strong external radiation field or complex dynamics could be the reason for this large chemical timescale difference.

One of the limitations of MUSCLE is that the physical structure (radial temperature and density profiles) is static within each evolutionary stage (IRDC, HMPO, HMC, and UCH_{II}). In reality, these properties do change on timescales smaller than the chemical timescales derived here; in addition, the dynamics (e.g., gas inflow) are important factors to consider. Currently, 3D time-dependent physical models in combination with a full chemical network are computationally expensive. Therefore, we use the approach of our quasi-static physical model by considering the four different evolutionary stages. More sophisticated physical-chemical models in the future are required to include 3D gas dynamics and the evolution of the density and temperature structure. In addition, a larger number of molecular column densities would better constrain the model parameter space (see Sect. 5).

2.6 Discussion

2.6.1 Physical structure of high-mass star-forming cores

Various methods were applied in the literature to observationally derive the density profiles of envelopes in HMSFRs (e.g., summarized in Table 6 in Gieser et al. 2019). Some of these studies

are based on observations with single-dish telescopes with beam sizes $> 10''$ tracing the clump scale envelope, while interferometric observations trace the core scale envelope. We selected studies in the literature for which the density structure was determined for a sample of cores or clumps and we extracted the typical sizes $\langle r \rangle$ from their studies. The results in comparison with our study are shown in Fig. 2.10. At scales of 1 pc down to 0.01 pc, it seems that the density index p lies between 1.7 and 2.0, which is close to the values inferred in low-mass star-forming regions (Motte & André 2001). To investigate this further, we observed the CORE regions with the NIKA2 instrument at the IRAM 30m telescope and an analysis of the density structure at clump scales will follow (Beuther et al. in preparation).

The observationally-derived density and temperature profiles ($q = 0.4 \pm 0.1$ and $p = 2.0 \pm 0.2$) are in agreement with theoretical studies of HMSF, but the physics of how massive stars form is still not fully understood. Currently, theoretical models propose the formation of high-mass stars through: a monolithic collapse of turbulent cores (McKee & Tan 2002, 2003); protostellar collisions and coalescence in dense clusters (Bonnell et al. 1998; Bonnell & Bate 2002); or competitive accretion in clusters (Bonnell et al. 2001; Smith et al. 2009; Hartmann et al. 2012; Murray & Chang 2012). The density and temperature structure are important parameters of the initial cloud and proceeding clump and core scales. For example, early star formation models by Shu (1977) and Shu et al. (1987) that model the gravitational collapse of an isothermal sphere find that $p = 2$ in the outer envelope and $p = 1.5$ in the inner region where the gas is free-falling onto the central region. McLaughlin & Pudritz (1996, 1997) used

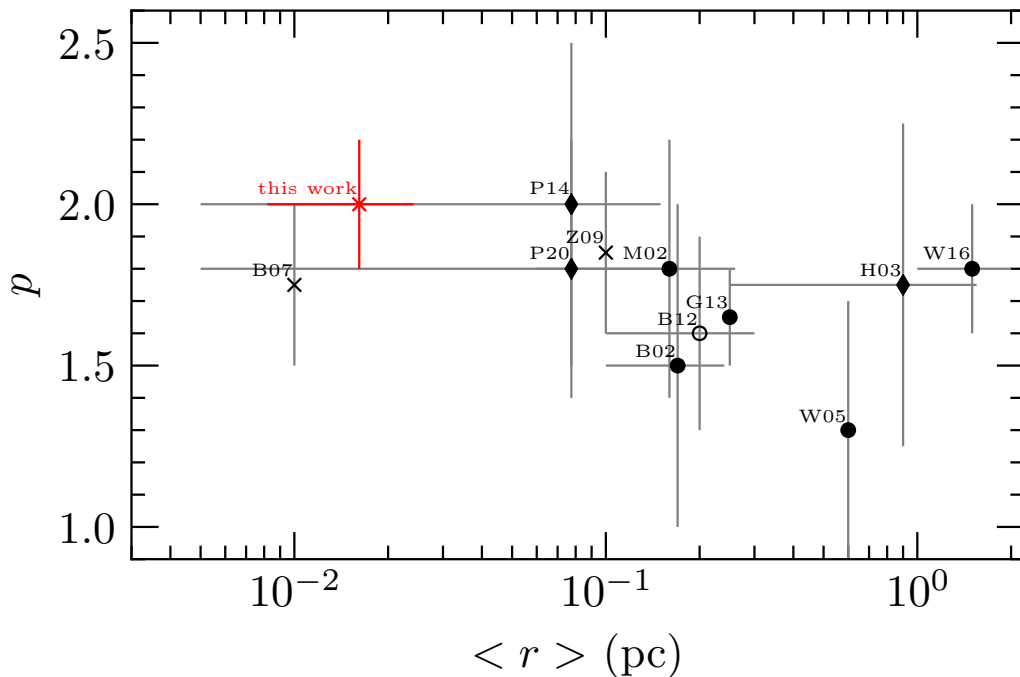


FIGURE 2.10: Literature comparison of the density power-law index p at different spatial scales, $\langle r \rangle$. Studies based on interferometric observations are marked by a “×”, (sub)mm single-dish observations by a “●”, multi-wavelength observations by a “◆”, and mid-infrared observations by a “○”.

References. M02: Mueller et al. (2002); B02: Beuther et al. (2002a); H03: Hatchell & van der Tak (2003); W05: Williams et al. (2005); B07: Beuther et al. (2007b); Z09: Zhang et al. (2009); B12: Butler & Tan (2012); G13: Giannetti et al. (2013); P14: Palau et al. (2014); W16: Wyrowski et al. (2016); P20: Palau et al. (2021).

a logatropic equation of state and a non-isothermal sphere and find that at an initial density profile of $p = 1$, the profile steepens to $p = 1.5$ after the collapse. In the turbulent core model by McKee & Tan (2002, 2003) the authors assume $p = 1.5$ based on observational constraints. In Bonnell et al. (1998) the density profile in the outer region has the form $p = 2$ and a shallower, near-uniform profile in the central region. Murray & Chang (2012) explore their models by varying p from 0 (uniform), 1, and 2 (isothermal).

The density structure is important for the physical and chemical evolution of HMSFRs. It is therefore important to quantify the initial density profile on cloud to clump and cores scales and how it changes with time. While theoretical models usually do not predict, but rather assume a given density profile, observations of HMSFRs on different scales can help to narrow down the parameter space (see Fig. 2.10). Hydrodynamic simulations reported by Chen et al. (2021) investigate how changes of p in giant molecular clouds with an initial radius of 20 pc affect massive star cluster formation. They find that for steep density profiles, $p = 2$, there is a centrally concentrated cluster, while for shallower profiles, hierarchical fragmentation occurs. Hydrodynamic simulations from Girichidis et al. (2011) show that massive protostars form only in clouds with a density index of $p = 1.5$ or $p = 2.0$, while for uniform or Bonnor-Ebert-like profiles, a large fraction of low-mass stars form. The authors found that turbulence and the initial density profile are important aspects for the evolution of the cloud and the formation of clusters.

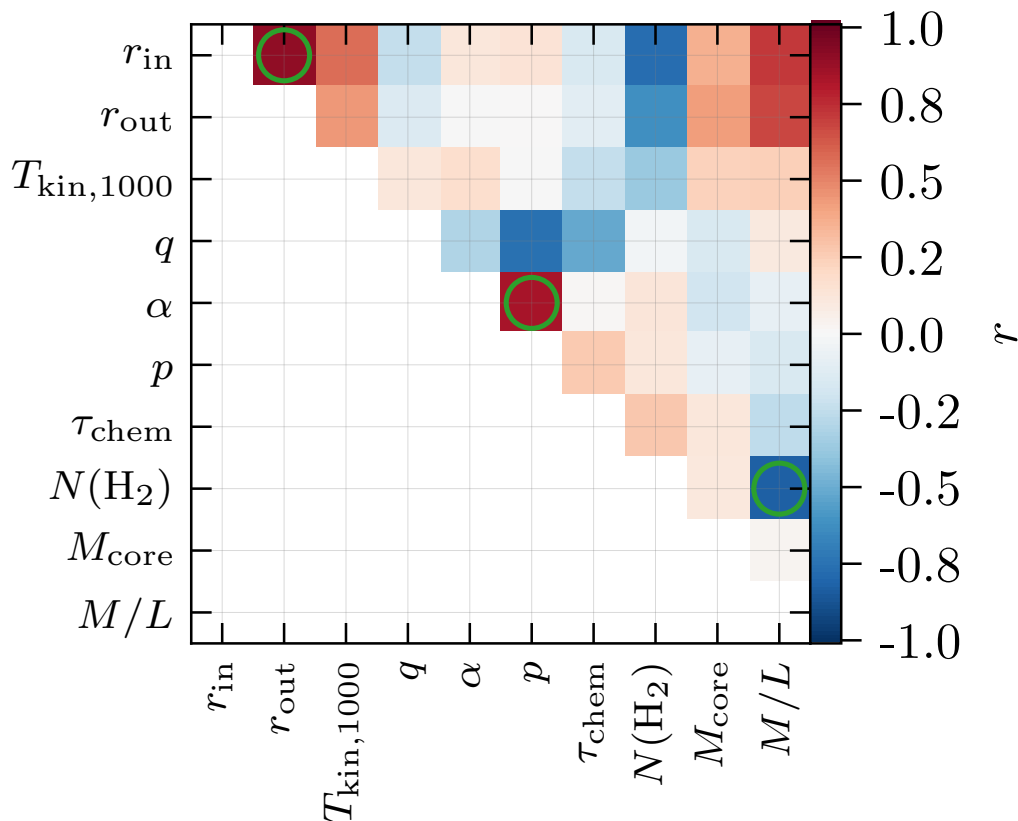


FIGURE 2.11: Spearman correlation coefficient r for the derived physical and chemical core parameters listed in Table 2.3. Values higher than 0.8 are marked by a green circle.

We study the correlations of all core properties shown in Table 2.3 using the Spearman correlation coefficient r . This statistical tool can be used to check if two data sets have a positive correlation ($r = 1$), negative correlation ($r = -1$), or no correlation ($r = 0$). We assume that

a high correlation exists if $r > 0.8$. For example, Feng et al. (2020) finds a negative correlation for the H_2 column density and dust temperature for cold high-mass clumps using the Spearman correlation coefficient, r . A big advantage compared to the Pearson correlation coefficient is that linear, as well as nonlinear, correlations are considered in the calculation of r . In addition, we add the M/L ratio of the region listed in Table 1 in Beuther et al. (2018a) as a parameter for each core. However, the interpretation is difficult as multiple cores within a region have the same M/L ratio. A mean chemical timescale is used in the computation of r for cores for which only a time range can be estimated (Table 2.3).

The results for the correlation coefficient, r , are shown in Fig. 2.11, where all pairs with a correlation > 0.8 are highlighted. Unfortunately, a small sample of only 22 cores does not allow us to find many strong correlations. Observations of many HMSFRs at core scales are required to study these relations in a better statistical way, which will be possible, for example, with the ALMAGAL survey, an ongoing ALMA large program observing more than 1 000 HMSFRs. A high correlation is found between the inner and outer radius, which is due to the fact that we are resolution-limited and the regions are located at different distances. The correlation between p and α is due to Eq. (2.3). However, we find a strong negative correlation between the M/L ratio and the H_2 column density of the cores, so more evolved cores have a higher beam-convolved H_2 column density. The M/L ratio, proposed to be a good tracer of the evolutionary stage, is investigated in the following section.

2.6.2 Mass-to-luminosity ratio as a tracer of evolutionary trends

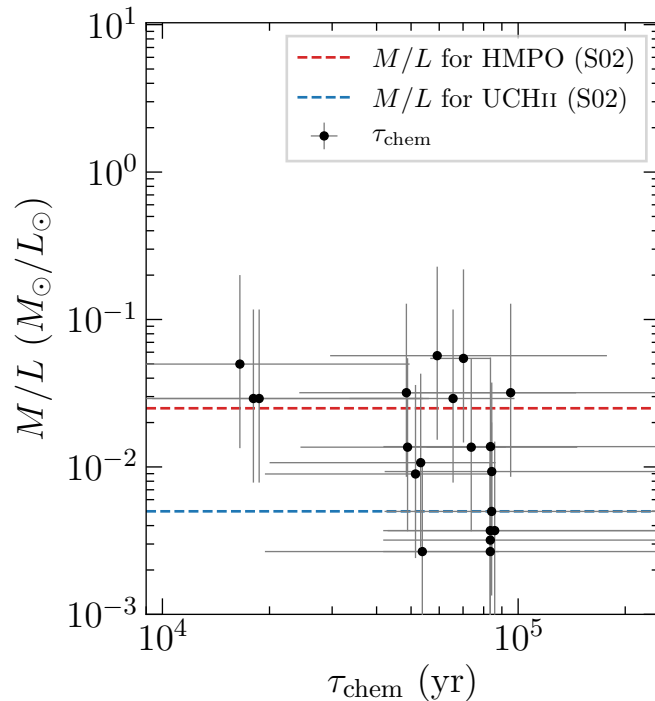


FIGURE 2.12: Comparison of the M/L ratio and chemical timescales τ_{chem} . The mass M and luminosity L for each region are taken from Beuther et al. (2018a). The horizontal dashed lines correspond to average M/L ratios for HMPOs (red) and UCHII regions (blue) taken from Sridharan et al. (2002).

Sridharan et al. (2002) found that the distance-independent mass-to-luminosity ratio M/L of UCHII regions is lower (~ 0.005) than the ratio of HMPOs (~ 0.025), as UCHII regions are more evolved and thus more luminous. This has also been confirmed by observations of large samples

of HMSFRs, for instance, by Molinari et al. (2008, 2010); Maud et al. (2015a); Molinari et al. (2016); Urquhart et al. (2018); Molinari et al. (2019). In Fig. 2.12 we plot the region-average M/L ratio taken from Table 1 in Beuther et al. (2018a) against the estimated chemical timescales τ_{chem} . The chemical timescale and a factor 2 uncertainty is shown for cores with a clear best-fit model. For cores with estimated chemical timescale ranges, the mean chemical timescale are shown with error bars spanning over the time range. The luminosities L have uncertainties on the order of $\sim 30\%$ (Mottram et al. 2011b) and the masses M calculated in Beuther et al. (2018a) are expected to be uncertain within a factor of 3. We also show the average M/L ratio for HMPOs and UCHII regions derived by Sridharan et al. (2002). We corrected the M/L ratios of Sridharan et al. (2002) by a factor of 0.5, as M was taken from Beuther et al. (2002a) where the reported values for M were lower by a factor of 2 (Beuther et al. 2005a). The cores G108.75 1 and 2 are excluded here, because no consistent continuum data is available to reliably derive the mass (Beuther et al. 2018a). There is a tendency such that the older cores have a lower M/L ratio. However, as the M/L ratios are determined on much larger scales and we resolve multiple cores within each region, it is difficult to compare these properties.

Estimating the chemical timescales with MUSCLE shows that a line-rich spectrum does not have to imply that a core is more evolved compared to a core with a line-poor spectrum. For example, the line-poor core 1 in IRAS 23033 is estimated to be older than the line-richer cores 2 and 3. When a hot core evolves to become a UCHII region, the strong protostellar radiation destroys molecules. Hence line-poor spectra can be found at early and at late evolutionary stages. Observations of more species would be helpful to better constrain the chemical model.

For G138.2957, G139.9091, and S106 we are not able to derive radial temperature profiles from the temperature maps (Fig. A.1). In G139.9091 and S106 there is no emission at the adopted $10\sigma_{\text{line,map}}$ level. There is diffuse emission of H_2CO in G138.2957, but it is too diffuse to derive a radial temperature profile. The spectra of these regions are line-poor and only simple species are detected (^{13}CO , C^{18}O , SO , H_2CO , see Fig. A.3). Based on the shape of the 1.37 mm continuum emission, G139.9091 and S106 have isolated cores with no significant envelope emission, while G138.2957 has diffuse dust emission (Fig. 2.3). Therefore one may conclude that G139.9091 and S106 are already more evolved and probably have $\tau_{\text{chem}} > 100\,000$ yr. S106 is a well studied bipolar HII region (e.g., Roberts et al. 1995; Schneider et al. 2007). G139.9091 is associated with a HII region as well (e.g., Kurtz et al. 1994; Purser 2017; Obonyo et al. 2019). G138.2957 could be in a very young strongly depleted phase with $\tau_{\text{chem}} < 20\,000$ yr or could be an evolved region and the diffuse emission is due to the disruption by the protostellar radiation. With observations of G138.2957 at 5.8 cm and 20 cm, a core component with an associated synchrotron jet is seen toward the location of the 1.37 mm continuum peak and the position has an associated infrared source (Obonyo et al. 2019). This suggests that G138.2957 is an evolved embedded cluster and not a young region. Deep observations at radio wavelengths ($\sim 5\text{--}50$ GHz) would also provide information on the presence of UCHII regions within the CORE sample. We find that for the known HII regions, we only detect simple species such as CO isotopologues, H_2CO suggesting that a large fraction of the larger molecules are already destroyed in this stage.

2.6.3 Correlations between chemical species

In this section, we aim to establish which molecules show a correlation via chemical links or temperature effects. We compute the Spearman correlation coefficient r for the molecular column density pair combinations relative to $N(\text{C}^{18}\text{O})$. SO_2 , $\text{HC}_3\text{N};v_7 = 1$, and $\text{HC}_3\text{N};v_7 = 2$ are excluded from this analysis as there are less than 20 column density data points. Ideally, we would compare the correlations of relative abundance pairs relative to $N(\text{H}_2)$, but due to

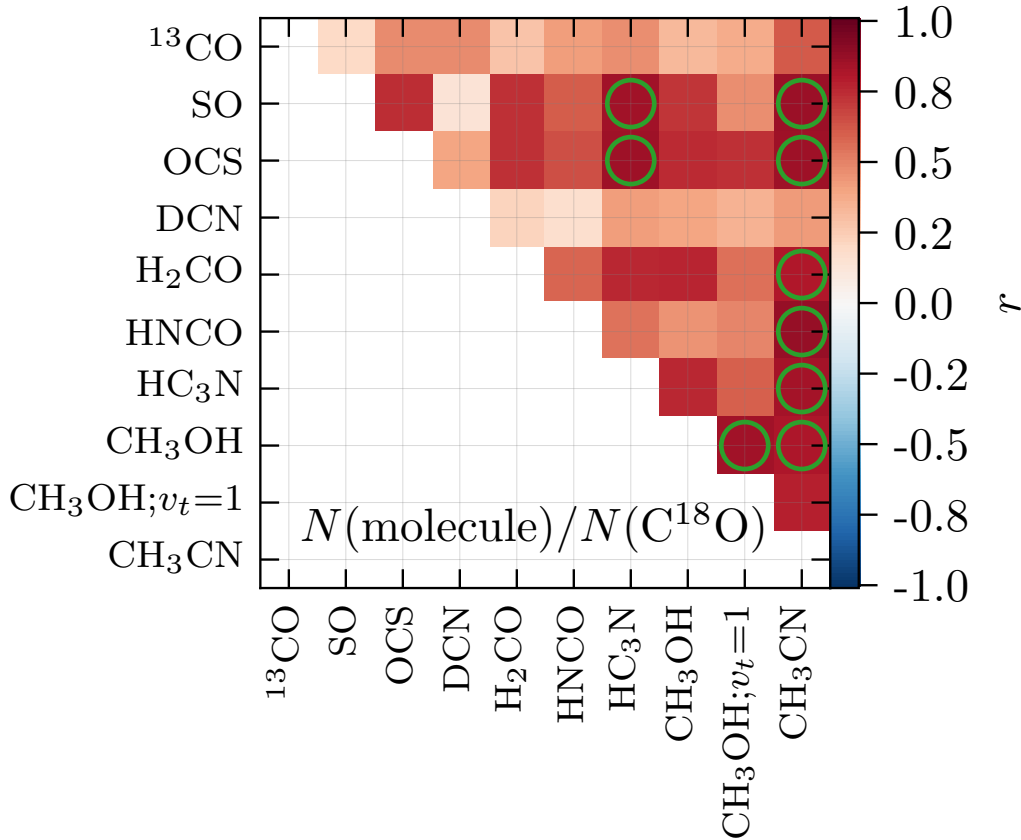


FIGURE 2.13: Spearman correlation coefficient r for pairs of molecular column densities relative to $N(\text{C}^{18}\text{O})$. Values higher than 0.8 are marked by a green circle.

the issue of the missing flux, we use $N(\text{C}^{18}\text{O})$, which is also detected toward all positions and is optically thin (Table A.2). Comparing the correlation between column density pairs, we ultimately face the issue that toward higher densities, the column density is also higher (as discussed in Sect. 2.4.2). The core and non-core positions were equally considered in the calculation of r and the results for all column density pairs are shown in Fig. 2.13.

In general, all pairs show a positive correlation, $r > 0$. High correlation coefficients ($r > 0.8$) are found between pairs of the following molecules: HC_3N –SO, HC_3N –OCS, CH_3CN –SO, CH_3CN –OCS, CH_3CN – H_2CO , CH_3CN –HNCO, CH_3CN – HC_3N , CH_3OH – $\text{CH}_3\text{OH};v_t = 1$, CH_3CN – CH_3OH . The lowest correlations are found for ^{13}CO and DCN, where there is no correlation with any species. In the case of ^{13}CO this is most likely due to a high optical depth (Table A.2), so the column density cannot be reliably derived. The case of DCN is more puzzling, but a more detailed study of the deuteration would be required. Unfortunately, the CORE spectral setup covers only the DCN 3–2 line, so follow-up observations of deuterated species are necessary to study how deuterium chemistry behaves on such scales (see Sect. 5).

Methyl cyanide (CH_3CN) shows a strong positive correlation with most other species, including S-bearing and N-bearing species. A correlation of HC_3N – CH_3CN can be explained by gas-phase N-chemistry in the envelope gas (Bergner et al. 2017). We find that OCS is correlated with other dense gas tracers (HC_3N and CH_3CN). A correlation exists between CH_3OH and CH_3CN even though there is no chemical link between methanol and methyl cyanide. Such a correlation has also been found toward low-mass star-forming regions (Bergner et al. 2017; Belloche et al. 2020) and toward the massive star-forming region G10.6–0.4 (Law et al. 2021). Belloche et al. (2020) argued that this is a temperature effect caused by chemically unrelated

species having been evaporated from icy grain mantles by energetic processes. Additional high angular resolution observations of SiO would be helpful for studying the impact of shocks in greater detail (see Sect. 5). In the 1D physical-chemical modeling of HMSFRs with MUSCLE by Gerner et al. (2014), CH₃CN, and CH₃OH are co-spatial in radial abundance profiles toward the inner hot core region. Urquhart et al. (2019) find that the line integrated ratios of S- and N-bearing species are positively correlated with the dust temperature in a sample of high-mass star-forming clumps. Gratier et al. (2013) found that CH₃CN is much more abundant in the photo-dissociation region (PDR) of the Horsehead nebula than the associated cold and dense core. This is consistent with the detection by Purcell et al. (2006) of 3 mm lines of CH₃CN in 58 candidate hot molecular cores in a sample of 83 methanol maser-selected star-forming regions. The authors detected CH₃CN in isolated methanol maser sites and found that CH₃CN is more prevalent and brighter when a UCHII region is present, independently of the distance to the source. Guzmán et al. (2014) proposed that correlated abundances of CH₃OH and CH₃CN could be related to photochemistry, for instance, by photodesorption.

The column densities relative to $N(\text{C}^{18}\text{O})$ show in general positive correlations. The N-bearing and S-bearing species seem to be chemically related by high temperature gas-phase chemistry. The strong non-correlation of DCN with any observed species requires high angular resolution follow-up observations of deuterated molecules toward these HMSFRs (e.g., N₂D⁺, DCO⁺). The correlation between CH₃CN and CH₃OH can be due to a mutual evaporation temperature or due to photo-desorption.

Computing the Spearman correlation coefficient r of the chemical timescales, τ_{chem} , (Table 2.3) with the observed column densities N (Fig. 2.8) and with the relative abundances $N/N(\text{C}^{18}\text{O})$ (Fig. A.2) for all 22 cores, we do not find strong correlations for most of the molecular column densities and relative abundances with the chemical timescale. We use the mean chemical timescale for cores for which only a time range can be estimated. Positive correlations of the column density and relative abundance with the chemical timescale ($r = 0.5 - 0.9$) are found for SO₂, HNCO, HC₃N; $v_7 = 1$, and CH₃OH; $v_t = 1$. We only detect HC₃N; $v_7 = 2$ in cores, which have a chemical timescale estimated to be $> 80\,000$ yr. This suggests that vibrationally and torsionally excited states of molecules are good indicators for a more evolved region, as these transitions have higher upper energy levels (Table A.2) and are only excited at a high kinetic temperature. We propose that SO₂ and HNCO are also good tracers of the evolutionary stage, however, this has to be investigated using a larger statistical sample.

2.6.4 Comparison of physical and chemical timescales

In the following, we compare the estimated chemical timescales with commonly applied physical timescales. The free-fall timescale, τ_{ff} , is the time it takes for a spherical object to fully collapse under the influence of gravity with no additional forces. It only depends on the initial density, ρ :

$$\tau_{\text{ff}} = \sqrt{\frac{3\pi}{32G\rho(\text{H}_2)}}, \quad (2.4)$$

where G is the gravitational constant and $\rho(\text{H}_2)$ the initial H₂ mass density. The crossing timescale is the time it takes to cross the system once:

$$\tau_{\text{cross}} = \frac{R}{v}, \quad (2.5)$$

with clump radius, R , and velocity dispersion, v .

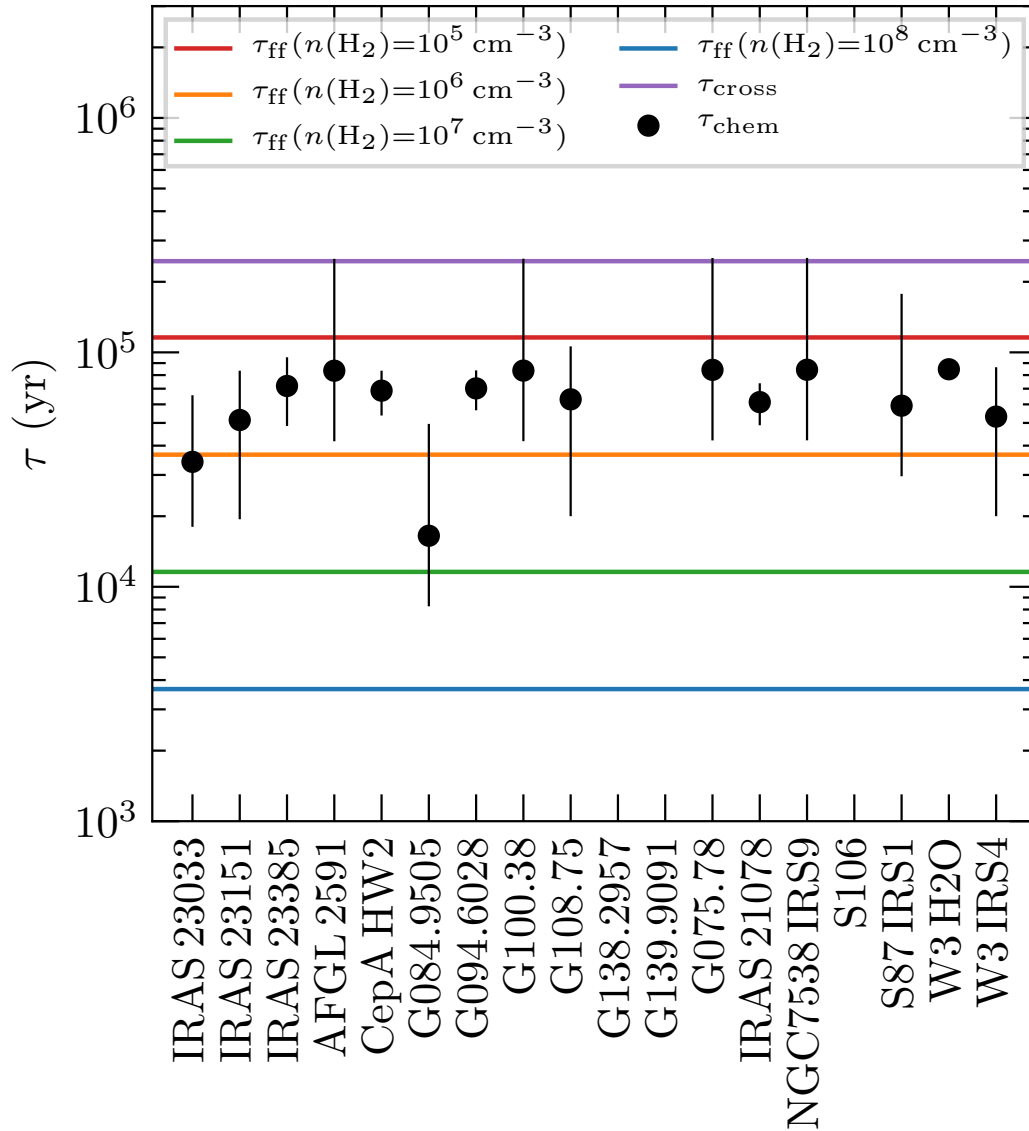


FIGURE 2.14: Comparison of the free-fall timescale, τ_{ff} , and crossing timescale, τ_{cross} , (colored lines), and chemical timescale, τ_{chem} , (black data points).

A comparison between the free-fall timescales for corresponding H_2 number densities of 10^5 cm^{-3} , 10^6 cm^{-3} , 10^7 cm^{-3} , and 10^8 cm^{-3} , crossing timescale (assuming $R = 1 \text{ pc}$ and $v = 4 \text{ km s}^{-1}$, Elmegreen 2000), and the chemical timescales of the regions estimated with MUSCLE is shown in Fig. 2.14. A mean chemical timescale is used for cores for which only a time range can be determined. We then calculate the mean chemical timescale for regions associated with multiple cores. In these cases, the errorbars indicate the range of chemical timescales. For regions associated with only one core, we assume an uncertainty of a factor of two for cores with a clear best-fit chemical timescale or the errorbars indicate the estimated time range for cores for which we can only determine a time range. The derived chemical timescales are in agreement with an initial clump density of $10^5 - 10^6 \text{ cm}^{-3}$. Indeed, observations suggest that IRDCs have densities $n(\text{H}_2) > 10^5 \text{ cm}^{-3}$ (e.g., Carey et al. 1998). The estimated crossing time is an upper limit, in agreement with the scenario that suggests that star formation occurs within a few crossing times (Elmegreen 2000). The agreement of the physical timescales with

the chemical timescales shows that even though the physical-chemical model is pseudo-time-dependent, the estimates are feasible, especially when a homogeneous data set and analysis is used.

Other forces such as magnetic fields and turbulence can slow down or prevent collapse and are important in the initial diffuse ISM (Ballesteros-Paredes et al. 2007; Burge et al. 2016). However, in the diffuse ISM, molecules, with the exception of H_2 , have not formed yet. Our zero point for the chemical timescales is when the density reaches 10^4 cm^{-3} and for the free-fall timescale, we also assume densities $\geq 10^4 \text{ cm}^{-3}$. In Beuther et al. (2018a), we showed that the fragmentation scales that we observe are in agreement with thermal Jeans fragmentation, thus turbulent Jeans fragmentation is not significant here. This is fully consistent with the results found in a different sample by Palau et al. (2015). The role of magnetic fields in the CORE regions are being investigated by polarization observations with the SMA (Beuther et al. in preparation).

2.7 Summary and conclusions

In this work, we study the physical and chemical structure of 18 high-mass star-forming regions using the CORE 1 mm continuum and spectral line data. We quantify the chemical content for in total 120 positions including in total 22 cores. Combining the CORE observations with the physical-chemical model MUSCLE, we estimate the chemical timescales of the cores. Our main conclusions are summarized as follows:

1. Using H_2CO and CH_3CN line emission, we derived temperature maps of the regions. We identify “cores” as objects having a clear radially decreasing temperature profile. We fit these radial temperature profiles and obtained an average power-law index $q = 0.4 \pm 0.1$, excluding three outliers with $q \geq 1$, which is in agreement with theoretical predictions and calculations.
2. The 1.37 mm continuum visibility profiles of the cores reveal a mean density power-law index of $p = 2.0 \pm 0.2$. Comparing these high-resolution density profiles to previous single-dish and interferometric studies, the density profiles appear to stay roughly constant between $p = 1.7 - 2.0$ from scales of 1 pc down to 1 000 au. The molecular hydrogen column density $N(\text{H}_2)$ has a mean of $1.5 \times 10^{24} \text{ cm}^{-2}$ toward the 120 positions and the core mass M_{core} of the 22 cores has a mean of $4.1 M_{\odot}$.
3. We derived molecular column densities of 11 species by fitting their spectral lines with XCLASS. Spearman correlation coefficients are evaluated for all molecule pairs. We find high correlations between N-bearing and S-bearing species that are chemically related through high temperature gas-phase chemistry. High correlations are also found for molecules that are not chemically related (CH_3CN and CH_3OH), but for which the correlation results from a common evaporation temperature or photo-desorption.
4. We applied the physical-chemical model MUSCLE to the observed column densities of each core to estimate the chemical timescale τ_{chem} . We find a spread in age from $\tau_{\text{chem}} \sim 20\,000 - 100\,000 \text{ yr}$ and a mean chemical timescale of $\sim 60\,000 \text{ yr}$. Multiple cores within a region show that there can be an age gradient for largely separated cores (e.g., toward IRAS 23033 and G108.75), while close cores have a similar chemical timescale (e.g., toward IRAS 21078 and W3 H2O) suggesting a sequential star formation.
5. A strong correlation is found between the peak column density $N(\text{H}_2)$ of the 22 cores and the M/L ratio of the region. In addition, we find a trend that older cores have a lower M/L

ratio. However, a larger sample is required to study the physical and chemical properties on core scales in more detail.

6. We compare the chemical timescale with physical timescales. We find that the chemical timescale is consistent with a free-fall timescale of the initial clump, at a density of 10^5 cm^{-3} and 10^6 cm^{-3} , which is consistent with density values typically found toward IRDCs. The chemical timescales are smaller than a crossing time of the parental clump.
7. We improved the quality (both intensity and noise) of the NOEMA continuum and spectral line data by applying self-calibration. All of the standard and self-calibrated CORE data are publically available².

The CORE data reveal a large physical and chemical diversity on scales down to ~ 300 au. Here, we use the molecular column densities of 120 positions toward the 18 high-mass star-forming regions to quantify the chemical content, with an emphasis on 22 cores. The case study of AFGL 2591 had already revealed complex structures around a single hot core (Gieser et al. 2019) using high-resolution interferometric observations. As a next step, evolutionary trends of the physical and chemical properties of fragmented cores need to be further investigated.

²<https://www.mpia.de/core>

Chapter 3

Clustered star formation at early evolutionary stages: Physical and chemical analysis of two young star-forming regions

This chapter is based on Gieser et al. (2022), published in Astronomy & Astrophysics, 657, A3. I led this study under the supervision of Henrik Beuther. The ISOSS J22478+6357 NOEMA data were calibrated by Henrik Beuther. I calibrated the ISOSS J23053+5953 NOEMA data and the IRAM 30m observations of both regions, and performed the imaging of the NOEMA continuum and NOEMA+IRAM 30m spectral line data for both regions. Science-ready data products of the Herschel and Spitzer observations were taken from the Herschel Science Archive¹ and from the Spitzer Heritage Archive², respectively. The continuum and kinematic properties are presented in Beuther et al. (2021), where I provided the H₂CO temperature maps that are also presented in this chapter. I carried out the analysis of the continuum and spectral line data, radiative transfer modeling with XCLASS (Möller et al. 2017), and physical-chemical modeling with MUSCLE. The initial chemical conditions from the Gerner et al. (2014, 2015) study with MUSCLE were provided by Dmitry Semenov. The histogram of oriented gradients (HOG) code was provided by Juan Soler and I applied it to the spectral line data. The text in the publication was written by me, I created the figures and all 22 co-authors provided comments for the manuscript.

3.1 Context

The process of high-mass star formation during the earliest evolutionary stages and the change over time of the physical and chemical properties of individual fragmented cores are still not fully understood. We aim to characterize the physical and chemical properties of fragmented cores during the earliest evolutionary stages in two very young star-forming regions.

In this work, we study the core properties in the two young and cold intermediate- to high-mass star-forming regions ISOSS J22478+6357 and ISOSS J23053+5953. The data were obtained as an extension of the CORE project (“CORE-extension”) with both regions observed in multiple pointings creating large mosaics and the new PolyFiX correlator increasing the spectral bandwidth by a factor of four. An overview and the analysis of the fragmentation and kinematic properties is presented in Beuther et al. (2021). These two additional regions are at very early evolutionary stages, similar to typical infrared dark clouds (IRDCs), with $T_{\text{clump}} \approx 20$ K (Ragan et al. 2012). Thus, these two sources complement the CORE sample with regions that tend to occupy an earlier phase in the evolutionary sequence of HMSF (Beuther et al. 2007a). Both regions were selected based on targets of the ISOPHOT Serendipity Survey (ISOSS) observing the sky during slew times at 170 μm (Krause et al. 2004).

¹<https://archives.esac.esa.int/hsa/whsa/>

²<https://sha.ipac.caltech.edu/applications/Spitzer/SHA/>

NORthern Extended Millimeter Array (NOEMA) 1.3 mm data are used in combination with archival mid- and far-infrared Spitzer and Herschel telescope observations to construct and fit the spectral energy distributions of individual fragmented cores. The radial density profiles are inferred from the 1.3 mm continuum visibility profiles, and the radial temperature profiles are estimated from H₂CO rotation temperature maps. Molecular column densities are derived with the line fitting tool XCLASS. The physical and chemical properties are combined by applying the physical-chemical model MUlti Stage CLoud code (MUSCLE) in order to constrain the chemical timescales of a few line-rich cores. The morphology and spatial correlations of the molecular emission are analyzed using the histogram of oriented gradients (HOG) method.

An overview of the 1.3 mm observations with NOEMA, the core fragmentation properties, and a detailed analysis of the kinematic properties of ISOSS J22478+6357 and ISOSS J23053+5953 are presented in Beuther et al. (2021). We expand the analysis with a detailed investigation of the molecular lines detected at 1.3 mm. In addition, we used archival MIR and far-infrared (FIR) data to study the clustered nature of both regions. The MIR observations reveal emission of more evolved protostars while the FIR emission traces the cold dust emission.

3.2 Sample

ISOSS J22478+6357

The ISOSS J22478+6357 region was first identified with the Infrared Astronomical Satellite (IRAS) as IRAS 22460+6341 (Beichman et al. 1988), and is also known as J224749.9+635647 (Di Francesco et al. 2008). We note that the associated IRAS source (Kerton & Brunt 2003) is spatially offset by $\sim 41''$ from the studied IR and mm counterparts in this and other more recent studies (Hennemann et al. 2008; Ragan et al. 2012; Bihl et al. 2015; Beuther et al. 2021). Wide-field Infrared Survey Explorer (WISE) images at 12 and 22 μm show extended emission around the IRAS source, which can be interpreted as a signpost of intermediate-mass star formation (Lundquist et al. 2014). With Herschel observations using the Photodetector Array Camera and Spectrometer (PACS, Poglitsch et al. 2010) instrument as part of the Earliest Phases of Star Formation (EPoS) program, Ragan et al. (2012) determine a kinematic distance of $d = 3.23^{+0.61}_{-0.60}$ kpc (using the model by Reid et al. 2009) and a total gas mass of $104 M_{\odot}$ within a total of seven resolved clumps. The systemic velocity v_{LSR} is -39.7 km s^{-1} . The region is located in the outer galaxy, $d_{\text{gal}} = 9.7$ kpc away from the Galactic center.

A detailed study of a few ISOSS regions, including ISOSS J22478+6357, is presented in Hennemann et al. (2008). These authors detect two submm clumps with the Submillimetre Common User Bolometer Array (SCUBA) at the James Clerk Maxwell Telescope (JCMT) at 450 μm and 850 μm , “SMM1 E” and “SMM1 W,” with sizes of 0.14 pc and 0.24 pc, gas masses of $64 M_{\odot}$ and $116 M_{\odot}$, and dust temperatures of 15 K and 14 K, respectively. By fitting the SED of a bright MIR source, one of the more evolved YSOs in the SMM1 E clump is classified as an intermediate-mass star with central mass $M_{\star} = 6 - 8.5 M_{\odot}$ and a system age of $10^6 - 6 \times 10^6$ yr. Using the 850 μm JCMT SCUBA observations, Bihl et al. (2015) estimate a total gas mass of $140 M_{\odot}$ in ISOSS J22478+6357.

ISOSS J23053+5953

The region ISOSS J23053+5953 was originally identified as a point source by IRAS under the identifier IRAS 23032+5937 (Beichman et al. 1988). In the literature it is also known as J230523.6+595356 (Di Francesco et al. 2008) or G109.995-00.282 (Rosolowsky et al. 2010). With the Bolocam Galactic Plane Survey (BGPS), a 1.1 mm flux of 0.826 Jy is derived within a

radius of $R = 38.''32$ (Rosolowsky et al. 2010). Schlingman et al. (2011) estimate the following properties using the BGPS data: $M = 130 M_{\odot}$, beam average density $n = 3\,000\text{ cm}^{-3}$, volume averaged density $n = 840\text{ cm}^{-3}$, free-fall timescale $\tau_{\text{ff}} = 1.4 \times 10^6\text{ yr}$, and crossing timescale $\tau_{\text{cross}} = 4.0 \times 10^5\text{ yr}$.

Single-dish observations with a linear resolution of $\approx 0.3 - 1\text{ pc}$ reveal molecular line emission toward the region with line widths of $1.5 - 5\text{ km s}^{-1}$ (e.g., CO, CS, HCO^+ , N_2H^+ , CH_3CCH , CH_3CHO ; Harju et al. 1993; Wouterloot et al. 1993; Bronfman et al. 1996; Alakoz et al. 2002; Shirley et al. 2013; Vasyunina et al. 2014). Based on NH_3 observations with the Effelsberg 100m telescope, the kinetic temperature was estimated to be $\sim 15\text{ K}$ (Wouterloot et al. 1988; Harju et al. 1993). Vasyunina et al. (2014) estimate a kinetic temperature of $31 \pm 1\text{ K}$ based on CH_3CCH line emission. Early studies found that there are two velocity components in molecular line emission, for example, for NH_3 (at -52.3 km s^{-1} and -50.8 km s^{-1} , Wouterloot et al. 1988), H_2O (at -52.3 km s^{-1} and -49.5 km s^{-1} , Wouterloot et al. 1993), and CS (at -51.8 km s^{-1} and -51.2 km s^{-1} , Larionov et al. 1999).

Very Large Array (VLA) and Effelsberg 100m observations of the NH_3 (1,1) and (2,2) lines at an angular resolution of $4''$ are analyzed by Bihl et al. (2015). These authors find a steep velocity gradient of $>30\text{ km s}^{-1}\text{ pc}^{-1}$ toward the region suggesting a dynamical collapse and/or converging gas flow. With JCMT SCUBA $850\text{ }\mu\text{m}$ observations, a total gas mass of $610 M_{\odot}$ is estimated by the authors in ISOSS J23053+5953. The kinematic data of the CORE-extension project further resolve this steep velocity gradient in DCO^+ (3 – 2) being higher than $50\text{ km s}^{-1}\text{ pc}^{-1}$ (Beuther et al. 2021).

Wouterloot & Walmsley (1986) and Wouterloot et al. (1993) detected H_2O maser emission. But no H_2O maser emission was detected in follow-up studies (Comoretto et al. 1990; Palagi et al. 1993; Palla et al. 1993; Slysh et al. 1999; Valdettaro et al. 2001; Sunada et al. 2007), so the presence or potential variability of H_2O maser emission remains unclear. No CH_3OH maser emission was detected (Wouterloot et al. 1993; Kalenskii & Sobolev 1994).

ISOSS J23053+5953 is a target of the EPoS survey as well (Ragan et al. 2012). The authors derive a gas mass of $488 M_{\odot}$ within three resolved clumps and a kinematic distance of $d = 4.31^{+0.64}_{-0.62}\text{ kpc}$ at a systemic velocity of -52.5 km s^{-1} (using the model by Reid et al. 2009). This is in agreement with other distance estimates, for example, by Yang et al. (2002, $d = 4.82\text{ kpc}$), Schlingman et al. (2011, $d = 4.253\text{ kpc}$), Ellsworth-Bowers et al. (2015, $d = 4.44^{+0.74}_{-0.70}\text{ kpc}$), and the Planck Collaboration et al. (2016, $d = 5.07\text{ kpc}$). With a Galactocentric distance of $d_{\text{gal}} \approx 10\text{ kpc}$ (Wouterloot & Brand 1989; Ellsworth-Bowers et al. 2015) the region is located in the outer galaxy as well.

Birkmann et al. (2007) find a young and accreting massive protostar toward one of the clumps with an associated outflow. The line profile of the optically thick HCO^+ 3 – 2 transition indicates infalling material with self-absorption in the red-shifted line wing compared the optically thin H^{13}CO^+ 3 – 2 isotopologue.

Pitann et al. (2011) studied the region using Spitzer observations with the InfraRed Array Camera (IRAC, Fazio et al. 2004) and the Multiband Imaging Photometer for Spitzer (MIPS, Rieke et al. 2004) instruments. These authors find that the region, harboring a cluster of sources, has extended polycyclic aromatic hydrocarbons (PAH) emission and warm dust components. In addition, the emission of forbidden transitions of FeII, SiII, and SiI imply post-shocked gas that occurred by a J-shock. This is confirmed by the detection of high-energy H_2 transitions from $S(0)$ to $S(7)$ with excitation energies ranging between $510 - 7200\text{ K}$. These authors do not find an indication of a photodissociation region (PDR).

3.3 Observations

3.3.1 CORE-extension data

The NOEMA mosaic observations were taken in February and March 2019 with ten antennas in the A, C, and D array configurations at 1.3 mm (Band 3) using the PolyFiX correlator. ISOSS J22478+6357 and ISOSS J23053+5953 were observed with six and four NOEMA pointings, respectively. A summary of both regions, for example, the coordinates and velocities, is shown in Table 3.1. Complementary IRAM 30m observations in the same frequency range, to include short-spacing information of the spectral line data, were obtained using EMIR (Carter et al. 2012) in June 2019.

TABLE 3.1: Overview of the CORE-extension sample. The distance, d , and systemic velocity, v_{LSR} , are taken from Ragan et al. (2012). The calculation of the $^{12}\text{C}/^{13}\text{C}$ and $^{16}\text{O}/^{18}\text{O}$ isotopic ratios is based on Wilson & Rood (1994), including the dependence on the Galactocentric distance, d_{gal} . The Galactic height, z_{gal} , is also listed.

	α (J2000)	δ (J2000)	d (kpc)	d_{gal} (kpc)	z_{gal} (pc)	v_{LSR} (km s $^{-1}$)	$^{12}\text{C}/^{13}\text{C}$	$^{16}\text{O}/^{18}\text{O}$
ISOSS J22478+6357	22:47:49.23	+63:56:45.3	3.23	9.7	270	-39.7	80	607
ISOSS J23053+5953	23:05:22.47	+59:53:52.6	4.31	10.4	11	-51.7	86	649

NOEMA data

The NOEMA data were calibrated using the CLIC package in GILDAS³. The PolyFiX correlator simultaneously covers ~ 8 GHz in two sidebands (lower sideband, LSB, and upper sideband, USB) and in the two orthogonal linear polarizations (horizontal and vertical) with a fixed channel spacing of 2 MHz (~ 2.7 km s $^{-1}$ at 1.3 mm). Rest frequencies from 213.3 GHz to 221.3 GHz in the LSB and from 228.7 GHz to 236.7 GHz in the USB were covered by the observations. High-resolution units with a channel spacing of 62.5 kHz (~ 0.084 km s $^{-1}$ at 1.3 mm) were placed within the broadband correlator units.

The NOEMA 1 mm data of the original CORE sample consisted of single pointing observations toward each region, which allowed us to self-calibrate these data sets with the GILDAS `selfcal` task (a detailed description of the method is explained in Sect. 2.2.4). Since self-calibration of mosaic observations is currently not possible, we use the standard calibrated NOEMA data for the CORE-extension data presented in Beuther et al. (2021) and in this work.

IRAM 30m data

The EMIR data were calibrated using the CLASS package in GILDAS. The EMIR instrument consists of four basebands with a width of ~ 4 GHz in each baseband: the lower outer (LO, 213.5 – 217.5 GHz), lower inner (LI, 217.3 – 221.3 GHz), upper inner (UI, 229.2 – 233.2 GHz), and upper outer (UO, 233.0 – 237.0 GHz) baseband. The chosen Fast Fourier Transform Spectrometer (FTS) backend delivers a channel separation of 200 kHz (~ 0.27 km s $^{-1}$ at 1.3 mm). The half power beam width (HPBW) is 11.''8 in the lower basebands and 11.''2 in the upper basebands. After an initial inspection of the data, spiky channels caused by noise artifacts were filled with Gaussian noise. The antenna temperature T_{A}^* was converted to main beam temperature T_{mb} using $T_{\text{mb}} = \frac{F_{\text{eff}}}{B_{\text{eff}}} \times T_{\text{A}}^*$ with $F_{\text{eff}} = 0.915$ and $B_{\text{eff}} = 0.57$ (Sect. 1.4.1).

³<https://www.iram.fr/IRAMFR/GILDAS/>

TABLE 3.2: Emission lines detected in the CORE-extension regions. Line properties are taken from either the CDMS (Müller et al. 2005) or JPL (Pickett et al. 1998) databases. The CH₃CN 12₀ – 11₀ transition is partially blended with CH₃CN 12₁ – 11₁ at 220.743 GHz.

Molecule (Transition)	Rest frequency ν_0 (GHz)	Einstein coefficient $\log A_{ul}$ (log s ⁻¹)	Upper energy level E_u/k_B (K)	Ref.
SO (5 ₅ – 4 ₄)	215.221	-3.9	44	JPL
DCO ⁺ (3 – 2)	216.113	-2.6	21	CDMS
H ₂ S (2 _{2,0} – 2 _{1,1})	216.710	-4.3	84	CDMS
CH ₃ OH (5 _{1,4} – 4 _{2,3} E)	216.946	-4.9	56	CDMS
SiO (5 – 4)	217.105	-3.3	31	JPL
c-C ₃ H ₂ (6 _{1,6} – 5 _{0,5})	217.822	-3.2	39	JPL
H ₂ CO (3 _{0,3} – 2 _{0,2})	218.222	-3.6	21	JPL
HC ₃ N (24 – 23)	218.325	-3.1	131	JPL
CH ₃ OH (4 _{2,3} – 3 _{1,2} E)	218.440	-4.3	45	CDMS
H ₂ CO (3 _{2,2} – 2 _{2,1})	218.476	-3.8	68	JPL
H ₂ CO (3 _{2,1} – 2 _{2,0})	218.760	-3.8	68	JPL
OCS (18 – 17)	218.903	-4.5	100	JPL
C ¹⁸ O (2 – 1)	219.560	-6.2	16	JPL
HNCO (10 _{0,10} – 9 _{0,9})	219.798	-3.8	58	CDMS
H ₂ ¹³ CO (3 _{1,2} – 2 _{1,1})	219.909	-3.6	33	JPL
SO (6 ₅ – 5 ₄)	219.949	-3.9	35	JPL
CH ₃ OH (8 _{0,8} – 7 _{1,6} E)	220.079	-4.6	97	CDMS
¹³ CO (2 – 1)	220.399	-6.2	16	JPL
CH ₃ CN (12 ₀ – 11 ₀)	220.747	-3.2	69	JPL
CH ₃ OH (8 _{1,8} – 7 _{0,7} E)	229.759	-4.4	89	CDMS
CO (2 – 1)	230.538	-6.2	17	JPL
OCS (19 – 18)	231.061	-4.4	111	JPL
¹³ CS (5 – 4)	231.221	-3.6	33	JPL
N ₂ D ⁺ (3 – 2)	231.322	-2.7	22	JPL
SO ₂ (4 _{2,2} – 3 _{1,3})	235.152	-4.1	19	JPL
HC ₃ N (26 – 25)	236.513	-3.0	153	JPL

Imaging

The NOEMA continuum and combined NOEMA + IRAM 30m (“merged”) spectral line data were imaged using the MAPPING package in GILDAS. Primary beam correction was applied to the final continuum and spectral line data products.

In a first inspection of the NOEMA spectral line data of both regions, we identified all detected emission lines. An overview of all lines and their properties is shown in Table 3.2. All of these emission lines were covered by the IRAM 30m EMIR observations, and hence the interferometric and single-dish data can be combined in order to recover missing flux filtered out by the interferometer. If available, we used the data obtained with the high-resolution units smoothed to a spectral resolution of 0.5 km s⁻¹ to increase the signal-to-noise ratio (S/N) and otherwise with the low-resolution basebands smoothed to a spectral resolution of 3.0 km s⁻¹ to increase the S/N .

The continuum is extracted from the low-resolution spectral line data by masking out all channels with line emission using the `uv_filter` and `uv_continuum` tasks. The continuum

data in the LSB and USB were merged with the task `uv_merge`. The continuum data were CLEANed with natural weighting using the Clark algorithm (Clark 1980). The synthesized beam ($\theta_{\text{maj}} \times \theta_{\text{min}}$, PA) and noise σ_{cont} of the continuum image are $0.''92 \times 0.''73$, 50° and $0.057 \text{ mJy beam}^{-1}$ for ISOSS J22478+6357 and $0.''84 \times 0.''74$, 67° and $0.16 \text{ mJy beam}^{-1}$ for ISOSS J23053+5953. Short-spacing information is only available for the spectral line data, so spatial filtering affects the continuum data. In Beuther et al. (2021) it is estimated that only 10 – 20% of the total flux is recovered by the NOEMA observations.

The continuum was subtracted from the spectral line data with the task `uv_baseline`. For each visibility, a baseline is fitted and subtracted with all channels of line emission masked out (listed in Table 3.3). The NOEMA observations were combined with the IRAM 30m data using the `uvshort` task.

The continuum-subtracted spectral line data were CLEANed with natural weighting using the SDI algorithm (Steer et al. 1984) for lines with extended emission within the field-of-view (all CO isotopologues, SO, SiO, and H₂CO) and with the Clark algorithm (Clark 1980) for lines with less extended emission. A detailed comparison of these two CLEAN algorithms applied to the CORE region W3 IRS4 is presented in Mottram et al. (2020). The properties of the spectral line data products are summarized in Table 3.3. The line noise σ_{line} , computed in emission-free channels, is $\sim 0.2 \text{ K channel}^{-1}$ and $\sim 0.07 \text{ K channel}^{-1}$ in the high-resolution and low-resolution line data, respectively.

3.3.2 Archival data

In addition to the high angular resolution NOEMA data at 1.3 mm, we used archival MIR to FIR observations obtained with the Spitzer and Herschel space telescopes to study the clustered nature of the regions and constrain the SEDs. For both regions, archival data covering the full field-of-view (FOV) of the NOEMA mosaic exists.

In the FIR, both regions were targets in the Herschel key program EPoS and the properties of the cold dust are analyzed in Ragan et al. (2012). Three photometric bands of the PACS instrument at 70, 100, and 160 μm , with angular resolutions of $\sim 5''$, $\sim 7''$, and $\sim 12''$, respectively, cover the peak of the SED of cold dust emission. Science-ready data products were taken from the Herschel Science Archive.

The Spitzer IRAC instrument has four photometric bands at 3.6, 4.5, 5.8, and 8.0 μm . The angular resolution is $1'' - 2''$, so comparable to the 1.3 mm observations with NOEMA. The Spitzer MIPS observations at 24 μm have an angular resolution of $7''$. The 70 μm MIPS data were not used, as the Herschel PACS 70 μm data have a higher angular resolution. Science-ready data products were obtained from the Spitzer Heritage Archive. For a detailed description of the Spitzer observations, we refer to Hennemann et al. (2008) for ISOSS J22478+6357 and to Birkmann et al. (2007) and Pitann et al. (2011) for ISOSS J23053+5953.

TABLE 3.3: Overview of the merged (combined NOEMA + IRAM 30m) spectral line data products. The line properties are summarized in Table 3.2. Lines with extended emission are CLEANed with the SDI algorithm (Steer et al. 1984) and species with compact emission are CLEANed with the Clark algorithm (Clark 1980). Transitions covered by the high-resolution units are re-binned to a velocity resolution of 0.5 km s^{-1} and transitions only covered by the low-resolution units of PolyFiX have a velocity resolution of 3.0 km s^{-1} . It is marked if the transition is detected (\checkmark) or not (\times) in the line integrated intensity maps (Sect. 3.5.2).

Molecule (Transition)	CLEAN algorithm	Spectral resolution δv (km s^{-1})	ISOSS J22478+6357				ISOSS J23053+5953			
			Synthesized beam		Line noise σ_{line} (K channel^{-1})	Detected?	Synthesized beam		Line noise σ_{line} (K channel^{-1})	Detected?
			$\theta_{\text{maj}} \times \theta_{\text{min}}$ ("×")	PA ($^{\circ}$)			$\theta_{\text{maj}} \times \theta_{\text{min}}$ ("×")	PA ($^{\circ}$)		
SO ($5_5 - 4_4$)	SDI	3.0	0.98×0.77	50	0.072	\checkmark	0.91×0.78	58	0.061	\checkmark
DCO ⁺ ($3 - 2$)	Clark	0.5	0.97×0.77	50	0.17	\checkmark	0.90×0.78	60	0.17	\checkmark
H ₂ S ($2_{2,0} - 2_{1,1}$)	Clark	3.0	0.97×0.77	51	0.067	\times	0.90×0.78	59	0.065	\checkmark
CH ₃ OH ($5_{1,4} - 4_{2,3E}$)	Clark	3.0	0.96×0.78	63	0.069	\times	0.90×0.78	59	0.067	\checkmark
SiO ($5 - 4$)	SDI	0.5	0.97×0.77	50	0.21	\checkmark	0.90×0.78	59	0.19	\checkmark
c-C ₃ H ₂ ($6_{1,6} - 5_{0,5}$)	Clark	3.0	0.97×0.77	50	0.086	\checkmark	0.89×0.77	59	0.072	\checkmark
H ₂ CO ($3_{0,3} - 2_{0,2}$)	SDI	0.5	0.97×0.78	50	0.23	\checkmark	0.89×0.77	59	0.17	\checkmark
HC ₃ N ($24 - 23$)	Clark	0.5	0.98×0.77	50	0.17	\times	0.89×0.77	60	0.16	\checkmark
CH ₃ OH ($4_{2,3} - 3_{1,2E}$)	Clark	0.5	0.97×0.77	51	0.17	\checkmark	0.89×0.77	59	0.16	\checkmark
H ₂ CO ($3_{2,2} - 2_{2,1}$)	SDI	0.5	0.97×0.77	49	0.17	\checkmark	0.89×0.77	59	0.17	\checkmark
H ₂ CO ($3_{2,1} - 2_{2,0}$)	SDI	0.5	0.96×0.80	68	0.17	\checkmark	0.89×0.77	59	0.19	\checkmark
OCS ($18 - 17$)	Clark	0.5	0.97×0.77	50	0.15	\times	0.89×0.77	59	0.15	\checkmark
C ¹⁸ O ($2 - 1$)	SDI	0.5	0.92×0.82	81	0.19	\checkmark	0.89×0.77	59	0.18	\checkmark
HNCO ($10_{0,10} - 9_{0,9}$)	Clark	3.0	0.96×0.77	50	0.072	\times	0.89×0.77	59	0.059	\checkmark
H ₂ ¹³ CO ($3_{1,2} - 2_{1,1}$)	Clark	3.0	0.97×0.77	49	0.078	\times	0.88×0.77	60	0.056	\checkmark
SO ($6_5 - 5_4$)	SDI	3.0	0.96×0.77	50	0.085	\checkmark	0.88×0.77	61	0.062	\checkmark
CH ₃ OH ($8_{0,8} - 7_{1,6E}$)	Clark	3.0	0.96×0.76	50	0.076	\times	0.88×0.77	59	0.058	\checkmark
¹³ CO ($2 - 1$)	SDI	0.5	0.96×0.77	50	0.20	\checkmark	0.88×0.76	60	0.19	\checkmark
CH ₃ CN ($12_0 - 11_0$)	Clark	0.5	0.96×0.76	50	0.20	\times	0.88×0.76	59	0.17	\checkmark
CH ₃ OH ($8_{1,8} - 7_{0,7E}$)	Clark	0.5	0.94×0.74	49	0.17	\checkmark	0.84×0.74	63	0.18	\checkmark
CO ($2 - 1$)	SDI	0.5	0.93×0.74	48	0.25	\checkmark	0.83×0.73	62	0.29	\checkmark

TABLE 3.3: continued.

Molecule (Transition)	CLEAN algorithm	Spectral resolution δv (km s ⁻¹)	ISOSS J22478+6357				ISOSS J23053+5953			
			Synthesized beam		Line noise	Detected?	Synthesized beam		Line noise	Detected?
			$\theta_{\text{maj}} \times \theta_{\text{min}}$ ("×")	PA (°)	σ_{line} (K channel ⁻¹)		$\theta_{\text{maj}} \times \theta_{\text{min}}$ ("×")	PA (°)	σ_{line} (K channel ⁻¹)	
OCS (19 – 18)	Clark	0.5	0.93×0.74	49	0.21	✗	0.83×0.73	62	0.17	✓
¹³ CS (5 – 4)	Clark	0.5	0.93×0.74	48	0.21	✗	0.83×0.73	61	0.21	✓
N ₂ D ⁺ (3 – 2)	Clark	0.5	0.93×0.74	48	0.21	✓	0.83×0.73	61	0.19	✓
SO ₂ (4 _{2,2} – 3 _{1,3})	Clark	0.5	0.92×0.72	48	0.20	✗	0.82×0.72	61	0.18	✓
HC ₃ N (26 – 25)	Clark	0.5	0.91×0.72	49	0.24	✗	0.82×0.71	61	0.23	✓

3.4 Continuum

The NOEMA 1.3 mm continuum data reveal the compact dust emission in the two star-forming regions. The sub-arcsecond resolution achieved with NOEMA allows us to study individual fragmented millimeter (mm) cores. In this section, the core properties are analyzed using the NOEMA 1.3 mm continuum emission in combination with archival MIR and FIR data.

3.4.1 Fragmentation properties

The NOEMA 1.3 mm continuum data are shown in Fig. 3.1 for ISOSS J22478+6357 and ISOSS J23053+5953. In both regions, the continuum data reveal a large number of fragmented mm cores. In total, ten bright mm cores with $S/N > 20$ are detected, four in ISOSS J22478+6357 and six in ISOSS J23053+5953.

The fragmentation properties are studied in detail in Beuther et al. (2021). By applying the `clumpfind` algorithm (Williams et al. 1994) to the continuum data, 15 and 14 individual mm cores can be identified for ISOSS J22478+6357 and ISOSS J23053+5953, respectively. The cores are labeled in Fig. 3.1. In this study, we investigate the physical and chemical properties of these 29 cores. An overview and summary of the results from Beuther et al. (2021), including the core position, 1.3 mm peak intensity I_{peak} , 1.3 mm integrated flux F_{1300} , and outer radius r_{out} derived with `clumpfind`, is presented in Table 3.4.

A comparison of the NOEMA 1.3 mm continuum and archival MIR and FIR observations obtained with the Spitzer and Herschel space telescopes is presented in Fig. 3.3. The Spitzer IRAC and MIPS observations highlight evolved protostars. The Herschel PACS observations at 70, 100, and 160 μm trace the cold dust emission on clump scales. The mm cores have counterparts not only at FIR wavelengths, such that they are embedded in the cold clumps, but there are also a few cores that are MIR-bright (e.g., mm core 13 in ISOSS J22478+6357 and mm core 2 in ISOSS J23053+5953). The SED of mm cores with associated Spitzer IRAC sources are constructed and modeled in Sect. 3.4.3.

Based on the 1.3 mm continuum peak intensity I_{peak} and integrated flux F_{1300} of each core, Beuther et al. (2021) calculate the molecular hydrogen column density $N(\text{H}_2)$ and core mass M_{core} assuming optically thin dust emission. For the kinetic temperature T_{kin} , the H_2CO rotation temperature $T(\text{H}_2\text{CO})$ was used assuming LTE conditions (Sect. 3.5.4). In order to check if the assumption of optically thin dust emission is valid, we computed the 1.3 mm continuum optical depth τ_{cont} at the position of the peak intensity according to Eq. (1.47).

The continuum optical depth, τ_{cont} , as well as $N(\text{H}_2)$, M_{core} , and T_{kin} for each core are summarized in Table 3.4. The optical depth is < 0.01 for all 29 cores; therefore, the assumption of optically thin dust emission is valid.

The core masses M_{core} , derived from the integrated 1.3 mm flux, vary between 0.04 and 4.61 M_{\odot} (Table 3.4). This indicates that most of the mm cores form low- and intermediate-mass stars. The sum of all core masses is 17 M_{\odot} and 23 M_{\odot} in ISOSS J22478+6357 and ISOSS J23053+5953, respectively. The mass estimates using single-dish observations (Ragan et al. 2012; Bihr et al. 2015) are a factor of 10 – 30 higher than estimated from the 1.3 mm NOEMA data. The interferometric observations of the dust continuum suffer from spatially filtering the extended emission, the estimated core masses are therefore only lower limits. The single-dish observations at FIR wavelengths from Herschel PACS and JCMT SCUBA reveal that both regions have a large gas mass reservoir of a few 100 M_{\odot} (Ragan et al. 2012; Bihr et al. 2015). This provides a mass reservoir for further growth and indicates that mass assembly is not complete. Bright MIR sources suggest the presence of at least intermediate-mass protostars in both regions.

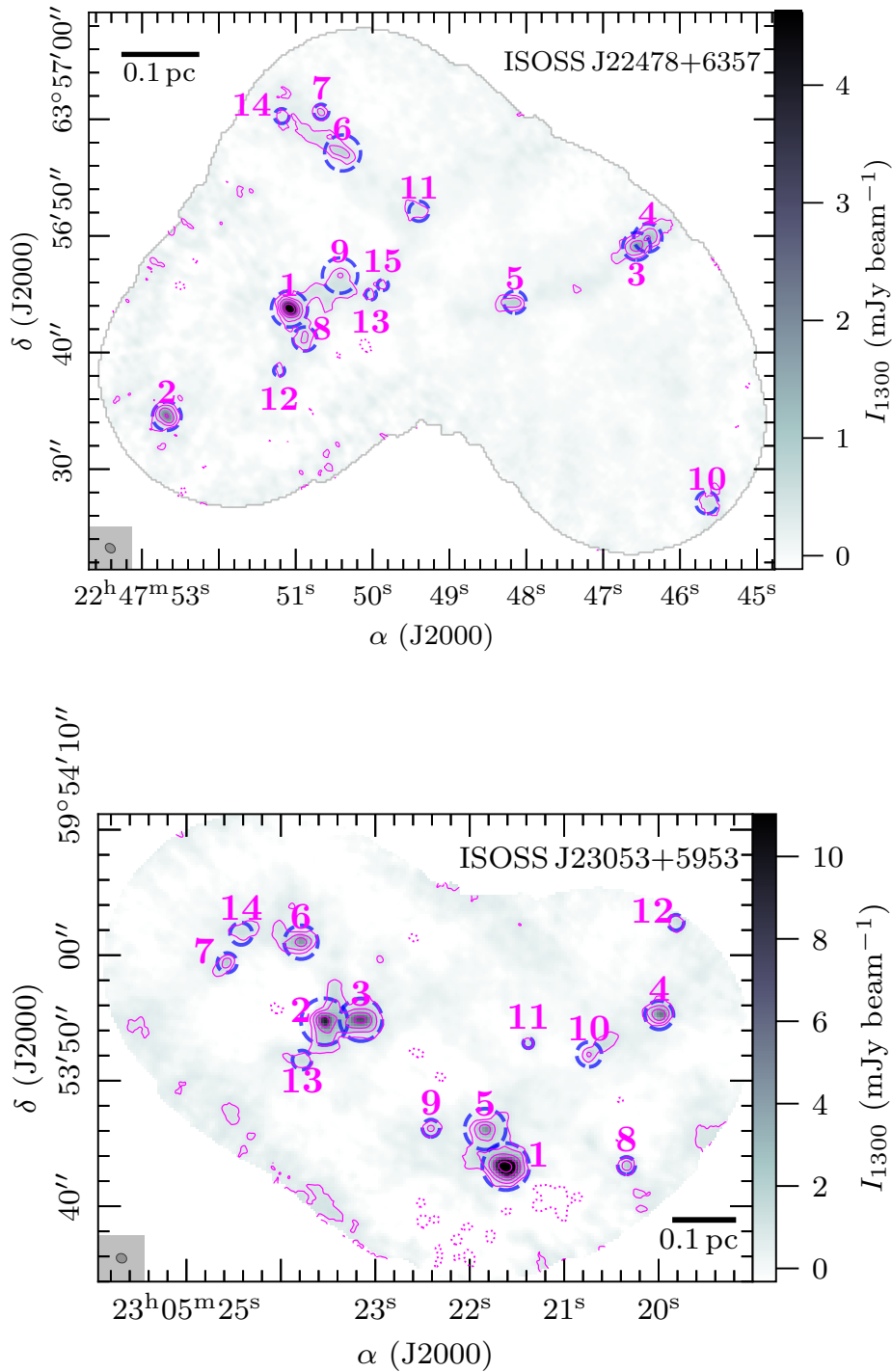


FIGURE 3.1: NOEMA 1.3 mm continuum emission of the CORE-extension regions (*top panel*: ISOSS J22478+6357 and *bottom panel*: ISOSS J23053+5953). The NOEMA continuum data are presented in color scale and pink contours. The dotted pink contour marks the $-5\sigma_{\text{cont}}$ level. Solid pink contour levels are 5, 10, 20, 40, and $80\sigma_{\text{cont}}$. All mm cores identified in Beuther et al. (2021) are labeled in pink. The core outer radius r_{out} is indicated by a dashed blue circle. The synthesized beam is shown in the bottom left corner. A linear spatial scale of 0.1 pc is indicated by a black scale bar.

Birkmann et al. (2007) derive core masses of 26, 4.4, and $4.4 M_{\odot}$ for cores 1, 2, and 3, respectively, in ISOSS J23053+5953 using 1.3 mm observations. These values are higher than the estimates by Beuther et al. (2021). As in the calculation by Birkmann et al. (2007) the

assumed kinetic temperature was derived from lower dust temperatures based on the single-dish observations. The estimated core mass of mm core 13 in ISOSS J22478+6357 is low ($0.44 M_{\odot}$), but Hennemann et al. (2008) infers that this MIR source (their “source 3”) has a central mass of $6 - 8.5 M_{\odot}$ using the YSO SED models by Robitaille et al. (2007). By applying the same SED models to mm core 2 (their “SMM East”) in ISOSS J23053+5953, Pitann et al. (2011) estimate a central mass of $4.1 - 6.6 M_{\odot}$, whereas Beuther et al. (2021) derive a core mass of $2.51 M_{\odot}$.

The calculation of the core mass depends strongly on the assumed temperature. In Beuther et al. (2021), core masses are also derived assuming a uniform temperature of 20 K. In cases when the kinetic temperature is actually higher, derived from the H_2CO rotation temperature maps (Sect. 3.5.4), the core masses are overestimated by a factor of a few. While the assumption of a low temperature at clump scales is valid, the high angular resolution data reveals that some mm cores already harbor protostars that heat up the surrounding envelope. Differences in the mass estimates are also caused by a higher assumed gas-to-dust mass ratio (150, Beuther et al. 2021) instead of the canonical value of 100 used in the literature. Given the mass reservoir and that the regions are in an early evolutionary stage and thus gas accretion will continue for a few $10^5 - 10^6$ yr, some of the low-mass cores might form intermediate- to high-mass protostars in the future.

TABLE 3.4: Overview of the cores in the CORE-extension sample. The coordinates, peak intensity I_{peak} , integrated flux F_{1300} , outer radius r_{out} , T_{kin} obtained from the H_2CO rotation temperature map, core mass M_{core} , and molecular hydrogen column density $N(\text{H}_2)$ are taken from Beuther et al. (2021). The systemic velocity v_{LSR} of each core is estimated from the optically thin $\text{C}^{18}\text{O } 2-1$ line (Sect. 3.5.6). The continuum optical depth τ_{cont} is calculated according to Eq. (1.47) in Sect. 3.4.1. The presence of protostellar outflows are investigated in Sect. 3.5.1 using $\text{CO } 2-1$ line wing emission. Cores with an associated bipolar outflow are marked with a \checkmark , whereas cores with no or no clear bipolar outflow signature are marked with a \times . The last column lists Herschel clumps studied by Ragan et al. (2012) associated with the mm cores (Fig. 3.3). We note that due to poor angular resolutions at FIR wavelengths, multiple mm cores can be embedded within a Herschel clump. Here we list for the mm cores the closest clump considering the clump peak intensity.

Core	Coordinates		v_{LSR} (km s^{-1})	I_{peak} (mJy beam^{-1})	F_{1300} (mJy)	r_{out} (au)	T_{kin} (K)	M_{core} (M_{\odot})	$N(\text{H}_2)$ (10^{22} cm^{-2})	τ_{cont} (10^{-3})	CO outflow	Herschel clump
	α (J2000)	δ (J2000)										
ISOSS J22478+6357 1	22:47:51.08	+63:56:43.7	-39.8	7.69	12.59	5 007	42	1.84	27.4	7.0	\checkmark	...
ISOSS J22478+6357 2	22:47:52.68	+63:56:34.5	-39.7	2.38	5.14	3 967	13	3.33	37.5	9.8	\checkmark	...
ISOSS J22478+6357 3	22:47:46.56	+63:56:49.1	-39.0	1.80	4.02	3 841	33	0.78	8.5	2.2	\checkmark	...
ISOSS J22478+6357 4	22:47:46.42	+63:56:49.8	-39.1	1.25	3.49	3 915	22	1.1	9.6	2.5	\checkmark	clump 1
ISOSS J22478+6357 5	22:47:48.15	+63:56:44.3	-40.1	0.89	2.02	3 108	37	0.34	3.7	0.9	\checkmark	clump 3
ISOSS J22478+6357 6	22:47:50.39	+63:56:57.1	-40.5	0.78	4.08	4 986	27	0.97	4.5	1.2	\times	clump 5
ISOSS J22478+6357 7	22:47:50.67	+63:57:00.6	-41.0	0.73	0.79	2 096	10	0.76	17.1	4.5	\times	...
ISOSS J22478+6357 8	22:47:50.88	+63:56:41.2	-39.0	0.68	1.90	3 326	27	0.47	4.1	1.0	\times	...
ISOSS J22478+6357 9	22:47:50.42	+63:56:46.6	-40.7	0.62	3.91	4 891	10	3.76	14.5	3.8	\times	...
ISOSS J22478+6357 10	22:47:45.65	+63:56:27.1	-39.5	0.56	1.38	3 060	10	1.32	13.1	3.5	\times	...
ISOSS J22478+6357 11	22:47:49.40	+63:56:52.1	-39.3	0.47	1.07	2 768	18	0.45	4.8	1.2	\times	...
ISOSS J22478+6357 12	22:47:51.22	+63:56:38.4	-38.8	0.40	0.40	1 510	57	0.04	1.0	0.3	\times	...
ISOSS J22478+6357 13	22:47:50.02	+63:56:45.0	-40.4	0.37	0.37	1 510	15	0.19	4.7	1.2	\times	clump 4
ISOSS J22478+6357 14	22:47:51.18	+63:57:00.3	-40.9	0.36	0.52	2 039	27	0.13	2.2	0.6	\times	...
ISOSS J22478+6357 15	22:47:49.87	+63:56:45.8	-39.9	0.35	0.35	1 510	20	0.12	3.0	0.8	\times	...
ISOSS J23053+5953 1	23:05:21.62	+59:53:43.2	-52.2	18.38	62.67	8 063	186	3.29	13.2	4.1	\checkmark	clump 2
ISOSS J23053+5953 2	23:05:23.54	+59:53:54.7	-52.0	9.82	35.39	8 018	139	2.51	9.5	3.0	\times	clump 3
ISOSS J23053+5953 3	23:05:23.15	+59:53:54.9	-51.3	7.55	30.09	7 324	67	4.61	15.8	5.0	\times	...
ISOSS J23053+5953 4	23:05:19.99	+59:53:55.2	-51.5	5.88	11.76	4 916	33	3.95	27.0	8.6	\times	...
ISOSS J23053+5953 5	23:05:21.84	+59:53:46.1	-51.0	4.92	18.08	7 055	112	1.61	6.0	1.9	\times	...

TABLE 3.4: continued.

Core	Coordinates		v_{LSR} (km s ⁻¹)	I_{peak} (mJy beam ⁻¹)	F_{1300} (mJy)	r_{out} (au)	T_{kin} (K)	M_{core} (M_{\odot})	$N(\text{H}_2)$ (10 ²² cm ⁻²)	τ_{cont} (10 ⁻³)	CO outflow	Herschel clump
	α (J2000)	δ (J2000)										
ISOSS J23053+5953 6	23:05:23.79	+59:54:01.0	-52.2	4.57	13.02	5 793	88	1.5	7.2	2.2	X	...
ISOSS J23053+5953 7	23:05:24.57	+59:53:59.4	-52.4	2.32	3.53	3 349	54	0.69	6.2	1.9	X	...
ISOSS J23053+5953 8	23:05:20.34	+59:53:43.2	-51.9	2.29	2.94	2 993	38	0.84	9.0	2.8	X	...
ISOSS J23053+5953 9	23:05:22.41	+59:53:46.2	-51.8	1.88	2.52	2 970	92	0.28	2.8	0.9	✓	...
ISOSS J23053+5953 10	23:05:20.74	+59:53:52.1	-51.8	1.73	4.76	4 264	30	1.8	9.0	2.8	✓	...
ISOSS J23053+5953 11	23:05:21.38	+59:53:53.0	-51.8	1.50	1.50	1 737	26	0.67	9.1	2.9	X	...
ISOSS J23053+5953 12	23:05:19.82	+59:54:02.6	-51.7	1.46	1.89	2 681	39	0.53	5.6	1.8	X	...
ISOSS J23053+5953 13	23:05:23.78	+59:53:51.7	-52.4	1.39	2.56	3 262	61	0.44	3.2	1.0	X	...
ISOSS J23053+5953 14	23:05:24.42	+59:54:01.7	-52.3	1.29	3.51	3 808	116	0.3	1.5	0.5	X	...

3.4.2 Radial density profiles

Observations of individual high-mass cores suggest that the density profiles of the gas and dust envelope around the forming protostars can be described by power-law profiles with density power-law indices p (Eq. 2.2) typically ranging from 1.5 to 2.0 (e.g., Beuther et al. 2007b; Zhang et al. 2009; Palau et al. 2014, 2021; Gómez et al. 2021, and Sect. 2.3.3). The density profiles can be inferred, for example, from the radial intensity profiles of the dust continuum emission (van der Tak et al. 2000; Beuther et al. 2002a; Palau et al. 2014). While the aforementioned studies are based on single-dish observations, the interferometric continuum data suffer from significantly spatially filtering the extended emission (Beuther et al. 2021). This effect can cause intensity profiles in the image domain to be much steeper than in reality and result in too steep ($p > 3$) density profiles. In order to overcome this problem, we therefore analyze the continuum data in the uv plane - excluding the regime of missing baselines - in order to estimate the power-law index p of each core. The same method to infer the core density profiles as presented in Sect. 2.3.3 is applied to the mm cores. Assuming optically thin dust emission (which is valid for all cores, Table 3.4), the power-law index p can be calculated from the power-law index of the azimuthally averaged visibility amplitudes $\bar{V} \sim s^\alpha$ (taking into account both the real and imaginary components), with uv distance s (Eq. 2.3, e.g., Adams 1991; Looney et al. 2003).

Many of the fainter mm cores are only marginally or not resolved. In order to reliably derive the radial density and temperature profiles, we restrict the analysis to mm cores that are detected with $S/N > 20$ in the 1.3 mm continuum data. This is the case for cores 1 – 4 in ISOSS J22478+6357 and cores 1 – 6 in ISOSS J23053+5953.

The azimuthally averaged visibility amplitude \bar{V} and its standard deviation were computed for each core with the `uvamp` task in MIRIAD (Sault et al. 1995) considering the real and imaginary components. The phase center was shifted to the location of the core (Table 3.4). The visibilities were binned in a bin size of $20 \text{ k}\lambda$ up to $600 \text{ k}\lambda$, which corresponds to the longest NOEMA baseline (774 m).

The computation of the azimuthally averaged visibility amplitudes of a certain core can be influenced by other mm-bright cores in the field (e.g., in ISOSS J23053+5953 mm core 2 is close to mm core 3, Fig. 3.1). Thus, before the radial visibility amplitudes of a certain core were computed, we first subtracted the emission of the remaining four brightest cores in the region. Using the `uv_fit` task in GILDAS MAPPING, we found that the emission of the mm cores is modeled best by fitting two circular Gaussian functions with a full width half maximum (FWHM) of $0.''5$, and $2.''0$, respectively, in order to take into account both compact and extended emission. The flux of the two components was varied for each core separately in order to take into account that the cores have a varying morphology (e.g., compact core or a compact core embedded in a more extended envelope). The model emission of the four remaining brightest mm cores, described each by the two Gaussian functions, was then subtracted from the original uv data set. We carefully checked, for each core, that the emission of the four brightest remaining cores was subtracted correctly by imaging the cores-subtracted uv data set.

As an example, after core 3 in ISOSS J23053+5953, the four remaining brightest cores within the FOV are cores 1, 2, 4, and 5 (Table 3.4). We first fitted and subtracted the model emission of cores 1, 2, 4, and 5 with the `uv_fit` task. We imaged this cores-subtracted uv data set and validated that the emission of cores 1, 2, 4, and 5 was removed without affecting the emission of core 3. Then we shifted the phase center in the cores-subtracted uv data to the location of core 3 and computed the azimuthally averaged visibility amplitudes using the `uvamp` task as described above.

The azimuthally averaged visibility profiles for cores 1 – 4 in ISOSS J22478+6357 and cores 1 – 6 in ISOSS J23053+5953 are shown in Fig. 3.2. The radial visibility profiles of most of the

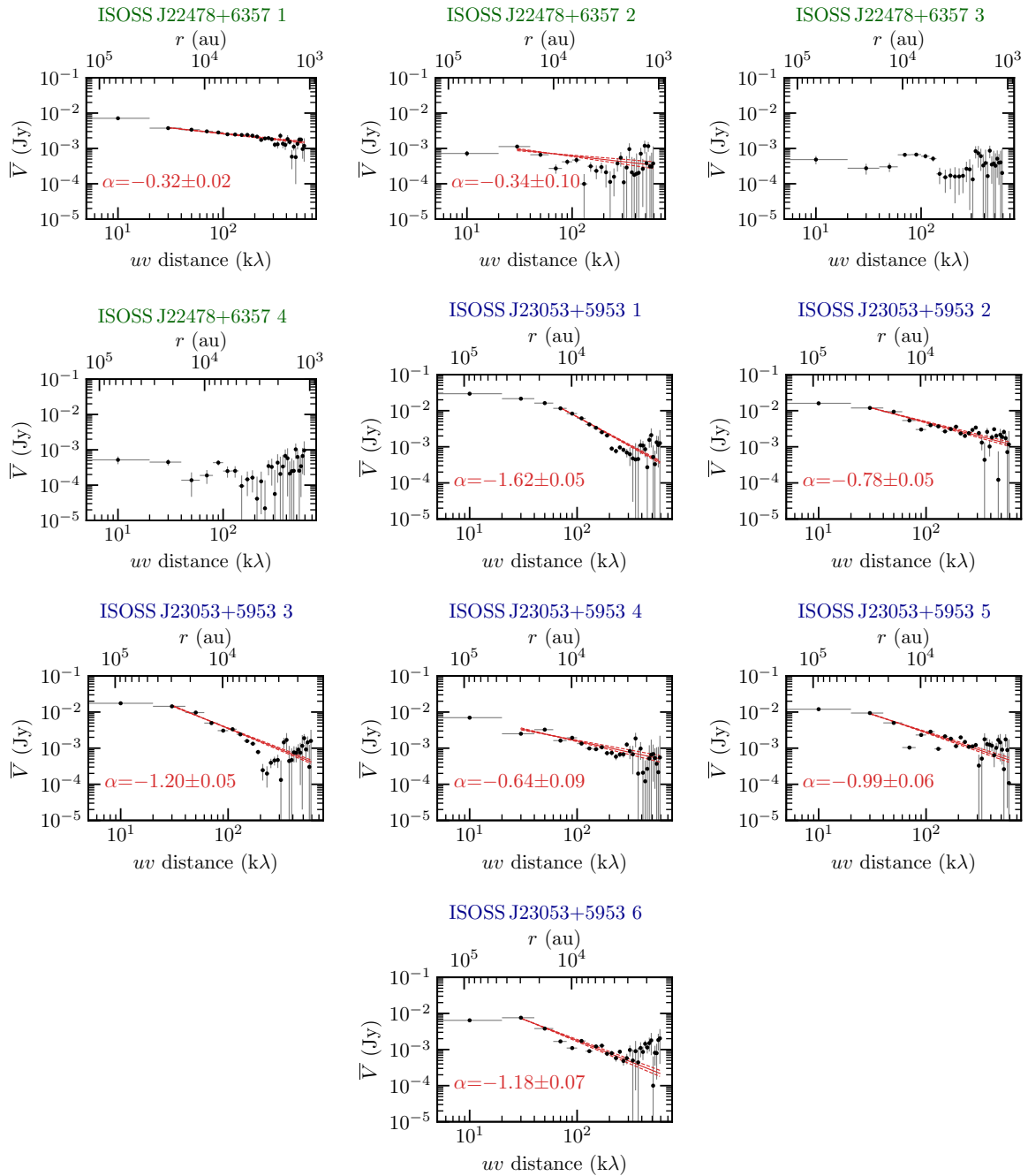


FIGURE 3.2: Radial visibility profiles of cores 1 – 4 in ISOSS J22478+6357 and cores 1 – 6 in ISOSS J23053+5953. The azimuthally averaged visibility amplitudes \bar{V} , considering the real and imaginary components, are shown in black. The bottom x-axis shows the uv distance and the top x-axis is converted to the corresponding linear spatial scale. A fit to the data and its uncertainties ($\pm 1\sigma$) are shown by the red solid and dashed lines, respectively.

cores follow a single power-law profile. Only at the shortest baselines, at 0 – 20 $k\lambda$, the profiles flatten for most of the resolved cores. The flattening at short uv distances is caused by spatial filtering since the shortest baseline is ~ 18 m. In general, at large uv distances (> 300 $k\lambda$), there is an increased scatter of the data points due to the fact that the number of long baselines of the NOEMA interferometer is smaller compared to the number of short baselines. This also causes an increase in the uncertainties of the binned data points. Cores 3 and 4 in ISOSS J22478+6357 have a flat profile, since these cores are only marginally resolved (Fig. 3.1). The visibility profile

of core 1 in ISOSS J23053+5953 flattens at uv distances $<60 k\lambda$. A large bipolar molecular outflow is observed toward this core (Sect. 3.5.1) that might impact the radial profile of the dust envelope.

Cores 3 and 4 in ISOSS J22478+6357 and cores 2 and 3 in ISOSS J23053+5953 are very close, $1.''2$ (3 900 au) and $2.''9$ (12 000 au), respectively (Fig. 3.1). The subtraction of the emission of the nearby cores is difficult in these cases, since the cores are embedded within a common envelope.

In order to estimate the density profile according to Eq. (2.2), we fitted the observed visibility profiles with a power-law profile for uv distances ranging between 20 – 600 $k\lambda$ for all cores except for core 1 in ISOSS J23053+5953. Here, we fitted the visibility profile between 60 – 600 $k\lambda$ not considering the flat distribution toward the smaller baselines. Since the visibility profiles of cores 3 and 4 ISOSS J22478+6357 are flat, we do not fit their profiles. The temperature power-law index q , required for the calculation of p , is derived in Sect. 3.5.5 and varies between 0.1 and 1 (Table 3.5).

The results for α and p are summarized in Table 3.5. The density power-law index ranges between 1 – 2. A detailed discussion and comparison with the density profiles of 22 cores in the more evolved CORE sample (Sect. 2.3.3) is given in Sect. 3.7.1.

TABLE 3.5: Physical structure and chemical timescales of the cores (with $S/N > 20$ in the continuum data) in the CORE-extension sample. The outer radius r_{out} and core mass M_{core} are taken from Beuther et al. (2021). The radial temperature profile (Eq. 2.1), described by T_{500} , the temperature at a radius of 500 au, and the power-law index q , are derived from the H_2CO temperature maps in Sect. 3.5.5. The density power-law index p is derived from the 1.3 mm continuum visibilities in Sect. 3.4.2. The chemical age τ_{chem} of cores, with eight or more detected species in the spectral line data and for which both density and temperature profiles could be derived, is estimated in Sect. 3.6.2.

Core	r_{out} (au)	M_{core} (M_{\odot})	T_{500} (K)	q	α	p	τ_{chem} (10^4 yr)
ISOSS J22478+6357 1	5007	1.84	105.8 ± 9.4	0.95 ± 0.05	-0.32 ± 0.02	1.73 ± 0.05	3.1
ISOSS J22478+6357 2	3967	3.33	-0.34 ± 0.10
ISOSS J22478+6357 3	3841	0.78	57.5 ± 20.1	0.72 ± 0.26
ISOSS J22478+6357 4	3915	1.10
ISOSS J23053+5953 1	8063	3.29	247.0 ± 22.8	0.38 ± 0.05	-1.62 ± 0.05	1.00 ± 0.07	1.9
ISOSS J23053+5953 2	8018	2.51	181.7 ± 14.1	0.14 ± 0.03	-0.78 ± 0.05	2.08 ± 0.06	1.9
ISOSS J23053+5953 3	7324	4.61	-1.20 ± 0.05
ISOSS J23053+5953 4	4916	3.95	-0.64 ± 0.09
ISOSS J23053+5953 5	7055	1.61	99.8 ± 17.1	0.14 ± 0.10	-0.99 ± 0.06	1.87 ± 0.12	...
ISOSS J23053+5953 6	5793	1.50	153.2 ± 5.5	0.29 ± 0.02	-1.18 ± 0.07	1.53 ± 0.07	1.8

3.4.3 Spectral energy distribution

The cold clumps toward both regions are studied by Ragan et al. (2012) using Herschel PACS observations at 70, 100, and 160 μm . Both regions were also observed with the Spitzer space telescope at 3.6, 4.5, 5.8, and 8.0 μm using the IRAC instrument and at 24 μm using the MIPS instrument. An overview of these archival data sets in comparison with the NOEMA 1.3 mm emission is shown in Fig. 3.3.

In the ISOSS J22478+6357 region, all mm cores are embedded within the $R \approx 0.1$ pc sized Herschel clumps. A clump with strong 70 μm emission is detected toward the southwest with no associated 1.3 mm continuum emission (“clump 2”). This source also shows strong emission in the Spitzer IRAC and MIPS data. This suggests a more evolved source where the cold dust

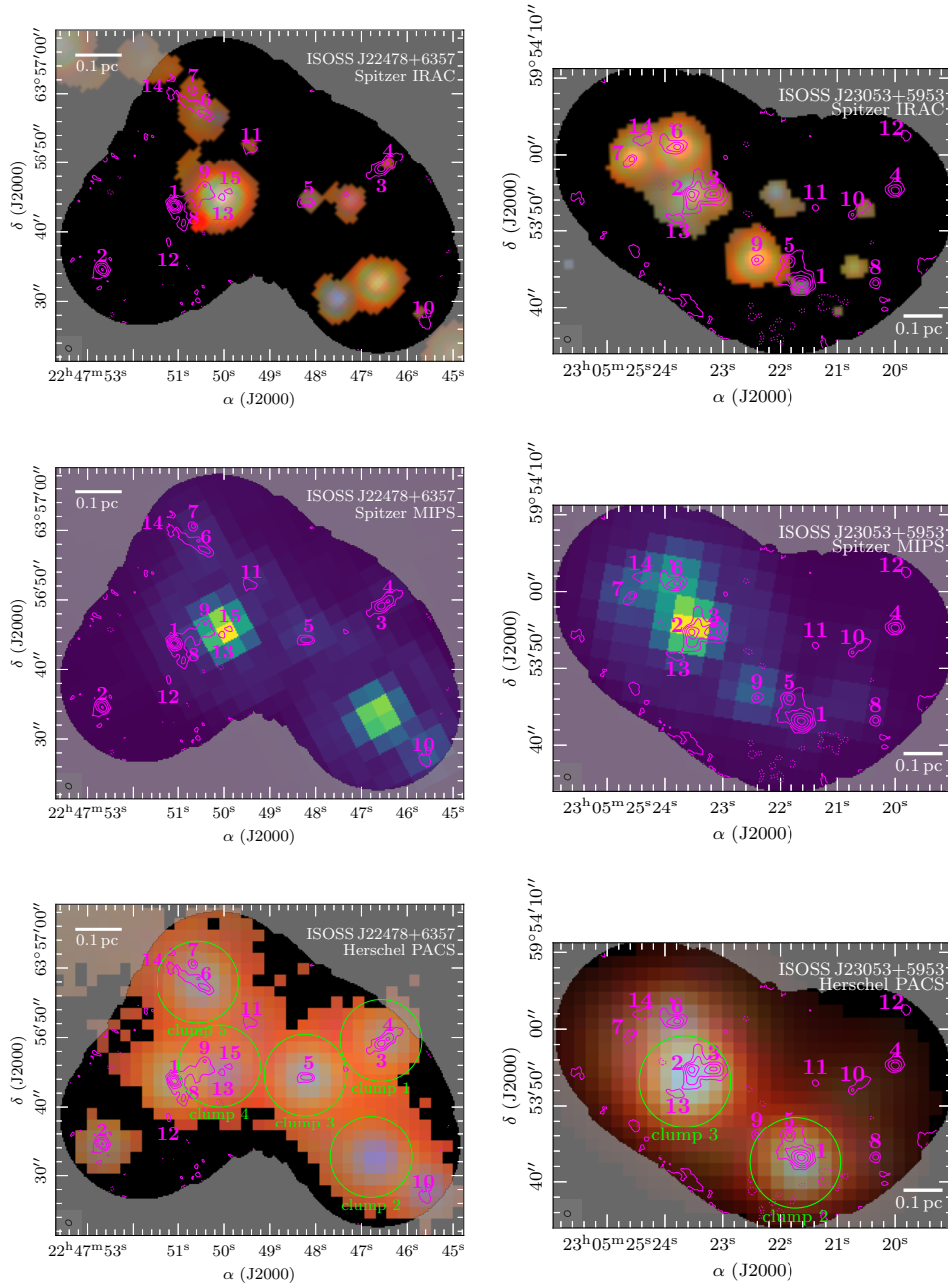


FIGURE 3.3: Multi-wavelength overview of ISOSS J22478+6357 (*left panel*) and ISOSS J23053+5953 (*right panel*). The *top panels* show a Spitzer IRAC composite RGB image at 4.5 (blue), 5.8 (green), and 8.0 μm (red). The *middle panels* show Spitzer MIPS data at 24 μm . The *bottom panels* show a composite RGB image of Herschel PACS observations at 70 (blue), 100 (green), and 160 μm (red). The Herschel clumps studied in Ragan et al. (2012) are indicated by green circles and labeled in green. In all panels, the NOEMA continuum data are shown in pink contours. The dotted pink contour marks the $-5\sigma_{\text{cont}}$ level. Solid pink contour levels are 5, 10, 20, 40, and $80\sigma_{\text{cont}}$. All mm cores identified in Beuther et al. (2021) are labeled in pink. The synthesized beam of the NOEMA continuum data is shown in the bottom left corner. A linear spatial scale of 0.1 pc is indicated by a white scale bar.

envelope was already disrupted by the protostar. The strongest MIR source is around the mm cores 13 and 15. These two mm cores, with a projected separation of $\sim 4\,200$ au, might in reality be the remaining dust envelope that is currently being disrupted by the protostar. Hennemann et al. (2008) find that this YSO is an intermediate-mass protostar. Cores 4, 5, and 6 also have bright counterparts in the Spitzer IRAC data.

The spatial extent of the two Herschel clumps in ISOSS J23053+5953 is larger, $R \approx 0.2 - 0.3$ pc, compared to the clumps in ISOSS J22478+6357. While cores 2, 3, 6, 7, 13, 14 are embedded in the northeastern clump peaking toward core 2, cores 1, 4, 5, 8, 9, 10, and 11 are associated with the southwestern clump peaking toward cores 1 and 5. MIR emission is detected around the following cores in ISOSS J23053+5953: cores 1, 2, 6, 7, 9, and 14. The southwestern clump is elongated toward core 12, but no significant FIR emission is detected there. There is also no corresponding MIR counterpart. Located at the edge of the primary beam with enhanced noise, core 12 might be an artifact.

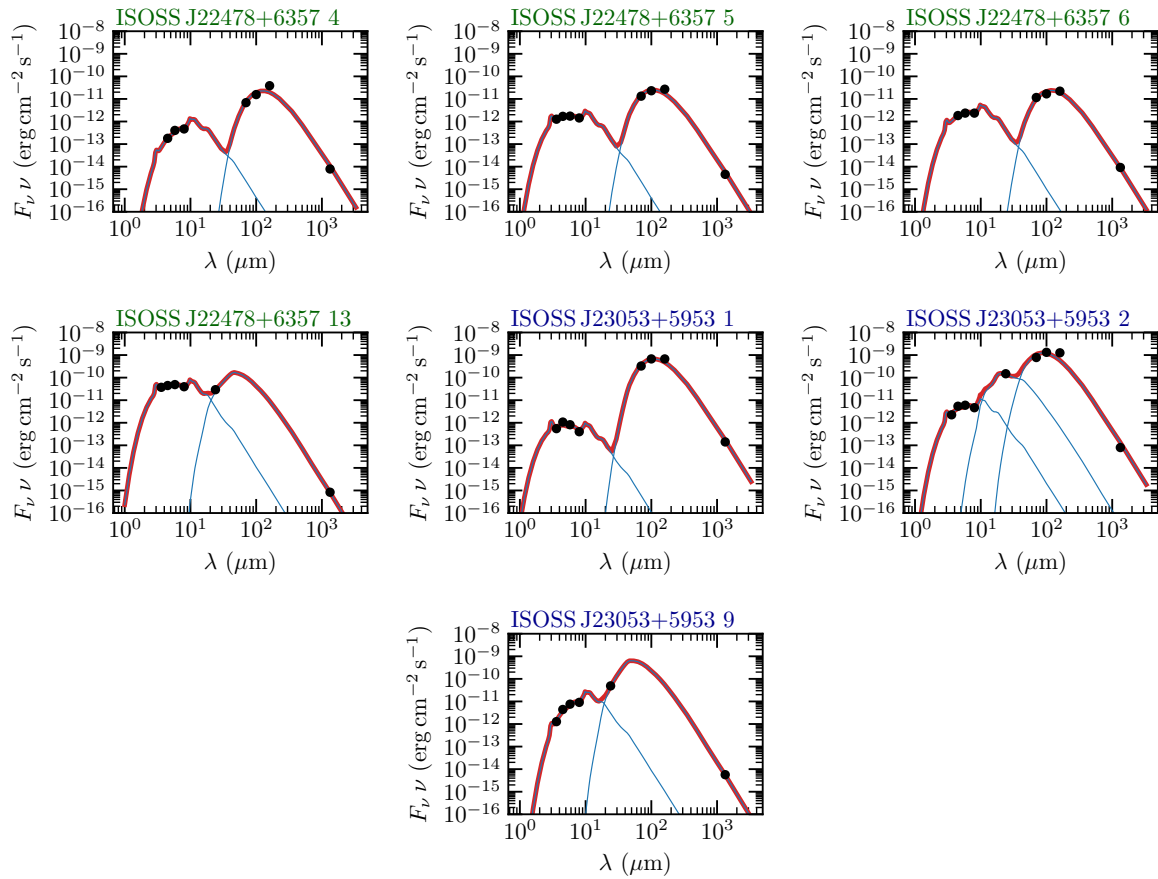


FIGURE 3.4: Spectral energy distribution of mm cores with associated Spitzer IRAC emission in at least three bands. The flux densities (black points) are obtained from Spitzer IRAC (3.6, 4.5, 5.8, and 8.0 μm), Spitzer MIPS (24 μm), Herschel PACS (70, 100, and 160 μm), and NOEMA 1.3 mm observations (Table 3.4 and 3.6). The total SED fit is shown by a red line and individual components are indicated by blue lines.

The temperature and bolometric luminosity of the cold clumps are derived by Ragan et al. (2012) with Herschel PACS observations by fitting the SED. Following the nomenclature of Ragan et al. (2012), clumps 1 – 5 toward ISOSS J22478+6357 and clumps 2 and 3 toward ISOSS J23053+5953 were covered by our observations (Fig. 3.3). In ISOSS J22478+6357, the five clumps have a temperature ranging between 18 – 21 K and bolometric luminosity between 7 – 10 L_{\odot} . For ISOSS J23053+5953, in the northeastern (clump 3) and southwestern

clump (clump 2) the dust temperature is 21 and 22 K and the bolometric luminosity is $441 L_{\odot}$ and $869 L_{\odot}$, respectively. However, the Spitzer data show that there is an additional warmer component.

We therefore refitted the SED of the cores with clear MIR counterparts in order to derive a more reliable estimate of the bolometric luminosity L . There are sources detected in the Spitzer data with no mm counterpart; however, in the following analysis we only focused on the sources with mm counterparts. It should be noted that while the Spitzer IRAC and NOEMA observations have a comparable angular resolution, the angular resolution of the Spitzer MIPS and Herschel PACS data is lower (Sect. 3.3.2). Smoothing the data to a common resolution would smear out all core features; instead, we performed a conservative cross-matching of the Spitzer MIPS sources and Herschel PACS clumps with the mm cores, as explained below.

In order to derive fluxes of the sources in the Spitzer IRAC and MIPS data, we performed aperture photometry using the `photutils` package. Background subtraction was performed by clipping sources with emission $>3\sigma$ and then the median was computed and subtracted from the data. The DAOFIND algorithm (Stetson 1987) was used to identify sources with emission $>5\sigma$. A circular aperture with a radius of $2.''4$ and $7.''6$ was used to calculate the flux of the extracted sources in the IRAC and MIPS data, respectively. We did not subtract the background with a background annulus due to the crowded fields in the IRAC data. Instead we subtracted the background using the median value in the region as described above. The Spitzer sources are cross-matched to the closest mm core, if the projected distance is $<1''$ and $<4''$ for the IRAC and MIPS data, respectively. Aperture correction was applied to the derived fluxes, with a correction factor of 1.215, 1.233, 1.366, 1.568, and 1.61 for the fluxes at 3.6, 4.5, 5.8, 8.0, and $24 \mu\text{m}$, respectively (Reach et al. 2005; Engelbracht et al. 2007).

In order to reliably fit the SED, we require that the mm cores are detected in three or four IRAC bands and therefore fitted the SED of evolved protostars. As a second further constraint, the core must either be detected at $24 \mu\text{m}$ or be associated with a Herschel clump peaking toward the position of the mm core (Table 3.4). This ensures that the mm flux can be accurately fitted with a cold component. For example, in the case of cores 6 and 7 in ISOSS J23053+5953, the mm cores have strong Spitzer IRAC counterparts; however, due to the poor angular resolution in the FIR, the Herschel clump (“clump 3” in Fig. 3.3) is not resolved toward these cores and peaks toward core 2 instead. While the warm component can be estimated with the Spitzer IRAC fluxes, a second cold component based on the mm flux cannot be constrained with only one data point. On the other hand, around core 13 in ISOSS J22478+6357, the Herschel clump (“clump 4” in Fig. 3.3) is not resolved also showing significant emission toward core 1. In this case, the Herschel PACS data points are not included in the fitting, but the strong $24 \mu\text{m}$ MIPS flux provided an additional data point peaking toward core 13. In summary, we can construct the SED from MIR to mm wavelengths for cores 4, 5, 6, and 13 in ISOSS J22478+6357 and for cores 1, 2, and 9 in ISOSS J23053+5953.

The fluxes of the Herschel PACS clumps are taken from Ragan et al. (2012), for which we cross-match the studied clumps to the closest mm core if one is detected (Table 3.4). The FIR observations resolve linear scales of $0.1 - 0.2 \text{ pc}$ (Fig. 3.3), so the fluxes are integrated over a much larger area compared to the NOEMA 1.3 mm and Spitzer IRAC data. The 1.3 mm fluxes are taken from Beuther et al. (2021) and are listed in Table 3.4. The MIR and FIR photometric data points are listed in Table 3.6 and the core SEDs are shown in Fig. 3.4.

For each core, we fit the SED with two or three components of a modified black body (Eq. 1.49),

$$B_{\nu}(T) = \frac{F_{\nu}\eta d^2}{\kappa_{\nu}M}, \quad (3.1)$$

in order to estimate the temperature and bolometric luminosity (see also Beuther & Steinacker

2007; Beuther et al. 2010; Linz et al. 2010; Ragan et al. 2012). The wavelength-dependent dust opacities, κ_ν , are taken from Ossenkopf & Henning (1994) for densities of 10^6 cm^{-3} and 10^5 yr of coagulation and with thin ice mantles. In consistency with all previous CORE and CORE-extension studies, we assume a gas-to-dust mass ratio of $\eta = 150$ ($\eta = \frac{M_{\text{gas}}}{M_{\text{H}}} / \frac{M_{\text{dust}}}{M_{\text{H}}}$, with $\frac{M_{\text{gas}}}{M_{\text{H}}} = 1.4$ and $\frac{M_{\text{dust}}}{M_{\text{H}}} = 0.0091$; Table 1.4 and 23.1 in Draine 2011, respectively). This is higher than the typically assumed ratio of 100; however, recent observations suggest that η increases with Galactocentric distance d_{gal} (Giannetti et al. 2017). These authors find a relation, where $\eta = 130 - 320$ at $d_{\text{gal}} = 10 \text{ kpc}$. For most cores, two components were sufficient to model their SED; however, for core 2 in ISOSS J23053+5953, three components were required to reliably model all photometric data points.

The results of the temperature T_i and luminosity L_i of each i -th component, and total bolometric luminosity L are summarized in Table 3.6. The fitted total SED as well as each component are shown in Fig. 3.4. The contribution of cold dust with $T \approx 20 - 40 \text{ K}$ is not sufficient to explain the observed fluxes at MIR wavelengths. In addition to the cold component, one or two warmer components with $T = 400 - 600 \text{ K}$ are required to reliably fit the SED (Table 3.6). This gives further evidence that some of the mm cores contain YSOs in a more evolved stage.

As an example for mm core 1 in ISOSS J23053+5953, two components with $T = 23 \text{ K}$ and $T = 620 \text{ K}$ are required to properly reproduce the FIR+mm and MIR fluxes, respectively. A strong $24 \mu\text{m}$ source is detected toward mm core 2 in ISOSS J23053+5953, for which three components with $T = 28 \text{ K}$, $T = 109 \text{ K}$, and $T = 479 \text{ K}$ are needed to describe the full SED.

One uncertainty arises from the fact that, even though the MIR and FIR sources are associated with the mm cores, the angular resolution of the observations from MIR to mm wavelengths vary and thus the fluxes are integrated over different angular sizes. This effect is particularly strong for the $160 \mu\text{m}$ fluxes whose observed fluxes are usually higher than the fluxes derived from the SED fit (Fig. 3.4).

TABLE 3.6: Photometry of mm cores with associated Spitzer IRAC sources (Fig. 3.3) and SED fit results (Fig. 3.4). The photometry of the Spitzer IRAC and MIPS data is described in Sect. 3.4.3. The Herschel PACS fluxes are taken from Ragan et al. (2012) by cross-matching the position of the clumps and the mm cores (Table 3.4). Due to poor angular resolutions at FIR wavelengths, core 13 in ISOSS J22478+6357 and core 9 in ISOSS J23053+5953 cannot be assigned to a Herschel clump and therefore their SEDs are not fitted in the FIR regime. In order to fit the full SED of the cores, two or three components are required. The temperature T_i and luminosity L_i of the i -th component, as well as the total bolometric luminosity $L = \sum_i L_i$, are presented. The M/L ratio is calculated from the core mass M_{core} divided by the total bolometric luminosity L .

Core	Spitzer					Herschel			SED fit							M/L (M_{\odot}/L_{\odot})
	IRAC				MIPS	PACS			T_1	L_1	T_2	L_2	T_3	L_3	L	
	$F_{3.6}$ (mJy)	$F_{4.5}$ (mJy)	$F_{5.8}$ (mJy)	$F_{8.0}$ (mJy)	F_{24} (mJy)	F_{70} (Jy)	F_{100} (Jy)	F_{160} (Jy)	(K)	(L_{\odot})	(K)	(L_{\odot})	(K)	(L_{\odot})	(L_{\odot})	
ISOSS J22478+6357 4	...	0.3	0.8	1.2	...	0.2	0.5	2.1	375	0.3	20	7.0	7.4	1.5×10^{-1}
ISOSS J22478+6357 5	1.5	2.5	3.3	3.8	...	0.3	0.8	1.4	548	1.0	24	7.9	8.9	3.8×10^{-2}
ISOSS J22478+6357 6	...	2.8	4.6	6.3	...	0.3	0.6	1.2	464	1.5	21	7.5	9.0	1.1×10^{-1}
ISOSS J22478+6357 13	44.7	67.0	95.0	105.4	234.0	552	27.3	54	47.0	74.3	2.6×10^{-3}
ISOSS J23053+5953 1	0.7	1.6	1.6	1.1	...	7.6	22.5	35.9	620	0.7	23	379.3	380.1	8.7×10^{-3}
ISOSS J23053+5953 2	2.7	8.1	11.5	12.4	1190.0	18.2	44.1	67.0	479	5.7	109	83.0	28	706.6	795.3	3.2×10^{-3}
ISOSS J23053+5953 9	1.5	6.6	14.7	24.3	391.0	374	11.4	48	333.7	345.1	8.1×10^{-4}

3.5 Spectral line emission

In this section, we study the composition of the molecular gas by analyzing the 1.3 mm spectral line data. In the analysis of the original CORE data set (Sect. 2.4.2) the low-resolution data were used, which provided a continuous spectrum. However, as ISOSS J22478+6357 and ISOSS J23053+5953 are much colder and younger with typical line widths $<3 \text{ km s}^{-1}$ (compared to a mean line width of 6 km s^{-1} in the original CORE sample, Sect. 2.4.2) we used the high-resolution ($\sim 0.5 \text{ km s}^{-1}$) data if a high-resolution unit was placed toward the line. The properties of the spectral line data products (such as velocity resolution, synthesized beam, line noise σ_{line}) are summarized in Table 3.3.

3.5.1 Molecular outflows

Molecular outflows are ubiquitous in low- and high-mass star-forming regions indicating indirectly the presence of gas accretion toward protostars (e.g., Beuther et al. 2002b; Wu et al. 2004; Zhang et al. 2005; Kölligan & Kuiper 2018). In low-mass star-forming regions, both the disk and outflow are commonly observed around protostars. Toward high-mass protostars, large bipolar outflows are found (e.g., Beuther et al. 2002b; Arce et al. 2007; Frank et al. 2014), but disk structures remain challenging to observe (e.g., Cesaroni et al. 2017; Ahmadi et al. 2019; Maud et al. 2019; Beltrán 2020; Johnston et al. 2020).

We used the integrated CO 2 – 1 emission in the blue- and red-shifted line wings to search for molecular outflows in ISOSS J22478+6357 and ISOSS J23053+5953. The blue- and red-shifted integrated intensity was computed from $v_{\text{LSR}} - 21 \text{ km s}^{-1}$ to $v_{\text{LSR}} - 6 \text{ km s}^{-1}$ and from $v_{\text{LSR}} + 6 \text{ km s}^{-1}$ to $v_{\text{LSR}} + 21 \text{ km s}^{-1}$, respectively. The results are shown in Fig. 3.5 for ISOSS J22478+6357 and ISOSS J23053+5953.

Both regions show multiple bipolar outflow signatures, indicated by arrows in Fig. 3.5. In Table 3.4 we list all mm cores with molecular outflows seen in CO 2 – 1. We find outflow signatures toward cores 1 – 5 in ISOSS J22478+6357. The outflow toward core 1 is collimated. The outflow around core 2 has a quadrupolar morphology, similar to the outflow of the intermediate-mass YSO IRAS 22198+6336 (Sánchez-Monge et al. 2010). Either the quadrupolar shape arises from the cavity walls of a wide-angle outflow or two distinct outflows of unresolved multiple protostars are present. Toward the northwest of core 5 there could be a bipolar outflow with no associated mm continuum core. All outflow directions show a preferred orientation from the northeast to the southwest and are almost parallel with respect to each other. The orientation of the outflows are perpendicular to the filamentary gas traced by DCO⁺ for ISOSS J22478+6357 (Fig. B.2). Core 11 might have a north-south bipolar outflow, but the signature is not clear.

In ISOSS J23053+5953 a large scale bipolar outflow is seen toward core 1 with the red- and blue-shifted lobes directed toward the northwest and southeast, respectively. A small projected outflow is observed toward core 9, which might be either a very young outflow just being launched or the result of an inclination effect. The CO 2 – 1 line profile of core 9 is not significantly broader than the one of core 1, so an inclination effect is unlikely. Core 10 also hosts an outflow that is partially overlapping with the red-shifted outflow of core 1. Toward the northeast of ISOSS J23053+5953, red- and blue-shifted emission is detected around the location of cores 2, 3, 6, 7, 13, and 14; however, no clear outflow directions can be identified. For example, toward both cores 7 and 6 there is a weak signature of northeast-southwest bipolar outflows. We discuss in Sect. 3.5.3 that the region shows a steep velocity gradient toward these cores caused by a colliding flow, which is also seen in the CO line wing emission. It is therefore difficult to determine if these cores host outflows or not.

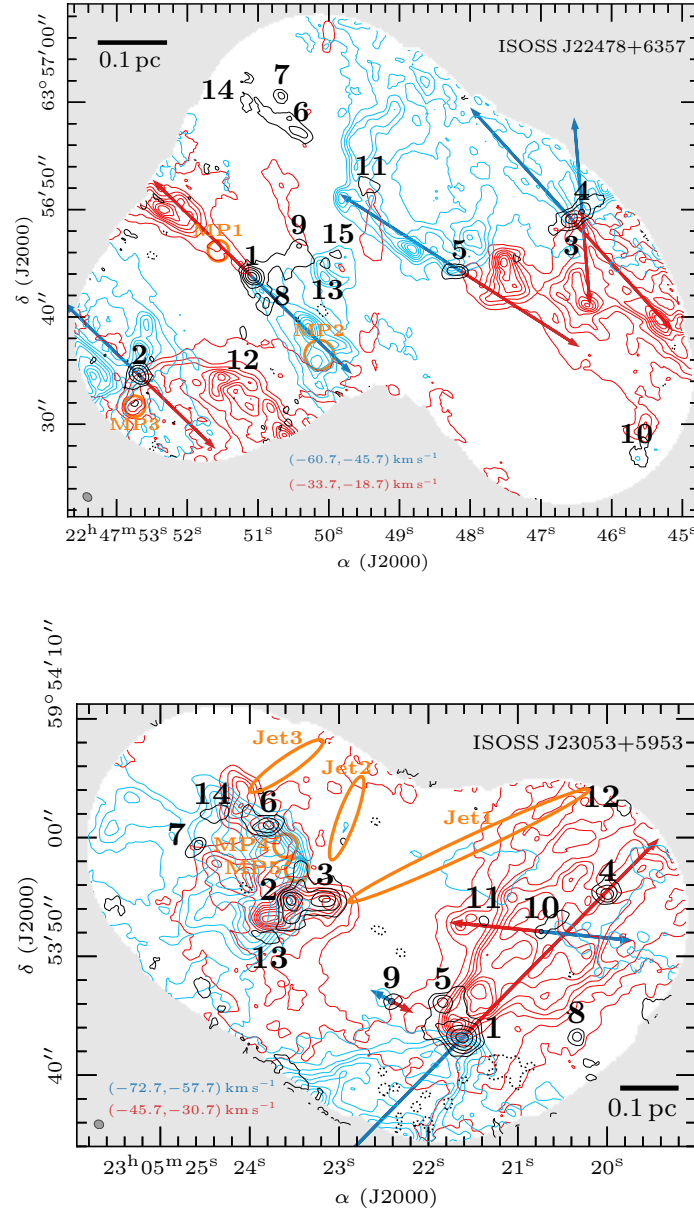


FIGURE 3.5: CO 2 – 1 outflows in ISOSS J22478+6357 (*top panel*) and ISOSS J23053+5953 (*bottom panel*). The blue and red contours show the integrated intensity of the blue- and red-shifted line wings, respectively. The intensity is integrated over $v_{\text{LSR}} - 21$ to $v_{\text{LSR}} - 6$ and over $v_{\text{LSR}} + 6$ to $v_{\text{LSR}} + 21$ km s⁻¹ for the blue- and red-shifted integrated intensity, respectively. The corresponding velocity ranges are shown in each panel. Contour levels range from 10% – 90% of the peak integrated intensity with steps of 10%. In ISOSS J22478+6357 the red- and blue-shifted peak integrated intensity is 45 K km s⁻¹ and 47 K km s⁻¹ and in ISOSS J23053+5953 it is 112 K km s⁻¹ and 140 K km s⁻¹, respectively. Red- and blue-shifted outflow directions are indicated by red and blue arrows, respectively. The NOEMA 1.3 mm continuum data are shown in black contours. The dotted black contour marks the $-5\sigma_{\text{cont}}$ level. Solid black contour levels are 5, 10, 20, 40, and 80 σ_{cont} . All mm cores identified in Beuther et al. (2021) are labeled in black. Positions with a peak in molecular emission, but no associated continuum (“molecular peaks,” MP) are indicated by orange circles (Sect. 3.5.2). Jet-like structures, seen in SiO 5 – 4 emission, are indicated by orange ellipses (Fig. 3.7). The synthesized beam of the continuum data is shown in the bottom left corner. The synthesized beam of the spectral line data is similar. A linear spatial scale of 0.1 pc is indicated by a black scale bar.

Toward ISOSS J23053+5953 clear detections of line wings from -60 km s^{-1} to -40 km s^{-1} were found using the CO 1 – 0 line observed with the IRAM 30m telescope at an angular resolution of $21''$ (Wouterloot et al. 1989). These authors derived the outflow properties and estimated a total outflow mass of $M_{\text{out}} = 14.2 - 34.2 M_{\odot}$, momentum of $P_{\text{out}} = 71.8 - 172.4 M_{\odot} \text{ km s}^{-1}$, energy of $E_{\text{out}} = (40.5 - 97.4) \times 10^{44} \text{ ergs}$, a size of $R_{\text{out}} = 1 \text{ pc}$ for both blue- and red-shifted lobes, and an outflow timescale of $\tau_{\text{out}} = 10^5 \text{ yr}$. Their outflow can be assigned to the large scale outflow from mm core 1 with a red-shifted lobe directed toward the northwest and the blue-shifted lobe directed toward the southeast (Fig. 6 in Wouterloot et al. 1989).

Comparing the mass outflow rate of core 1, $\dot{M}_{\text{out}} = \frac{M_{\text{out}}}{\tau_{\text{out}}} \approx 2 \times 10^{-4} M_{\odot} \text{ yr}^{-1}$ with the mass outflow rates of low- to high-mass YSOs (Fig. 11 in Henning et al. 2000), suggests that core 1 will form an intermediate- to high-mass star (see also Beuther et al. 2002b; Wu et al. 2004, 2005; López-Sepulcre et al. 2009; Maud et al. 2015b, for a comparison of the mass outflow rate and bolometric luminosity). The outflow has also been tentatively detected by Birkmann et al. (2007) using Plateau de Bure Interferometer (PdBI) observations of CO 2 – 1 (we note that the red- and blue-shifted outflow directions are swapped in their Fig. 3).

The molecular outflows observed with NOEMA in both regions can be assigned to mm cores; however, their extent is larger than the observed mosaic, so a larger FOV would be required to properly derive the outflow properties (such as mass, momentum, energy, and timescale) of individual outflows. The multiplicity of bipolar outflows suggests that ongoing clustered star formation is occurring in both regions. A recent study of the properties of the molecular outflow of core 1 in ISOSS J23053+5953 is presented in Rodríguez et al. (2021) using observations with the Submillimeter Array (SMA) and the VLA. These authors detect compact cm emission toward the mm core, suggesting the presence of an ionized jet. The larger FOV of the SMA primary beam allowed them to properly derive the outflow properties, with $M_{\text{out}} = 45.2 \pm 12.6 M_{\odot}$ and $\tau_{\text{out}} = 1.5 - 7.2 \times 10^4 \text{ yr}$. The resulting outflow rate $\dot{M}_{\text{out}} \approx 10^{-3} M_{\odot} \text{ yr}^{-1}$ is even higher than previously determined by single-dish observations (Wouterloot et al. 1989). A further discussion of the protostellar outflows in ISOSS J22478+6357 and ISOSS J23053+5953 is given in Sect. 3.7.1.

3.5.2 Spatial morphology and correlations

The spectral setup covers in total 26 emission lines detected in at least one of the two regions and an overview of the transition properties is shown in Table 3.2. We detect simple species consisting of 2 – 5 atoms (CO, ^{13}CO , C^{18}O , ^{13}CS , SO, H_2S , OCS, SO_2 , H_2CO , H_2^{13}CO , HNC, HC_3N); deuterated ions (N_2D^+ , DCO^+); the shock tracer SiO; the cyclic molecule $\text{c-C}_3\text{H}_2$; and two complex organic molecules (CH_3OH , CH_3CN).

Line integrated intensity

In order to investigate the spatial morphology of each emission line, we computed the integrated intensity around the region systemic velocity from $v_{\text{LSR}} - 3 \text{ km s}^{-1}$ to $v_{\text{LSR}} + 3 \text{ km s}^{-1}$. The systemic velocity v_{LSR} for both regions is listed in Table 3.1. This velocity range covers 3 and 13 channels in the low- and high-resolution data, respectively. The integrated intensity (“moment 0”) maps for strong transitions of three key species, H_2CO ($3_{0,3} - 2_{0,2}$), SiO ($5 - 4$), and CH_3OH ($4_{2,3} - 3_{1,2}E$) are shown in Figs. 3.6, 3.7, and 3.8, respectively. The moment 0 maps of the remaining lines are shown in Appendix B.1. The noise in the integrated intensity maps $\sigma_{\text{int.intensity}}$ was calculated by considering the velocity resolution (δv), line noise (σ_{line}), and number of channels (#channels): $\sigma_{\text{int.intensity}} = \delta v \times \sigma_{\text{line}} \sqrt{\text{\#channels}}$. In all integrated intensity maps, only locations with an integrated intensity $> 3\sigma_{\text{int.intensity}}$ are presented.

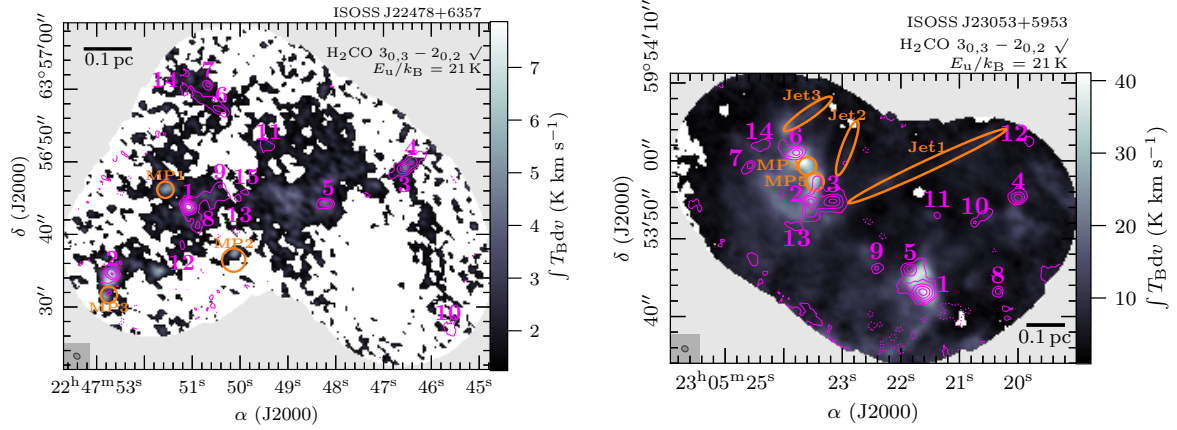


FIGURE 3.6: Line integrated intensity map of $\text{H}_2\text{CO } 3_{0,3} - 2_{0,2}$. The integrated intensity of the transition with a threshold of $S/N \geq 3$ is presented in color scale. The line intensity is integrated from a velocity of $v_{\text{LSR}} - 3 \text{ km s}^{-1}$ to $v_{\text{LSR}} + 3 \text{ km s}^{-1}$. It is marked if the transition is detected (\checkmark) or not (\times), further explained in Sect. 3.5.2. The NOEMA 1.3 mm continuum data are shown in pink contours. The dotted pink contour marks the $-5\sigma_{\text{cont}}$ level. Solid pink contour levels are 5, 10, 20, 40, and $80\sigma_{\text{cont}}$. All mm cores identified in Beuther et al. (2021) are labeled in pink. Positions with a peak in molecular emission, but no associated continuum (“molecular peaks,” MP) are indicated by orange circles (Sect. 3.5.2). Jet-like structures, seen in $\text{SiO } 5 - 4$ emission, are indicated by orange ellipses (Fig. 3.7). The synthesized beam of the continuum data is shown in the bottom left corner. The synthesized beam of the spectral line data is similar. A linear spatial scale of 0.1 pc is indicated by a black scale bar.

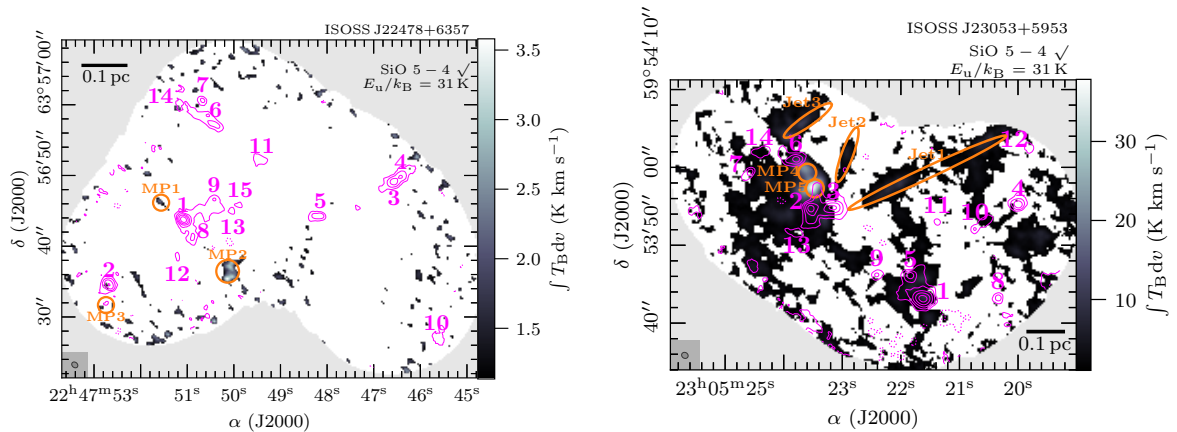


FIGURE 3.7: The same as Fig. 3.6, but for $\text{SiO } 5 - 4$.

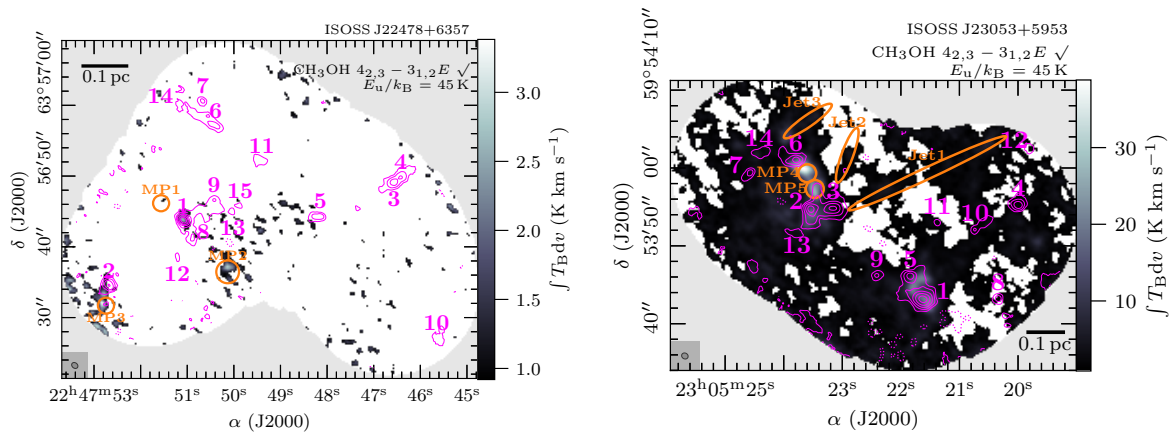


FIGURE 3.8: The same as Fig. 3.6, but for $\text{CH}_3\text{OH } 4_{2,3} - 3_{1,2}E_{\nu}$.

The properties of the line data products, such as synthesized beam and line noise, are summarized in Table 3.3. It can be clearly seen in the integrated intensity maps that the noise is not uniform throughout the mosaic increasing toward the edge. For a comparison between the two regions, regardless of whether a transition shows significant emission throughout the FOV, we carefully investigated each line integrated intensity map, especially for the fainter lines, and searched for spatially resolved emission with $S/N > 3$ that is not caused by noise artifacts. In Table 3.3 and in the integrated intensity maps we indicate for each region if the line is considered as detected (\checkmark) or not (\times) in the integrated intensity map. For example, the OCS 18 – 17 line (Fig. B.9) is clearly detected (\checkmark) in ISOSS J23053+5953 toward core 1, 2 and 6, whereas in ISOSS J22478+6357 the line emission is irregular and caused by noise artifacts and therefore marked as not detected (\times). In Sect. 3.5.6, molecular column densities are derived from the core spectrum and there it was checked separately, if the transition has emission $> 3\sigma_{\text{line}}$.

While all transitions are detected in ISOSS J23053+5953, ISOSS J22478+6357 is more line-poor, with many transitions at higher upper energy levels ($E_u/k_B \gtrsim 50$ K) not detected (Table 3.3). In both regions, the emission of the three CO isotopologues (CO, ^{13}CO , C^{18}O , Figs. B.18, B.15, and B.10, respectively) is widespread across the FOV. The optically thick CO and ^{13}CO lines trace the outer parts of the cloud and/or clump structure, while even the optically thin C^{18}O emission is detected everywhere in the FOV. The detected H_2CO transitions (Figs. 3.6, B.7, and B.8) have extended emission in both regions. H_2CO is a good thermometer at temperatures < 100 K and therefore its emission is used in Sect. 3.5.4 to create temperature maps of the regions.

In ISOSS J22478+6357, the line-richest object is core 1 with emission peaks of H_2CO , CH_3OH , SO, $c\text{-C}_3\text{H}_2$ (Figs. 3.6, 3.8, B.1, B.5, B.7, B.8, B.13, and B.17). The DCO^+ and N_2D^+ emission (Figs. B.2 and B.21) peak toward core 2, but both molecules also have large scale filamentary emission that is connecting the mm cores. H_2CO (Fig. 3.6) and SO (Figs. B.1 and B.13) also show emission peaks toward core 2. The cyclic molecule $c\text{-C}_3\text{H}_2$ has distinct emission peaks toward cores 1, 3, and 4 (Fig. B.5) tracing UV irradiated gas (e.g., Pety et al. 2005; Fontani et al. 2012; Mottram et al. 2020). There is no known PDR or UCHII region nearby and the emission peaks are co-spatial with the continuum peak of the cores. This suggests that the irradiation stems from the central protostar. Complementary observations at cm wavelengths would draw a clearer picture about the presence of any UCHII region.

We find locations in ISOSS J22478+6357 with strong molecular emission, but no 1.3 mm continuum counterpart. Toward the northeast and southwest of core 1 there are two molecular

peaks (MPs), MP1 and MP2, seen clearly in H_2CO $3_{0,3} - 2_{0,2}$ (Fig. 3.6) and SO $6_5 - 5_4$ emission (Fig. B.13). The fact that these MPs are located at both sides of core 1 suggests that they are most likely shocked regions caused by the bipolar outflow of core 1 (Fig. 3.5). The dust emission toward the MPs can be too faint to be detected at our sensitivity limit, but due to shocks dust grain destruction of the mm-sized grains into undetectable μm -sized fragments might play a role as well. Toward the south of core 2, we also find a molecular emission peak only associated with faint 1.3 mm continuum emission (MP3). This is clearly seen in H_2CO $3_{0,3} - 2_{0,2}$ (Fig. 3.6), CH_3OH $4_{2,3} - 3_{1,2E}$ (Fig. 3.8), and both SO transitions (Figs. B.1 and B.13). MP3 is connected to the red-shifted outflow cavity of core 2 (Fig. 3.5). ISOSS J22478+6357 is generally line-poor with simple species tracing the envelope, in which the cores are embedded. Molecular emission peaks with no mm continuum counterpart can be linked to molecular outflows, thus tracing shocked gas. Here, molecules, such as SO , H_2CO , and CH_3OH , which were initially frozen on the dust grains, are evaporated into the gas-phase by the shock. Toward most of the cores, no distinct molecular emission is detected. This suggests that the cores are still too cold to have high molecular abundances in the gas-phase.

ISOSS J23053+5953 is richer in line emission compared to ISOSS J22478+6357 (Table 3.3). Most of the molecular emission peaks at core 1, with some species peaking at cores 2 and 6. Core 1 has spatial emission peaks of SO (Figs. B.1 and B.13), ^{13}CS (Fig. B.20), H_2S (Fig. B.3), OCS (Figs. B.9 and B.19), H_2CO (Figs. 3.6, B.7, and B.8), HC_3N (Figs. B.6 and B.23), and CH_3OH (Figs. 3.8, B.4, B.14, and B.17).

Core 2 has a prominent emission peak in the CH_3OH $5_{1,4} - 4_{2,3}$ line (Fig. B.4), but also in OCS (Figs. B.9 and B.19), HNCO (Fig. B.11), and CH_3CN (B.16) emission. Core 6 also shows many emission peaks and in comparison to core 1, strong emission of HNCO (Fig. B.11), $c\text{-C}_3\text{H}_2$ (Fig. B.5), and CH_3CN (Fig. B.16) is detected here, but also SO (Figs. B.1 and B.13), OCS (Figs. B.9 and B.19), and H_2S (Fig. B.3).

Similar to ISOSS J22478+6357, DCO^+ is distributed throughout the FOV (Fig. B.2). Toward core 3, DCO^+ emission peaks toward the north, while N_2D^+ emission (Fig. B.21) peaks toward the west. A possible scenario could be that there is a severe depletion of CO in the western position resulting in a low DCO^+ abundance. This is further discussed in Sect. 3.7.2.

The cavity of the red-shifted outflow lobe of core 1 (Sect. 3.5.1) is seen between cores 1 and 5 in H_2CO (Fig. 3.6), CH_3OH (Figs. 3.8, B.4, B.14, and B.17), SiO (Fig. 3.7), and SO (Figs. B.1 and B.13), and HNCO (Fig. B.11) emission. The bipolar outflow is also seen as a dark lane in CO (Fig. B.18). In SiO (Fig. 3.7) and SO (Figs. B.1 and B.13), three jets can be identified toward the north of the region (labeled as Jet1, Jet2, and Jet3 in the integrated intensity maps). Jet1 is also seen in H_2CO emission (Fig. 3.6). While we do not find clear outflow signatures of the cores in this location, these jet features might indeed be caused by protostellar outflows (Sect. 3.5.1).

Toward the south of core 6 and toward the north of core 2, two emission peaks can be identified (MP4 and MP5) seen in H_2CO (Figs. 3.6, B.7, and B.8), H_2^{13}CO (Fig. B.12), CH_3OH (Figs. 3.8, B.4, B.14, and B.17), SiO (Fig. 3.7), SO (Figs. B.1 and B.13), SO_2 (Fig. B.22), HC_3N (Figs. B.6 and B.23), OCS (Figs. B.9 and B.19), and HNCO (Fig. B.11) emission. DCO^+ emission is only enhanced toward MP5 (Fig. B.2). It could be that MP4 and MP5 are connected to potential molecular outflows as it is the case for MP1, MP2, and MP3 seen in SO , SiO , and H_2CO emission toward ISOSS J22478+6357. Unfortunately, the CO $2 - 1$ line wing emission toward the location around cores 2, 3, and 6 is very complex and it is not possible to identify clear bipolar outflow signatures (Fig. 3.5). While we cannot rule out the presence of protostellar outflows causing these shocked regions, it coincides with a steep large scale velocity gradient, for example, seen in NH_3 (Bühr et al. 2015) and DCO^+ (Beuther et al. 2021), which hints at the presence of a colliding flow. This velocity gradient is further investigated in Sect.

3.5.3.

The emission of MP4 is elongated to the northeast toward mm core 6. All species having an enhanced emission toward MP4 and MP5 are known to trace shocked regions caused by protostellar outflows (Leurini et al. 2011; Benedettini et al. 2013; Moscadelli et al. 2013; Shimajiri et al. 2015; Palau et al. 2017; Tychoniec et al. 2019; Okoda et al. 2020; Taquet et al. 2020). There is enhanced $c\text{-C}_3\text{H}_2$ emission toward the north and south of core 2 (Fig. B.5) that could potentially trace, in addition to the colliding flow, a bipolar outflow.

A ring-like structure is seen in H_2CO emission in (Fig. 3.6) and in CO absorption (Fig. B.18) connecting the core 6, MP4, MP5, and core 2. This dynamically complex region might be an overlap of a colliding flow and the presence of protostellar outflows.

Spatial correlations

To quantify the spatial correlation of the detected molecular emission lines, we applied the histogram of oriented gradients (HOG) method, for which a detailed description is given in Soler et al. (2019). In summary, HOG computes the relative orientation of the local intensity gradients of two position-position-velocity (PPV) cubes I_{ijl}^A and I_{ijm}^B , where i and j run over the spatial axes and l and m over the spectral axes.

With the increasing bandwidth of correlators, sensitivity, and number of observed regions, it has become challenging to compare the spatial distribution of molecular emission and it is basically impossible to do that by eye on a channel-by-channel basis. The correlation function can also be used to study spatial correlations of the integrated intensity (e.g., Guzmán et al. 2018; Law et al. 2021). The HOG method also allows us to find a similar spatial morphology between two transitions. As the comparison is carried out in each velocity channel, potential velocity offsets between two molecules can be identified for example (Soler et al. 2019).

For the two regions in this study, we are able to compare the results obtained with HOG with the morphology of the integrated intensity maps (Sect. 3.5.2). However, for future line surveys toward star-forming regions and the analysis of the spatial morphology of the original CORE sample, HOG provides a convenient method to compare the line emission at high angular resolution and to find and study spatial correlations of molecular emission.

The projected Rayleigh statistic, V , is a statistical test to determine whether the distribution of angles ϕ_{ijlm} between the gradients is nonuniform and peaked at a particular angle (see, e.g., Durand & Greenwood 1958; Batschelet 1972; Jow et al. 2018). In this application, the angle of interest is 0 degrees, which corresponds to the alignment of the iso-intensity contours in the PPV cubes.

In our application, we accounted for the statistical correlation brought in by the beam by introducing the statistical weights w_{ij} . Relative orientation angles of local intensity gradients ϕ_{ijlm} are computed after applying a Gaussian filter with kernel size Δ . The weighting is either $w_{ijlm} = \frac{\delta}{\Delta}$ with pixel size δ or $w_{ijlm} = 0$ in noisy regions. The projected Rayleigh statistic V_{lm} quantifies the amount of spatial correlation between the velocity channels l and m of two PPV cubes and is calculated from

$$V_{lm} = \frac{\sum_{ij} w_{ijlm} \cos(2\phi_{ijlm})}{\sqrt{\sum_{ij} \frac{w_{ijlm}^2}{2}}}. \quad (3.2)$$

Hence high values of V_{lm} correspond to a high spatial correlation, while low values of V_{lm} correspond to low or no spatial correlation, for example, when comparing two velocity channels dominated by noise. To recover the smallest spatial scales, we adopted a kernel size Δ equal to the synthesized beam. For both regions, we compare all pairs of detected

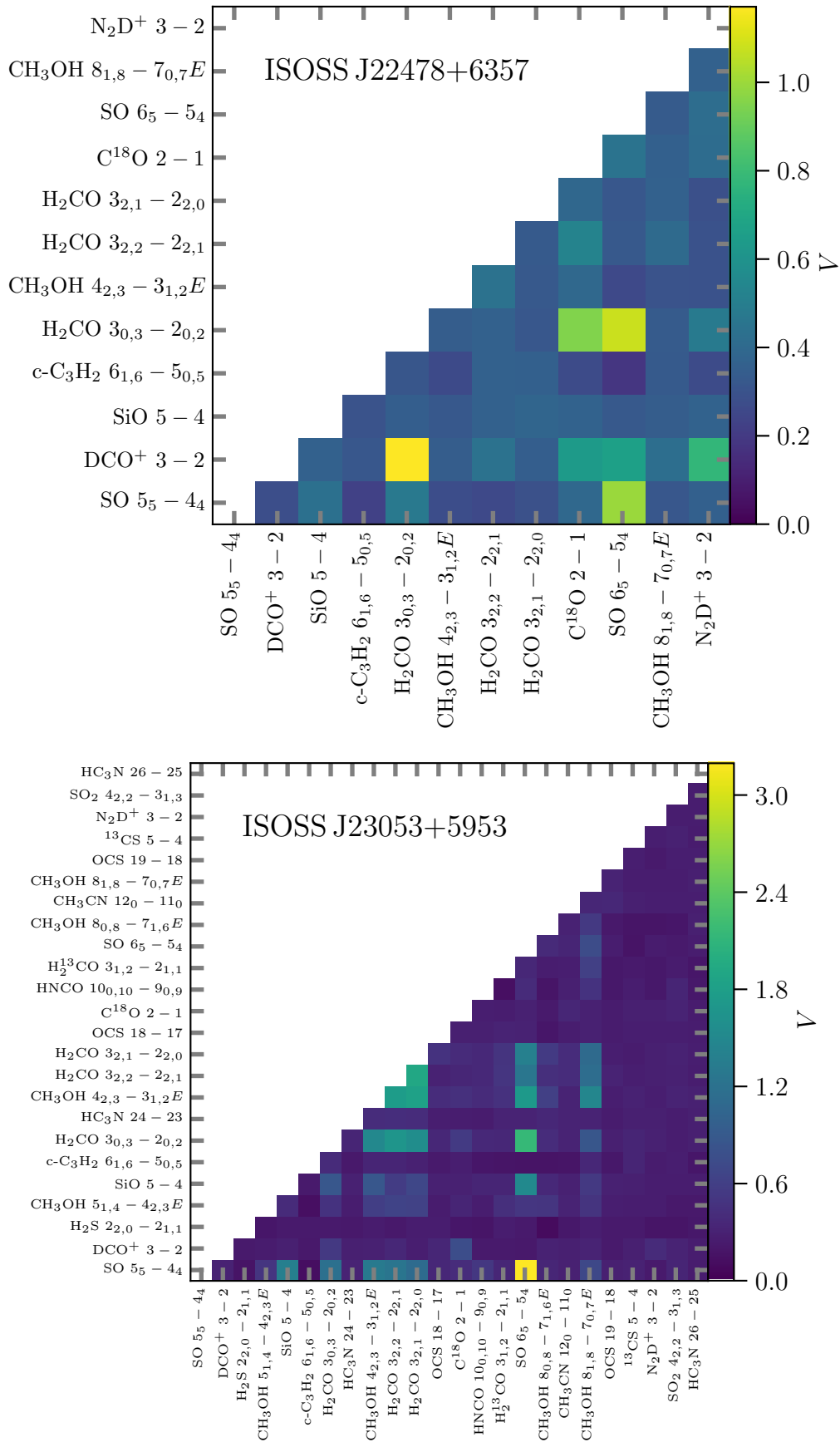


FIGURE 3.9: HOG results for ISOSS J22478+6357 and ISOSS J23053+5953. The peak projected Rayleigh statistic V is shown for each transition pair (Sect. 3.5.2). Examples of high spatial correlations in velocity space are shown in Fig. 3.10.

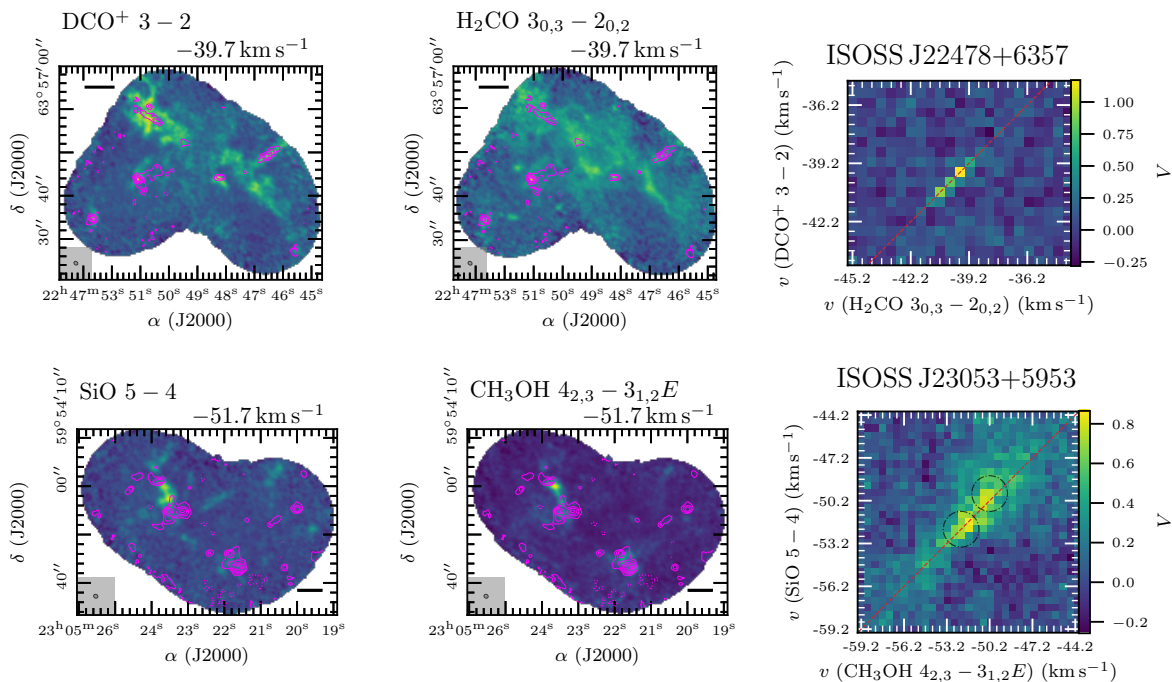


FIGURE 3.10: HOG correlation results for DCO^+ ($3-2$) and H_2CO ($3_{0,3}-2_{0,2}$) in ISOSS J22478+6357 (*top panel*) and for SiO ($5-4$) and CH_3OH ($4_{2,3}-3_{1,2}E$) in ISOSS J23053+5953 (*bottom panel*). Emission maps of the channels with the highest correlation are shown in the *left* and *middle* panels. The NOEMA 1.3 mm continuum data are shown in pink contours. The dotted pink contour marks the $-5\sigma_{\text{cont}}$ level. Solid pink contour levels are 5, 10, 20, 40, and $80\sigma_{\text{cont}}$. The synthesized beam of the continuum data is shown in the bottom left corner. The synthesized beam of the spectral line data is similar. A linear spatial scale of 0.1 pc is indicated by a black scale bar. The projected Rayleigh statistic V , computed for all velocity pairs, is shown in the *right panel*. The red dashed line indicates equal velocity in both transitions. For ISOSS J23053+5953, the velocity regime around the two velocity components seen in line emission at $v \approx -52 \text{ km s}^{-1}$ and -50 km s^{-1} (Sect. 3.5.3) are highlighted by black dash-dotted circles.

emission lines listed in Table 3.3, except for the optically thick CO and ^{13}CO transitions. For all transitions, the emission was compared in channels within a velocity range between $v_{\text{LSR}} - 7.5 \text{ km s}^{-1}$ and $v_{\text{LSR}} + 7.5 \text{ km s}^{-1}$. The only exception is the H_2CO $3_{0,3}-2_{0,2}$ line observed toward ISOSS J22478+6357, which lies at the edge of the high-resolution unit. Here we only considered a velocity range between $v_{\text{LSR}} - 5.5 \text{ km s}^{-1}$ and $v_{\text{LSR}} + 5.5 \text{ km s}^{-1}$. The peak projected Rayleigh statistic V for all transitions is shown in Fig. 3.9 for ISOSS J22478+6357 and ISOSS J23053+5953. A detailed example of two transitions with a high spatial correlation for each region is shown in Fig. 3.10.

In ISOSS J22478+6357, many transitions are not detected and thus excluded from the analysis (detections and non-detections for both regions are listed in Table 3.3). The low-energy transitions of H_2CO and SO have a high correlation. C^{18}O , DCO^+ , and H_2CO trace large scale emission. As expected, high correlations of transitions of the same species are found (H_2CO and SO). The high correlation between DCO^+ and N_2D^+ is originating from the strong emission around mm core 2.

For ISOSS J23053+5953 we also find high correlations among combinations of transitions of the same species, which is the case for SO, H_2CO , and CH_3OH . While transitions with higher upper energy levels are generally less extended, the emission stems from the same location. The observed SiO transition shows a high correlation with both SO transitions toward the outflow of core 1, Jet1, and the shocked region caused by the putative colliding flow where MP4 and

MP5 are located. With the exception of cores 1, 2, and 6 in ISOSS J23053+5953, the molecular emission does not peak toward the cores, which would be expected if the gas temperatures are already high enough to evaporate species frozen on the dust grains or allow efficient gas-phase chemistry reactions. On the contrary, the emission of SO, SiO, H₂CO, and CH₃OH transitions peak toward the shocked region (MP4 and MP5).

In summary, with HOG we are able to find molecular species that show a high spatial correlation. This can be the case for chemically related species (e.g., H₂CO and CH₃OH) and for species tracing physical conditions such as shocks (e.g., SiO and SO). As expected, multiple transitions of the same molecule also have a high spatial correlation (e.g., for transitions of SO, H₂CO, and CH₃OH). In addition, the kinematic features of the molecular line emission can be studied in detail. We do not find significant velocity offsets for species with a high spatial correlation, but the two velocity components in ISOSS J23053+5953 can be clearly identified in Fig. 3.10 (bottom right panel) at -52 km s^{-1} and at -50 km s^{-1} and are indicated by black dash-dotted circles in the figure.

3.5.3 Kinematic properties

A detailed study of the kinematic properties using the NOEMA + IRAM 30m observations of ISOSS J22478+6357 and ISOSS J23053+5953 is presented in Beuther et al. (2021). DCO⁺ is a good tracer of the early stages of HMSF (e.g., Gerner et al. 2015).

Using the DCO⁺ 3 – 2 transition, both regions show distinct emission features (Fig. B.2). The integrated line intensity shows that the 15 cores in ISOSS J22478+6357 are connected by filamentary structures (Fig. B.2). Multiple velocity components are resolved toward substructures within the region and the line widths (FWHM) are small, on the order of $\sim 1 \text{ km s}^{-1}$ (Beuther et al. 2021). The DCO⁺ line integrated intensity of ISOSS J23053+5953 does not show filamentary, but extended emission with many emission peaks close, but slightly offset from the core positions (Fig. B.2). There are two distinct velocity components, $v \approx -53 \text{ km s}^{-1}$ in the southeast direction and $v \approx -51 \text{ km s}^{-1}$ in the northwest direction (Beuther et al. 2021). This velocity gradient has already been reported by Bihl et al. (2015) using NH₃ emission at lower angular resolution and can be explained by a colliding gas flow triggering star formation. The line widths of individual DCO⁺ components are also small within the region, $\Delta v \leq 1.5 \text{ km s}^{-1}$, the only exceptions being cores 1 and 2 with $\Delta v > 2 \text{ km s}^{-1}$ (Beuther et al. 2021). The thermal line width is 0.2 km s^{-1} at 20 K (Beuther et al. 2021).

The presence of two velocity components is seen in various molecular tracers using single-dish (Wouterloot et al. 1988, 1993; Larionov et al. 1999) and interferometric observations (Bihl et al. 2015; Beuther et al. 2021). In Beuther et al. (2021) the DCO⁺ (3 – 2) intensity-weighted peak velocity (“moment 1”) map is shown to highlight the velocity gradients. For a more complete picture, we show in Fig. B.24 moment 1 maps of all observed lines with extended emission (¹³CO, C¹⁸O, SO, SiO, DCO⁺, H₂CO, and CH₃OH) with the exception of the optically thick CO 2 – 1 transition. The velocity gradient is clearly seen in all transitions. This velocity gradient is suggested to be caused by a colliding flow (Bihl et al. 2015; Beuther et al. 2021).

Another tracer of the dynamical processes in the regions is SiO. SiO is produced in shocked regions, for example, due to outflows, disk winds or converging gas flows. In a shock, silicon is sputtered off the grains and subsequently forms SiO in the gas-phase (Schilke et al. 1997). Using the SiO 5 – 4 transition, significant emission is only detected toward the south in ISOSS J22478+6357 with no nearby continuum source. In Sect. 3.5.1, we find that this emission peak is shocked gas that is directed along the blue-shifted side of the outflow of core 1. In ISOSS J23053+5953, the spatial extent of the line integrated intensity of the SiO 5 – 4 is much larger peaking between cores 2, 3, and 6. Jet-like features (Jet1 and Jet2), which might

be protostellar outflows originating from core 3, are seen toward the north of the region. SiO emission is also seen between cores 1 and 5 and likely caused by the outflow of core 1 (Sect. 3.5.1).

3.5.4 Formaldehyde distribution

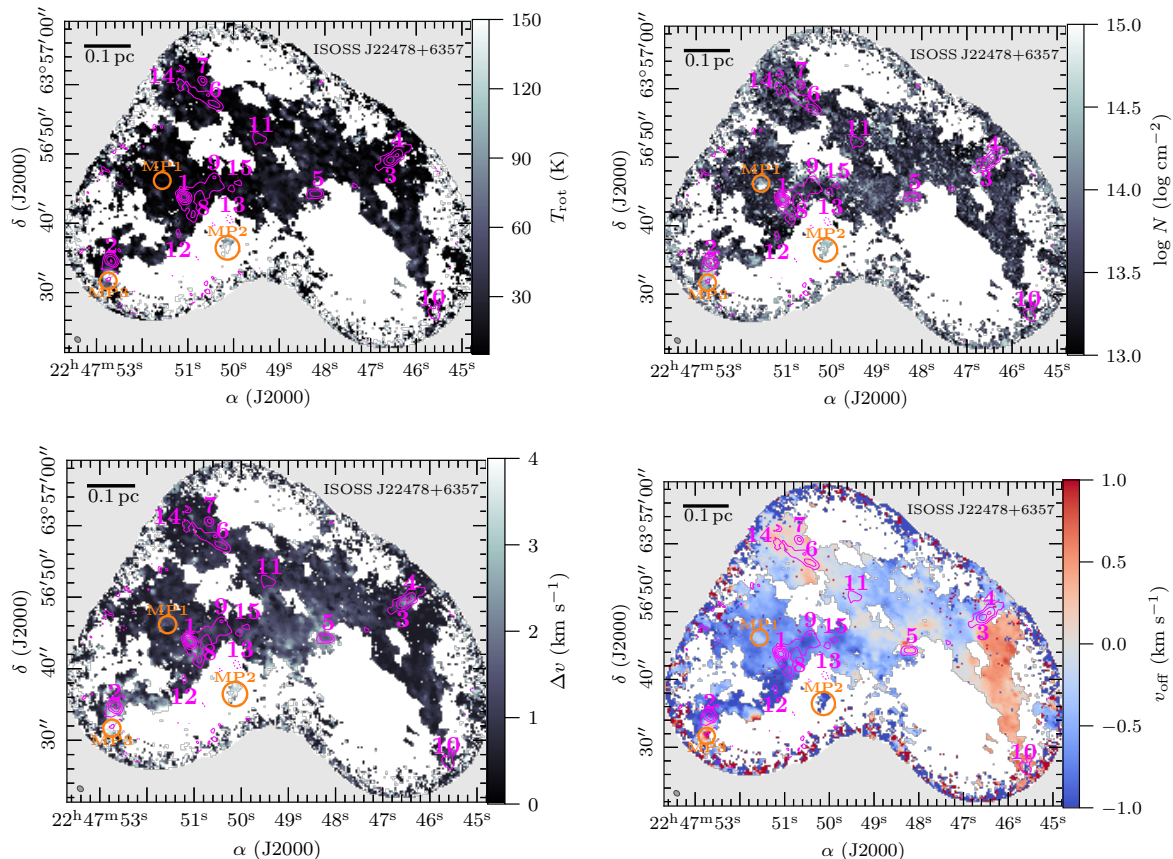


FIGURE 3.11: H_2CO parameter maps of ISOSS J22478+6357 derived with XCLASS. The fit parameter maps (T_{rot} , N , Δv , v_{off}) for H_2CO are presented in color scale. The NOEMA 1.3 mm continuum data are shown in pink contours. The dotted pink contour marks the $-5\sigma_{\text{cont}}$ level. Solid pink contour levels are 5, 10, 20, 40, and $80\sigma_{\text{cont}}$. All mm cores identified in Beuther et al. (2021) are labeled in pink. Positions with a peak in molecular emission, but no associated continuum (“molecular peaks,” MP) are indicated by orange circles (Sect. 3.5.2). The synthesized beam of the continuum data is shown in the bottom left corner. The synthesized beam of the spectral line data is similar. A linear spatial scale of 0.1 pc is indicated by a black scale bar.

The spectral line data can be used to derive molecular properties such as the rotation temperature T_{rot} and column density N in each pixel and to create parameter maps within the full FOV with XCLASS (Sect. 1.5.2). It is computationally expensive to apply this method for all pixels and all detected molecules (Table 3.3); therefore, we only applied this pixel-by-pixel analysis to formaldehyde (H_2CO), for which we detect three transitions. For the regions of the original CORE sample, temperature maps are also derived using the high-density tracer CH_3CN (Sect. 2.3.2), but since it is not detected in ISOSS J22478+6357 and the emission is not extended in ISOSS J23053+5953, only H_2CO can be used to probe the gas temperature.

We employ XCLASS to derive the following parameter set for a molecule: source size θ_{source} , rotation temperature T_{rot} (“excitation temperature”), column density N , line width Δv , and offset

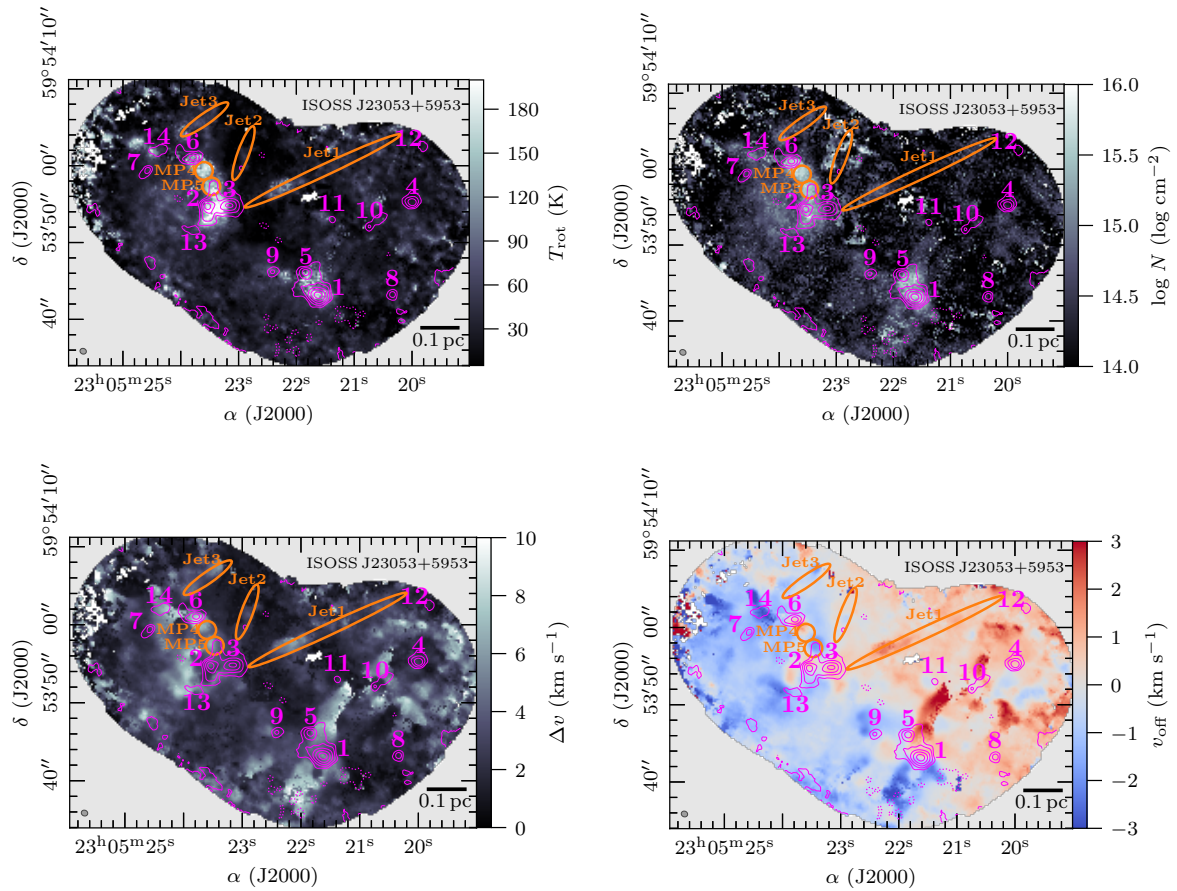


FIGURE 3.12: The same as Fig. 3.11, but for ISOSS J23053+5953. Jet-like structures, seen in SiO 5 – 4 emission, are indicated by orange ellipses (Fig. 3.7).

velocity v_{off} with respect to the local standard of rest v_{LSR} . The method is introduced in Sect. 1.5.2 and a detailed description of the used XCLASS setup is given in Appendix B.2.

The H_2CO rotation temperature maps are already presented in Beuther et al. (2021). Assuming $T_{\text{kin}} \approx T_{\text{rot}}$, the H_2CO rotation temperature was used as input to estimate the H_2 column density $N(\text{H}_2)$ and core mass M_{core} from the 1.3 mm continuum data (Table 3.4). Pixels with $T_{\text{rot}} < 3$ K are only found toward the edge of the FOV where the noise is high and the fits are unreliable.

The H_2CO parameter maps of ISOSS J22478+6357 are shown in Fig. 3.11. The rotation temperature T_{rot} is generally low varying between 10 – 50 K. Toward MP2 there is a $\approx 3'' \times 3''$ region with a high rotation temperature, $T_{\text{rot}} > 150$ K. As discussed in Sect. 3.5.1 and 3.5.2, this location is directed along the blue-shifted outflow of core 1 and is a shocked region with an enhanced H_2CO abundance and temperature increase. This can be seen in the column density map where $N(\text{H}_2\text{CO})$ is highest toward the core positions with strong mm continuum emission, but also toward this shocked region. The line widths are small, on the order of 1 km s^{-1} . The line width significantly increases at the positions of MP2 and MP3 with $\Delta v > 3 \text{ km s}^{-1}$. A small east-west velocity gradient within the region is observed in the H_2CO envelope with v_{off} varying between $\pm 1 \text{ km s}^{-1}$.

The H_2CO parameter maps of ISOSS J23053+5953 are shown in Fig. 3.12. The average rotation temperature is slightly higher with an average of $T_{\text{rot}} \approx 70$ K compared to ISOSS J22478+6357. A high increase with rotation temperatures > 150 K is observed toward

MP4 and MP5, in cores 2 and 13, and toward cores 1 and 5. We note that the highest temperatures are not located toward the continuum peak positions of the cores, but are offset and/or between the cores. This implies that the cores themselves are still cold, in agreement with temperature estimates using NH_3 (Bihr et al. 2015), but shocks increase the local gas temperature and enhance the H_2CO abundance by a factor of two, and increase the line width. The shocked region in the northeast is associated with a colliding flow and potential outflows, while the shocked region between cores 1 and 5 is most likely associated with the strong outflow of core 1, which is also seen by strong velocity gradients in v_{off} (see Sect. 3.5.1 for a discussion of the outflows in the regions). Surrounding core 4 a ring-like structure of increase in T_{rot} , Δv , and v_{off} can be observed, which could be caused by the red-shifted outflow of core 1.

In summary, the H_2CO parameter maps reveal the large scale gas distribution in both regions. We find that the temperature is enhanced toward the MPs that are caused by shocks. At this high angular resolution, we find that the temperature is higher in some locations compared to estimates using the Herschel PACS observations (~ 20 K, Ragan et al. 2012). Toward some mm cores and the shocked locations, the H_2CO column density and line width are enhanced as well. A small east-west velocity gradient is observed in ISOSS J22478+6357, while in ISOSS J22478+6357 there is a steep velocity gradient from the northeast to the southwest.

3.5.5 Radial temperature profiles

The derived H_2CO temperature maps can be used to create radial temperature profiles of the mm cores. To be consistent with the analysis of the density profiles (Sect. 3.4.2), we only applied the following analysis to cores with $S/N > 20$. Radial temperature profiles were extracted from the H_2CO temperature map for cores 1 – 4 in ISOSS J22478+6357 and for cores 1 – 6 in ISOSS J23053+5953. We binned the data with a bin size $0.5 \times \Delta r$ corresponding to half of the average beam size ($\Delta r = \frac{\theta_{\text{maj}} + \theta_{\text{min}}}{2}$). The radial temperature profile for cores 1 – 4 in ISOSS J22478+6357 and cores 1 – 6 in ISOSS J23053+5953 are shown in Fig. 3.13. Cores 3 and 4 in ISOSS J22478+6357 are close so their temperature profiles overlap.

We fitted the data assuming a power-law profile according to Eq. (2.1). We excluded the inner-most data point, which is diluted by the beam, and only fitted the data up to the bin that contains the outer radius r_{out} (Table 3.4). The outer radius r_{out} of each core is taken from (Beuther et al. 2021) and estimated by applying the `clumpfind` algorithm (Williams et al. 1994) to the 1.3 mm continuum data. For the characteristic radius and temperature we used $r_{500} = 500$ au and $T_{500} = T(r_{500})$. Flat temperature profiles (core 4 in ISOSS J22478+6357 and core 4 in ISOSS J23053+5953) or profiles that have an increasing temperature at increasing radii (core 2 in ISOSS J22478+6357 and core 3 in ISOSS J23053+5953) were not fitted.

The results for $T(r_{500})$, and q are summarized in Table 3.5. The temperature $T(r_{500})$ varies between 60 and 250 K indicating that some protostars have already heated up their surrounding envelope. The temperature power-law index q varies between 0.1 and 1.0. The results are consistent with results obtained in low- and high-mass cores (e.g., Shirley et al. 2000; Palau et al. 2014, , and Sect. 2.3.2). A comparison of the temperature profile with the cores of the CORE sample is discussed in Sect. 3.7.1.

For cores 1 and 2 in ISOSS J22478+6357, there is a significant temperature increase for $r > r_{\text{out}}$. The H_2CO temperature map (Fig. 3.11) reveals that toward the shocked gas of MP2 and MP3 the obtained rotation temperature is higher (> 100 K) compared to the ambient gas ($\approx 20 - 30$ K). Thus, the radial temperature increase for $r > r_{\text{out}}$ is related to the bipolar outflows of cores 1 and 2 (Sect. 3.5.1). The radial temperature increase of core 2 is also connected to the fact that it is located at the edge of the temperature map, where the temperature fits are unreliably due to an increase in noise (Fig. 3.11).

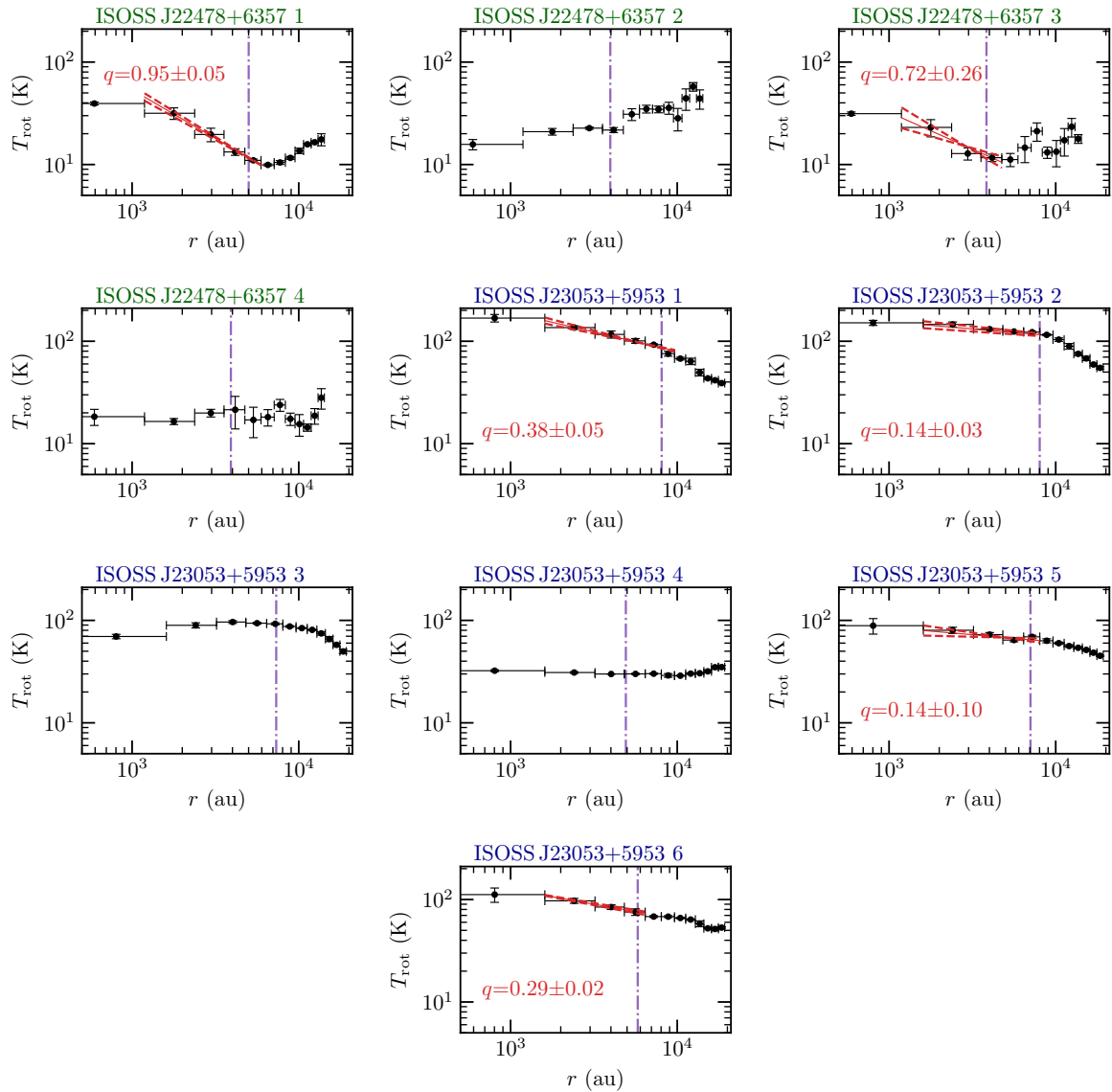


FIGURE 3.13: Radial temperature profiles for cores 1 – 4 in ISOSS J22478+6357 and cores 1 – 6 in ISOSS J23053+5953. The radial H_2CO temperature profile is shown by the black data points. The outer radius r_{out} , estimated with the `clumpfind` algorithm in the continuum data (Table 3.4), is indicated by the dash-dotted purple vertical line. A fit to the data and its uncertainties ($\pm 1\sigma$) are shown by the red solid and dashed lines, respectively.

Flat temperature profiles are observed if the temperature gradient is not resolved. In addition, a flat profile can be observed if protostellar heating is not yet high enough to heat up the envelope. A high optical depth of the H_2CO lines could have an impact toward the densest regions of the cores, but since we can clearly derive temperature gradients for the densest cores (e.g., core 1 in ISOSS J23053+5953), line optical depth effects causing unreliable temperature estimates should not be an issue for the less dense cores. For the more evolved CORE regions we find that only in evolved HMSFRs containing HMCs the H_2CO temperature maps are not reliable in the densest central regions (Sect. 2.3.2). In these cases, CH_3CN was used as a thermometer instead.

3.5.6 Molecular column densities

We quantify the molecular content by analyzing the molecular column densities N with XCLASS (Sect. 1.5.2) detected toward spectra of the 29 cores. The general setup of our XCLASS method is described in Appendix B.2. Here, we use the `myXCLASSFit` function to estimate the molecular column densities of detected molecules (Table 3.3). For each core, all species were fitted with one emission component. The column densities of the species are an input for the physical-chemical modeling of the cores (Sect. 3.6). We excluded CO and ^{13}CO from the XCLASS fitting because of the high optical depth, and only fitted the optically thin C^{18}O line. H_2^{13}CO and SO_2 were also excluded, as there is no strong emission toward the 29 cores. Our physical-chemical model does not include shock chemistry; therefore, the column density of SiO was not derived either. It should be noted that the abundances of other species are also affected by shock chemistry (e.g., Palau et al. 2017), in the case of our observations we see shocked regions in enhanced SO, H_2CO , and CH_3OH emission (see Sect. 3.5.2).

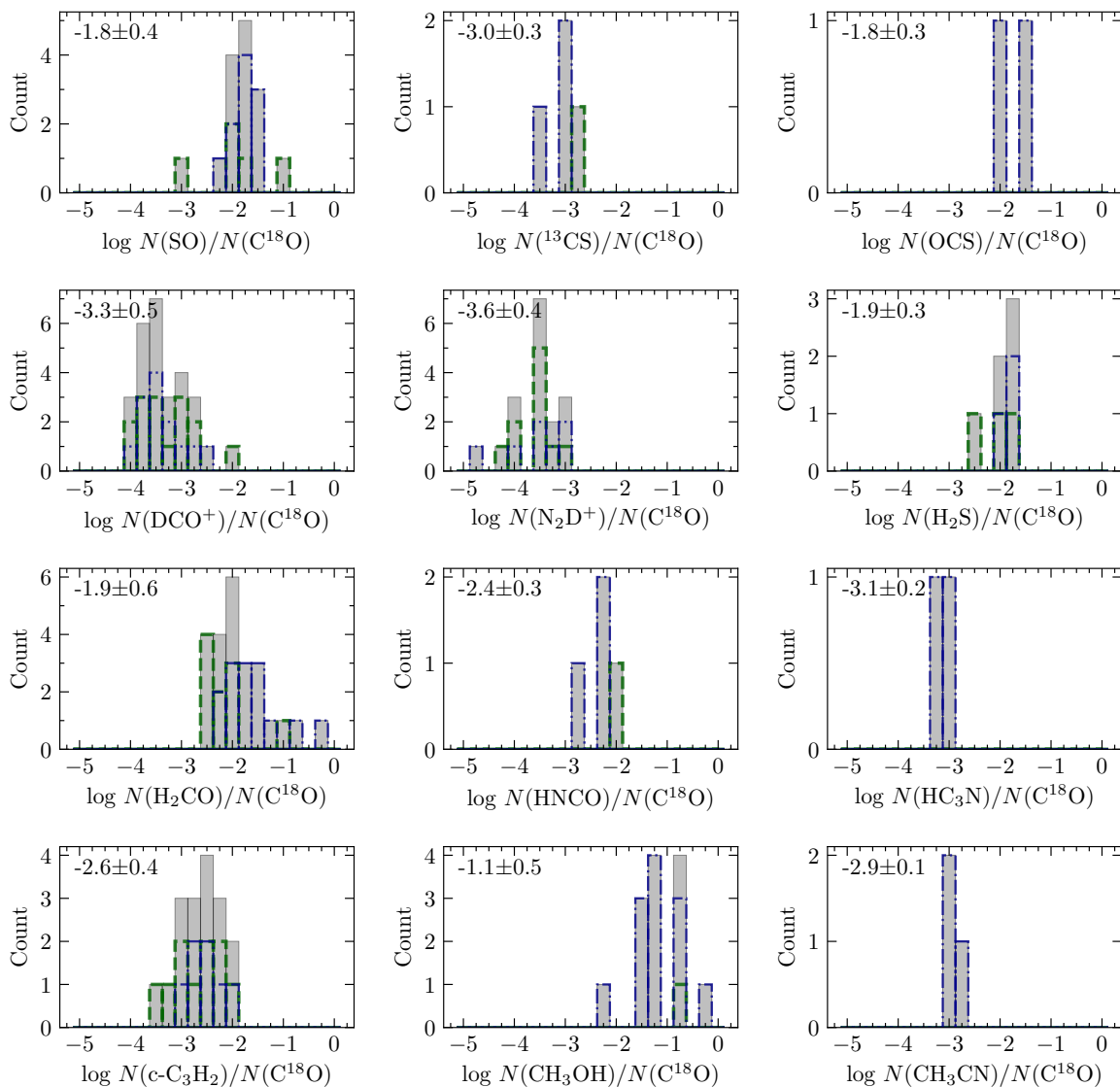


FIGURE 3.14: Abundance histograms (relative to C^{18}O) of all species fitted with XCLASS. The gray histogram shows the combined results of all 29 cores. The mean and standard deviation are shown in the top left corner. The green dashed and blue dash-dotted histograms show the results for the cores in ISOSS J22478+6357 and ISOSS J23053+5953, respectively.

Tables B.1 and B.2 summarize the best-fit column density for all 29 cores and species fitted with XCLASS. Upper limits are given, if the model peak intensity is $<3\sigma_{\text{line}}$, considering all transitions of a molecule. Upper limits are also given in cases where the upper column density error is larger than a factor of ten and when the lower column density error is zero. With these two additional constraints, unreliable fits can be further discarded (Sect. 2.4.2).

As an example, we show for all fitted transitions the observed and XCLASS modeled spectra of core 1 in ISOSS J23053+5953 in Fig. B.26. Most of the transitions show a Gaussian-shaped line profile. The $\text{H}_2\text{CO } 3_{0,3} - 2_{0,2}$ line is affected by self-absorption toward the systemic velocity and has broad line wings due to the bipolar outflow. The blue-shifted peak has a lower intensity than the red-shifted peak. This asymmetry arises from the outflowing gas being partially absorbed along the line-of-sight. The outflow is also seen in OCS 18 – 17 and 19 – 18 transitions having a weak double peaked line profile. The intensity of the CH_3OH lines that were only observed at a spectral resolution of 3 km s^{-1} is overproduced by a factor of two in the XCLASS best-fit spectrum. The upper energy levels of these transitions are not significantly different from the remaining transitions observed with the high-resolution units. This mismatch is most likely due to the differences in spectral resolution, as the remaining two transitions are fitted well. In the low-resolution spectra, the emission of a few lines, for example for SO, is broader than the frequency range considered in the fit. This enabled that, in XCLASS, the non-Gaussian line wings caused by the outflows do not have a strong impact, which might cause broad features in the fitted line profile. For the remaining cores, the line widths are smaller and therefore the fit frequency range is sufficient to consider the emission of the full line. An example of the observed and XCLASS modeled spectra of core 1 in ISOSS J22478+6357 is presented in Fig. B.25, for which clearly fewer emission lines are detected, and hence column densities for less species can be estimated.

For all species, we computed the abundance relative to $N(\text{C}^{18}\text{O})$ and abundance histograms are shown in Fig. 3.14. As the H_2 column density is derived from the NOEMA 1.3 mm continuum emission (Beuther et al. 2021) and suffers from spatial filtering, we use $N(\text{C}^{18}\text{O})$ for a reliable comparison instead (Sect. 2.4.2). Each panel shows the results considering all cores, and separate histograms for ISOSS J22478+6357 and ISOSS J23053+5953 are presented as well. The logarithmic mean and standard variation of the abundance relative to $N(\text{C}^{18}\text{O})$ considering both regions are shown in each panel. Some species are only detected toward ISOSS J23053+5953 (OCS, HC_3N , and CH_3CN). For SO, ^{13}CS , DCO^+ , N_2D^+ , H_2S , $c\text{-C}_3\text{H}_2$, and CH_3OH both regions have a similar abundance. However, the H_2CO abundance is about one order of magnitude higher in ISOSS J23053+5953 cores compared to the cores in ISOSS J22478+6357. A comparison of the mean abundance found toward the ISOSS regions compared to the CORE regions is given in Sect. 3.7.1.

3.6 Physical-chemical modeling

By analyzing the molecular line emission in Sect. 3.5.6, we find that the molecular content varies between the mm cores. Chemical timescales τ_{chem} of individual cores can be estimated with the physical-chemical model MUSCLE. The model was originally developed to study the evolutionary timescales of the IRDC, HMPO, HMC, and UCHII stages using single-dish observations of 59 HMSFRs (Gerner et al. 2014, 2015). A detailed description of the physical-chemical model is given in Sect. 2.5.

MUSCLE was applied to high angular resolution observations of the CORE pilot regions, NGC 7538S and NGC 7538IRS1 (Feng et al. 2016). In both regions, the cores have short chemical timescales of 11 000-12 000 yr. The model parameters were investigated in detail with CORE observations of the well-studied HMC AFGL 2591 VLA3 (Gieser et al. 2019), for which

the derived chemical timescale is in agreement with estimates derived in the literature. A complete physical-chemical analysis of 22 cores in the CORE sample is presented in Chapter 2. The estimated chemical timescales varies from 20 000 – 100 000 yr. The chemical composition of the molecular gas of the cores varies even within a single region. An explanation for this variety is subsequent star formation. A few CORE targets contain UCHII regions, such as S106 or G139.9091, which both already show emission at cm wavelengths. Toward these regions, compact mm cores are found in the 1.3 mm continuum emission, but not many emission lines are detected, with the exception of CO isotopologues, SO, and H₂CO. In these cases, molecules are destroyed by the protostellar radiation and thus the spectra are line-poor compared to spectra toward HMCs of the CORE sample.

3.6.1 Model setup

MUSCLE consists of a static spherically symmetric model core described by 40 radial grid points coupled the time-dependent gas-grain chemical network ALCHEMIC (Semenov et al. 2010). The density $n(r)$ and temperature $T(r)$ profiles are described by power-law profiles up to a radius r_{out} , according to Eq. (2.2) and (2.1), respectively. From an inner radius r_{in} and inward, both density and temperature reach a constant plateau, $n(r \leq r_{\text{in}}) = n_{\text{in}}$ and $T(r \leq r_{\text{in}}) = T_{\text{in}}$.

We used the same model parameters for the dust properties, interstellar radiation field, and initial chemical conditions used in the study of the 22 cores of the CORE sample, summarized in Table 2.3. Instead of running the model with only 100 logarithmic steps up to $\tau_{\text{model}} = 100\,000$ yr (Sect. 2.5), we used a finer grid of 999 logarithmic steps up to $\tau_{\text{model}} = 10^7$ yr. For the inner radius r_{in} we chose 500 au (Table 3.5). For the cores of the CORE sample the outer radius r_{out} was determined from the temperature profiles (Sect. 2.3.2), but for the ISOSS cores, we used the outer radius derived from the `clumpfind` analysis presented in Beuther et al. (2021) and summarized in Table 3.4.

We used the molecular hydrogen column density $N(\text{H}_2)$ derived from the 1.3 mm continuum emission (Table 3.4). Short-spacing information is available for the spectral line data; however, the continuum data are obtained with NOEMA only, so missing flux can be an issue. Column densities derived with XCLASS of the following molecules were included in the model: C¹⁸O, ¹³CS, SO, OCS, DCO⁺, N₂D⁺, H₂S, H₂CO, HNCO, HC₃N, c-C₃H₂, CH₃OH, and CH₃CN. The chemical network ALCHEMIC does not consider isotopologues except for a sophisticated deuterium (D) network, thus the column densities of C¹⁸O and ¹³CS were converted to the column density of their main isotopologue (CO and CS) using the isotopic ratio calculations from Wilson & Rood (1994) depending on the Galactocentric distance d_{gal} . The ¹²C/¹³C isotopic ratio is 80 and 86 and the ¹⁶O/¹⁸O isotopic ratio is 607 and 649 for ISOSS J22478+6357 and ISOSS J23053+5953, respectively (Table 3.1). The ¹²C/¹³C isotopic ratios are in agreement with a study by Giannetti et al. (2014). These authors predict a ratio between 40 – 90 and between 45 – 95 at the corresponding Galactocentric distance for ISOSS J22478+6357 and ISOSS J23053+5953, respectively.

A static spherically symmetric physical model is not sufficient to describe the protostellar evolution where the temperature and density are gradually increasing. However, coupling a chemical network with thousands of reactions to a hydrodynamical model is computationally expensive. As complex molecules, such as CH₃OH, are observed toward both regions, a simple chemical network would not be sufficient to describe the formation of all observed molecular species. Instead, we approximate the warm-up and density increase as step functions of several evolutionary stages with different temperature and density profiles. Using a sample of 59 HMFRS, Gerner et al. (2014, 2015) created template initial chemical conditions for the IRDC, HMPO, HMC and UCHII stage. For each core, we ran MUSCLE with IRDC, HMPO and HMC

initial chemical conditions, referred to as the HMPO, HMC, and UCH_{II} model, respectively, to derive the best-fit chemical timescale τ_{chem} (see also Sect. 2.5). While we follow this nomenclature, it is not our goal to classify the cores into these evolutionary stages (Sect. 2.5.1).

For each initial condition model, the chemical age τ_{chem} was estimated from the best match of the modeled and observed column densities. The physical properties of each core were fixed and set to the observed physical properties (p , q , T_{500} , listed in Table 3.5). Therefore, the observed molecular column densities (Tables B.1 and B.2) constrained the best-fit model. As both regions are in general line-poor, only cores, for which at least eight of the in total 14 column density points are considered as detections and good fits and not upper limits, are modeled with MUSCLE. This includes four cores: core 1 in ISOSS J22478+6357 and cores 1, 2, and 6 in ISOSS J23053+5953.

Not all three initial condition models were considered for each core. The cores gradually warm up due to the protostellar radiation and a temperature decrease with increasing time would be unphysical. We therefore required that the observed temperature of the core at r_{in} is equal or higher than the temperature at r_{in} of the initial condition model, $T_{\text{in}} \geq T_{\text{in,init}}$.

In each time step, the modeled radial abundance profiles are converted to beam convolved column densities with the same beam size as in the observations assumed. The modeled and observed column densities of the input molecules are compared by a least χ^2 analysis. We used a weighted χ^2 , taking into account the percentage of well modeled molecules Y : $\bar{\chi}^2 = \frac{\chi^2}{Y^2}$. The model with the lowest $\bar{\chi}^2$ was then considered as the best-fit model. The column density of a molecule is well modeled if the modeled and observed column densities agree within a factor of ten. The chemical timescale is the sum of the timescale of the initial condition model τ_{init} and of the core model τ_{model} : $\tau_{\text{chem}} = \tau_{\text{init}} + \tau_{\text{model}}$.

3.6.2 Chemical timescales

The best-fit chemical timescales are summarized in Table 3.5 for each modeled core. Detailed model results for each initial condition model are presented in Table B.3. Following the analysis of the mm cores of the original CORE sample (Sect. 2.5), we assume that the chemical timescales are uncertain by a factor of two (see also Gerner et al. 2014, 2015). A comparison of the observed and modeled column density is shown in Fig. 3.15 for all four modeled cores. Since in MUSCLE a factor of ten uncertainty for the modeled column densities is assumed and none for the observed column densities when deciding if a molecule is well modeled or not, we only show error bars for the modeled column density data points.

In the ISOSS J22478+6357 region, only core 1 can be modeled with MUSCLE and the estimated chemical timescale is 31 000 yr. This is in agreement with the fact that the region is young and still in a cold stage. With most molecules still frozen on the dust grains or not formed yet, the spectra appear line-poor. The modeled SO and H₂S column densities are both higher than a factor of ten compared to the observed column densities. As discussed in Gerner et al. (2014) and in Sect. 2.5, the sulfur chemistry, especially SO, is poorly understood and is also affected by the presence of shocks. The elemental sulfur abundance had to be increased in the Gerner et al. (2014, 2015) models in order to properly explain the observed column densities of S-bearing species, but even in their case, the SO abundances could not be explained with MUSCLE. The same issue was found when modeling the 22 cores of the original CORE sample (Sect. 2.5). It is still under debate where and in what form sulfur is locked, for example, on the grains as OCS or H₂S or in the gas-phase as neutral S (e.g., Goicoechea et al. 2021, and references within).

For core 1 in ISOSS J23053+5953, we estimate a chemical timescale of 19 000 yr. Both HMPO and UCH_{II} model have a similar χ^2 of 0.458 and 0.457, respectively. However, the number of well-modeled molecules is higher for the HMPO model (71.4%) than for the UCH_{II}

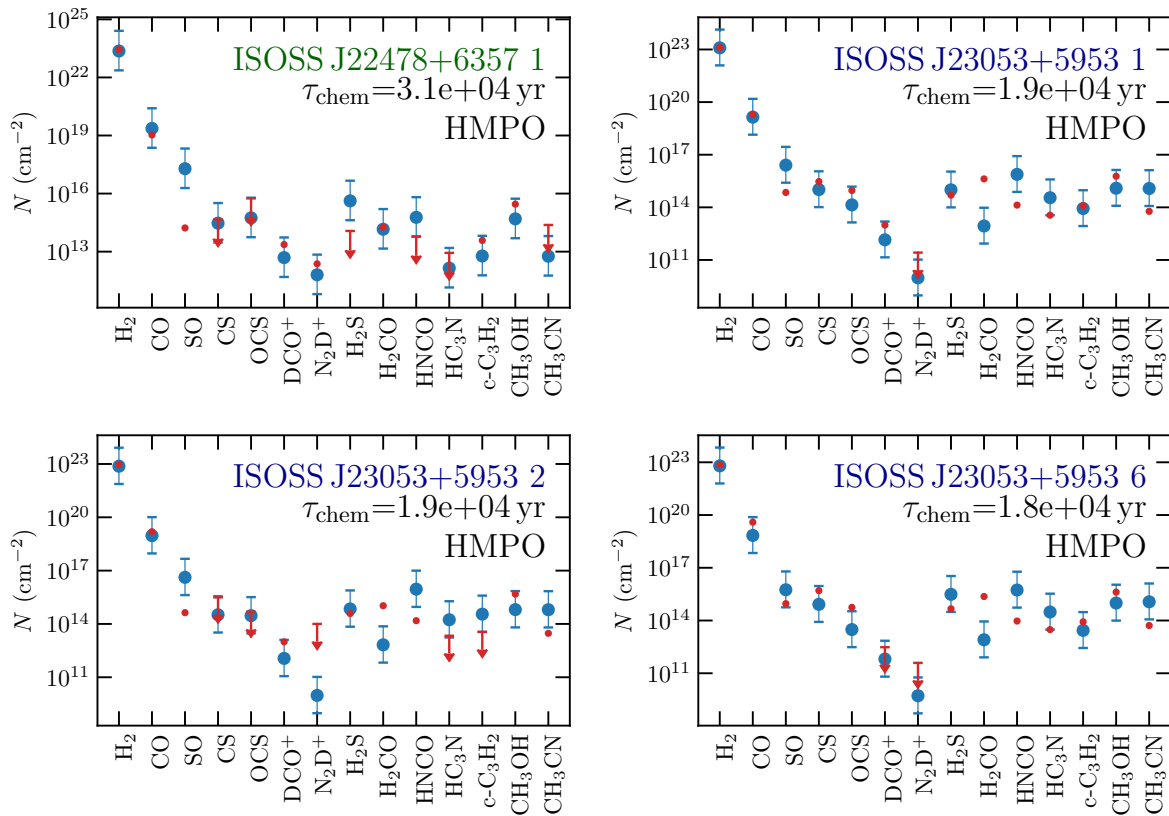


FIGURE 3.15: Comparison of the observed and modeled column densities for core 1 in ISOSS J22478+6357 and cores 1, 2, and 6 in ISOSS J23053+5953 modeled with MUSCLE. The observed column density is shown in red and upper limits are indicated by arrows (Tables B.1 and B.2). The column densities of the MUSCLE best-fit model are shown by the blue data points assuming a factor of ten uncertainty.

model (64.3%), so the weighted $\bar{\chi}^2$ is lower for the HMPO model. In the physical-chemical analysis of the CORE sample, cores with $\tau_{\text{chem}} > 80\,000$ yr show emission from vibrationally excited lines that are not detected in the two ISOSS regions. In addition, the observed spectra toward the CORE cores with $\tau_{\text{chem}} > 80\,000$ show typical hot-core type spectra and with more emission lines detected compared to core 1 in ISOSS J23053+5953. This suggests that the HMPO model is indeed the more realistic model. The best-fit chemical age for cores 2 and 6 are similar to the chemical timescale of core 1, 19 000 yr and 18 000 yr, respectively.

The MUSCLE model overestimates the SO column density for all cores except for core 6 in ISOSS J23053+5953. The H₂CO column density is underestimated by MUSCLE for all cores except core 1 in ISOSS J22478+6357. These species are difficult to model with MUSCLE since the sulfur chemistry was already an issue in the initial abundance models by Gerner et al. (2014, 2015) and shock chemistry is not included, which is important to consider, for example, for outflow sources having enhances SO and H₂CO emission (see also Sect. 3.5.2). A comparison of the chemical timescales τ_{chem} of the four CORE-extension cores with the 22 cores of the CORE sample is discussed in Sect. 3.7.1.

3.7 Discussion

The core properties of both regions are discussed and compared with the results of the 22 cores of the original more evolved CORE sample (Chapter 2) in Sect. 3.7.1. A more detailed discussion of the complex dynamics in ISOSS J23053+5953 is given in Sect. 3.7.2.

3.7.1 Core properties

Both regions, located in the outer galaxy ($d_{\text{gal}} \approx 10$ kpc), fragment into a total of 29 mm cores (with $S/N \geq 5$) as revealed by the high angular resolution observations with NOEMA at 1.3 mm (Beuther et al. 2021). Herschel observations at FIR wavelengths show that the mm cores are embedded in cold clumps (Ragan et al. 2012) and MIR observations with the IRAC and MIPS instruments on the Spitzer space telescope reveal that multiple mm cores have MIR counterparts (Fig. 3.3). This suggests that in both regions star formation is occurring subsequently with some more evolved sources already becoming bright at MIR wavelengths. The strong mm cores with no or a weak associated MIR sources are likely younger. In this case, the luminosity of the protostars is still too faint and/or the protostars are still too embedded.

Clustered star formation

The total clump masses of the cold gas are $104 M_{\odot}$ and $488 M_{\odot}$ for ISOSS J22478+6357 and ISOSS J23053+5953 (Ragan et al. 2012). Tackenberg et al. (2012) estimate that a gas reservoir of $1000 M_{\odot}$ is required to form a $20 M_{\odot}$ star on clump scales at a size of $R \approx 0.3 - 1.0$ pc. This suggests that in ISOSS J22478+6357 low- and intermediate-mass stars can form. This is in agreement with the results of Hennemann et al. (2008) who estimate that the bright MIR source toward mm core 13 is forming an intermediate-mass star. But, toward ISOSS J23053+5953, core 1 with its strong bipolar outflow (Wouterloot et al. 1989; Rodríguez et al. 2021) and being embedded within a large gas reservoir (Birkmann et al. 2007) is an accreting intermediate-mass protostar, destined to become a high-mass star (see, e.g., Beuther et al. 2007a).

The SED fitting (Sect. 3.4.3) shows that for individual cores the bolometric luminosity is not only dominated by the FIR emission of the cold dust, but a significant contribution can arise at MIR wavelengths. In ISOSS J22478+6357, the strong mm cores 1 and 2 have no associated MIR source, while in ISOSS J23053+5953 mm cores 1 and 2 can be associated with MIR emission. Some of the faint mm cores show MIR emission, for example, core 13 in ISOSS J22478+6357 is the brightest in the MIR. As both regions harbor young intermediate- to high-mass protostars (mm-bright) surrounded by more evolved low-mass YSOs (MIR-bright) suggests that clustered subsequent star formation occurs. It seems that first a generation of low-mass stars form, with bright emission in the near-infrared (NIR) and MIR, and then higher-mass protostars, bright at mm wavelengths, form afterward. As an example, in ISOSS J22478+6357 the MIR-bright source toward mm core 13 has an estimated age of $\sim 1 - 6$ Myr (Hennemann et al. 2008) and for the nearby mm core 1 we derive a shorter chemical timescale of 31 000 yr (Table 3.5). While the angular resolution of the Spitzer IRAC and NOEMA observations is comparable and resolve the core features, the lower angular resolution of the Spitzer MIPS and Herschel PACS data trace the clump scales, in which multiple cores can be embedded (Fig. 3.3). Unfortunately, high angular resolution observations at FIR wavelengths, which would significantly improve the SED fit and bolometric luminosity estimate of cold components toward individual mm cores, are currently not possible (e.g., Linz et al. 2021).

In both regions a small cluster is undergoing active star formation (Fig. 3.3). Kumar et al. (2003a) studied young star-forming regions that are classified as precursors to UCHII regions with no free-free emission detected at radio wavelengths. Using observations in the NIR and FIR, these authors found that the regions form stars in a clustered mode. Toward the young massive protocluster IRAS 22134+5834, a massive protostar shows strong emission in the FIR and has a weak radio continuum, while the surrounding protostars on the other hand are bright in the NIR (Kumar et al. 2003b; Palau et al. 2013; Wang et al. 2016). This is an indication for an early phase of massive star formation with protostars at a range of evolutionary stages. This is also observed toward both ISOSS regions in our study where strong mm cores and bright MIR

sources coexist (Fig. 3.3). The formation and evolution of massive stars is much faster, but it is also commonly observed that high-mass protostars are surrounded by a cluster of more evolved low-mass protostars (see also e.g., Kumar et al. 2006).

This is in agreement with the scenario proposed by Kumar et al. (2020) that low-mass star formation occurs in filaments, while HMSF occurs in hubs, which take longer to assemble. Thus, high-mass protostars are observed to be surrounded by more evolved low-mass protostars. We find that in ISOSS J22478+6357, the mm cores are embedded within filamentary structures, whereas in ISOSS J23053+5953 the system consist of two bigger clumps resembling more of a hub (Sect. 3.5.2). This also supports the theory that star formation occurs at the intersection of filaments and gas hubs, and that the growing massive cores could be fed by fresh matter from and/or via these filaments (e.g., Myers 2009; Peretto et al. 2013; Tigé et al. 2017; Kumar et al. 2020). However, it is difficult from an observational point of view to observe this possible gas accretion from large to small scales. Both ISOSS J22478+6357 and ISOSS J23053+5953 seem to be embedded in a filament-hub system as observed with the Herschel Spectral and Photometric Imaging REceiver (SPIRE). But currently no velocity information of these structures is available and thus follow-up line observations of a larger FOV are required in order to investigate the clustered star-formation properties in both regions.

Another explanation could be that additional external feedback triggers a further generation of stars. In ISOSS J23053+5953, the colliding flow could have triggered further star formation at the colliding front toward cores 2, 3, and 6. In ISOSS J22478+6357 the nearby IRAS source, which could be an expanding HII region, but has not been studied, could have an impact on the cluster.

Physical properties

In both regions, clear signatures of protostellar outflows are observed in line wings of the CO 2 – 1 transition (Fig. 3.5). For comparison, Zhang et al. (2007) find multiple collimated outflows toward the high-mass protocluster AFGL 5142 with CO, SO, and SiO observations. In AFGL 5142, the bipolar outflows are randomly oriented and the outflows are associated with mm cores. In the filamentary IRDC G28.34+0.06 P1, Wang et al. (2011) detect mm cores aligned in a filamentary structure. Even though the cores show no line emission except for CO, all cores harbor bipolar jet-like CO outflows. The outflows are oriented almost parallel to each other and perpendicular to the filament structure. The molecular outflows are observed in SO, SiO, H₂CO, and CH₃OH emission as well (Zhang et al. 2015).

This is similar to the line-poor mm cores toward ISOSS J22478+6357, for which the outflows are aligned and perpendicular to the filamentary gas as well (Fig. 3.5). This suggests that for protostars forming along filaments, there is a preferred orientation of the outflows and that the filaments can provide gas that can be accreted. The magnetic field morphology is a topic for future investigations since the magnetic field is typically also oriented perpendicular to the high-density filaments (e.g., Soler et al. 2017).

On the other hand, the outflows that can clearly be identified in ISOSS J23053+5953 do not have a preferred orientation. There is no clear signature of a filament, but rather the presence of two massive clumps (Fig. 3.3) and a colliding flow toward the location of the mm cores (Fig. B.24). Similar to AFGL 5142, outflows toward more massive star-forming regions are influenced by the gravitational interaction between the protostars, which might cause the outflows to precess and change their orientation with time (for detailed simulations of high-mass outflows, see, e.g., Peters et al. 2014).

The physical structure, specifically the radial temperature and density profile, is analyzed for the ten strongest cores within both regions. The 1.3 mm visibility profiles (Fig. 3.2) were used

to estimate the density power-law index p of five cores (Table 3.5). We derive a mean density power-law index of $p = 1.6 \pm 0.4$. The same analysis was applied to 22 cores of the original CORE sample (Sect. 2.3.3), with a mean of $p = 2.0 \pm 0.2$. This suggests that from the IRDC to HMC stage, the density profile does not change significantly within these short evolutionary timescales. In Sect. 2.6.1 the mean density power-law index was compared to results at various spatial scales in the literature. It is found that p does not change from clump to core scales. A mean value of $p \approx 2$ is also found toward low-mass star-forming regions (Motte & André 2001). Hence a density profile around two appears to be present over a broad range in evolutionary timescale as well as protostellar mass. The density profile of an initial (high-mass) starless core and in a more evolved UCH_{II} region phase might differ from the intermediate IRDC, HMPO, and HMC stage, though.

The radial temperature profile of the cores (Fig. 3.13) is derived from the H₂CO rotation temperature maps (Figs. 3.11 and 3.12). The mean temperature power-law index is $q = 0.4 \pm 0.3$ ranging between $q = 0.1 - 1$ within the six mm cores with a radially decreasing temperature profile (Table 3.5). In some cores, we do not observe a radial temperature gradient, which might not be resolved by our observations. For the cores of the original CORE sample, H₂CO and, in addition, CH₃CN temperature maps were used to estimate the temperature profiles of individual cores. The mean temperature power-law index of the 22 cores of the original CORE sample is $q = 0.4 \pm 0.1$, which is predicted from theoretical calculations (Emerson 1988; Osorio et al. 1999; van der Tak et al. 2000) and similar to the value found toward the ISOSS cores.

It is expected that the initially cold cores develop a radially decreasing temperature profile due to protostellar heating. The fact that the density and temperature power-law index are similar from the IRDC to HMC phase suggests that the density and temperature gradient form very early on and stay roughly constant. Since observational constraints of the temperature and density profiles at core scales are still scarce, our findings provide useful constraints for physical models and simulations, but in addition, the density and temperature structure are crucial for chemical models as well (Sect. 3.6).

Comparing results of the H₂CO temperature maps (Table 3.5) and the temperature of individual components in the SED fit (Table 3.6) reveals a temperature gradient of decreasing gas temperature at increasing spatial scale. The Herschel observations tracing the larger scale clumps at 0.1 – 0.3 pc reveal a cold component of ~ 20 K. Thus, the mm cores form within a cold clump. The CORE-extension observations show that at a spatial scale of $\approx 3\,000 - 4\,000$ au the gas temperature increases toward the cores, with H₂CO rotation temperatures up to ~ 200 K. The MIR sources appear as point sources in the Spitzer IRAC observations. The strong MIR emission arises from the close vicinity of the protostar and reveals a hot component of 400 – 600 K toward the mm cores with MIR counterparts.

Molecular gas

Both ISOSS J22478+6357 and ISOSS J23053+5953 appear line-poor compared to many regions in the original CORE sample. In total, 26 transitions can be identified (Table 3.2), all of them toward ISOSS J23053+5953, while toward ISOSS J22478+6357 only 14 transitions are detected (Table 3.3). Toward the regions of the CORE sample, strong line emission of SO₂, vibrationally excited HC₃N and torsionally excited CH₃OH and less abundant isotopologues, such as O¹³CS and ³⁴SO₂ are commonly detected in the spectra. In addition, more transitions of HNCO and CH₃CN with higher upper energy levels are detected. This contrast is in agreement with the fact that the gas temperature and density in ISOSS J22478+6357 and ISOSS J23053+5953 are lower suggesting that these regions are less evolved.

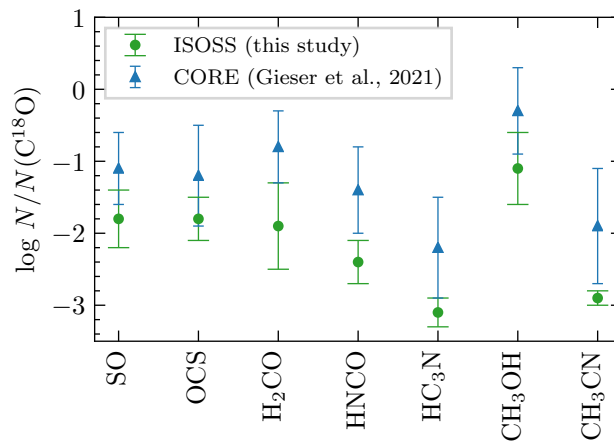


FIGURE 3.16: Mean abundances (relative to C^{18}O) and standard deviation of the cores in both ISOSS regions (green circles) in comparison with the cores in the CORE sample (blue triangles, Sect. 2.4.2). Only species that were studied both in this study (Chapter 3, Gieser et al. 2022) and in Chapter 2 (Gieser et al. 2021) are shown.

The mm cores are embedded in an envelope seen in H_2CO and DCO^+ emission (Figs. 3.6 and B.2). While both regions have similar clump properties (Ragan et al. 2012), the high angular resolution data reveal complex dynamics that affect the molecular gas of the regions (Sects. 3.5.2 and 3.5.3).

While ISOSS J22478+6357 is more quiescent and line-poor, a colliding flow is creating a large shocked region in ISOSS J23053+5953 that is seen in line-rich emission knots (MP4 and MP5), which are not associated with the mm cores and are in a steep velocity gradient (Fig. B.24). In both sources, the temperatures are low throughout the region, so most of the molecules around individual cores are either still frozen onto the dust grains or have not yet formed. Shocked regions are caused either by bipolar outflows (MP1, MP2, and MP3 in ISOSS J22478+6357, Fig. 3.5) or by a large scale colliding flow in ISOSS J23053+5953 (MP4 and MP5, Fig. B.24). These shocks are traced by emission of SO, SiO, H_2CO , and CH_3OH (e.g., Figs. B.1, 3.7, 3.6, and B.4). The presence of molecular outflows, which might also create shocks, toward mm cores surrounding MP4 and MP5 cannot be ruled out.

The mean abundance, relative to $N(\text{C}^{18}\text{O})$ and standard deviation of the 29 cores in both ISOSS regions in comparison with the mean abundance of the 22 cores in the CORE sample is shown in Fig. 3.16. Only abundances of species that were analyzed in both studies are shown. While there is clearly a scatter for the ISOSS and more evolved CORE cores, which is most likely caused by individual cores being at slightly different evolutionary stages, the mean abundances of all species of the ISOSS cores are about an order of magnitude lower than the mean abundances of the CORE cores. This can be interpreted in an evolutionary sense that most of the species are still depleted early on and the gas-phase abundances and gas density increase during the evolution of the cores.

The molecular emission in the large mosaics allows us to investigate different physical processes. The larger scale molecular cloud is traced by CO isotopologues (CO , ^{13}CO , and C^{18}O , Figs. B.18, B.15, and B.10), with even C^{18}O being detected everywhere in the FOV. We find that DCO^+ and H_2CO are also good tracers of the larger scale emission, that is, the filamentary structure in ISOSS J22478+6357 and the clumps in ISOSS J23053+5953 (Figs. B.2 and 3.6). Distinct molecular emission peaking toward the mm cores (SO , ^{13}CS , OCS, DCO^+ , N_2D^+ , H_2S , H_2CO , H_2^{13}CO , HNCO, HC_3N , $c\text{-C}_3\text{H}_2$, CH_3OH and CH_3CN) is seen for cores 1 and 2 in ISOSS J22478+6357 and for cores 1, 2, and 6 in ISOSS J23053+5953. Bipolar molecular

outflows are traced by broad CO line wing emission (Fig. B.18), SO (Figs. B.1 and B.13), SiO (Fig. 3.7), H₂CO (Fig. 3.6), H₂¹³CO (Fig. B.12), and CH₃OH (Fig. 3.8).

Multiple molecular emission peaks in molecular emission are detected in both regions (MPs 1 – 5). Qiu & Zhang (2009) detect a MP in the HMSFR HH 80-81 also with no mm continuum counterpart. In their case, a CO outflow arises from this molecular core, while in our case, the molecular emission, which also is not associated with any mm continuum, stems from shocks caused by outflows and a colliding flow.

Physical-chemical modeling results

In Sect. 2.5, the physical-chemical model MUSCLE is applied to 22 cores in order to estimate the chemical timescale, τ_{chem} , and a mean of 60 000 yr, with a spread of 20 000 – 100 000 yr, is estimated. It is not possible to apply MUSCLE to all cores in ISOSS J22478+6357 and ISOSS J23053+5953 as the spectra are in general line-poor. The mean chemical timescale of the ISOSS cores is 20 000 yr. The 1.3 mm spectral setup is ideal to study the molecular emission around cores in the HMPO and HMC stage (Chapter 2), but in the IRDC stage spectra appear line-poor (Figs. B.25 and B.26). Complementary observations at 3 mm with many simple species, including their deuterated counterparts, in the ground state levels would help to better constrain the chemical timescales of the mm cores in ISOSS J22478+6357, but also of the line-poor mm cores in the original CORE sample.

For ISOSS J22478+6357 we are only able to model core 1 that shows the most emission lines compared to the remaining cores in the region. As expected from the low temperature in the region, the estimated chemical timescale is low ($\sim 31\,000$ yr). The remaining strong mm cores hosting bipolar outflows as well, are most likely in an early evolutionary stage, where more species are still frozen onto the grains, which is also seen in low kinetic temperatures of the cores (Table 3.4). The estimated chemical timescale of core 1 in ISOSS J22478+6357 is $\approx 10\,000$ yr higher compared to the mm cores in ISOSS J23053+5953. Since M_{core} and T_{500} are low, this low-mass protostar cannot reach densities as high as in core 1 in ISOSS J23053+5953 in order to have a more complex molecular content. The ISOSS J22478+6357 cluster seems slightly older, with a MIR-bright YSO around mm core 13 at an estimated system age of 10^6 yr (Hennemann et al. 2008) already present.

Core 1 in ISOSS J23053+5953 is most likely a young intermediate- to high-mass protostar with a strong bipolar outflow at an estimated chemical timescale of $\approx 20\,000$ yr. The single-dish observations reported in Vasyunina et al. (2014), centered on core 1, show the presence of a few more complex organic molecules, such as CH₃CCH and CH₃CHO, detected at 2 and 3 mm. This indicates the onset of some more complex chemistry toward this particular core. Unresolved CH₃CN emission in our NOEMA data toward the continuum peak already suggests that the inner parts already reach high temperatures and densities (Fig. B.16). For cores 2 and 6 in ISOSS J23053+5953, we also estimate a comparable chemical timescale. Both can be associated with MIR sources as well (Fig. 3.3), both significantly brighter in the MIR than core 1, and also have distinct MPs in the line integrated intensity maps (Sect. 3.5.2).

Correlations

Using the CORE and CORE-extension observations, the physical and chemical properties of 32 fragmented mm cores were studied in detail (ten cores in this chapter and 22 cores in Chapter 2). The following derived properties are investigated for correlations: the 1.3 mm peak intensity and integrated flux (I_{peak} and F_{1300}), the kinetic temperature estimated from the H₂CO temperature map (T_{kin}), core mass M_{core} , molecular hydrogen column density $N(\text{H}_2)$, kinetic temperature at

$r = 500$ au obtained from the radial temperature profile T_{500} , visibility, density, and temperature power-law index (α , p , and q), chemical timescale (τ_{chem}), and M/L ratio.

The absolute flux calibration of the NOEMA data is expected to be 20% or better. We therefore assume a 20% uncertainty for I_{peak} and F_{1300} . Using the MCMC error estimation algorithm, the uncertainty of the H_2CO rotation temperature estimated with XCLASS is $\sim 30\%$ (Table A.1). Since T_{kin} is approximated by $T_{\text{rot}}(\text{H}_2\text{CO})$, we assume a 30% uncertainty for T_{kin} . The core mass and H_2 column density are uncertain by a factor of three (taking into account further uncertainties of, for example, the distance, gas-to-dust mass ratio, and dust absorption coefficient, Beuther et al. 2021). The uncertainties for T_{500} , α , p , and q are taken from the uncertainty of the fit (Table 3.5). The chemical timescales are estimated to be uncertain by a factor of two (Sect. 3.6.2). The M/L ratio ($M/L = \frac{M_{\text{core}}}{L}$, Table 3.6) is assumed to be uncertain by a factor of three. The M/L ratio of the CORE cores, based on single-dish observations and taken from Beuther et al. (2018a), is an average of the whole region. But for the ISOSS cores we are able to constrain the M/L ratio on core scales (Sect. 3.4.3). For completeness, we also show the clump-averaged M/L ratio taken from Ragan et al. (2012) of the ISOSS cores that have an associated Herschel clump peaking toward the core (core-clump associations are listed in Table 3.4). The clump-averaged M/L ratio of the ISOSS cores is shown in red in Fig. 3.17, but not considered in the calculation of the correlation coefficient.

In order to find correlations or anticorrelations, we computed the Spearman correlation coefficient r_S (Cohen 1988) for all parameter combinations. If $r_S = 1$, a positive correlation exists and if $r_S = -1$ an anticorrelation exists between the parameters. For uncorrelated parameters, $r_S = 0$ holds. All parameter pairs with $|r_S| \geq 0.4$ are shown in Fig. 3.17. The ISOSS and CORE cores are shown in green and blue, respectively.

A high correlation exists between I_{peak} and F_{1300} , but the figure reveal that the cores of the ISOSS regions are fainter than the cores of the CORE regions with a small overlap in between. This correlation spans over four orders of magnitude highlighting that the CORE-extension cores are a complement of the CORE cores. Brighter mm cores also have a higher kinetic temperature T_{kin} . As $N(\text{H}_2)$ and M_{core} are computed from I_{peak} and F_{1300} , respectively, we find a high correlation here as well. Thus, M_{core} and $N(\text{H}_2)$ also have a high correlation. T_{kin} and T_{500} correlate with $N(\text{H}_2)$ and M_{core} , respectively.

The temperature index q is anticorrelated with the density index p , such that cores with flatter temperature profiles have a steeper density profile. A strong correlation between α and p can be attributed to Eq. (2.2). We do not find correlations for α , p , and q with other physical parameters. The mean indices for the density and temperature power-law indices are similar in both studies, implying that these parameters do not change significantly from the IRDC to HMC stage.

Both the peak intensity and H_2 column density of the mm cores correlate with τ_{chem} such that brighter mm cores with higher H_2 column densities have a higher estimated chemical timescale. The M/L ratio is a tracer of the evolutionary trend such that more evolved proto-stars have a lower M/L ratio (e.g., Sridharan et al. 2002; Molinari et al. 2008, 2010; Maud et al. 2015a; Molinari et al. 2016; Urquhart et al. 2018; Molinari et al. 2019). The peak intensity, integrated flux, and H_2 column density of the mm cores are anticorrelated with the M/L ratio. As would be expected as a tracer of the evolutionary trend, the chemical timescale τ_{chem} is also anticorrelated with the M/L ratio.

The correlation of the physical parameters of the mm cores in the CORE and CORE-extension sample reveal that some of the studied physical properties change with time: cores with a high mm brightness also have a higher temperature, core mass, H_2 column density and lower M/L ratio. This suggests that the initial low-mass cores gain mass with time while also increasing the gas temperature and density. Both the M/L ratio and chemical timescales τ_{chem}

are tracers of the evolutionary sequence. It is difficult to determine the bolometric luminosity L of cores, which are clearly resolved in MIR and mm observations, but not at FIR wavelengths (Fig. 3.3). Since it is currently impossible to reach sub-arcsecond resolutions at FIR wavelengths (e.g., Linz et al. 2021), more reliable SED fits remain challenging, especially in crowded regions (Sect. 3.4.3). However, chemical timescales estimated with MUSCLE are determined by the observed molecular column densities, for which sub-arcsecond resolution observations are possible with current interferometers. We do not find that the indices of the temperature and density power-law profiles have a high correlation with the remaining parameters suggesting that they are set very early on and do not change significantly from the IRDC to HMC stage.

3.7.2 Dynamics in ISOSS J23053+5953

In ISOSS J23053+5953 a colliding gas flow creates enhanced abundances of shock tracers such as SO, ^{13}CS , SiO, OCS, SO_2 , H_2CO , H_2^{13}CO , HC_3N , CH_3OH , and CH_3CN (indicated as MP4 and MP5 in the integrated intensity maps, Sect. 3.5.2). These shocked locations reveal molecules that were initially depleted. Therefore, it allows us to investigate which molecules already resided on the grains. In addition, SiO is created by Si sputtered off the grains and forming SiO in the gas-phase (Schilke et al. 1997). These emission peaks are spatially located at a velocity gradient seen clearly for all species with extended emission (Fig. B.24). However, since both cores 2 and 6 are young protostars, molecular outflows are expected to be present, but difficult to identify (Fig. 3.5).

Core 2, which is embedded within a common dust envelope with core 3 (Fig. 3.1), shows emission of $c\text{-C}_3\text{H}_2$ (Fig. B.5) toward the north and south of the mm core. This might trace an outflow cavity, but a clear outflow direction cannot be inferred due to the complex dynamics. We therefore conclude that a colliding flow creates a shocked region between cores 2, 3, and 6, but protostellar outflows are most likely present as well.

Colliding flows are found in other regions of the Galaxy. For example, in the well-known giant molecular cloud complex NGC 6334, colliding flows are reported in the source known as “V” by Juárez et al. (2017), where two velocity components separated about 2.4 km s^{-1} are seen in H^{13}CO^+ , with SiO emission at the intermediate velocities and also at the interface of the two flows (Fig. 7 of Juárez et al. 2017). Multiple IR, cm, and mm sources are found at the flow interface as well (Figs. 1 and 4 of Juárez et al. 2017). Overall, the similarities of NGC 6334 V and ISOSS J23053+5953 are remarkable, despite clearly being located in different parts of the Galaxy. Converging flows are also reported in DR21(OH) (Csengeri et al. 2011), Orion (Lee et al. 2013), G035.39-00.33 (Jiménez-Serra et al. 2014), G0.253+0.016 (Johnston et al. 2014), the Galactic Center (Schwörer et al. 2019), the Musca filament (Bonne et al. 2020), and G+0.693-0.03 (Zeng et al. 2020).

Toward core 3 in ISOSS J23053+5953, a chemical differentiation between DCO^+ peaking toward the north (Fig. B.2) and N_2D^+ peaking toward the west (Fig. B.21) of the mm core is observed. In general, N_2D^+ is less depleted than DCO^+ due to N_2 residing longer in the gas-phase compared to CO and CO leading to an enhancement of deuterated species (Emprechtinger et al. 2009). Due to the fact that all CO isotopologues show wide spread emission, the difference between the two species might not be due to CO freeze-out. Murillo et al. (2018) also find spatially offset emission of these two species in the cold envelope of the low-mass protostar IRAS 16293-2422. In their models, the different locations of the molecular emission are due to a temperature effect, where DCO^+ is located in a colder region at the disk-envelope interface. The colliding flow might have caused a temperature change toward core 3 or the spatial difference might be caused by potential molecular outflows. Two jet-like features are observed in SiO (Jet1 and Jet2), both pointing to core 3 (Fig. 3.7).

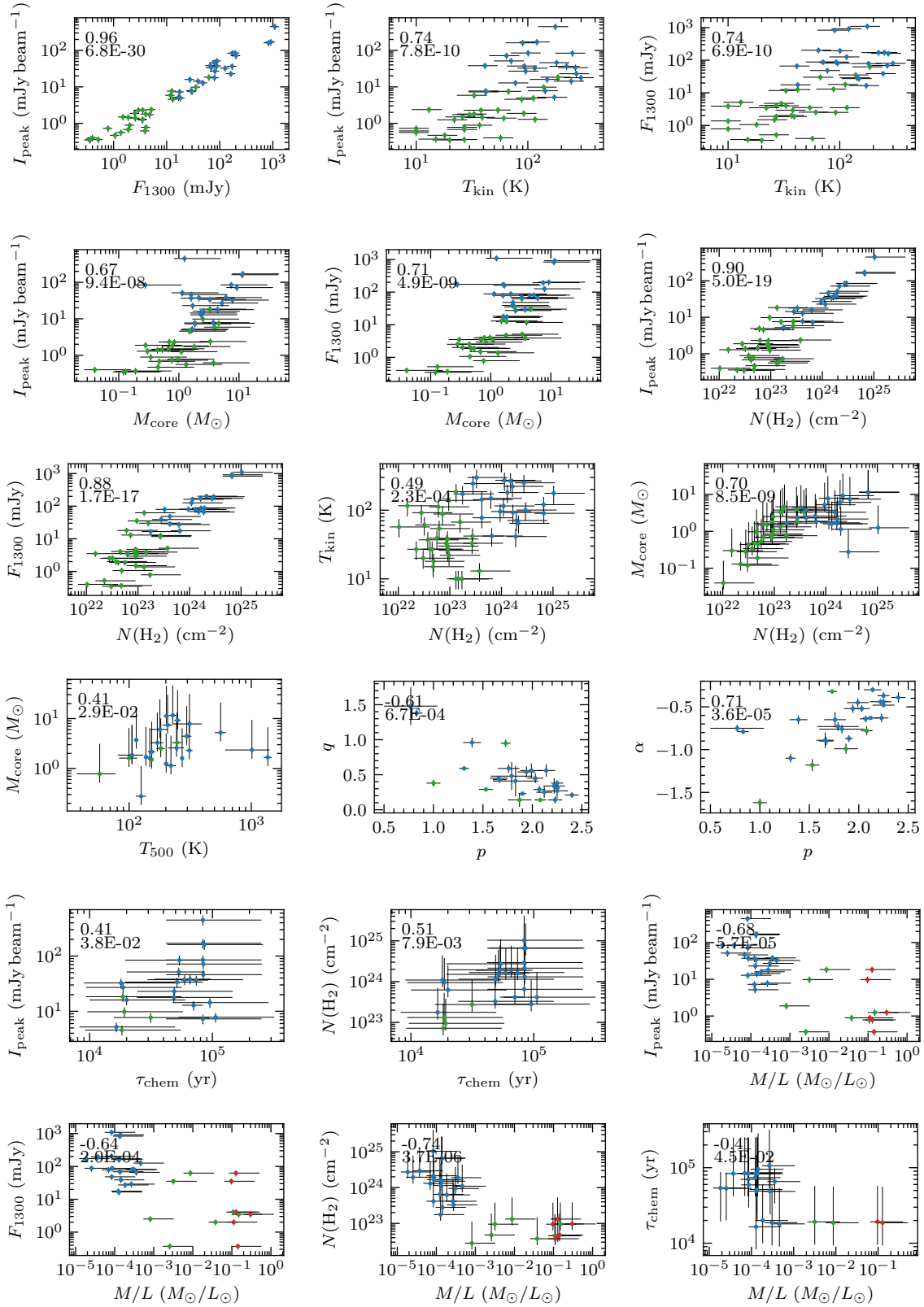


FIGURE 3.17: Core parameters with a Spearman correlation coefficient of $|r_s| \geq 0.4$. The results for the cores in ISOSS J22478+6357 and ISOSS J23053+5953 are shown in green (this work, Tables 3.4, 3.5, and 3.6) and the results for the cores of the original CORE sample are presented in blue (Chapter 2). In each panel, the correlation coefficient r_s and p -value are shown in the top left corner. For completeness, the clump-average M/L ratio taken from Ragan et al. (2012) of the corresponding ISOSS cores (Table 3.4) is shown in red.

3.8 Summary and conclusions

We used high angular resolution observations at 1.3 mm of the young star-forming regions ISOSS J22478+6357 and ISOSS J23053+5953 and MIR and FIR archival data from the Spitzer and Herschel telescopes to study the physical and chemical properties of fragmented mm cores. This study (CORE-extension) is a follow-up of the CORE large program, for which the fragmentation and physical-chemical properties of fragmented cores toward HMSFRs classified as HMPOs, HMCs, and UCHII regions are presented in Beuther et al. (2018a) and Chapter 2, respectively. Here, we focused on the physical (temperature and density profiles, outflows) and chemical properties of younger mm cores.

Our main results are summarized as follows:

1. Comparing the 1.3 mm continuum with Spitzer IRAC and MIPS observations, we find that some of the fainter mm cores already have strong MIR counterparts suggesting clustered subsequent star formation occurring in both regions. A generation of more evolved low-mass protostars surrounds the younger intermediate- and high-mass protostars. The bolometric luminosity of the cores, which can be resolved in the MIR and FIR, was estimated from fitting their SEDs from MIR to mm wavelengths. Two or three temperature components were necessary to properly fit the full SEDs.
2. The radial density profile was inferred from the 1.3 mm continuum visibilities and the radial temperature profile was inferred from H₂CO rotation temperature maps. We assumed that both profiles follow a power-law profile, and we derive a mean density and temperature power-law index of $p = 1.6 \pm 0.4$ and $q = 0.4 \pm 0.3$, respectively. We find similar values toward the cores of the original more evolved CORE sample (Chapter 2), suggesting that both the radial density and temperature power-law index do not change significantly from the IRDC to HMC stage.
3. The 1.3 mm spectra are generally line-poor, compared to spectra observed in the original CORE sample, and mostly simple species with low upper energy levels are detected. Molecular column densities were inferred with XCLASS. The abundances (relative to C¹⁸O) of the cores compared to the cores of the original CORE sample (Chapter 2) are about one order of magnitude lower suggesting that most species are still depleted in the younger ISOSS sources studied here.
4. The CO (2 – 1) line wing emission reveals multiple bipolar molecular outflows in both regions. In ISOSS J22478+6357, we find five mm cores with outflows that are aligned almost parallel in the plane of the sky. These mm cores are connected by a filamentary structure seen in DCO⁺ and the outflows are perpendicular to this filament. A large scale bipolar outflow is seen toward core 1 in ISOSS J23053+5953, which is a high-mass protostar.
5. Most of the mm cores do not show distinct molecular emission peaks (except for cores 1 and 2 in ISOSS J22478+6357, and for cores 1, 2, and 6 in ISOSS J23053+5953). Multiple molecular emission peaks are detected within the FOV in both regions with no associated mm continuum cores for transitions of SO, SiO, H₂CO, and CH₃OH being well-known shock tracers. These regions can be linked to bipolar outflows ISOSS J22478+6357 and a combination of a colliding flow and outflows in ISOSS J23053+5953 creating shocks in the gas surrounding the mm cores.

6. We applied the statistical tool HOG to the line data in both regions to find velocity channels with a high spatial correlation between two molecular transitions. As expected, transitions of the same species have a high correlation, but also the shock-tracing species and the molecules tracing the larger scale emission are spatially correlated with no significant velocity offsets. With HOG it will be possible for future programs to easily identify spatial correlations in a large sample of regions and many detected transitions on a channel-by-channel comparison.
7. A large scale velocity gradient is seen in ISOSS J23053+5953 toward the cores 2, 3 and 6. Between these cores, a colliding flow is creating a shock enhancing the abundances of many detected species. This colliding flow might have triggered further star formation.
8. With the physical-chemical model MUSCLE, we estimate chemical timescales of four cores with the highest number of detected species and for which we were able to derive density and temperature profiles. We find a mean chemical timescale of 20 000 yr, while for the cores of the original more evolved CORE sample a mean of 60 000 yr is derived (Sect. 2.5). Most cores in the ISOSS regions are in an early evolutionary phase, which is supported by the shorter chemical timescales, smaller molecular abundances, and lower temperatures. However, we also find some more evolved cores in the region with higher temperatures, signposts of complex chemistry and MIR signatures that indicates subsequent on-going star formation (cores 1 and 6 in ISOSS J23053+5953).
9. Comparing the mm core properties studied in the ISOSS and CORE regions, we find that some properties clearly change with time. The 1.3 mm peak intensity and integrated flux, core mass, H₂ column density, and kinetic temperature of a mm core increase with time, since these properties are anticorrelated with the M/L ratio and correlated with the chemical timescale τ_{chem} .

The CORE and CORE-extension studies reveal that sub-arcsecond angular resolution observations are required in order to investigate the properties of fragmented cores that show complex dynamical and chemical properties on these spatial scales (<10 000 au). The number of observed and analyzed mm cores is still not high; however, this analysis demonstrates a pathway for ongoing and future large programs targeting hundreds or thousands of embedded young (high-mass) protostars. The 1.3 mm setup of the CORE project is not ideal for studying the molecular composition in young and cold regions in the IRDC phase, as well as in evolved UCH_{II} regions. High angular resolution observations at 3 mm covering the ground-state transitions of many simple species, including many deuterated molecules, would provide a better insight on the earliest evolutionary stages. An intriguing result of this study is that both regions harboring young intermediate- and high-mass protostars are already embedded in a cluster of more evolved low-mass MIR-bright YSOs.

Chapter 4

Unveiling the physical properties during high-mass star formation with ALMA from infrared dark clouds to ultra-compact H_{II} regions

The content of this chapter is based on a paper in preparation by Gieser et al. (in preparation) that will be submitted to Astronomy & Astrophysics.

4.1 Context

During the formation of high-mass stars, the physical and chemical properties on core scales are diverse as revealed in the CORE and CORE-extension regions using sub-arcsecond interferometric NOEMA observations at 1 mm wavelengths (Chapters 2 and 3). To increase our sample size of HMSFRs and to explore both physical and chemical properties at 3 mm wavelengths, I am leading an ALMA project (Cycle 6, project code: 2018.1.00424.S, PI: Caroline Gieser) targeting in total 11 HMSFRs in Band 3 covering the full evolutionary sequence during HMSF (Sect. 1.2) - from cold IRDCs to evolved UCH_{II} regions. The ALMA continuum and spectral line observations with an angular resolution of $\approx 1''$ allow us to study the fragmentation and physical properties on core scales (< 0.1 pc) and characterize the molecular content of the cores and in the surrounding structures they are embedded in.

The 3 mm spectral setup (Table C.2) covers a variety of molecular lines targeting, for example, high- and low-density and temperature regimes, photochemistry, shocks and outflows, and C-/O-/N-/S- bearing species. Since molecule formation and destruction depends heavily on the underlying physical conditions (Sect. 1.3), with this sample covering multiple evolutionary stages we are able to probe the evolution of physical properties and molecular abundances with time.

In this chapter, we study the fragmentation properties based on the ALMA 3 mm continuum and analyze the temperature and density profiles of the fragments. Furthermore, we investigate how the properties change along the evolutionary sequence taking into account the results from the CORE and CORE-extension regions (Chapters 2 and 3). Future studies (Sect. 5.2) will be dedicated to a detailed chemical analysis targeting a variety of processes, for example the formation of COMs, isotopologues and isomers, shocks, and outflows and we aim to improve the initial chemical conditions of MUSCLE (Sect. 1.3.3).

4.2 Sample

The 11 targets were selected from the chemical study by Gerner et al. (2014, 2015) targeting 59 HMSFRs at all evolutionary phases during HMSF. Their analysis was based on observations with single-dish telescopes (e.g., with the IRAM 30m telescope) that can not resolve individual fragmented cores at the typical distances of HMSFRs of a few kpc. In addition, protostars at various evolutionary stages can be present within one clump as revealed by the CORE and CORE-extension NOEMA observations (Chapters 2 and 3). We therefore observed 11 regions with ALMA in Cycle 6 at 3 mm wavelengths at an angular resolution of $\approx 1''$.

In Table 4.1 the basic properties such as the phase center and region velocity are summarized with additional information about the large scale clump properties taken from the APEX Telescope Large Area Survey of the Galaxy (ATLASGAL, Urquhart et al. 2018). A short introduction of each region is given in the following. Mass and luminosity estimates in those descriptions might differ from the ATLASGAL results shown in Table 4.1, for example, due to a different assumed source distance. Within this chapter, we consistently use the distance d and clump properties (L , M , T_{dust}) taken from the ATLASGAL survey (Table 4.1). Archival MIR and FIR observations with the APEX, Herschel, and Spitzer telescopes are presented in Appendix C.2 in Figs. C.1 – C.11.

TABLE 4.1: Overview of the ALMA sample.

Region	ATLASGAL clump properties ^(*)						
	α (J2000)	δ (J2000)	v_{LSR} (km s ⁻¹)	d (kpc)	T (K)	$\log M$ (log M_{\odot})	$\log L$ (log L_{\odot})
IRDC G11.11–4	18:10:28.30	–19:22:31.5	+29.2	2.9	16	3.0	2.8
IRDC 18223–3	18:25:08.40	–12:45:15.5	+45.3	3.4	13	3.1	2.7
IRDC 18310–4	18:33:39.42	–08:21:10.4	+86.5	5.9	13	3.0	2.5
HMPO IRAS 18089	18:11:51.52	–17:31:28.9	+33.8	2.5	23	3.1	4.3
HMPO IRAS 18182	18:21:09.21	–14:31:45.5	+59.1	4.7	25	3.1	4.3
HMPO IRAS 18264	18:29:14.68	–11:50:24.0	+43.6	3.3	20	3.2	3.9
HMC G9.62+0.19	18:06:14.92	–20:31:39.2	+4.4	5.2	32	3.5	5.4
HMC G10.47+0.03	18:08:38.20	–19:51:50.1	+67.8	8.6	25	4.4	5.7
HMC G34.26+0.15	18:53:18.54	+01:14:57.9	+58.0	1.6	29	3.2	4.8
UCHII G10.30–0.15	18:08:55.92	–20:05:54.6	+13.5	3.6	30	3.3	5.2
UCHII G13.87+0.28	18:14:35.95	–16:45:36.5	+48.3	3.9	34	3.1	5.1

(*): taken from Urquhart et al. (2018).

IRDC G11.11–4 (Fig. C.1)

The IRDC G11.11–4, also referred to as the “Snake”, is a filamentary cloud (Carey et al. 1998) that shows a spatial correlation between dust extinction maps and submm emission (Johnstone et al. 2003; Henning et al. 2010, see also Fig. C.1). Henning et al. (2010) detected 18 cores along the filament, two of them with masses $>50 M_{\odot}$. Wang et al. (2014) studied the hierarchical fragmentation from scales of 1 pc down to 0.01 pc in the filament and found chemical differentiation between fragmented cores indicating that the cores are at different evolutionary phases.

We observed with ALMA the region referred to as “P1” in the literature which already shows signatures of active star formation by 8 μm emission, a molecular outflow (Johnstone

et al. 2003), and the presence of CH₃OH and H₂O masers (Pillai et al. 2006b). By modeling the SED of the dust continuum, Pillai et al. (2006b) infer a luminosity of $1\,200 L_{\odot}$ that is powered by a Zero Age Main Sequence (ZAMS) star of $8 M_{\odot}$. These authors infer an envelope mass and temperature of $500 M_{\odot}$ and 19 K, respectively, and elevated temperatures around the protostar (≈ 60 K). Rosero et al. (2014) detected radio continuum emission at 1.3 cm and 6 cm with the VLA which they attributed to a thermal ionized jet, while at 3 mm wavelengths the emission is dominated by dust.

IRDC 18223–3 (Fig. C.2)

IRDC 18223–3 (“peak 3” studied by Beuther et al. 2002a) is located in the same filament as IRAS 18223–1243, an HII region (Bronfman et al. 1996) with bright radio continuum emission (Dewangan et al. 2018). Beuther et al. (2005b) studied the region with the PdBI at 3 mm wavelengths, while no emission is detected at MIR wavelengths except for weak emission at $4.5 \mu\text{m}$ around the source tracing shock-excited gas by an outflow. The fact that there is no MIR source detected in the Spitzer IRAC bands and only a small outflow mass of $M_{\text{out}} = 3.4 M_{\odot}$ is estimated, the authors suspected that this source is a very young protostar before the HMPO phase.

Weak protostellar MIR emission became detectable with more sensitive Spitzer MIPS observations at 24 and $70 \mu\text{m}$ (Beuther & Steinacker 2007). These authors fit the SED and find that most of the mass ($M \approx 580 M_{\odot}$) is enclosed at low temperatures of $T \approx 15$ K, while a small fraction ($M \approx 0.01 M_{\odot}$) has elevated temperatures of $T \geq 51$ K with a total luminosity of $180 L_{\odot}$ and thus the source is expected to evolve into a high-mass star. The outflow is directed from the northwest-southeast with a disk that is likely to be edge-on (Fallscheer et al. 2009).

Beuther et al. (2015b) studied the larger scale filament with PdBI mosaic observations and these authors detect 12 cores with a separation of 0.4 pc which is consistent with thermal Jeans fragmentation. However, a high mass-to-length ratio of $\approx 1\,000 M_{\odot}$ in the filament requires additional support against further collapse. The filament and its environment were studied by Dewangan et al. (2018) with ¹³CO line emission. These authors find two clouds at slightly different velocities at 45 km s^{-1} and 51 km s^{-1} that seem to be connected at the intermediate velocities suggesting that about 1 Myr ago a cloud-cloud collision could have occurred which could then have triggered the formation of high-mass stars.

IRDC 18310–4 (Fig. C.3)

IRDC 18310–4 (“peak 4” in Beuther et al. 2002a) is located in the same filament as IRAS 18310–0825. The region, being dark up to $100 \mu\text{m}$, was a prestellar clump candidate with a mass reservoir of $\approx 800 M_{\odot}$ without any signposts of active star formation (Beuther et al. 2013). The line width of N₂H⁺ decreases toward the center of the clump (Tackenberg et al. 2014).

Weak $70 \mu\text{m}$ emission was detected toward one of the fragments (Beuther et al. 2015a) and the magnetic field is relatively weak (≈ 2.6 mG) compared to more evolved HMPOs and HMCs (Beuther et al. 2018b). Recent ALMA observations revealed that among 11 cores with masses ranging from 1.1 to $19 M_{\odot}$ at least four cores show outflows traced by CO and SiO emission such that star formation has been taking place for at least 10^4 yr (Morii et al. 2021).

HMPO IRAS 18089 (Fig. C.4)

IRAS 18089–1732 is a massive HMPO with $M \approx 2\,000 M_{\odot}$ with H₂O and CH₃OH maser emission (Beuther et al. 2004). The authors found a collimated north-south outflow revealed by SiO emission, while CH₃OCHO emission is confined to the central core region with a velocity

gradient almost perpendicular to the outflow tracing the rotating envelope/disk structure. Sub-arcsecond resolution observations show that the core does not further fragment (Beuther et al. 2005c), however, the variability of CH₃OH maser emission with a period of ≈ 30 d could be explained by a binary system (Goedhart et al. 2009).

The rich molecular content and a temperature of 350 K derived with CH₃CN indicates that the central region has already formed a hot core in the inner region (Beuther et al. 2005c). Sanhueza et al. (2021) studied the region at 700 au scales with ALMA and find that the dust and magnetic field have spiral-like filamentary features and the H¹³CO⁺ emission shows a complex velocity gradient suggesting that the filaments are rotating and infalling. An analysis of the energy budget shows that gravity is dominant over rotation, turbulence, and the magnetic field (Sanhueza et al. 2021). The authors estimate an infall rate of $0.9 - 2.5 \times 10^{-4} M_{\odot} \text{ yr}^{-1}$.

HMPO IRAS 18182 (Fig. C.5)

HMPO IRAS 18182 is a massive isolated core with $M \approx 1500 M_{\odot}$ and $L \approx 10^{4.3} L_{\odot}$ (Beuther et al. 2002a) with detected OH, H₂O, and CH₃OH maser emission (Sanna et al. 2010). Beuther et al. (2006) resolve no further fragmentation down to their angular resolution of 3'' and derive a temperature of 150 K in the central region using CH₃CN line emission. The authors find that the outflow has a quadrupolar morphology and that the molecular emission peaks 1 – 2'' off from the continuum peak position. With multi-epoch CH₃OH maser observations, Sanna et al. (2010) estimate that the central object has a mass of $35 M_{\odot}$ assuming that the emission stems from a rotating disk.

HMPO IRAS 18264 (Fig. C.6)

IRAS 18264 is an extended green object (EGO) with widespread emission in 4.5 μm Spitzer data that rises from shocked H₂ in the outflow (Cyganowski et al. 2008) and has associated H₂O and CH₃OH masers (Beuther et al. 2002c; Chen et al. 2011). Issac et al. (2020) find that IRAS 18264 is a protocluster with multiple radio as well as mm components detected. The C¹⁷O line has an inverse P-Cygni profile tracing infalling material and multiple bipolar outflows are traced by C¹⁸O (Issac et al. 2020).

HMC G9.62+0.19 (Fig. C.7)

The G9.62+0.19 star-forming complex consists of protostars at different evolutionary stages, from an embedded HMC to evolved UCHII regions, revealed by multi-wavelength observations from NIR to radio wavelengths (Cesaroni et al. 1994; Testi et al. 1998; Linz et al. 2005). The NIR emission is not only dominated by the SED of the YSO, but there are also contributions of the circumstellar matter and outflows, and the non-detection of the UCHII regions is consistent with a high extinction (Linz et al. 2005).

High angular resolution observations at 1 mm carried out by Liu et al. (2017) reveal that the filament contains at least 12 dense cores at different evolutionary stages from starless cores to the known UCHII regions, with three cores harboring molecular outflows. The authors propose that the expanding UCHII regions compress the gas of the clump in a filament in which sequential star formation is then triggered. The feedback of the UCHII regions results in a lack of low-mass star formation (Liu et al. 2017).

Liu et al. (2020) studied the spatial correlation of the molecular emission using ALMA 3 mm observations using the HOG method (Soler et al. 2019) that we also applied to the molecular lines of the CORE-extension regions in Sect. 3.5.2. The authors find that the molecules can be grouped to species that either trace extended emission (CS, HCN, HCO⁺), shocks (SiO),

or the dense cores (SO, H¹³CN, HC₃N, CH₃OH). Widespread SiO emission with narrow line widths seems to stem from either colliding flows or the H_{II} regions (Liu et al. 2020). A sketch of the regions with the dense cores at evolutionary stages under the influence of the H_{II} regions is given in Fig. 10 in Liu et al. (2017) and Fig. 20 in Liu et al. (2020).

HMC G10.47+0.03 (Fig. C.8)

The G10.47+0.03 region contains several MIR sources including a HMC, as well as multiple UCH_{II} regions and strong maser activity (Pascucci et al. 2004, and references within). Cesaroni et al. (2010) found that three UCH_{II} regions are located within the HMC itself. Based on CH₃CN line emission the temperature in the innermost 1.''5 is estimated to be 160 K (Olmí et al. 1996). Molecular emission lines reveals that there is outflowing gas as well as infalling material (Rolffs et al. 2011). These authors find that the density toward the central 10 000 au flattens due to pressure (e.g., thermal, turbulent, wind-driven) driving expansion. Gorai et al. (2020) detect precursors of prebiotic molecules toward the HMC, including HNCO, NH₂CHO, and CH₃NCO and by applying a chemical model these authors find that these molecules are chemically linked.

HMC G34.26+0.15 (Fig. C.9)

G34.26+0.15 contains a cometary UCH_{II} region and two unresolved UCH_{II} regions (Reid & Ho 1985). The cometary UCH_{II} region harbors a line-rich HMC (MacDonald et al. 1996). Mookerjea et al. (2007) find that the HMC is externally heated by the UCH_{II} region with no internal heating. Toward the region, many COMs such as CH₃OCHO, CH₃OCH₃, and NH₂CHO are detected (Mookerjea et al. 2007). Ammonia (NH₃) lines have inverse P-Cygni profiles indicating infalling material (Hajigholi et al. 2016).

UCH_{II} G10.30–0.15 (Fig. C.10)

The UCH_{II} region G10.30–0.15 is part of the W31 star-forming complex containing a cluster of stars and YSOs at different evolutionary stages (Beuther et al. 2011) and a large scale bipolar H_{II} region launched by a massive O8–O9 star (Deharveng et al. 2015). The UCH_{II} region G10.30–0.15 is associated with CH₃OH maser emission and the central object is a B0 star (Deharveng et al. 2015). These authors studied the clustered nature of the W31 region and find that five clumps, including the clump containing G10.30–0.15 at the waist of the bipolar H_{II} region, are a result of triggered star formation.

UCH_{II} G13.87+0.28 (Fig. C.11)

G13.87+0.28 is a cometary UCH_{II} region, with a bright head and an extended low brightness tail. The morphology and kinematics of the ionized and molecular gas is consistent with a bow shock launched by a stellar wind of a massive O6.5 ZAMS star (Garay et al. 1994). High velocity components of 22 GHz water masers are likely associated with an outflow (Xi et al. 2015).

4.3 Observations

In this chapter, we use the ALMA 3 mm observations toward the sample in combination with archival MIR, FIR, and cm data with the Spitzer, Herschel, and APEX telescopes, and the VLA.

The ALMA data calibration and imaging procedure is explained in Sect. 4.3.1 and an overview of the archival data is given in Sect. 4.3.2.

4.3.1 ALMA

The ALMA observations were carried out during Cycle 6 with the project code 2018.1.00424.S (PI: Caroline Gieser). In total, 12 science targets were observed in Band 3 covering a (non-continuous) spectral range (SPR) from 86–110 GHz in three different spectral setups (referred to as SPR1, SPR2, and SPR3) and in total 39 spectral windows (spws). In order to reduce off-source time, the regions were grouped in three fields (referred to as Field 1, Field 2 and Field 3, last column in Table 4.2). One of the observed science targets turned out to be a misclassified UCHII region (Wood & Churchwell 1989) and is in fact a planetary nebula (Walsh et al. 2003; Thompson et al. 2006) and is not further discussed in the following analysis.

The initial goal of the observations was to observe all regions with three array configurations, two with the “12m-array” (C43-4 and C43-1) and one with the Atacama Compact Array (ACA, also referred to as the “7m-array”) covering spatial scales from 1” to 60”. Since not all observations could be carried out during Cycle 6, the intermediate C43-1 configuration is missing for the most part, however, the uv coverage of the C43-4 and ACA configurations have a sufficient overlap in order to successfully combine the data. For Field 2/SPR3, the C43-4 configuration is missing, however, these regions were observed with the C43-1 configuration instead. For the remaining fields and spectral setups, the C43-1 configuration was not observed, but data in the C43-4 configuration is available. Therefore, the angular resolution of Field 2/SPR3 is lower ($\approx 3''$) compared to the SPR3 line data products of Field 1 and Field 3 ($\approx 1''$).

A summary of all ALMA observations - including the array configuration, observation date, PWV and minimum and maximum baseline - is presented in Table C.1. During the observations from October 2018 until May 2019, the PWV ranged from 1 – 6 mm sufficient for observations at 3 mm wavelengths. The baselines cover 9–1 400 m (except for Field 2/SPR3 9–310 m). In contrast to the CORE and CORE-extension observations (Chapters 2 and 3), we do not have complementary single-dish line observations to recover missing short-spacing information, we therefore filter out spatial scales $>60''$ in both the continuum and spectral line data.

The covered frequency ranges and spectral resolution of each of the 39 spws is summarized in Table C.2. In total, there are 36 spws with a spectral resolution of 244 kHz ($\approx 0.8 \text{ km s}^{-1}$ at 3 mm) covering 0.12 GHz each and 3 spws with a lower spectral resolution of 1 MHz ($\approx 3 \text{ km s}^{-1}$ at 3 mm) covering 1.9 GHz each. The line width of the three low-resolution spws is not sufficient to resolve the line widths of the IRDCs ($\lesssim 3 \text{ km s}^{-1}$), however, for the remaining regions, the line emission can be spectrally resolved.

Calibration

The data of each observation block (Table C.1) were calibrated using the CASA pipeline (CASA version 5.4.0). When multiple observations were carried out for each SPR, field and array configuration, the data were merged using the `concat` task. Science targets were extracted from the calibrated uv tables using the `split` task.

In order to extract the 3 mm continuum, we computed an average spectrum for each region, array configuration, and spw in order to determine all line-free channels. All line-free channels were merged using the `concat` task to create a continuum table containing all SPRs and array configurations. To increase the S/N , the continuum visibilities were averaged over 30 s at a central frequency of 98.3 GHz (corresponding to $\approx 3 \text{ mm}$).

The continuum is subtracted from the spectral line data using the `uvcontsub` task by fitting a first-order polynomial to the line-free channels. Using the `concat` task, all array configurations

were merged for each SPR. With the `split` task, for each spw a uv table of the merged spectral line data is created.

Self-calibration and imaging

TABLE 4.2: Overview of the ALMA 3 mm continuum data products.

Region	Beam		Noise σ_{cont} (mJy beam ⁻¹)	Peak intensity $I_{3\text{mm}}^{\text{region}}$ (mJy beam ⁻¹)	Flux density $F_{3\text{mm}}^{\text{region}}$ (mJy)	Field
	$\theta_{\text{maj}} \times \theta_{\text{min}}$ ("×")	PA (°)				
IRDC G11.11-4	1.0×0.8	104	0.033	1.4	15	Field 2
IRDC 18223-3	1.0×0.7	108	0.022	2.9	23	Field 3
IRDC 18310-4	1.0×0.7	111	0.022	1.2	4.0	Field 3
HMPO IRAS 18089	0.8×0.7	101	0.057	24	130	Field 2
HMPO IRAS 18182	1.1×0.7	107	0.029	13	90	Field 3
HMPO IRAS 18264	1.0×0.7	108	0.031	9.9	130	Field 3
HMC G9.62+0.19	0.9×0.7	104	0.049	58	640	Field 2
HMC G10.47+0.03	0.8×0.7	100	0.25	340	830	Field 2
HMC G34.26+0.15	0.8×0.7	118	1.8	2 500	7 100	Field 1
UCHII G10.30-0.15	1.0×0.8	104	0.041	18	1 000	Field 2
UCHII G13.87+0.28	1.0×0.8	105	0.065	7.0	1 800	Field 2

The ALMA continuum and spectral line data are imaged using the `tclean` task. All data are CLEANed using the Hogbom algorithm (Högbom 1974) with Briggs weighting (Briggs 1995) using a robust parameter of 0.5.

In order to increase the S/N , we perform phase self-calibration of the continuum data using a similar method adopted for the CORE NOEMA data (Sect. 2.2.4) and apply the solutions to the spectral line data. First, a shallow model of the continuum data is created using `tclean` with a stopping criterion of either 2 000 CLEAN components or a peak residual intensity of 0.1 mJy beam⁻¹. In a first self-calibration loop, the gains based on the source model are determined using the `gaincal` task with a solution interval of 120 s. The gain solutions are applied with the `applycal` task using the “calonly” mode, that does not flag baselines for which the S/N is too small for self-calibration ($S/N < 3$), therefore long baselines with low S/N are not self-calibrated but kept in the uv table in order to enable a high angular resolution. In the second and third self-calibration loop, the number of iterations increases to 4 000 and 8 000, the peak residual intensity decreases to 0.05 mJy beam⁻¹ and 0.025 mJy beam⁻¹, and the solution interval is decreased to 60 s and 30 s, respectively.

The final self-calibrated continuum data are then imaged with a stopping criterion of either 8 000 CLEAN components or a peak residual intensity of 0.025 mJy beam⁻¹ with a pixel size of 0."15. An overview of the continuum data products for each region is presented in Table 4.2. The synthesized beam size is $\approx 1''$. For most regions, except for HMC G9.62+0.19 and HMC G10.47+0.03, the continuum noise σ_{cont} is smaller than 0.1 mJy beam⁻¹. The HMC G9.62+0.19 and HMC G10.47+0.03 regions are bright continuum sources and the spectra do not have many line-free emission channels, which results in a higher continuum noise. Table 4.2 also shows the continuum peak intensity $I_{3\text{mm}}^{\text{region}}$ and region-integrated flux density $F_{3\text{mm}}^{\text{region}}$ considering emission with $S/N > 5$.

A comparison between the standard-calibrated and self-calibrated continuum data of the HMC G9.62+0.19 region is presented in Fig. 4.1. This region has a similar complex morphology as the W3 IRS4 region of the CORE sample (Fig. 2.1). Strong noise artifacts throughout the

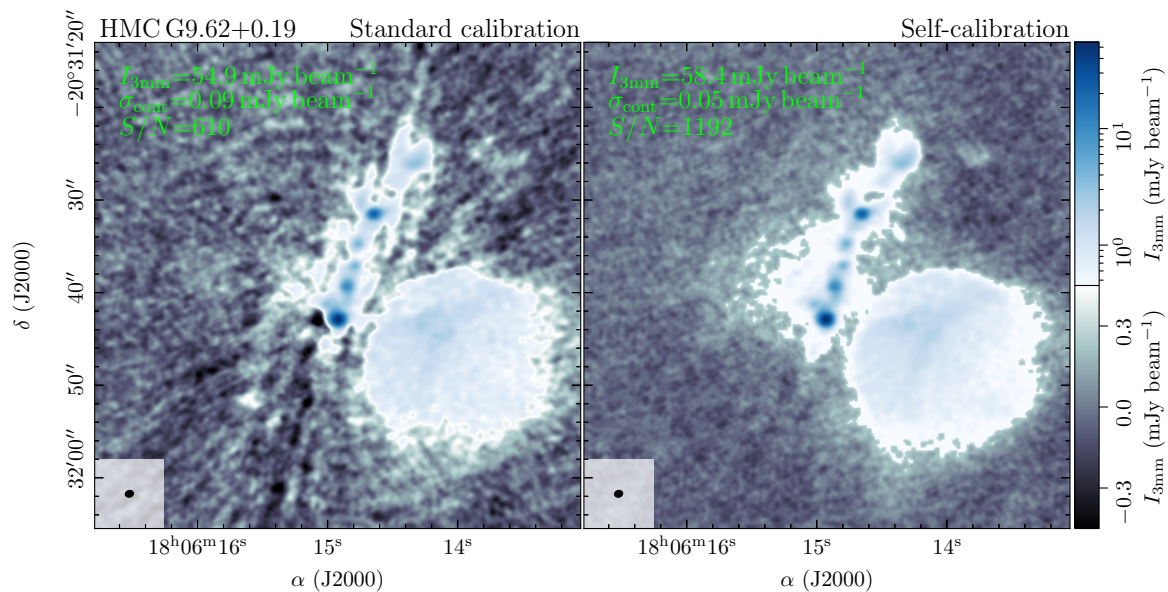


FIGURE 4.1: Comparison of CASA standard calibrated (*left panel*) and CASA self-calibrated (*right panel*) HMC G9.62+0.19 ALMA continuum data. In each panel, the beam size is shown in the bottom left corner. The linear grey-scale and logarithmic blue-scale color map highlight the continuum intensity between $-5\sigma_{\text{cont}}$ to $+5\sigma_{\text{cont}}$ and between $+5\sigma_{\text{cont}}$ and peak intensity $I_{3\text{mm}}^{\text{region}}$ of the standard calibrated data, respectively. These color scales are inspired by the MeerKAT 1.28 GHz Galactic center mosaic presented in Heywood et al. (2022).

FOV due to incorrect phases are clearly corrected by the phase self-calibration procedure decreasing the continuum noise σ_{cont} by a factor of two. The peak intensity is slightly enhanced as well. Overall, the S/N is increased by a factor of two from ≈ 610 to ≈ 1200 due to phase self-calibration in the HMC G9.62+0.19 region.

The gain solutions of the phase self-calibrated continuum data are applied to all 39 spws using the `applycal` task, keeping non self-calibrated visibilities with $S/N < 3$ in order to not flag long baseline data. The spectral line data are imaged with a pixel size of $0.''15$ (except for Field 2/SPR3 where the pixel scale is $0.''5$). The CLEAN stopping criterion of the 36 high-resolution spws is a peak residual intensity of 20 mJy beam^{-1} (except for Field 2/SPR3 where the threshold is 28 mJy beam^{-1}). The 3 low-resolution spws are CLEANed with a stopping criterion of 10 mJy beam^{-1} of the peak residual intensity.

In this work, we focus on the physical properties of fragmented objects within the regions, we therefore only utilize a few emission lines. H(40) α emission is used to estimate for which regions there is an expected contribution of free-free emission at 3 mm (Sect. 4.4.2). Molecular line emission of HCN, HNC, CH₃CN, and CH₃¹³CN is used to estimate the temperature structure in the regions (Sect. 4.5). The line properties are summarized in Table 4.3.

The spectral line data products of the lines analyzed in this work are summarized in Table 4.4. For each field and SPR, a mean value for the beam size and line noise are given. The line noise σ_{line} in the low-resolution spw containing the H(40) α emission is $\approx 0.1 \text{ K}$, while the line noise in the high-resolution spws containing the HCN, HNC, CH₃CN, and CH₃¹³CN is $\approx 0.7 \text{ K}$ (except for Field 2/SPR3, $\approx 0.1 \text{ K}$). For the purpose of this work, for all regions in Field 2, the HCN spectral line data are imaged using the same baselines, pixel size, and stopping criterion as the HNC observations have (Table C.1) since we use the HCN-to-HNC intensity ratio to estimate the temperature in the regions (Sect. 4.5) that requires the same angular resolution for both lines.

TABLE 4.3: Emission lines detected and analyzed in the ALMA regions.

Line	Frequency	Einstein	Upper energy	Catalog	ALMA spw
	ν_0	coefficient	level		
	(GHz)	$\log A_{ul}$	E_u/k_B		
		($\log s^{-1}$)	(K)		
H(40) α	99.023	SPR2 spw6
HCN 1 – 0	88.630	–4.6	4.3	CDMS	SPR1 spw5
HNC 1 – 0	90.664	–4.6	4.4	CDMS	SPR3 spw9
CH ₃ CN 5 ₄ – 4 ₄	91.959	–4.8	127.5	JPL	SPR3 spw13
CH ₃ CN 5 ₃ – 4 ₃	91.971	–4.6	77.5	JPL	SPR3 spw13
CH ₃ CN 5 ₂ – 4 ₂	91.980	–4.4	41.8	JPL	SPR3 spw13
CH ₃ CN 5 ₁ – 4 ₁	91.985	–4.4	20.4	JPL	SPR3 spw13
CH ₃ CN 5 ₀ – 4 ₀	91.987	–4.4	13.2	JPL	SPR3 spw13
CH ₃ ¹³ CN 5 ₄ – 4 ₄	91.913	–4.6	127.5	JPL	SPR3 spw11
CH ₃ ¹³ CN 5 ₃ – 4 ₃	91.926	–4.4	77.5	JPL	SPR3 spw11
CH ₃ ¹³ CN 5 ₂ – 4 ₂	91.935	–4.3	41.8	JPL	SPR3 spw11
CH ₃ ¹³ CN 5 ₁ – 4 ₁	91.940	–4.2	20.4	JPL	SPR3 spw11
CH ₃ ¹³ CN 5 ₀ – 4 ₀	91.942	–4.2	13.2	JPL	SPR3 spw11

TABLE 4.4: Overview of the ALMA spectral line data products.

Line	Field 1				Field 2				Field 3			
	Beam		Noise		Beam		Noise		Beam		Noise	
	$\theta_{\text{maj}} \times \theta_{\text{min}}$	PA	σ_{line}		$\theta_{\text{maj}} \times \theta_{\text{min}}$	PA	σ_{line}		$\theta_{\text{maj}} \times \theta_{\text{min}}$	PA	σ_{line}	
	("×")	(°)	(K)		("×")	(°)	(K)		("×")	(°)	(K)	
H(40) α	1.5×1.2	122	0.12		1.9×1.0	105	0.12		1.5×1.0	111	0.11	
HCN 1 – 0	0.9×0.8	97	0.73		4.2×2.5	104	0.02		0.9×0.7	102	0.52	
HNC 1 – 0	0.8×0.7	80	0.84		4.2×2.5	104	0.08		1.0×0.7	104	0.66	
CH ₃ CN $J=5-4, K=0-4$	0.8×0.7	72	0.85		4.2×2.5	104	0.09		1.1×0.7	98	0.59	
CH ₃ ¹³ CN $J=5-4, K=0-4$	0.8×0.7	75	0.78		4.2×2.5	104	0.09		0.9×0.7	102	0.66	

4.3.2 Archival data

We use archival MIR, FIR, and cm data in order to create a multi-wavelength picture of each region. The cm data is used to estimate the free-free contribution in the ALMA 3 mm continuum data (Sect. 1.5.1)

Spitzer IRAC 4.5 μm and MIPS (24 μm) data are taken from the Spitzer Heritage Archive. Herschel PACS 160 μm data products are taken from the Herschel Science Archive. A more detailed description of the Spitzer IRAC and MIPS and Herschel PACS instruments is given in Sect. 3.3.2. In order to study the large scale environment, we use Herschel SPIRE 250 μm observations (with an angular resolution of $\approx 18''$) taken from the Herschel Science Archive.

The clump properties are taken from the APEX Telescope Large Area Survey of the Galaxy (ATLASGAL) that covers all of our target regions. The 870 μm observations with APEX using the Large APEX BOlometer CAmera (LABOCA) have an angular resolution of $19.''2$ (Schuller et al. 2009). The properties of the clumps used in this study are taken from Urquhart et al. (2018) and listed in Table 4.1.

Radio continuum observations at 5 GHz (6 cm) were taken with the VLA as part of the COordinated Radio aNd Infrared Survey for High-mass star formation (CORNISH) project

(Hoare et al. 2012) for five regions in our sample. The synthesized beam is $1.''5 \times 1.''5$ with a sensitivity of ≈ 0.3 mJy beam $^{-1}$.

4.4 Continuum

In this section, we analyze the fragmentation properties in the regions and classify the fragmented objects. The free-free contribution in the 3 mm continuum data for evolved cores and UCHII regions is estimated from archival cm data (Sect. 4.4.2).

The ALMA 3 mm continuum data is presented in Fig. 4.2 which consists not only of dust emission but also of free-free emission in regions containing evolved protostars. All regions show some level of fragmentation, with some being dominated by a single core (e.g., IRDC G11.11–4 and HMPO IRAS 18089), while others have a number of bright mm cores (e.g., HMPO IRAS 18182 and HMPO IRAS 18264). In IRDC 18223–3 and HMC G9.62+0.19 the mm cores are aligned in a filamentary structure. The three UCHII regions (referred to as A, B, and C in the literature, e.g., Mookerjee et al. 2007) are clearly resolved in HMC G34.26+0.15. The UCHII regions G10.30–0.15 and G13.87+0.28 show extended 3 mm emission in the shape of cometary halos. In HMC G9.62+0.19 there is an extended cometary UCHII region toward the south-west of a filament containing the mm cores.

4.4.1 Fragmentation

In order to quantify the fragmentation in the continuum data, we use the `clumpfind` algorithm (Williams et al. 1994) that was also used to identify the mm cores in the CORE and CORE-extension sample (Beuther et al. 2018a, 2021). The algorithm groups the continuum emission into individual “clumps” and we choose a starting level of $5\sigma_{\text{cont}}$ and contour spacing of $5\sigma_{\text{cont}}$. The minimum number of pixels in a core is set to 20, which covers a slightly smaller area than one synthesized beam.

The properties (position, peak intensity, integrated flux, radius) of all clumps extracted by the `clumpfind` algorithm are listed in Table C.3. The positions are given relative to the phase center (Table 4.1) and the fragments are sorted by peak intensity. The radius is calculated from the area A covered by each identified clump by $r_{\text{out}} = \sqrt{\frac{A}{\pi}}$.

Since the three cometary UCHII regions (UCHII G10.30–0.15 1, UCHII G13.87+0.28 1, and HMC G9.62+0.19 9, Fig. 4.2) have extended clumpy morphology, we exclude the area covered by these cometary UCHII regions from the `clumpfind` analysis and treat them as individual structures in our analysis. The peak intensity and integrated flux are computed over the area covered by the cometary UCHII regions.

With additional 5 GHz data of the CORNISH project and observed H(40) α line, we can further classify the fragmented sources in the 3 mm continuum data. The 3 mm continuum emission reveals that mm cores are embedded in extended envelopes which can themselves be clumpy. We therefore carefully check each “clump” identified by the `clumpfind` algorithm and categorize them into either “mm cores” or “envelope clumps” based on a visual inspection (last column in Table C.3). Compact mm cores with detected H(40) α and 5 GHz emission (Sect. 4.4.2) are classified to be “UCHII regions”. The three extended UCHII regions are classified as “cometary UCHII regions” in Table C.3. In the following, “protostellar sources” refer to all fragments classified as mm cores and (cometary) UCHII regions. While the envelope clumps might also contain protostellar objects, we refrain from analyzing their properties in this work due to insufficient sensitivity and angular resolution.

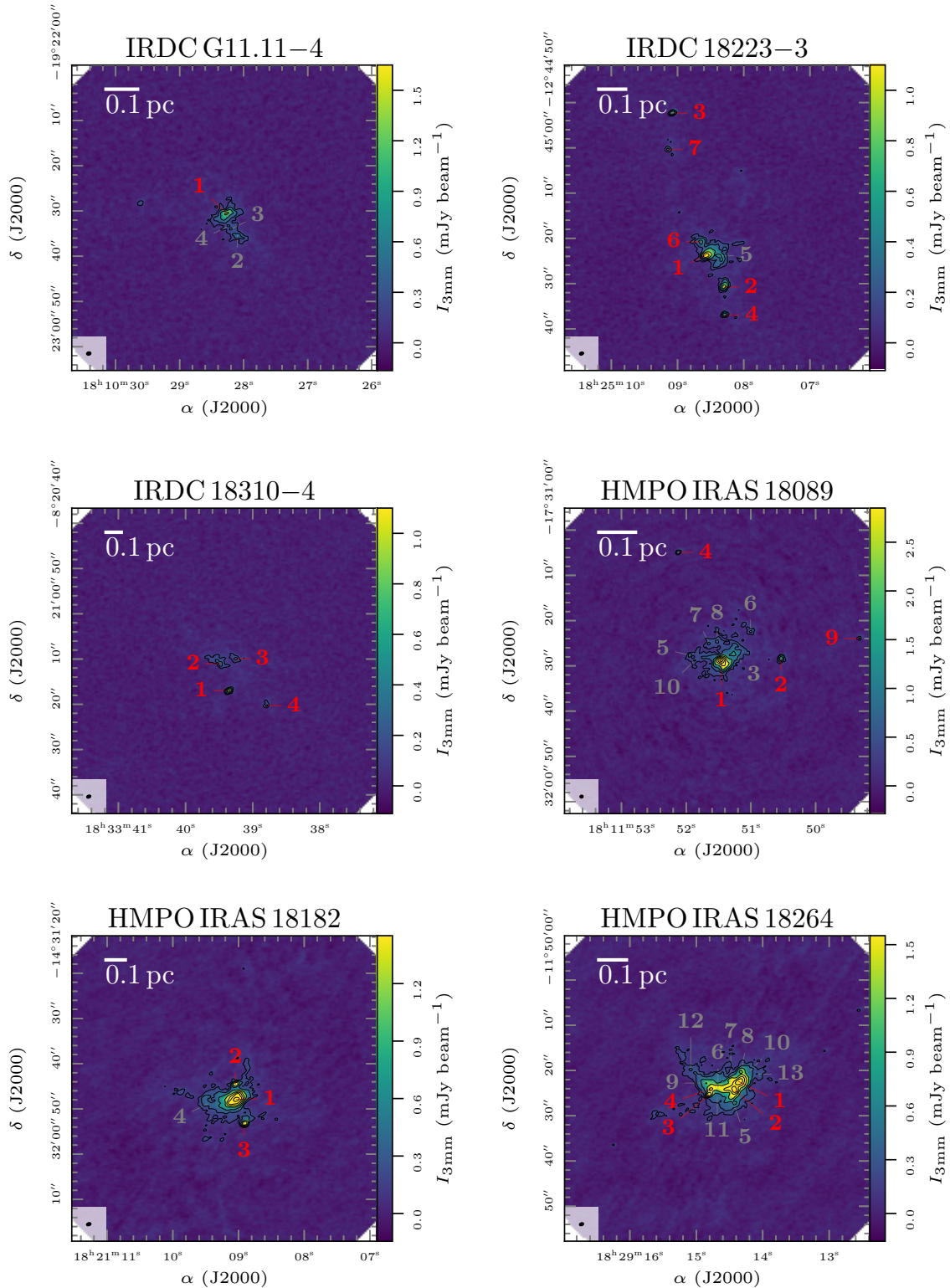


FIGURE 4.2: ALMA 3 mm continuum images of the sample. In each panel, the continuum data of the region is shown in color and black contours. The dotted black contour marks the $-5\sigma_{\text{cont}}$ level. The solid black contours start at $5\sigma_{\text{cont}}$ and contour steps increase by a factor of 2 (e.g., 5, 10, 20, $40\sigma_{\text{cont}}$). The synthesized beam size is shown in the bottom left corner. The bar in the top left corner indicates a linear spatial scale of 0.1 pc. The continuum noise and synthesized beam size are listed in Table 4.2. The continuum fragments are classified into mm cores (red), (cometary) UCHII regions (orange), and envelope clumps (grey), further explained in Sect. 4.4.1.

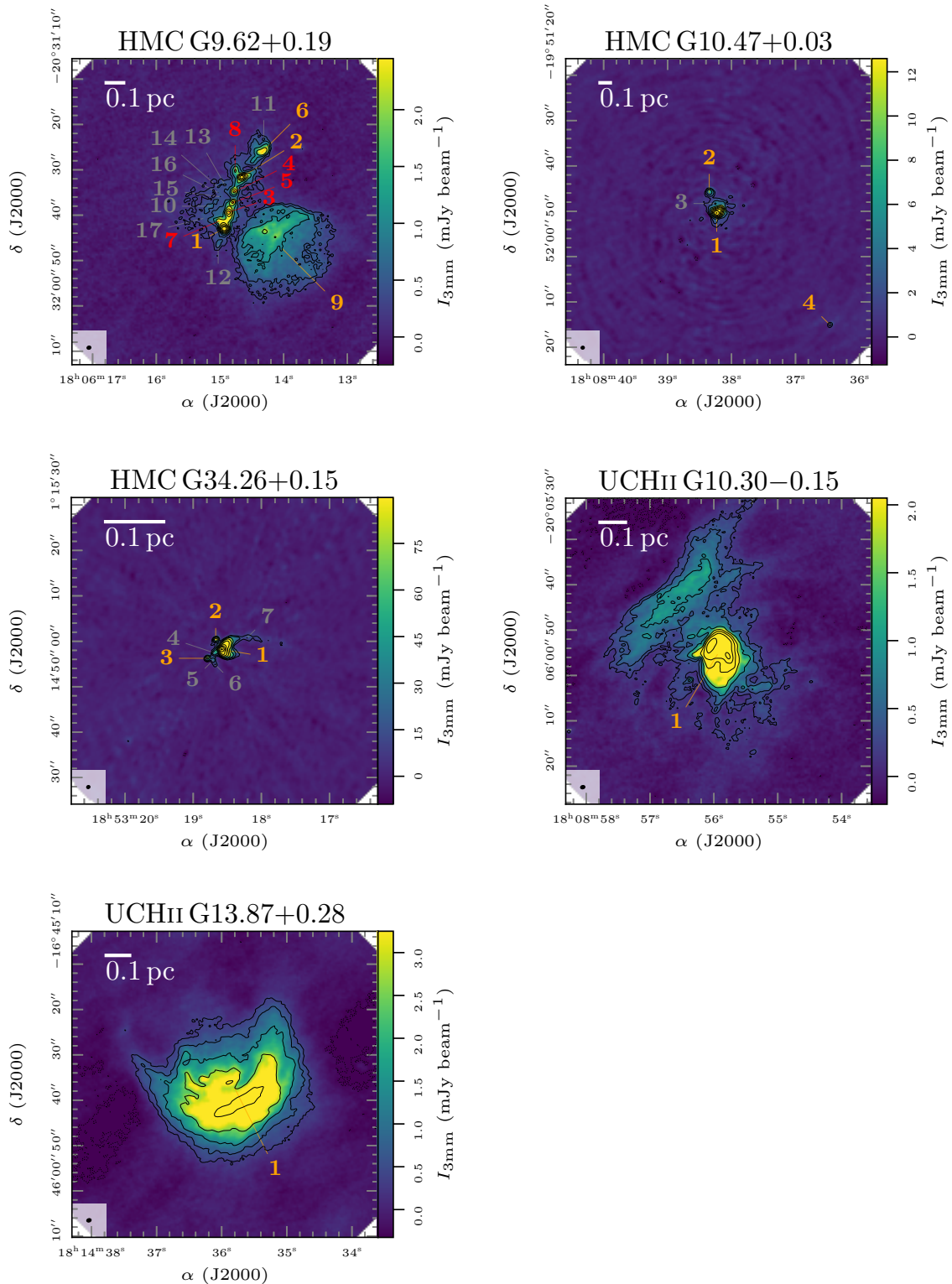


FIGURE 4.2 (cont.): ALMA 3 mm continuum of the sample. In each panel, the continuum data of the region is shown in color and black contours. The dotted black contour marks the $-5\sigma_{\text{cont}}$ level. The solid black contours start at $5\sigma_{\text{cont}}$ and contour steps increase by a factor of 2 (e.g., 5, 10, 20, $40\sigma_{\text{cont}}$). The synthesized beam size is shown in the bottom left corner. The bar in the top left corner indicates a linear spatial scale of 0.1 pc. The continuum noise and synthesized beam size are listed in Table 4.2. The continuum fragments are classified into mm cores (red), (cometary) UCHII regions (orange), and envelope clumps (grey), further explained in Sect. 4.4.1.

In total, we extract 27 mm cores, 33 envelope clumps, 9 UCH_{II} regions, and 3 cometary UCH_{II} regions. Excluding the envelope clumps, the peak intensity and integrated flux of the fragments covers 5 orders of magnitudes from 0.25 to 2 500 mJy beam⁻¹ and 0.29 to 6 600 mJy, respectively and the radii range from 1 200 to 66 000 au.

In the following analysis, we derive the temperature and density profiles ($T \sim r^{-q}$ and $n \sim r^{-p}$), H₂ column density $N(\text{H}_2)$, and mass M of the mm cores and (cometary) UCH_{II} regions excluding the envelope clump positions. In order to reliably estimate the H₂ column density and mass (Sect. 4.7), free-free emission that can have a significant contribution at 3 mm wavelengths has to be subtracted first from the ALMA 3 mm continuum in order to determine the pure 3 mm dust emission (Sect. 4.4.2).

4.4.2 Free-free emission

In the CORE and CORE-extension sample, the NOEMA 1 mm continuum emission arises from optically thin dust emission toward the cores (Sects. 2.3.1 and 3.4.1, respectively). At 3 mm wavelengths, an additional contribution from free-free emission can be present for more evolved cores toward the HMC and UCH_{II} regions (Fig. 1.9). Free-free emission arises from free electrons scattering of ions (Condon & Ransom 2016). In order to reliably estimate the H₂ column density and mass (Sect. 4.7), the free-free contribution at 3 mm wavelengths is estimated using archival VLA data of the CORNISH project (Hoare et al. 2012). The CORNISH project is a 5 GHz (6 cm) radio continuum survey with the VLA covering the Galactic plane at $10^\circ < l < 65^\circ$ and $|b| < 1^\circ$ at an angular resolution of 1.''5 with the primary aim to study UCH_{II} regions. At high frequencies, the free-free emission is optically thin and the spectrum is described by Eq. (1.50).

Hydrogen recombination lines can reveal locations in HMSFRs that contain free electrons. Our ALMA 3 mm spectral setup covers the H(40) α recombination line that allows us to estimate in which regions there is a significant contribution of free-free emission at 3 mm. For each region, the H(40) α line integrated intensity is computed from $\nu_{\text{LSR}} - 50 \text{ km s}^{-1}$ to $\nu_{\text{LSR}} + 50 \text{ km s}^{-1}$ and the integrated intensity maps are shown in Fig. C.12. In all IRDCs and HMPOs, there is no H(40) α intensity detected at our line sensitivity of $\approx 0.1 \text{ K}$ (Table 4.4) which is expected since these regions are young. In contrast, all HMCs and UCH_{II} regions show at least in some parts H(40) α emission. Thus the ALMA 3 mm continuum emission is dominated by dust for all IRDCs and HMPOs and a composite of dust and free-free emission for the HMCs and UCH_{II} regions.

For two HMCs (except for HMC G9.62+0.19) and both UCH_{II} regions CORNISH data is available. Since the traced spatial scales of the ALMA and VLA observations are not the same, spatial filtering hinders a direct comparison. Therefore, we reimage the ALMA 3 mm continuum data of the four regions with the same VLA baselines (2–300 k λ), pixel scale (0.''25), and synthesized beam (1.''5). The reimaged ALMA continuum data are shown in color and in green contours ($\pm 5\sigma_{\text{cont}}$) in the left panel Fig. 4.3. In addition the VLA 5 GHz CORNISH data are shown by red contours ($\pm 5\sigma_{\text{cont}}$). The free-free emission at 5 GHz is extrapolated to 98.3 GHz (3 mm) according to Eq. (1.50) for all pixels that have a $S/N \geq 5$ in both the reimaged ALMA and VLA data (center panel in Fig. 4.3). The dust emission is then estimated by subtracting the extrapolated free-free emission from the 3 mm continuum, $I_{\text{dust},3\text{mm}} = I_{3\text{mm}} - I_{\text{ff},3\text{mm}}$.

The integrated flux density of the reimaged ALMA 3 mm continuum $F_{3\text{mm}}$, free-free flux density at 3 mm $F_{\text{ff},3\text{mm}}$, and dust flux density at 3 mm $F_{\text{dust},3\text{mm}}$ for all fragments in the four regions with detected 5 GHz emission are summarized in Table 4.5. All of these fragments are classified as ‘‘UCH_{II} regions’’ (Sect. 4.4.1, Table C.3). The integrated flux densities are

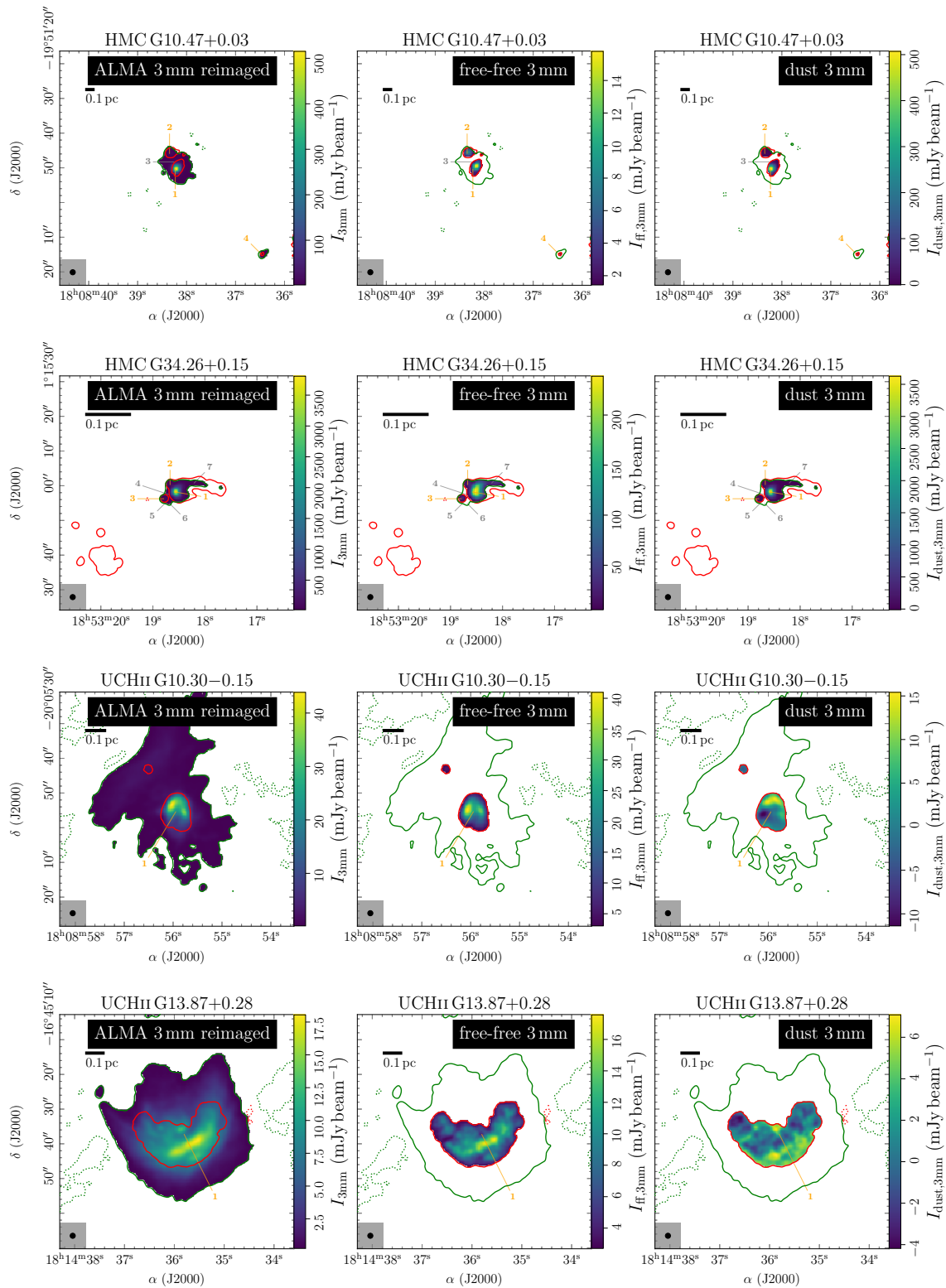


FIGURE 4.3: Estimate of the free-free contribution at 3 mm. In each panel, the VLA 5 GHz (Hoare et al. 2012) and reimagined ALMA 3 mm $\pm 5\sigma$ continuum levels are indicated by red and green contours, respectively (dotted: -5σ and solid: $+5\sigma$). In color, the reimagined ALMA 3 mm continuum $I_{3\text{mm}}$ (left panel), free-free contribution at 3 mm based on VLA 5 GHz emission $I_{\text{ff},3\text{mm}}$ (center panel), and dust emission at 3 mm $I_{\text{dust},3\text{mm}}$ (right panel) are shown. In the center and right panel only emission where both the ALMA and VLA data have a $S/N > 5$ are shown in color. The synthesized beam size is shown in the bottom left corner. The continuum fragments are classified into mm cores (red), (cometary) UCHII regions (orange), and envelope clumps (grey), further explained in Sect. 4.4.1.

TABLE 4.5: Free-free contribution at 3 mm in the ALMA regions. The estimates for HMC G9.62+0.19 are taken from Liu et al. (2020). For the remaining regions, the free-free emission is estimated from CORNISH 5 GHz data (Fig. 4.3).

	$F_{3\text{mm}}$	$F_{\text{ff},3\text{mm}}$	$F_{\text{dust},3\text{mm}}$	$F_{\text{ff},3\text{mm}}/F_{3\text{mm}}$	type
	(mJy)			(%)	
HMC G9.62+0.19 1	98.8	73.0	25.8	73.9	UCHII
HMC G9.62+0.19 2	40.9	2.0	38.9	4.9	UCHII
HMC G9.62+0.19 6	32.6	32.0	0.6	98.2	UCHII
HMC G9.62+0.19 9	437.0	359.0	78.0	82.2	comet. UCHII
HMC G10.47+0.03 1	655.4	24.0	631.5	3.7	UCHII
HMC G10.47+0.03 2	16.5	8.0	8.6	48.2	UCHII
HMC G10.47+0.03 4	1.0	0.4	0.6	39.8	UCHII
HMC G34.26+0.15 1	6334.3	776.4	5558.0	12.3	UCHII
HMC G34.26+0.15 2	98.5	20.8	77.7	21.1	UCHII
HMC G34.26+0.15 3	56.8	14.0	42.8	24.6	UCHII
UCHII G10.30-0.15 1	514.3	483.5	59.6	94.0	comet. UCHII
UCHII G13.87+0.28 1	1069.1	886.6	182.5	82.9	comet. UCHII

computed only considering the pixels that have a $S/N \geq 5$ in both the reimagined ALMA and VLA data. The percentage of free-free contribution at 3 mm is presented as well in Table 4.5. For HMC G9.62+0.19 we show literature results for fragments with detected $\text{H}(40)\alpha$ emission taken from Liu et al. (2020). While for a few UCHII regions (e.g., HMC G9.62+0.19 2 and HMC G10.47+0.03 1) the free-free emission contributes less than 10% to the 3 mm continuum, the cometary UCHII regions are dominated by free-free emission (>80%) at 3 mm.

For HMC G34.26+0.15 1 we might underestimate the free-free contribution at 3 mm since Mookerjea et al. (2007) estimate that at 3 mm the continuum is completely dominated by free-free emission. Therefore, we likely overestimate the mass and column density in Sect. 4.7. Toward HMC G10.47+0.03 1, Cesaroni et al. (2010) detect with VLA 6 cm observations three sources, A, B1, and B2 at a higher angular resolution of $0.''1$. These authors derive an integrated flux density of $F_{\text{ff},6\text{cm}} = 52.5$ mJy for these three sources, corresponding to $F_{\text{ff},3\text{mm}} = 39$ mJy, while with the CORNISH data we estimate $F_{\text{ff},3\text{mm}} = 24$ mJy (Table 4.5). We might therefore also slightly overestimate the 3 mm dust emission for HMC G10.47+0.03 1. Interestingly, there is an offset between the peak of the ALMA and VLA data for HMC G10.47+0.03 1, where the ALMA peaks toward the south-east, and the VLA data peaks toward the north-west (Fig. 4.3). The ALMA continuum peaks toward the sources B1 and B2 and the VLA data peaks toward the source A studied by Cesaroni et al. (2010).

4.5 Temperature structure

The temperature in the densest regions in IRDCs is typically very low, $T < 20$ K (Carey et al. 1998), but as protostars form, they heat up their surrounding gas and dust and eventually the envelope is completely disrupted. On clump scales, the temperature can be estimated from fitting the SED of the dust continuum emission (e.g., with Herschel observations, Ragan et al. 2012), but the angular resolution is not sufficient to resolve individual cores within their parental clumps. Molecular line emission can also be used to estimate the temperature, for example H_2CO and CH_3CN (Sects. 2.3.2 and 3.5.4, Rodón et al. 2012; Gieser et al. 2019; Lin et al.

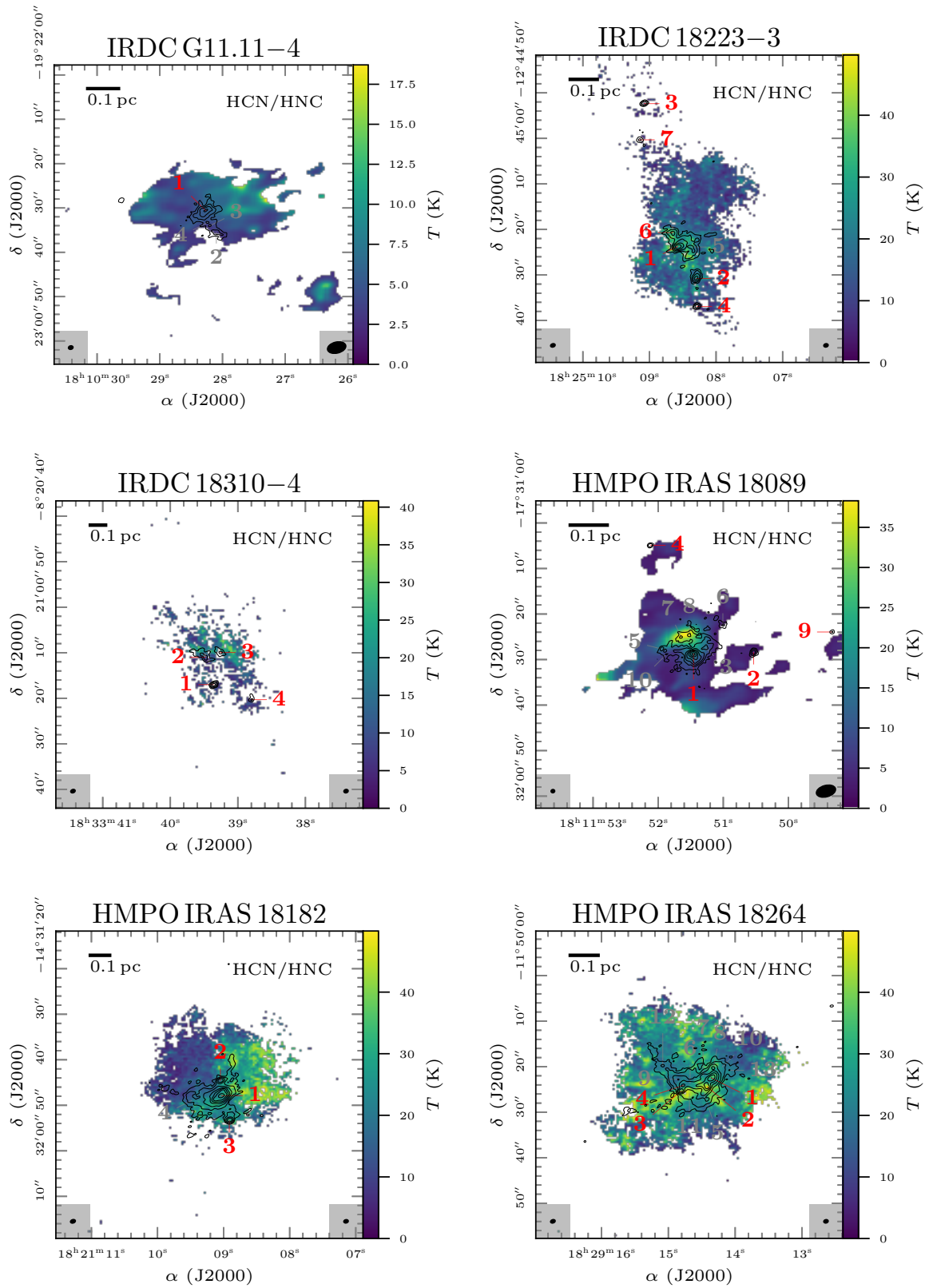


FIGURE 4.4: Temperature maps derived with the HCN-to-HNC intensity ratio. In each panel, the temperature is shown in color and the 3 mm continuum in black contours. The dotted black contour marks the $-5\sigma_{\text{cont}}$ level. The solid black contours start at $5\sigma_{\text{cont}}$ and contour steps increase by a factor of 2 (e.g., 5, 10, 20, $40\sigma_{\text{cont}}$). The synthesized beam size of the continuum and line data is shown in the bottom left and right corner, respectively. The continuum fragments are classified into mm cores (red), (cometary) UCHII regions (orange), and envelope clumps (grey), further explained in Sect. 4.4.1.

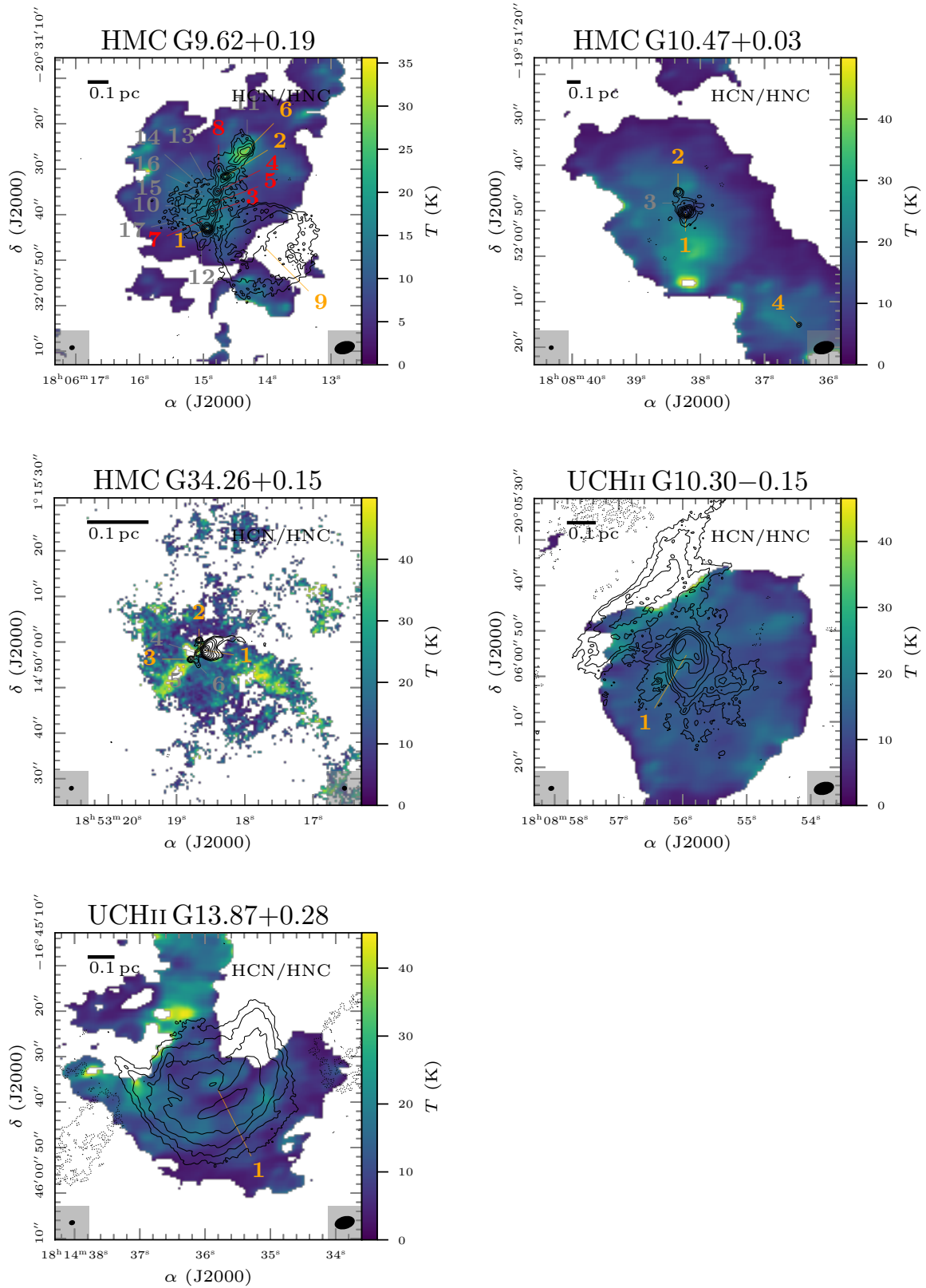


FIGURE 4.4 (cont.): Temperature maps derived with the HCN-to-HNC intensity ratio. In each panel, the temperature is shown in color and the 3 mm continuum in black contours. The dotted black contour marks the $-5\sigma_{\text{cont}}$ level. The solid black contours start at $5\sigma_{\text{cont}}$ and contour steps increase by a factor of 2 (e.g., 5, 10, 20, 40 σ_{cont}). The synthesized beam size of the continuum and line data is shown in the bottom left and right corner, respectively. The continuum fragments are classified into mm cores (red), (cometary) UCHII regions (orange), and envelope clumps (grey), further explained in Sect. 4.4.1.

2022). Recently, Hacar et al. (2020) reported that between 15 K and 50 K the HCN-to-HNC intensity ratio provides a good estimate of the temperature.

In this section we use both the HCN-to-HNC intensity ratio, tracing the cold extended gas, and CH₃CN and CH₃¹³CN line emission, tracing warmer gas, to create temperature maps for all regions. Azimuthal-averaged temperature profiles are computed for all mm cores to estimate the temperature power-law index q (Eq. 2.1).

4.5.1 HCN-to-HNC intensity ratio

Hacar et al. (2020) find an empirical relation between the gas temperature and the HCN-to-HNC line integrated intensity ratio $\frac{I(\text{HCN})}{I(\text{HNC})}$. These authors used IRAM 30m observations of the 1 – 0 transition of HCN and HNC and compared the line integrated intensity ratios with kinetic temperature estimates derived from NH₃ observations. The empirical relation derived by Hacar et al. (2020) follows:

$$\begin{aligned}
 T &= 10 \times \frac{I(\text{HCN})}{I(\text{HNC})} && \text{if } \frac{I(\text{HCN})}{I(\text{HNC})} \leq 4 \\
 T &= 3 \times \left(\frac{I(\text{HCN})}{I(\text{HNC})} - 4 \right) + 40 && \text{if } \frac{I(\text{HCN})}{I(\text{HNC})} > 4.
 \end{aligned}
 \tag{4.1}$$

Our observational setup covers the 1 – 0 transition of HCN and HNC (Table 4.3) and therefore we use their approach to estimate the kinetic temperature of the low-density and low-temperature gas. This method is also useful for more extended regions where no CH₃CN line emission is detected. The HCN and HNC line data products are summarized in Table 4.4. For both molecules, the integrated intensity is computed from $v_{\text{LSR}} - 30$ to $v_{\text{LSR}} + 30$ km s⁻¹. The noise in the integrated intensity maps is estimated from σ_{line} (Table 4.4) and the number of channels n_{channel} : $\sigma_{\text{int.intensity}} = \sqrt{n_{\text{channel}}} \times \sigma_{\text{line}} \times \delta v$, with $\delta v \approx 0.8$ km s⁻¹. All pixels with a $S/N < 3$ in the integrated intensity map are masked out. Since the HCN line is in SPR1 and HNC in SPR3, for which all regions in Field 2 (Table 4.1) have a poorer resolution of $\approx 3''$, we imaged the HCN spectral line data using the same baselines as the HNC spectral line data (Sect. 4.3.1). The temperature is calculated according to Eq. (4.1) from the HCN-to-HNC intensity ratio. We further mask all pixels with $T_{\text{kin}} < T_{\text{CMB}} = 2.73$ K and $T_{\text{kin}} > 50$ K.

The temperature maps derived with the HCN-to-HNC intensity ratio are presented in Fig. 4.4. In most cases, the temperature maps are more extended than the 3 mm continuum due to HCN and HNC having large scale emission. Broad line wings of bipolar outflows can affect the line intensities (e.g., toward HMC G34.26+0.15). In HMPO IRAS 18182 a large scale E-W temperature gradient can be observed. The UCHII region in the position HMC G9.62+0.19 6 heats up the environment with elevated temperatures in the surrounding envelope.

Since this method is only valid up to ≈ 50 K (Hacar et al. 2020) and the HCN and HNC lines can become optically thick in the densest regions, we use CH₃CN and CH₃¹³CN in the next section to probe the temperature in the high-density and high-temperature regions.

4.5.2 Methyl cyanide

In Chapter 2 we used CH₃CN line emission to infer the temperature structure in the CORE sample using the radiative transfer tool XCLASS. A detailed description of XCLASS is given in Sect. 1.5.2. While the CORE 1 mm spectral setup covered the CH₃CN $J = 12 - 11$ K-ladder ($E_{\text{u}}/k_{\text{B}} = 69 - 530$ K), in the ALMA 3 mm setup the $J = 5 - 4$ transitions are covered ($E_{\text{u}}/k_{\text{B}} = 13 - 130$ K for CH₃CN and CH₃¹³CN, Table 4.3). Extended CH₃¹³CN emission is only

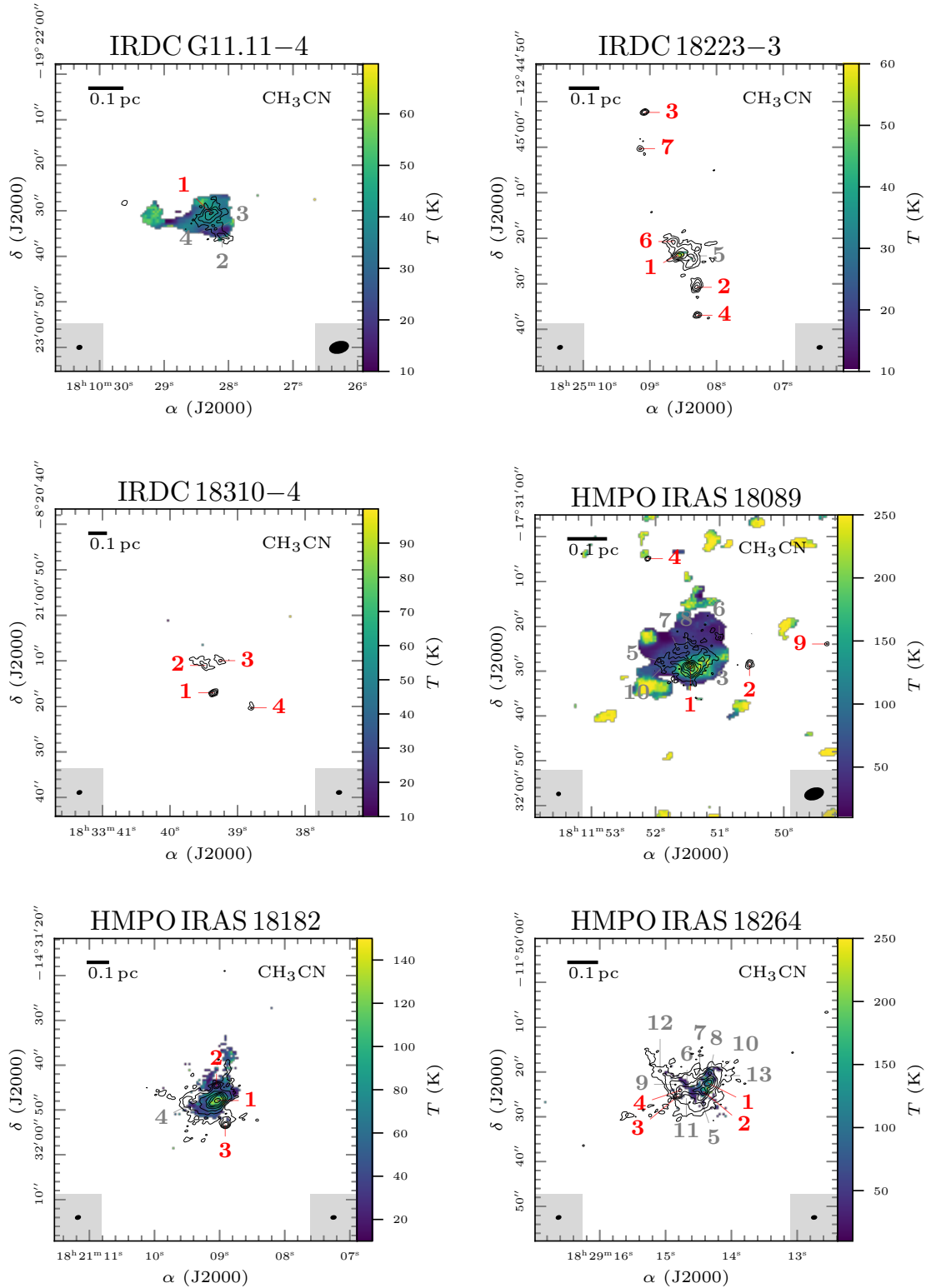


FIGURE 4.5: Temperature maps derived with CH_3CN . In each panel, the temperature is shown in color and the 3 mm continuum in black contours. The dotted black contour marks the $-5\sigma_{\text{cont}}$ level. The solid black contours start at $5\sigma_{\text{cont}}$ and contour steps increase by a factor of 2 (e.g., 5, 10, 20, $40\sigma_{\text{cont}}$). The synthesized beam size of the continuum and spectral line data are shown in the bottom left and right corner, respectively. The continuum fragments are classified into mm cores (red), (cometary) UCHII regions (orange), and envelope clumps (grey), further explained in Sect. 4.4.1. The clumpy features surrounding HMPO IRAS 18089 are caused by side lobes.

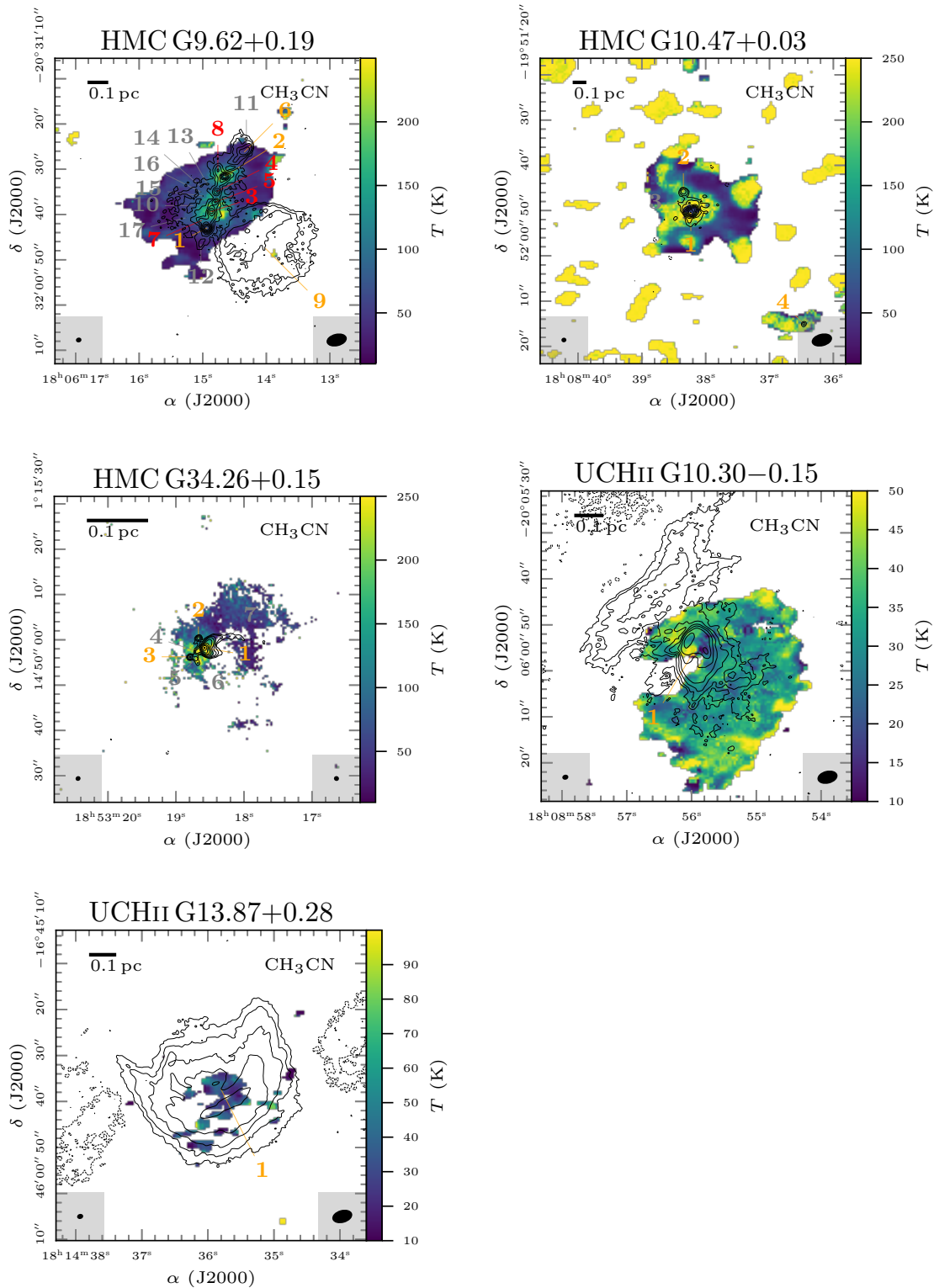


FIGURE 4.5 (cont.): Temperature maps derived with CH_3CN . In each panel, the temperature is shown in color and the 3 mm continuum in black contours. The dotted black contour marks the $-5\sigma_{\text{cont}}$ level. The solid black contours start at $5\sigma_{\text{cont}}$ and contour steps increase by a factor of 2 (e.g., 5, 10, 20, $40\sigma_{\text{cont}}$). The synthesized beam size of the continuum and spectral line data are shown in the bottom left and right corner, respectively. The continuum fragments are classified into mm cores (red), (cometary) UCHII regions (orange), and envelope clumps (grey), further explained in Sect. 4.4.1. The clumpy features surrounding HMC G10.47+0.03 are caused by side lobes.

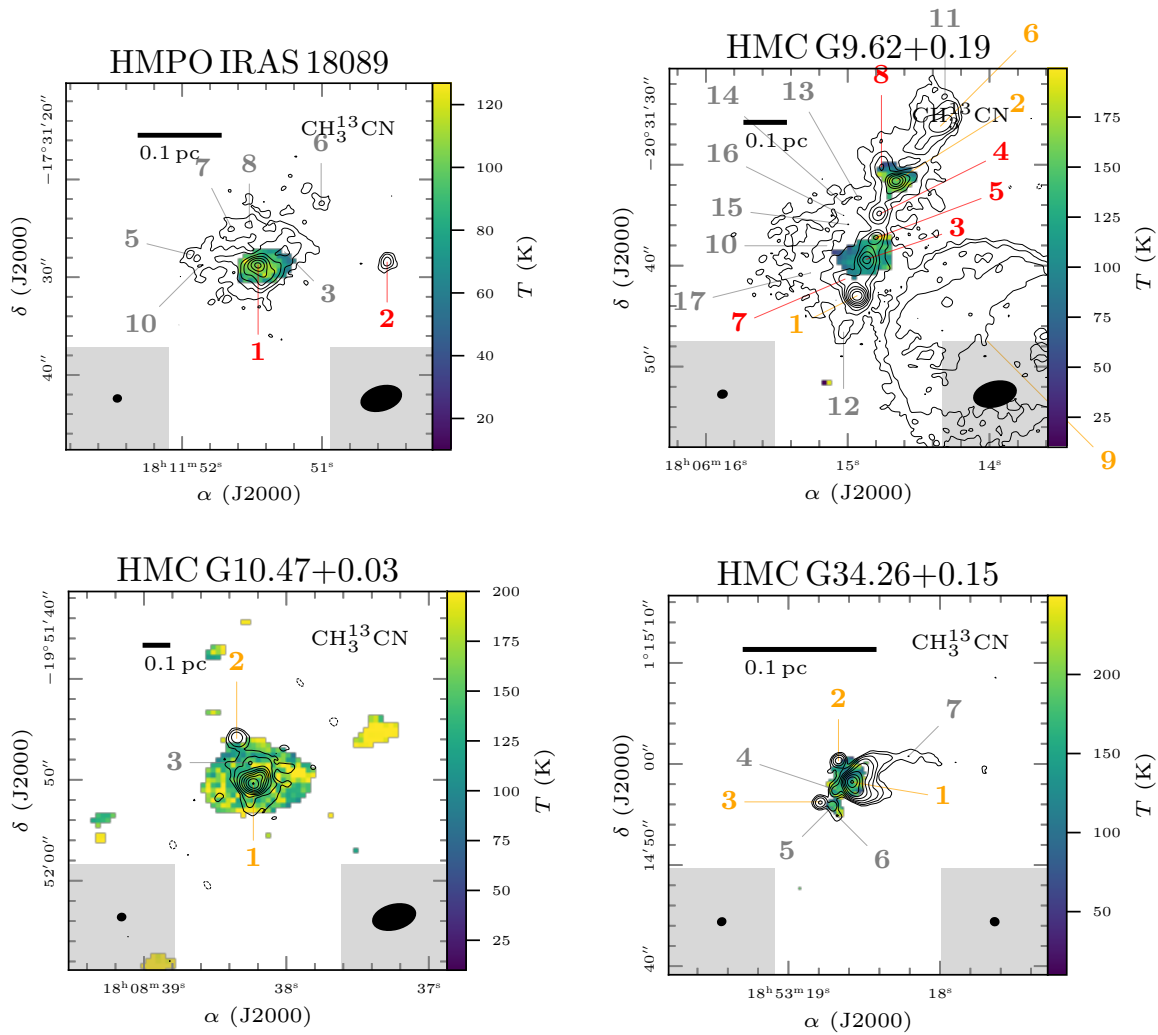


FIGURE 4.6: Temperature maps derived with $\text{CH}_3^{13}\text{CN}$. In each panel, the temperature is shown in color and the 3 mm continuum in black contours. The dotted black contour marks the $-5\sigma_{\text{cont}}$ level. The solid black contours start at $5\sigma_{\text{cont}}$ and contour steps increase by a factor of 2 (e.g., 5, 10, 20, $40\sigma_{\text{cont}}$). The synthesized beam size of the continuum and spectral line data are shown in the bottom left and right corner, respectively. The continuum fragments are classified into mm cores (red), (cometary) UCHII regions (orange), and envelope clumps (grey), further explained in Sect. 4.4.1.

detected toward the three HMCs and HMPO IRAS 18089, and due to a high optical depth of the main isotopologue, $\text{CH}_3^{13}\text{CN}$ can thus more reliably trace the temperature of denser regions.

With `myXCLASSmapfit`, we fit all pixels with a peak intensity $>5\sigma_{\text{line}}$ in the spectrum (Table 4.4) using CH_3CN for all 11 regions and $\text{CH}_3^{13}\text{CN}$ for the four regions in which emission is detected. Each parameter range (T_{rot} , N , θ_{Source} , Δv , and v_{off}) is adjusted for each region and molecule, since the sample covers a broad range of densities and temperatures. We therefore iteratively adjust the parameter ranges that result in relatively smooth parameter maps without too many outliers due to bad fits. When many lines are optically thick, the algorithm converges to high temperatures (Sect. 2.3.2), we therefore set the highest possible temperature to 250 K. To trace hotter gas layers, observations of CH_3CN and $\text{CH}_3^{13}\text{CN}$ transitions with higher upper energy levels are required.

The temperature maps of CH_3CN and $\text{CH}_3^{13}\text{CN}$ are presented in Figs. 4.5 and 4.6, respectively. Toward the likely youngest region in our sample, IRDC 18310–4, CH_3CN is not

detected. In IRDC 18223–3, the temperature can only be estimated toward the 3 mm continuum peak position. In IRDC G11.11–4, the CH₃CN emission is already more extended with $T \approx 50$ K. From the IRDCs to the HMCs, the peak temperature is clearly increasing up to ≈ 250 K (that is the upper limit set in XCLASS). Bright CH₃CN emission in HMPO IRAS 18089 and HMC G10.47+0.03 causes strong side lobes which can be seen as artifacts toward the edges surrounding the central region. A temperature plateau is reached toward the continuum peak positions in the HMCs, and in these cases CH₃¹³CN is a better temperature probe. CH₃¹³CN is less extended, but clearly traces high temperatures >150 K in the four regions with detected CH₃¹³CN emission. The cometary UCHII region in HMC G9.62+0.19 (source 9) produces a temperature increase of ≈ 150 K toward the edge of the filament which otherwise has a lower temperature of ≈ 50 K in the envelope.

The temperature map of UCHII G10.30–0.15 is very extended toward the west, and no CH₃CN is detected toward the east facing the bipolar HII region. In UCHII G13.87+0.28 the temperature map is less extended with CH₃CN being present in the cometary halo. In both UCHII regions, the kinetic temperature is very low, with $T < 50$ K. There are two possible explanations for such a low temperature: either CH₃CN is present in the cold gas envelope or the line emission is produced by non-LTE effects. However, since the HCN-to-HNC intensity ratio method also infers temperatures $\lesssim 50$ K, the first explanation seems to be more likely. Therefore, the extended molecular emission in the cometary UCHII regions seems to stem from an envelope that either stayed cold during the evolution of the protostars or is cooling due to the expanding UCHII region.

4.5.3 Radial temperature profiles

The temperature maps created with the HCN-to-HNC intensity ratio, CH₃CN, and CH₃¹³CN allow us to derive radial temperature profiles of the mm cores and (cometary) UCHII regions that are approximated by a power-law profile with temperature power-law index q , $T \sim r^{-q}$ (Eq. 2.1). For each of the sources and temperature tracers, the azimuthal-averaged temperature profile is calculated along seven beams, that is sufficient to fully resolve the radial profiles, starting at the continuum peak position of the source (Table C.3). The temperature profiles are binned in steps of half the synthesized beam size.

In order to derive the radial temperature profile, we fit a power-law profile (Eq. 2.1) to continuous profiles that are resolved along at least two beams and that are radially decreasing. In the fitting, we exclude the innermost data point that is smeared out by the limiting beam size (highlighted as a gray shaded area in Fig. 4.7) if more than three data points are otherwise available in the fit. The profiles are fitted as long as continuous data points are available and as long as the profiles are not increasing with increasing radius along two data points. The fit results including the inner radius r_{in} , temperature $T_{\text{in}} = T(r_{\text{in}})$, and temperature power-law index q are listed in Table C.4. The radial temperature profiles are shown in Fig. 4.7 for all protostellar sources that could be fitted by a power-law.

The temperature profiles derived from the HCN-to-HNC intensity ratio tracing the colder envelope are flat $q \approx 0.05 - 0.3$, while the CH₃CN profiles tracing the hotter gas can be steeper with values ranging between $q \approx 0.1 - 0.8$. The temperature profiles are steep $q > 0.5$ toward sources that are classified to harbor hot cores. The observed CH₃¹³CN radial profiles (five sources in total) are either not resolved or flat and are therefore not fitted.

The beam-averaged temperature \bar{T} for all three tracers is computed for all sources in order to estimate the H₂ column density and mass (Sect. 4.7). The results of the beam-averaged temperatures are summarized in Table C.5. By constraint, the HCN-to-HNC intensity ratio only traces temperatures up to 50 K, in addition, the low upper energy level ($E_{\text{u}}/k_{\text{B}} = 4$ K) of

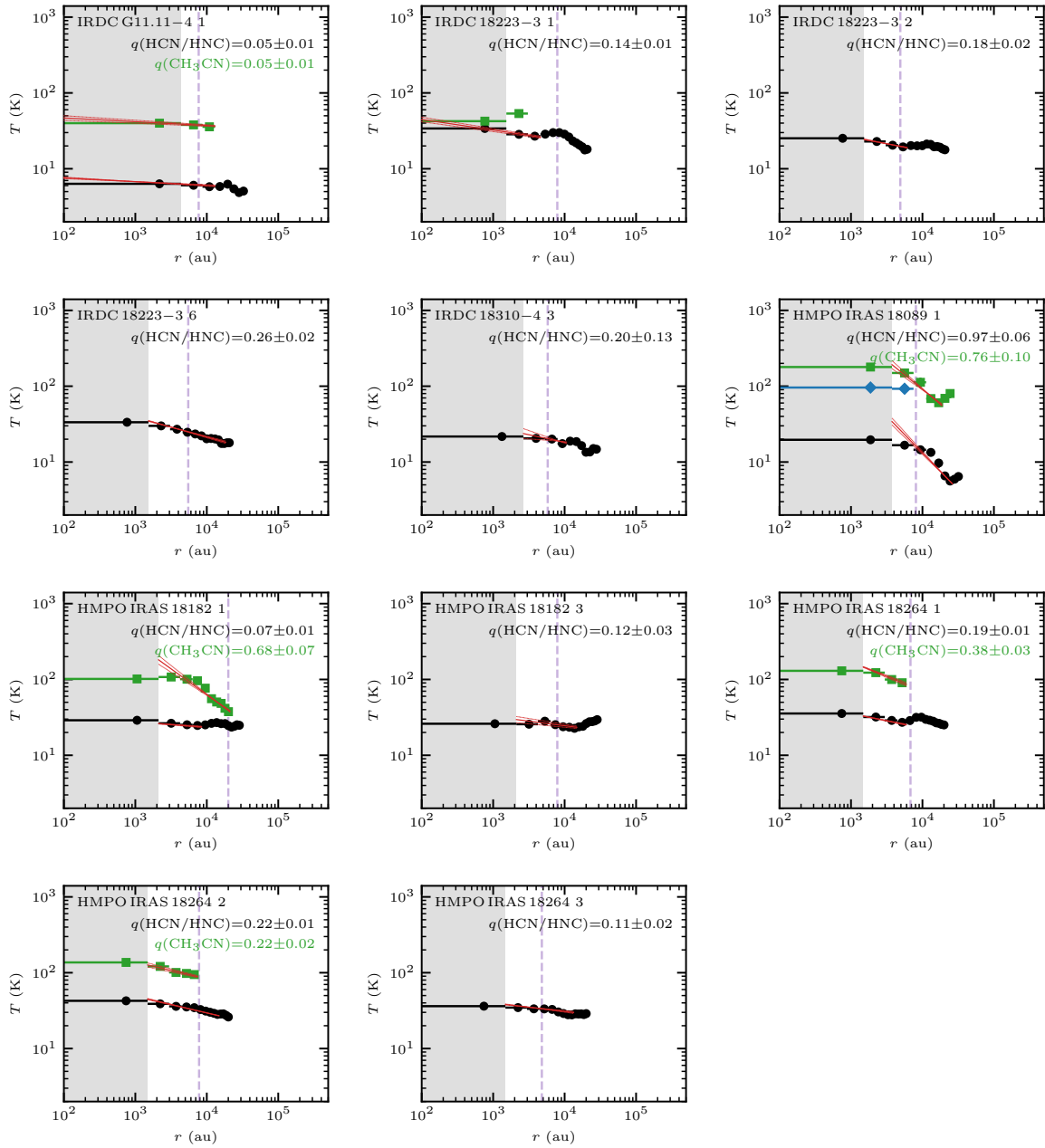


FIGURE 4.7: Radial temperature profiles. The profiles extracted from the HCN-to-HNC intensity ratio (Fig. 4.4), CH_3CN (Fig. 4.5), and $\text{CH}_3^{13}\text{CN}$ (Fig. 4.6) temperature maps are shown by black circles, green squares, and blue diamonds, respectively. The inner unresolved region (one beam radius) is shown as a grey-shaded area. The dashed purple vertical line indicates the outer radius r_{out} of the continuum (Table C.3). A power-law fit and its 1σ uncertainty to resolved and radially decreasing profiles is shown by the red solid and dashed lines, respectively (Sect. 4.5.3).

the HCN and HNC emission line is only sensitive to the colder envelope and might become optically thick toward the densest regions. Therefore, the temperatures might be considerably lower compared to the temperatures derived with CH_3CN and $\text{CH}_3^{13}\text{CN}$. In most cases, the $\text{CH}_3^{13}\text{CN}$ beam-averaged temperature is lower than the CH_3CN beam-averaged temperature. This can be attributed to the fact that if most CH_3CN transitions become optically thick, the fitting algorithm in XCLASS converges toward the upper limit of the rotation temperature that we set to 250 K for the ALMA regions. We find the same effect for the CORE regions, where in regions with a high H_2CO line optical depth, the derived H_2CO rotation temperature is higher

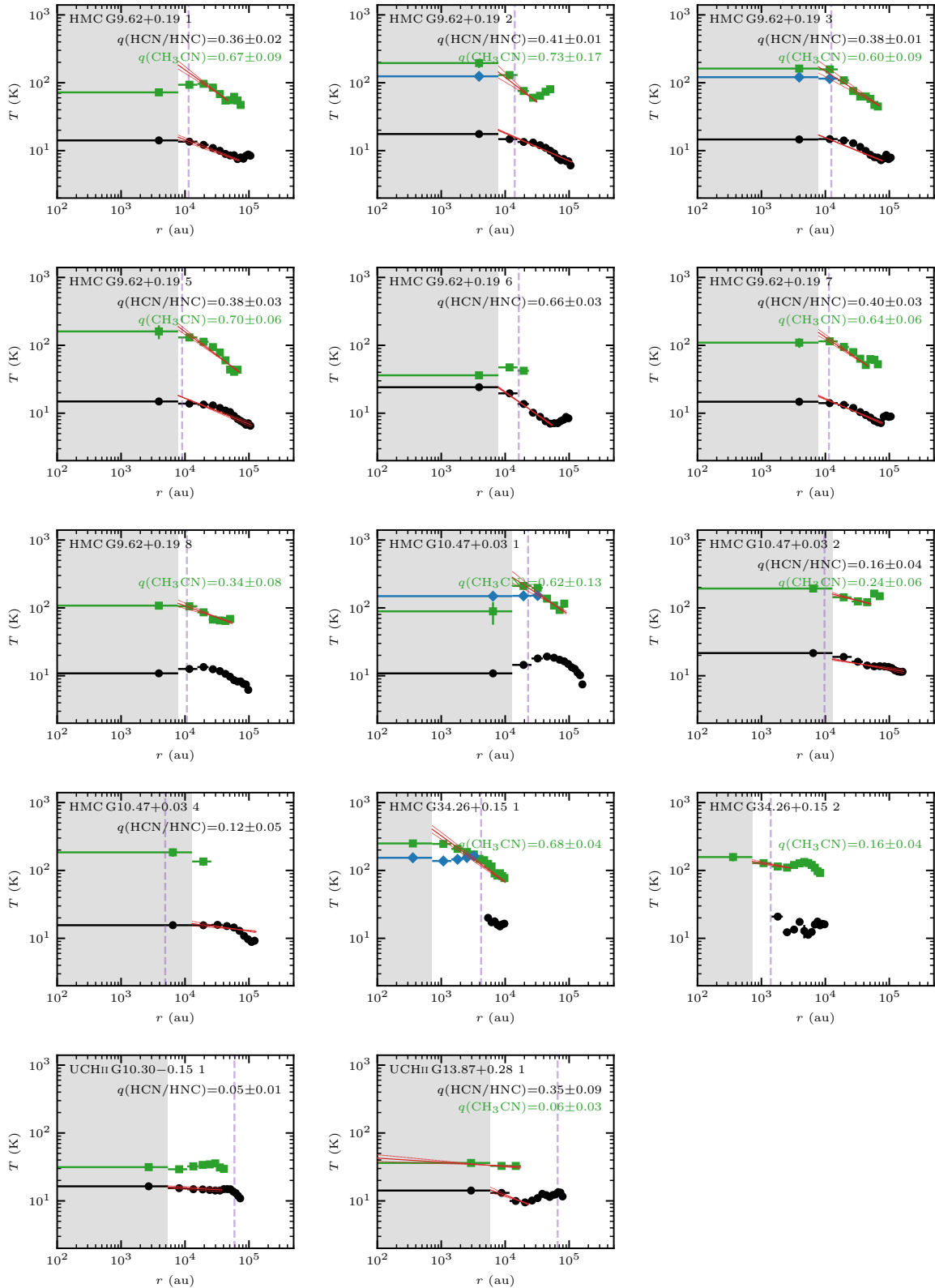


FIGURE 4.7 (cont.): Radial temperature profiles. The profiles extracted from the HCN-to-HNC intensity ratio (Fig. 4.4), CH_3CN (Fig. 4.5), and $\text{CH}_3^{13}\text{CN}$ (Fig. 4.6) temperature maps are shown by black circles, green squares, and blue diamonds, respectively. The inner unresolved region (one beam radius) is shown as a grey-shaded area. The dashed purple vertical line indicates the outer radius r_{out} (Table C.3). A power-law fit and its 1σ uncertainty to resolved and radially decreasing profiles is shown by the red solid and dashed lines, respectively (Sect. 4.5.3).

than the CH₃CN rotation temperature (Fig. A.1). In Sect. 4.8 we discuss evolutionary trends of the temperature profiles and compare the results with the CORE and CORE-extension regions (Chapters 2 and 3).

4.6 Density profiles

In this section, we derive radial density profiles of the mm cores and (cometary) UCH_{II} regions using the 3 mm continuum data. As discussed already in Sects. 2.3.3 and 3.4.2, interferometric observations filter out extended emission and missing flux can therefore be an issue. The radial density profile with power-law index p ($n \sim r^{-p}$, Eq. 2.2) can be best estimated from the continuum data in the uv plane considering the visibility and temperature power-law indices, α and q , with $p = \alpha - q + 3$ (Eq. 2.3). Since bright nearby sources can affect the visibility profiles, we first subtract the emission of other mm cores and UCH_{II} regions (Sect. 4.6.1) and then compute and fit the complex-averaged visibility profiles \bar{V} (Sect. 4.6.2).

4.6.1 Source subtraction

For each mm core or UCH_{II} region, we subtract the emission of the remaining mm cores and UCH_{II} regions within a target region by modeling their emission with a circular Gaussian profile using the task `uvmodel fit` in CASA. Since the three extended cometary UCH_{II} regions (Table C.3) have a complex morphology and cannot be described by a simple model, we do not subtract their emission.

The source model is Fourier-transformed to the uv plane with the `ft` task in CASA and subtracted from the data using the `uvsb` task in CASA. Source subtraction is only necessary when multiple mm cores and/or UCH_{II} regions are present within one region, therefore this step is not necessary for IRDC G11.11–4, UCH_{II} G10.30–0.15, and UCH_{II} G13.87+0.28 (Fig. 4.2, Table C.3). For the remaining regions, we carefully check by imaging the source-subtracted data that the emission of each source is approximately removed and does not affect the emission of nearby sources.

As an example, before computing the visibility profile of mm core 2 in IRDC 18310–4, we subtract the emission of the remaining mm cores 1, 3, and 4. The continuum data of the (cometary) UCH_{II} regions contain not only dust, but also free-free emission that might have an impact on the visibility profiles.

4.6.2 Visibility profiles

The complex-averaged visibility profiles \bar{V} as a function of uv distance are computed using the `plotms` task in CASA. The phase center is shifted to the corresponding source position (Table C.3). For a comparison how the source-subtraction is impacting the visibility profiles, we also compute the complex-averaged visibility profiles \bar{V} using the original 3 mm continuum data with no source subtraction.

Since the number of long baselines is much smaller than the number of short baselines, the visibility profiles are binned with variable bin sizes of 3, 15, and 60 $k\lambda$ in the ranges of 0 – 15, 15 – 120, and 120 – 600 $k\lambda$, respectively. Since the shortest baseline corresponds to $\approx 2.3 k\lambda$, the first binned data point (0 – 3 $k\lambda$) is expected to suffer from missing flux. The visibility profiles are shown in Fig. 4.8 for all mm cores and (cometary) UCH_{II} regions.

In contrast to the CORE and CORE-extension mm cores (Figs. 2.6 and 3.2, respectively) which all have visibility profiles that can be described by a single power-law, $\bar{V} \sim s^\alpha$, most of the sources in this ALMA sample are better described by two power-laws with a steeper profile

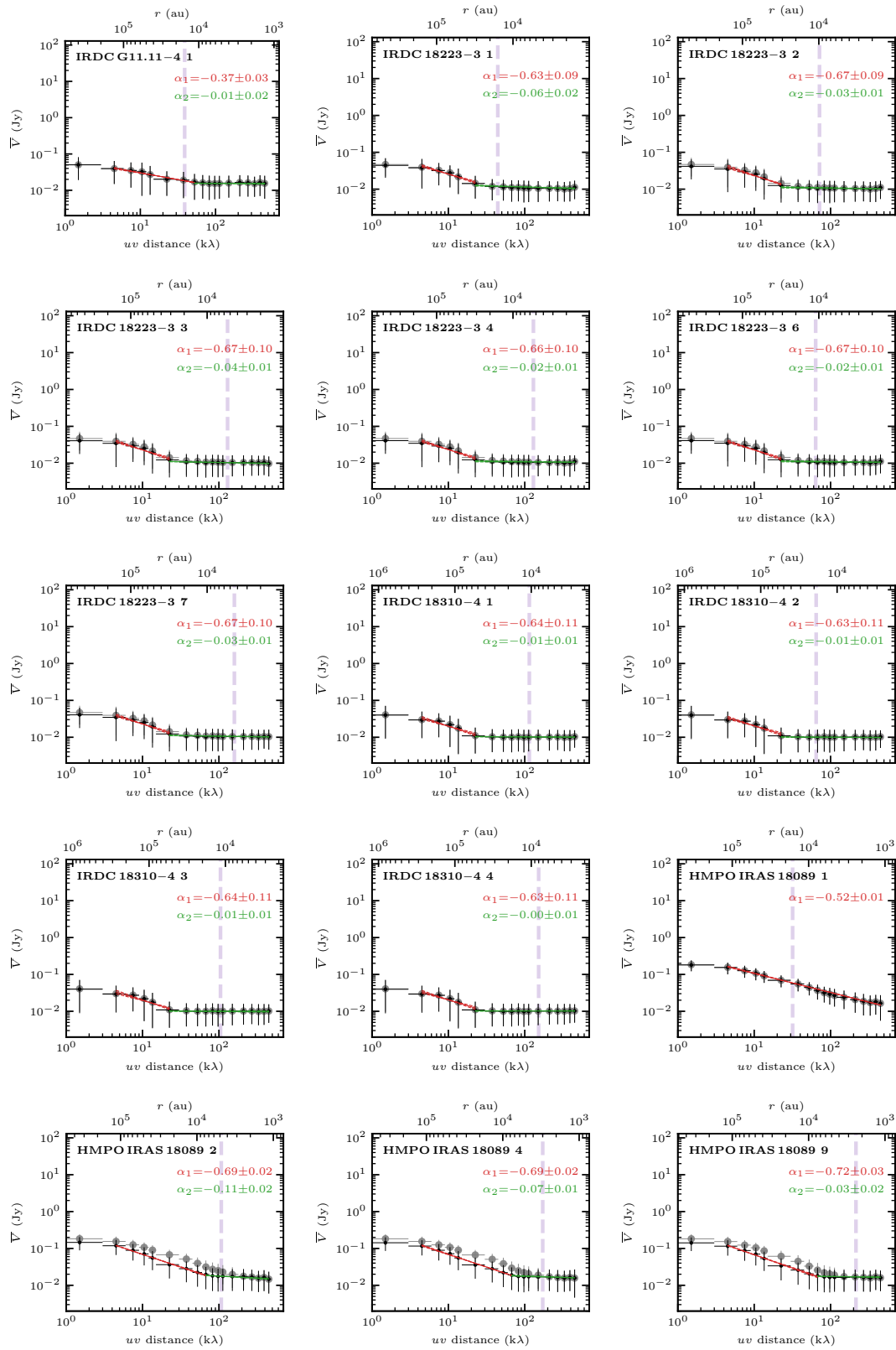


FIGURE 4.8: Visibility profiles of the mm cores and (cometary) UCHII regions. The profile of the non-core and core-subtracted data is shown in grey and black, respectively (further explained in Sect. 4.6.1). Depending on the shape of the profile, one or two power-law profiles are fitted to the core-subtracted data shown in red and green, respectively. The bottom axis shows the uv distance in $k\lambda$ and the top axis is the corresponding spatial scale. The purple dashed line indicates the diameter of the mm cores/HII regions (Table C.3).

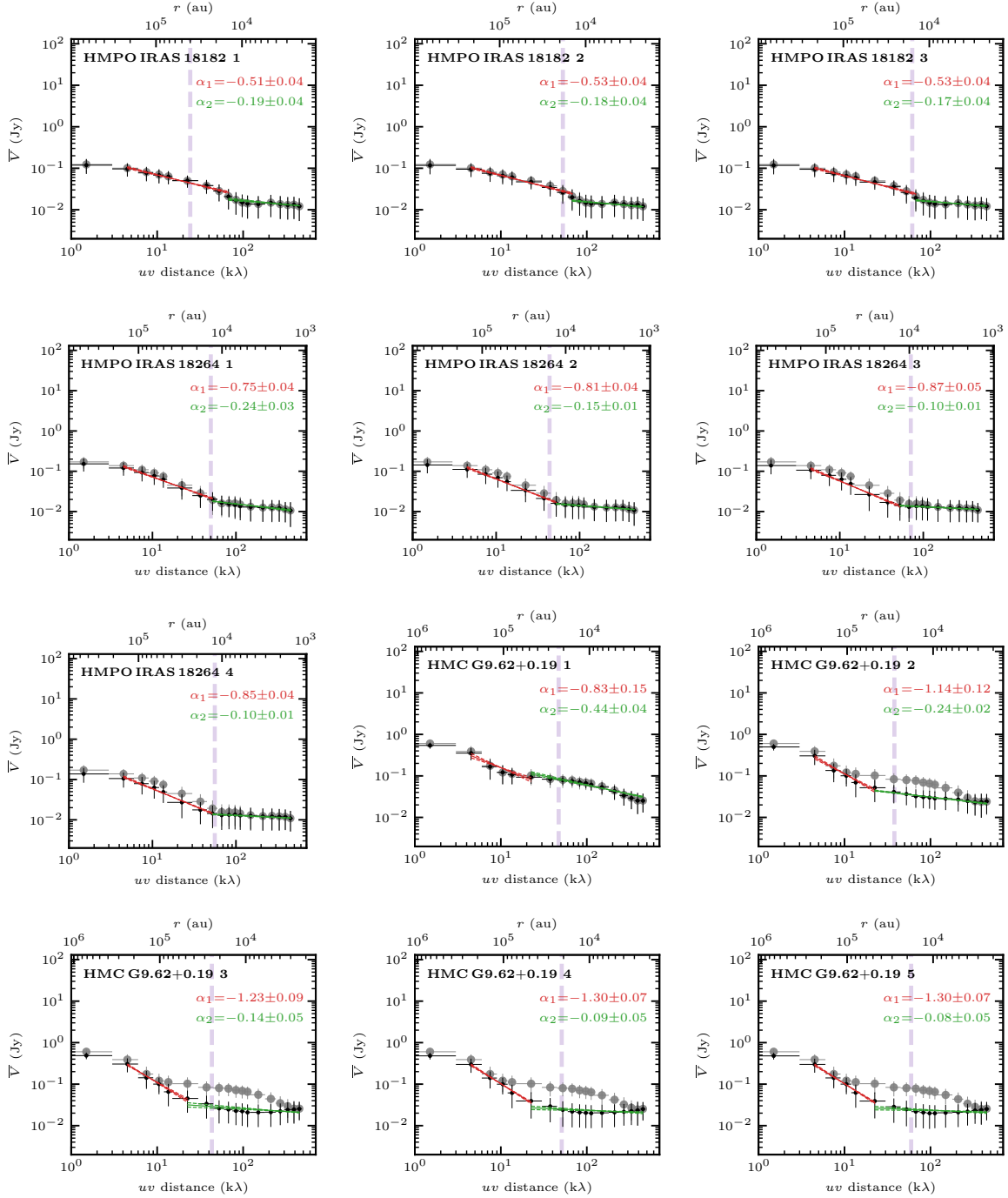


FIGURE 4.8 (cont.): Visibility profiles of the mm cores and (cometary) UCHII regions. The profile of the non-core and core-subtracted data is shown in grey and black, respectively (further explained in Sect. 4.6.1). Depending on the shape of the profile, one or two power-law profiles are fitted to the core-subtracted data shown in red and green, respectively. The bottom axis shows the uv distance in $k\lambda$ and the top axis is the corresponding spatial scale. The purple dashed line indicates the diameter of the mm cores/HII regions (Table C.3).

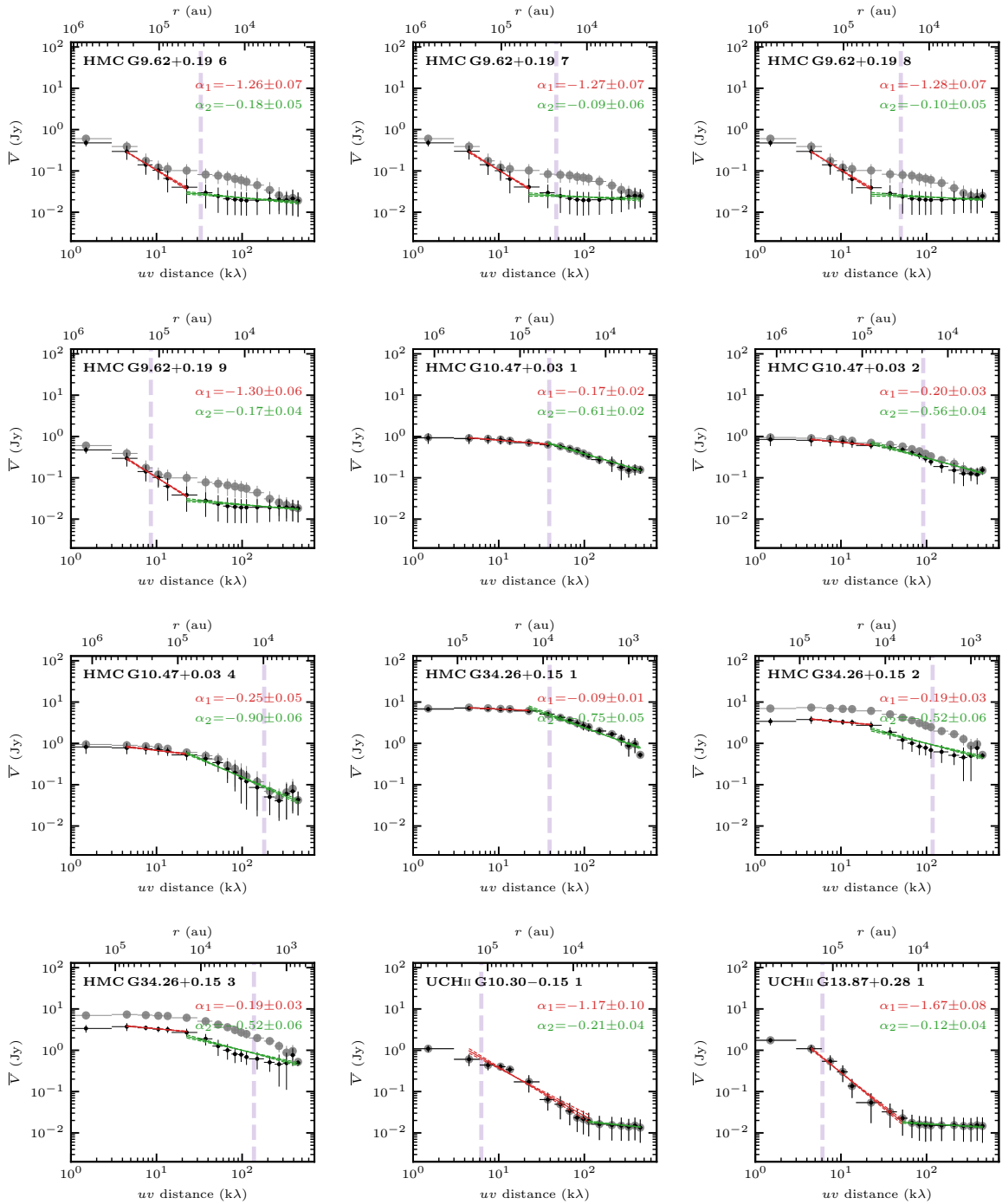


FIGURE 4.8 (cont.): Visibility profiles of the mm cores and (cometary) UCHII regions. The profile of the non-core and core-subtracted data is shown in grey and black, respectively (further explained in Sect. 4.6.1). Depending on the shape of the profile, one or two power-law profiles are fitted to the core-subtracted data shown in red and green, respectively. The bottom axis shows the uv distance in $k\lambda$ and the top axis is the corresponding spatial scale. The purple dashed line indicates the diameter of the mm cores/HII regions (Table C.3).

at short baselines (large spatial scales) and a flatter profile at longer baselines (small spatial scales). In these cases we therefore fit two power-law profiles with α_1 and α_2 , and only one power-law profile ($\alpha_1 = \alpha_2$) otherwise. The first binned data point suffering from missing flux is excluded from the fit. The corresponding density profiles are calculated according to Eq. (2.3) using the temperature power-law index q measured toward the source. The results for α_1 , α_2 , p_1 , and p_2 are summarized in Table C.6.

In Fig. 4.8 it is clearly visible that the source subtraction can have a big impact on the visibility profiles when bright sources are located within the region (e.g., for sources in the HMC G9.62+0.19 and HMC G34.26+0.15 regions). Toward bright sources, the visibility profiles flatten at short uv distances which can be attributed to the continuum emission becoming optically thick (the continuum optical depth τ_v^{cont} is listed in Table C.5, see Sect. 4.7). In these cases, the calculation of the density power-law index p_1 does not provide reliable results since optically thin emission is assumed in Eq. (2.3).

When multiple sources are present within one region, the visibility slope at clump scales (α_1) are similar (Table C.6). This can be explained by the fact that at small baselines, the cores are all covered by such short baselines (and corresponding larger angular resolution) and even though the phase center is shifted to the source position, it does not impact the clump scale in which the cores are embedded in. Except for the sources with a flattening at small uv distances, there is a trend such that the visibility profiles α_1 steepen from the IRDC to UCHII regions implying a flattening of the density profile p_1 . The visibility slope at core scales (α_2) are nearly flat implying unresolved sources in the IRDC stages and become then also steeper with $p_2 \approx 2$. A detailed discussion of the physical structure and evolutionary trends is presented in Sect. 4.8.

4.7 Molecular hydrogen column density and mass estimates

The H_2 column density $N(\text{H}_2)$ and mass M of the sources can be estimated from the 3 mm continuum emission according to Eq. (1.48) and (1.49), respectively, with the assumption that the emission stems from dust and is optically thin. Therefore, for (cometary) UCHII regions with a free-free contribution at 3 mm, we correct the peak intensity $I_{3\text{mm}}$ and integrated flux $F_{3\text{mm}}$ by the fraction of estimated free-free emission listed in Table 4.5. For the temperature, we assume either the beam-averaged temperature based on the $\text{CH}_3^{13}\text{CN}$ temperature maps if detected, CH_3CN if otherwise detected, and HCN-to-HNC intensity ratio otherwise (Table C.5). We use the same parameters as for the CORE and CORE-extension regions with gas-to-dust mass ratio $\eta = 150$ (Draine 2011) and mean molecular weight $\mu = 2.8$ (Kauffmann et al. 2008). The dust opacity is extrapolated from 1.3 mm ($\kappa_0 = 0.9 \text{ g cm}^{-2}$, Ossenkopf & Henning 1994) to 3 mm wavelengths with $\kappa_\nu = \kappa_0 \left(\frac{\nu}{\nu_0}\right)^\beta$, resulting in $\kappa_\nu = 0.12 \text{ g cm}^{-2}$ assuming $\beta = 2$.

The results for $N(\text{H}_2)$ and M are summarized in Table C.5. The optical depth τ_v^{cont} calculated according to Eq. (1.47) is also listed in Table C.5. Since the properties are derived from interferometric observations, the results are lower limits due to potential missing flux. For HMC G34.26+0.15 1, the optical depth cannot be estimated since the numerator is larger than the denominator in Eq. (1.47), most likely because we overestimate the 3 mm dust emission as discussed in Sect. 4.4.2, and therefore the optical depth is estimated to be high. For the remaining sources, the optical depth τ_v^{cont} is much smaller than 1. However, in HMC G10.47+0.03 and HMC G34.26+0.15 in some sources the optical depth becomes larger, $\tau_v^{\text{cont}} > 0.1$, which can be also seen in a flattening of the visibility profiles α_1 (Fig. 4.8) at small baselines. Indeed, the brightness temperatures (Eq. 1.44) are high toward the continuum peak position in HMC G10.47+0.03 and HMC G34.26+0.15 with $T_B \approx 40 \text{ K}$ and $T_B \approx 300 \text{ K}$, respectively, while for the remaining regions $T_B < 10 \text{ K}$. The H_2 column densities vary between

$7 \times 10^{22} \text{ cm}^{-2}$ and $6 \times 10^{26} \text{ cm}^{-2}$ and the masses range between 0.3 and $200 M_{\odot}$. These estimated masses suggest that many of the protostellar sources can develop into massive stars. The highest mass is found toward HMC G10.47+0.03 1 with $M \approx 200 M_{\odot}$. Cesaroni et al. (2010) detect three sources toward this position at 1.6 cm with the VLA at a higher angular resolution of $0.''1$. This indicates that this region is currently forming a compact cluster of massive stars.

4.8 Discussion

In this chapter, we analyze the 3 mm continuum and spectral line emission toward a sample of 11 HMSFRs observed with ALMA in order to characterize the physical properties. The 3 mm continuum data reveal a high degree of fragmentation (Fig. 4.2) and fragmented objects are classified into mm cores (compact 3 mm emission), UCHII regions (with compact 3 mm emission, H(40) α , and cm emission), cometary UCHII regions (with extended 3 mm emission, H(40) α , and cm emission), and envelope clumps (Table C.3).

In Sect. 4.8.1, the region properties (peak intensity $I_{3\text{mm}}^{\text{region}}$ and flux density $F_{3\text{mm}}^{\text{region}}$) derived with the ALMA observations are related to the clump properties derived from the ATLASGAL survey. In Sect. 4.8.2 the evolutionary trends of the physical properties on core scales are discussed and compared with the results of the CORE (Chapter 2) and CORE-extension (Chapter 3) studies.

4.8.1 Evolutionary trends of the clump properties

All regions in our ALMA sample are also covered by the ATLASGAL survey (Schuller et al. 2009) targeting dust emission on clump scales in the Galactic plane. The $870 \mu\text{m}$ images are presented in Figs. C.1 – C.11. The sizes of the clumps cover roughly the FOV of the ALMA 3 mm observations, we therefore compare in this section the ATLASGAL clump properties with the ALMA 3 mm peak intensity $I_{3\text{mm}}^{\text{region}}$ and flux density $F_{3\text{mm}}^{\text{region}}$ of each region.

The distance d , luminosity L , mass M , and dust temperature T_{dust} are taken from the ATLASGAL study by Urquhart et al. (2018) and are listed in Table 4.1. The clump distances d are estimated using different methods, including maser parallaxes and kinematic distances based on radial velocities. The luminosity, mass, and dust temperature are derived by fitting the SED (Eq. 3.1) using additional MIR and FIR data from, for example, the Galactic Legacy Infrared Mid-Plane Survey Extraordinaire (GLIMPSE, Benjamin et al. 2003), the MIPS GALactic plane survey (MIPSGAL, Carey et al. 2009), and the Herschel infrared Galactic Plane Survey (Hi-GAL Molinari et al. 2010).

The ALMA 3 mm peak intensity $I_{3\text{mm}}^{\text{region}}$ and flux density $F_{3\text{mm}}^{\text{region}}$ are listed in Table 4.2. The flux density is integrated using all pixels with emission $>5\sigma_{\text{cont}}$. In contrast to the single-dish observations with Spitzer, Herschel, and APEX telescopes used for the SED fit in Urquhart et al. (2018), the interferometric ALMA observations suffer from spatial filtering that can be an issue especially for the extended UCHII regions that have widespread emission within the full ALMA primary beam (Fig. 4.2). In addition, at 3 mm wavelengths, there is an additional contribution from free-free emission toward evolved regions (Sect. 4.4.2).

In Fig. 4.9 the following clump parameters are presented: d , L/M , T_{dust} , $I_{3\text{mm}}^{\text{region}}$, and $F_{3\text{mm}}^{\text{region}}$. The L/M ratio is an indicator of evolutionary stage (e.g., Sridharan et al. 2002; Molinari et al. 2008, 2010; Maud et al. 2015a; Molinari et al. 2016; Urquhart et al. 2018; Molinari et al. 2019). In color, the different evolutionary stages are highlighted. In order to quantify potential correlations, we use the Spearman correlation coefficient r_s , that is zero for uncorrelated data and ± 1 for correlated and anticorrelated data, respectively (Cohen 1988). The p -value indicates the

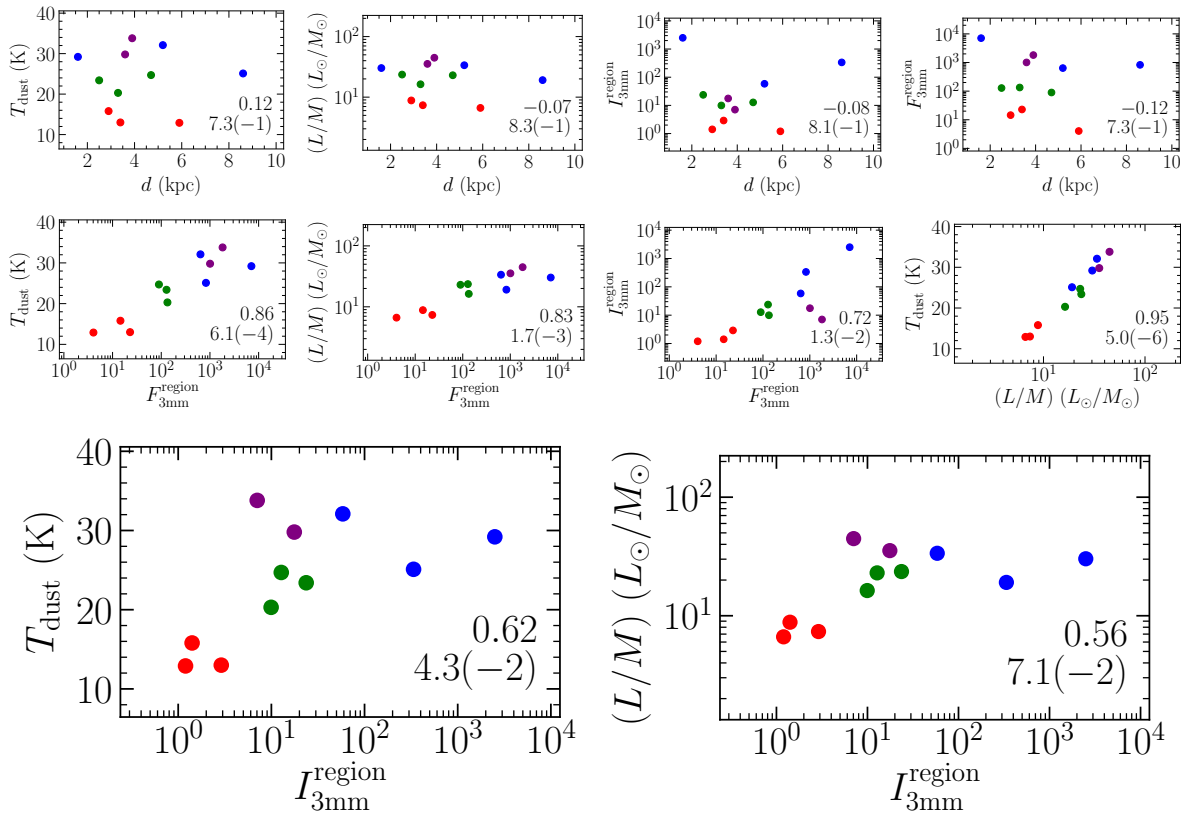


FIGURE 4.9: Comparison of the clump parameters of the ALMA sample. The temperature T_{dust} , luminosity L , mass M , and distance d are listed in Table 4.1 and are taken from the ATLASGAL survey (Schuller et al. 2009; Urquhart et al. 2018). The region peak intensity $I_{3\text{mm}}^{\text{region}}$ and flux density $F_{3\text{mm}}^{\text{region}}$ of the ALMA 3 mm continuum data is listed in Table 4.2. The colors of the data points highlight the four evolutionary stages (red: IRDC, green: HMPO, blue: HMC, and purple: UCHII region). The Spearman correlation coefficient r_s and p -value, with $a(b)=a \times 10^b$, are shown in the bottom right corner.

probability that an uncorrelated data set would have with this Spearman correlation coefficient value. The Spearman correlation coefficient r_s and p -value are shown in Fig. 4.9 for each parameter pair.

The top row in Fig. 4.9 shows the dependence of the parameters as a function of distance d . With $|r_s| < 0.12$ for all parameters, T_{dust} , L/M , $I_{3\text{mm}}^{\text{region}}$, and $F_{3\text{mm}}^{\text{region}}$ are not correlated with distance d . This implies that our sample is not biased by distance such that more luminous regions would be at larger distances. However, there are clear evolutionary trends, highlighted in different colors, for T_{dust} , L/M , and $F_{3\text{mm}}^{\text{region}}$, with these values increasing with evolutionary stages (but independent of distance). For example, the dust temperature T_{dust} increases from ≈ 15 K (IRDCs), ≈ 20 K (HMPOs), ≈ 30 K (HMCs and UCHII regions). For the peak intensity $I_{3\text{mm}}^{\text{region}}$, this trend is seen from the IRDC to the HMC stages, and for the UCHII regions, the peak intensity $I_{3\text{mm}}^{\text{region}}$ decreases compared to the HMC stage. Since both UCHII regions have a cometary morphology with extended emission (Fig. 4.2), the decrease of $I_{3\text{mm}}^{\text{region}}$ compared to previous evolutionary stages can be explained by the expanding envelope driven by the central protostar (Fig. 1.1) resulting in a lower surface brightness.

For the remaining parameter pairs (excluding the distance d), we find positive correlations with $r_s \geq 0.56$ (all panels in the second and third row in Fig. 4.9). The values of T_{dust} , L/M , and $F_{3\text{mm}}^{\text{region}}$ increase with evolutionary stage.

The evolutionary trends of ≈ 5000 ATLASGAL clumps are investigated by Urquhart et al.

(2022) using a slightly different evolutionary scheme (quiescent, protostellar, YSO, HII region). The clumps were classified based on additional MIR and FIR data from GLIMPSE, MIPS GAL, and Hi-GAL. For example, quiescent clumps have no counterpart at wavelengths of 70 μm and below and YSOs have 70 μm , 24 μm and 4 – 8 μm counterparts, but show no cm emission. Based on the cumulative distribution of T_{dust} and L/M , Urquhart et al. (2022) also found that these parameters increase with evolutionary stage.

Despite the fact that our ALMA sample covers only 11 HMSFRs compared to, for example, the $\approx 10\,000$ clumps studied in the ATLASGAL survey, we still cover a broad range in clump properties as shown in Fig. 4.9. The four evolutionary stages form relatively distinct regions in these correlation plots, and in the next section we will investigate if and how the physical properties in HMSFRs correlate on core scales, such as the temperature and density profiles, and mass. Since a high degree of fragmentation is observed in our ALMA sample (Fig. 4.2 and Table C.3), it is expected that the evolutionary trends become less prominent due to multiple mm cores and/or UCHII regions, potentially at different evolutionary stages, present within a single HMSFR.

4.8.2 Evolutionary trends on core scales

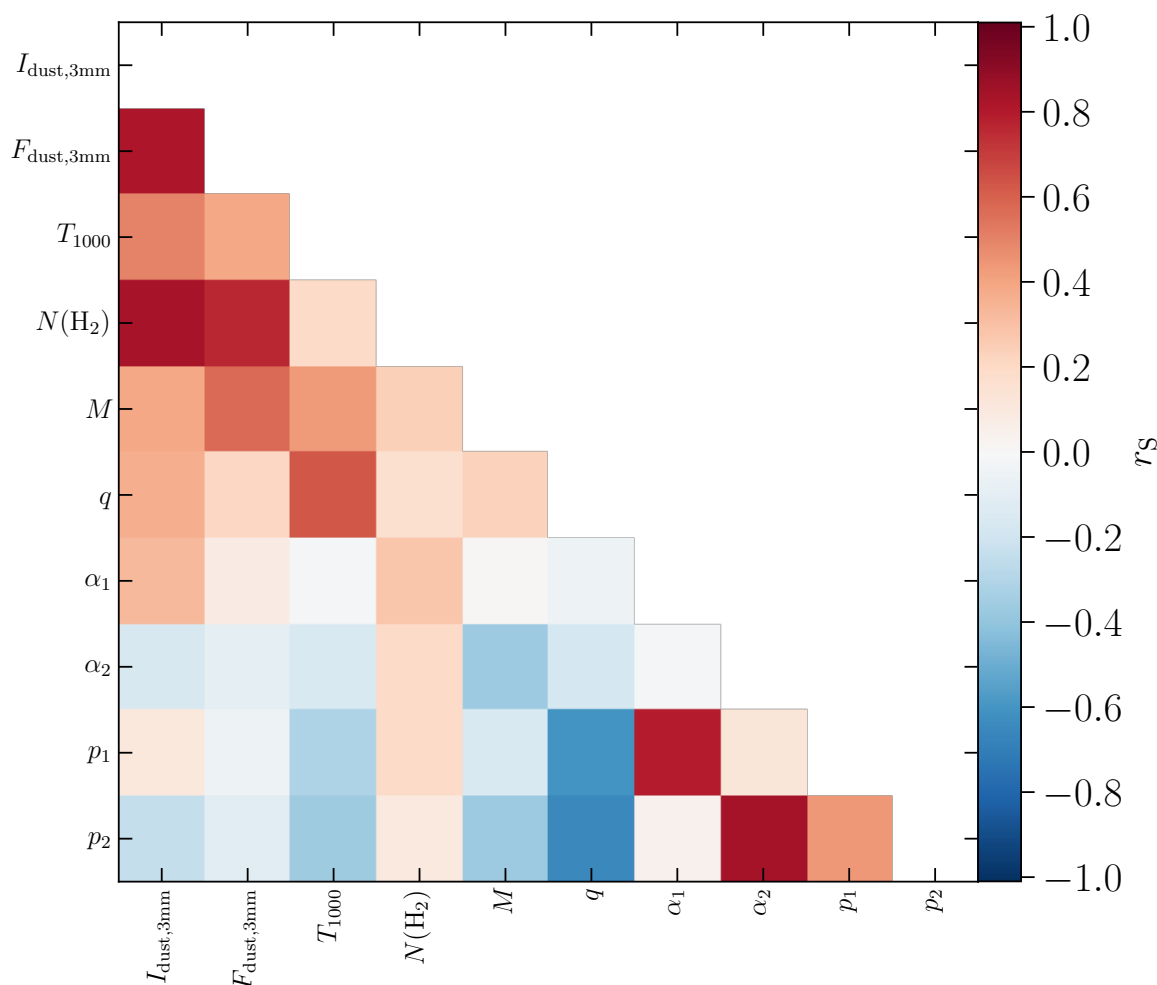


FIGURE 4.10: Correlations of the physical parameters of the ALMA, CORE, and CORE-extension samples.

In this section, we compare the physical parameters on core scales, i.e., the physical structure of the mm cores and (cometary) UCHII regions of the ALMA sample analyzed in this chapter and the mm cores of the CORE and CORE-extension sample (Chapters 2 and 3). We focus on the following physical properties that were derived in all three studies.

The 3 mm peak intensity $I_{\text{dust},3\text{mm}}$ and integrated flux density $F_{\text{dust},3\text{mm}}$ of the dust emission is estimated from the continuum data. For the ALMA sample, we use the free-free corrected 3 mm continuum data (Sect. 4.4.2). For the CORE and CORE-extension sample, we extrapolate the 1 mm peak intensity and flux density to 3 mm wavelengths assuming $I_\nu \sim \nu^2$ and $F_\nu \sim \nu^2$ (Eq. 1.43). The masses M and H_2 column density $N(\text{H}_2)$ are calculated according to Eq. 1.49 and 1.48, respectively.

In order to account for the fact that the regions are at various distances and were observed at different angular resolutions, we extrapolate the radial temperature profiles to a common radius of 1 000 au, $T_{1000} = T(r = 1\,000\text{ au})$. The radial temperature profiles are taken from the H_2CO , CH_3CN , and $\text{CH}_3^{13}\text{CN}$ temperature maps derived with XCLASS or the temperature map derived using the HCN-to-HNC intensity ratio (Hacar et al. 2020).

The observed temperature power-law index q is derived from the radial temperature profiles and the visibility power-law index α is calculated from the continuum visibility profiles. Since we find that most of the ALMA sources are best fitted by two power-law profiles, α_1 and α_2 , we assume $\alpha_1 = \alpha_2 = \alpha$ for the CORE and CORE-extension mm cores and check for correlations for both profiles separately. The indices α_1 and α_2 roughly correspond to the clump and core scales, respectively (Sect. 4.6).

The density profiles p_1 and p_2 are calculated according to Eq. (2.3) using α_1 and α_2 , respectively. We use for each source the observed temperature power-law index q . Therefore, we have two density power-law indices, p_1 and p_2 tracing the clump and core scales, respectively. For the mm cores in the CORE and CORE extension sample $p_1 = p_2$ holds.

In total, we derive in this thesis a complete set of these physical parameters for 52 protostellar sources: 22 mm cores in the CORE sample (Chapter 2); 5 mm cores in the CORE-extension sample (Chapter 3); and 15 mm cores, 8 UCHII regions and 2 cometary UCHII regions in the ALMA sample (this chapter). To investigate potential correlations between pairs of these parameters, we compute the Spearman correlation coefficient. Figure 4.10 summarizes the Spearman correlation coefficient r_S for all parameter pairs. In addition, in Fig. 4.11 the parameter pairs with $|r_S| > 0.5$ are shown. In the following, we focus on the discussion of these parameter pairs.

We find positive correlations of $I_{\text{dust},3\text{mm}}$ with $F_{\text{dust},3\text{mm}}$, T_{1000} , and $N(\text{H}_2)$. The integrated flux density $F_{\text{dust},3\text{mm}}$ is positively correlated with $N(\text{H}_2)$ and M . Evolutionary trends for these parameters are clearly seen from IRDCs to the UCHII regions. The peak intensity is lower for the cometary UCHII regions compared to the other sources. From UCHII regions to cometary UCHII regions, the dust peak intensity, dust flux density, temperature, and H_2 column density decrease significantly. This can be explained by the fact that the protostellar radiation disrupts the surrounding gas and dust envelope that is expanding. The surface brightness (corresponding to the intensity) is therefore decreasing as well and since the dust is slowly expelled into the more diffuse ISM, the flux density within our limited sensitivity decreases as well.

With the observed CH_3CN and $\text{CH}_3^{13}\text{CN}$ emission lines and our angular resolution, we can trace gas layers up to 200 – 250 K, however, higher J-transitions are required to further constrain the temperature profiles in higher density regions. In addition, the angular resolution and line sensitivity only allows for the radial temperature profiles to be only marginally resolved, typically only along 2 – 3 beams, that are difficult to fit. The increasing mass with evolutionary stage is a clear indicator that mass accretion continues from the young mm cores in IRDCs to the evolved UCHII region phase.

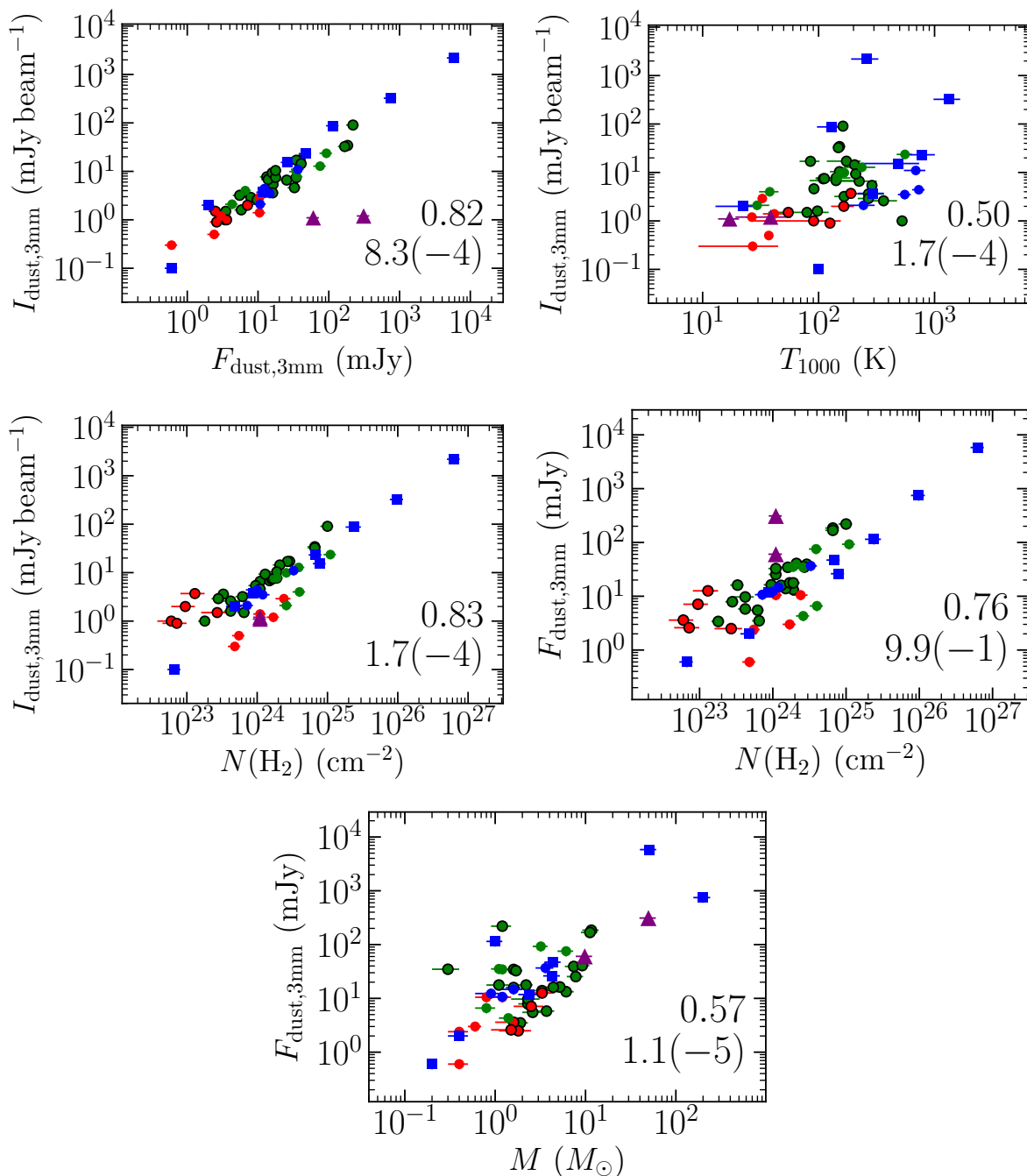


FIGURE 4.11: Correlations with $|r_S| > 0.5$ of the physical parameters of the ALMA, CORE, and CORE-extension sample. The color of the data points highlight the four evolutionary stages (red: IRDC, green: HMPO, blue: HMC, and purple: UCHII region). The data points of the mm cores of the CORE (green) and CORE-extension (red) sample are enclosed in black rings. The mm cores, UCHII and cometary UCHII regions are shown by circles, squares and triangles, respectively. The Spearman correlation coefficient r_S and p -value, with $a(b)=a \times 10^b$, are shown in each panel.

The positive correlation between the pair of α_1 and p_1 and of α_2 and p_2 is due to the fact that p is calculated considering α in Eq. (2.3). If the flat visibility slopes $\alpha_1 > -0.3$ are not considered since these are optically thick UCHII regions (Sect. 4.6), there is a clear trend such that the density profile on clump scales, p_1 , flattens from the IRDC ($p_1 \approx 2.2$) to (cometary) UCHII region phase ($p_1 \approx 1.2$). This can be explained by the fact that steep density profiles are expected for collapsing and accreting clumps, while feedback of the massive stars disrupts the

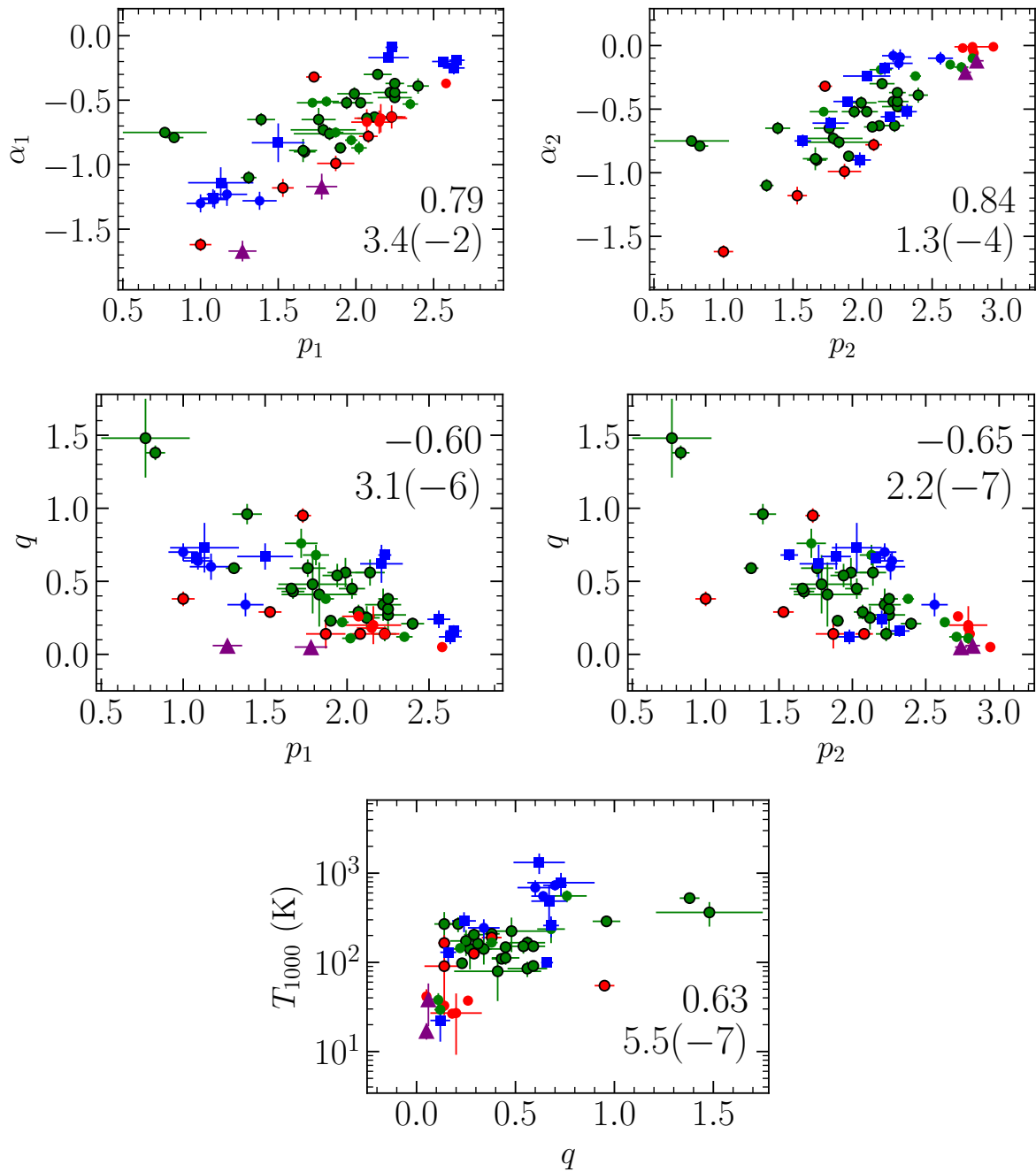


FIGURE 4.11 (cont.): Correlations with $|r_S| > 0.5$ of the physical parameters of the ALMA, CORE, and CORE-extension sample. The color of the data points highlight the four evolutionary stages (red: IRDC, green: HMPO, blue: HMC, and purple: UCHII region). The data points of the mm cores of the CORE (green) and CORE-extension (red) sample are enclosed in black rings. The mm cores, UCHII and cometary UCHII regions are shown by circles, squares and triangles, respectively. The Spearman correlation coefficient r_S and p -value, with $a(b)=a \times 10^b$, are shown in each panel.

surrounding envelope. This flattening of the density power-law index on clump scales has also been observed by Beuther et al. (2002a) where their “strong molecular sources” have $p \approx 1.9$ and their more evolved “cm sources” have $p \approx 1.5$. On the other hand, evolutionary trends of the density profile, p_2 , are not so clear. On core scales, most of the objects seem to be collapsing and accreting toward the gravitational center and thus toward $p_2 \approx 2$ a high density of mm cores of HMPOs and HMCs and UCHII regions is found. This is also the mean value found toward the 22 cores of the CORE sample (Fig. 2.5).

The observed temperature power-law index q is anti-correlated with the density power-law indices p_1 and p_2 . There is a clear evolutionary trend such that the temperature profiles steepens from the IRDC ($q \approx 0.1$) to the UCHII regions ($q \approx 0.7$), while for the cometary UCHII regions the profiles become flat. This suggests that an embedded source is steadily heating up the envelope. This is also confirmed by the fact that the slope q becomes steeper with T_{1000} increasing from 20 K up to 1 000 K. The cometary UCHII regions have a low value of T_{1000} (20 – 50 K). An increase of the temperature power-law index q has been observed toward several HMCs in the literature (Beltrán et al. 2018; Mottram et al. 2020). We also find in the analysis of the 22 mm cores of the CORE sample, that the distribution of q has a spread (Fig. 2.5). The four data points with $q > 0.9$ are most likely outliers due to unreliable fits. In the HMC models by Nomura & Millar (2004) and Osorio et al. (2009), in which the temperature profile is calculated self-consistently, the temperature profiles also steepen on core scales with $q > 0.4$.

An unexpected result of the density profiles is that for most of the sources in the ALMA sample, we find that the visibility profiles follow at least two power-law profiles (Sect. 4.6), while for the CORE and CORE-extension samples, a single power-law profile was sufficient. The traced spatial scales of NOEMA and ALMA are not too different (2 – 500 k λ and 10 – 600 k λ , respectively), but NOEMA has less long baselines resulting a higher noise at long baselines in the visibility profiles (Figs. 2.6 and 3.2) compared to ALMA (Fig. 4.8). To test if the two power-law slopes are an effect of observed wavelength (1 mm versus 3 mm), we aim to obtain additional 3 mm observations of the CORE sample (Sect. 5.2). The fact that the sources in the ALMA regions show two power-law slopes can be explained by the young mm cores in the IRDCs containing unresolved point sources. In an inside-out collapse picture, the mm cores grow in mass and size, and the density profile of the cores in the HMPOs aligns with the underlying clump density profile. In these cases, a single visibility power-law profile is observed, in our cases for the CORE sample (Fig. 2.6) and for core 1 in HMPO IRAS18089. In the HMC stage, the mm continuum becomes optically thick and therefore a break occurs in the visibility profile and in the UCHII region stage when the envelope is expanding, the complex spatial morphology (Fig. 4.2) is anyway difficult to explain by a simple power-law profile assuming spherical symmetry.

We find evolutionary trends on core scales, but there are clear overlaps in contrast to the larger scale clump properties discussed in Sect. 4.8.1. In our analysis of the physical properties, we assume that the envelopes are spherically symmetric, however, the presence of outflows and the observed inclination might also impact, for example, the temperature and density profiles. In addition, a single classification of the evolutionary stage of a HMSFRs based on the clump properties is not sufficient to describe the evolutionary stages on core scales. We therefore aim to use in a future study our physical-chemical modeling with MUSCLE to derive chemical timescales, τ_{chem} , in combination with MIR, FIR, and cm data in order to better characterize and classify individual protostellar sources in clustered HMSFRs.

4.9 Summary and conclusions

In this chapter we analyze ALMA 3 mm continuum and line observations of 11 high-mass star-forming regions at evolutionary stages from young infrared dark clouds to evolved ultra-compact HII regions. In addition, we make use of archival data at MIR, FIR, and cm wavelengths in order to characterize the environment of the regions. In particular, we make use of VLA 5 GHz observations to distinguish between dust and free-free emission in the ALMA 3 mm continuum data.

At an angular resolution of $\approx 1''$, we observe a high degree of fragmentation in the regions. We classify the fragments into protostellar sources and envelope clumps. The protostellar

sources are divided further into mm cores, UCHII regions (compact mm and additional H(40) α and cm emission) and cometary UCHII regions (extended mm and additional H(40) α and cm emission) for which we detect 27, 8, and 3 sources, respectively. Our findings are summarized as follows:

1. We create temperature maps using the HCN-to-HNC intensity ratio to trace the low-temperature regime and with XCLASS we model and fit CH₃CN and CH₃¹³CN line emission to trace the high-temperature regime. Radial temperature profiles with power-law index q are computed for all protostellar sources. We find that there is a spread in q between $\approx 0.1 - 0.8$.
2. The density profiles are estimated from the 3 mm continuum visibility profiles. In contrast to the CORE and CORE-extension regions (Chapters 2 and 3), most of the visibility profiles are best explained by two profiles with varying slope α_1 and α_2 instead of a single profile. The visibility slopes α_1 and α_2 approximately trace the clump and core scales, respectively. The estimated density power-law index p_1 and p_2 varies between 1 and 2.6 and 1.6 and 3, respectively.
3. Using the dust peak intensity $I_{\text{dust},3\text{mm}}$ and integrated flux density $F_{\text{dust},3\text{mm}}$ of the 3 mm dust emission, we estimate the mass and H₂ column density of the protostellar sources. We find a large spread in H₂ column density, $N(\text{H}_2) \approx 10^{23} - 10^{26} \text{ cm}^{-2}$ and mass, $M \approx 0.2 - 200 M_{\odot}$ within the protostellar sources.
4. Comparing the 3 mm peak intensity and region-integrated flux density ($I_{3\text{mm}}^{\text{region}}$ and $F_{3\text{mm}}^{\text{region}}$) with clump properties (T_{dust} , L/M) derived by the ATLASGAL survey (Urquhart et al. 2018), we find that there are clear evolutionary trends of T_{dust} , L/M , and $F_{3\text{mm}}^{\text{region}}$ increasing from IRDC to UCHII regions. The peak intensity $I_{3\text{mm}}^{\text{region}}$ is increasing from the IRDC to HMC stage and then significantly decreases in the UCHII regions. This can be explained by the fact that the expanding extended envelope has a low surface brightness compared to compact cores in the IRDC to HMC stages. Even though our sample consists of only 11 regions, we still cover a broad range in physical properties on clump scales.
5. We combined the physical structure derived in this study with the results of the CORE and CORE extension sample (Chapters 2 and 3, respectively) and analyzed a sample of a total of 52 protostellar sources for correlations and evolutionary trends. We find that the temperature at a characteristic radius of 1 000 au, T_{1000} , is increasing with evolutionary stage and at the same time, the temperature power-law index q steepens from $q \approx 0.1$ to $q \approx 0.7$ from the IRDC to UCHII regions. The cometary UCHII regions have a flat temperature profile and a low temperature in the extended envelope. The density profile p_1 on clump scales, flattens from $p_1 \approx 2.2$ in the IRDC stage to $p_1 \approx 1.2$ in UCHII regions, while for the density profile p_2 on core scales, we do not find clear evolutionary trends, but a mean of $p \approx 2$. These results provide invaluable observational constraints for physical models describing the formation of high-mass stars.

In this study, we focused on the characterization of the physical properties in this ALMA sample. In a next step, the properties of the molecular gas will be analyzed, further explained in Sect. 5.2. We also aim to combine the physical and chemical properties in our MUSCLE model in order to estimate chemical timescales τ_{chem} of the protostellar sources. With additional MIR, FIR, and cm data at high angular resolution, we aim to better characterize and classify the evolutionary stages on core scales, instead of clump scales, considering that multiple fragments are typically embedded within a single clump.

Chapter 5

Summary and outlook

5.1 Summary of this thesis

Even though how stars are born has been studied for many decades, we still have not fully understood all processes in star formation, in particular how massive stars form is still an active field of research in modern astronomy. It is challenging to capture the early stages of high-mass star formation in observations, since massive stars are less common compared to their low-mass counterparts, located at typical distances >1 kpc, and their evolution is fast ($\approx 10^5$ yr).

In the past, many surveys containing a large number of high-mass star-forming regions have been conducted using single-dish telescopes tracing the cloud (>1 pc) and clump (0.1 – 1 pc) structures, but most interferometric studies tracing the core scales (<0.1 pc) have been carried out only toward a single or a small number of regions. With the increasing sensitivity of modern interferometers (Table 1.1), sample studies containing a large number of regions are proceeding and allow us to better characterize high-mass star-forming regions at core scales. The evolutionary stages during the formation of high-mass stars can be classified into roughly four categories based on their observed properties (Fig. 1.1): infrared dark cloud (IRDC) – high-mass protostellar object (HMPO) – hot molecular core (HMC) – ultra-compact HII (UCHII) region. This thesis focuses on understanding the physical and chemical processes during the formation of high-mass stars on core scales.

I analyzed a sample of high-mass star-forming regions classified to be HMPOs that are part of the “CORE” project - a NOEMA large program targeting a total of 18 regions with sub-arcsecond resolution continuum and spectral line observations at 1.3 mm. The goals of the CORE project are to investigate the fragmentation (Beuther et al. 2018a; Suri et al. 2021), kinematic (Ahmadi et al. 2018; Bosco et al. 2019; Cesaroni et al. 2019; Mottram et al. 2020; Moscadelli et al. 2021), and basic chemical properties (Feng et al. 2016; Gieser et al. 2019, and Chapter 2) during the formation of high-mass stars. Within this thesis, I characterized in particular the physical and chemical properties of 22 fragmented mm cores in the CORE sample (Chapter 2).

The core spectra (Fig. A.3) reveal a large diversity in the molecular content and I used the radiative transfer code XCLASS (Möller et al. 2017, Sect. 1.5.2) to derive molecular column densities (Fig. 2.8, e.g., of SO, OCS, HC₃N, and CH₃OH). In addition, rotation temperature maps of the regions were created with the gas thermometers H₂CO and CH₃CN using XCLASS (Fig. A.1) to infer the radial temperature profile, $T \sim r^{-q}$ (Eq. 2.1), of the cores. By analyzing the continuum visibilities (Fig. 2.6), it is possible to then derive the radial density profile, $n \sim r^{-p}$ (Eq. 2.2). The observed properties (temperature and density profile, molecular content) were combined with the physical-chemical model MUSCLE (MULTI Stage CLOUD code, Sect. 1.3.3) to estimate a chemical timescale τ_{chem} for each core.

For the first time, the temperature and density structure was determined on core scales in

a sample of high-mass star-forming regions directly from observations, and the results in general agree with theoretical predictions of temperature and density power-law distributions with indices around 0.4 (Fig. 2.5) and 2.0 (Fig. 2.7), respectively. The precise knowledge of the physical structure provides an important constraint for simulations and chemical models. For both power-law slopes, there is a spread, but the number of mm cores was not sufficient to conclude if this spread is real or due to uncertainties. The chemical timescale of the cores derived with MUSCLE varies between 20 000 yr and 100 000 yr (Fig. 2.14). Thus, the variety in molecular abundances observed in the core spectra can be explained by an age spread of the cores. When multiple cores are detected in a region, age gradients are found suggesting subsequent star formation. Comparing the chemical timescale τ_{chem} with the free-fall timescale τ_{ff} , we find that it is consistent with an initial clump density of $10^5 - 10^6 \text{ cm}^{-3}$ that is a typical value found toward IRDCs (e.g., Carey et al. 1998).

The CORE sample was complemented by mosaic NOEMA observations of the young and cold star-forming regions ISOSS J22478+6357 and ISOSS J23053+5953 (“CORE-extension”), both classified to be in the IRDC stage. We first analyzed the fragmentation properties and kinematics in both regions (Beuther et al. 2021) and then characterized the physical and chemical properties (Chapter 3).

Even though both regions are line-poor (Figs. B.25 and B.26) compared to the regions of the more evolved CORE sample (Fig. A.3), the molecular emission reveals a complex morphology (Sect. 3.5.2). Molecules such as SO, SiO, H₂CO, and CH₃OH trace shocks in the environment of the cores and I could associate these shocks to protostellar outflows and to colliding gas flows. The mean chemical timescale of the cores in the two CORE-extension regions is lower ($\approx 20\,000$ yr) compared to the more evolved cores in the original CORE sample ($\approx 60\,000$ yr). Combining the results of Chapters 2 and 3, we find a correlation of the chemical timescale τ_{chem} and the L/M ratio, an independent age indicator (e.g., Sridharan et al. 2002; Molinari et al. 2008).

Comparing the NOEMA 1.3 mm CORE-extension observations with archival Spitzer MIR data (Fig. 3.3) and by fitting the spectral energy distribution of individual cores (Fig. 3.4), we find that more evolved MIR-bright low-mass YSOs surround mm-bright cores with no or only weak MIR emission. This suggests that first a population of low-mass stars forms and only at later times high-mass protostars are able to assemble, a scenario suggested, for example, by Kumar et al. (2020).

The initial chemical conditions in the physical-chemical model MUSCLE are based on the study by Gerner et al. (2014, 2015) targeting 59 high-mass star-forming regions covering all evolutionary stages from IRDCs to UCH_{II} regions. These studies were based on single-dish observations targeting the clump scales of each region. I therefore revisited a sub-sample of 11 regions with ALMA observations at 3 mm wavelengths and an angular resolution of $\approx 1''$ tracing the core scales. Our ALMA sample also covers all evolutionary stages from IRDCs to UCH_{II} regions allowing us to investigate evolutionary trends of the physical and chemical properties.

The 3 mm continuum emission shows a high degree of fragmentation including three extended cometary UCH_{II} regions. Archival cm observations with the VLA reveal that the 3 mm continuum emission of all HMC and UCH_{II} regions consists not only of dust, but also of free-free emission. This is in agreement with H(40) α emission being detected toward these locations. The fragmentation of the cores is quantified by applying the `clumpfind` algorithm (Williams et al. 1994). The fragments are classified into envelope clumps, that are not further analyzed, and (potential) protostellar sources. These protostellar sources are further classified into mm cores (with compact 3 mm emission), UCH_{II} regions (with compact 3 mm emission and bright cm sources), and cometary UCH_{II} regions (extended 3 mm emission and bright cm sources). The ALMA 3 mm continuum and spectral line data is used to infer the physical structure of

the protostellar sources, in particular the density and temperature profiles. The mass M and hydrogen column density $N(\text{H}_2)$ are derived using the (free-free corrected) 3 mm continuum data.

Since all regions in our ALMA sample are part of the ATLASGAL survey (Schuller et al. 2009), targeting the larger clump scales of the regions (Figs. C.1 – C.11), we compare the peak intensity $I_{3\text{mm}}^{\text{region}}$ and flux density $F_{3\text{mm}}^{\text{region}}$ of each region with properties derived from the ATLASGAL study by Urquhart et al. (2018), specifically T_{dust} and L/M . We find that $F_{3\text{mm}}^{\text{region}}$, T_{dust} , and L/M increases from IRDCs to UCHII regions, while for $I_{3\text{mm}}^{\text{region}}$ we find this trend only from IRDCs to HMCs. The peak intensity is significantly decreased for UCHII regions. This can be explained by the expanding envelope of the UCHII regions that results in a lower surface brightness.

Correlations and evolutionary trends of the physical properties of the protostellar sources of the ALMA sample were investigated in combination with the mm cores of the CORE and CORE-extension sample (Chapters 2 and 3). In total, we derived a complete set of physical properties for 52 sources, including 42 mm cores, 8 UCHII regions, and 2 cometary UCHII regions. We find that the temperature $T_{1000} = T(r = 1000 \text{ au})$ and mass M increases from the mm cores in the IRDCs to the UCHII regions and at the same time the temperature profile q steepens from $q \approx 0.1$ to $q \approx 0.7$. The slope of the density profiles on larger clump scales, p_1 , flattens from mm cores in the IRDCs to evolved UCHII regions from $p_1 \approx 2.4$ to $p_1 \approx 1.2$. Evolutionary trends of the density profile on smaller core scales, p_2 , are less clear, but the data points cluster around $p_2 \approx 2$. These evolutionary trends provide helpful observational constraints for physical models of high-mass star formation.

While in our first study targeting 22 mm cores in the CORE sample (Chapter 2) we were not able to study evolutionary trends, extending our sample (Chapters 3 and 4) allowed us to perform a more detailed statistical analysis of the physical properties. In the next section, follow-up projects targeting in particular the chemical properties on core scales are discussed that will allow us to further characterize high-mass star-forming regions.

5.2 Outlook

In this thesis I showed that with modern interferometers it is now possible to characterize individual fragmented cores in high-mass star-forming regions with sub-arcsecond resolution observations at (sub)mm wavelengths and to conduct a statistical analysis of the physical and chemical properties (Chapters 2, 3, and 4). In the coming years, I aim to investigate the following open questions:

- **How do the chemical properties - such as the molecular abundances and spatial morphology - evolve during high-mass star formation?**
- **What forms first in a cluster: high- or low-mass stars?**
- **Which molecular tracers can determine certain physical parameters best?**

The physical and chemical core properties can be best studied using interferometric observations at (sub)mm wavelengths (e.g., with ALMA, NOEMA, and the SMA), by applying the methods I developed in this thesis. The clustered nature of star-forming regions is probed by complementary archival Spitzer MIR and Herschel FIR data. Thus, a multi-wavelength picture of high-mass star formation can be constructed on core scales allowing a detailed investigation of, for example, the time evolution of the molecular abundances in a large statistical sample. In addition, the physical properties of cores, containing potential high-mass protostars, should

be compared to what is found toward low-mass protostars. In the following, some projects are mentioned that address the above mentioned topics and open questions.

“CORE+”: Deuterium and shock chemistry in high-mass star-forming regions

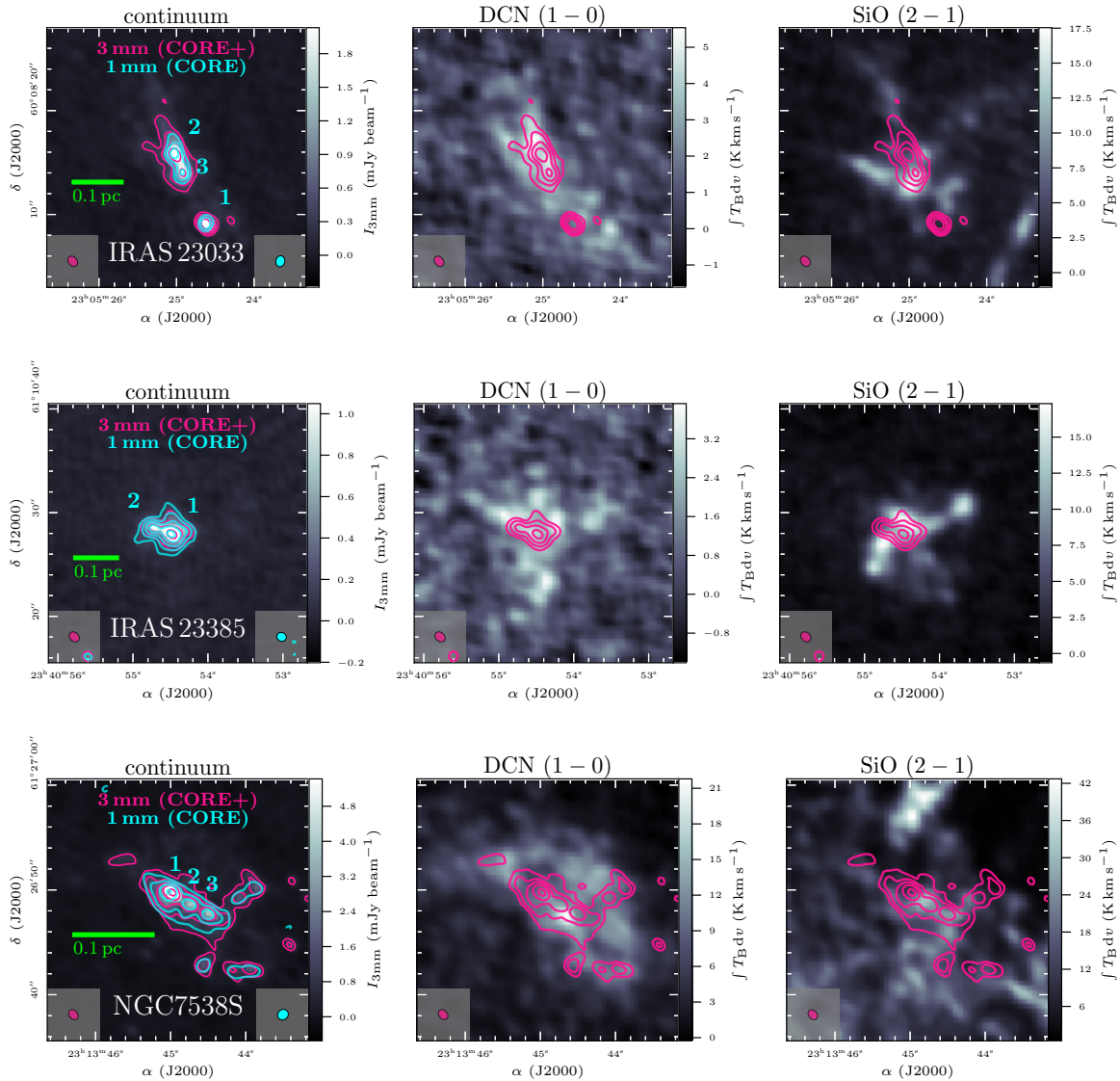


FIGURE 5.1: CORE+ continuum (*left panel*) and spectral line data products (*middle and right panels*, Gieser et al. in preparation). In the *left panel*, the NOEMA 3 mm continuum is presented in color. The *middle and right panels* show in color the integrated intensity maps of DCN (1 – 0) and SiO (2 – 1) line emission, respectively. The NOEMA 3 mm and 1 mm continuum data is shown in pink and cyan contours, respectively. The dotted contour marks the $-5\sigma_{\text{cont}}$ level and the solid black contours start at $5\sigma_{\text{cont}}$ and contour steps increase by a factor of 2 (e.g., 5, 10, 20, $40\sigma_{\text{cont}}$). The synthesized beam size of the 3 mm and 1 mm data is shown in the bottom left and bottom right corner, respectively. The green bar indicates a linear spatial scale of 0.1 pc. The analyzed mm cores, in Chapter 2 for IRAS 23033 and IRAS 23385 and in Feng et al. (2016) for the CORE pilot region NGC 7538S, are labeled in cyan.

The spectral line data of the CORE 1 mm observations allowed us to study the dense gas in the regions (Chapter 2); however, the 4 GHz bandpass of the old WideX correlator did not cover emission lines of many basic molecules (Table A.2). In order to conduct a more detailed

chemical survey, with emphasis on the deuteration level and the impact of shocks, I am leading the NOEMA + IRAM 30m telescope observing program at 3 mm wavelengths “CORE+: Deuterium and shock chemistry during high-mass star formation” (PI: Caroline Gieser, project codes W20AV and 190-20) using the new PolyFiX correlator providing a bandwidth of 16 GHz. Additional topics that will be investigated include the chemical segregation between C-, O-, N- and S-bearing species (e.g., seen toward the AFGL 2591 hot core, Gieser et al. 2019), the ionization level using HCO^+ and N_2H^+ isotopologues, and molecular outflows can be characterized with SiO. Furthermore, the 1 mm and 3 mm NOEMA continuum data allow us to study the dust spectral index.

Some cores are line-poor in the 1 mm spectra and, since in MUSCLE the chemical timescales are constrained by the observed molecular column densities, it was in some cases difficult to estimate a chemical timescale (Sects. 2.5 and 3.6). Therefore, a larger number of observed molecules yield an invaluable additional constraint in the chemical model.

During the winter semester 2020/2021, we obtained CORE+ observations of two regions of the original CORE sample (IRAS 23033 and IRAS 23385, Table 2.1) and the CORE pilot region NGC 7538S (Feng et al. 2016). Self-calibrated CORE+ data of the IRAS 23033, IRAS 23385, and NGC 7538S regions are presented in Fig. 5.1. While the angular resolution at 3 mm is slightly poorer than at 1 mm, both data sets are still comparable when imaged with robust and natural weighting, respectively. The deuteration level shows local inhomogeneities among the cores and outflows can be identified with the shock-tracing molecule SiO. Interestingly, with our physical-chemical modeling we find that core 1 in IRAS 23033 is older ($\tau_{\text{chem}} > 34\,000$ yr) than cores 2 and 3 ($\tau_{\text{chem}} \approx 20\,000$ yr) with an age gradient along the filament (Table 2.3). Toward cores 2 and 3, the deuteration, as observed in the DCN $1-0$ line, is higher, while for the more evolved core 1, DCN emission is more confined to the surrounding envelope of the core.

The CORE+ observations at 3 mm provide an important piece to the creation of a multi-wavelength picture of all CORE regions. All regions are now observed with the SMA at 345 GHz as well (PI: Henrik Beuther). While the primary goal of the SMA observations is to characterize the magnetic field morphology using dust polarization measurements, the spectral line data of the SMA observations obtained with a broad bandwidth of 32 GHz give unprecedented further insight into the molecular content toward the CORE regions.

Unveiling the physical properties during high-mass star formation with ALMA from infrared dark clouds to ultra-compact HII regions: proceeding projects

The CORE survey focused only on a comparatively narrow range of evolutionary stages, where most of the regions are classified to be HMPOs. Therefore, we extended our sample with regions at different evolutionary phases ranging from IRDCs up to UCHII regions (Chapter 4). The initial chemical conditions in our physical-chemical model MUSCLE were taken from a detailed chemical study by Gerner et al. (2014, 2015) consisting of a sample of 59 high-mass star-forming regions. These studies were based on single-dish observations at low angular resolution with typical beam sizes $>10''$ that do not resolve individual cores. Multiple cores at different evolutionary stages can be present within one beam (Fig. 4.2), thus, the spectra analyzed in Gerner et al. (2014, 2015) only provided a rough region-average.

We therefore selected a sub-sample of 11 regions of the original sample studied by Gerner et al. (2014, 2015) and successfully obtained 3 mm observations with ALMA at an angular resolution of $\approx 1''$. In a first study, we analyzed the physical properties on core scales with a focus on the analysis of the continuum data and a few spectral lines (Chapter 4). However, with a total of 39 spectral windows that provide a total bandwidth of ≈ 10 GHz with hundreds of

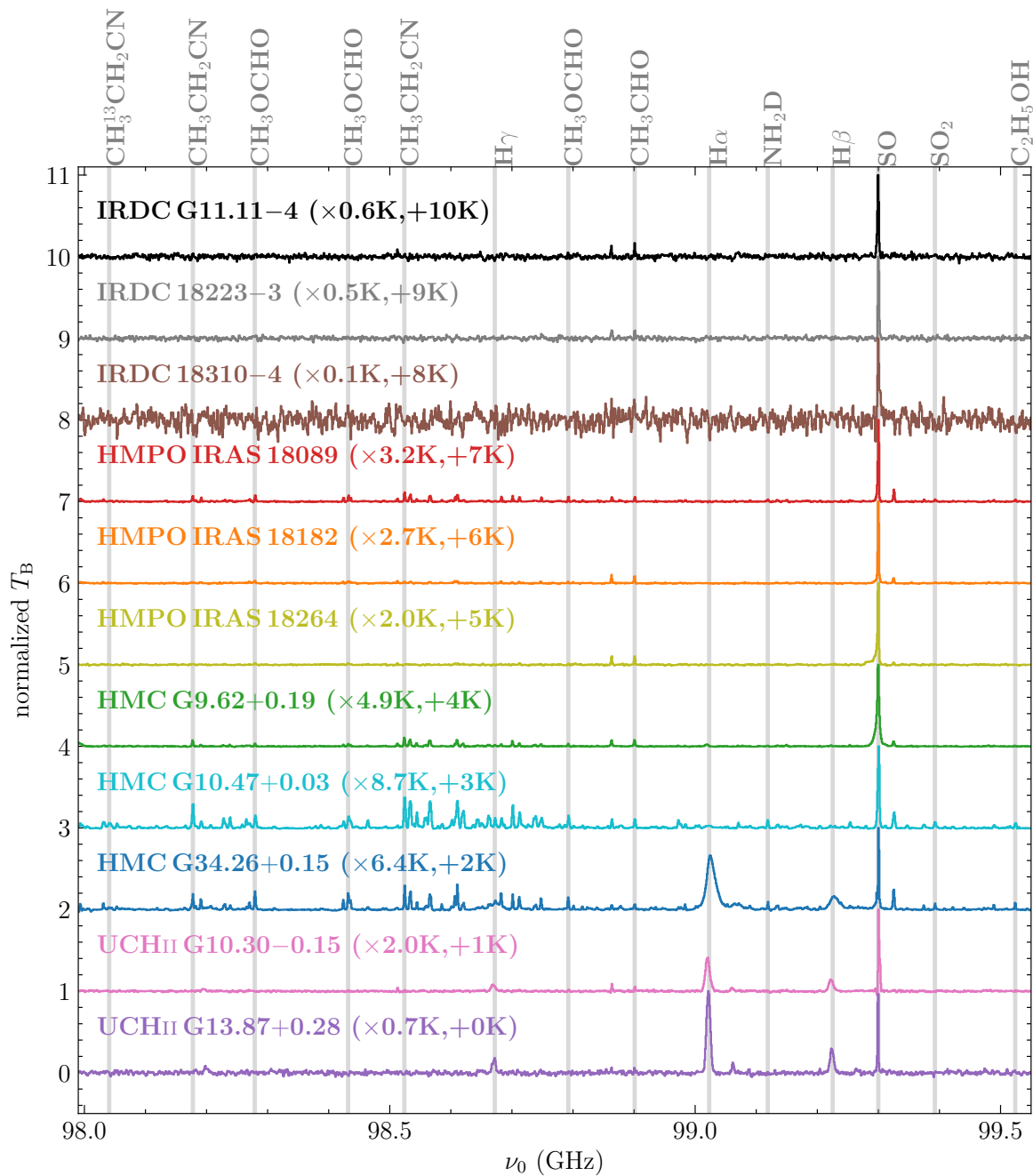


FIGURE 5.2: ALMA 3 mm mean spectra (SPR2 6, Table C.2) of the central $10'' \times 10''$ in each region (Gieser et al. in preparation). The spectra are normalized to the peak intensity in each spectrum. Some lines are labeled and highlighted by grey vertical lines.

emission lines detected toward the HMCs (Table C.2), it is possible to conduct a comprehensive chemical analysis of the molecular gas. The detected molecules range from simple species (e.g., CO isotopologues, H^{13}CO^+ , H^{13}CN , N_2H^+ , SiO, SO, SO_2 , OCS, HNC, $c\text{-C}_3\text{H}_2$) to a variety of complex organic molecules (COMs, e.g., CH_3CN , CH_3OH , $\text{CH}_3\text{CH}_2\text{CN}$, CH_3COCH_3). A mean spectrum computed in the central $10'' \times 10''$ in one of the low-resolution spectral windows (SPR2 6, Table C.2) are presented in Fig. 5.2 for each region. Clearly, the amount of detected emission lines increases from IRDC to HMC regions and then decreases again for the UCH II regions.

This data set, consisting of sensitive continuum and spectral line data, enables us to expand

our comprehensive study of high-mass star formation over all important evolutionary stages with a significantly increased coverage of molecular species. In addition, it allows us to improve the initial chemical conditions of our model that are currently based on single-dish observations at low angular resolution (Gerner et al. 2014, 2015). In a first study presented in Chapter 4 an overview of the ALMA observations and analysis of the physical structure (temperature and density profiles) is presented and including a comparison with the results of the CORE and CORE-extension regions (Chapters 2 and 3). In the forthcoming years, a series of studies will be carried out that uses the rich molecular line data to investigate the following chemical processes:

- Molecular column densities of N-/O-/S-bearing species and COMs are derived with the line fitting tool XCLASS (Möller et al. 2017). This allows us to study, for example, isotopologue ratios (e.g., OCS and O¹³CS) and isomer ratios (e.g., HCN and HNC) and their local spatial variations.
- The radiation field in the regions can be probed by H¹³CO⁺, N₂H⁺, and c-C₃H₂.
- Shocks and outflows are studied by investigating the line wings of SiO and CO emission profiles.
- The histogram of oriented gradients method (Soler et al. 2019) allows us to study the spatial morphology of the molecular emission and to find velocity-resolved correlations among different species, as tested in Chapter 3 for the CORE-extension regions, to further understand the formation of molecules in the interstellar medium.
- Chemical timescales of fragmented cores are estimated with MUSCLE to investigate, for example, if we find more regions with subsequent star formation (Chapters 2 and 3).

Star formation processes traced by the James Webb Space Telescope

On the 25th of December 2021, all astronomers received a big and expensive Christmas present with the launch of the James Webb Space Telescope (JWST, Gardner et al. 2006) operating at NIR and MIR wavelengths. The telescope mirror consisting of 18 hexagonal mirror segments has a diameter of 6.5 m. By now (April 2022), JWST has reached the orbit around the Lagrange point L_2 of the Earth and Sun and its instruments are currently being commissioned. Figure 5.3 shows an image of the alignment of the mirror segments with the Near Infrared Camera (NIRCam, Rieke et al. 2005). While the bright source in the center is the star 2MASS J17554042+6551277, in the background faint distant galaxies are revealed.

With JWST, many topics in astrophysics can be investigated, for example, cosmology, exoplanets and their atmospheres, but also star and planet formation. The Mid InfraRed Instrument (MIRI, Rieke et al. 2015) includes a spectrograph operating from 5 μm to 28 μm at an angular resolution of 0.''2 – 1''. The guaranteed time program “MIRI EC Protostars Survey”¹ (PI: Ewine van Dishoeck) targets both low- and high-mass protostars with MIRI. The scientific goals are to study, for example, jets and outflows, disks, accretion rates, and the chemical composition in the ices and in the gas-phase. Molecules such as H₂, H₂O, and CO₂, as well as atomic lines such as NeII, FeII, and SiI can be studied in the MIR. Two high-mass protostars of this JWST project, namely IRAS 23385 and HMPO IRAS 18089 were studied in this thesis (Chapter 2 and 4, respectively) and thus a comparison of the interferometric mm observations with the upcoming JWST MIR data will be possible at a similar angular resolution.

In this thesis, I characterized the physical and chemical properties of a sample of high-mass star-forming regions focusing on interferometric observations at mm wavelengths. However,

¹Official project name to be decided.



FIGURE 5.3: Mirror alignment of JWST with the NIRC*am* instrument (image credit: NASA/STScI). The bright star in the center is 2MASS J17554042+6551277.

some processes discussed in this section still need to be investigated with follow-up projects, in particular the chemical properties of the molecular gas and why there is such a large diversity. The future of detailed high angular resolution studies of high-mass star formation is bright, not only at mm wavelengths, but also in the MIR with upcoming JWST observations.

Bibliography

- Adams, F. C. 1991, *ApJ*, 382, 544
- Adams, W. S. 1941, *ApJ*, 93, 11
- Ahmadi, A., Beuther, H., Mottram, J. C., et al. 2018, *A&A*, 618, A46
- Ahmadi, A., Kuiper, R., & Beuther, H. 2019, *A&A*, 632, A50
- Alakoz, A. V., Kalenskii, S. V., Promislov, V. G., Johansson, L. E. B., & Winnberg, A. 2002, *Astronomy Reports*, 46, 551
- Albertsson, T., Semenov, D. A., Vasyunin, A. I., Henning, T., & Herbst, E. 2013, *ApJS*, 207, 27
- Allamandola, L. J., Tielens, A. G. G. M., & Barker, J. R. 1985, *ApJL*, 290, L25
- Allamandola, L. J., Tielens, A. G. G. M., & Barker, J. R. 1989, *ApJS*, 71, 733
- ALMA Partnership, Brogan, C. L., Pérez, L. M., et al. 2015, *ApJL*, 808, L3
- André, P., Di Francesco, J., Ward-Thompson, D., et al. 2014, in *Protostars and Planets VI*, ed. H. Beuther, R. S. Klessen, C. P. Dullemond, & T. Henning, 27
- Andrews, S. M., Huang, J., Pérez, L. M., et al. 2018, *ApJL*, 869, L41
- Arce, H. G., Shepherd, D., Gueth, F., et al. 2007, in *Protostars and Planets V*, ed. B. Reipurth, D. Jewitt, & K. Keil, 245
- Avenhaus, H., Quanz, S. P., Garufi, A., et al. 2018, *ApJ*, 863, 44
- Ballesteros-Paredes, J., Klessen, R. S., Mac Low, M. M., & Vazquez-Semadeni, E. 2007, in *Protostars and Planets V*, ed. B. Reipurth, D. Jewitt, & K. Keil, 63
- Batschelet, E. 1972, *Recent Statistical Methods for Orientation Data*, Vol. 262, 61
- Beichman, C. A., Neugebauer, G., Habing, H. J., Clegg, P. E., & Chester, T. J. 1988, *Infrared Astronomical Satellite (IRAS) Catalogs and Atlases. Volume 1: Explanatory Supplement.*, Vol. 1
- Belloche, A., Maury, A. J., Maret, S., et al. 2020, *A&A*, 635, A198
- Belloche, A., Müller, H. S. P., Menten, K. M., Schilke, P., & Comito, C. 2013, *A&A*, 559, A47
- Beltrán, M. 2020, *arXiv e-prints*, arXiv:2005.06912
- Beltrán, M. T., Cesaroni, R., Rivilla, V. M., et al. 2018, *A&A*, 615, A141
- Beltrán, M. T. & de Wit, W. J. 2016, *A&AR*, 24, 6
- Benedettini, M., Viti, S., Codella, C., et al. 2013, *MNRAS*, 436, 179
- Benjamin, R. A., Churchwell, E., Babler, B. L., et al. 2003, *PASP*, 115, 953
- Bergeron, H., Rougeau, N., Sidis, V., et al. 2008, *Journal of Physical Chemistry A*, 112, 11921
- Bergner, J. B., Öberg, K. I., Garrod, R. T., & Graninger, D. M. 2017, *ApJ*, 841, 120
- Bertin, M., Romanzin, C., Doronin, M., et al. 2016, *ApJL*, 817, L12
- Beuther, H., Churchwell, E. B., McKee, C. F., & Tan, J. C. 2007a, *Protostars and Planets V*, 165
- Beuther, H., Gieser, C., Suri, S., et al. 2021, *A&A*, 649, A113
- Beuther, H., Henning, T., Linz, H., et al. 2015a, *A&A*, 581, A119
- Beuther, H., Henning, T., Linz, H., et al. 2010, *A&A*, 518, L78
- Beuther, H., Hunter, T. R., Zhang, Q., et al. 2004, *ApJL*, 616, L23
- Beuther, H., Leurini, S., Schilke, P., et al. 2007b, *A&A*, 466, 1065
- Beuther, H., Linz, H., Henning, T., et al. 2011, *A&A*, 531, A26
- Beuther, H., Linz, H., Tackenberg, J., et al. 2013, *A&A*, 553, A115
- Beuther, H., Mottram, J. C., Ahmadi, A., et al. 2018a, *A&A*, 617, A100
- Beuther, H., Ragan, S. E., Johnston, K., et al. 2015b, *A&A*, 584, A67

- Beuther, H., Schilke, P., Menten, K. M., et al. 2002a, *ApJ*, 566, 945
- Beuther, H., Schilke, P., Menten, K. M., et al. 2005a, *ApJ*, 633, 535
- Beuther, H., Schilke, P., Sridharan, T. K., et al. 2002b, *A&A*, 383, 892
- Beuther, H., Soler, J. D., Vlemmings, W., et al. 2018b, *A&A*, 614, A64
- Beuther, H., Sridharan, T. K., & Saito, M. 2005b, *ApJL*, 634, L185
- Beuther, H. & Steinacker, J. 2007, *ApJL*, 656, L85
- Beuther, H., Walsh, A., Schilke, P., et al. 2002c, *A&A*, 390, 289
- Beuther, H., Zhang, Q., Sridharan, T. K., & Chen, Y. 2005c, *ApJ*, 628, 800
- Beuther, H., Zhang, Q., Sridharan, T. K., Lee, C. F., & Zapata, L. A. 2006, *A&A*, 454, 221
- Bieniek, R. J. & Dalgarno, A. 1979, *ApJ*, 228, 635
- Bihl, S., Beuther, H., Linz, H., et al. 2015, *A&A*, 579, A51
- Birkmann, S. M., Krause, O., Hennemann, M., et al. 2007, *A&A*, 474, 883
- Bizzocchi, L., Tamassia, F., Laas, J., et al. 2017, *ApJS*, 233, 11
- Bolatto, A. D., Wolfire, M., & Leroy, A. K. 2013, *ARA&A*, 51, 207
- Bonne, L., Bontemps, S., Schneider, N., et al. 2020, *A&A*, 644, A27
- Bonnell, I. A. 2007, in *Astronomical Society of the Pacific Conference Series*, Vol. 367, *Massive Stars in Interactive Binaries*, ed. N. St.-Louis & A. F. J. Moffat, 303
- Bonnell, I. A. & Bate, M. R. 2002, *MNRAS*, 336, 659
- Bonnell, I. A., Bate, M. R., Clarke, C. J., & Pringle, J. E. 2001, *MNRAS*, 323, 785
- Bonnell, I. A., Bate, M. R., & Zinnecker, H. 1998, *MNRAS*, 298, 93
- Bosco, F., Beuther, H., Ahmadi, A., et al. 2019, *A&A*, 629, A10
- Briggs, D. S. 1995, PhD thesis, New Mexico Institute of Mining and Technology
- Bronfman, L., Nyman, L. A., & May, J. 1996, *A&AS*, 115, 81
- Burge, C. A., Van Loo, S., Falle, S. A. E. G., & Hartquist, T. W. 2016, *A&A*, 596, A28
- Butler, M. J. & Tan, J. C. 2012, *ApJ*, 754, 5
- Carey, S. J., Clark, F. O., Egan, M. P., et al. 1998, *ApJ*, 508, 721
- Carey, S. J., Noriega-Crespo, A., Mizuno, D. R., et al. 2009, *PASP*, 121, 76
- Carruthers, G. R. 1970, *ApJL*, 161, L81
- Carter, M., Lazareff, B., Maier, D., et al. 2012, *A&A*, 538, A89
- Caselli, P., Walmsley, C. M., Zucconi, A., et al. 2002, *ApJ*, 565, 344
- Cesaroni, R., Beuther, H., Ahmadi, A., et al. 2019, *A&A*, 627, A68
- Cesaroni, R., Churchwell, E., Hofner, P., Walmsley, C. M., & Kurtz, S. 1994, *A&A*, 288, 903
- Cesaroni, R., Felli, M., Testi, L., Walmsley, C. M., & Olmi, L. 1997, *A&A*, 325, 725
- Cesaroni, R., Hofner, P., Araya, E., & Kurtz, S. 2010, *A&A*, 509, A50
- Cesaroni, R., Sánchez-Monge, Á., Beltrán, M. T., et al. 2017, *A&A*, 602, A59
- Charnley, S. B., Tielens, A. G. G. M., & Millar, T. J. 1992, *ApJL*, 399, L71
- Chen, X., Ellingsen, S. P., Shen, Z.-Q., Titmarsh, A., & Gan, C.-G. 2011, *ApJS*, 196, 9
- Chen, Y., Li, H., & Vogelsberger, M. 2021, *MNRAS*, 502, 6157
- Cheung, A. C., Rank, D. M., Townes, C. H., Thornton, D. D., & Welch, W. J. 1968, *PRL*, 21, 1701
- Cheung, A. C., Rank, D. M., Townes, C. H., Thornton, D. D., & Welch, W. J. 1969, *Nature*, 221, 626
- Churchwell, E. 2002, *ARA&A*, 40, 27
- Clark, B. G. 1980, *A&A*, 89, 377
- Cohen, J. 1988, *Statistical Power Analysis for the Behavioral Sciences* (Lawrence Erlbaum Associates)
- Comoretto, G., Palagi, F., Cesaroni, R., et al. 1990, *A&AS*, 84, 179
- Condon, J. J. & Ransom, S. M. 2016, *Essential Radio Astronomy*
- Crowther, P. A., Caballero-Nieves, S. M., Bostroem, K. A., et al. 2016, *MNRAS*, 458, 624

- Cruz-Díaz, G. A., Martín-Doménech, R., Muñoz Caro, G. M., & Chen, Y.-J. 2016, *A&A*, 592, A68
- Csengeri, T., Belloche, A., Bontemps, S., et al. 2019, *A&A*, 632, A57
- Csengeri, T., Bontemps, S., Schneider, N., et al. 2011, *ApJL*, 740, L5
- Cuppen, H. M., Walsh, C., Lamberts, T., et al. 2017, *Space Sci. Rev.*, 212, 1
- Cyganowski, C. J., Whitney, B. A., Holden, E., et al. 2008, *AJ*, 136, 2391
- Dame, T. M., Hartmann, D., & Thaddeus, P. 2001, *ApJ*, 547, 792
- de Bernardis, P., Ade, P. A. R., Bock, J. J., et al. 2000, *Nature*, 404, 955
- Deharveng, L., Zavagno, A., Samal, M. R., et al. 2015, *A&A*, 582, A1
- Dewangan, L. K., Ojha, D. K., Zinchenko, I., & Baug, T. 2018, *ApJ*, 861, 19
- Di Francesco, J., Johnstone, D., Kirk, H., MacKenzie, T., & Ledwosinska, E. 2008, *ApJS*, 175, 277
- Douglas, A. E. & Herzberg, G. 1941, *ApJ*, 94, 381
- Downes, D. 1989, in *Evolution of Galaxies: Astronomical Observations*, ed. I. Appenzeller, H. J. Habing, & P. Lena, Vol. 333, 351
- Draine, B. T. 2011, *Physics of the Interstellar and Intergalactic Medium* (Princeton: Princeton University Press)
- Duarte-Cabral, A., Bontemps, S., Motte, F., et al. 2013, *A&A*, 558, A125
- Dullemond, C. P. & Dominik, C. 2005, *A&A*, 434, 971
- Durand, D. & Greenwood, J. A. 1958, *The Journal of Geology*, 66, 229
- Ellsworth-Bowers, T. P., Rosolowsky, E., Glenn, J., et al. 2015, *ApJ*, 799, 29
- Elmegreen, B. G. 2000, *ApJ*, 530, 277
- Emerson, J. P. 1988, in *NATO Advanced Science Institutes (ASI) Series C*, Vol. 241, NATO Advanced Science Institutes (ASI) Series C, ed. A. K. Dupree & M. T. V. T. Lago, 21
- Emprechtinger, M., Caselli, P., Volgenau, N. H., Stutzki, J., & Wiedner, M. C. 2009, *A&A*, 493, 89
- Endres, C. P., Schlemmer, S., Schilke, P., Stutzki, J., & Müller, H. S. P. 2016, *Journal of Molecular Spectroscopy*, 327, 95
- Engelbracht, C. W., Blaylock, M., Su, K. Y. L., et al. 2007, *PASP*, 119, 994
- Fallscheer, C., Beuther, H., Zhang, Q., Keto, E., & Sridharan, T. K. 2009, *A&A*, 504, 127
- Fazio, G. G., Hora, J. L., Allen, L. E., et al. 2004, *ApJS*, 154, 10
- Feng, S., Beuther, H., Semenov, D., et al. 2016, *A&A*, 593, A46
- Feng, S., Li, D., Caselli, P., et al. 2020, *ApJ*, 901, 145
- Ferrarotti, A. S. & Gail, H. P. 2006, *A&A*, 447, 553
- Fontani, F., Palau, A., Busquet, G., et al. 2012, *MNRAS*, 423, 1691
- Foreman-Mackey, D., Hogg, D. W., Lang, D., & Goodman, J. 2013, *PASP*, 125, 306
- Frank, A., Ray, T. P., Cabrit, S., et al. 2014, in *Protostars and Planets VI*, ed. H. Beuther, R. S. Klessen, C. P. Dullemond, & T. Henning, 451
- Garay, G. & Lizano, S. 1999, *PASP*, 111, 1049
- Garay, G., Lizano, S., & Gomez, Y. 1994, *ApJ*, 429, 268
- Gardner, J. P., Mather, J. C., Clampin, M., et al. 2006, *SSR*, 123, 485
- Garrod, R. T. & Herbst, E. 2006, *A&A*, 457, 927
- Garrod, R. T., Widicus Weaver, S. L., & Herbst, E. 2008, *ApJ*, 682, 283
- Gatto, A., Walch, S., Naab, T., et al. 2017, *MNRAS*, 466, 1903
- Gerin, M. 2013, *The Molecular Universe*, ed. I. W. M. Smith, C. S. Cockell, & S. Leach (Berlin, Heidelberg: Springer Berlin Heidelberg), 35–72
- Gerner, T., Beuther, H., Semenov, D., et al. 2014, *A&A*, 563, A97
- Gerner, T., Shirley, Y. L., Beuther, H., et al. 2015, *A&A*, 579, A80
- Giannetti, A., Brand, J., Sánchez-Monge, Á., et al. 2013, *A&A*, 556, A16

- Giannetti, A., Leurini, S., Wyrowski, F., et al. 2017, *A&A*, 603, A33
- Giannetti, A., Wyrowski, F., Brand, J., et al. 2014, *A&A*, 570, A65
- Gieser, C., Beuther, H., Semenov, D., et al. 2021, *A&A*, 648, A66
- Gieser, C., Beuther, H., Semenov, D., et al. 2022, *A&A*, 657, A3
- Gieser, C., Semenov, D., Beuther, H., et al. 2019, *A&A*, 631, A142
- Girichidis, P., Federrath, C., Banerjee, R., & Klessen, R. S. 2011, *MNRAS*, 413, 2741
- Girichidis, P., Walch, S., Naab, T., et al. 2016, *MNRAS*, 456, 3432
- Goedhart, S., Langa, M. C., Gaylard, M. J., & Van Der Walt, D. J. 2009, *MNRAS*, 398, 995
- Goicoechea, J. R., Aguado, A., Cuadrado, S., et al. 2021, *A&A*, 647, A10
- Gómez, G. C., Vázquez-Semadeni, E., & Palau, A. 2021, *MNRAS*, 502, 4963
- Gorai, P., Bhat, B., Sil, M., et al. 2020, *ApJ*, 895, 86
- Gratier, P., Pety, J., Guzmán, V., et al. 2013, *A&A*, 557, A101
- Guelin, M. & Cernicharo, J. 2022, arXiv e-prints, arXiv:2201.06106
- Guzmán, A. E., Guzmán, V. V., Garay, G., Bronfman, L., & Hechenleitner, F. 2018, *ApJS*, 236, 45
- Guzmán, V. V., Pety, J., Gratier, P., et al. 2014, *Faraday Discussions*, 168, 103
- Gwinn, W. D., Turner, B. E., Goss, W. M., & Blackman, G. L. 1973, *ApJ*, 179, 789
- Hacar, A., Bosman, A. D., & van Dishoeck, E. F. 2020, *A&A*, 635, A4
- Hacar, A., Clark, S., Heitsch, F., et al. 2022, arXiv e-prints, arXiv:2203.09562
- Hajigholi, M., Persson, C. M., Wirström, E. S., et al. 2016, *A&A*, 585, A158
- Harju, J., Walmsley, C. M., & Wouterloot, J. G. A. 1993, *A&AS*, 98, 51
- Hartmann, L., Ballesteros-Paredes, J., & Heitsch, F. 2012, *MNRAS*, 420, 1457
- Hasegawa, T. I., Herbst, E., & Leung, C. M. 1992, *ApJS*, 82, 167
- Hatchell, J., Thompson, M. A., Millar, T. J., & MacDonald, G. H. 1998, *A&As*, 133, 29
- Hatchell, J. & van der Tak, F. F. S. 2003, *A&A*, 409, 589
- Heger, A., Fryer, C. L., Woosley, S. E., Langer, N., & Hartmann, D. H. 2003, *ApJ*, 591, 288
- Hennemann, M., Birkmann, S. M., Krause, O., & Lemke, D. 2008, *A&A*, 485, 753
- Henning, T., Linz, H., Krause, O., et al. 2010, *A&A*, 518, L95
- Henning, T., Schreyer, K., Launhardt, R., & Burkert, A. 2000, *A&A*, 353, 211
- Herbst, E. 1978, *ApJ*, 222, 508
- Herbst, E. & van Dishoeck, E. F. 2009, *ARA&A*, 47, 427
- Herrera, F., Lozano, M., & Verdegay, J. L. 1998, *Artificial intelligence review*, 12, 265
- Herrera, J., Huedo, E., Montero, R. S., & Llorente, I. M. 2005, in *European Grid Conference*, Springer, 315–322
- Herzberg, G. 1942, *Reviews of Modern Physics*, 14, 219
- Heywood, I., Rammala, I., Camilo, F., et al. 2022, *ApJ*, 925, 165
- Hildebrand, R. H. 1983, *QJRAS*, 24, 267
- Hoare, M. G., Purcell, C. R., Churchwell, E. B., et al. 2012, *PASP*, 124, 939
- Högbom, J. A. 1974, *A&AS*, 15, 417
- Horn, A., Møllendal, H., Sekiguchi, O., et al. 2004, *ApJ*, 611, 605
- Huntress, W. T., J. & Anicich, V. G. 1976, *ApJ*, 208, 237
- Indriolo, N., Neufeld, D. A., Gerin, M., et al. 2015, *ApJ*, 800, 40
- Issac, N., Tej, A., Liu, T., et al. 2020, *MNRAS*, 497, 5454
- Jiménez-Serra, I., Caselli, P., Fontani, F., et al. 2014, *MNRAS*, 439, 1996
- Johnston, K. G., Beuther, H., Linz, H., et al. 2014, *A&A*, 568, A56
- Johnston, K. G., Hoare, M. G., Beuther, H., et al. 2020, *ApJ*, 896, 35
- Johnstone, D., Fiege, J. D., Redman, R. O., Feldman, P. A., & Carey, S. J. 2003, *ApJL*, 588, L37
- Jow, D. L., Hill, R., Scott, D., et al. 2018, *MNRAS*, 474, 1018

- Juárez, C., Girart, J. M., Zamora-Avilés, M., et al. 2017, *ApJ*, 844, 44
- Kalenskii, S. V. & Sobolev, A. M. 1994, *Astronomy Letters*, 20, 91
- Kauffmann, J., Bertoldi, F., Bourke, T. L., Evans, N. J., I., & Lee, C. W. 2008, *A&A*, 487, 993
- Kerton, C. R. & Brunt, C. M. 2003, *A&A*, 399, 1083
- Klaassen, P. D., Johnston, K. G., Urquhart, J. S., et al. 2018, *A&A*, 611, A99
- Kölligan, A. & Kuiper, R. 2018, *A&A*, 620, A182
- Krause, O., Vavrek, R., Birkmann, S., et al. 2004, *Baltic Astronomy*, 13, 407
- Kroupa, P. 2001, *MNRAS*, 322, 231
- Krumholz, M. R. 2015, *Astrophysics and Space Science Library*, Vol. 412, *The Formation of Very Massive Stars*, ed. J. S. Vink, 43
- Krumholz, M. R., Klein, R. I., McKee, C. F., Offner, S. S. R., & Cunningham, A. J. 2009, *Science*, 323, 754
- Kuiper, G. P. 1938, *ApJ*, 88, 472
- Kuiper, R. & Hosokawa, T. 2018, *A&A*, 616, A101
- Kumar, M. S. N., Davis, C. J., & Bachiller, R. 2003a, *Ap&SS*, 287, 191
- Kumar, M. S. N., Keto, E., & Clerkin, E. 2006, *A&A*, 449, 1033
- Kumar, M. S. N., Ojha, D. K., & Davis, C. J. 2003b, *ApJ*, 598, 1107
- Kumar, M. S. N., Palmeirim, P., Arzoumanian, D., & Inutsuka, S. I. 2020, *A&A*, 642, A87
- Kurtz, S., Cesaroni, R., Churchwell, E., Hofner, P., & Walmsley, C. M. 2000, in *Protostars and Planets IV*, ed. V. Mannings, A. P. Boss, & S. S. Russell, 299–326
- Kurtz, S., Churchwell, E., & Wood, D. O. S. 1994, *ApJS*, 91, 659
- Larionov, G. M., Val'ts, I. E., Winnberg, A., et al. 1999, *A&AS*, 139, 257
- Larson, R. B. 1969, *MNRAS*, 145, 271
- Law, C. J., Zhang, Q., Öberg, K. I., et al. 2021, *ApJ*, 909, 214
- Le Bourlot, J., Le Petit, F., Pinto, C., Roueff, E., & Roy, F. 2012, *A&A*, 541, A76
- Lee, H. H., Roueff, E., Pineau des Forets, G., et al. 1998, *A&A*, 334, 1047
- Lee, K., Looney, L. W., Schnee, S., & Li, Z.-Y. 2013, *ApJ*, 772, 100
- Leroy, A. K., Schinnerer, E., Hughes, A., et al. 2021, *ApJS*, 257, 43
- Leurini, S., Codella, C., Zapata, L., et al. 2011, *A&A*, 530, A12
- Lin, Y., Wyrowski, F., Liu, H. B., et al. 2022, *A&A*, 658, A128
- Linz, H., Beuther, H., Gerin, M., et al. 2021, *Experimental Astronomy*
- Linz, H., Krause, O., Beuther, H., et al. 2010, *A&A*, 518, L123
- Linz, H., Stecklum, B., Henning, T., Hofner, P., & Brandl, B. 2005, *A&A*, 429, 903
- Liu, T., Evans, N. J., Kim, K.-T., et al. 2020, *MNRAS*, 496, 2790
- Liu, T., Lacy, J., Li, P. S., et al. 2017, *ApJ*, 849, 25
- Lizano, S. & Shu, F. H. 1989, *ApJ*, 342, 834
- Looney, L. W., Mundy, L. G., & Welch, W. J. 2003, *ApJ*, 592, 255
- López-Sepulcre, A., Codella, C., Cesaroni, R., Marcelino, N., & Walmsley, C. M. 2009, *A&A*, 499, 811
- Lundquist, M. J., Koblunicky, H. A., Alexander, M. J., Kerton, C. R., & Arvidsson, K. 2014, *ApJ*, 784, 111
- MacDonald, G. H., Gibb, A. G., Habing, R. J., & Millar, T. J. 1996, *A&AS*, 119, 333
- Mangum, J. G. & Shirley, Y. L. 2015, *PASP*, 127, 266
- Mangum, J. G. & Wootten, A. 1993, *ApJS*, 89, 123
- Marquardt, D. W. 1963, *Journal of the society for Industrial and Applied Mathematics*, 11, 431
- Mathis, J. S., Rumpl, W., & Nordsieck, K. H. 1977, *ApJ*, 217, 425
- Maud, L. T., Cesaroni, R., Kumar, M. S. N., et al. 2019, *A&A*, 627, L6
- Maud, L. T., Lumsden, S. L., Moore, T. J. T., et al. 2015a, *MNRAS*, 452, 637
- Maud, L. T., Moore, T. J. T., Lumsden, S. L., et al. 2015b, *MNRAS*, 453, 645

- McElroy, D., Walsh, C., Markwick, A. J., et al. 2013, *A&A*, 550, A36
- McGuire, B. A. 2018, *ApJS*, 239, 17
- McKee, C. F. & Ostriker, E. C. 2007, *ARA&A*, 45, 565
- McKee, C. F. & Ostriker, J. P. 1977, *ApJ*, 218, 148
- McKee, C. F. & Tan, J. C. 2002, *Nature*, 416, 59
- McKee, C. F. & Tan, J. C. 2003, *ApJ*, 585, 850
- McLaughlin, D. E. & Pudritz, R. E. 1996, *ApJ*, 469, 194
- McLaughlin, D. E. & Pudritz, R. E. 1997, *ApJ*, 476, 750
- Meynet, G., Maeder, A., Schaller, G., Schaerer, D., & Charbonnel, C. 1994, *A&AS*, 103, 97
- Molinari, S., Baldeschi, A., Robitaille, T. P., et al. 2019, *MNRAS*, 486, 4508
- Molinari, S., Merello, M., Elia, D., et al. 2016, *ApJL*, 826, L8
- Molinari, S., Pezzuto, S., Cesaroni, R., et al. 2008, *A&A*, 481, 345
- Molinari, S., Swinyard, B., Bally, J., et al. 2010, *PASP*, 122, 314
- Möller, T., Bernst, I., Panoglou, D., et al. 2013, *A&A*, 549, A21
- Möller, T., Endres, C., & Schilke, P. 2017, *A&A*, 598, A7
- Mookerjea, B., Casper, E., Mundy, L. G., & Looney, L. W. 2007, *ApJ*, 659, 447
- Morii, K., Sanhueza, P., Nakamura, F., et al. 2021, *ApJ*, 923, 147
- Moscadelli, L., Beuther, H., Ahmadi, A., et al. 2021, *A&A*, 647, A114
- Moscadelli, L., Li, J. J., Cesaroni, R., et al. 2013, *A&A*, 549, A122
- Motte, F. & André, P. 2001, *A&A*, 365, 440
- Motte, F., Bontemps, S., & Louvet, F. 2018, *Annual Review of Astronomy and Astrophysics*, 56, 41
- Motte, F., Bontemps, S., Schilke, P., et al. 2007, *A&A*, 476, 1243
- Mottram, J. C., Beuther, H., Ahmadi, A., et al. 2020, *A&A*, 636, A118
- Mottram, J. C., Hoare, M. G., Davies, B., et al. 2011a, *ApJL*, 730, L33
- Mottram, J. C., Hoare, M. G., Urquhart, J. S., et al. 2011b, *A&A*, 525, A149
- Mueller, K. E., Shirley, Y. L., Evans, Neal J., I., & Jacobson, H. R. 2002, *ApJS*, 143, 469
- Müller, H. S. P., Schlöder, F., Stutzki, J., & Winnewisser, G. 2005, *Journal of Molecular Structure*, 742, 215
- Murillo, N. M., van Dishoeck, E. F., van der Wiel, M. H. D., et al. 2018, *A&A*, 617, A120
- Murray, N. & Chang, P. 2012, *ApJ*, 746, 75
- Myers, P. C. 2009, *ApJ*, 700, 1609
- Myers, P. C. & Fuller, G. A. 1992, *ApJ*, 396, 631
- Nanni, A., Bressan, A., Marigo, P., & Girardi, L. 2013, *MNRAS*, 434, 2390
- Nava, L., Recchia, S., Gabici, S., et al. 2019, *MNRAS*, 484, 2684
- Nomura, H. & Millar, T. J. 2004, *A&A*, 414, 409
- Öberg, K. I., Guzmán, V. V., Walsh, C., et al. 2021, *ApJS*, 257, 1
- Obonyo, W. O., Lumsden, S. L., Hoare, M. G., et al. 2019, *MNRAS*, 486, 3664
- Okoda, Y., Oya, Y., Sakai, N., Watanabe, Y., & Yamamoto, S. 2020, *ApJ*, 900, 40
- Okuzumi, S., Tanaka, H., Kobayashi, H., & Wada, K. 2012, *ApJ*, 752, 106
- Olguin, F. A., Hoare, M. G., Johnston, K. G., et al. 2020, *MNRAS*, 498, 4721
- Oliveira, C. M., Hébrard, G., Howk, J. C., et al. 2003, *ApJ*, 587, 235
- Olmi, L., Cesaroni, R., & Walmsley, C. M. 1996, *A&A*, 307, 599
- Osorio, M., Anglada, G., Lizano, S., & D'Alessio, P. 2009, *ApJ*, 694, 29
- Osorio, M., Lizano, S., & D'Alessio, P. 1999, *ApJ*, 525, 808
- Ossenkopf, V. & Henning, T. 1994, *A&A*, 291, 943
- Padovani, M., Galli, D., & Glassgold, A. E. 2009, *A&A*, 501, 619
- Padovani, M., Galli, D., Ivlev, A. V., Caselli, P., & Ferrara, A. 2018, *A&A*, 619, A144
- Palagi, F., Cesaroni, R., Comoretto, G., Felli, M., & Natale, V. 1993, *A&AS*, 101, 153

- Palau, A., Ballesteros-Paredes, J., Vázquez-Semadeni, E., et al. 2015, *MNRAS*, 453, 3785
- Palau, A., Estalella, R., Girart, J. M., et al. 2014, *ApJ*, 785, 42
- Palau, A., Estalella, R., Girart, J. M., et al. 2007, *A&A*, 465, 219
- Palau, A., Fuente, A., Girart, J. M., et al. 2013, *ApJ*, 762, 120
- Palau, A., Walsh, C., Sánchez-Monge, Á., et al. 2017, *MNRAS*, 467, 2723
- Palau, A., Zhang, Q., Girart, J. M., et al. 2021, *ApJ*, 912, 159
- Palla, F., Cesaroni, R., Brand, J., et al. 1993, *A&A*, 280, 599
- Pascucci, I., Apai, D., Henning, T., Stecklum, B., & Brandl, B. 2004, *A&A*, 426, 523
- Pearson, T. J. & Readhead, A. C. S. 1984, *ARA&A*, 22, 97
- Penzias, A. A. & Burrus, C. A. 1973, *ARA&A*, 11, 51
- Peretto, N., Fuller, G. A., Duarte-Cabral, A., et al. 2013, *A&A*, 555, A112
- Perotti, G., Jørgensen, J. K., Fraser, H. J., et al. 2021, *A&A*, 650, A168
- Perotti, G., Rocha, W. R. M., Jørgensen, J. K., et al. 2020, *A&A*, 643, A48
- Peters, T., Klaassen, P. D., Mac Low, M.-M., et al. 2014, *ApJ*, 788, 14
- Peters, T., Mac Low, M.-M., Banerjee, R., Klessen, R. S., & Dullemond, C. P. 2010, *ApJ*, 719, 831
- Pety, J., Teyssier, D., Fossé, D., et al. 2005, *A&A*, 435, 885
- Pickett, H. M., Poynter, R. L., Cohen, E. A., et al. 1998, *JQSRT*, 60, 883
- Pillai, T., Wyrowski, F., Carey, S. J., & Menten, K. M. 2006a, *A&A*, 450, 569
- Pillai, T., Wyrowski, F., Menten, K. M., & Krügel, E. 2006b, *A&A*, 447, 929
- Pilling, M. J. 2013, *Chemical Processes in the Interstellar Medium*, ed. I. W. M. Smith, C. S. Cockell, & S. Leach (Berlin, Heidelberg: Springer Berlin Heidelberg), 73–113
- Pilling, S., Neves, R., Santos, A. C. F., & Boechat-Roberty, H. M. 2007, *A&A*, 464, 393
- Pitann, J., Hennemann, M., Birkmann, S., et al. 2011, *ApJ*, 743, 93
- Planck Collaboration, Ade, P. A. R., Aghanim, N., et al. 2016, *A&A*, 594, A28
- Poglitsch, A., Waelkens, C., Geis, N., et al. 2010, *A&A*, 518, L2
- Prasad, S. S. & Huntress, W. T., J. 1980, *ApJS*, 43, 1
- Purcell, C. R., Balasubramanyam, R., Burton, M. G., et al. 2006, *MNRAS*, 367, 553
- Purser, S. J. D. 2017, PhD thesis, University of Leeds
- Qin, S.-L., Wang, J.-J., Zhao, G., Miller, M., & Zhao, J.-H. 2008, *A&A*, 484, 361
- Qiu, K. & Zhang, Q. 2009, *ApJL*, 702, L66
- Radcliffe, J. F., Garrett, M. A., Beswick, R. J., et al. 2016, *A&A*, 587, A85
- Ragan, S., Henning, T., Krause, O., et al. 2012, *A&A*, 547, A49
- Rathborne, J. M., Jackson, J. M., & Simon, R. 2006, *ApJ*, 641, 389
- Reach, W. T., Megeath, S. T., Cohen, M., et al. 2005, *PASP*, 117, 978
- Reid, M. J. & Ho, P. T. P. 1985, *ApJL*, 288, L17
- Reid, M. J., Menten, K. M., Zheng, X. W., et al. 2009, *ApJ*, 700, 137
- Remijan, A. J., Markwick-Kemper, A., & ALMA Working Group on Spectral Line Frequencies. 2007, in *American Astronomical Society Meeting Abstracts*, Vol. 211, American Astronomical Society Meeting Abstracts, 132.11
- Rieke, G. H., Wright, G. S., Böker, T., et al. 2015, *PASP*, 127, 584
- Rieke, G. H., Young, E. T., Engelbracht, C. W., et al. 2004, *ApJS*, 154, 25
- Rieke, M. J., Kelly, D., & Horner, S. 2005, in *Society of Photo-Optical Instrumentation Engineers (SPIE) Conference Series*, Vol. 5904, *Cryogenic Optical Systems and Instruments XI*, ed. J. B. Heaney & L. G. Burriesci, 1–8
- Roberts, D. A., Crutcher, R. M., & Troland, T. H. 1995, *ApJ*, 442, 208
- Robitaille, T. P., Whitney, B. A., Indebetouw, R., & Wood, K. 2007, *ApJS*, 169, 328
- Rodón, J. A., Beuther, H., & Schilke, P. 2012, *A&A*, 545, A51
- Rodríguez, T. M., Hofner, P., Araya, E. D., et al. 2021, *ApJ*, 922, 66

- Rolfs, R., Schilke, P., Zhang, Q., & Zapata, L. 2011, *ApJ*, 536, A33
- Roman-Duval, J., Jackson, J. M., Heyer, M., Rathborne, J., & Simon, R. 2010, *ApJ*, 723, 492
- Rosen, A. L., Offner, S. S. R., Sadavoy, S. I., et al. 2020, *Space Sci. Rev.*, 216, 62
- Rosero, V., Hofner, P., McCoy, M., et al. 2014, *ApJ*, 796, 130
- Rosolowsky, E., Dunham, M. K., Ginsburg, A., et al. 2010, *ApJS*, 188, 123
- Sánchez-Monge, Á., Cesaroni, R., Beltrán, M. T., et al. 2013a, *A&A*, 552, L10
- Sánchez-Monge, Á., Kurtz, S., Palau, A., et al. 2013b, *ApJ*, 766, 114
- Sánchez-Monge, Á., Palau, A., Estalella, R., et al. 2010, *ApJL*, 721, L107
- Sánchez-Monge, Á., Schilke, P., Schmiedeke, A., et al. 2017, *A&A*, 604, A6
- Sanhueza, P., Girart, J. M., Padovani, M., et al. 2021, *ApJL*, 915, L10
- Sanna, A., Moscadelli, L., Cesaroni, R., et al. 2010, *A&A*, 517, A71
- Sault, R. J., Teuben, P. J., & Wright, M. C. H. 1995, in *Astronomical Society of the Pacific Conference Series*, Vol. 77, *Astronomical Data Analysis Software and Systems IV*, ed. R. A. Shaw, H. E. Payne, & J. J. E. Hayes, 433
- Schilke, P. 2015, in *EAS Publications Series*, Vol. 75, *EAS Publications Series*, 227–235
- Schilke, P., Walmsley, C. M., Pineau des Forets, G., & Flower, D. R. 1997, *A&A*, 321, 293
- Schlingman, W. M., Shirley, Y. L., Schenk, D. E., et al. 2011, *ApJS*, 195, 14
- Schneider, N., Csengeri, T., Hennemann, M., et al. 2012, *A&A*, 540, L11
- Schneider, N., Simon, R., Bontemps, S., Comerón, F., & Motte, F. 2007, *A&A*, 474, 873
- Schöier, F. L., van der Tak, F. F. S., van Dishoeck, E. F., & Black, J. H. 2005, *A&A*, 432, 369
- Schuller, F., Menten, K. M., Contreras, Y., et al. 2009, *A&A*, 504, 415
- Schwörer, A., Sánchez-Monge, Á., Schilke, P., et al. 2019, *A&A*, 628, A6
- Semenov, D., Hersant, F., Wakelam, V., et al. 2010, *A&A*, 522, A42
- Shimajiri, Y., Sakai, T., Kitamura, Y., et al. 2015, *ApJS*, 221, 31
- Shirley, Y. L., Ellsworth-Bowers, T. P., Svoboda, B., et al. 2013, *ApJS*, 209, 2
- Shirley, Y. L., Evans, Neal J., I., Rawlings, J. M. C., & Gregersen, E. M. 2000, *ApJS*, 131, 249
- Shu, F. H. 1977, *ApJ*, 214, 488
- Shu, F. H., Adams, F. C., & Lizano, S. 1987, *ARA&A*, 25, 23
- Slysh, V. I., Val'ts, I. E., Kalenskii, S. V., et al. 1999, *A&AS*, 134, 115
- Smith, I. W. M., Herbst, E., & Chang, Q. 2004, *MNRAS*, 350, 323
- Smith, R. J., Longmore, S., & Bonnell, I. 2009, *MNRAS*, 400, 1775
- Snyder, L. E., Buhl, D., Zuckerman, B., & Palmer, P. 1969, *PRL*, 22, 679
- Soler, J. D., Ade, P. A. R., Angilè, F. E., et al. 2017, *A&A*, 603, A64
- Soler, J. D., Beuther, H., Rugel, M., et al. 2019, *A&A*, 622, A166
- Solomon, P. M., Sanders, D. B., & Scoville, N. Z. 1979, in *The Large-Scale Characteristics of the Galaxy*, ed. W. B. Burton, Vol. 84, 35
- Sridharan, T. K., Beuther, H., Schilke, P., Menten, K. M., & Wyrowski, F. 2002, *ApJ*, 566, 931
- Steer, D. G., Dewdney, P. E., & Ito, M. R. 1984, *A&A*, 137, 159
- Stetson, P. B. 1987, *PASP*, 99, 191
- Sunada, K., Nakazato, T., Ikeda, N., et al. 2007, *PASJ*, 59, 1185
- Suri, S., Beuther, H., Gieser, C., et al. 2021, *A&A*, 655, A84
- Swings, P. & Rosenfeld, L. 1937, *ApJ*, 86, 483
- Syed, J., Wang, Y., Beuther, H., et al. 2020, *A&A*, 642, A68
- Tackenberg, J., Beuther, H., Henning, T., et al. 2014, *A&A*, 565, A101
- Tackenberg, J., Beuther, H., Henning, T., et al. 2012, *A&A*, 540, A113
- Tan, J. C., Beltrán, M. T., Caselli, P., et al. 2014, *Protostars and Planets VI*, 149
- Taquet, V., Codella, C., De Simone, M., et al. 2020, *A&A*, 637, A63
- Terzieva, R. & Herbst, E. 2000, *International Journal of Mass Spectrometry*, 201, 135
- Testi, L., Felli, M., Persi, P., & Roth, M. 1998, *A&A*, 329, 233

- Thompson, A. R., Moran, J. M., & Swenson, George W., J. 2001, *Interferometry and Synthesis in Radio Astronomy*, 2nd Edition
- Thompson, M. A., Hatchell, J., Walsh, A. J., MacDonald, G. H., & Millar, T. J. 2006, *A&A*, 453, 1003
- Tielens, A. G. G. M. 2005, *The Physics and Chemistry of the Interstellar Medium*
- Tielens, A. G. G. M. 2008, *ARA&A*, 46, 289
- Tielens, A. G. G. M. & Hagen, W. 1982, *A&A*, 114, 245
- Tigé, J., Motte, F., Russeil, D., et al. 2017, *A&A*, 602, A77
- Tobin, J. J., Looney, L. W., Li, Z.-Y., et al. 2016, *ApJ*, 818, 73
- Tychoniec, Ł., Hull, C. L. H., Kristensen, L. E., et al. 2019, *A&A*, 632, A101
- Urquhart, J. S., Figura, C., Wyrowski, F., et al. 2019, *MNRAS*, 484, 4444
- Urquhart, J. S., König, C., Giannetti, A., et al. 2018, *MNRAS*, 473, 1059
- Urquhart, J. S., Wells, M. R. A., Pillai, T., et al. 2022, *MNRAS*, 510, 3389
- Valdettaro, R., Palla, F., Brand, J., et al. 2001, *A&A*, 368, 845
- van der Tak, F. F. S., van Dishoeck, E. F., Evans, Neal J., I., & Blake, G. A. 2000, *ApJ*, 537, 283
- Vasyunina, T., Vasyunin, A. I., Herbst, E., et al. 2014, *ApJ*, 780, 85
- Vázquez-Semadeni, E., Gómez, G. C., Jappsen, A. K., Ballesteros-Paredes, J., & Klessen, R. S. 2009, *ApJ*, 707, 1023
- Vázquez-Semadeni, E., Palau, A., Ballesteros-Paredes, J., Gómez, G. C., & Zamora-Avilés, M. 2019, *MNRAS*, 490, 3061
- Wakelam, V., Herbst, E., Loison, J. C., et al. 2012, *ApJS*, 199, 21
- Wakelam, V., Loison, J.-C., Herbst, E., et al. 2015, *ApJS*, 217, 20
- Walsh, A. J., Macdonald, G. H., Alvey, N. D. S., Burton, M. G., & Lee, J. K. 2003, *A&A*, 410, 597
- Wang, K., Zhang, Q., Testi, L., et al. 2014, *MNRAS*, 439, 3275
- Wang, K., Zhang, Q., Wu, Y., & Zhang, H. 2011, *ApJ*, 735, 64
- Wang, Y., Audard, M., Fontani, F., et al. 2016, *A&A*, 587, A69
- Watanabe, N. & Kouchi, A. 2002, *ApJL*, 571, L173
- Weingartner, J. C. & Draine, B. T. 2001, *ApJ*, 548, 296
- Weinreb, S., Barrett, A. H., Meeks, M. L., & Henry, J. C. 1963, *Nature*, 200, 829
- Williams, J. P., de Geus, E. J., & Blitz, L. 1994, *ApJ*, 428, 693
- Williams, S. J., Fuller, G. A., & Sridharan, T. K. 2004, *A&A*, 417, 115
- Williams, S. J., Fuller, G. A., & Sridharan, T. K. 2005, *A&A*, 434, 257
- Wilson, R. W., Jefferts, K. B., & Penzias, A. A. 1970, *ApJL*, 161, L43
- Wilson, T. L., Rohlfs, K., & Hüttemeister, S. 2009, *Tools of Radio Astronomy*
- Wilson, T. L. & Rood, R. 1994, *ARA&A*, 32, 191
- Wolfire, M. G. & Cassinelli, J. P. 1987, *ApJ*, 319, 850
- Wood, D. O. S. & Churchwell, E. 1989, *ApJS*, 69, 831
- Woosley, S. & Janka, T. 2005, *Nature Physics*, 1, 147
- Wouterloot, J. G. A. & Brand, J. 1989, *A&AS*, 80, 149
- Wouterloot, J. G. A., Brand, J., & Fiegle, K. 1993, *A&AS*, 98, 589
- Wouterloot, J. G. A., Henkel, C., & Walmsley, C. M. 1989, *A&A*, 215, 131
- Wouterloot, J. G. A. & Walmsley, C. M. 1986, *A&A*, 168, 237
- Wouterloot, J. G. A., Walmsley, C. M., & Henkel, C. 1988, *A&A*, 203, 367
- Wu, Y., Wei, Y., Zhao, M., et al. 2004, *A&A*, 426, 503
- Wu, Y., Zhang, Q., Chen, H., et al. 2005, *AJ*, 129, 330
- Wyrowski, F., Güsten, R., Menten, K. M., et al. 2016, *A&A*, 585, A149
- Xi, H., Zhou, J., Esimbek, J., et al. 2015, *MNRAS*, 453, 4203
- Yang, J., Jiang, Z., Wang, M., Ju, B., & Wang, H. 2002, *ApJS*, 141, 157

-
- Zeng, S., Zhang, Q., Jiménez-Serra, I., et al. 2020, MNRAS, 497, 4896
Zhang, Q., Hunter, T. R., Beuther, H., et al. 2007, ApJ, 658, 1152
Zhang, Q., Hunter, T. R., Brand, J., et al. 2005, ApJ, 625, 864
Zhang, Q., Wang, K., Lu, X., & Jiménez-Serra, I. 2015, ApJ, 804, 141
Zhang, Q., Wang, Y., Pillai, T., & Rathborne, J. 2009, ApJ, 696, 268
Zhao, B., Tomida, K., Hennebelle, P., et al. 2020, SSR, 216, 43
Zinnecker, H. & Yorke, H. W. 2007, ARA&A, 45, 481
Zuckerman, B. & Dyck, H. M. 1986, ApJ, 311, 345

List of Figures

1.1	High-mass star formation scenario and evolutionary stages.	3
1.2	Sketch of a dust particle with an icy mantle and grain surface reaction mechanisms.	7
1.3	Antenna radiation pattern.	10
1.4	Principle of a two antenna interferometer.	12
1.5	Principle of a mixer and local oscillator.	14
1.6	NOEMA calibration steps.	14
1.7	Example of a NOEMA <i>uv</i> coverage.	15
1.8	Sketch of radiative transfer through a medium.	16
1.9	Spectral energy distribution of black body and free-free components.	18
1.10	Emission and absorption processes in atoms and molecules.	19
1.11	Molecule types.	20
1.12	Vibrational modes of carbon monoxide and water.	21
2.1	Comparison of GILDAS standard calibrated, CASA self-calibrated, and GILDAS self-calibrated W3 IRS4 continuum data.	30
2.2	Comparison of GILDAS standard calibrated and GILDAS self-calibrated broadband spectral line data of W3 IRS4.	31
2.3	NOEMA 1.37 mm continuum emission of the CORE regions.	35
2.4	Radial temperature profiles of the 22 cores.	40
2.5	Histogram of the temperature power-law index q	42
2.6	Radial 1.37 mm continuum visibility profiles of the 22 cores.	43
2.7	Histogram of the density power-law index p	45
2.8	Column density histograms.	49
2.9	Comparison of the observed and modeled column densities of the 22 cores.	53
2.10	Literature comparison of the density power-law index p at different spatial scales.	57
2.11	Spearman correlation coefficient r for the derived physical and chemical core parameters.	58
2.12	Comparison of the M/L ratio and chemical timescales τ_{chem}	59
2.13	Spearman correlation coefficient r for pairs of molecular column densities relative to $N(\text{C}^{18}\text{O})$	61
2.14	Comparison of the free-fall timescale, and crossing timescale, and chemical timescale.	63
3.1	NOEMA 1.3 mm continuum of the CORE-extension regions.	76
3.2	Radial visibility profiles of cores 1 – 4 in ISOSS J22478+6357 and cores 1 – 6 in ISOSS J23053+5953.	81
3.3	Multi-wavelength overview of ISOSS J22478+6357 and ISOSS J23053+5953.	83
3.4	Spectral energy distribution of mm cores with associated Spitzer IRAC emission in at least three bands.	84
3.5	CO 2 – 1 outflows in ISOSS J22478+6357 and ISOSS J23053+5953.	89
3.6	Line integrated intensity map of $\text{H}_2\text{CO } 3_{0,3} - 2_{0,2}$	91
3.7	Line integrated intensity map of SiO 5 – 4.	91

3.8	Line integrated intensity map of CH ₃ OH 4 _{2,3} – 3 _{1,2} E.	92
3.9	HOG results.	95
3.10	HOG correlation examples.	96
3.11	H ₂ CO parameter maps for ISOSS J22478+6357 derived with XCLASS.	98
3.12	H ₂ CO parameter maps for ISOSS J23053+5953 derived with XCLASS.	99
3.13	Radial temperature profiles for cores 1 – 4 in ISOSS J22478+6357 and cores 1 – 6 in ISOSS J23053+5953.	101
3.14	Abundance histograms (relative to C ¹⁸ O).	102
3.15	Comparison of the observed and modeled column densities for core 1 in ISOSS J22478+6357 and cores 1, 2, and 6 in ISOSS J23053+5953.	106
3.16	Comparison of the mean abundances (relative to C ¹⁸ O) of cores in the CORE and CORE-extension sample.	110
3.17	Core parameters with a Spearman correlation coefficient of $ r_s \geq 0.4$	114
4.1	Comparison of the standard calibrated and self-calibrated HMC G9.62+0.19 continuum data.	124
4.2	ALMA 3 mm continuum images of the sample.	127
4.3	Estimate of the free-free contribution at 3 mm based on CORNISH data.	130
4.4	Temperature maps derived with the HCN-to-HNC intensity ratio.	132
4.5	Temperature maps derived with CH ₃ CN.	135
4.6	Temperature maps derived with CH ₃ ¹³ CN.	137
4.7	Radial temperature profiles.	139
4.8	Visibility profiles of the mm cores and (cometary) UCHII regions.	142
4.9	Comparison of the clump parameters of the ALMA sample.	147
4.10	Correlations of the physical parameters of the ALMA, CORE, and CORE-extension samples.	148
4.11	Correlations of the physical parameters of the ALMA, CORE, and CORE-extension sample.	150
5.1	CORE+ continuum and spectral line data products.	158
5.2	ALMA 3 mm spectra.	160
5.3	Mirror alignment of JWST with the NIRCcam instrument.	162
A.1	Temperature maps derived with XCLASS.	187
A.2	Abundance ratio histograms.	193
A.3	Broadband spectrum toward each position.	209
B.1	Line integrated intensity map of SO 5 ₅ – 4 ₄	241
B.2	Line integrated intensity map of DCO ⁺ 3 – 2.	242
B.3	Line integrated intensity map of H ₂ S 2 _{2,0} – 2 _{1,1}	242
B.4	Line integrated intensity map of CH ₃ OH 5 _{1,4} – 4 _{2,3} E.	242
B.5	Line integrated intensity map of c-C ₃ H ₂ 6 _{1,6} – 5 _{0,5}	243
B.6	Line integrated intensity map of HC ₃ N 24 – 23.	243
B.7	Line integrated intensity map of H ₂ CO 3 _{2,2} – 2 _{2,1}	243
B.8	Line integrated intensity map of H ₂ CO 3 _{2,1} – 2 _{2,0}	244
B.9	Line integrated intensity map of OCS 18 – 17.	244
B.10	Line integrated intensity map of C ¹⁸ O 2 – 1.	244
B.11	Line integrated intensity map of HNCO 10 _{0,10} – 9 _{0,9}	245
B.12	Line integrated intensity map of H ₂ ¹³ CO 3 _{1,2} – 2 _{1,1}	245
B.13	Line integrated intensity map of SO 6 ₅ – 5 ₄	245

B.14	Line integrated intensity map of $\text{CH}_3\text{OH } 8_{0,8} - 7_{1,6}E$	246
B.15	Line integrated intensity map of $^{13}\text{CO } 2 - 1$	246
B.16	Line integrated intensity map of $\text{CH}_3\text{CN } 12_0 - 11_0$	246
B.17	Line integrated intensity map of $\text{CH}_3\text{OH } 8_{1,8} - 7_{0,7}E$	247
B.18	Line integrated intensity map of $\text{CO } 2 - 1$	247
B.19	Line integrated intensity map of $\text{OCS } 19 - 18$	247
B.20	Line integrated intensity map of $^{13}\text{CS } 5 - 4$	248
B.21	Line integrated intensity map of $\text{N}_2\text{D}^+ 3 - 2$	248
B.22	Line integrated intensity map of $\text{SO}_2 4_{2,2} - 3_{1,3}$	248
B.23	Line integrated intensity map of $\text{HC}_3\text{N } 26 - 25$	249
B.24	Intensity-weighted peak velocity (moment 1) maps of molecular lines with extended emission in ISOSS J23053+5953.	250
B.25	Example spectrum of all molecular transitions fitted with XCLASS toward core 1 in ISOSS J22478+6357.	256
B.26	Example spectrum of all molecular transitions fitted with XCLASS toward core 1 in ISOSS J23053+5953.	257
C.1	Overview of IRDC G11.11-4.	263
C.2	Overview of IRDC 18223-3.	264
C.3	Overview of IRDC 18310-4.	265
C.4	Overview of HMPO IRAS 18089.	266
C.5	Overview of HMPO IRAS 18182.	267
C.6	Overview of HMPO IRAS 18264.	268
C.7	Overview of HMC G9.62+0.19.	269
C.8	Overview of HMC G10.47+0.03.	270
C.9	Overview of HMC G34.26+0.15.	271
C.10	Overview of $\text{UCH}_{\text{II}} \text{G}10.30-0.15$	272
C.11	Overview of $\text{UCH}_{\text{II}} \text{G}13.87+0.28$	273
C.12	Integrated intensity maps of $\text{H}(40)\alpha$	282

List of Tables

1.1	Examples of radio single-dish telescopes and interferometers.	9
2.1	Overview of the CORE sample.	28
2.2	Overview of the CORE data products.	32
2.3	Physical structure and chemical timescales of the cores in the CORE sample.	46
2.4	MUSCLE input parameters.	52
3.1	Overview of the CORE-extension sample.	70
3.2	Emission lines detected in the CORE-extension regions.	71
3.3	Overview of the CORE-extension spectral line data products.	73
3.4	Overview of the cores in the CORE-extension sample.	78
3.5	Physical structure and chemical timescales of the cores in the CORE-extension sample.	82
3.6	Photometry and SED fit of mm cores with associated Spitzer IRAC sources.	87
4.1	Overview of the ALMA sample.	118
4.2	Overview of the ALMA 3 mm continuum data products.	123
4.3	Emission lines detected and analyzed in the ALMA regions.	125
4.4	Overview of the ALMA spectral line data products.	125
4.5	Free-free contribution at 3 mm in the ALMA regions.	131
A.1	Overview of the cores and non-core positions in the CORE sample.	180
A.2	Emission lines detected in the CORE regions.	185
A.3	Molecular column densities (^{13}CO , C^{18}O , SO , OCS , SO_2 , DCN , H_2CO) derived with XCLASS in the CORE sample.	195
A.4	Molecular column densities (HNCO , HC_3N , $\text{HC}_3\text{N};v_7=1$, $\text{HC}_3\text{N};v_7=2$, CH_3OH , $\text{CH}_3\text{OH};v_t=1$, CH_3CN) derived with XCLASS in the CORE sample.	202
A.5	MUSCLE results for cores in the CORE regions.	239
B.1	Molecular column densities (C^{18}O , SO , ^{13}CS , OCS , DCO^+ , N_2D^+ , H_2S) derived with XCLASS in the CORE-extension sample.	252
B.2	Molecular column densities (H_2CO , HNCO , HC_3N , $c\text{-C}_3\text{H}_2$, CH_3OH , CH_3CN) derived with XCLASS in the CORE-extension sample.	254
B.3	MUSCLE results for cores in the CORE-extension regions.	259
C.1	Overview of the ALMA 3 mm observation blocks.	261
C.2	Overview of the spectral windows observed with ALMA.	262
C.3	Overview of the cores, (cometary) UCHII regions, and envelope positions in the ALMA sample.	274
C.4	Radial temperature profiles in the ALMA sample.	276
C.5	H_2 column density and mass in the ALMA sample.	278
C.6	Visibility and density profiles in the ALMA sample.	280

Appendix A

Supplementary material for Chapter 2

A.1 Position properties

Table A.1 summarizes the properties of all 120 positions extracted within the 18 CORE regions which were analyzed in this study¹. The positions are also marked in Fig. 2.3 presenting the 1.37 mm continuum emission. Positions which show a clear temperature profile are labeled as “C” (core, further explained in Sect. 2.3.2).

¹This table is online available at <https://cdsarc.u-strasbg.fr/viz-bin/cat/J/A+A/648/A66>.

TABLE A.1: Overview of the cores and non-core positions in the CORE sample. The systemic velocity is derived from the C^{18}O 2 – 1 line (Sect. 2.4.2). The noise of the spectrum σ_{line} is computed in a line-free range from a rest-frequency of 219.00 GHz to 219.13 GHz. The continuum optical depth τ_{ν}^{cont} is calculated according to Eq. (1.47) and the H_2 column density $N(\text{H}_2)$ is calculated according to Eq. (1.48) using the continuum intensity $I_{1.37\text{mm}}$ and T_{kin} (Sect. 2.4.1). As the H_2 column density is derived from the 1.37 mm dust continuum emission and we do not have short-spacing information this should be considered as a lower limit due to potential missing flux.

Position	α J(2000)	δ J(2000)	v_{LSR} (km s^{-1})	σ_{line} (K)	T_{kin} (K)	$I_{1.37\text{mm}}$ (mJy beam^{-1})	τ_{ν}^{cont}	$N(\text{H}_2)$ (cm^{-2})
IRAS 23033 1 C	23:05:24.63	+60:08:09.2	-53.6	0.30	114.9±8.2	38.13	5.5(-2)	1.9(24)±4.0(23)
IRAS 23033 2 C	23:05:25.04	+60:08:15.8	-53.4	0.20	167.2±6.6	32.55	3.1(-2)	1.1(24)±2.2(23)
IRAS 23033 3 C	23:05:24.92	+60:08:13.9	-54.6	0.20	160.8±8.0	27.04	2.7(-2)	9.5(23)±2.0(23)
IRAS 23033 4	23:05:24.97	+60:08:15.0	-53.7	0.19	84.9±6.7	7.14	1.4(-2)	4.9(23)±1.1(23)
IRAS 23033 5	23:05:25.03	+60:08:17.3	-52.9	0.21	15.3±2.5	6.30	9.5(-2)	3.2(24)±9.7(23)
IRAS 23151 1 C	23:17:20.89	+59:28:47.6	-54.5	0.22	129.2±4.7	33.78	4.3(-2)	1.5(24)±3.1(23)
IRAS 23151 2	23:17:20.84	+59:28:47.0	-54.2	0.22	168.8±78.9	3.06	2.9(-3)	1.0(23)±5.4(22)
IRAS 23151 3	23:17:20.82	+59:28:48.4	-56.2	0.23	171.7±42.2	2.96	2.8(-3)	9.8(22)±3.2(22)
IRAS 23151 4	23:17:20.88	+59:28:49.0	-56.4	0.33	204.1±35.5	2.35	1.8(-3)	6.5(22)±1.7(22)
IRAS 23151 5	23:17:20.96	+59:28:46.2	-53.7	0.29	69.0±37.7	1.87	4.5(-3)	1.6(23)±1.0(23)
IRAS 23385 1 C	23:40:54.51	+61:10:28.0	-50.9	0.20	239.5±12.1	17.84	9.3(-3)	3.3(23)±6.8(22)
IRAS 23385 2 C	23:40:54.72	+61:10:28.5	-51.3	0.25	226.0±2.3	14.36	7.9(-3)	2.8(23)±5.6(22)
IRAS 23385 3	23:40:54.44	+61:10:27.7	-50.8	0.17	72.4±37.5	13.79	2.5(-2)	8.9(23)±5.2(23)
IRAS 23385 4	23:40:54.42	+61:10:27.0	-49.9	0.21	21.5±4.7	4.12	3.0(-2)	1.1(24)±3.7(23)
IRAS 23385 5	23:40:54.32	+61:10:28.2	-50.1	0.22	262.2±11.6	3.99	1.9(-3)	6.7(22)±1.4(22)
IRAS 23385 6	23:40:54.59	+61:10:27.3	-51.0	0.18	51.1±32.1	3.28	8.7(-3)	3.1(23)±2.2(23)
IRAS 23385 7	23:40:54.49	+61:10:29.4	-50.7	0.20	164.2±42.2	2.49	1.9(-3)	6.8(22)±2.2(22)
IRAS 23385 8	23:40:54.34	+61:10:27.2	-50.3	0.21	116.4±36.6	0.92	1.0(-3)	3.6(22)±1.4(22)
AFGL 2591 1 C	20:29:24.88	+40:11:19.4	-5.0	0.47	159.9±6.8	85.10	8.6(-2)	2.9(24)±6.0(23)
AFGL 2591 2	20:29:24.47	+40:11:24.0	-7.2	0.36	39.3±6.4	5.76	2.5(-2)	9.0(23)±2.4(23)
AFGL 2591 3	20:29:25.03	+40:11:21.3	-5.7	0.40	61.6±14.8	5.68	1.5(-2)	5.4(23)±1.8(23)
AFGL 2591 4	20:29:24.80	+40:11:20.5	-5.8	0.35	94.3±20.4	5.01	8.4(-3)	3.0(23)±9.1(22)

Notes. a(b) = $a \times 10^b$.

TABLE A.1: continued.

Position	α J(2000)	δ J(2000)	v_{LSR} (km s ⁻¹)	σ_{line} (K)	T_{kin} (K)	$I_{1.37\text{mm}}$ (mJy beam ⁻¹)	τ_{ν}^{cont}	$N(\text{H}_2)$ (cm ⁻²)
CepA HW2 1 C	22:56:17.98	+62:01:49.6	-7.7	0.97	238.2±11.4	448.50	3.4(-1)	1.0(25)±2.1(24)
CepA HW2 2 C	22:56:17.96	+62:01:46.2	-9.8	0.39	170.5±13.3	84.21	8.0(-2)	2.7(24)±5.9(23)
CepA HW2 3	22:56:17.87	+62:01:50.3	-7.4	0.48	124.9±8.7	28.63	3.7(-2)	1.3(24)±2.7(23)
CepA HW2 4	22:56:17.35	+62:01:54.8	-11.1	0.44	20.0±10.0	20.45	2.3(-1)	7.2(24)±4.9(24)
CepA HW2 5	22:56:17.89	+62:01:48.1	-9.4	0.42	273.8±8.5	14.19	8.0(-3)	2.8(23)±5.7(22)
G084.9505 1 C	20:55:32.50	+44:06:10.2	-34.3	0.15	169.0±0.8	5.19	5.0(-3)	1.8(23)±3.5(22)
G084.9505 2	20:55:32.22	+44:06:07.9	-34.5	0.17	81.8±3.6	3.38	6.9(-3)	2.4(23)±5.0(22)
G084.9505 3	20:55:32.13	+44:06:08.8	-34.2	0.14	77.0±22.5	2.18	4.7(-3)	1.7(23)±6.2(22)
G084.9505 4	20:55:32.30	+44:06:08.0	-34.0	0.15	111.2±36.4	2.05	3.0(-3)	1.1(23)±4.3(22)
G084.9505 5	20:55:32.41	+44:06:08.5	-34.2	0.14	53.7±42.5	1.68	5.4(-3)	1.9(23)±1.7(23)
G084.9505 6	20:55:32.16	+44:06:09.2	-34.2	0.17	111.2±37.9	1.27	1.9(-3)	6.7(22)±2.7(22)
G084.9505 7	20:55:32.31	+44:06:09.0	-34.7	0.17	33.3±4.2	1.15	6.4(-3)	2.3(23)±5.6(22)
G084.9505 8	20:55:32.38	+44:06:06.6	-33.9	0.17	57.2±27.2	1.04	3.1(-3)	1.1(23)±6.2(22)
G094.6028 1 C	21:39:58.27	+50:14:21.0	+29.0	0.26	183.8±45.4	12.84	1.2(-2)	4.2(23)±1.3(23)
G094.6028 2	21:39:58.16	+50:14:20.5	+30.0	0.18	39.1±17.7	2.18	1.0(-2)	3.7(23)±2.1(23)
G094.6028 3	21:39:58.11	+50:14:26.1	+28.4	0.25	50.9±0.0	2.11	7.5(-3)	2.7(23)±5.3(22)
G094.6028 4	21:39:58.31	+50:14:19.6	+28.3	0.19	37.8±8.5	2.05	1.0(-2)	3.6(23)±1.2(23)
G094.6028 5	21:39:58.13	+50:14:21.6	+29.0	0.17	21.7±5.0	2.00	1.9(-2)	6.9(23)±2.4(23)
G094.6028 6	21:39:58.05	+50:14:26.0	+28.2	0.29	65.8±38.7	1.86	5.0(-3)	1.8(23)±1.2(23)
G094.6028 7	21:39:58.22	+50:14:21.7	+29.0	0.20	26.7±11.7	1.70	1.3(-2)	4.5(23)±2.6(23)
G094.6028 8	21:39:58.59	+50:14:20.5	+28.9	0.30	16.7±4.4	1.32	1.8(-2)	6.4(23)±2.6(23)
G100.38 1 C	22:16:10.37	+52:21:34.1	-37.4	0.13	68.2±0.7	7.28	1.8(-2)	6.5(23)±1.3(23)
G100.38 2	22:16:10.48	+52:21:36.7	-37.3	0.16	37.4±0.0	1.21	5.9(-3)	2.1(23)±4.2(22)
G100.38 3	22:16:10.42	+52:21:37.1	-37.4	0.18	42.3±37.6	1.20	5.1(-3)	1.8(23)±1.9(23)
G100.38 4	22:16:10.58	+52:21:33.3	-37.6	0.18	14.7±6.1	0.99	1.6(-2)	5.5(23)±3.4(23)
G100.38 5	22:16:10.62	+52:21:36.1	-37.5	0.20	20.0±10.0	0.67	7.0(-3)	2.5(23)±1.7(23)

Notes. a(b) = a×10^b.

TABLE A.1: continued.

Position	α J(2000)	δ J(2000)	v_{LSR} (km s ⁻¹)	σ_{line} (K)	T_{kin} (K)	$I_{1.37\text{mm}}$ (mJy beam ⁻¹)	τ_{ν}^{cont}	$N(\text{H}_2)$ (cm ⁻²)
G108.75 1 C	22:58:47.41	+58:45:02.0	-51.0	0.15	111.2±8.2	16.01	1.8(-2)	6.2(23)±1.3(23)
G108.75 2 C	22:58:46.78	+58:45:03.6	-50.7	0.14	82.9±2.6	7.81	1.2(-2)	4.2(23)±8.4(22)
G108.75 3	22:58:46.97	+58:45:04.9	-50.9	0.16	39.1±17.5	6.24	2.1(-2)	7.6(23)±4.2(23)
G108.75 4	22:58:47.06	+58:45:04.6	-50.8	0.16	22.9±5.9	2.14	1.4(-2)	4.9(23)±1.8(23)
G108.75 5	22:58:46.89	+58:45:04.3	-50.8	0.13	155.7±75.4	0.97	7.5(-4)	2.7(22)±1.4(22)
G108.75 6	22:58:47.38	+58:45:03.5	-50.7	0.14	28.8±17.2	0.97	4.7(-3)	1.7(23)±1.2(23)
G138.2957 1	03:01:31.28	+60:29:12.7	-38.9	0.16	31.3±6.7	6.28	3.0(-2)	1.1(24)±3.4(23)
G138.2957 2	03:01:31.41	+60:29:12.4	-39.2	0.19	34.8±16.4	3.78	1.6(-2)	5.6(23)±3.3(23)
G138.2957 3	03:01:31.49	+60:29:12.2	-39.3	0.19	149.3±28.4	3.13	2.7(-3)	9.6(22)±2.7(22)
G138.2957 4	03:01:31.36	+60:29:18.5	-38.0	0.20	19.3±5.7	2.64	2.3(-2)	8.1(23)±3.5(23)
G138.2957 5	03:01:31.40	+60:29:19.3	-38.3	0.26	35.1±12.8	2.28	9.4(-3)	3.3(23)±1.6(23)
G138.2957 6	03:01:31.28	+60:29:13.9	-38.6	0.16	74.9±14.1	2.27	4.1(-3)	1.4(23)±4.1(22)
G138.2957 7	03:01:31.28	+60:29:10.6	-39.4	0.16	117.1±41.7	2.19	2.4(-3)	8.7(22)±3.7(22)
G138.2957 8	03:01:32.16	+60:29:18.7	-38.6	0.29	41.1±11.1	2.02	7.0(-3)	2.5(23)±9.1(22)
G138.2957 9	03:01:31.46	+60:29:18.9	-37.3	0.21	63.6±14.3	1.87	4.0(-3)	1.4(23)±4.5(22)
G138.2957 10	03:01:32.15	+60:29:19.9	-37.2	0.26	20.8±4.9	1.85	1.4(-2)	5.1(23)±1.8(23)
G138.2957 11	03:01:32.25	+60:29:17.7	-38.5	0.35	20.0±2.6	1.80	1.5(-2)	5.3(23)±1.4(23)
G138.2957 12	03:01:30.67	+60:29:12.9	-36.9	0.22	27.4±14.6	1.44	8.0(-3)	2.8(23)±1.9(23)
G139.9091 1	03:07:24.49	+58:30:42.8	-39.8	0.27	257.5±59.1	13.49	6.7(-3)	2.4(23)±7.4(22)
G139.9091 2	03:07:24.58	+58:30:53.0	-39.7	0.21	298.3±0.0	6.63	2.8(-3)	1.0(23)±2.0(22)
G139.9091 3	03:07:23.94	+58:30:52.5	-39.8	0.24	57.2±61.6	1.79	4.3(-3)	1.5(23)±1.8(23)
G139.9091 4	03:07:24.49	+58:30:50.3	-40.8	0.30	55.3±43.1	1.59	4.0(-3)	1.4(23)±1.2(23)
G075.78 1 C	20:21:44.02	+37:26:37.5	-6.9	0.38	176.8±0.3	71.67	6.2(-2)	2.1(24)±4.3(23)
G075.78 2	20:21:43.95	+37:26:39.3	-6.0	0.30	73.1±28.6	13.88	3.0(-2)	1.0(24)±4.9(23)
G075.78 3	20:21:44.10	+37:26:39.3	-6.7	0.31	64.7±23.2	4.20	1.0(-2)	3.6(23)±1.6(23)
G075.78 4	20:21:44.28	+37:26:38.0	-7.1	0.30	276.8±3.2	4.16	2.2(-3)	7.8(22)±1.6(22)

Notes. a(b) = a×10^b.

TABLE A.1: continued.

Position	α J(2000)	δ J(2000)	v_{LSR} (km s ⁻¹)	σ_{line} (K)	T_{kin} (K)	$I_{1.37\text{mm}}$ (mJy beam ⁻¹)	τ_{ν}^{cont}	$N(\text{H}_2)$ (cm ⁻²)
IRAS 21078 1 C	21:09:21.71	+52:22:37.1	-6.5	0.40	135.5±0.2	36.69	4.7(-2)	1.6(24)±3.3(23)
IRAS 21078 2 C	21:09:21.79	+52:22:35.7	-6.8	0.25	121.9±3.4	22.95	3.3(-2)	1.1(24)±2.3(23)
IRAS 21078 3	21:09:21.76	+52:22:36.8	-5.4	0.29	120.5±15.1	21.21	3.0(-2)	1.1(24)±2.6(23)
IRAS 21078 4	21:09:22.12	+52:22:34.6	-3.9	0.21	46.3±14.3	20.09	8.3(-2)	2.8(24)±1.1(24)
IRAS 21078 5	21:09:21.85	+52:22:32.0	-5.4	0.27	249.0±9.1	19.24	1.3(-2)	4.6(23)±9.3(22)
IRAS 21078 6	21:09:21.65	+52:22:38.6	-6.3	0.25	61.8±3.8	19.06	5.6(-2)	2.0(24)±4.1(23)
IRAS 21078 7	21:09:21.96	+52:22:36.9	-4.6	0.25	206.9±23.3	16.49	1.3(-2)	4.8(23)±1.1(23)
IRAS 21078 8	21:09:21.90	+52:22:35.4	-5.2	0.26	77.7±33.6	13.98	3.2(-2)	1.1(24)±5.6(23)
IRAS 21078 9	21:09:22.04	+52:22:35.2	-5.5	0.26	229.5±18.5	10.08	7.4(-3)	2.6(23)±5.7(22)
IRAS 21078 10	21:09:21.82	+52:22:38.0	-6.0	0.25	115.7±36.4	9.99	1.5(-2)	5.3(23)±2.0(23)
IRAS 21078 11	21:09:21.37	+52:22:38.1	-6.0	0.32	229.1±59.2	5.16	3.8(-3)	1.3(23)±4.4(22)
IRAS 21078 12	21:09:21.83	+52:22:34.0	-5.3	0.28	41.4±8.6	4.03	1.8(-2)	6.4(23)±2.0(23)
IRAS 21078 13	21:09:21.83	+52:22:33.0	-5.3	0.33	298.1±0.9	3.96	2.2(-3)	7.9(22)±1.6(22)
IRAS 21078 14	21:09:21.49	+52:22:38.8	-5.8	0.28	286.2±2.2	3.29	1.9(-3)	6.8(22)±1.4(22)
NGC7538 IRS9 1 C	23:14:01.75	+61:27:19.8	-56.5	0.64	200.5±0.9	46.09	3.7(-2)	1.3(24)±2.6(23)
NGC7538 IRS9 2	23:14:02.05	+61:27:19.7	-57.7	0.26	189.4±18.4	6.12	5.2(-3)	1.8(23)±4.1(22)
NGC7538 IRS9 3	23:14:02.21	+61:27:18.9	-58.4	0.27	194.6±21.8	4.65	3.8(-3)	1.4(23)±3.1(22)
NGC7538 IRS9 4	23:14:02.15	+61:27:20.1	-57.9	0.27	104.2±52.4	4.44	7.0(-3)	2.5(23)±1.4(23)
NGC7538 IRS9 5	23:14:01.64	+61:27:21.2	-58.5	0.22	263.4±7.7	3.27	2.0(-3)	7.0(22)±1.4(22)
NGC7538 IRS9 6	23:14:01.89	+61:27:20.9	-58.8	0.32	84.5±22.5	2.81	5.5(-3)	2.0(23)±6.8(22)
NGC7538 IRS9 7	23:14:02.02	+61:27:20.6	-58.5	0.27	203.8±29.4	2.71	2.1(-3)	7.6(22)±1.9(22)
NGC7538 IRS9 8	23:14:02.34	+61:27:19.8	-58.0	0.19	134.8±70.6	2.33	2.8(-3)	1.0(23)±5.8(22)
S87 IRS1 1 C	19:46:20.64	+24:35:38.8	+22.9	0.61	112.0±5.2	37.31	4.8(-2)	1.7(24)±3.4(23)
S87 IRS1 2	19:46:20.59	+24:35:36.6	+22.5	0.38	84.4±27.0	8.24	1.4(-2)	5.0(23)±2.0(23)
S87 IRS1 3	19:46:20.13	+24:35:29.4	+22.0	0.32	63.5±40.1	6.77	1.6(-2)	5.5(23)±4.0(23)
S87 IRS1 4	19:46:19.87	+24:35:28.4	+22.2	0.28	28.4±7.4	6.60	3.9(-2)	1.3(24)±5.0(23)
S87 IRS1 5	19:46:20.02	+24:35:28.8	+21.2	0.25	53.2±9.9	5.92	1.7(-2)	5.9(23)±1.7(23)

Notes. a(b) = a×10^b.

TABLE A.1: continued.

Position	α J(2000)	δ J(2000)	v_{LSR} (km s ⁻¹)	σ_{line} (K)	T_{kin} (K)	$I_{1.37\text{mm}}$ (mJy beam ⁻¹)	τ_{ν}^{cont}	$N(\text{H}_2)$ (cm ⁻²)
S87 IRS1 6	19:46:20.61	+24:35:37.4	+22.9	0.48	100.3±52.1	5.42	7.7(-3)	2.7(23)±1.6(23)
S87 IRS1 7	19:46:20.22	+24:35:32.0	+22.7	0.24	69.9±16.4	3.31	6.9(-3)	2.4(23)±7.9(22)
S87 IRS1 8	19:46:19.94	+24:35:30.2	+21.5	0.24	107.7±60.5	3.22	4.2(-3)	1.5(23)±9.3(22)
S87 IRS1 9	19:46:19.99	+24:35:31.7	+21.8	0.35	186.6±43.0	2.58	1.9(-3)	6.8(22)±2.1(22)
S106 1	20:27:26.77	+37:22:47.7	+0.5	0.24	64.3±63.4	150.47	5.2(-1)	1.4(25)±1.6(25)
S106 2	20:27:25.49	+37:22:48.4	-0.5	0.57	124.8±30.8	50.13	6.9(-2)	2.4(24)±7.7(23)
S106 3	20:27:25.51	+37:22:46.9	-0.8	0.75	64.2±12.5	19.13	5.3(-2)	1.8(24)±5.3(23)
S106 4	20:27:26.99	+37:22:50.5	-2.4	0.25	96.7±38.8	8.05	1.4(-2)	5.0(23)±2.3(23)
W3 H2O 1	02:27:03.85	+61:52:25.0	-47.1	0.54	124.2±28.3	456.29	1.3(0)	2.5(25)±7.9(24)
W3 H2O 2	02:27:03.90	+61:52:24.3	-46.8	0.41	81.0±9.1	317.19	1.5(0)	2.8(25)±6.5(24)
W3 H2O 3 C	02:27:04.71	+61:52:24.7	-51.7	0.97	176.6±10.9	170.41	2.0(-1)	6.6(24)±1.4(24)
W3 H2O 4 C	02:27:04.55	+61:52:24.7	-49.7	1.27	166.4±9.0	161.32	2.1(-1)	6.6(24)±1.4(24)
W3 H2O 5	02:27:04.42	+61:52:25.4	-48.1	0.42	109.0±21.4	42.75	8.0(-2)	2.7(24)±7.8(23)
W3 IRS4 1 C	02:25:31.35	+62:06:20.8	-44.7	0.44	173.0±15.4	51.50	5.6(-2)	1.9(24)±4.3(23)
W3 IRS4 2	02:25:31.97	+62:06:23.7	-46.6	0.63	48.2±10.6	20.76	9.0(-2)	3.1(24)±9.6(23)
W3 IRS4 3	02:25:31.50	+62:06:22.2	-43.9	0.46	61.3±19.4	16.36	5.3(-2)	1.9(24)±7.4(23)
W3 IRS4 4	02:25:31.04	+62:06:19.8	-44.6	0.45	251.5±9.5	10.46	7.6(-3)	2.7(23)±5.5(22)
W3 IRS4 5	02:25:31.50	+62:06:22.9	-44.5	0.43	27.9±3.1	10.02	8.1(-2)	2.8(24)±6.7(23)
W3 IRS4 6	02:25:31.62	+62:06:24.9	-44.6	0.39	4.8±29.0	5.91	1.3(-2)	4.7(23)±2.0(23)

Notes. a(b) = a×10^b.

A.2 Spectral line properties

In Table A.2 the properties of the spectral lines detected in the CORE sample are summarized.

TABLE A.2: Emission lines detected in the CORE regions taken from Splatalogue (Remijan et al. 2007). The entries are taken from the CDMS and JPL catalogs (Müller et al. 2005; Pickett et al. 1998). Blended lines are indicated by a ‡. The mean and maximum line optical depth for each transition, that is fitted with XCLASS for all spectra, are computed considering all 120 positions (see Sect. 2.4.2).

Molecule	Transition	ν (GHz)	$\log A_{ul}$ ($\log \text{s}^{-1}$)	E_u/k_B (K)	Catalog	$\tau_{\text{mean}}^{\text{line}}$	$\tau_{\text{max}}^{\text{line}}$
^{13}CO	2 – 1	220.399	–6.22	15.9	JPL	1.5(0)	2.1(2)
C^{18}O	2 – 1	219.560	–6.22	15.8	JPL	1.1(–1)	5.4(0)
SO	6 ₅ – 5 ₄	219.949	–3.87	35.0	JPL	2.7(–1)	8.3(0)
OCS	18 – 17	218.903	–4.52	99.8	JPL	4.3(–1)	2.4(1)
O^{13}CS	18 – 17	218.199	–4.52	99.5	JPL	2.0(–3)	3.4(–1)
SO ₂	22 _{7,15} – 23 _{6,18}	219.276	–4.67	352.8	JPL	2.8(–2)	5.6(–1)
$^{34}\text{SO}_2$	11 _{1,11} – 10 _{0,10}	219.355	–3.96	60.2	JPL	1.1(–2)	1.1(–1)
DCN	3 – 2	217.239	–3.34	20.9	CDMS	9.7(–2)	2.2(1)
H ₂ CO	3 _{0,3} – 2 _{0,2}	218.222	–3.55	21.0	JPL	6.2(–1)	2.5(1)
H ₂ CO	3 _{2,2} – 2 _{2,1}	218.476	–3.80	68.1	JPL	1.5(–1)	5.8(0)
H ₂ CO	3 _{2,1} – 2 _{2,0}	218.760	–3.80	68.1	JPL	1.3(–1)	8.5(0)
H ₂ ^{13}CO	3 _{1,2} – 2 _{1,1}	219.909	–3.59	32.9	JPL	1.5(–2)	7.9(–1)
HNCO	10 _{1,10} – 9 _{1,9}	218.981	–3.85	101.1	CDMS	6.5(–2)	2.3(0)
HNCO	10 _{3,8} – 9 _{3,7}	219.657	–3.92	433.0	CDMS	1.0(–2)	1.7(–1)
HNCO	10 _{3,7} – 9 _{3,6}	219.657	–3.92	433.0	CDMS	1.0(–2)	1.7(–1)
HNCO	10 _{2,9} – 9 _{2,8}	219.734	–3.87	228.3	CDMS	5.8(–2)	9.9(–1)
HNCO	10 _{2,8} – 9 _{2,7}	219.737	–3.87	228.3	CDMS	6.5(–2)	9.9(–1)
HNCO	10 _{0,10} – 9 _{0,9}	219.798	–3.83	58.0	CDMS	1.3(–1)	3.9(0)
HNCO	10 _{1,9} – 9 _{1,8}	220.585	–3.84	101.5	CDMS	9.1(–2)	2.3(0)
HC ₃ N	24 – 23	218.325	–3.08	131.0	JPL	8.3(–2)	1.3(0)
HC ₃ N; $v_7 = 1^\ddagger$	24 – 23, $l = 1e$	218.861	–3.08	452.1	CDMS
HC ₃ N; $v_7 = 1$	24 – 23, $l = 1f$	219.174	–3.08	452.3	CDMS	2.5(–2)	5.8(–1)
HC ₃ N; $v_7 = 2$	24 – 23, $l = 0$	219.675	–3.08	773.5	CDMS	3.4(–3)	6.8(–2)
HC ₃ N; $v_7 = 2$	24 – 23, $l = 2e$	219.707	–3.08	776.8	CDMS	4.2(–3)	6.6(–2)
HC ₃ N; $v_7 = 2^\ddagger$	24 – 23, $l = 2f$	219.742	–3.08	776.8	CDMS
HCC ^{13}CN	24 – 23	217.420	–3.09	130.4	CDMS	1.1(–3)	1.8(–2)
CH ₃ OH	20 _{1,19} – 20 _{0,20E}	217.887	–4.47	508.4	CDMS	1.4(–2)	5.3(–1)
CH ₃ OH	4 _{2,3} – 3 _{1,2E}	218.440	–4.33	45.5	CDMS	5.7(–1)	4.0(1)
CH ₃ OH	25 _{3,23} – 24 _{4,20E}	219.984	–4.69	802.2	CDMS	1.5(–3)	9.6(–2)
CH ₃ OH	23 _{5,18} – 22 _{6,17E}	219.994	–4.76	775.9	CDMS	1.5(–3)	9.4(–2)
CH ₃ OH	8 _{0,8} – 7 _{1,6E}	220.079	–4.60	96.6	CDMS	9.5(–2)	5.0(0)
CH ₃ OH ‡	10 _{5,6} – 11 _{4,8E}	220.401	–4.95	251.6	CDMS
CH ₃ OH; $v_t = 1$	6 _{1,5} – 7 _{2,5A}	217.299	–4.37	373.9	CDMS	4.1(–2)	1.6(0)
CH ₃ OH; $v_t = 1$	15 _{6,9} – 16 _{5,11A}	217.643	–4.72	745.6	CDMS	1.0(–2)	1.5(–1)
CH ₃ OH; $v_t = 1$	15 _{6,10} – 16 _{5,12A}	217.643	–4.72	745.6	CDMS	1.0(–2)	1.5(–1)
CH ₃ CN	12 ₈ – 11 ₈	220.476	–3.45	525.6	JPL	7.4(–3)	4.0(–1)
CH ₃ CN	12 ₇ – 11 ₇	220.539	–3.38	418.6	JPL	2.2(–2)	7.7(–1)
CH ₃ CN	12 ₆ – 11 ₆	220.594	–3.32	325.9	JPL	9.2(–2)	2.7(0)

Notes. a(b) = $a \times 10^b$.

TABLE A.2: continued.

Molecule	Transition	ν (GHz)	$\log A_{ul}$ ($\log \text{s}^{-1}$)	E_u/k_B (K)	Catalog	$\tau_{\text{mean}}^{\text{line}}$	$\tau_{\text{max}}^{\text{line}}$
CH ₃ CN	12 ₅ – 11 ₅	220.641	–3.28	247.4	JPL	5.9(–2)	2.1(0)
CH ₃ CN	12 ₄ – 11 ₄	220.679	–3.25	183.1	JPL	1.1(–1)	2.7(0)
CH ₃ CN	12 ₃ – 11 ₃	220.709	–3.22	133.2	JPL	2.7(–1)	8.2(0)
CH ₃ CN	12 ₂ – 11 ₂	220.730	–3.21	97.4	JPL	2.1(–1)	4.7(0)
CH ₃ CN	12 ₁ – 11 ₁	220.743	–3.20	76.0	JPL	4.5(–1)	6.7(0)
CH ₃ CN	12 ₀ – 11 ₀	220.747	–3.20	68.9	JPL	3.3(–1)	6.7(0)
CH ₃ ¹³ CN	12 ₆ – 11 ₆	220.486	–3.16	325.9	JPL	9.8(–4)	3.1(–2)
CH ₃ ¹³ CN	12 ₅ – 11 ₅	220.532	–3.12	247.4	JPL	5.7(–3)	4.8(–1)
CH ₃ ¹³ CN	12 ₄ – 11 ₄	220.570	–3.09	183.1	JPL	1.3(–3)	3.9(–2)
CH ₃ ¹³ CN	12 ₃ – 11 ₃	220.600	–3.06	133.1	JPL	1.5(–2)	6.4(–1)
CH ₃ ¹³ CN	12 ₂ – 11 ₂	220.621	–3.05	97.4	JPL	2.0(–3)	6.3(–2)
CH ₃ ¹³ CN	12 ₁ – 11 ₁	220.634	–3.04	76.0	JPL	1.4(–2)	1.0(0)
CH ₃ ¹³ CN	12 ₀ – 11 ₀	220.638	–3.03	68.8	JPL	6.4(–2)	2.1(0)

Notes. a(b) = $a \times 10^b$.

A.3 Temperature maps

Figure A.1 shows the H₂CO and CH₃CN temperature maps derived with XCLASS for each CORE region (Sect. 2.3.2). Each core position is marked in red and the derived outer radii from the radial temperature profiles are indicated by dashed red circles.

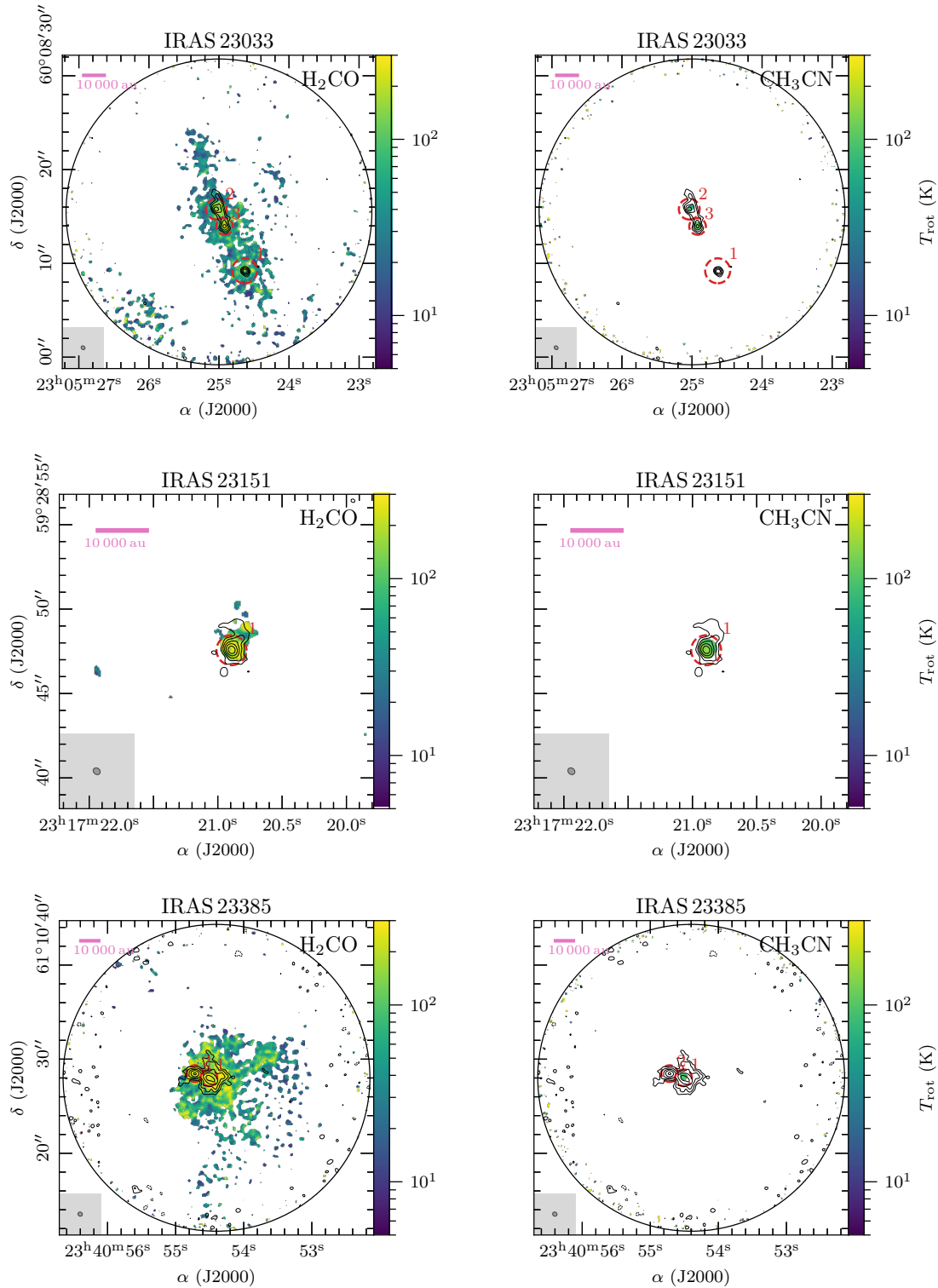


FIGURE A.1: Temperature maps derived with XCLASS. Each panel shows in color the temperature map (left: H_2CO , right: CH_3CN) and in black contours the 1.37 mm continuum emission. The dashed black contours show the $-5\sigma_{\text{cont}}$ emission and the solid black contours start at $5\sigma_{\text{cont}}$ with steps increasing by a factor of two (see Table 2.2 for values of σ_{cont} for each region). Each core is marked in red and the dashed red circle indicates the outer radius of the radial temperature fit (Sect. 2.3.2). The beam size is shown in the bottom left corner in each panel. The pink bar in the top left corner indicates a linear spatial scale of 10 000 au. The primary beam size is indicated by a black circle and for regions with no extended H_2CO temperature map a smaller field of view is shown.

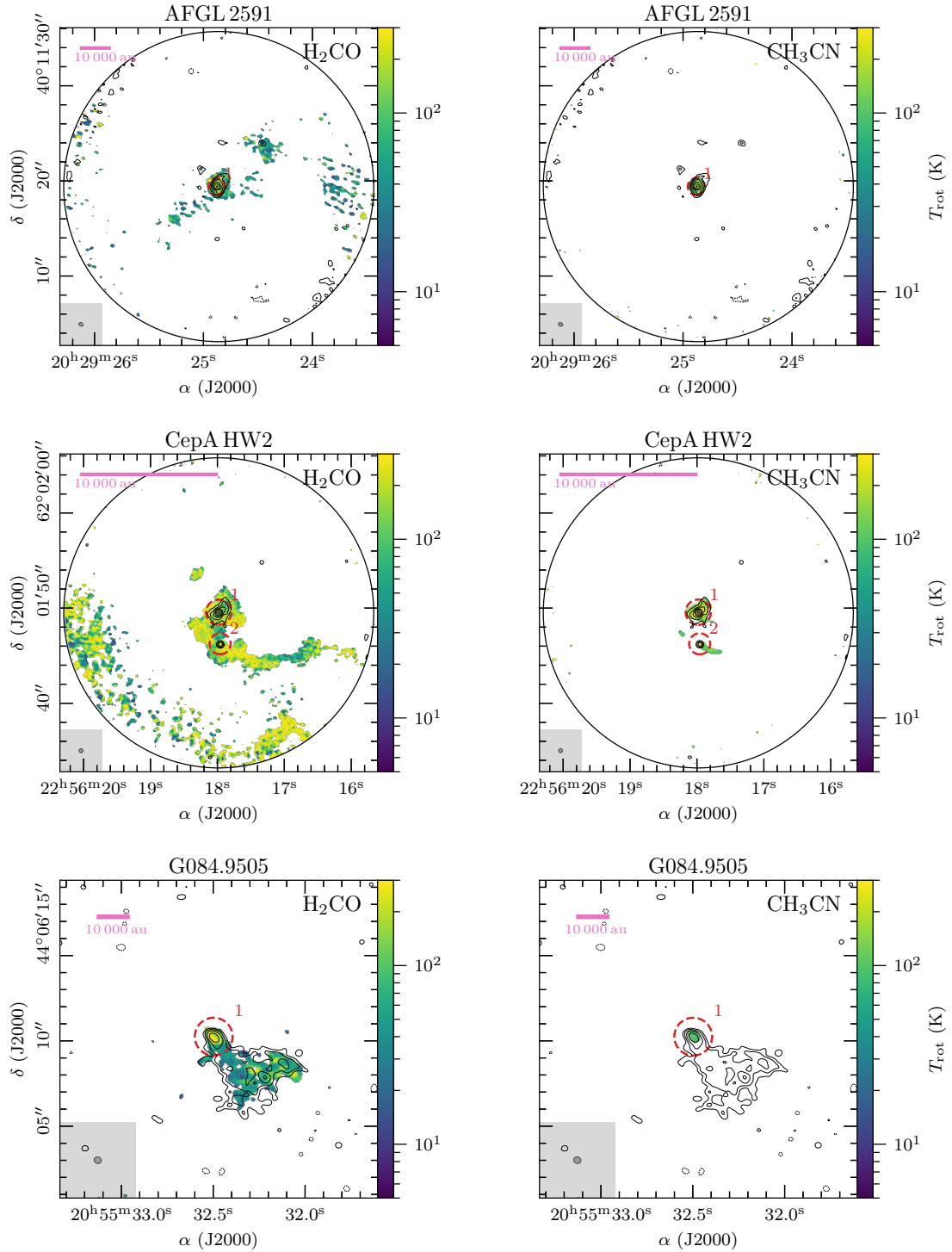


FIGURE A.1 (cont.): Temperature maps derived with XCLASS. Each panel shows in color the temperature map (*left*: H₂CO, *right*: CH₃CN) and in black contours the 1.37 mm continuum emission. The dashed black contours show the $-5\sigma_{\text{cont}}$ emission and the solid black contours start at $5\sigma_{\text{cont}}$ with steps increasing by a factor of two (see Table 2.2 for values of σ_{cont} for each region). Each core is marked in red and the dashed red circle indicates the outer radius of the radial temperature fit (Sect. 2.3.2). The beam size is shown in the bottom left corner in each panel. The pink bar in the top left corner indicates a linear spatial scale of 10 000 au. The primary beam size is indicated by a black circle and for regions with no extended H₂CO temperature map a smaller field of view is shown.

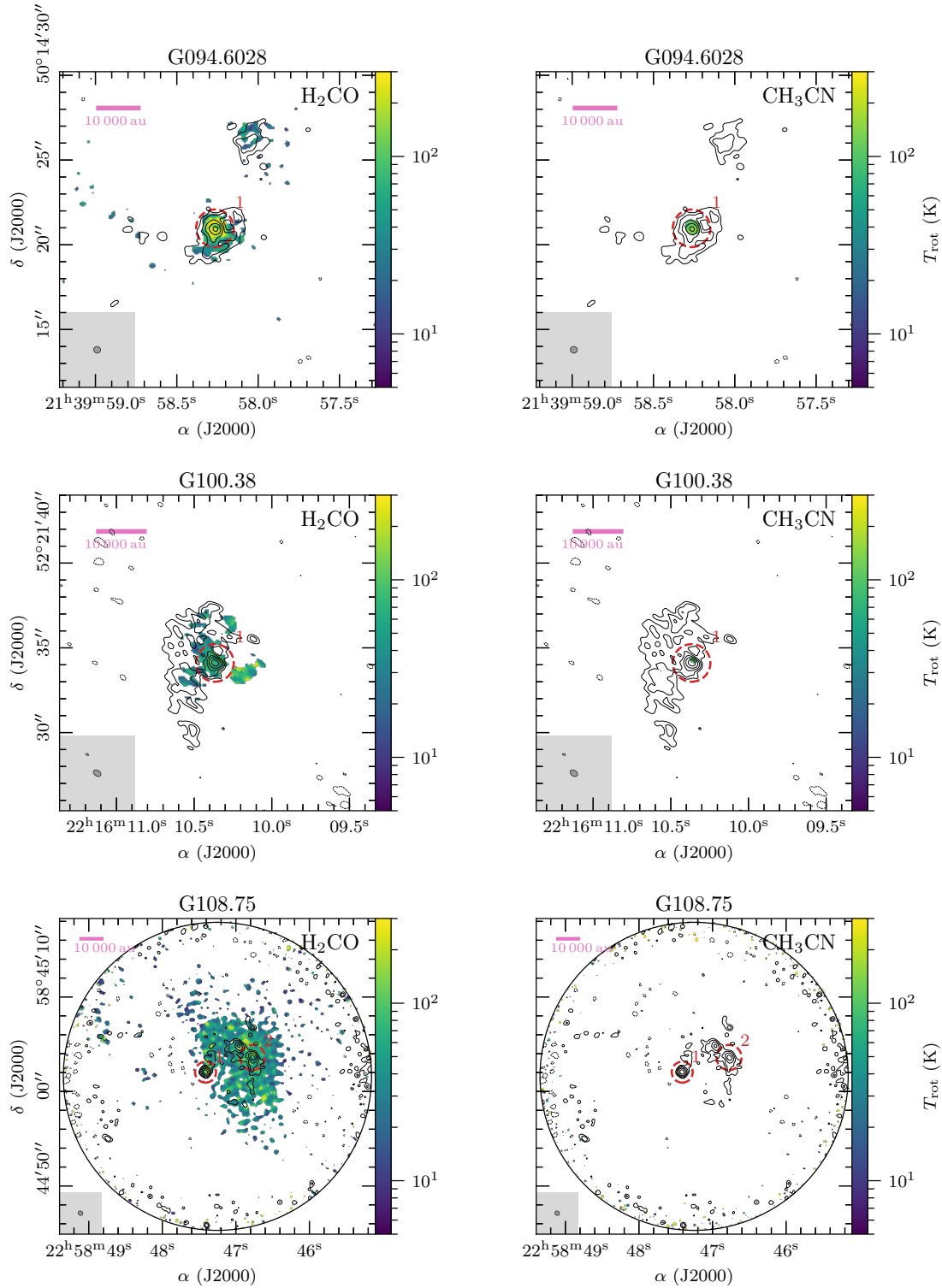


FIGURE A.1 (cont.): Temperature maps derived with XCLASS. Each panel shows in color the temperature map (*left*: H₂CO, *right*: CH₃CN) and in black contours the 1.37 mm continuum emission. The dashed black contours show the $-5\sigma_{\text{cont}}$ emission and the solid black contours start at $5\sigma_{\text{cont}}$ with steps increasing by a factor of two (see Table 2.2 for values of σ_{cont} for each region). Each core is marked in red and the dashed red circle indicates the outer radius of the radial temperature fit (Sect. 2.3.2). The beam size is shown in the bottom left corner in each panel. The pink bar in the top left corner indicates a linear spatial scale of 10 000 au. The primary beam size is indicated by a black circle and for regions with no extended H₂CO temperature map a smaller field of view is shown.

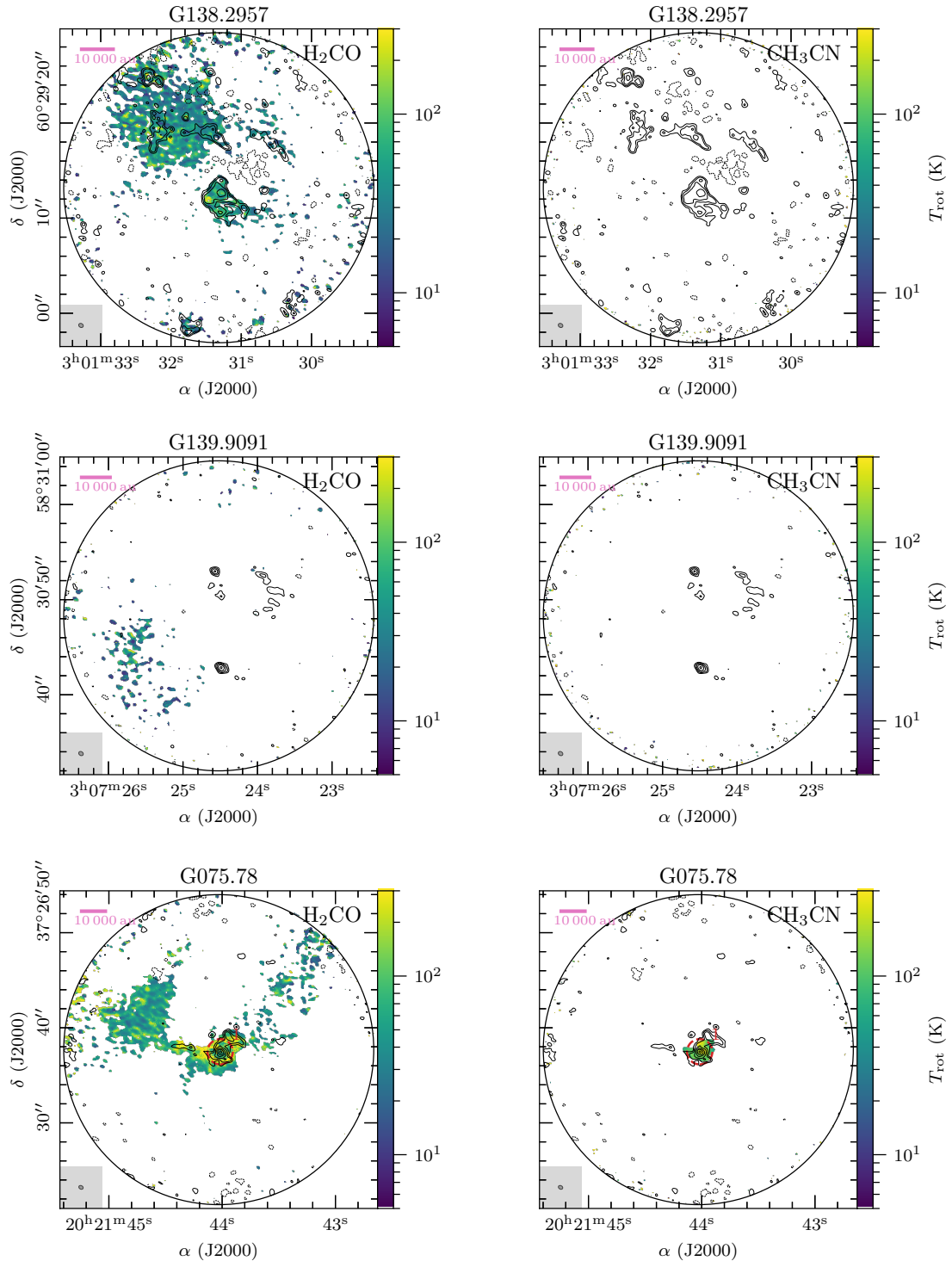


FIGURE A.1 (cont.): Temperature maps derived with XCLASS. Each panel shows in color the temperature map (*left*: H₂CO, *right*: CH₃CN) and in black contours the 1.37 mm continuum emission. The dashed black contours show the $-5\sigma_{\text{cont}}$ emission and the solid black contours start at $5\sigma_{\text{cont}}$ with steps increasing by a factor of two (see Table 2.2 for values of σ_{cont} for each region). Each core is marked in red and the dashed red circle indicates the outer radius of the radial temperature fit (Sect. 2.3.2). The beam size is shown in the bottom left corner in each panel. The pink bar in the top left corner indicates a linear spatial scale of 10 000 au. The primary beam size is indicated by a black circle and for regions with no extended H₂CO temperature map a smaller field of view is shown.

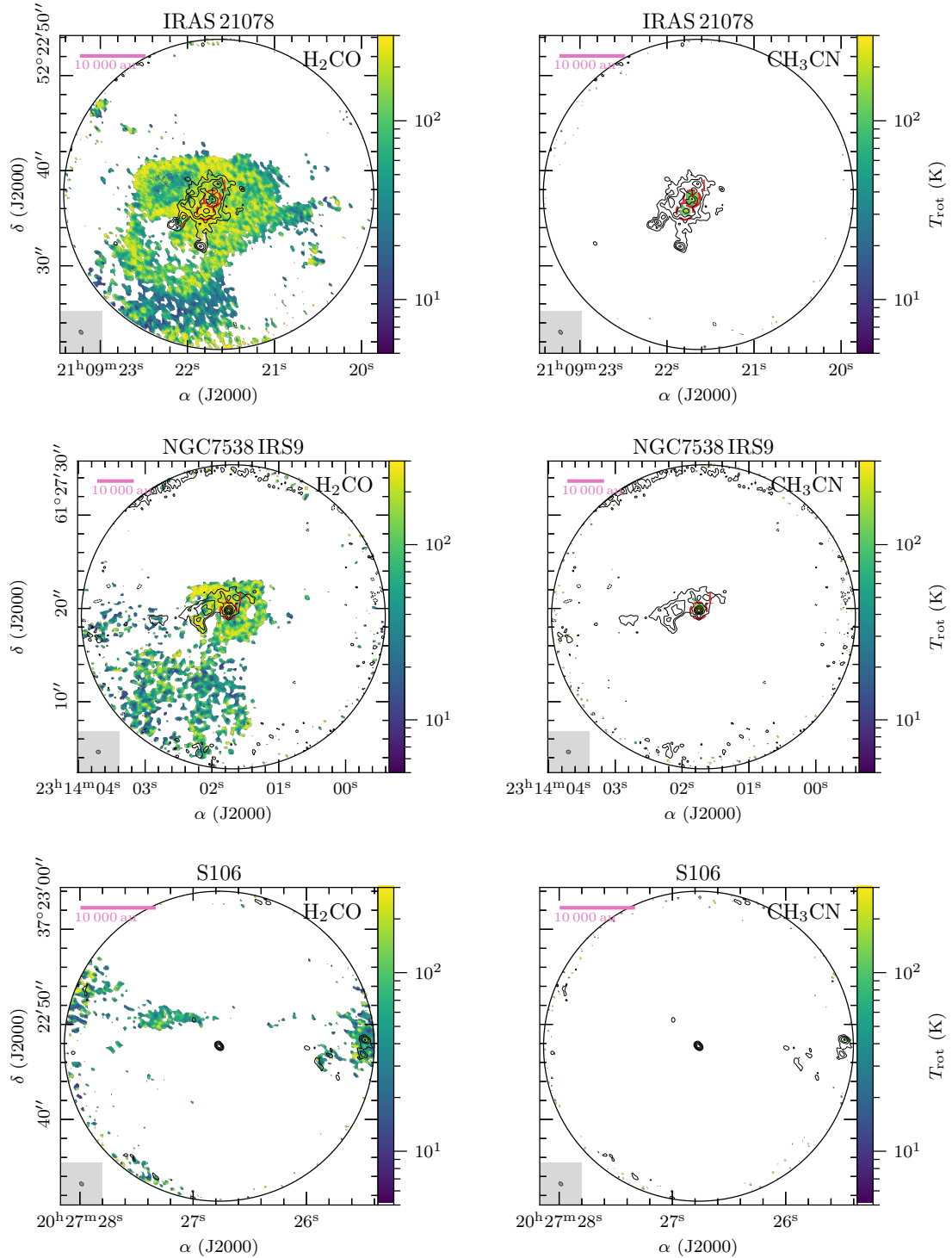


FIGURE A.1 (cont.): Temperature maps derived with XCLASS. Each panel shows in color the temperature map (*left*: H₂CO, *right*: CH₃CN) and in black contours the 1.37 mm continuum emission. The dashed black contours show the $-5\sigma_{\text{cont}}$ emission and the solid black contours start at $5\sigma_{\text{cont}}$ with steps increasing by a factor of two (see Table 2.2 for values of σ_{cont} for each region). Each core is marked in red and the dashed red circle indicates the outer radius of the radial temperature fit (Sect. 2.3.2). The beam size is shown in the bottom left corner in each panel. The pink bar in the top left corner indicates a linear spatial scale of 10 000 au. The primary beam size is indicated by a black circle and for regions with no extended H₂CO temperature map a smaller field of view is shown.

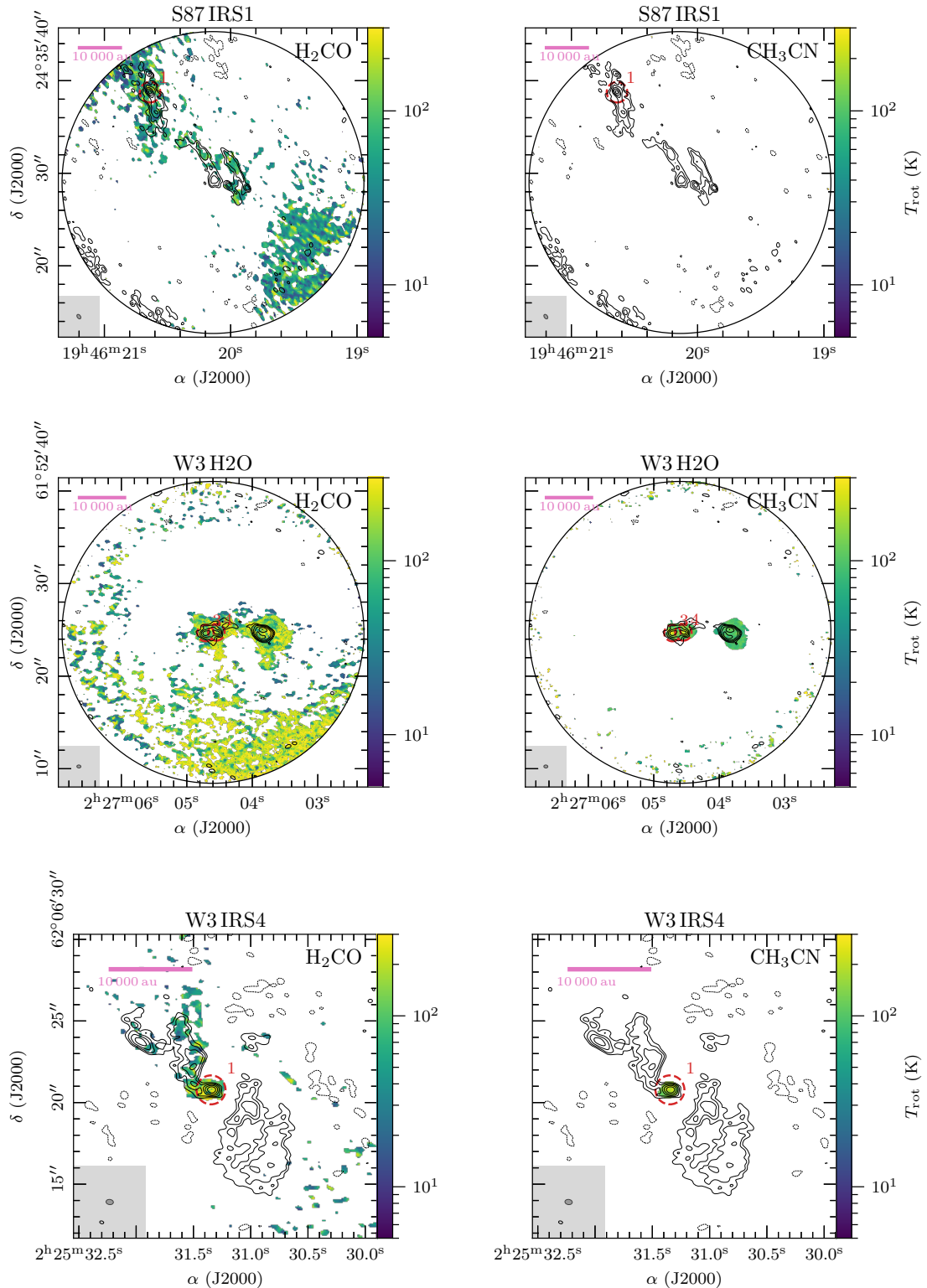


FIGURE A.1 (cont.): Temperature maps derived with XCLASS. Each panel shows in color the temperature map (*left*: H_2CO , *right*: CH_3CN) and in black contours the 1.37 mm continuum emission. The dashed black contours show the $-5\sigma_{\text{cont}}$ emission and the solid black contours start at $5\sigma_{\text{cont}}$ with steps increasing by a factor of two (see Table 2.2 for values of σ_{cont} for each region). Each core is marked in red and the dashed red circle indicates the outer radius of the radial temperature fit (Sect. 2.3.2). The beam size is shown in the bottom left corner in each panel. The pink bar in the top left corner indicates a linear spatial scale of 10 000 au. The primary beam size is indicated by a black circle and for regions with no extended H_2CO temperature map a smaller field of view is shown.

A.4 Abundance histograms

Figure A.2 shows a histogram of the abundance ratio relative to $N(\text{C}^{18}\text{O})$ for each molecule complementary to the column density histograms discussed in Sect. 2.4.2.

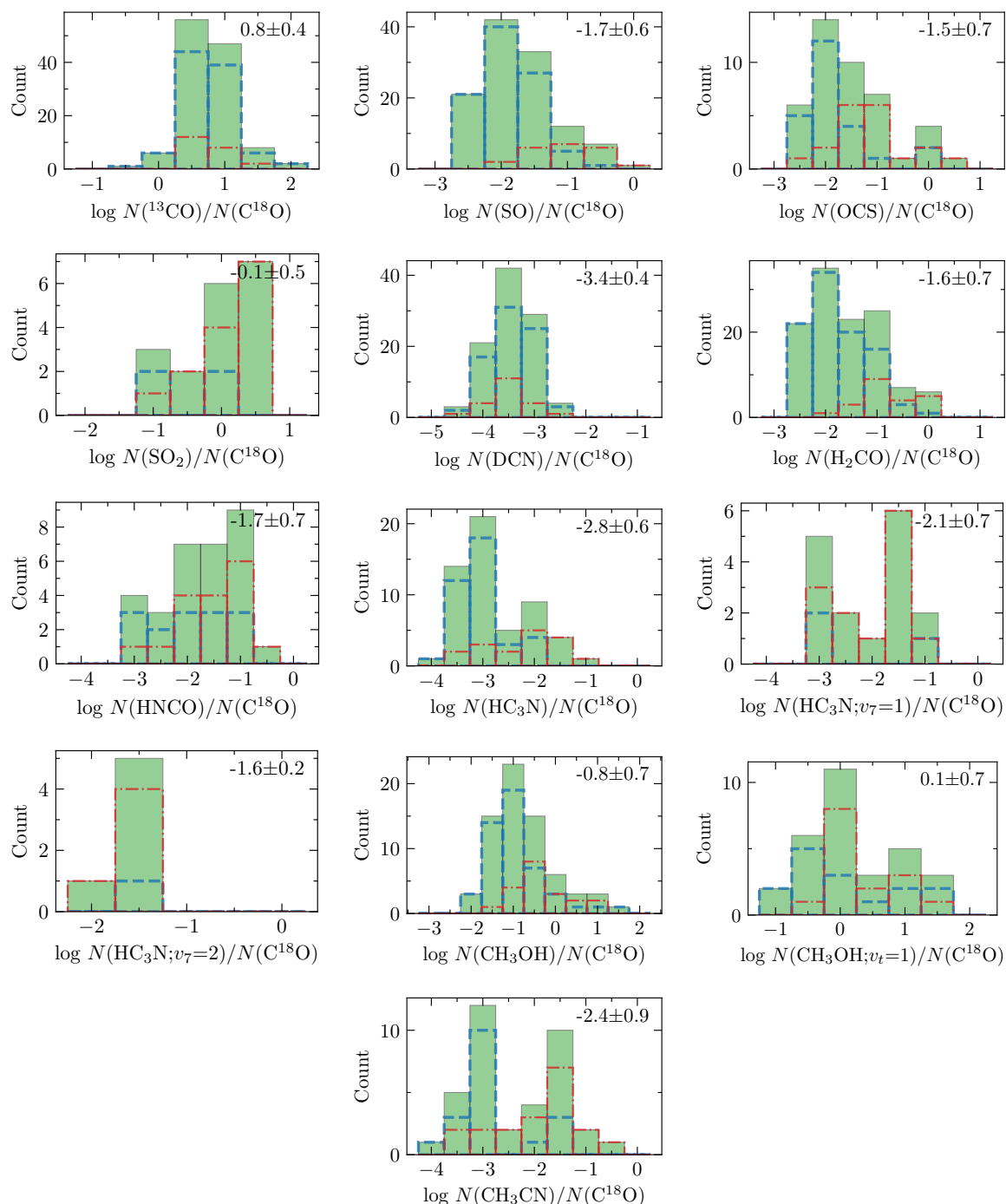


FIGURE A.2: Abundance ratio histograms. Abundance ratio histograms of all 120 positions are shown in green (upper limits are not included). Separate abundance ratio histograms of the core and non-core positions are indicated by the dash-dotted red and dashed blue lines, respectively.

A.5 Column density results

Tables A.3 and A.4 show the derived column densities for all molecules fitted with XCLASS (Sect. 2.4.2)². The upper and lower errors are estimated using the MCMC error estimation algorithm in XCLASS. If the fitting results do not match our defined criteria for a good fit (further explained in Sect. 2.4.2), the results are considered as upper limits.

²The tables are online available at <https://cdsarc.u-strasbg.fr/viz-bin/cat/J/A+A/648/A66>.

TABLE A.3: Molecular column densities (^{13}CO , C^{18}O , SO , OCS , SO_2 , DCN , H_2CO) derived with XCLASS in the CORE sample.

Position	$N(^{13}\text{CO})$ (cm^{-2})	$N(\text{C}^{18}\text{O})$ (cm^{-2})	$N(\text{SO})$ (cm^{-2})	$N(\text{OCS})$ (cm^{-2})	$N(\text{SO}_2)$ (cm^{-2})	$N(\text{DCN})$ (cm^{-2})	$N(\text{H}_2\text{CO})$ (cm^{-2})
IRAS 23033 1	8.4(17) ^{+9.1(16)} _{-1.2(17)}	5.3(16) ^{+5.8(16)} _{-1.7(16)}	1.7(15) ^{+1.7(15)} _{-3.5(14)}	<9.5(14)	<1.1(16)	<1.5(13)	7.3(15) ^{+2.4(15)} _{-1.5(15)}
IRAS 23033 2	7.6(17) ^{+1.8(17)} _{-8.4(16)}	1.9(17) ^{+1.0(17)} _{-3.9(16)}	2.5(16) ^{+1.1(16)} _{-4.6(15)}	9.5(15) ^{+5.0(15)} _{-1.3(15)}	3.4(16) ^{+3.1(16)} _{-1.4(16)}	1.4(14) ^{+7.7(13)} _{-2.9(13)}	2.9(16) ^{+2.3(15)} _{-4.7(15)}
IRAS 23033 3	1.2(18) ^{+1.7(17)} _{-1.0(17)}	2.6(17) ^{+5.4(16)} _{-4.5(16)}	2.8(16) ^{+1.6(15)} _{-1.5(15)}	2.4(16) ^{+4.3(15)} _{-3.7(15)}	4.7(16) ^{+3.2(16)} _{-1.4(16)}	8.3(13) ^{+1.4(13)} _{-8.0(12)}	6.6(16) ^{+1.4(16)} _{-5.1(15)}
IRAS 23033 4	8.2(17) ^{+2.8(17)} _{-9.6(16)}	2.4(17) ^{+6.4(16)} _{-6.0(16)}	2.3(15) ^{+2.1(15)} _{-8.0(14)}	<1.8(14)	<1.4(16)	7.2(13) ^{+7.7(13)} _{-3.2(13)}	3.4(15) ^{+1.2(15)} _{-9.2(14)}
IRAS 23033 5	8.0(17) ^{+2.0(17)} _{-7.4(16)}	1.3(17) ^{+1.8(17)} _{-3.2(16)}	6.3(14) ^{+1.2(14)} _{-5.0(14)}	<3.9(14)	<1.3(16)	1.3(14) ^{+2.1(13)} _{-4.8(13)}	2.2(15) ^{+1.1(15)} _{-1.3(15)}
IRAS 23151 1	1.8(18) ^{+2.5(17)} _{-1.5(17)}	6.9(17) ^{+1.0(17)} _{-7.4(16)}	4.0(16) ^{+1.5(15)} _{-5.5(15)}	1.5(16) ^{+3.3(15)} _{-1.5(15)}	5.1(17) ^{+3.8(16)} _{-1.9(16)}	4.4(13) ^{+9.9(13)} _{-3.4(13)}	3.8(16) ^{+5.4(15)} _{-6.8(15)}
IRAS 23151 2	6.4(17) ^{+6.9(16)} _{-1.1(17)}	2.1(17) ^{+7.5(16)} _{-3.2(16)}	7.9(15) ^{+1.8(15)} _{-1.2(15)}	7.6(14) ^{+8.2(13)} _{-6.5(14)}	<1.8(16)	6.0(13) ^{+9.2(13)} _{-4.1(13)}	9.1(15) ^{+1.6(15)} _{-3.5(15)}
IRAS 23151 3	6.7(17) ^{+1.2(17)} _{-1.0(17)}	4.0(17) ^{+5.9(16)} _{-6.2(16)}	8.3(15) ^{+5.2(15)} _{-1.9(15)}	2.0(15) ^{+1.1(16)} _{-7.5(14)}	<1.5(16)	2.1(13) ^{+1.2(14)} _{-1.2(13)}	3.1(15) ^{+9.7(14)} _{-6.2(14)}
IRAS 23151 4	2.8(17) ^{+1.1(17)} _{-5.6(16)}	2.3(17) ^{+9.5(16)} _{-3.2(16)}	3.3(15) ^{+1.1(15)} _{-3.8(14)}	7.1(14) ^{+1.5(14)} _{-5.8(14)}	<2.7(16)	2.8(13) ^{+1.6(13)} _{-1.6(13)}	2.5(15) ^{+5.9(14)} _{-9.8(14)}
IRAS 23151 5	9.5(18) ^{+4.8(16)} _{-8.9(16)}	1.3(17) ^{+5.1(16)} _{-4.4(16)}	4.3(15) ^{+1.2(15)} _{-9.4(14)}	<3.7(14)	<1.5(16)	7.1(13) ^{+2.2(14)} _{-3.8(13)}	7.7(14) ^{+1.4(15)} _{-2.7(14)}
IRAS 23385 1	9.3(17) ^{+2.3(17)} _{-1.5(17)}	2.6(17) ^{+1.4(17)} _{-3.5(16)}	1.1(16) ^{+3.8(15)} _{-1.6(15)}	1.2(16) ^{+1.7(15)} _{-2.1(15)}	<1.5(16)	9.8(13) ^{+6.3(13)} _{-2.8(13)}	2.8(16) ^{+4.7(15)} _{-2.8(15)}
IRAS 23385 2	6.2(17) ^{+2.2(17)} _{-1.1(17)}	2.1(17) ^{+1.6(17)} _{-2.8(16)}	2.2(15) ^{+1.9(15)} _{-7.5(14)}	1.3(15) ^{+6.2(15)} _{-6.9(14)}	<1.7(18)	2.3(13) ^{+1.1(14)} _{-1.0(13)}	1.9(16) ^{+6.0(15)} _{-4.6(15)}
IRAS 23385 3	4.3(17) ^{+5.9(16)} _{-1.1(17)}	2.3(17) ^{+1.5(17)} _{-3.5(16)}	5.6(15) ^{+2.1(15)} _{-2.4(15)}	9.6(14) ^{+1.9(15)} _{-4.2(14)}	<2.0(16)	1.3(14) ^{+8.6(13)} _{-3.7(13)}	2.1(16) ^{+5.7(15)} _{-4.4(15)}
IRAS 23385 4	1.0(18) ^{+1.9(17)} _{-1.9(17)}	9.5(16) ^{+1.2(17)} _{-2.8(16)}	4.6(15) ^{+1.8(15)} _{-1.3(15)}	8.9(14) ^{+1.8(14)} _{-7.2(14)}	<1.6(16)	4.3(13) ^{+3.1(13)} _{-2.4(13)}	2.4(16) ^{+7.2(15)} _{-4.7(15)}
IRAS 23385 5	5.8(17) ^{+2.1(17)} _{-1.6(17)}	7.1(16) ^{+8.2(16)} _{-3.3(16)}	4.3(15) ^{+1.0(15)} _{-1.4(15)}	<6.1(14)	<1.2(16)	4.4(13) ^{+1.0(14)} _{-3.1(13)}	1.2(16) ^{+4.5(15)} _{-2.7(15)}
IRAS 23385 6	6.5(17) ^{+1.5(17)} _{-1.7(17)}	1.2(17) ^{+8.6(16)} _{-4.6(16)}	3.5(15) ^{+1.7(15)} _{-8.0(14)}	<2.6(14)	<1.1(16)	7.6(13) ^{+2.1(14)} _{-6.5(13)}	1.3(16) ^{+5.3(15)} _{-1.4(15)}
IRAS 23385 7	1.3(18) ^{+3.3(17)} _{-3.7(17)}	1.2(17) ^{+7.4(16)} _{-5.3(16)}	1.4(16) ^{+6.9(15)} _{-7.4(15)}	<8.8(14)	<1.0(16)	3.1(13) ^{+3.8(13)} _{-1.5(13)}	1.6(16) ^{+1.1(16)} _{-5.7(15)}
IRAS 23385 8	3.8(18) ^{+5.4(17)} _{-6.8(17)}	8.4(16) ^{+5.0(16)} _{-4.8(16)}	1.3(15) ^{+4.9(14)} _{-3.6(14)}	1.6(15) ^{+1.2(16)} _{-6.7(14)}	<3.8(16)	5.7(13) ^{+3.5(14)} _{-1.7(13)}	6.1(15) ^{+2.1(15)} _{-1.9(15)}

 Notes. a(b) = $a \times 10^b$

TABLE A.3: continued.

Position	$N(^{13}\text{CO})$ (cm^{-2})	$N(\text{C}^{18}\text{O})$ (cm^{-2})	$N(\text{SO})$ (cm^{-2})	$N(\text{OCS})$ (cm^{-2})	$N(\text{SO}_2)$ (cm^{-2})	$N(\text{DCN})$ (cm^{-2})	$N(\text{H}_2\text{CO})$ (cm^{-2})
AFGL 2591 1	4.6(18) ^{+3.1(17)} _{-2.4(17)}	4.1(17) ^{+6.0(16)} _{-3.6(16)}	1.1(17) ^{+3.8(15)} _{-6.8(15)}	4.1(16) ^{+5.7(15)} _{-4.2(15)}	1.3(18) ^{+2.2(17)} _{-1.3(17)}	1.1(14) ^{+4.6(13)} _{-3.3(13)}	5.0(16) ^{+7.9(15)} _{-3.8(15)}
AFGL 2591 2	6.6(17) ^{+1.5(17)} _{-6.8(16)}	6.0(17) ^{+9.7(16)} _{-5.9(16)}	1.3(15) ^{+7.1(14)} _{-6.1(14)}	<1.6(15)	<1.3(16)	<1.0(13)	1.4(15) ^{+3.9(14)} _{-4.3(14)}
AFGL 2591 3	6.3(17) ^{+2.0(17)} _{-1.0(17)}	2.7(17) ^{+3.1(16)} _{-4.9(16)}	4.8(15) ^{+2.0(16)} _{-2.8(15)}	<1.7(17)	<2.4(16)	4.7(13) ^{+4.4(13)} _{-1.2(13)}	1.0(15) ^{+1.0(15)} _{-2.1(14)}
AFGL 2591 4	9.8(17) ^{+1.7(17)} _{-9.9(16)}	1.9(17) ^{+8.3(16)} _{-2.2(16)}	6.3(15) ^{+1.6(15)} _{-1.2(15)}	<1.5(15)	<2.1(16)	2.8(13) ^{+1.1(14)} _{-1.8(13)}	2.4(15) ^{+1.2(15)} _{-3.9(14)}
CepA HW2 1	1.1(18) ^{+4.8(17)} _{-2.4(17)}	5.6(17) ^{+1.4(17)} _{-6.2(16)}	1.4(17) ^{+2.3(16)} _{-1.9(16)}	3.6(16) ^{+9.3(15)} _{-2.0(15)}	1.3(18) ^{+1.2(17)} _{-1.1(17)}	1.4(14) ^{+4.1(13)} _{-6.4(13)}	5.4(17) ^{+4.8(16)} _{-3.0(16)}
CepA HW2 2	1.1(18) ^{+1.4(17)} _{-1.5(17)}	5.6(17) ^{+4.8(16)} _{-9.9(16)}	5.1(16) ^{+2.1(16)} _{-5.5(15)}	1.2(16) ^{+2.3(16)} _{-2.1(15)}	3.3(17) ^{+1.2(17)} _{-5.2(16)}	2.2(13) ^{+1.1(13)} _{-1.9(13)}	8.6(16) ^{+2.9(16)} _{-1.0(16)}
CepA HW2 3	2.2(18) ^{+2.6(17)} _{-4.1(17)}	7.5(17) ^{+5.5(16)} _{-5.0(16)}	3.0(16) ^{+6.8(15)} _{-4.6(15)}	2.0(16) ^{+5.5(15)} _{-2.5(15)}	9.1(16) ^{+1.5(16)} _{-1.3(16)}	9.2(14) ^{+1.6(13)} _{-2.9(13)}	5.4(16) ^{+1.2(16)} _{-6.8(15)}
CepA HW2 4	9.9(18) ^{+2.3(16)} _{-2.3(16)}	1.2(17) ^{+5.3(16)} _{-5.9(16)}	<1.1(14)	<1.0(14)	<1.7(16)	<9.7(12)	<1.8(14)
CepA HW2 5	9.9(17) ^{+1.3(17)} _{-1.1(17)}	2.9(17) ^{+1.1(17)} _{-4.6(16)}	1.2(16) ^{+1.4(15)} _{-2.7(15)}	<7.5(14)	<1.0(16)	3.7(13) ^{+8.7(13)} _{-2.3(13)}	8.8(15) ^{+2.8(15)} _{-7.8(14)}
G084.9505 1	5.9(17) ^{+2.3(17)} _{-1.2(17)}	1.1(17) ^{+9.3(16)} _{-3.1(16)}	2.7(15) ^{+2.9(14)} _{-7.2(14)}	3.4(15) ^{+2.0(15)} _{-7.4(14)}	<8.2(17)	1.1(14) ^{+3.6(13)} _{-2.7(13)}	1.8(16) ^{+6.5(15)} _{-1.3(15)}
G084.9505 2	2.5(17) ^{+1.3(17)} _{-1.1(16)}	4.1(16) ^{+1.4(16)} _{-2.9(16)}	1.0(15) ^{+5.9(14)} _{-3.2(14)}	<4.7(14)	<1.2(16)	6.2(12) ^{+3.2(12)} _{-5.1(12)}	7.6(14) ^{+9.1(14)} _{-1.8(14)}
G084.9505 3	1.1(17) ^{+1.2(17)} _{-1.4(16)}	5.1(16) ^{+4.7(16)} _{-2.5(16)}	1.4(15) ^{+1.2(15)} _{-4.5(14)}	<1.5(14)	<1.0(16)	1.8(13) ^{+4.6(13)} _{-1.4(13)}	3.4(15) ^{+4.4(15)} _{-8.2(14)}
G084.9505 4	1.5(17) ^{+4.3(16)} _{-4.7(16)}	2.6(16) ^{+2.5(16)} _{-4.1(15)}	1.6(15) ^{+6.7(14)} _{-7.6(14)}	<1.9(14)	<3.5(18)	1.4(13) ^{+6.9(13)} _{-5.0(12)}	1.3(15) ^{+1.0(15)} _{-6.7(14)}
G084.9505 5	6.8(17) ^{+4.1(17)} _{-1.5(17)}	9.3(16) ^{+1.6(17)} _{-2.7(16)}	1.8(15) ^{+6.2(14)} _{-1.2(15)}	<2.3(14)	<1.2(16)	4.9(13) ^{+6.6(13)} _{-3.5(13)}	6.7(14) ^{+5.8(14)} _{-3.6(14)}
G084.9505 6	2.2(17) ^{+1.7(17)} _{-2.1(16)}	5.3(16) ^{+2.4(16)} _{-2.7(16)}	2.0(15) ^{+1.5(15)} _{-1.2(15)}	8.9(14) ^{+3.0(15)} _{-4.2(14)}	<4.0(16)	1.1(13) ^{+1.3(12)} _{-9.6(12)}	2.3(15) ^{+3.1(15)} _{-1.5(15)}
G084.9505 7	6.7(17) ^{+4.0(17)} _{-1.8(17)}	1.1(17) ^{+7.4(16)} _{-5.2(16)}	2.0(15) ^{+2.5(15)} _{-9.6(14)}	8.3(14) ^{+1.7(15)} _{-4.9(14)}	<1.0(16)	1.5(13) ^{+6.9(12)} _{-1.3(13)}	6.0(14) ^{+5.5(14)} _{-3.7(14)}
G084.9505 8	4.1(17) ^{+1.4(17)} _{-1.2(17)}	4.9(16) ^{+4.3(16)} _{-2.3(16)}	4.2(14) ^{+1.7(14)} _{-3.1(14)}	<5.5(14)	<3.0(16)	2.6(12) ^{+3.8(12)} _{-1.2(12)}	7.7(14) ^{+3.8(14)} _{-5.4(14)}
G094.6028 1	1.5(18) ^{+3.5(17)} _{-1.0(17)}	3.1(16) ^{+1.8(16)} _{-9.5(15)}	2.7(16) ^{+4.0(15)} _{-3.5(15)}	3.2(16) ^{+8.4(15)} _{-6.6(15)}	6.5(16) ^{+2.9(16)} _{-2.8(16)}	1.0(14) ^{+6.0(13)} _{-1.5(13)}	4.1(16) ^{+8.0(15)} _{-9.7(15)}

Notes. a(b) = a×10^b

TABLE A.3: continued.

Position	$N(^{13}\text{CO})$ (cm^{-2})	$N(\text{C}^{18}\text{O})$ (cm^{-2})	$N(\text{SO})$ (cm^{-2})	$N(\text{OCS})$ (cm^{-2})	$N(\text{SO}_2)$ (cm^{-2})	$N(\text{DCN})$ (cm^{-2})	$N(\text{H}_2\text{CO})$ (cm^{-2})
G094.6028 2	3.4(17) ^{+1.5(17)} _{-6.0(16)}	6.4(16) ^{+1.9(16)} _{-4.1(16)}	1.0(15) ^{+1.0(14)} _{-8.4(14)}	<2.9(14)	<1.3(16)	6.9(13) ^{+2.0(13)} _{-3.1(13)}	5.9(14) ^{+5.4(14)} _{-8.9(13)}
G094.6028 3	1.1(18) ^{+2.3(17)} _{-4.9(17)}	1.2(17) ^{+8.0(16)} _{-4.1(16)}	4.8(14) ^{+1.2(15)} _{-1.6(14)}	<1.3(14)	<1.3(16)	3.6(13) ^{+8.9(12)} _{-3.2(13)}	5.5(14) ^{+9.8(14)} _{-1.6(14)}
G094.6028 4	4.0(17) ^{+1.5(17)} _{-6.2(16)}	6.2(16) ^{+4.0(16)} _{-2.9(16)}	1.3(15) ^{+4.6(14)} _{-6.7(14)}	<1.3(15)	<1.2(16)	5.2(13) ^{+5.5(13)} _{-2.0(13)}	7.1(14) ^{+6.1(14)} _{-2.8(14)}
G094.6028 5	4.7(17) ^{+3.6(16)} _{-1.2(17)}	5.3(16) ^{+6.4(16)} _{-2.5(16)}	2.8(14) ^{+4.1(14)} _{-4.1(13)}	<4.0(14)	<1.0(16)	5.8(13) ^{+1.8(14)} _{-2.6(13)}	5.5(14) ^{+9.8(13)} _{-4.2(14)}
G094.6028 6	1.3(18) ^{+1.4(17)} _{-2.8(17)}	8.2(16) ^{+3.8(16)} _{-2.7(16)}	1.0(15) ^{+5.9(14)} _{-3.8(14)}	<1.1(15)	<1.3(16)	2.8(13) ^{+3.0(13)} _{-2.0(13)}	7.1(14) ^{+6.5(14)} _{-2.9(14)}
G094.6028 7	5.3(17) ^{+1.1(17)} _{-9.4(16)}	5.7(16) ^{+6.7(15)} _{-4.0(16)}	5.3(14) ^{+4.2(13)} _{-4.1(14)}	8.8(14) ^{+2.4(15)} _{-4.5(14)}	<1.2(16)	1.5(13) ^{+9.4(13)} _{-4.4(12)}	3.7(14) ^{+2.0(14)} _{-2.4(14)}
G094.6028 8	4.8(17) ^{+3.3(17)} _{-7.7(16)}	4.8(16) ^{+4.4(16)} _{-2.0(16)}	<2.5(14)	<1.9(14)	<1.8(16)	<1.9(12)	1.2(14) ^{+1.6(13)} _{-2.5(13)}
G100.38 1	6.6(17) ^{+1.5(17)} _{-1.2(17)}	1.7(17) ^{+1.6(17)} _{-5.0(16)}	1.6(16) ^{+2.7(15)} _{-2.4(15)}	2.0(15) ^{+4.0(15)} _{-1.5(15)}	4.3(16) ^{+1.9(16)} _{-1.1(16)}	2.7(13) ^{+3.3(12)} _{-2.4(13)}	4.9(15) ^{+1.8(15)} _{-1.3(15)}
G100.38 2	5.5(17) ^{+1.9(17)} _{-1.0(17)}	2.2(17) ^{+1.7(17)} _{-6.9(16)}	1.8(15) ^{+2.5(15)} _{-6.7(14)}	<1.0(18)	<1.3(16)	<6.5(12)	4.3(14) ^{+4.0(14)} _{-2.1(14)}
G100.38 3	3.6(17) ^{+5.6(16)} _{-3.3(16)}	1.4(17) ^{+7.8(16)} _{-3.5(16)}	8.4(14) ^{+5.3(14)} _{-6.4(14)}	<6.7(16)	<3.0(16)	<1.0(13)	3.1(14) ^{+2.0(14)} _{-1.6(14)}
G100.38 4	7.1(16) ^{+4.5(16)} _{-3.7(16)}	1.7(17) ^{+6.8(16)} _{-6.7(16)}	2.6(15) ^{+4.4(15)} _{-1.8(15)}	<1.4(14)	<8.9(17)	<9.0(12)	1.2(15) ^{+3.5(14)} _{-1.1(15)}
G100.38 5	2.7(17) ^{+3.0(17)} _{-1.6(17)}	9.0(16) ^{+7.7(16)} _{-4.8(16)}	1.1(15) ^{+1.1(14)} _{-9.2(14)}	<4.4(14)	<1.2(16)	<7.1(12)	<1.1(14)
G108.75 1	6.9(17) ^{+3.1(16)} _{-8.5(16)}	2.1(17) ^{+1.8(17)} _{-2.9(16)}	3.8(15) ^{+2.5(14)} _{-6.7(14)}	8.9(14) ^{+4.6(14)} _{-7.2(14)}	<1.9(16)	4.1(13) ^{+3.7(14)} _{-2.2(13)}	6.6(15) ^{+2.9(15)} _{-1.7(15)}
G108.75 2	4.4(17) ^{+1.6(17)} _{-2.3(17)}	5.2(16) ^{+1.4(16)} _{-3.2(16)}	1.0(15) ^{+6.5(14)} _{-4.6(14)}	<1.9(14)	<2.7(18)	5.0(13) ^{+2.3(13)} _{-4.4(13)}	3.5(15) ^{+3.4(15)} _{-1.1(15)}
G108.75 3	4.3(17) ^{+3.8(16)} _{-6.3(16)}	5.8(16) ^{+4.6(16)} _{-3.0(16)}	6.0(14) ^{+6.6(14)} _{-3.1(14)}	<1.4(14)	<1.1(16)	2.0(13) ^{+2.3(13)} _{-1.5(13)}	8.4(14) ^{+4.3(14)} _{-4.5(14)}
G108.75 4	4.5(17) ^{+7.8(16)} _{-4.5(16)}	1.3(17) ^{+1.5(17)} _{-6.1(16)}	5.2(14) ^{+7.3(14)} _{-2.3(14)}	<5.4(15)	<1.0(16)	1.4(13) ^{+3.7(13)} _{-9.0(12)}	1.7(15) ^{+3.1(15)} _{-3.9(14)}
G108.75 5	4.8(17) ^{+5.6(17)} _{-1.4(17)}	5.0(16) ^{+4.9(16)} _{-2.5(16)}	1.2(15) ^{+3.1(15)} _{-6.9(14)}	3.5(14) ^{+9.8(14)} _{-7.3(13)}	<1.0(16)	5.2(13) ^{+1.0(14)} _{-4.5(13)}	3.9(15) ^{+2.4(14)} _{-2.6(15)}
G108.75 6	8.8(17) ^{+2.7(17)} _{-1.2(17)}	1.0(17) ^{+1.1(17)} _{-3.9(16)}	1.2(15) ^{+2.8(15)} _{-6.7(14)}	<2.6(14)	<1.1(16)	1.1(14) ^{+7.4(13)} _{-6.8(13)}	8.5(14) ^{+1.0(15)} _{-2.5(14)}

Notes. a(b) = $a \times 10^b$

TABLE A.3: continued.

Position	$N(^{13}\text{CO})$ (cm^{-2})	$N(\text{C}^{18}\text{O})$ (cm^{-2})	$N(\text{SO})$ (cm^{-2})	$N(\text{OCS})$ (cm^{-2})	$N(\text{SO}_2)$ (cm^{-2})	$N(\text{DCN})$ (cm^{-2})	$N(\text{H}_2\text{CO})$ (cm^{-2})
G138.2957 1	6.3(17) ^{+1.9(17)} _{-6.7(16)}	6.1(16) ^{+4.1(16)} _{-2.6(16)}	1.1(15) ^{+1.4(14)} _{-9.8(14)}	<2.1(14)	<1.2(16)	3.6(13) ^{+5.6(13)} _{-1.4(13)}	4.8(14) ^{+3.2(14)} _{-2.9(14)}
G138.2957 2	4.0(17) ^{+5.9(16)} _{-2.9(16)}	1.5(17) ^{+7.0(16)} _{-4.0(16)}	1.0(15) ^{+1.2(15)} _{-8.1(14)}	<9.9(17)	<1.0(16)	7.8(13) ^{+2.2(14)} _{-3.4(13)}	5.0(14) ^{+3.7(14)} _{-2.5(14)}
G138.2957 3	7.4(17) ^{+1.8(17)} _{-1.7(17)}	1.7(17) ^{+1.1(17)} _{-5.7(16)}	1.4(15) ^{+1.6(15)} _{-6.9(14)}	<5.5(14)	<2.4(18)	1.1(14) ^{+1.2(14)} _{-1.4(13)}	1.6(15) ^{+1.5(15)} _{-4.0(14)}
G138.2957 4	1.3(18) ^{+7.0(17)} _{-4.5(17)}	1.9(17) ^{+1.0(17)} _{-8.0(16)}	1.8(15) ^{+2.6(15)} _{-6.8(14)}	<5.0(14)	<1.5(16)	9.7(13) ^{+9.6(13)} _{-8.5(13)}	4.3(14) ^{+1.4(14)} _{-1.8(14)}
G138.2957 5	6.0(17) ^{+1.9(17)} _{-8.2(16)}	1.7(17) ^{+9.6(16)} _{-6.1(16)}	9.9(14) ^{+8.5(14)} _{-6.0(14)}	<1.0(14)	<2.4(16)	1.8(13) ^{+7.2(13)} _{-1.0(13)}	6.4(14) ^{+3.4(14)} _{-1.9(14)}
G138.2957 6	6.4(17) ^{+3.2(17)} _{-1.2(17)}	4.2(16) ^{+5.9(16)} _{-1.3(16)}	8.4(14) ^{+2.8(15)} _{-3.9(14)}	<4.1(14)	<6.3(18)	4.8(13) ^{+8.9(13)} _{-3.1(13)}	1.1(15) ^{+1.8(15)} _{-5.2(14)}
G138.2957 7	6.2(17) ^{+1.7(17)} _{-1.6(17)}	6.1(16) ^{+3.9(16)} _{-1.2(16)}	4.8(14) ^{+5.6(14)} _{-2.9(14)}	<1.7(14)	<1.1(16)	1.2(14) ^{+7.1(13)} _{-5.2(13)}	1.2(15) ^{+1.5(15)} _{-4.6(14)}
G138.2957 8	7.2(17) ^{+1.2(17)} _{-7.5(16)}	1.0(17) ^{+8.8(16)} _{-4.7(16)}	1.2(15) ^{+9.7(14)} _{-4.5(14)}	<6.1(14)	<2.0(16)	<1.3(13)	9.4(14) ^{+6.6(14)} _{-3.9(14)}
G138.2957 9	7.9(17) ^{+1.2(17)} _{-1.8(17)}	1.9(17) ^{+1.2(17)} _{-6.3(16)}	7.6(14) ^{+8.4(14)} _{-1.7(14)}	<8.7(14)	1.5(16) ^{+9.8(15)} _{-1.3(15)}	1.9(13) ^{+5.4(13)} _{-1.3(13)}	1.5(15) ^{+2.3(15)} _{-1.9(14)}
G138.2957 10	5.5(17) ^{+6.4(17)} _{-4.6(16)}	7.1(16) ^{+4.8(16)} _{-3.8(16)}	1.1(15) ^{+8.3(14)} _{-6.2(14)}	<7.2(14)	<1.7(16)	<1.4(13)	7.2(14) ^{+7.9(14)} _{-8.8(13)}
G138.2957 11	1.1(18) ^{+2.6(17)} _{-9.6(16)}	1.1(17) ^{+2.0(17)} _{-3.9(16)}	9.2(14) ^{+9.7(14)} _{-4.7(14)}	<9.2(15)	<8.9(18)	<7.2(12)	1.7(15) ^{+1.9(15)} _{-9.0(14)}
G138.2957 12	3.9(17) ^{+2.7(17)} _{-1.2(17)}	1.1(17) ^{+7.9(16)} _{-4.0(16)}	1.3(15) ^{+6.2(14)} _{-1.0(15)}	<3.2(14)	<1.7(18)	5.6(13) ^{+3.5(13)} _{-4.8(13)}	7.1(14) ^{+1.3(15)} _{-3.7(14)}
G139.9091 1	3.4(17) ^{+1.4(17)} _{-5.6(16)}	2.1(16) ^{+1.4(16)} _{-3.4(15)}	<3.8(14)	<1.1(14)	<8.3(18)	<8.4(12)	1.1(15) ^{+1.3(14)} _{-9.6(14)}
G139.9091 2	1.4(18) ^{+4.0(17)} _{-2.6(17)}	5.3(16) ^{+4.6(16)} _{-2.1(16)}	1.9(15) ^{+1.2(15)} _{-5.2(14)}	<3.0(14)	<1.6(16)	<2.2(13)	1.3(15) ^{+6.5(14)} _{-1.0(15)}
G139.9091 3	6.6(17) ^{+9.3(16)} _{-7.0(16)}	5.6(16) ^{+3.1(16)} _{-2.7(16)}	5.7(14) ^{+7.6(14)} _{-2.9(14)}	<1.0(18)	<1.0(16)	5.8(13) ^{+2.5(14)} _{-3.0(13)}	3.6(14) ^{+9.9(14)} _{-1.0(14)}
G139.9091 4	1.2(18) ^{+1.6(17)} _{-4.7(17)}	1.0(17) ^{+2.6(16)} _{-4.3(16)}	5.6(14) ^{+1.9(14)} _{-3.9(14)}	<1.9(14)	<1.0(16)	<1.2(13)	7.2(14) ^{+5.8(14)} _{-5.1(14)}
G075.78 1	2.2(18) ^{+5.2(17)} _{-2.9(17)}	3.1(17) ^{+6.9(16)} _{-3.9(16)}	1.5(17) ^{+2.4(16)} _{-1.7(16)}	2.0(16) ^{+3.8(15)} _{-8.6(14)}	8.0(17) ^{+5.4(16)} _{-6.2(16)}	1.2(14) ^{+2.6(13)} _{-3.1(13)}	5.8(16) ^{+2.2(16)} _{-7.5(15)}
G075.78 2	9.0(17) ^{+2.6(17)} _{-7.3(16)}	5.6(17) ^{+8.3(16)} _{-6.0(16)}	1.8(16) ^{+4.8(15)} _{-3.1(15)}	<1.4(14)	<1.1(16)	9.6(13) ^{+7.3(13)} _{-2.1(13)}	1.9(15) ^{+1.4(15)} _{-5.9(14)}

Notes. a(b) = $a \times 10^b$

TABLE A.3: continued.

Position	$N(^{13}\text{CO})$ (cm^{-2})	$N(\text{C}^{18}\text{O})$ (cm^{-2})	$N(\text{SO})$ (cm^{-2})	$N(\text{OCS})$ (cm^{-2})	$N(\text{SO}_2)$ (cm^{-2})	$N(\text{DCN})$ (cm^{-2})	$N(\text{H}_2\text{CO})$ (cm^{-2})
G075.78 3	6.4(17) ^{+2.9(17)} _{-7.4(16)}	2.4(17) ^{+7.7(16)} _{-8.2(16)}	2.1(15) ^{+8.8(14)} _{-6.6(14)}	<3.2(14)	<1.1(17)	<6.3(12)	7.3(14) ^{+3.4(14)} _{-2.1(14)}
G075.78 4	2.0(18) ^{+3.1(17)} _{-5.7(17)}	1.6(17) ^{+5.7(16)} _{-3.5(16)}	2.2(15) ^{+9.4(14)} _{-5.6(14)}	<3.5(14)	<2.7(16)	1.3(14) ^{+8.1(13)} _{-3.1(13)}	8.3(15) ^{+2.2(15)} _{-1.0(15)}
IRAS 21078 1	2.9(18) ^{+4.8(17)} _{-1.8(17)}	3.1(17) ^{+9.1(16)} _{-4.0(16)}	3.7(16) ^{+3.9(15)} _{-2.0(15)}	6.2(16) ^{+7.9(15)} _{-3.9(15)}	4.1(17) ^{+1.2(17)} _{-1.3(17)}	9.4(13) ^{+9.6(13)} _{-3.5(13)}	4.8(17) ^{+3.2(16)} _{-3.0(16)}
IRAS 21078 2	1.7(18) ^{+2.1(17)} _{-1.2(17)}	3.6(17) ^{+1.2(17)} _{-6.1(16)}	1.3(16) ^{+2.2(15)} _{-1.9(15)}	1.5(16) ^{+7.9(15)} _{-3.7(15)}	<1.3(16)	1.6(14) ^{+1.4(14)} _{-2.0(13)}	4.4(16) ^{+8.8(15)} _{-6.1(15)}
IRAS 21078 3	1.8(18) ^{+1.2(17)} _{-5.0(16)}	4.8(17) ^{+7.4(16)} _{-5.3(16)}	9.5(15) ^{+2.2(15)} _{-1.8(15)}	2.1(16) ^{+1.8(15)} _{-3.0(15)}	<1.5(16)	9.8(13) ^{+9.1(13)} _{-1.9(13)}	6.5(16) ^{+1.2(16)} _{-1.2(16)}
IRAS 21078 4	9.6(17) ^{+4.8(17)} _{-1.9(17)}	5.7(16) ^{+1.9(16)} _{-3.5(16)}	6.7(14) ^{+5.8(14)} _{-4.1(14)}	<3.4(14)	<1.9(16)	4.1(13) ^{+2.4(13)} _{-2.4(13)}	1.6(15) ^{+1.3(15)} _{-2.5(14)}
IRAS 21078 5	5.3(17) ^{+2.5(17)} _{-1.4(17)}	6.5(16) ^{+7.6(16)} _{-3.1(16)}	1.4(15) ^{+1.0(15)} _{-3.6(14)}	1.7(15) ^{+6.2(15)} _{-1.2(15)}	<1.2(16)	1.6(13) ^{+1.6(13)} _{-1.3(13)}	2.1(15) ^{+1.6(13)} _{-5.6(14)}
IRAS 21078 6	9.2(17) ^{+8.7(16)} _{-1.2(17)}	4.6(17) ^{+9.4(16)} _{-6.5(16)}	2.8(15) ^{+1.3(15)} _{-1.1(14)}	1.9(15) ^{+3.0(15)} _{-1.4(15)}	<1.1(16)	7.6(13) ^{+4.2(13)} _{-3.2(13)}	1.2(16) ^{+1.0(16)} _{-4.1(15)}
IRAS 21078 7	8.7(17) ^{+5.9(17)} _{-1.1(17)}	1.7(17) ^{+1.4(17)} _{-6.4(16)}	1.9(15) ^{+3.3(14)} _{-4.8(14)}	<1.0(14)	<2.4(18)	1.3(14) ^{+7.0(13)} _{-3.8(13)}	4.8(15) ^{+1.2(15)} _{-1.4(15)}
IRAS 21078 8	5.8(17) ^{+1.3(17)} _{-1.5(17)}	1.7(17) ^{+1.1(17)} _{-6.7(16)}	3.7(15) ^{+1.2(15)} _{-9.0(14)}	1.0(15) ^{+1.2(14)} _{-8.8(14)}	<9.8(17)	1.3(14) ^{+8.5(13)} _{-3.7(13)}	3.9(15) ^{+1.8(15)} _{-7.2(14)}
IRAS 21078 9	3.2(17) ^{+1.3(17)} _{-5.3(16)}	8.5(16) ^{+1.4(16)} _{-4.9(16)}	1.7(15) ^{+8.6(14)} _{-4.8(14)}	<1.9(14)	<6.5(16)	4.6(13) ^{+6.1(13)} _{-2.0(12)}	5.2(15) ^{+5.9(14)} _{-1.4(15)}
IRAS 21078 10	7.1(17) ^{+1.5(17)} _{-1.2(17)}	1.3(17) ^{+8.1(16)} _{-3.6(16)}	7.6(15) ^{+4.8(15)} _{-1.9(15)}	7.9(14) ^{+1.1(15)} _{-5.8(14)}	<1.2(16)	5.0(13) ^{+5.9(13)} _{-3.4(13)}	2.7(16) ^{+2.0(16)} _{-5.7(15)}
IRAS 21078 11	7.1(17) ^{+2.7(17)} _{-1.1(17)}	1.6(17) ^{+2.2(16)} _{-5.2(16)}	4.0(15) ^{+2.1(15)} _{-8.1(14)}	<1.1(15)	<1.4(16)	<8.5(14)	4.0(15) ^{+3.6(15)} _{-7.7(14)}
IRAS 21078 12	1.0(18) ^{+5.5(17)} _{-4.8(17)}	1.5(17) ^{+1.7(17)} _{-7.9(16)}	1.8(15) ^{+8.2(14)} _{-6.7(14)}	2.3(15) ^{+5.6(15)} _{-1.8(15)}	<1.4(16)	8.5(13) ^{+6.3(13)} _{-2.6(13)}	1.1(16) ^{+4.1(15)} _{-1.7(15)}
IRAS 21078 13	4.0(17) ^{+3.1(17)} _{-7.0(16)}	3.0(16) ^{+1.8(16)} _{-2.0(16)}	1.1(15) ^{+8.3(14)} _{-2.3(14)}	<2.2(14)	<1.0(19)	1.3(13) ^{+9.9(12)} _{-2.2(12)}	4.7(15) ^{+1.3(15)} _{-4.7(14)}
IRAS 21078 14	1.7(18) ^{+5.7(17)} _{-2.4(17)}	1.3(17) ^{+7.1(16)} _{-5.6(16)}	1.2(15) ^{+1.5(14)} _{-1.6(14)}	<4.3(14)	<1.6(16)	2.1(13) ^{+2.1(13)} _{-1.7(13)}	2.0(16) ^{+6.9(15)} _{-4.3(15)}
NGC7538 IRS9 1	2.4(18) ^{+6.3(17)} _{-3.3(17)}	2.2(17) ^{+1.1(17)} _{-5.3(16)}	4.0(16) ^{+4.3(15)} _{-4.7(15)}	2.1(16) ^{+4.7(15)} _{-1.7(15)}	7.0(17) ^{+1.7(17)} _{-2.0(17)}	1.1(14) ^{+2.8(13)} _{-2.7(13)}	3.1(17) ^{+5.5(16)} _{-3.2(16)}
NGC7538 IRS9 2	9.1(17) ^{+2.2(17)} _{-2.1(17)}	1.2(17) ^{+5.9(16)} _{-4.7(16)}	2.1(15) ^{+6.8(14)} _{-5.2(14)}	1.9(15) ^{+4.9(15)} _{-1.2(15)}	<1.5(16)	4.6(13) ^{+4.8(13)} _{-4.1(13)}	4.1(15) ^{+1.5(15)} _{-1.1(15)}

Notes. a(b) = $a \times 10^b$

TABLE A.3: continued.

Position	$N(^{13}\text{CO})$ (cm^{-2})	$N(\text{C}^{18}\text{O})$ (cm^{-2})	$N(\text{SO})$ (cm^{-2})	$N(\text{OCS})$ (cm^{-2})	$N(\text{SO}_2)$ (cm^{-2})	$N(\text{DCN})$ (cm^{-2})	$N(\text{H}_2\text{CO})$ (cm^{-2})
NGC7538 IRS9 3	6.6(17) ^{+9.9(16)} _{-5.8(16)}	1.3(17) ^{+9.8(16)} _{-4.0(16)}	1.8(15) ^{+2.4(14)} _{-5.6(14)}	<3.0(14)	<1.4(18)	1.3(14) ^{+5.6(13)} _{-3.9(13)}	4.3(15) ^{+2.2(15)} _{-6.9(14)}
NGC7538 IRS9 4	1.6(18) ^{+4.3(17)} _{-2.8(17)}	7.4(16) ^{+4.1(16)} _{-1.6(16)}	2.7(14) ^{+4.2(14)} _{-4.1(13)}	<3.5(14)	<1.0(16)	1.1(14) ^{+5.3(13)} _{-2.5(13)}	1.2(15) ^{+9.5(14)} _{-6.1(14)}
NGC7538 IRS9 5	6.8(18) ^{+1.5(18)} _{-1.0(18)}	2.6(17) ^{+6.0(16)} _{-6.7(16)}	1.1(15) ^{+2.7(14)} _{-3.7(14)}	<2.8(14)	<6.3(18)	5.9(13) ^{+8.1(13)} _{-3.0(13)}	2.1(16) ^{+7.6(15)} _{-5.6(15)}
NGC7538 IRS9 6	8.0(17) ^{+1.2(17)} _{-1.3(17)}	2.6(17) ^{+1.8(17)} _{-6.3(16)}	2.1(15) ^{+1.2(15)} _{-6.7(14)}	1.6(15) ^{+3.4(15)} _{-9.7(14)}	<2.2(16)	5.7(13) ^{+9.3(13)} _{-4.4(13)}	1.2(16) ^{+1.5(15)} _{-1.6(15)}
NGC7538 IRS9 7	6.9(17) ^{+3.3(17)} _{-1.3(17)}	2.2(17) ^{+8.6(16)} _{-5.2(16)}	2.0(15) ^{+5.1(14)} _{-4.1(14)}	1.6(15) ^{+2.5(14)} _{-1.5(15)}	<1.7(16)	5.0(13) ^{+2.1(13)} _{-3.2(13)}	1.3(16) ^{+5.4(15)} _{-3.8(15)}
NGC7538 IRS9 8	4.6(17) ^{+5.8(16)} _{-7.5(16)}	1.6(17) ^{+2.5(16)} _{-5.6(16)}	8.7(14) ^{+1.1(15)} _{-4.8(14)}	<1.0(14)	<1.4(16)	4.3(13) ^{+4.7(13)} _{-2.0(13)}	1.4(15) ^{+1.1(15)} _{-6.0(14)}
S87 IRS1 1	1.1(18) ^{+2.2(17)} _{-1.0(17)}	1.7(17) ^{+1.4(17)} _{-5.5(16)}	1.8(15) ^{+1.7(15)} _{-8.7(14)}	<1.1(15)	<3.8(16)	2.7(13) ^{+2.9(13)} _{-2.0(13)}	2.6(15) ^{+3.3(15)} _{-1.3(15)}
S87 IRS1 2	5.4(17) ^{+5.8(16)} _{-7.1(16)}	2.2(17) ^{+1.3(17)} _{-1.1(16)}	5.8(14) ^{+2.0(14)} _{-2.8(14)}	<6.4(15)	<1.1(16)	7.7(13) ^{+1.3(14)} _{-3.2(13)}	1.0(15) ^{+1.3(15)} _{-1.9(14)}
S87 IRS1 3	5.0(17) ^{+9.3(16)} _{-4.4(16)}	1.7(17) ^{+3.7(16)} _{-6.3(16)}	7.1(14) ^{+6.3(14)} _{-2.4(14)}	<2.5(14)	<1.3(16)	<4.3(12)	6.6(14) ^{+6.7(14)} _{-2.5(14)}
S87 IRS1 4	6.8(17) ^{+3.9(17)} _{-3.3(16)}	1.4(17) ^{+9.1(16)} _{-3.9(16)}	8.4(14) ^{+1.2(15)} _{-4.9(14)}	<5.1(14)	<1.5(16)	2.0(13) ^{+9.1(12)} _{-1.7(13)}	6.5(14) ^{+1.9(14)} _{-2.0(14)}
S87 IRS1 5	1.0(18) ^{+5.3(16)} _{-1.1(17)}	1.1(17) ^{+5.5(16)} _{-5.1(16)}	3.7(15) ^{+1.1(15)} _{-1.6(14)}	<3.8(14)	<2.7(16)	<1.1(12)	1.0(15) ^{+1.6(15)} _{-2.1(14)}
S87 IRS1 6	1.9(18) ^{+6.3(17)} _{-7.9(17)}	1.8(17) ^{+3.8(16)} _{-5.7(16)}	6.6(14) ^{+7.3(14)} _{-2.6(14)}	<5.6(14)	<1.2(18)	1.1(14) ^{+2.1(14)} _{-8.2(13)}	1.2(15) ^{+1.7(15)} _{-5.3(14)}
S87 IRS1 7	5.6(17) ^{+9.9(16)} _{-5.7(16)}	1.4(17) ^{+5.5(16)} _{-7.9(16)}	4.2(14) ^{+3.1(14)} _{-8.9(13)}	<1.1(14)	<2.4(16)	9.7(13) ^{+1.9(13)} _{-4.1(13)}	1.1(15) ^{+1.1(15)} _{-4.1(14)}
S87 IRS1 8	3.9(18) ^{+7.6(17)} _{-7.6(17)}	1.2(17) ^{+1.8(17)} _{-5.6(16)}	6.3(14) ^{+2.4(14)} _{-3.7(14)}	<1.4(14)	<1.0(16)	8.5(13) ^{+4.3(14)} _{-5.9(13)}	1.1(15) ^{+1.2(15)} _{-3.0(14)}
S87 IRS1 9	7.4(17) ^{+9.6(16)} _{-1.2(17)}	1.6(17) ^{+1.3(17)} _{-6.2(16)}	2.0(15) ^{+9.0(14)} _{-8.1(13)}	<1.3(14)	<1.6(18)	<1.2(13)	2.5(15) ^{+1.2(15)} _{-1.1(15)}
S106 1	5.7(17) ^{+1.5(17)} _{-1.2(17)}	3.8(16) ^{+1.8(16)} _{-2.3(16)}	<2.3(14)	<4.0(14)	<1.3(16)	<2.2(12)	3.0(14) ^{+2.4(14)} _{-1.3(14)}
S106 2	1.3(18) ^{+3.6(17)} _{-1.0(17)}	3.3(17) ^{+1.6(17)} _{-5.1(16)}	1.6(16) ^{+5.2(15)} _{-2.0(15)}	5.2(15) ^{+2.4(15)} _{-1.6(15)}	<2.7(16)	1.9(14) ^{+7.4(13)} _{-5.3(13)}	1.7(16) ^{+3.8(15)} _{-2.6(15)}
S106 3	1.4(18) ^{+2.2(17)} _{-1.3(17)}	7.6(17) ^{+4.3(16)} _{-4.0(16)}	2.0(15) ^{+1.4(15)} _{-6.9(14)}	<1.6(15)	<5.7(16)	2.1(14) ^{+9.0(13)} _{-2.4(13)}	2.8(15) ^{+9.7(14)} _{-7.1(14)}

Notes. a(b) = $a \times 10^b$

TABLE A.3: continued.

Position	$N(^{13}\text{CO})$ (cm^{-2})	$N(\text{C}^{18}\text{O})$ (cm^{-2})	$N(\text{SO})$ (cm^{-2})	$N(\text{OCS})$ (cm^{-2})	$N(\text{SO}_2)$ (cm^{-2})	$N(\text{DCN})$ (cm^{-2})	$N(\text{H}_2\text{CO})$ (cm^{-2})
S106 4	6.8(17) ^{+1.3(17)} _{-1.3(17)}	2.5(17) ^{+4.6(16)} _{-3.2(16)}	9.0(14) ^{+4.8(14)} _{-7.4(14)}	<3.8(14)	<2.5(16)	1.3(14) ^{+5.2(13)} _{-3.1(13)}	9.3(14) ^{+4.4(14)} _{-5.6(14)}
W3 H2O 1	3.8(17) ^{+1.3(17)} _{-8.1(16)}	5.3(16) ^{+4.0(16)} _{-2.3(16)}	8.6(15) ^{+6.0(15)} _{-2.6(15)}	3.2(16) ^{+4.8(15)} _{-3.4(15)}	5.0(16) ^{+1.7(16)} _{-1.5(16)}	1.2(14) ^{+2.6(13)} _{-2.6(13)}	1.9(16) ^{+5.2(15)} _{-3.4(15)}
W3 H2O 2	5.7(17) ^{+5.3(16)} _{-4.9(16)}	1.7(16) ^{+2.2(15)} _{-6.6(15)}	4.0(15) ^{+9.8(14)} _{-9.4(14)}	1.3(16) ^{+2.8(15)} _{-1.3(15)}	2.9(16) ^{+2.1(16)} _{-1.2(16)}	3.7(13) ^{+2.2(13)} _{-1.6(13)}	1.0(16) ^{+3.1(15)} _{-8.6(14)}
W3 H2O 3	3.9(18) ^{+1.1(17)} _{-2.5(17)}	4.4(17) ^{+3.6(16)} _{-4.9(16)}	6.9(16) ^{+1.1(16)} _{-5.4(15)}	4.7(17) ^{+5.5(16)} _{-4.9(16)}	5.7(17) ^{+1.6(17)} _{-7.1(16)}	2.4(14) ^{+2.8(13)} _{-1.7(13)}	1.3(17) ^{+2.7(16)} _{-1.5(16)}
W3 H2O 4	1.3(18) ^{+1.3(17)} _{-1.2(17)}	3.9(17) ^{+6.7(16)} _{-3.9(16)}	1.6(17) ^{+1.6(16)} _{-2.1(16)}	8.5(17) ^{+1.5(16)} _{-1.5(16)}	7.7(17) ^{+6.8(16)} _{-7.6(16)}	4.4(14) ^{+3.2(13)} _{-2.0(13)}	2.2(17) ^{+2.5(16)} _{-2.2(16)}
W3 H2O 5	1.1(18) ^{+3.0(17)} _{-2.4(17)}	8.1(17) ^{+3.6(16)} _{-5.1(16)}	2.5(16) ^{+3.3(15)} _{-2.9(15)}	1.4(17) ^{+5.5(16)} _{-2.6(16)}	<1.4(16)	1.3(14) ^{+8.9(13)} _{-1.6(13)}	5.7(16) ^{+1.6(16)} _{-1.5(16)}
W3 IRS4 1	3.0(18) ^{+1.6(17)} _{-2.8(17)}	1.4(17) ^{+2.5(16)} _{-3.7(16)}	7.6(16) ^{+5.5(15)} _{-2.2(15)}	2.0(16) ^{+7.4(15)} _{-5.4(15)}	4.4(17) ^{+2.8(16)} _{-1.8(16)}	3.9(13) ^{+8.1(13)} _{-3.2(13)}	4.0(16) ^{+6.3(15)} _{-7.9(15)}
W3 IRS4 2	7.5(17) ^{+1.6(17)} _{-5.8(16)}	3.4(17) ^{+3.4(16)} _{-5.5(16)}	1.7(15) ^{+8.6(14)} _{-6.8(14)}	<1.0(14)	<1.7(18)	8.4(13) ^{+1.6(14)} _{-4.5(12)}	1.3(15) ^{+4.5(14)} _{-4.7(14)}
W3 IRS4 3	1.1(18) ^{+2.1(17)} _{-7.9(16)}	5.0(17) ^{+7.7(16)} _{-6.7(16)}	3.5(15) ^{+2.6(15)} _{-3.0(14)}	<9.0(14)	<1.5(16)	3.4(13) ^{+1.8(14)} _{-1.2(13)}	1.2(15) ^{+5.6(14)} _{-2.7(14)}
W3 IRS4 4	1.5(18) ^{+2.8(17)} _{-1.9(17)}	5.9(17) ^{+4.0(16)} _{-1.1(17)}	1.3(15) ^{+8.1(14)} _{-4.3(14)}	<1.0(15)	<1.7(16)	<5.9(12)	2.1(15) ^{+1.2(15)} _{-8.9(14)}
W3 IRS4 5	7.3(17) ^{+3.2(17)} _{-2.9(16)}	5.5(17) ^{+5.8(16)} _{-6.3(16)}	1.6(15) ^{+8.8(14)} _{-2.7(14)}	<1.6(15)	<2.1(16)	5.3(13) ^{+4.0(13)} _{-3.0(13)}	2.4(15) ^{+5.1(14)} _{-1.0(15)}
W3 IRS4 6	1.2(18) ^{+7.0(16)} _{-1.2(17)}	5.4(17) ^{+3.8(16)} _{-8.3(16)}	1.2(15) ^{+6.8(14)} _{-2.1(14)}	<9.0(14)	<1.1(16)	3.4(13) ^{+5.5(13)} _{-2.6(13)}	2.5(15) ^{+2.2(15)} _{-1.0(15)}

Notes. a(b) = $a \times 10^b$

TABLE A.4: Molecular column densities (HNCO, HC₃N, HC₃N;*v*₇=1, HC₃N;*v*₇=2, CH₃OH, CH₃OH;*v*_t=1, CH₃CN) derived with XCLASS in the CORE sample.

Position	$N(\text{HNCO})$ (cm ⁻²)	$N(\text{HC}_3\text{N})$ (cm ⁻²)	$N(\text{HC}_3\text{N};v_7=1)$ (cm ⁻²)	$N(\text{HC}_3\text{N};v_7=2)$ (cm ⁻²)	$N(\text{CH}_3\text{OH})$ (cm ⁻²)	$N(\text{CH}_3\text{OH};v_t=1)$ (cm ⁻²)	$N(\text{CH}_3\text{CN})$ (cm ⁻²)
IRAS 23033 1	<3.6(15)	<1.7(14)	<2.3(16)	<1.0(17)	1.5(16) ^{+9.0(15)} _{-6.5(15)}	<1.9(16)	<2.7(13)
IRAS 23033 2	1.3(15) ^{+7.3(14)} _{-6.3(14)}	9.9(14) ^{+6.2(14)} _{-1.9(14)}	<1.1(14)	<1.0(16)	5.3(16) ^{+5.3(15)} _{-1.1(16)}	7.5(16) ^{+7.7(16)} _{-6.6(16)}	4.6(14) ^{+6.9(13)} _{-3.3(13)}
IRAS 23033 3	5.5(15) ^{+2.7(15)} _{-1.5(15)}	3.3(15) ^{+5.8(14)} _{-5.9(14)}	8.5(14) ^{+9.5(14)} _{-4.5(14)}	<5.5(16)	8.5(16) ^{+3.6(16)} _{-1.2(16)}	1.8(17) ^{+6.0(16)} _{-6.4(16)}	1.8(15) ^{+2.7(14)} _{-2.4(14)}
IRAS 23033 4	3.6(16) ^{+3.7(15)} _{-3.1(16)}	1.1(14) ^{+2.3(14)} _{-6.4(13)}	<8.4(14)	<6.0(16)	1.1(16) ^{+2.9(16)} _{-7.0(15)}	<1.3(16)	<5.0(13)
IRAS 23033 5	<8.3(14)	5.4(13) ^{+3.4(13)} _{-3.7(13)}	<1.1(14)	<2.3(16)	<8.6(14)	<5.9(15)	<3.1(13)
IRAS 23151 1	1.5(16) ^{+2.7(15)} _{-1.9(15)}	4.3(14) ^{+1.2(15)} _{-2.2(14)}	<1.6(14)	<1.0(16)	1.8(17) ^{+4.8(16)} _{-3.2(16)}	7.5(17) ^{+3.7(17)} _{-2.5(17)}	1.2(16) ^{+6.2(15)} _{-2.9(15)}
IRAS 23151 2	4.9(14) ^{+7.5(14)} _{-3.0(14)}	<1.0(13)	<3.9(15)	<1.0(16)	1.9(16) ^{+2.5(16)} _{-1.2(16)}	1.6(17) ^{+4.6(16)} _{-1.6(17)}	2.1(14) ^{+1.8(14)} _{-9.8(13)}
IRAS 23151 3	<2.2(14)	<3.0(13)	<1.1(15)	<4.0(16)	8.6(15) ^{+2.6(16)} _{-4.5(15)}	<5.4(15)	9.8(13) ^{+1.1(14)} _{-2.1(13)}
IRAS 23151 4	<1.7(14)	<3.1(13)	<6.4(15)	<3.2(16)	9.1(15) ^{+1.8(16)} _{-8.8(15)}	<5.1(16)	<1.2(14)
IRAS 23151 5	<1.1(14)	<3.2(13)	<3.3(15)	<6.1(16)	<1.3(15)	<1.5(18)	<7.2(13)
IRAS 23385 1	4.1(14) ^{+2.8(14)} _{-1.2(14)}	1.2(15) ^{+2.7(14)} _{-3.1(14)}	<1.6(14)	<3.8(16)	2.6(16) ^{+4.2(15)} _{-3.7(15)}	3.2(17) ^{+2.5(18)} _{-2.5(17)}	4.1(14) ^{+7.6(13)} _{-3.6(13)}
IRAS 23385 2	<7.8(14)	9.1(13) ^{+1.6(14)} _{-6.1(13)}	<1.0(14)	<4.1(15)	2.5(16) ^{+9.3(15)} _{-6.2(15)}	<2.9(16)	7.2(13) ^{+1.3(14)} _{-3.6(13)}
IRAS 23385 3	<3.1(14)	2.3(14) ^{+1.5(14)} _{-8.5(13)}	<9.7(15)	<2.2(15)	2.6(16) ^{+2.3(16)} _{-1.0(16)}	3.2(16) ^{+1.8(17)} _{-2.5(16)}	1.4(14) ^{+2.0(14)} _{-4.4(13)}
IRAS 23385 4	<7.9(14)	9.0(13) ^{+1.3(14)} _{-6.4(13)}	<3.6(14)	<1.4(15)	2.6(16) ^{+1.5(16)} _{-5.6(15)}	5.4(16) ^{+9.0(16)} _{-5.1(16)}	1.0(14) ^{+1.0(14)} _{-5.1(13)}
IRAS 23385 5	<3.5(14)	1.4(14) ^{+9.6(14)} _{-5.6(13)}	<2.5(16)	<2.4(16)	2.4(16) ^{+2.1(16)} _{-8.3(15)}	<5.1(16)	<9.4(13)
IRAS 23385 6	<3.9(15)	1.1(14) ^{+2.5(14)} _{-8.6(13)}	<9.7(15)	<1.5(16)	2.1(16) ^{+4.1(16)} _{-7.7(15)}	2.6(16) ^{+4.1(15)} _{-2.5(16)}	9.8(13) ^{+3.8(14)} _{-3.2(13)}
IRAS 23385 7	7.4(15) ^{+1.9(16)} _{-7.0(15)}	1.0(14) ^{+1.7(14)} _{-8.0(13)}	<1.0(14)	<2.6(15)	1.8(16) ^{+1.4(16)} _{-2.4(15)}	<1.9(16)	<1.1(14)
IRAS 23385 8	<6.9(14)	<4.1(13)	<1.5(16)	<2.1(15)	1.6(16) ^{+1.3(16)} _{-5.3(15)}	<4.8(16)	<9.2(13)

Notes. a(b) = a×10^b

TABLE A.4: continued.

Position	$N(\text{HNCO})$ (cm^{-2})	$N(\text{HC}_3\text{N})$ (cm^{-2})	$N(\text{HC}_3\text{N};v_7=1)$ (cm^{-2})	$N(\text{HC}_3\text{N};v_7=2)$ (cm^{-2})	$N(\text{CH}_3\text{OH})$ (cm^{-2})	$N(\text{CH}_3\text{OH};v_t=1)$ (cm^{-2})	$N(\text{CH}_3\text{CN})$ (cm^{-2})
AFGL 2591 1	1.8(16) ^{+2.2(15)} _{-8.5(14)}	3.9(15) ^{+4.2(14)} _{-3.8(14)}	9.9(15) ^{+1.7(15)} _{-8.3(14)}	4.2(15) ^{+7.2(14)} _{-5.8(14)}	2.0(17) ^{+5.2(16)} _{-2.4(16)}	3.0(17) ^{+6.8(16)} _{-6.7(16)}	1.6(16) ^{+2.6(15)} _{-1.9(15)}
AFGL 2591 2	<1.8(14)	<1.2(14)	7.0(14) ^{+8.1(14)} _{-5.3(14)}	<6.3(16)	<4.5(15)	<4.8(16)	<3.4(14)
AFGL 2591 3	<1.0(14)	<1.5(13)	<9.7(15)	<7.8(16)	<1.3(16)	<4.3(16)	<1.0(13)
AFGL 2591 4	<2.5(14)	1.7(14) ^{+6.1(14)} _{-8.3(13)}	<1.0(14)	<8.0(16)	2.3(16) ^{+3.0(16)} _{-2.2(16)}	<3.0(16)	<1.6(13)
CepA HW2 1	9.1(16) ^{+1.9(15)} _{-1.8(15)}	7.6(15) ^{+8.1(14)} _{-6.1(14)}	1.3(16) ^{+6.4(14)} _{-6.1(14)}	2.1(16) ^{+3.5(15)} _{-5.2(15)}	3.6(17) ^{+4.3(16)} _{-1.3(16)}	1.3(18) ^{+4.6(17)} _{-9.4(16)}	1.4(16) ^{+8.9(15)} _{-1.2(15)}
CepA HW2 2	8.7(15) ^{+9.9(14)} _{-2.4(15)}	<2.8(14)	6.4(14) ^{+1.4(15)} _{-2.0(14)}	<6.6(15)	2.2(16) ^{+2.6(16)} _{-8.9(15)}	<1.4(15)	3.9(15) ^{+1.3(15)} _{-7.0(14)}
CepA HW2 3	5.5(15) ^{+9.4(14)} _{-4.5(14)}	9.3(14) ^{+4.4(14)} _{-2.1(14)}	9.9(14) ^{+1.0(15)} _{-4.9(14)}	<1.1(15)	5.4(17) ^{+8.6(16)} _{-3.3(16)}	5.6(18) ^{+7.6(17)} _{-5.5(17)}	1.7(16) ^{+4.0(15)} _{-2.2(15)}
CepA HW2 4	<1.0(14)	<3.7(14)	<8.9(14)	<6.0(16)	<1.2(14)	<2.4(15)	<1.0(13)
CepA HW2 5	<1.0(14)	<3.4(13)	<9.7(15)	<1.0(16)	6.8(16) ^{+1.5(17)} _{-2.7(16)}	5.4(16) ^{+3.9(16)} _{-5.2(16)}	<1.2(13)
G084.9505 1	8.9(14) ^{+2.7(14)} _{-2.0(14)}	1.9(14) ^{+7.9(13)} _{-1.5(14)}	1.0(14) ^{+8.8(11)} _{-9.2(10)}	<1.0(16)	4.6(16) ^{+1.6(16)} _{-1.2(16)}	1.0(17) ^{+1.5(17)} _{-7.4(16)}	5.8(14) ^{+2.5(14)} _{-1.2(14)}
G084.9505 2	<1.2(14)	<5.2(13)	<1.0(14)	<2.0(15)	4.4(15) ^{+2.8(16)} _{-3.6(15)}	<1.3(15)	<1.1(13)
G084.9505 3	<1.6(14)	<4.7(13)	<1.5(14)	<1.1(16)	5.3(15) ^{+5.1(15)} _{-1.3(15)}	<2.3(17)	<1.5(13)
G084.9505 4	6.9(14) ^{+7.1(14)} _{-5.1(14)}	4.1(14) ^{+1.0(15)} _{-3.7(14)}	<1.3(16)	<1.0(16)	2.3(15) ^{+1.7(15)} _{-1.5(15)}	<1.2(17)	<1.7(13)
G084.9505 5	<7.9(14)	<1.4(13)	<6.1(16)	<1.0(16)	2.1(15) ^{+4.5(15)} _{-1.7(15)}	<1.1(17)	<2.1(13)
G084.9505 6	<1.0(14)	<1.9(13)	<6.7(14)	<6.3(16)	5.1(15) ^{+5.6(15)} _{-2.7(15)}	1.4(16) ^{+1.9(16)} _{-1.2(16)}	<2.9(13)
G084.9505 7	<1.1(16)	<2.0(13)	<1.3(14)	<3.4(16)	<5.2(15)	<4.1(17)	<2.0(13)
G084.9505 8	<3.6(14)	<1.0(17)	<1.1(14)	<4.4(16)	<2.0(16)	<5.3(15)	<1.2(17)
G094.6028 1	4.4(15) ^{+3.2(14)} _{-6.7(14)}	2.3(15) ^{+1.1(15)} _{-4.4(14)}	6.5(14) ^{+8.0(14)} _{-5.0(14)}	<1.0(16)	1.9(17) ^{+5.0(16)} _{-1.4(16)}	1.1(18) ^{+6.5(17)} _{-2.4(17)}	2.3(15) ^{+3.2(14)} _{-4.0(14)}
G094.6028 2	<1.6(16)	<2.5(13)	<1.0(14)	<5.5(15)	<7.8(15)	2.8(16) ^{+7.8(16)} _{-2.3(16)}	<8.7(16)

Notes. a(b) = $a \times 10^b$

TABLE A.4: continued.

Position	$N(\text{HNCO})$ (cm^{-2})	$N(\text{HC}_3\text{N})$ (cm^{-2})	$N(\text{HC}_3\text{N};v_7=1)$ (cm^{-2})	$N(\text{HC}_3\text{N};v_7=2)$ (cm^{-2})	$N(\text{CH}_3\text{OH})$ (cm^{-2})	$N(\text{CH}_3\text{OH};v_t=1)$ (cm^{-2})	$N(\text{CH}_3\text{CN})$ (cm^{-2})
G094.6028 3	<2.8(14)	<1.0(13)	<5.7(14)	<1.3(15)	<1.7(15)	<3.1(16)	<2.0(17)
G094.6028 4	<1.5(16)	7.6(13) ^{+7.5(13)} -5.5(13)	<3.3(16)	<1.6(15)	<1.4(15)	<4.9(16)	<1.7(13)
G094.6028 5	6.3(15) ^{+5.8(16)} -5.4(15)	<2.2(13)	<1.2(15)	<4.5(16)	<1.8(15)	<1.1(17)	<1.9(17)
G094.6028 6	<1.0(14)	<1.0(13)	<1.2(14)	<4.7(15)	<2.9(15)	<1.5(17)	<1.0(13)
G094.6028 7	<3.6(14)	<2.6(13)	<2.4(14)	<1.0(16)	<3.6(15)	3.4(16) ^{+9.6(16)} -3.2(16)	<5.3(13)
G094.6028 8	<4.6(14)	<1.6(13)	<1.4(14)	<1.5(15)	<1.4(15)	<2.3(16)	<2.3(13)
G100.38 1	9.1(14) ^{+3.3(14)} -2.1(14)	<1.2(14)	<2.2(15)	<1.1(16)	1.6(16) ^{+4.1(16)} -1.5(16)	<4.7(15)	2.1(14) ^{+1.1(14)} -5.2(13)
G100.38 2	<1.7(14)	<2.4(13)	<5.2(14)	<2.4(16)	<1.0(15)	<1.1(16)	<7.3(13)
G100.38 3	<2.8(14)	<1.9(13)	<1.7(15)	<1.2(16)	<1.9(15)	<4.5(15)	<1.3(13)
G100.38 4	<1.1(14)	<8.3(13)	<2.0(15)	<1.0(15)	<2.8(15)	<1.8(16)	<5.4(16)
G100.38 5	<2.0(14)	<4.9(13)	<2.9(14)	<1.0(15)	<9.0(14)	2.2(16) ^{+2.8(16)} -1.7(16)	<3.4(13)
G108.75 1	<3.8(14)	6.3(13) ^{+1.3(14)} -1.5(13)	<3.5(14)	<1.0(15)	1.2(16) ^{+2.5(16)} -1.0(16)	<3.8(17)	7.8(13) ^{+1.2(14)} -5.3(13)
G108.75 2	<2.1(14)	<3.1(13)	<6.7(14)	<2.8(16)	<8.6(17)	<6.0(16)	<1.6(13)
G108.75 3	<1.0(17)	<1.3(13)	<1.6(14)	<1.5(16)	2.2(15) ^{+1.8(15)} -2.1(15)	<7.9(16)	<3.9(13)
G108.75 4	<1.9(14)	<2.8(13)	<4.0(14)	<1.2(15)	5.7(15) ^{+1.6(16)} -4.6(15)	<6.6(16)	<3.5(13)
G108.75 5	<3.1(14)	<1.3(13)	<1.9(14)	<1.5(15)	3.7(15) ^{+1.8(16)} -3.1(15)	<6.7(15)	<3.5(13)
G108.75 6	<1.0(17)	4.3(13) ^{+1.2(14)} -1.5(13)	<1.5(14)	<1.2(15)	<1.5(16)	<2.1(16)	<8.4(16)
G138.2957 1	<1.2(15)	<7.4(13)	<1.0(14)	<1.6(15)	<1.0(19)	<1.2(16)	<1.3(13)
G138.2957 2	<5.1(14)	<3.1(13)	<1.5(14)	<1.0(17)	<3.3(15)	<4.5(16)	<1.9(13)
G138.2957 3	<2.9(14)	6.6(13) ^{+1.5(14)} -3.1(13)	<2.0(14)	<8.5(16)	<6.1(15)	<2.6(16)	<1.9(13)
G138.2957 4	2.9(14) ^{+6.1(14)} -5.2(13)	<1.9(13)	<5.4(16)	<1.5(15)	<2.3(15)	<6.0(16)	<1.1(14)

Notes. a(b) = $a \times 10^b$

TABLE A.4: continued.

Position	$N(\text{HNCO})$ (cm^{-2})	$N(\text{HC}_3\text{N})$ (cm^{-2})	$N(\text{HC}_3\text{N};v_7=1)$ (cm^{-2})	$N(\text{HC}_3\text{N};v_7=2)$ (cm^{-2})	$N(\text{CH}_3\text{OH})$ (cm^{-2})	$N(\text{CH}_3\text{OH};v_t=1)$ (cm^{-2})	$N(\text{CH}_3\text{CN})$ (cm^{-2})
G138.2957 5	<2.2(15)	<2.1(13)	<1.4(14)	<6.1(16)	<2.5(15)	<2.3(16)	<8.5(17)
G138.2957 6	<4.3(14)	<1.4(13)	<2.4(16)	<1.3(16)	<3.8(15)	<8.6(15)	<1.5(15)
G138.2957 7	<1.0(17)	<5.4(13)	<1.0(14)	<2.1(15)	<1.3(16)	<1.3(17)	<2.3(13)
G138.2957 8	<2.2(14)	<1.6(15)	<1.0(15)	<6.8(16)	1.3(16) ^{+1.2(16)} _{-1.2(16)}	<1.0(19)	<1.0(13)
G138.2957 9	<1.1(14)	<3.3(13)	<9.7(16)	<1.7(16)	<1.0(16)	<7.2(16)	<1.6(16)
G138.2957 10	<1.1(14)	<1.7(13)	<3.8(14)	<1.5(16)	<3.4(15)	<8.4(17)	<8.1(14)
G138.2957 11	<3.9(14)	<3.9(13)	<1.4(14)	<1.5(16)	<3.6(15)	<3.2(16)	<1.1(14)
G138.2957 12	<1.0(14)	<5.9(13)	<1.0(14)	<1.0(16)	<1.4(15)	<5.9(15)	<1.3(13)
G139.9091 1	<1.1(14)	<7.4(13)	<6.5(14)	<2.0(15)	<8.7(14)	<3.5(16)	<6.0(13)
G139.9091 2	<2.2(14)	<2.0(13)	<9.7(15)	<1.4(15)	<2.8(15)	<2.9(18)	<2.6(17)
G139.9091 3	<1.9(14)	<7.7(13)	<9.7(15)	<1.5(16)	<7.4(14)	<2.4(15)	<1.0(15)
G139.9091 4	<2.9(14)	<1.0(13)	<1.8(14)	<1.5(16)	<2.3(15)	<4.7(16)	<6.2(13)
G075.78 1	1.5(16) ^{+1.1(15)} _{-1.8(15)}	6.2(15) ^{+5.3(14)} _{-5.9(14)}	1.6(16) ^{+7.7(14)} _{-5.5(15)}	1.1(16) ^{+3.4(15)} _{-1.8(15)}	1.8(17) ^{+2.2(16)} _{-2.9(16)}	3.9(17) ^{+2.4(17)} _{-5.7(16)}	8.2(15) ^{+1.6(15)} _{-1.1(15)}
G075.78 2	<1.8(14)	<1.3(13)	<8.3(14)	<1.0(16)	<2.1(15)	<2.3(15)	<1.0(13)
G075.78 3	<3.1(14)	<1.1(13)	<7.5(15)	<1.9(15)	<1.3(15)	<7.9(18)	<1.0(13)
G075.78 4	<1.1(14)	<1.2(13)	<3.6(14)	<4.8(15)	1.3(16) ^{+2.9(15)} _{-1.2(16)}	<6.1(16)	<3.3(13)
IRAS 21078 1	4.1(16) ^{+4.6(15)} _{-2.8(15)}	6.5(15) ^{+1.7(15)} _{-1.1(15)}	4.3(15) ^{+1.4(15)} _{-1.1(15)}	<1.4(15)	1.3(18) ^{+1.4(17)} _{-7.0(16)}	2.3(18) ^{+1.7(17)} _{-2.3(17)}	1.5(16) ^{+2.2(15)} _{-1.6(15)}
IRAS 21078 2	5.0(15) ^{+2.5(15)} _{-1.0(15)}	3.7(14) ^{+6.5(14)} _{-2.1(13)}	2.6(14) ^{+3.0(14)} _{-8.7(13)}	<1.0(16)	1.9(17) ^{+5.7(16)} _{-3.7(16)}	4.0(17) ^{+5.1(16)} _{-4.5(16)}	2.5(15) ^{+8.6(14)} _{-5.4(14)}
IRAS 21078 3	1.2(15) ^{+6.4(14)} _{-1.6(14)}	5.0(14) ^{+2.4(14)} _{-1.6(14)}	<4.7(14)	9.0(15) ^{+4.2(16)} _{-3.1(15)}	6.6(17) ^{+2.7(17)} _{-1.3(17)}	1.2(18) ^{+1.2(17)} _{-2.9(17)}	4.0(15) ^{+8.3(14)} _{-1.2(15)}
IRAS 21078 4	<1.0(14)	1.2(14) ^{+1.2(14)} _{-6.8(13)}	<4.7(14)	<1.0(16)	<1.2(16)	<9.3(17)	<1.5(13)
IRAS 21078 5	<1.5(14)	<8.3(13)	<5.7(14)	<1.1(15)	7.5(15) ^{+4.0(15)} _{-1.5(15)}	<6.0(16)	<9.0(13)
IRAS 21078 6	<1.9(14)	1.8(14) ^{+2.2(14)} _{-8.9(13)}	<9.7(15)	<1.2(16)	3.1(16) ^{+2.2(16)} _{-1.3(16)}	<5.5(15)	5.1(13) ^{+4.4(13)} _{-1.7(13)}

Notes. a(b) = $a \times 10^b$

TABLE A.4: continued.

Position	$N(\text{HNCO})$ (cm^{-2})	$N(\text{HC}_3\text{N})$ (cm^{-2})	$N(\text{HC}_3\text{N};v_7=1)$ (cm^{-2})	$N(\text{HC}_3\text{N};v_7=2)$ (cm^{-2})	$N(\text{CH}_3\text{OH})$ (cm^{-2})	$N(\text{CH}_3\text{OH};v_t=1)$ (cm^{-2})	$N(\text{CH}_3\text{CN})$ (cm^{-2})
IRAS 21078 7	<5.2(14)	<9.1(13)	<9.4(14)	<1.0(16)	7.1(15) ^{+8.6(15)} _{-2.5(15)}	<1.4(16)	<1.6(16)
IRAS 21078 8	<2.5(14)	1.8(14) ^{+7.5(13)} _{-1.6(14)}	<1.0(14)	<1.0(16)	2.9(16) ^{+6.6(15)} _{-1.3(16)}	<8.8(15)	1.5(14) ^{+1.0(14)} _{-7.1(13)}
IRAS 21078 9	<1.1(14)	1.5(14) ^{+5.1(13)} _{-1.0(14)}	<4.5(14)	<1.0(16)	2.6(16) ^{+2.5(16)} _{-9.4(15)}	<6.1(18)	<2.6(13)
IRAS 21078 10	7.9(14) ^{+2.4(14)} _{-6.2(14)}	1.9(14) ^{+3.0(14)} _{-8.9(13)}	<8.7(14)	<7.2(16)	2.5(16) ^{+1.4(16)} _{-5.5(15)}	2.3(16) ^{+8.3(15)} _{-2.1(16)}	2.1(14) ^{+8.8(13)} _{-8.5(13)}
IRAS 21078 11	<3.3(14)	<8.3(13)	<1.1(15)	<1.2(15)	5.5(17) ^{+8.1(17)} _{-4.8(17)}	<4.4(16)	1.5(14) ^{+1.0(14)} _{-6.1(13)}
IRAS 21078 12	<1.4(14)	1.6(14) ^{+1.1(14)} _{-1.4(14)}	<1.0(14)	<2.9(16)	1.8(16) ^{+1.2(16)} _{-4.3(15)}	<3.5(16)	1.5(14) ^{+3.9(14)} _{-5.2(13)}
IRAS 21078 13	<8.4(14)	<1.1(14)	<1.3(14)	<1.0(15)	2.9(16) ^{+3.4(16)} _{-1.6(16)}	<3.7(16)	<2.9(14)
IRAS 21078 14	<1.9(14)	9.4(13) ^{+2.1(14)} _{-5.0(13)}	<1.4(14)	<5.4(15)	2.6(16) ^{+3.6(16)} _{-9.7(15)}	<1.9(16)	<3.8(13)
NGC7538 IRS9 1	9.8(16) ^{+7.9(14)} _{-2.7(14)}	3.8(15) ^{+4.1(15)} _{-1.0(15)}	4.7(15) ^{+1.2(15)} _{-9.7(14)}	<5.2(15)	9.1(16) ^{+4.2(16)} _{-2.0(16)}	3.3(17) ^{+2.4(17)} _{-1.2(17)}	8.7(15) ^{+2.5(15)} _{-1.3(15)}
NGC7538 IRS9 2	<1.9(14)	<2.0(13)	<3.6(14)	<7.3(16)	5.2(15) ^{+2.5(16)} _{-2.8(15)}	<3.4(15)	<4.2(17)
NGC7538 IRS9 3	<1.2(14)	8.1(13) ^{+5.1(13)} _{-7.0(13)}	<1.8(14)	<1.3(16)	7.6(15) ^{+4.6(16)} _{-6.0(15)}	<2.6(16)	<6.2(16)
NGC7538 IRS9 4	<1.0(14)	<2.8(14)	<2.0(14)	<3.0(16)	3.4(15) ^{+7.7(15)} _{-2.9(15)}	<9.9(18)	<1.4(14)
NGC7538 IRS9 5	<1.6(14)	1.0(14) ^{+1.9(14)} _{-5.1(13)}	<1.0(14)	<6.6(16)	9.1(15) ^{+9.2(15)} _{-4.7(15)}	<9.9(15)	<5.1(13)
NGC7538 IRS9 6	<6.6(14)	2.5(14) ^{+4.4(14)} _{-1.4(14)}	<2.4(14)	<1.0(16)	4.6(16) ^{+3.9(16)} _{-8.5(15)}	<2.1(16)	1.3(14) ^{+1.4(13)} _{-3.2(13)}
NGC7538 IRS9 7	<7.8(16)	<9.1(13)	<1.1(16)	<3.2(16)	3.5(15) ^{+2.9(15)} _{-3.2(15)}	<2.2(15)	<7.0(13)
NGC7538 IRS9 8	<1.6(14)	5.8(13) ^{+1.1(14)} _{-3.3(13)}	<2.2(14)	<4.0(16)	4.4(15) ^{+1.4(16)} _{-3.9(15)}	<6.3(15)	<2.5(13)
S87 IRS1 1	<3.2(16)	<1.5(13)	<2.4(14)	<1.1(15)	<1.8(15)	<1.5(16)	<1.7(17)
S87 IRS1 2	<3.6(14)	6.7(13) ^{+6.6(12)} _{-5.6(13)}	<3.1(15)	<1.0(16)	<1.7(16)	<2.5(17)	<3.1(13)

Notes. a(b) = $a \times 10^b$

TABLE A.4: continued.

Position	$N(\text{HNCO})$ (cm^{-2})	$N(\text{HC}_3\text{N})$ (cm^{-2})	$N(\text{HC}_3\text{N};v_7=1)$ (cm^{-2})	$N(\text{HC}_3\text{N};v_7=2)$ (cm^{-2})	$N(\text{CH}_3\text{OH})$ (cm^{-2})	$N(\text{CH}_3\text{OH};v_t=1)$ (cm^{-2})	$N(\text{CH}_3\text{CN})$ (cm^{-2})
S87 IRS1 3	<1.0(14)	<2.0(13)	<2.9(14)	<1.5(16)	<5.1(18)	<1.3(16)	<3.8(13)
S87 IRS1 4	<2.7(14)	1.2(14) ^{+6.5(13)} _{-9.9(13)}	<2.8(14)	<1.4(15)	3.4(15) ^{+8.4(15)} _{-2.9(15)}	<5.1(16)	<2.8(13)
S87 IRS1 5	<3.3(16)	<1.7(13)	<3.1(14)	<1.5(16)	<1.4(14)	<2.2(18)	<9.0(13)
S87 IRS1 6	<1.0(14)	<2.2(13)	<1.4(14)	<1.3(15)	2.7(15) ^{+5.0(15)} _{-2.4(15)}	<2.0(16)	<9.3(13)
S87 IRS1 7	1.5(14) ^{+1.4(14)} _{-5.2(12)}	1.6(14) ^{+2.0(14)} _{-7.9(13)}	<1.4(14)	<3.4(16)	<4.4(15)	<1.5(18)	<2.5(13)
S87 IRS1 8	<3.1(14)	<1.8(13)	<2.3(16)	<1.2(15)	<1.1(16)	7.5(17) ^{+5.5(17)} _{-7.4(17)}	<1.0(13)
S87 IRS1 9	<1.5(14)	<1.3(13)	<1.5(14)	<2.9(16)	<1.4(16)	<1.8(16)	<1.0(18)
S106 1	<1.1(14)	<8.6(13)	<4.5(16)	<2.8(16)	<1.6(15)	<1.5(16)	<3.7(14)
S106 2	2.2(15) ^{+5.5(14)} _{-7.5(14)}	2.0(15) ^{+1.0(15)} _{-5.7(14)}	<6.5(14)	<3.8(15)	<3.4(16)	<2.2(16)	4.1(14) ^{+8.0(13)} _{-6.7(13)}
S106 3	<5.4(14)	2.3(14) ^{+7.3(13)} _{-3.8(13)}	<3.3(14)	<2.1(16)	<1.4(16)	<1.1(17)	<2.6(14)
S106 4	<1.0(14)	8.2(13) ^{+5.1(14)} _{-8.1(12)}	<2.0(14)	<1.0(16)	<6.4(14)	<8.3(15)	<1.0(14)
W3 H2O 1	2.4(15) ^{+1.3(15)} _{-4.1(14)}	4.0(14) ^{+6.0(14)} _{-1.1(14)}	<7.1(14)	<1.8(16)	2.0(18) ^{+3.2(17)} _{-1.2(17)}	1.4(18) ^{+4.7(17)} _{-1.7(17)}	2.2(15) ^{+7.1(14)} _{-5.3(14)}
W3 H2O 2	4.8(14) ^{+2.5(14)} _{-3.4(14)}	2.2(14) ^{+9.0(14)} _{-5.6(13)}	9.9(14) ^{+5.3(15)} _{-1.8(14)}	<1.9(15)	1.1(17) ^{+2.0(16)} _{-1.2(16)}	4.4(17) ^{+2.5(17)} _{-2.1(17)}	5.4(14) ^{+6.4(13)} _{-4.7(13)}
W3 H2O 3	5.2(16) ^{+2.1(14)} _{-3.9(15)}	8.8(15) ^{+9.4(14)} _{-1.0(15)}	1.2(16) ^{+1.2(15)} _{-1.1(15)}	1.2(16) ^{+3.3(15)} _{-2.1(15)}	1.4(18) ^{+8.5(16)} _{-4.4(16)}	3.1(18) ^{+2.6(17)} _{-2.0(17)}	6.0(16) ^{+1.0(16)} _{-1.0(16)}
W3 H2O 4	6.7(16) ^{+1.6(15)} _{-2.9(15)}	6.9(15) ^{+1.1(15)} _{-3.3(14)}	4.2(16) ^{+1.0(16)} _{-1.2(16)}	1.6(16) ^{+3.0(15)} _{-1.1(15)}	2.9(18) ^{+2.9(17)} _{-1.8(17)}	2.5(18) ^{+7.5(16)} _{-1.3(17)}	1.5(17) ^{+1.7(16)} _{-1.2(16)}
W3 H2O 5	6.7(14) ^{+1.8(15)} _{-4.4(14)}	3.1(15) ^{+5.9(14)} _{-7.1(14)}	<5.4(14)	<4.5(16)	4.1(16) ^{+1.3(16)} _{-9.8(15)}	<1.5(16)	5.0(14) ^{+7.9(13)} _{-5.7(13)}
W3 IRS4 1	1.3(16) ^{+1.8(15)} _{-8.9(14)}	1.9(15) ^{+4.9(14)} _{-3.9(14)}	7.8(14) ^{+1.7(15)} _{-3.6(14)}	<3.3(16)	1.8(17) ^{+1.7(16)} _{-3.5(16)}	3.0(17) ^{+1.4(17)} _{-4.6(16)}	6.7(15) ^{+2.5(15)} _{-1.3(15)}
W3 IRS4 2	<8.7(16)	2.5(14) ^{+2.4(14)} _{-7.5(13)}	<1.7(14)	<8.7(15)	2.1(16) ^{+1.1(17)} _{-1.9(16)}	<2.0(18)	<2.2(13)
W3 IRS4 3	<1.0(15)	2.2(14) ^{+3.0(14)} _{-8.0(13)}	<1.7(14)	<2.5(15)	1.7(16) ^{+3.8(16)} _{-1.0(16)}	<1.2(17)	<3.2(14)

Notes. a(b) = $a \times 10^b$

TABLE A.4: continued.

Position	$N(\text{HNCO})$ (cm^{-2})	$N(\text{HC}_3\text{N})$ (cm^{-2})	$N(\text{HC}_3\text{N};v_7=1)$ (cm^{-2})	$N(\text{HC}_3\text{N};v_7=2)$ (cm^{-2})	$N(\text{CH}_3\text{OH})$ (cm^{-2})	$N(\text{CH}_3\text{OH};v_t=1)$ (cm^{-2})	$N(\text{CH}_3\text{CN})$ (cm^{-2})
W3 IRS4 4	<1.0(14)	<5.4(13)	<1.7(14)	<3.8(15)	<5.4(15)	<2.6(16)	<2.6(17)
W3 IRS4 5	<1.0(14)	$1.2(14)_{-7.3(13)}^{+1.5(14)}$	<6.7(14)	<3.1(16)	<1.6(15)	<2.1(18)	<1.3(14)
W3 IRS4 6	<6.1(14)	$7.8(13)_{-3.2(13)}^{+1.3(14)}$	<2.5(14)	<2.3(15)	$5.0(15)_{-1.8(15)}^{+3.6(15)}$	<1.2(18)	$1.7(14)_{-8.3(13)}^{+1.2(14)}$

Notes. $a(b) = a \times 10^b$

A.6 Spectra

In Fig. A.3 the observed spectrum and corresponding XCLASS fit is presented for all 120 positions analyzed in Sect. 2.4.2. In addition, the line optical depth τ_{ν}^{line} (Eq. 1.71) computed with XCLASS is shown.

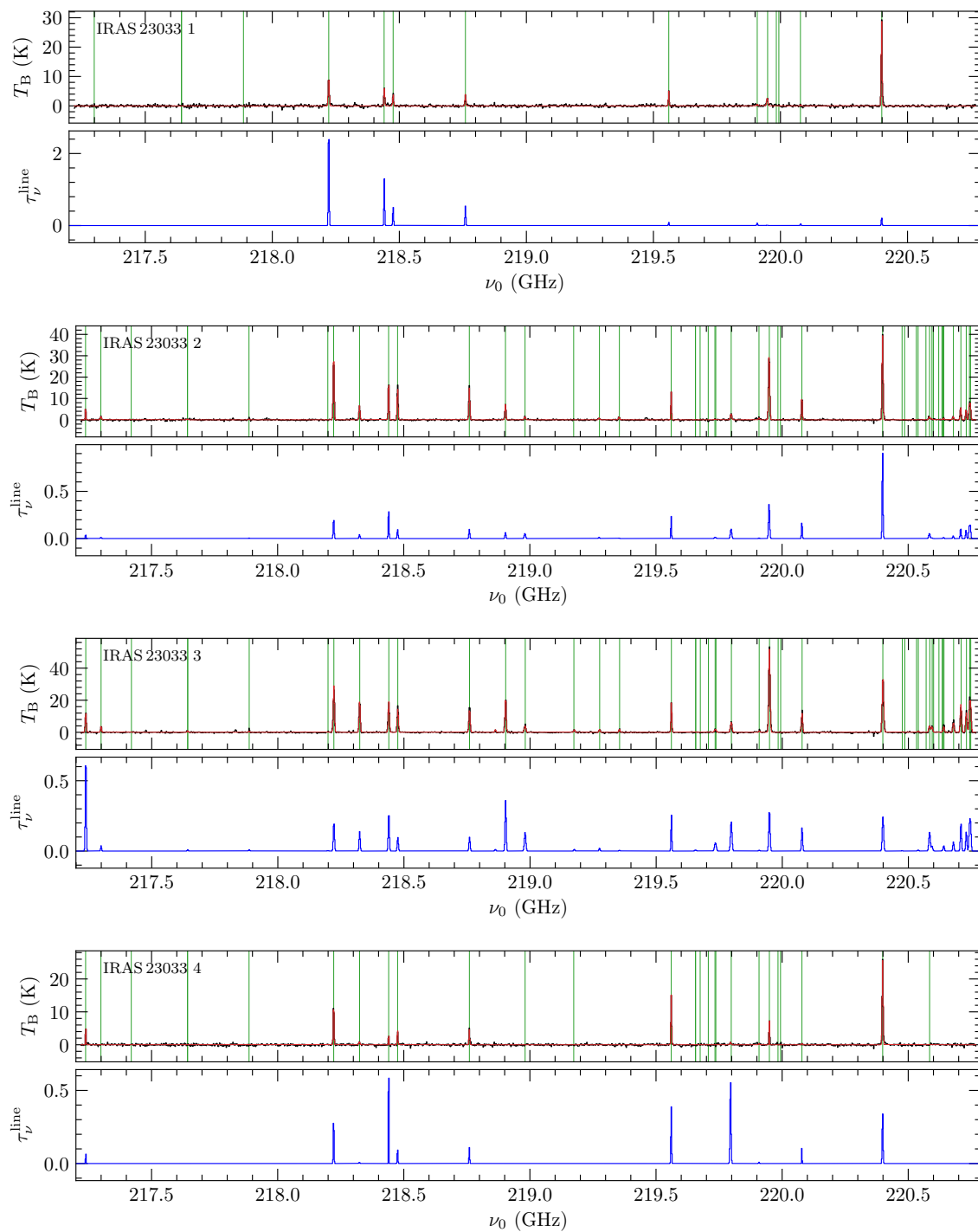


FIGURE A.3: Broadband spectrum toward each position. *Top panel:* Observed (black line) spectrum and XCLASS fit (red line) for all 120 analyzed positions. Fitted molecular transitions are indicated by green vertical lines. *Bottom panel:* Optical depth profile (blue line) of all fitted transitions for all 120 analyzed positions.

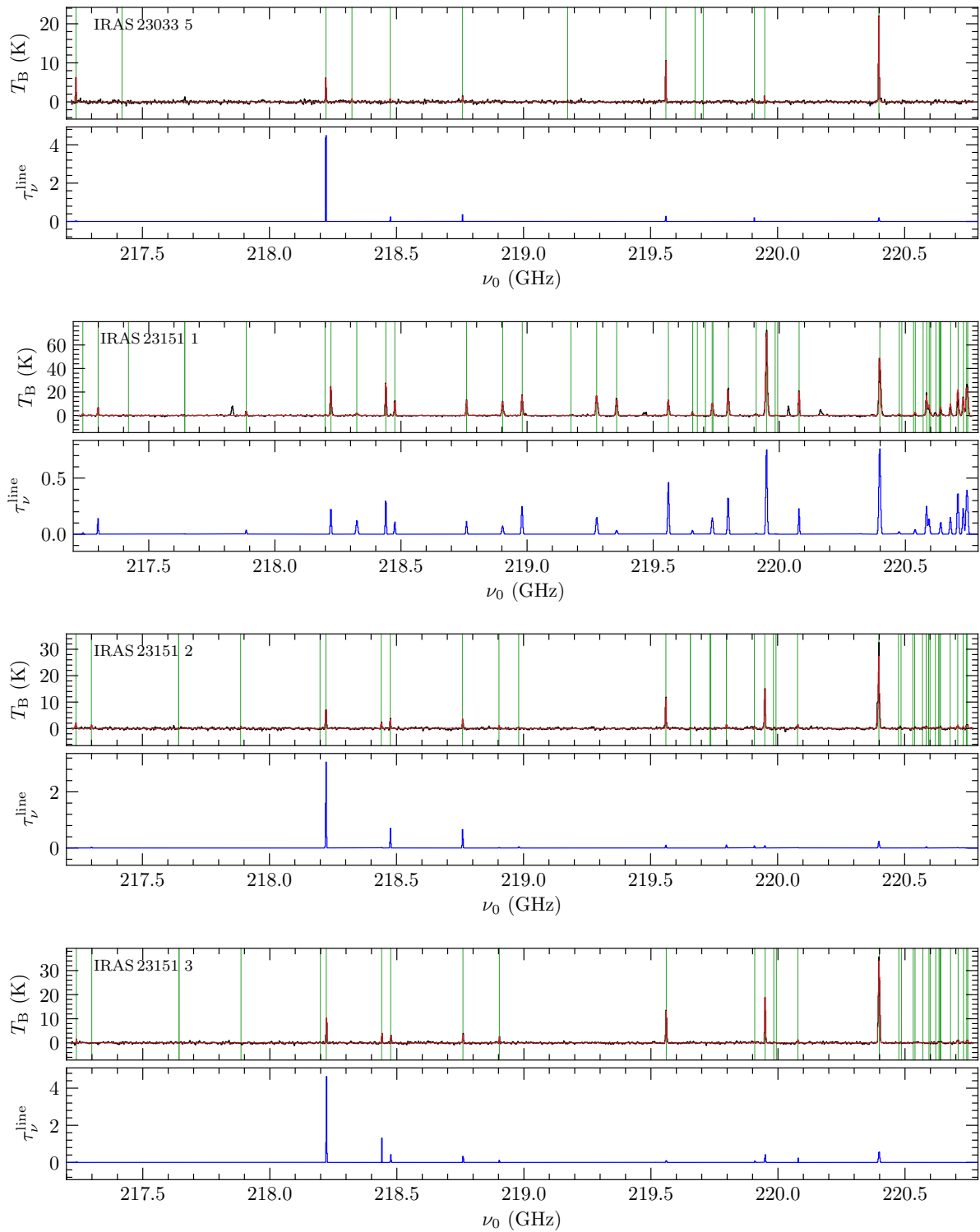


FIGURE A.3 (cont.): Broadband spectrum toward each position. *Top panel:* Observed (black line) spectrum and XCLASS fit (red line) for all 120 analyzed positions. Fitted molecular transitions are indicated by green vertical lines. *Bottom panel:* Optical depth profile (blue line) of all fitted transitions for all 120 analyzed positions.

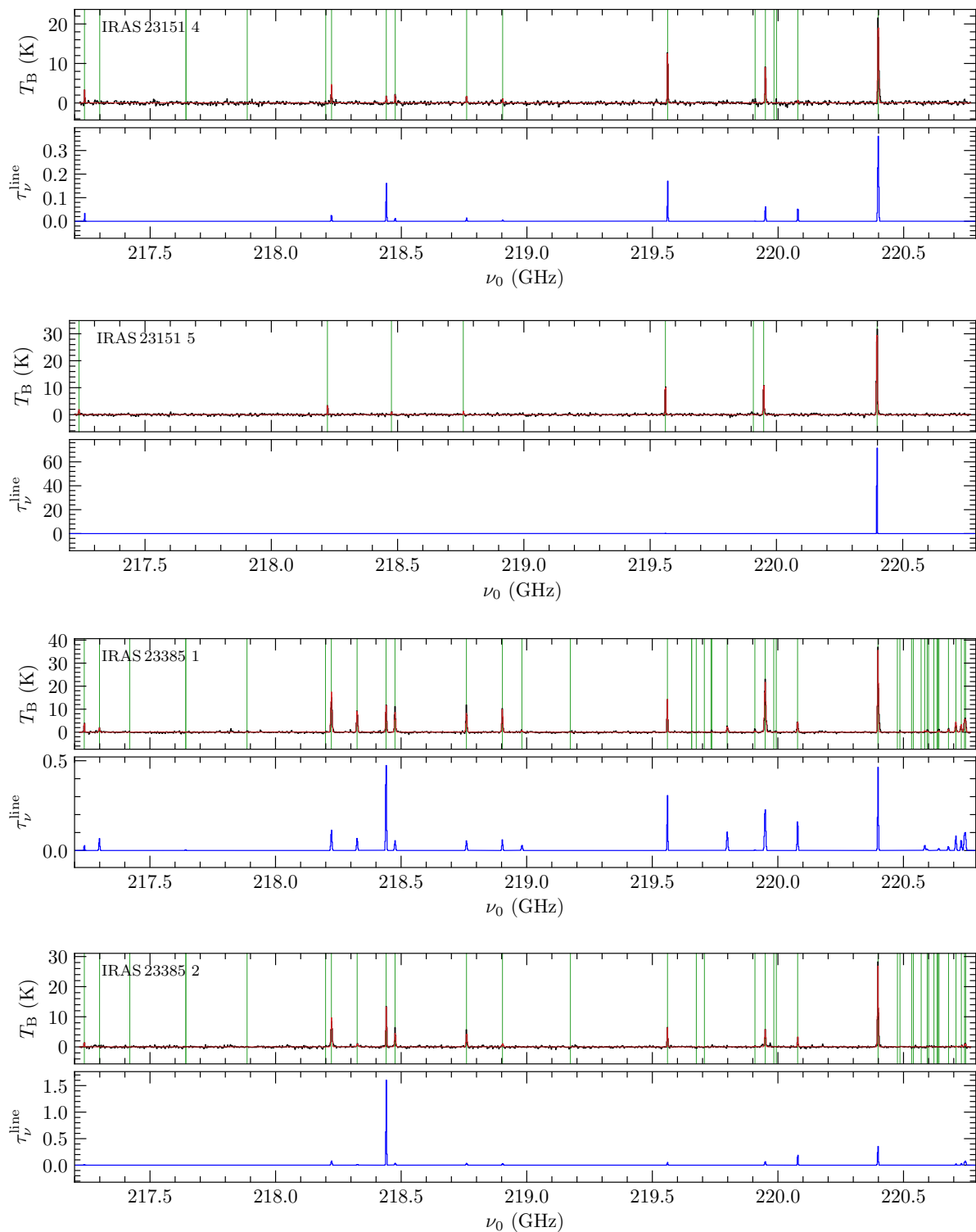


FIGURE A.3 (cont.): Broadband spectrum toward each position. *Top panel:* Observed (black line) spectrum and XCLASS fit (red line) for all 120 analyzed positions. Fitted molecular transitions are indicated by green vertical lines. *Bottom panel:* Optical depth profile (blue line) of all fitted transitions for all 120 analyzed positions.

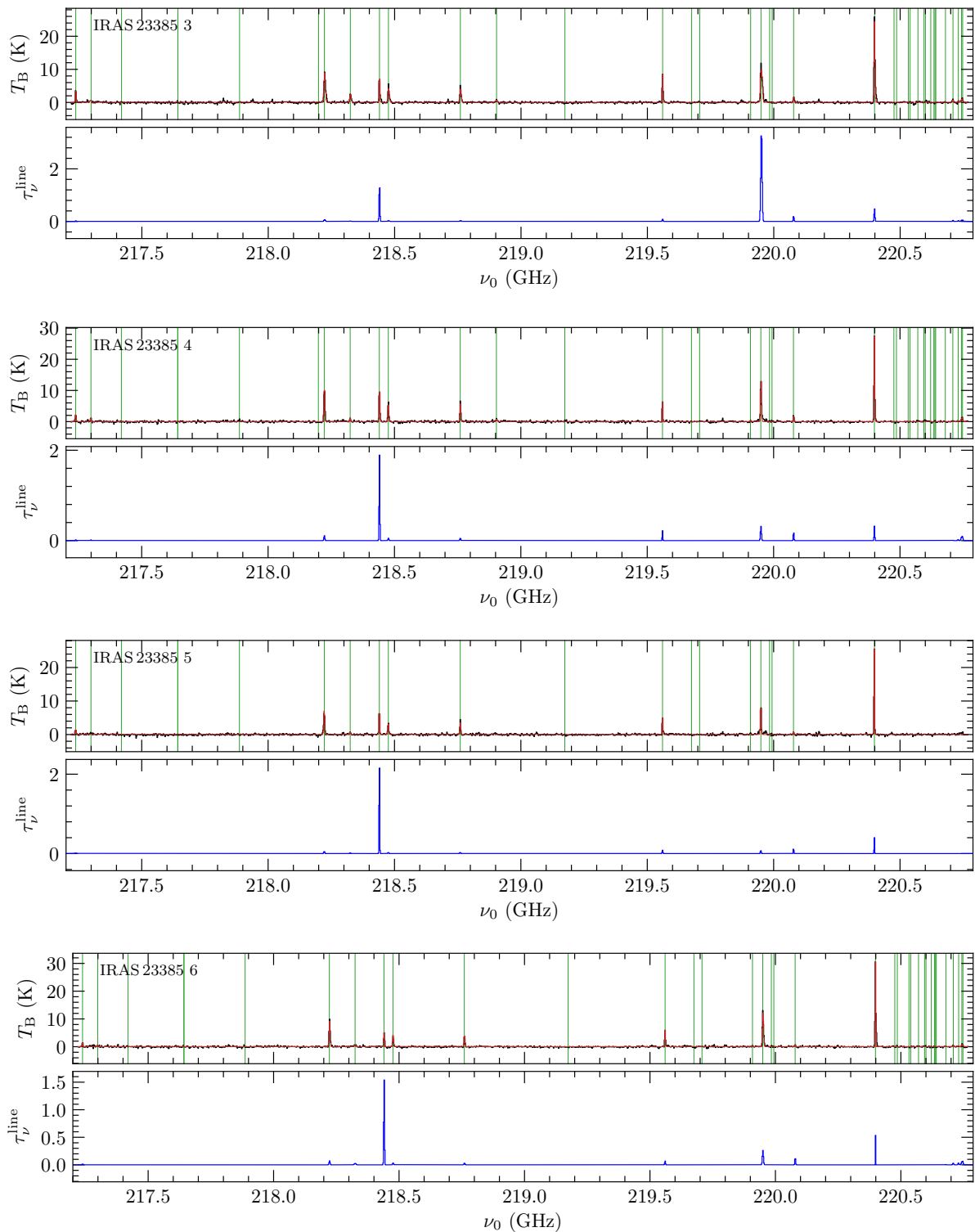


FIGURE A.3 (cont.): Broadband spectrum toward each position. *Top panel:* Observed (black line) spectrum and XCLASS fit (red line) for all 120 analyzed positions. Fitted molecular transitions are indicated by green vertical lines. *Bottom panel:* Optical depth profile (blue line) of all fitted transitions for all 120 analyzed positions.

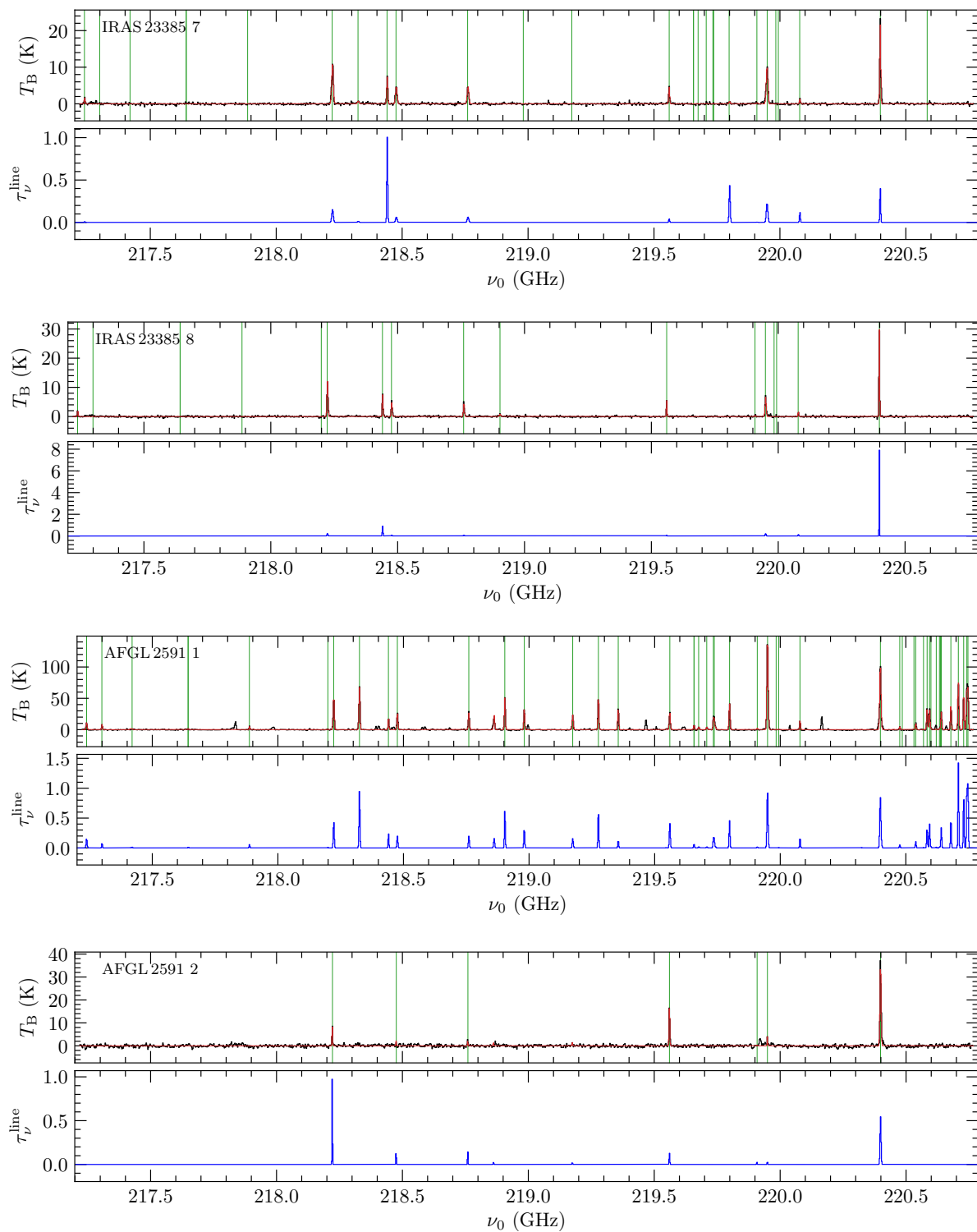


FIGURE A.3 (cont.): Broadband spectrum toward each position. *Top panel:* Observed (black line) spectrum and XCLASS fit (red line) for all 120 analyzed positions. Fitted molecular transitions are indicated by green vertical lines. *Bottom panel:* Optical depth profile (blue line) of all fitted transitions for all 120 analyzed positions.

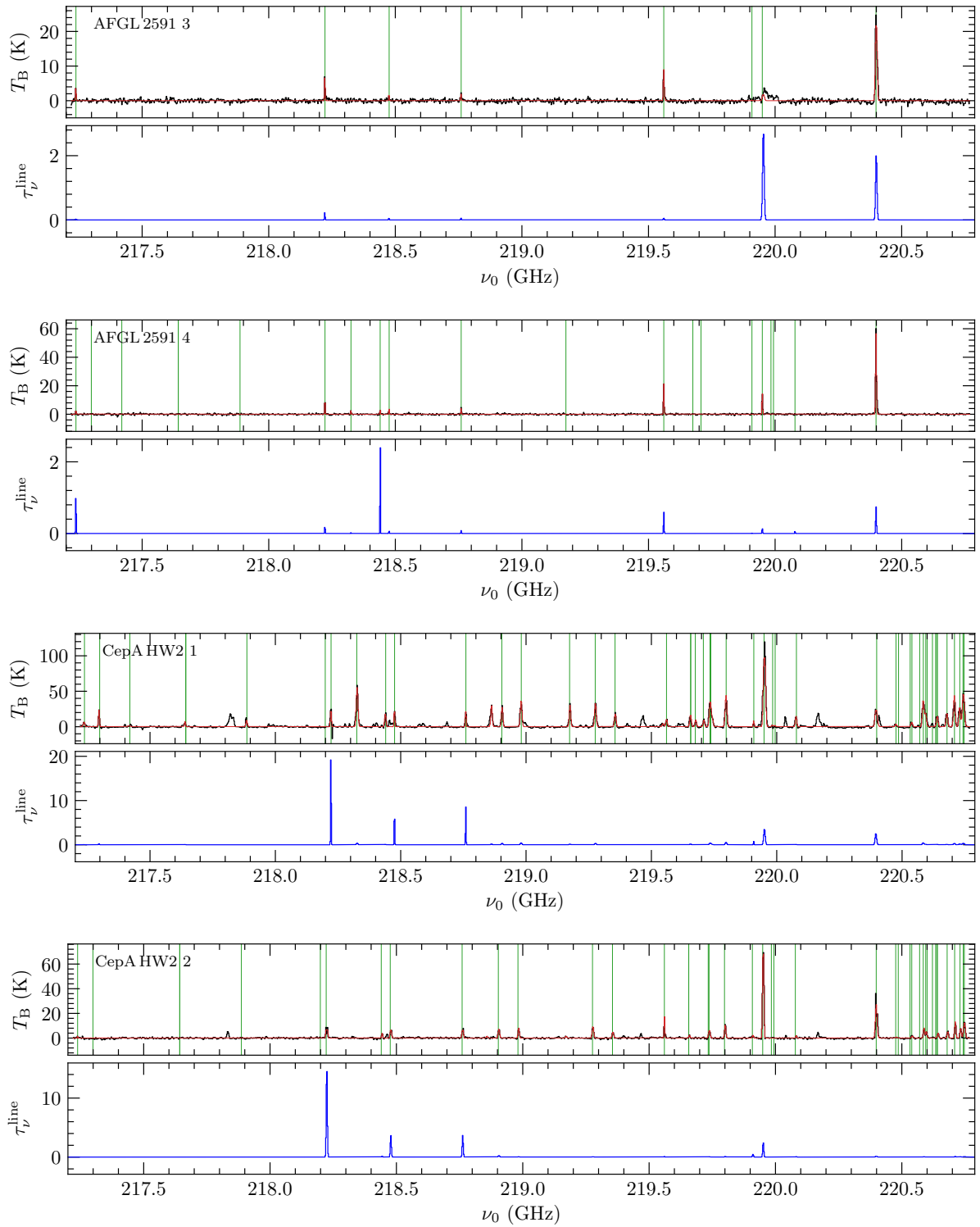


FIGURE A.3 (cont.): Broadband spectrum toward each position. *Top panel:* Observed (black line) spectrum and XCLASS fit (red line) for all 120 analyzed positions. Fitted molecular transitions are indicated by green vertical lines. *Bottom panel:* Optical depth profile (blue line) of all fitted transitions for all 120 analyzed positions.

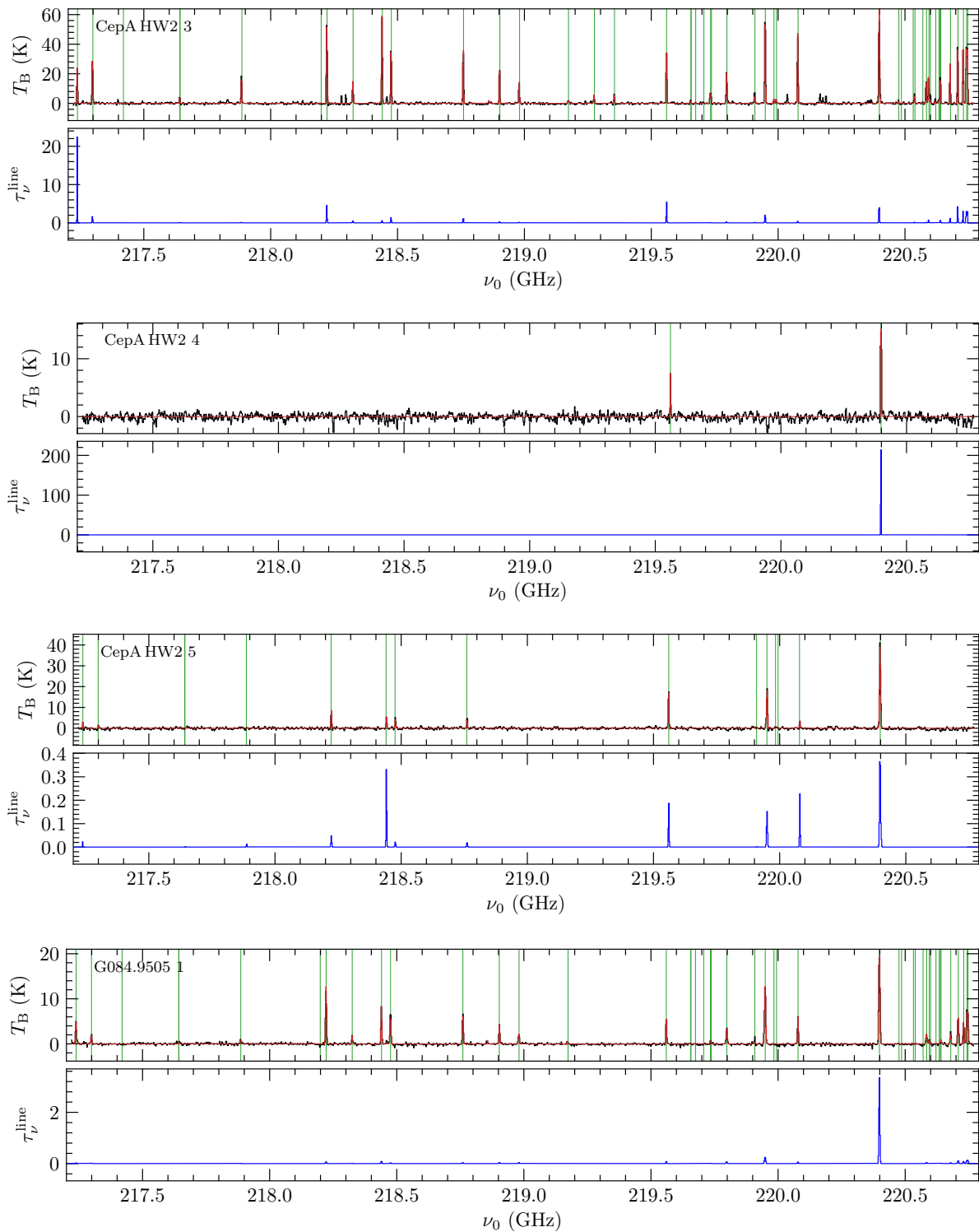


FIGURE A.3 (cont.): Broadband spectrum toward each position. *Top panel:* Observed (black line) spectrum and XCLASS fit (red line) for all 120 analyzed positions. Fitted molecular transitions are indicated by green vertical lines. *Bottom panel:* Optical depth profile (blue line) of all fitted transitions for all 120 analyzed positions.

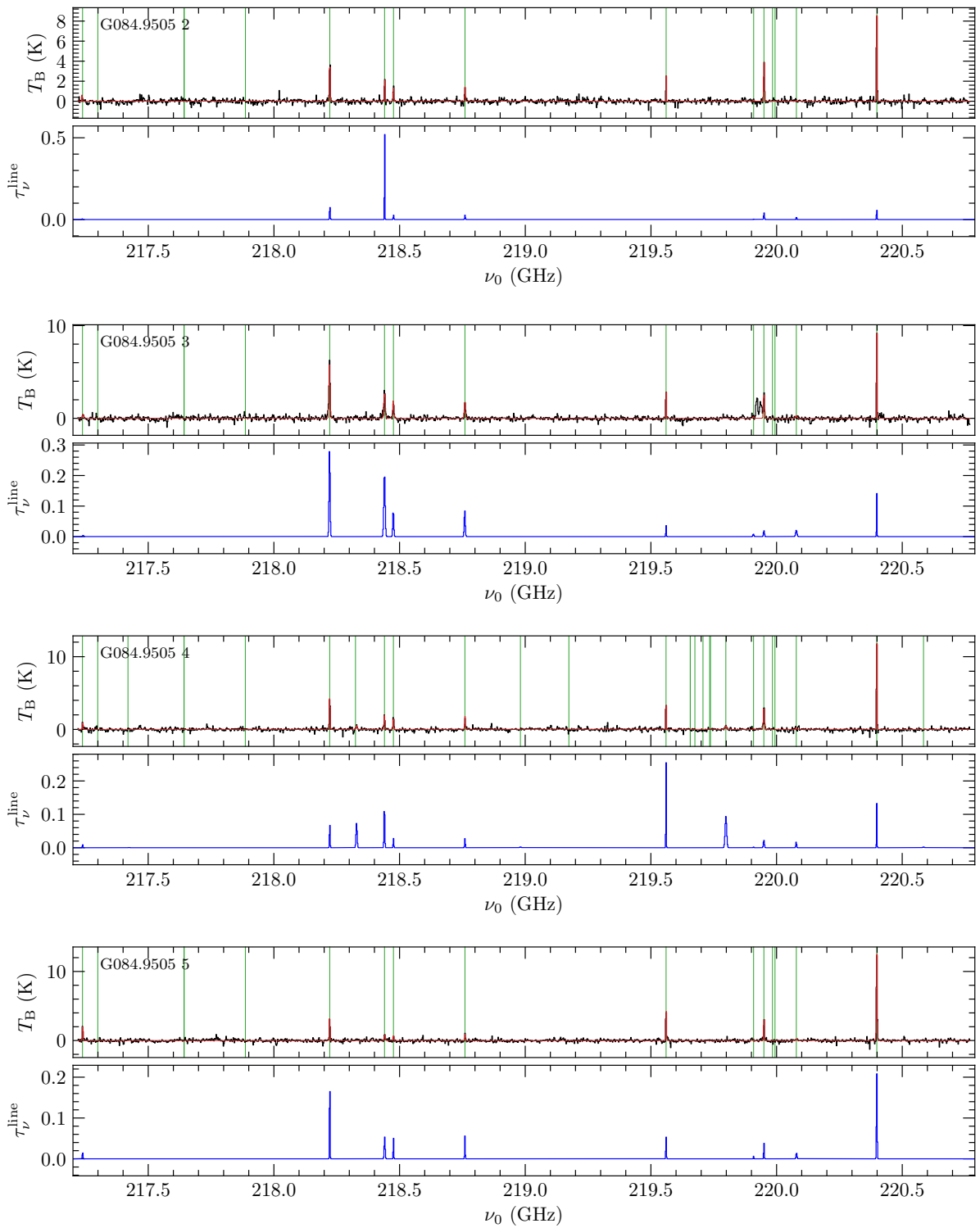


FIGURE A.3 (cont.): Broadband spectrum toward each position. *Top panel:* Observed (black line) spectrum and XCLASS fit (red line) for all 120 analyzed positions. Fitted molecular transitions are indicated by green vertical lines. *Bottom panel:* Optical depth profile (blue line) of all fitted transitions for all 120 analyzed positions.

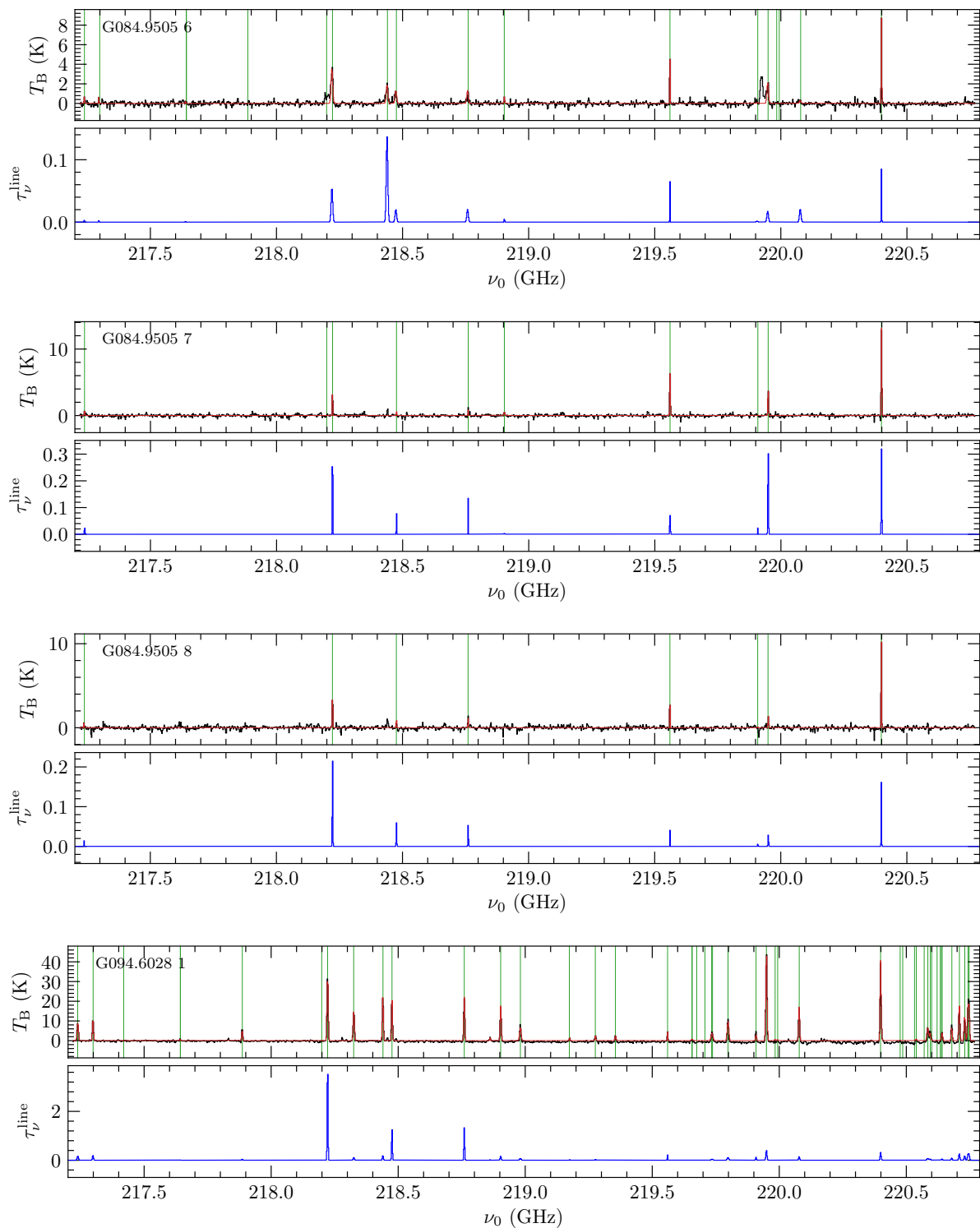


FIGURE A.3 (cont.): Broadband spectrum toward each position. *Top panel:* Observed (black line) spectrum and XCLASS fit (red line) for all 120 analyzed positions. Fitted molecular transitions are indicated by green vertical lines. *Bottom panel:* Optical depth profile (blue line) of all fitted transitions for all 120 analyzed positions.

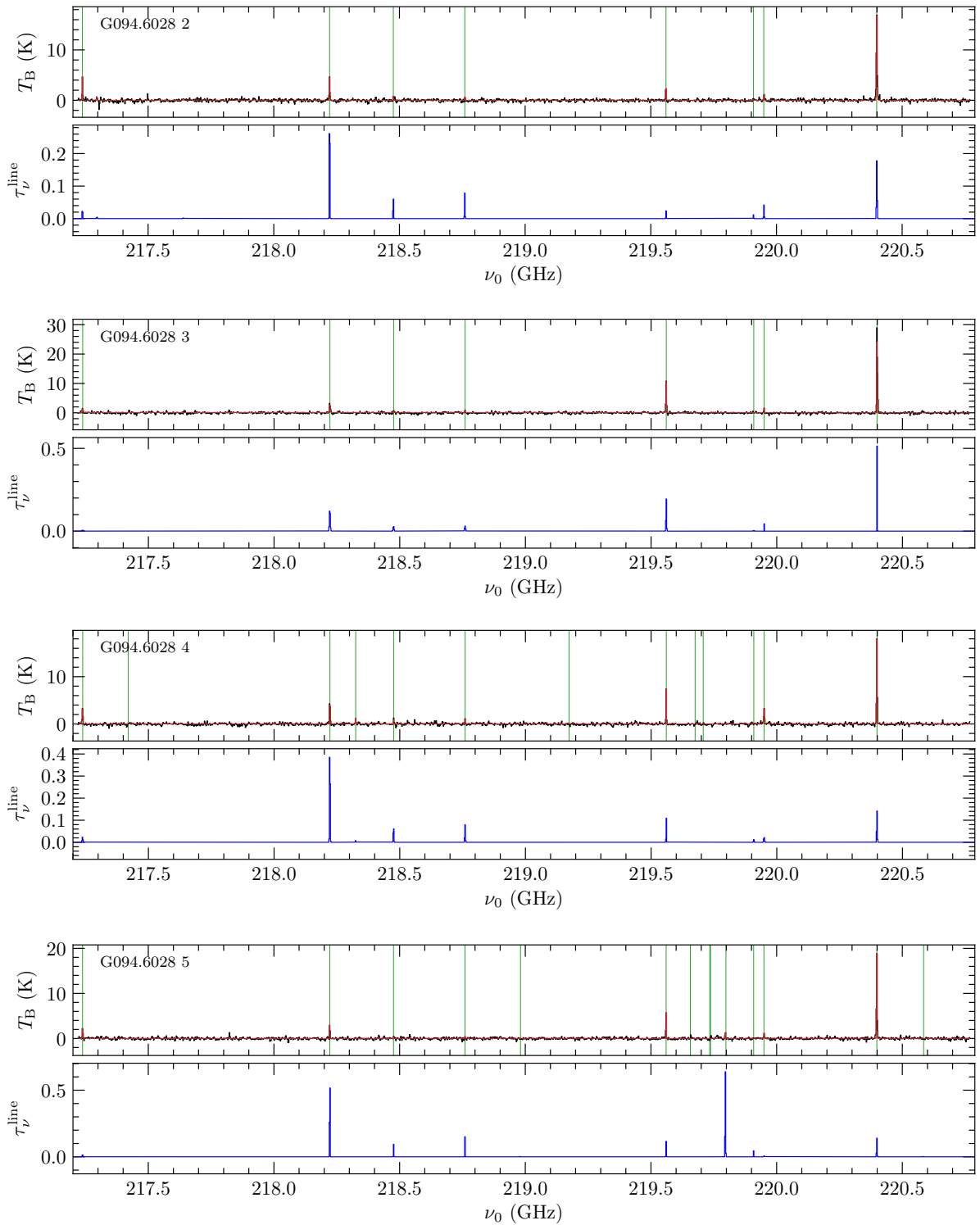


FIGURE A.3 (cont.): Broadband spectrum toward each position. *Top panel:* Observed (black line) spectrum and XCLASS fit (red line) for all 120 analyzed positions. Fitted molecular transitions are indicated by green vertical lines. *Bottom panel:* Optical depth profile (blue line) of all fitted transitions for all 120 analyzed positions.

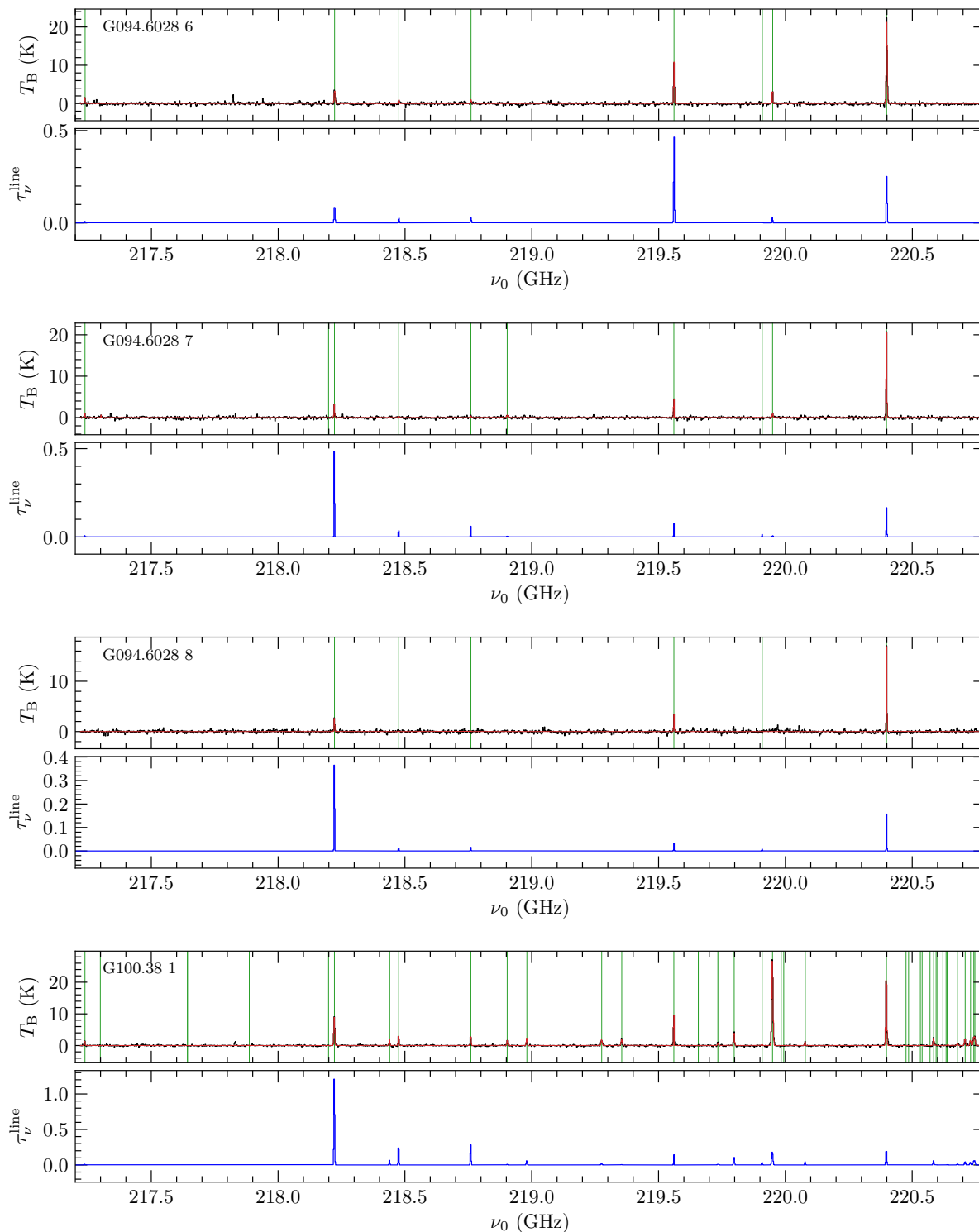


FIGURE A.3 (cont.): Broadband spectrum toward each position. *Top panel:* Observed (black line) spectrum and XCLASS fit (red line) for all 120 analyzed positions. Fitted molecular transitions are indicated by green vertical lines. *Bottom panel:* Optical depth profile (blue line) of all fitted transitions for all 120 analyzed positions.

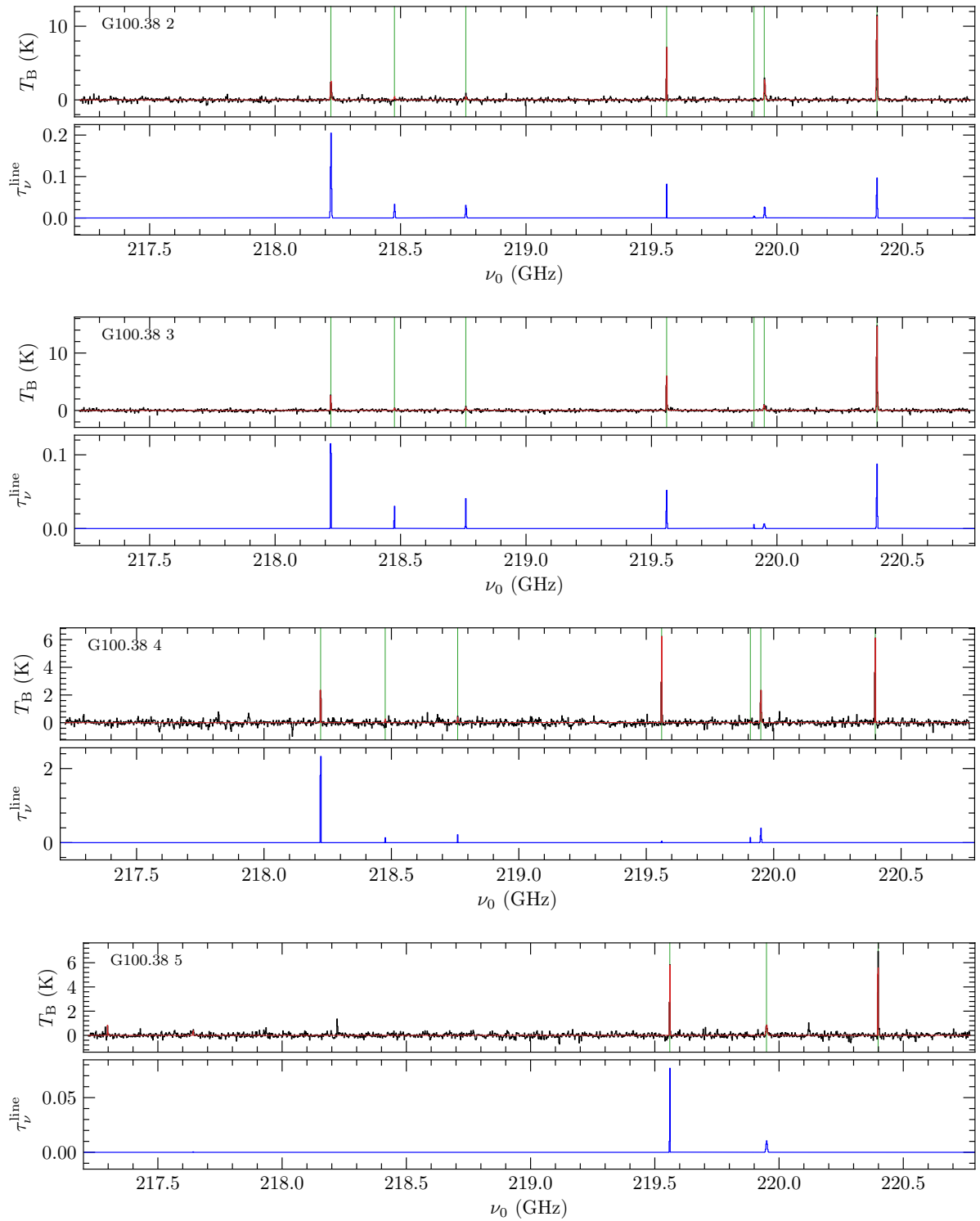


FIGURE A.3 (cont.): Broadband spectrum toward each position. *Top panel:* Observed (black line) spectrum and XCLASS fit (red line) for all 120 analyzed positions. Fitted molecular transitions are indicated by green vertical lines. *Bottom panel:* Optical depth profile (blue line) of all fitted transitions for all 120 analyzed positions.

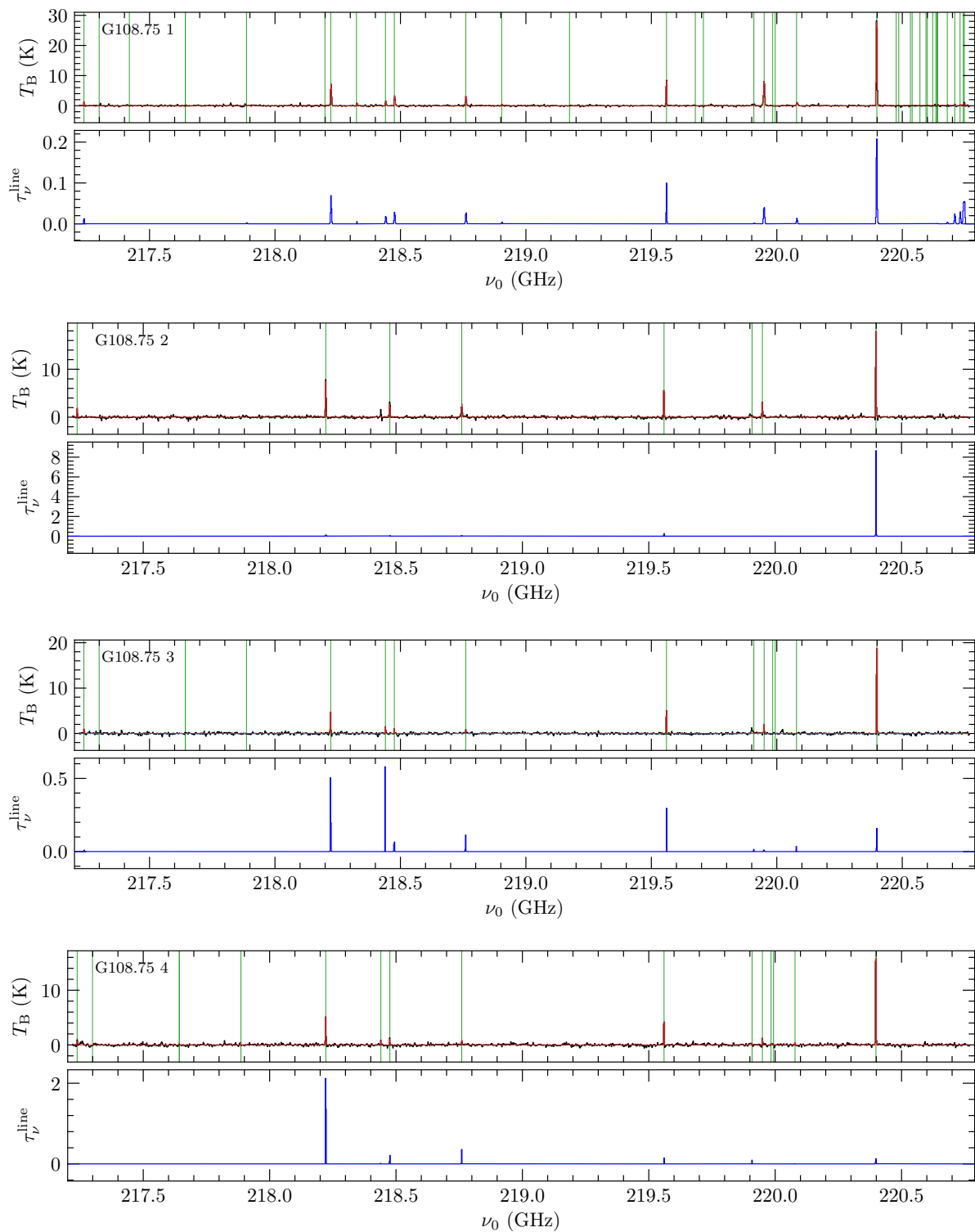


FIGURE A.3 (cont.): Broadband spectrum toward each position. *Top panel:* Observed (black line) spectrum and XCLASS fit (red line) for all 120 analyzed positions. Fitted molecular transitions are indicated by green vertical lines. *Bottom panel:* Optical depth profile (blue line) of all fitted transitions for all 120 analyzed positions.

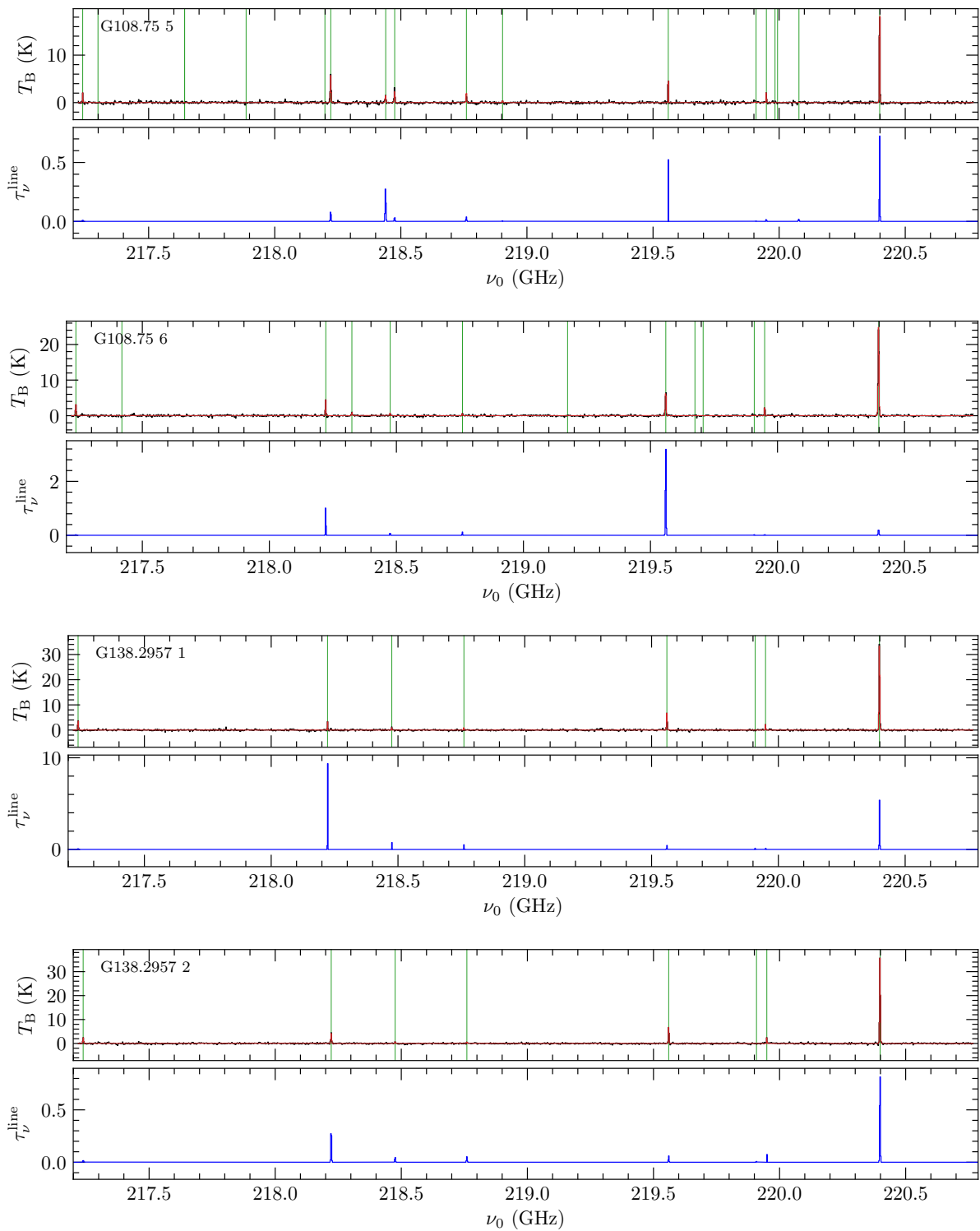


FIGURE A.3 (cont.): Broadband spectrum toward each position. *Top panel:* Observed (black line) spectrum and XCLASS fit (red line) for all 120 analyzed positions. Fitted molecular transitions are indicated by green vertical lines. *Bottom panel:* Optical depth profile (blue line) of all fitted transitions for all 120 analyzed positions.

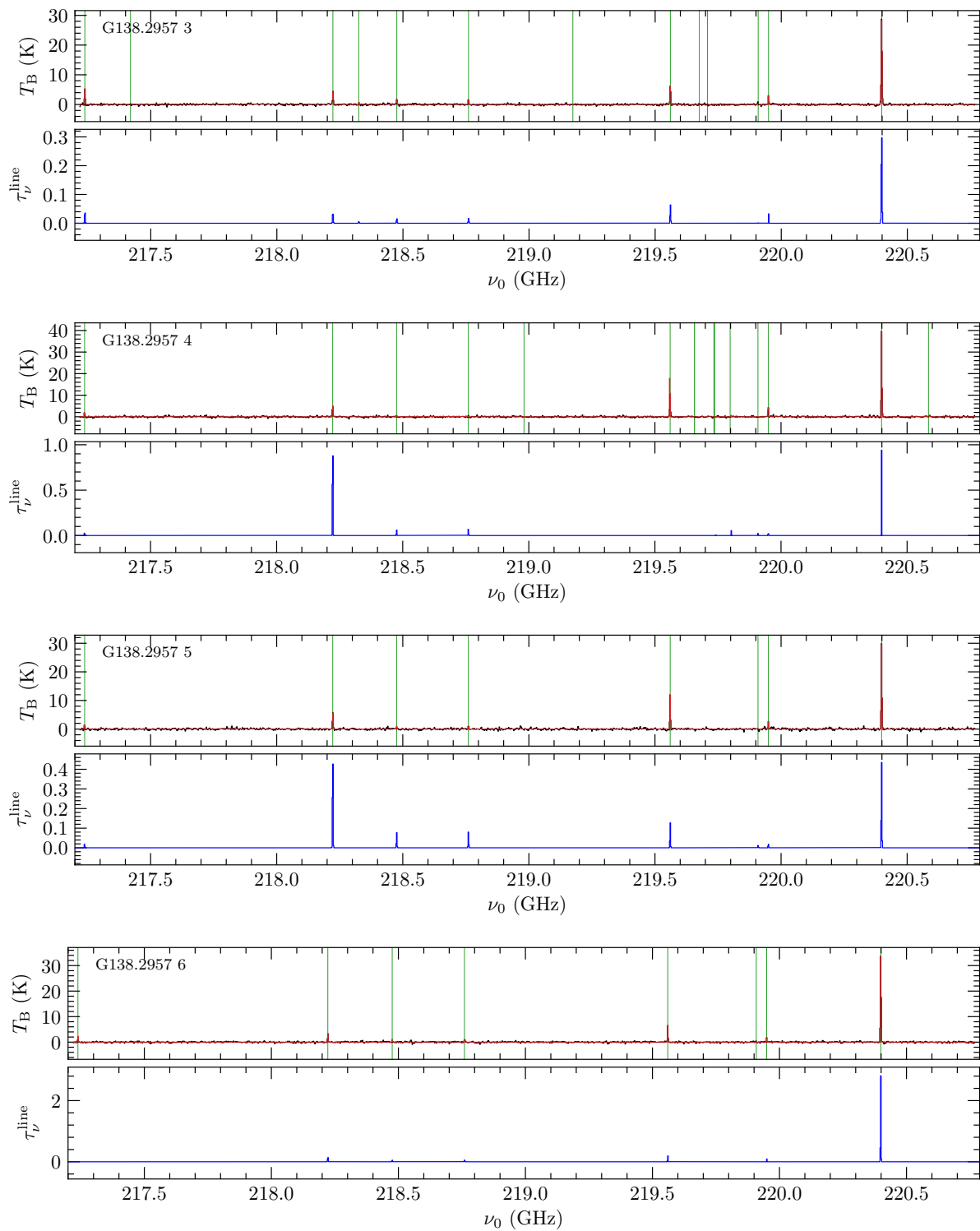


FIGURE A.3 (cont.): Broadband spectrum toward each position. *Top panel:* Observed (black line) spectrum and XCLASS fit (red line) for all 120 analyzed positions. Fitted molecular transitions are indicated by green vertical lines. *Bottom panel:* Optical depth profile (blue line) of all fitted transitions for all 120 analyzed positions.

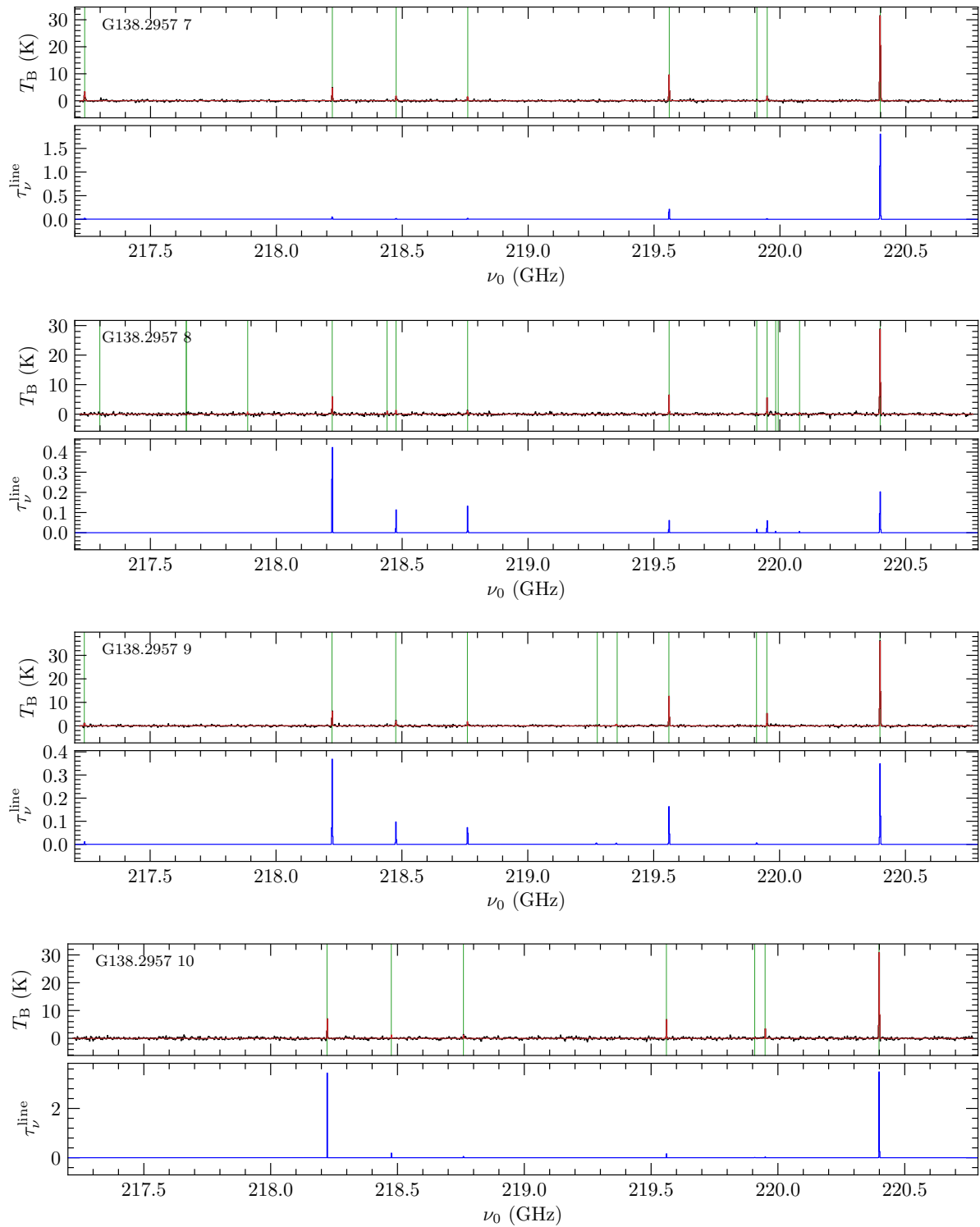


FIGURE A.3 (cont.): Broadband spectrum toward each position. *Top panel:* Observed (black line) spectrum and XCLASS fit (red line) for all 120 analyzed positions. Fitted molecular transitions are indicated by green vertical lines. *Bottom panel:* Optical depth profile (blue line) of all fitted transitions for all 120 analyzed positions.

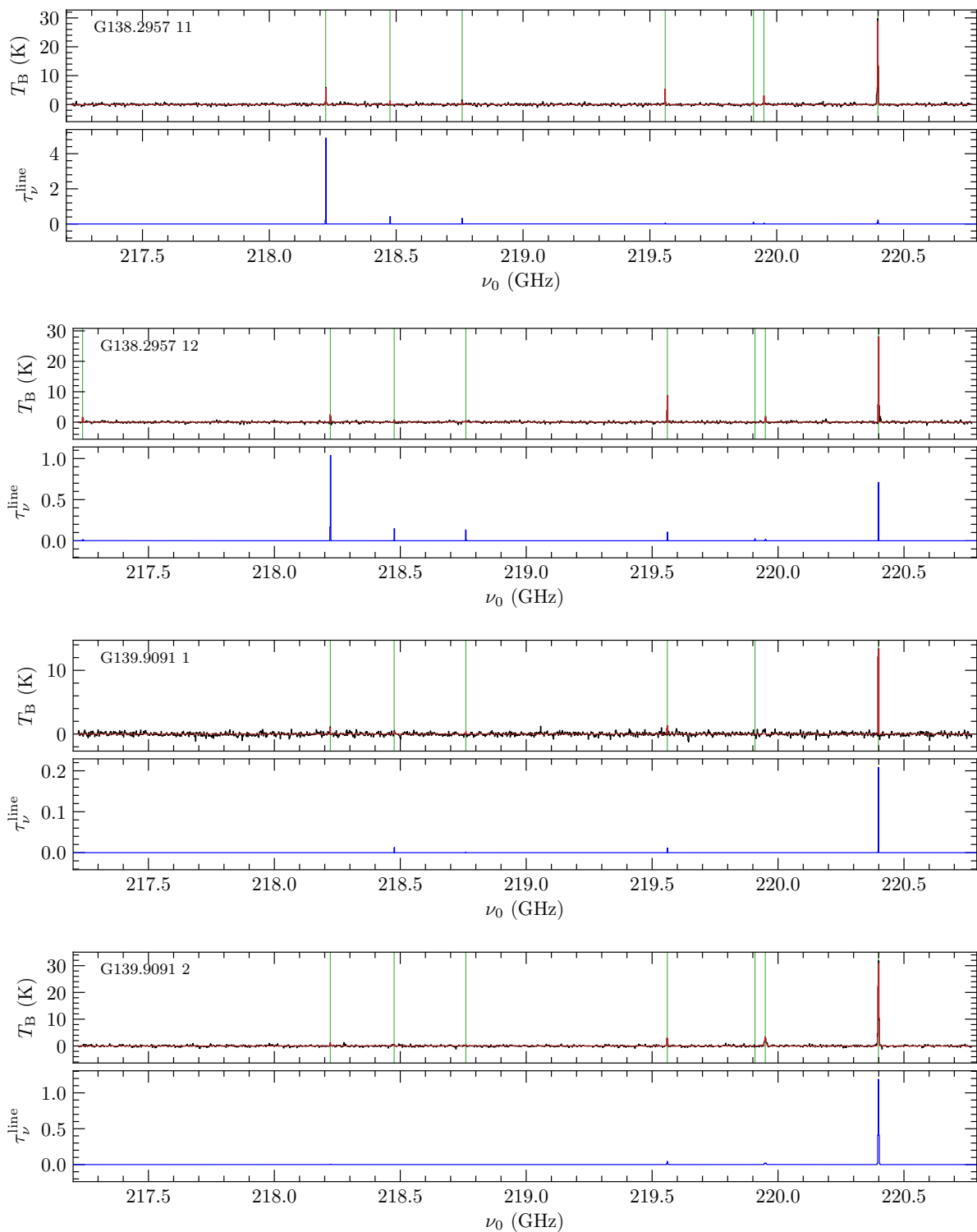


FIGURE A.3 (cont.): Broadband spectrum toward each position. *Top panel:* Observed (black line) spectrum and XCLASS fit (red line) for all 120 analyzed positions. Fitted molecular transitions are indicated by green vertical lines. *Bottom panel:* Optical depth profile (blue line) of all fitted transitions for all 120 analyzed positions.

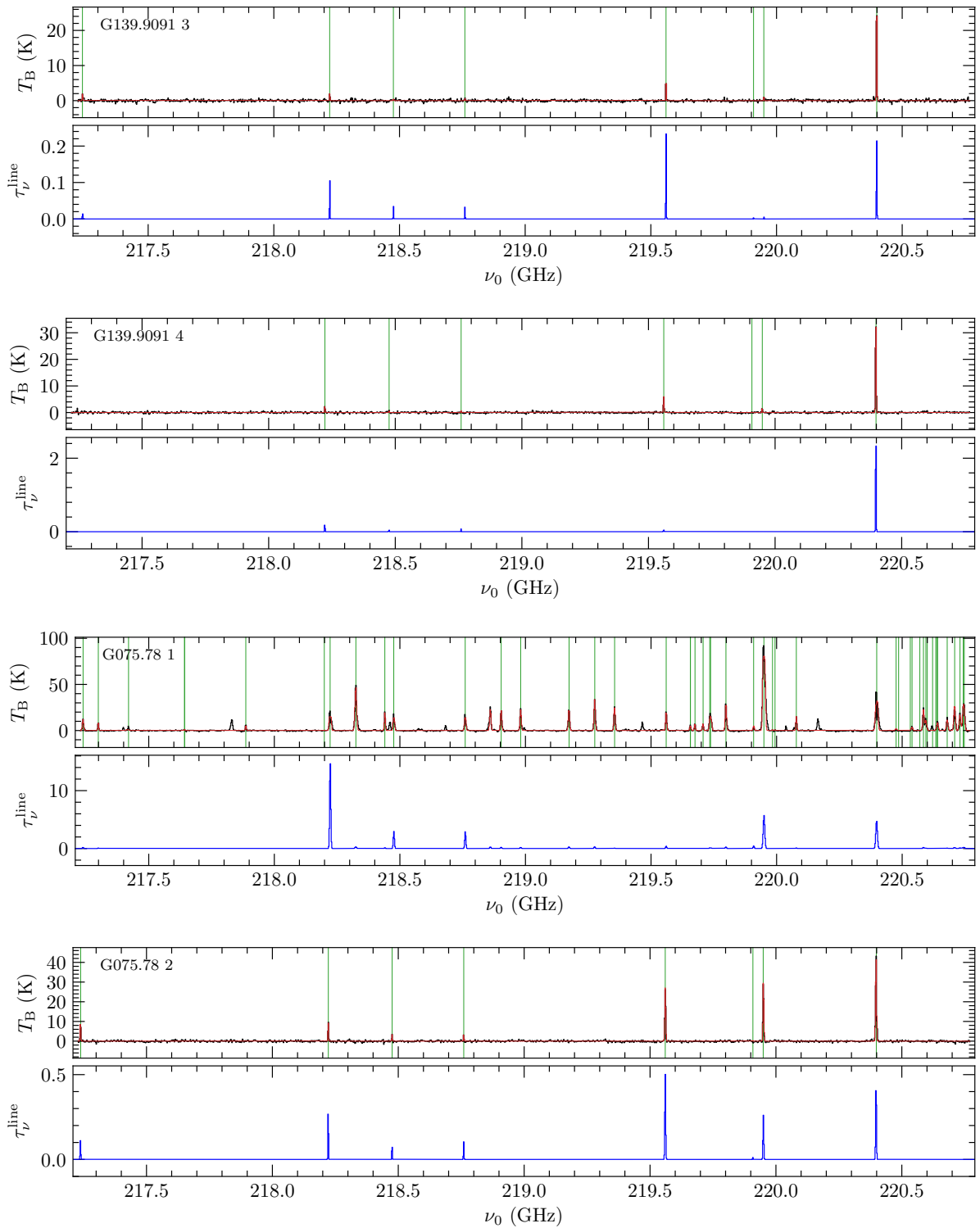


FIGURE A.3 (cont.): Broadband spectrum toward each position. *Top panel:* Observed (black line) spectrum and XCLASS fit (red line) for all 120 analyzed positions. Fitted molecular transitions are indicated by green vertical lines. *Bottom panel:* Optical depth profile (blue line) of all fitted transitions for all 120 analyzed positions.

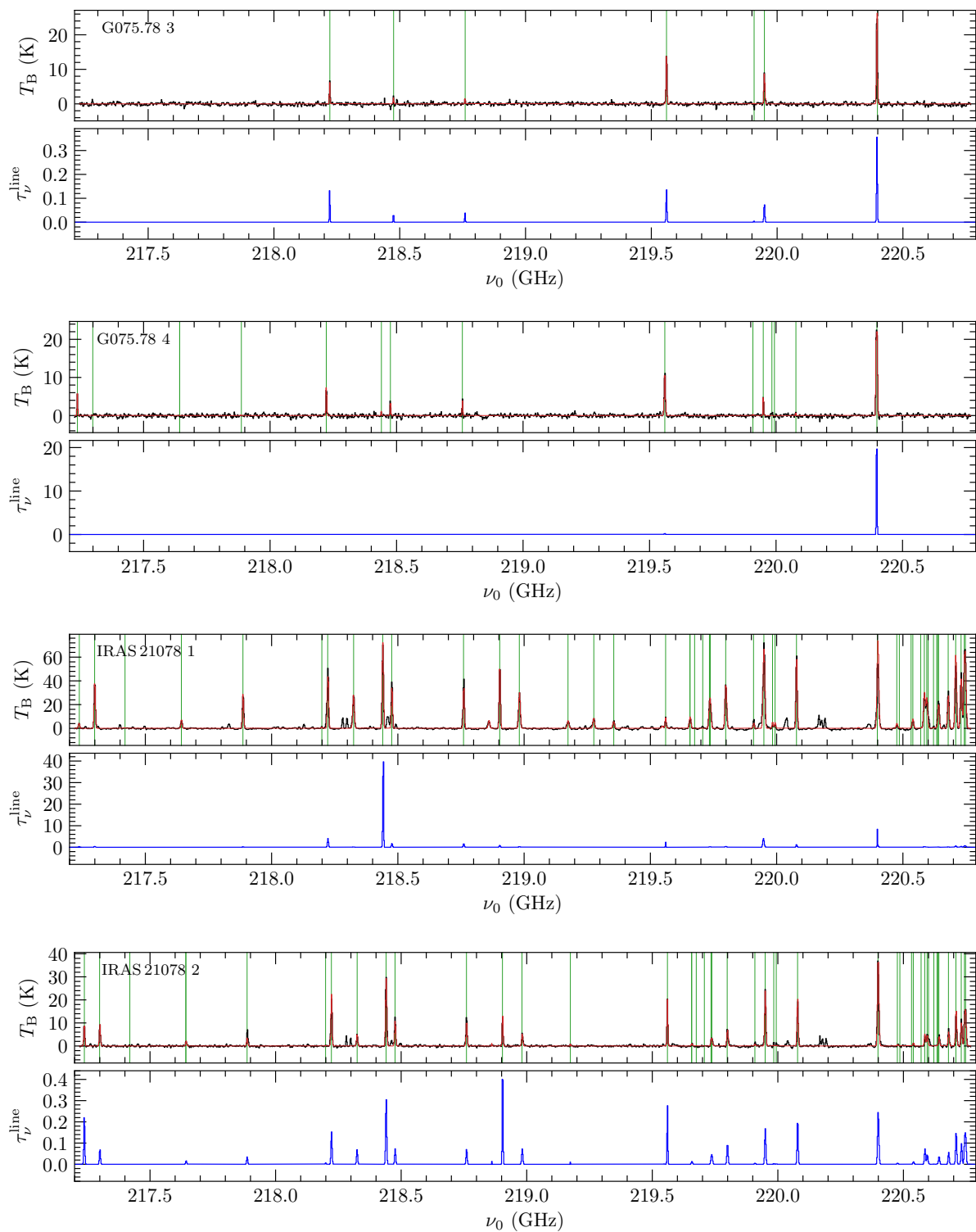


FIGURE A.3 (cont.): Broadband spectrum toward each position. *Top panel:* Observed (black line) spectrum and XCLASS fit (red line) for all 120 analyzed positions. Fitted molecular transitions are indicated by green vertical lines. *Bottom panel:* Optical depth profile (blue line) of all fitted transitions for all 120 analyzed positions.

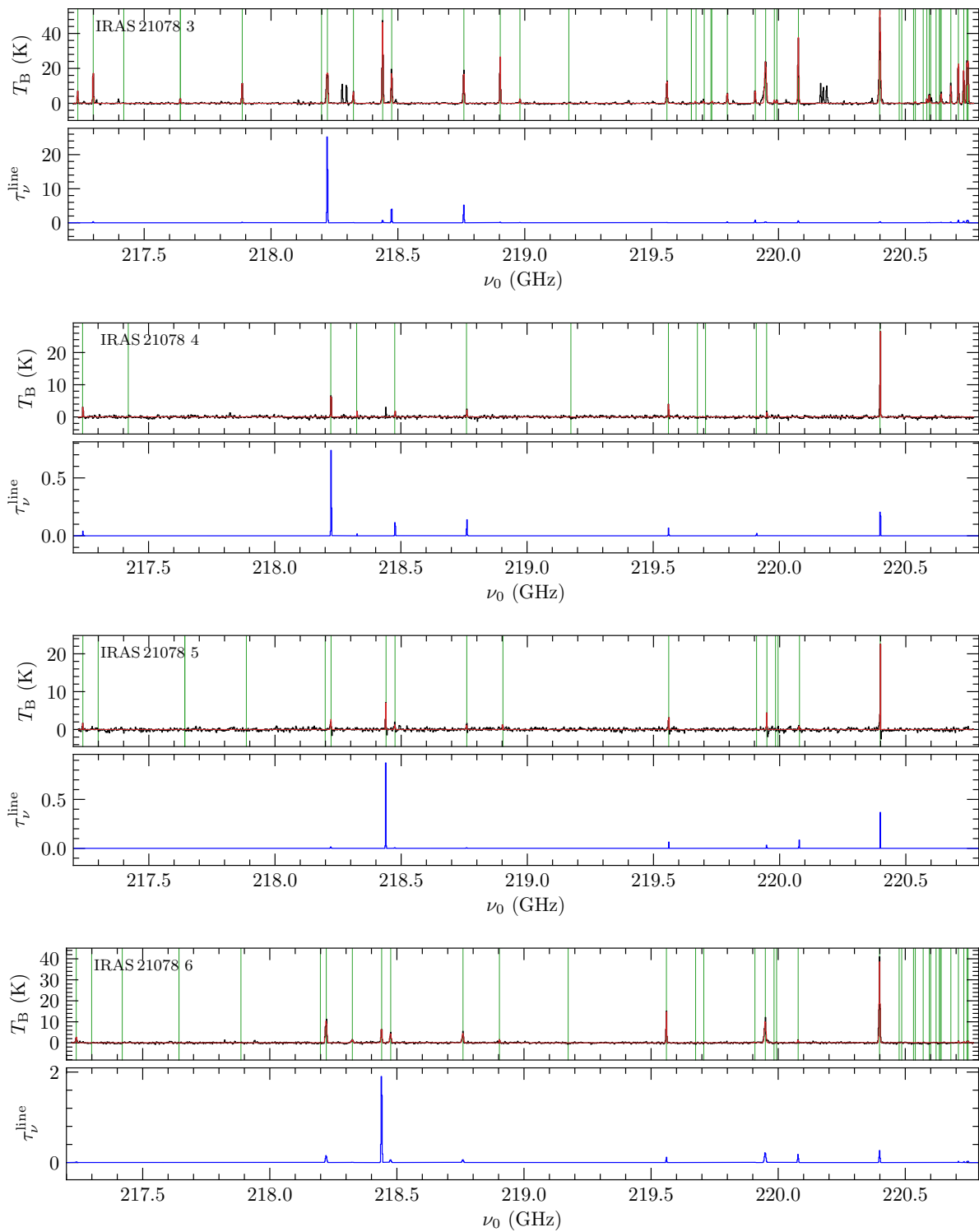


FIGURE A.3 (cont.): Broadband spectrum toward each position. *Top panel:* Observed (black line) spectrum and XCLASS fit (red line) for all 120 analyzed positions. Fitted molecular transitions are indicated by green vertical lines. *Bottom panel:* Optical depth profile (blue line) of all fitted transitions for all 120 analyzed positions.

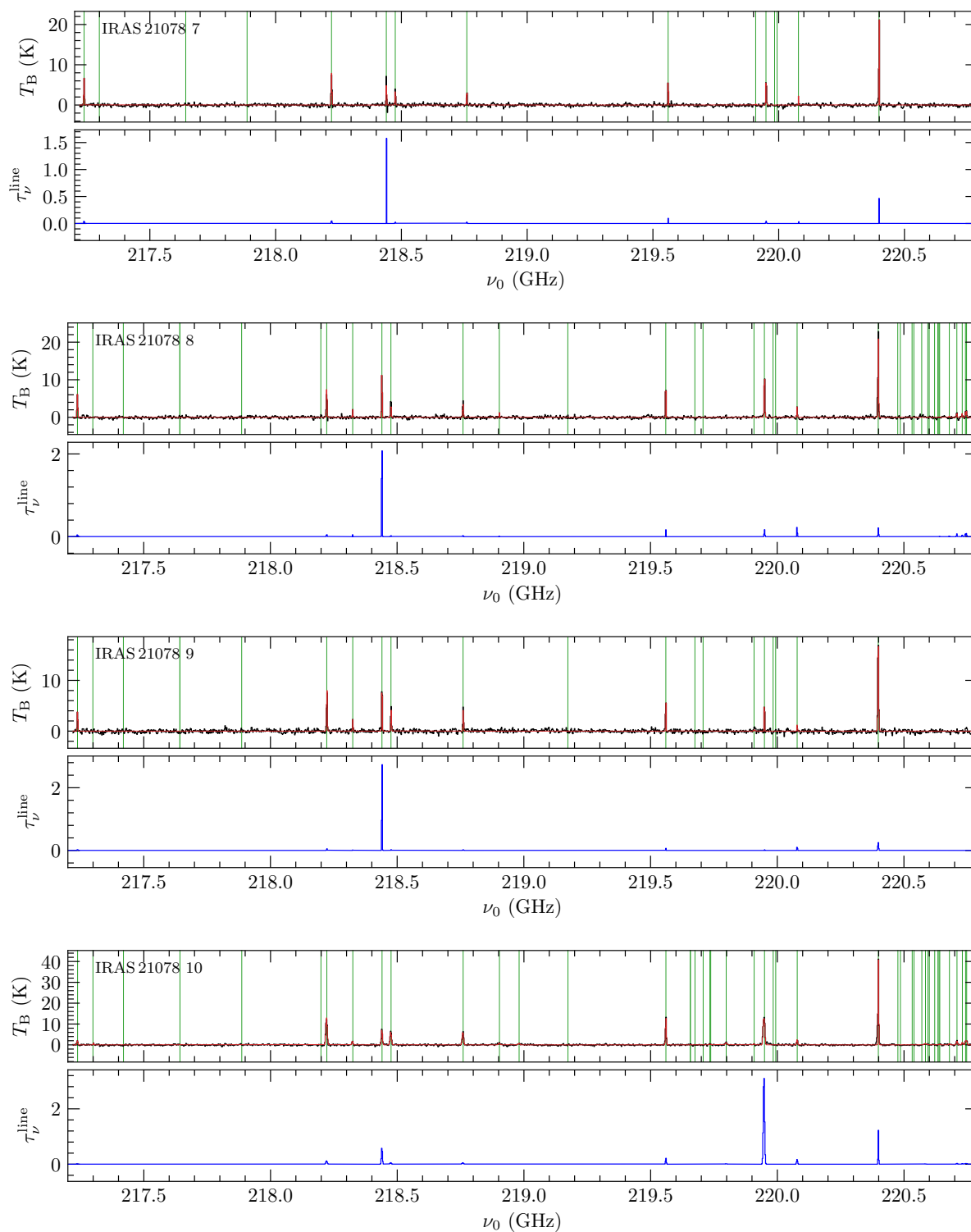


FIGURE A.3 (cont.): Broadband spectrum toward each position. *Top panel:* Observed (black line) spectrum and XCLASS fit (red line) for all 120 analyzed positions. Fitted molecular transitions are indicated by green vertical lines. *Bottom panel:* Optical depth profile (blue line) of all fitted transitions for all 120 analyzed positions.

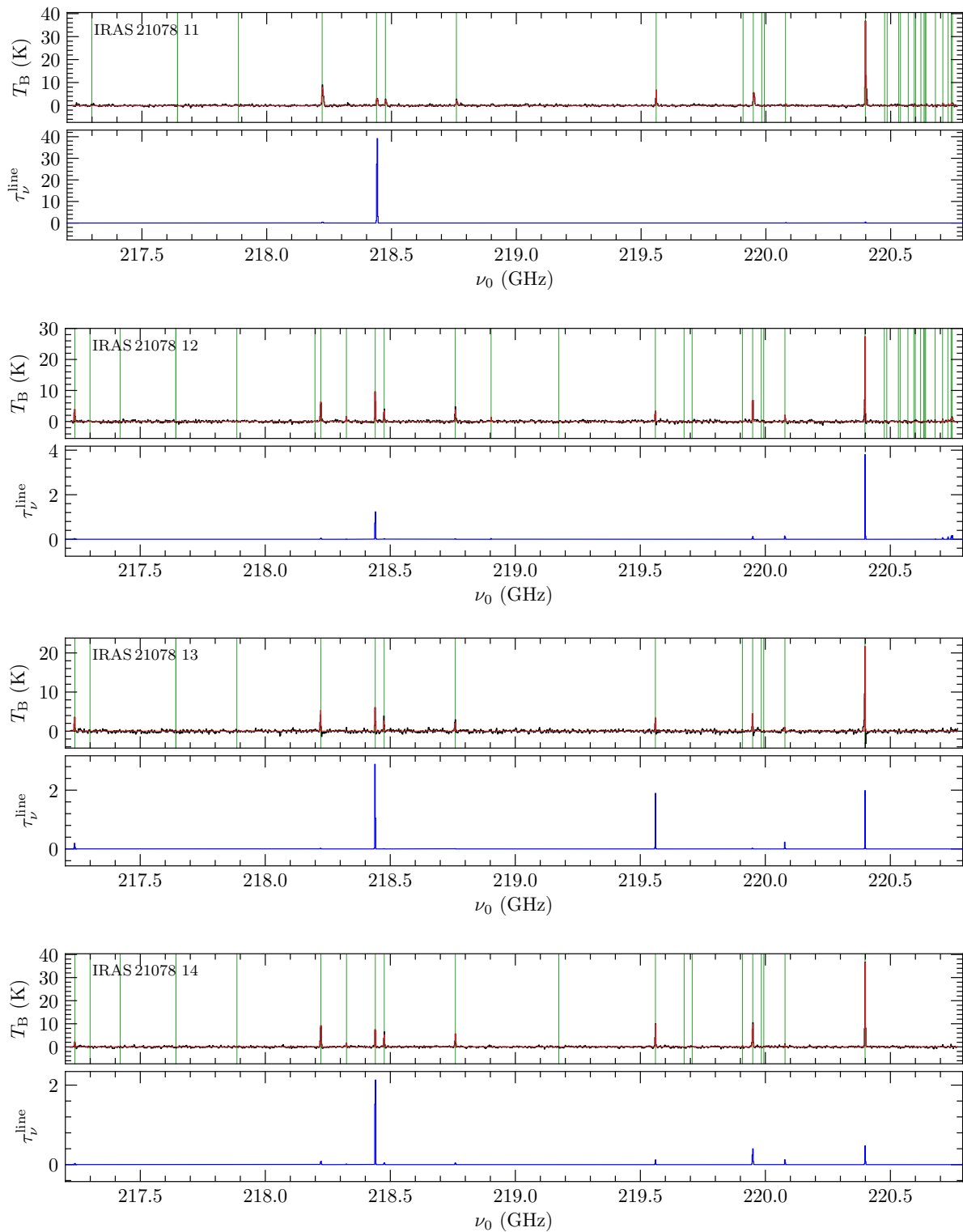


FIGURE A.3 (cont.): Broadband spectrum toward each position. *Top panel:* Observed (black line) spectrum and XCLASS fit (red line) for all 120 analyzed positions. Fitted molecular transitions are indicated by green vertical lines. *Bottom panel:* Optical depth profile (blue line) of all fitted transitions for all 120 analyzed positions.

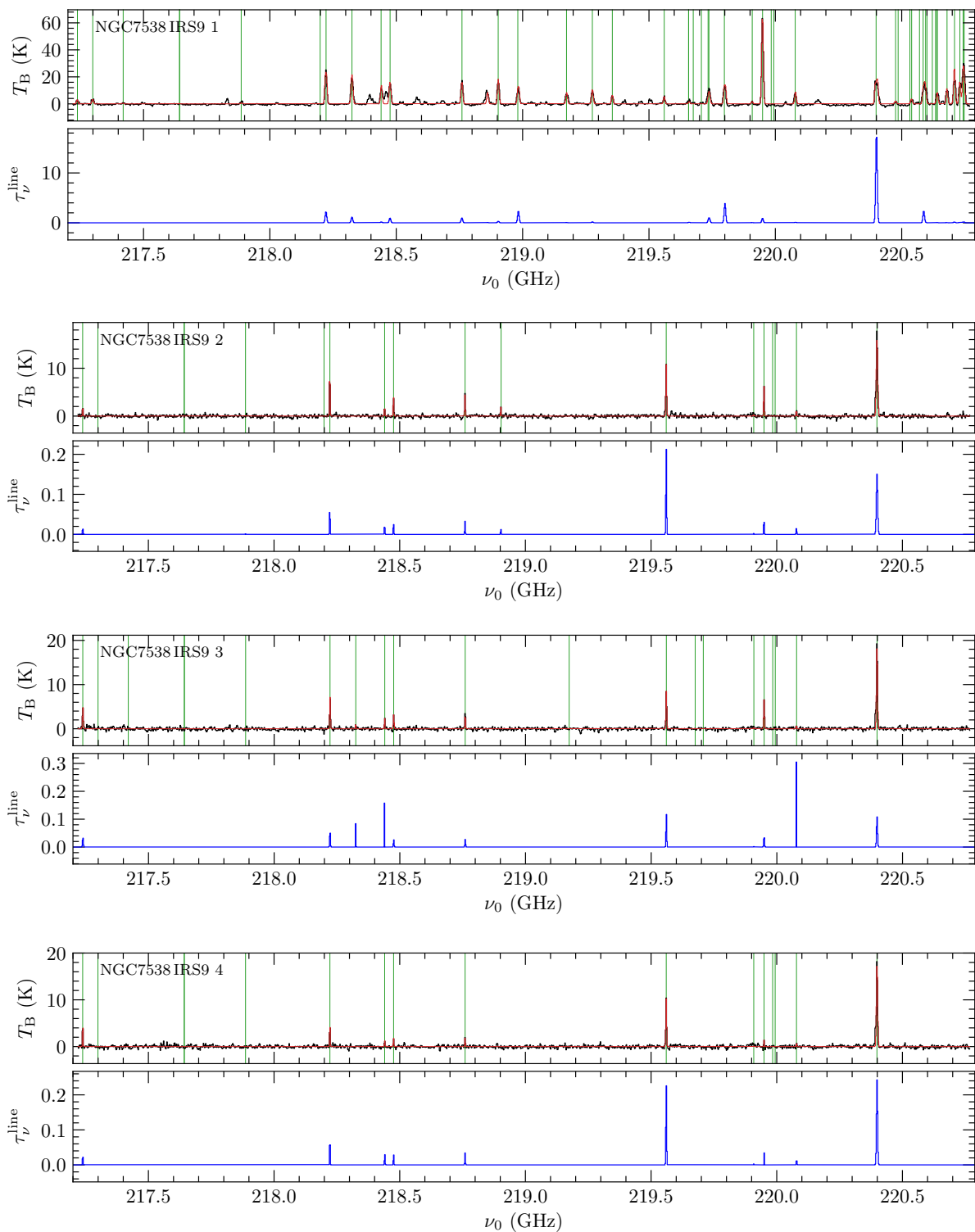


FIGURE A.3 (cont.): Broadband spectrum toward each position. *Top panel:* Observed (black line) spectrum and XCLASS fit (red line) for all 120 analyzed positions. Fitted molecular transitions are indicated by green vertical lines. *Bottom panel:* Optical depth profile (blue line) of all fitted transitions for all 120 analyzed positions.

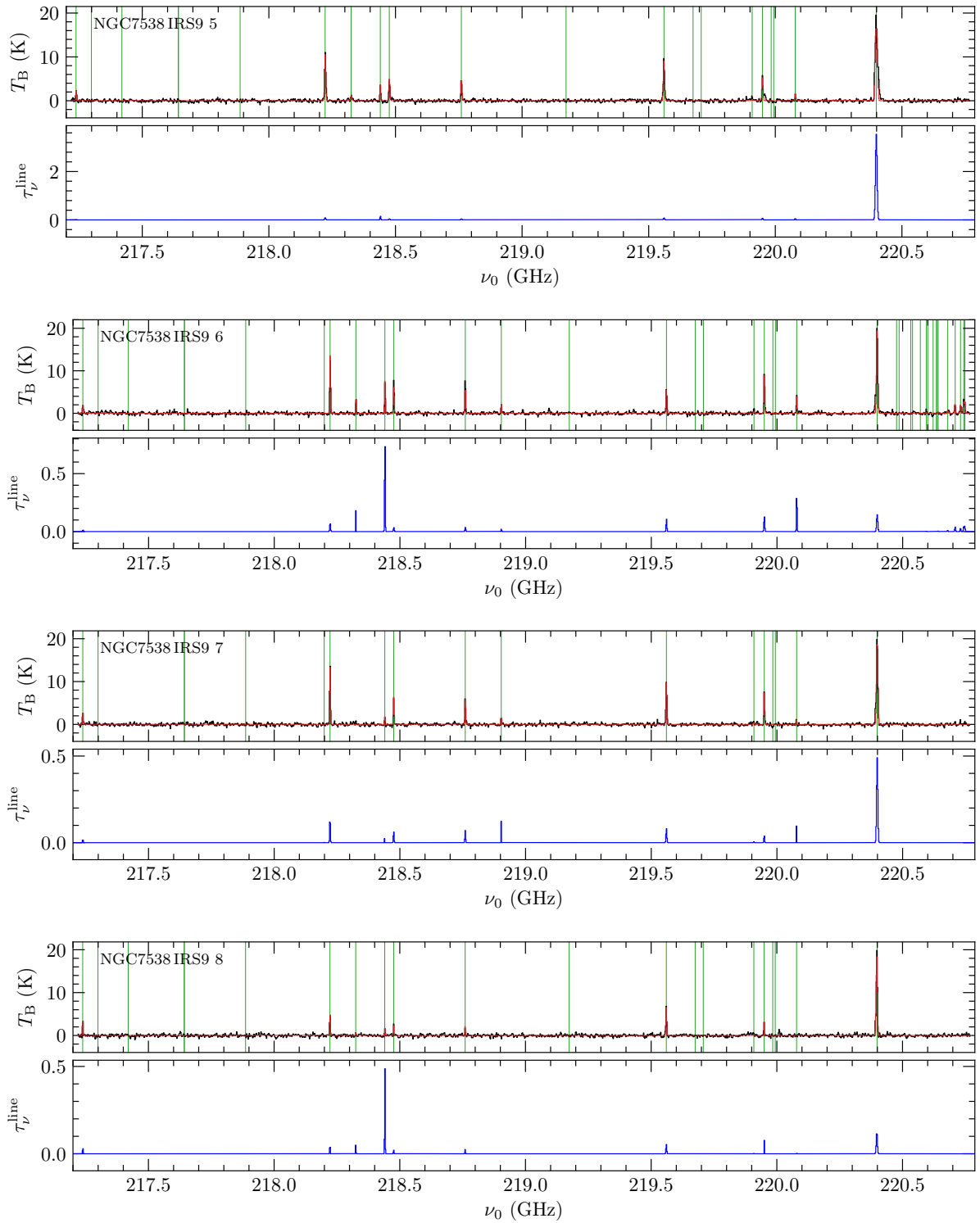


FIGURE A.3 (cont.): Broadband spectrum toward each position. *Top panel:* Observed (black line) spectrum and XCLASS fit (red line) for all 120 analyzed positions. Fitted molecular transitions are indicated by green vertical lines. *Bottom panel:* Optical depth profile (blue line) of all fitted transitions for all 120 analyzed positions.

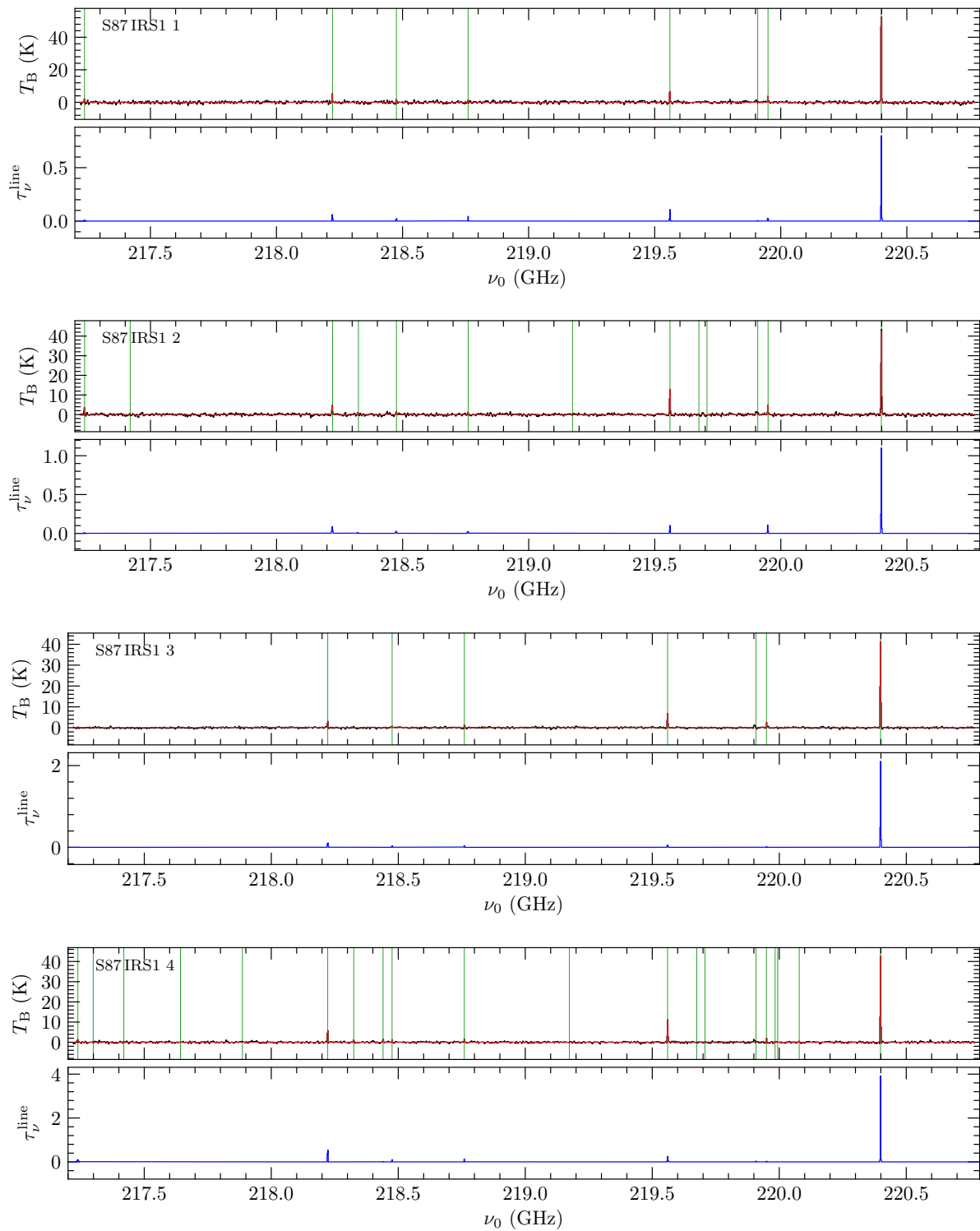


FIGURE A.3 (cont.): Broadband spectrum toward each position. *Top panel:* Observed (black line) spectrum and XCLASS fit (red line) for all 120 analyzed positions. Fitted molecular transitions are indicated by green vertical lines. *Bottom panel:* Optical depth profile (blue line) of all fitted transitions for all 120 analyzed positions.

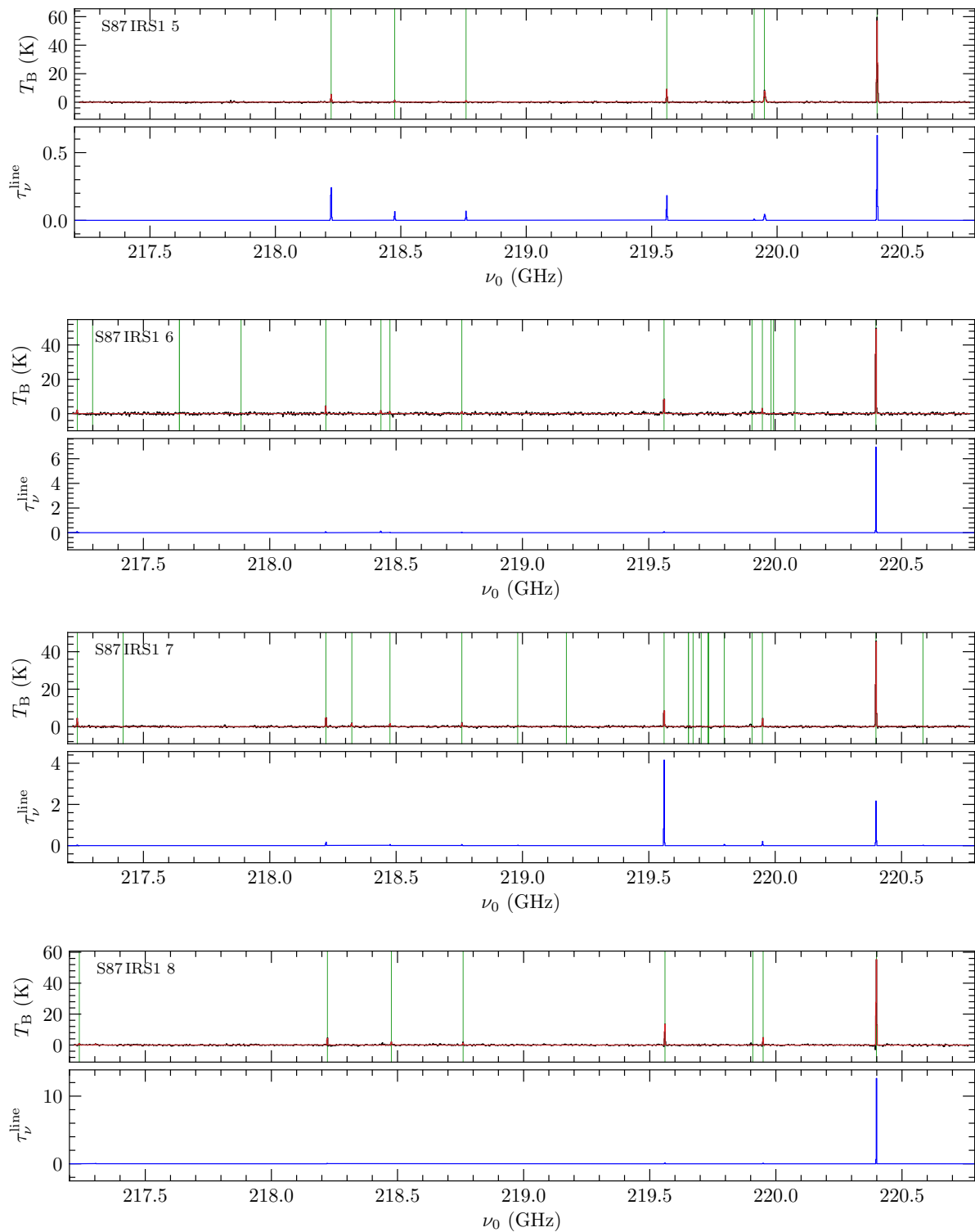


FIGURE A.3 (cont.): Broadband spectrum toward each position. *Top panel:* Observed (black line) spectrum and XCLASS fit (red line) for all 120 analyzed positions. Fitted molecular transitions are indicated by green vertical lines. *Bottom panel:* Optical depth profile (blue line) of all fitted transitions for all 120 analyzed positions.

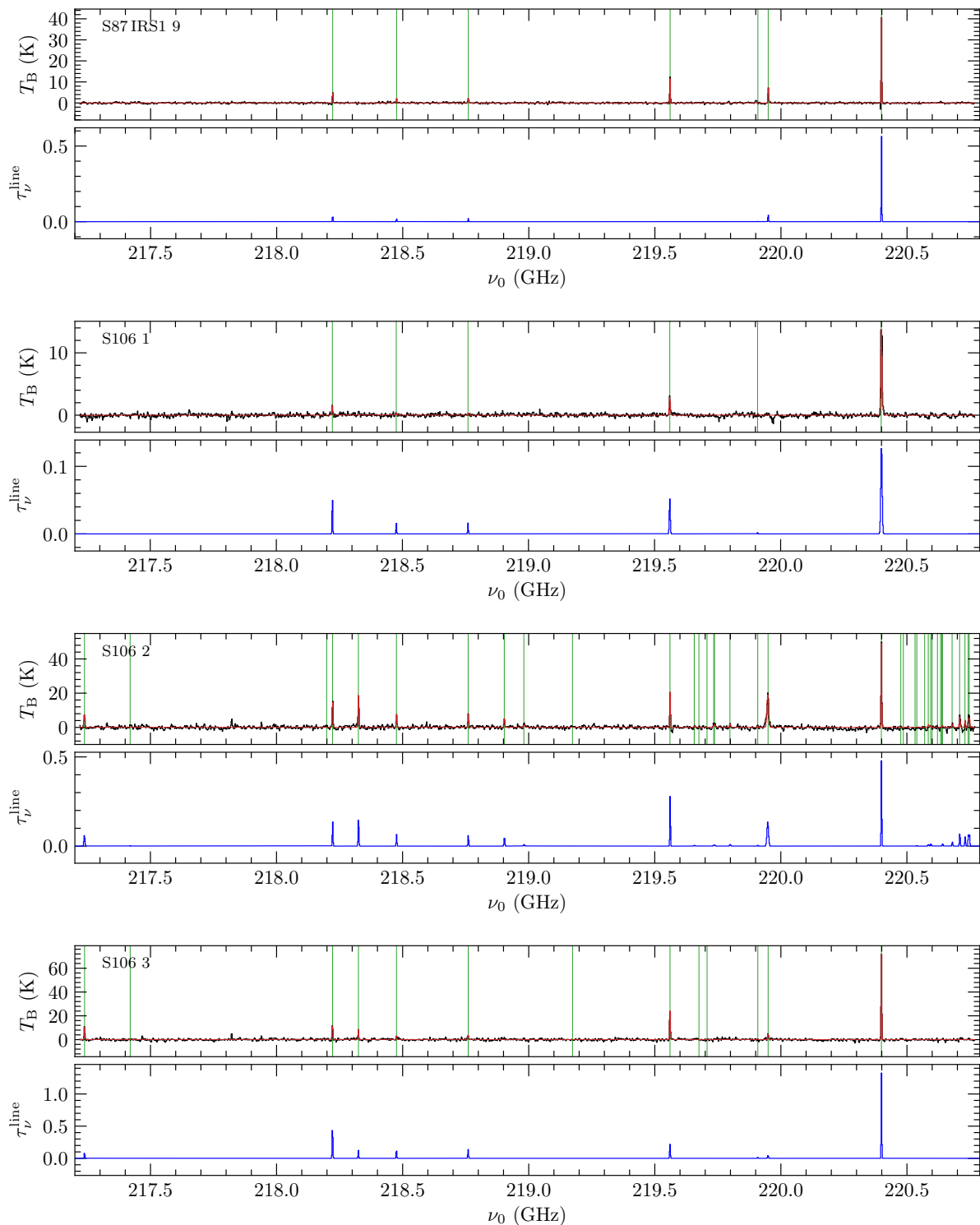


FIGURE A.3 (cont.): Broadband spectrum toward each position. *Top panel:* Observed (black line) spectrum and XCLASS fit (red line) for all 120 analyzed positions. Fitted molecular transitions are indicated by green vertical lines. *Bottom panel:* Optical depth profile (blue line) of all fitted transitions for all 120 analyzed positions.

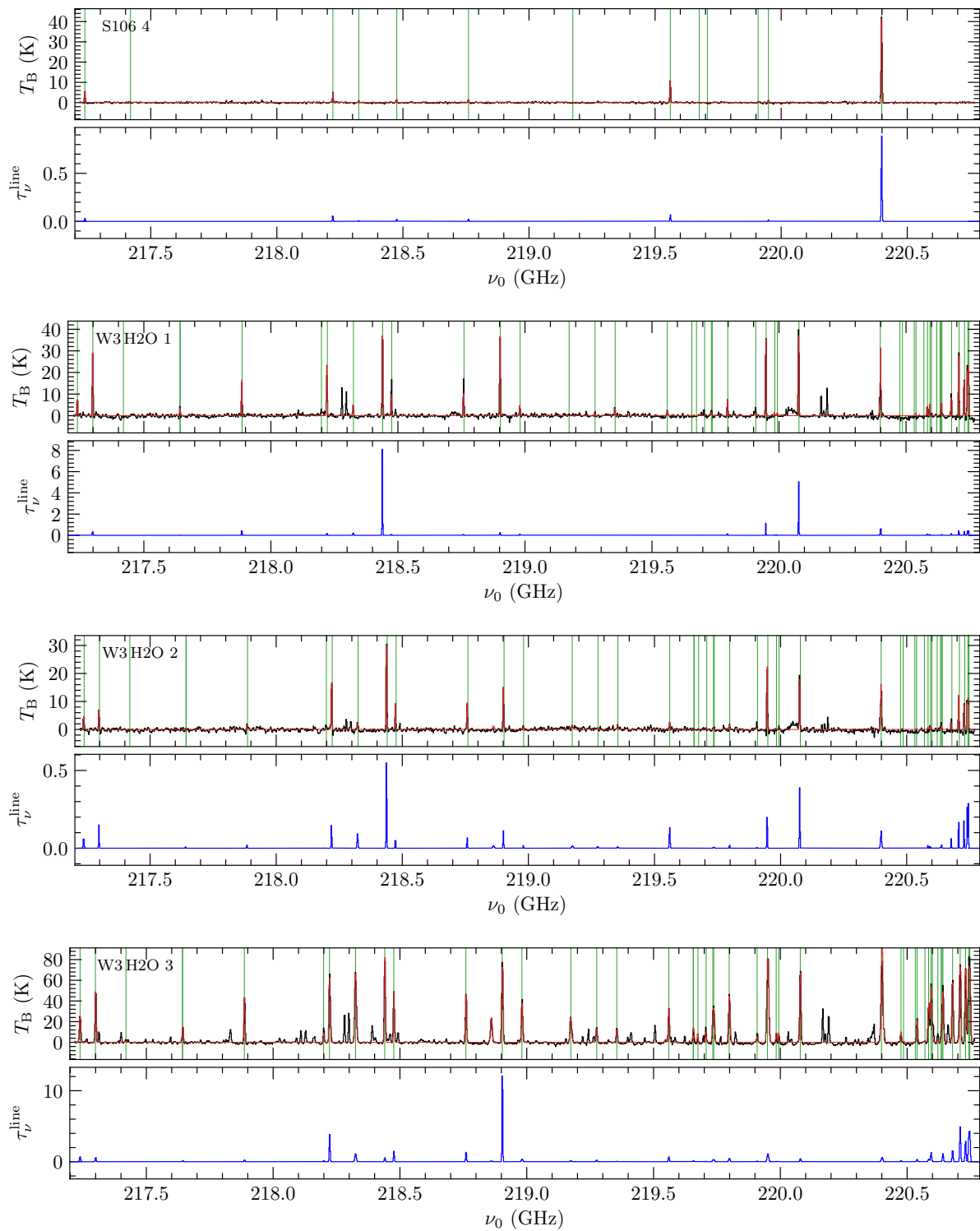


FIGURE A.3 (cont.): Broadband spectrum toward each position. *Top panel:* Observed (black line) spectrum and XCLASS fit (red line) for all 120 analyzed positions. Fitted molecular transitions are indicated by green vertical lines. *Bottom panel:* Optical depth profile (blue line) of all fitted transitions for all 120 analyzed positions.

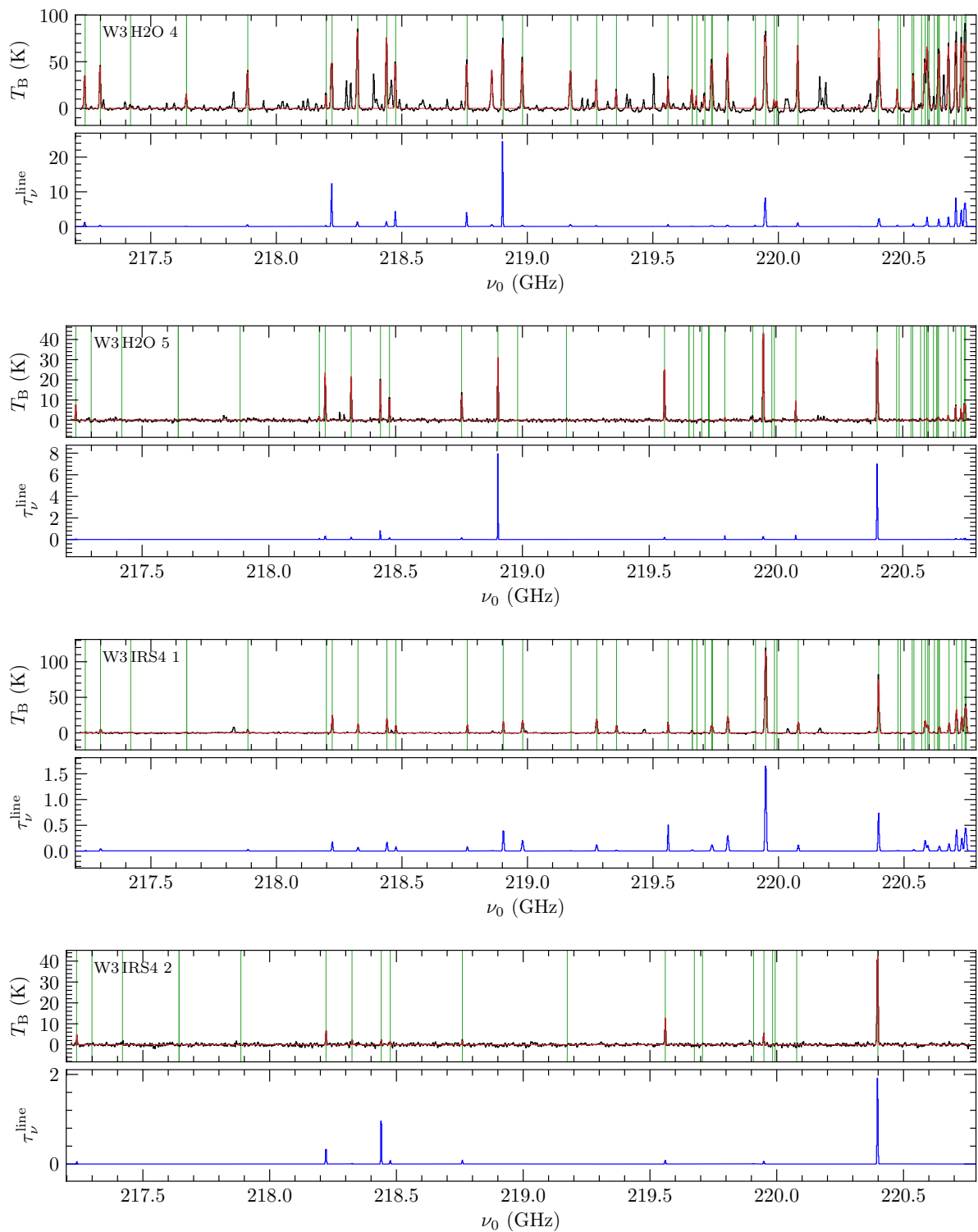


FIGURE A.3 (cont.): Broadband spectrum toward each position. *Top panel:* Observed (black line) spectrum and XCLASS fit (red line) for all 120 analyzed positions. Fitted molecular transitions are indicated by green vertical lines. *Bottom panel:* Optical depth profile (blue line) of all fitted transitions for all 120 analyzed positions.

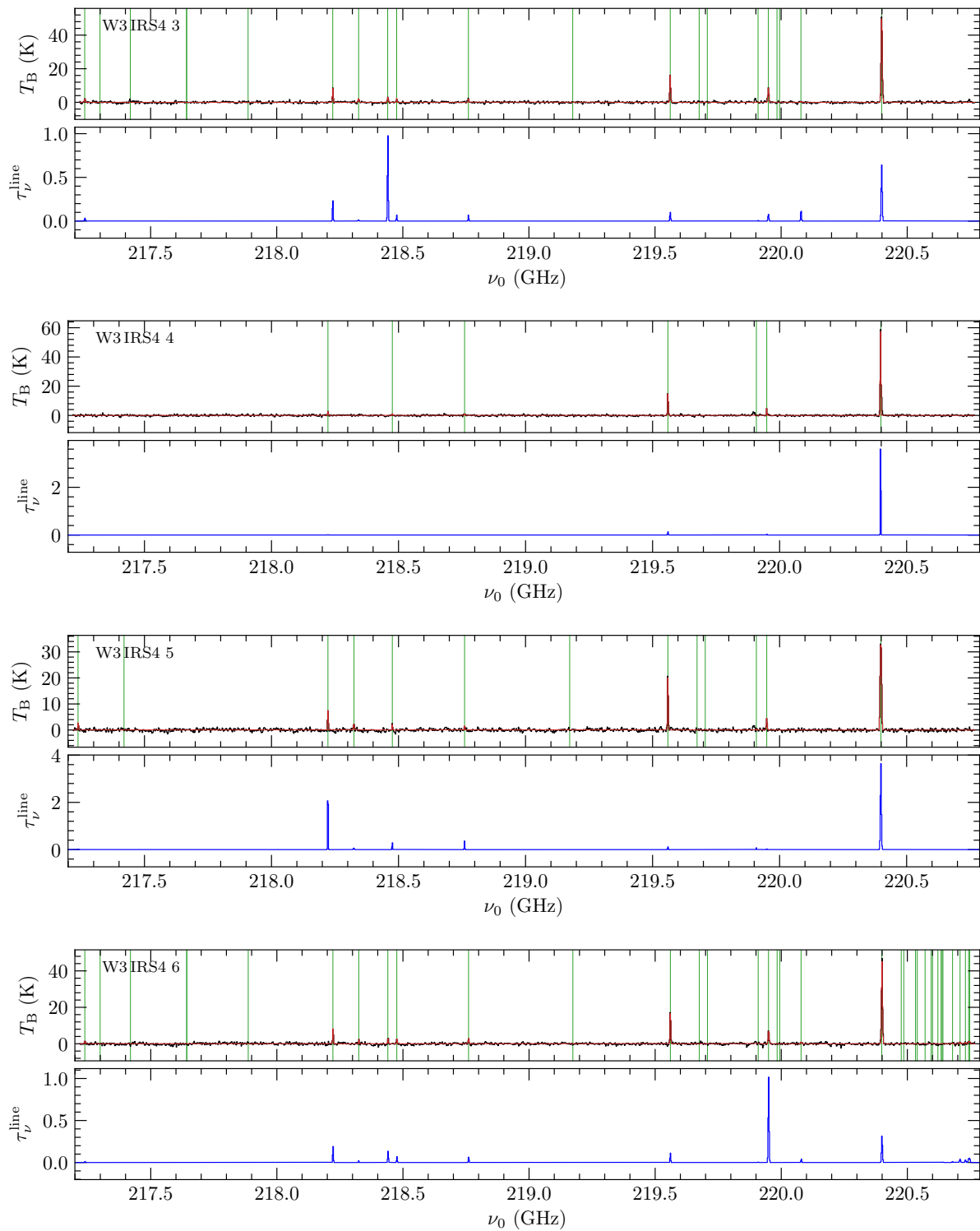


FIGURE A.3 (cont.): Broadband spectrum toward each position. *Top panel:* Observed (black line) spectrum and XCLASS fit (red line) for all 120 analyzed positions. Fitted molecular transitions are indicated by green vertical lines. *Bottom panel:* Optical depth profile (blue line) of all fitted transitions for all 120 analyzed positions.

A.7 Model results

Table A.5 shows the best-fit chemical timescale τ_{chem} , χ^2 value, and percentage of well modeled molecules Y for each initial condition model (HMPO, HMC, and UCHII model) for each core.

TABLE A.5: MUSCLE results for cores in the CORE regions. The best-fit chemical timescale τ_{chem} , χ^2 value, and percentage of well modeled molecules Y are shown for each initial condition model.

Core	HMPO model			HMC model			UCHII model		
	τ_{chem} (yr)	χ^2 (%)	Y (%)	τ_{chem} (yr)	χ^2 (%)	Y (%)	τ_{chem} (yr)	χ^2 (%)	Y (%)
IRAS 23033 1	33 574	0.339	64	73 271	0.346	64	97 675	0.336	64
IRAS 23033 2	18 019	0.525	64	49 046	0.589	64	104 065	0.589	55
IRAS 23033 3	18 705	0.517	64	50 019	0.559	64	96 415	0.567	64
IRAS 23151 1	19 415	0.458	64	49 222	0.557	64	83 510	0.444	82
IRAS 23385 1	17 547	0.581	55	48 510	0.498	55	87 011	0.644	45
IRAS 23385 2	20 729	0.545	55	48 510	0.602	45	95 268	0.465	55
AFGL 2591 1	17 884	0.508	64	54 635	0.562	64	83 510	0.441	82
CepA HW2 1	18 705	0.602	55	48 530	0.605	55	83 510	0.478	64
CepA HW2 2	19 415	0.459	73	48 812	0.616	45	88 141	0.454	73
G084.9505 1	16 510	0.475	55	48 510	0.533	55	83 510	0.537	55
G094.6028 1	17 884	0.593	55	56 611	0.521	64	83 784	0.536	55
G100.38 1	18 705	0.483	64	54 090	0.459	64	83 602	0.432	73
G108.75 1	20 011	0.485	73	48 602	0.608	55	87 011	0.610	55
G108.75 2	20 729	0.319	73	60 268	0.325	73	106 070	0.296	73
G075.78 1	18 330	0.471	64	49 547	0.532	64	84 222	0.410	82
IRAS 21078 1	17 157	0.602	73	55 234	0.509	64	92 402	0.516	73
IRAS 21078 2	18 168	0.601	55	48 876	0.542	64	84 884	0.575	55
NGC7538 IRS9 1	17 884	0.502	73	71 070	0.521	73	84 292	0.447	82
S87 IRS1 1	16 784	0.383	64	59 223	0.337	64	83 510	0.413	64
W3 H2O 3	17 547	0.590	55	48 876	0.579	45	83 510	0.532	64
W3 H2O 4	17 292	0.514	55	54 635	0.563	64	85 920	0.485	73
W3 IRS4 1	20 011	0.492	64	67 238	0.570	64	86 415	0.469	82

Appendix B

Supplementary material for Chapter 3

B.1 Moment maps

In Sect. 3.5.2 we compute the line integrated intensity in order to study and compare the spatial morphology of the molecular emission. The moment 0 map of H_2CO $3_{0,3} - 2_{0,2}$, SiO $5 - 4$, and CH_3OH $4_{2,3} - 3_{1,2}E$ are shown in Sect. 3.5.2 in Figs. 3.6, 3.7, and 3.8, respectively. Here, the line integrated intensity maps of the remaining transitions (Table 3.2) are presented in Figs. B.1 – B.23. The line emission was integrated from $v_{\text{LSR}} - 3 \text{ km s}^{-1}$ to $v_{\text{LSR}} + 3 \text{ km s}^{-1}$. The intensity-weighted peak velocity (moment 1) map of molecular lines with spatially extended emission in ISOSS J23053+5953 is shown in Fig. B.24.

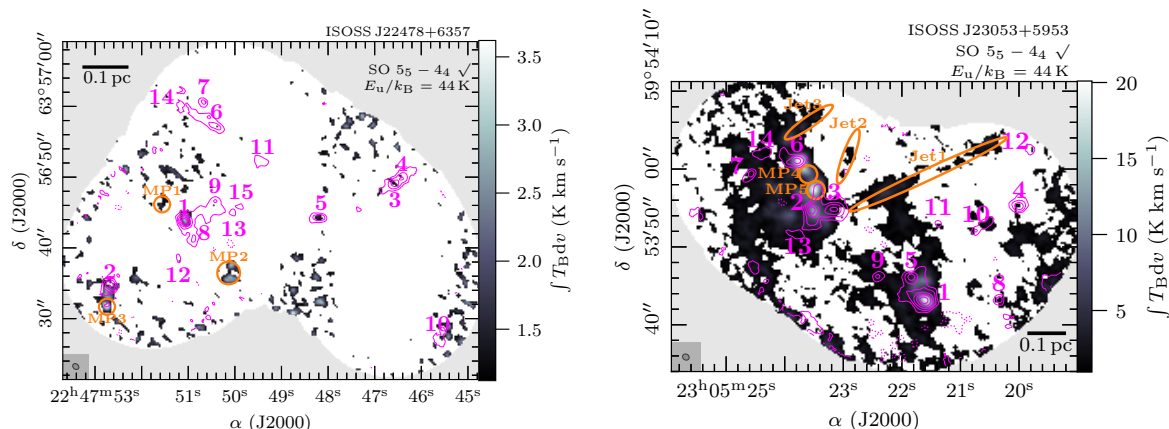
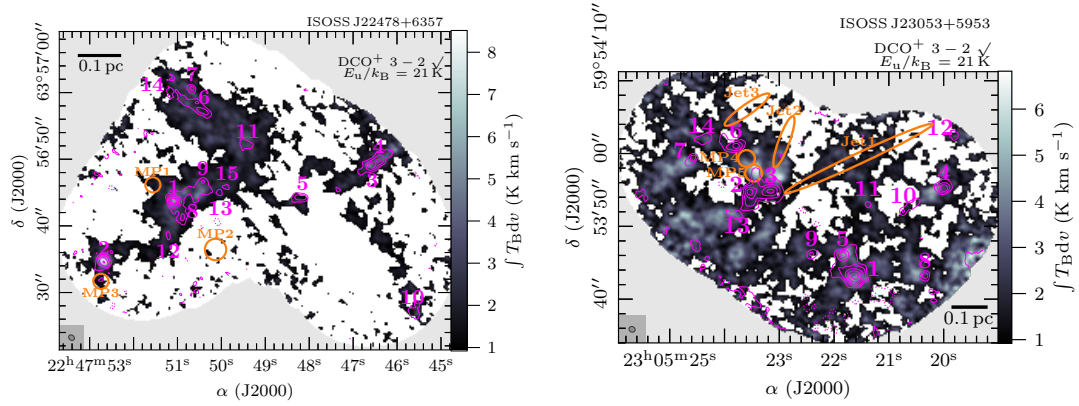
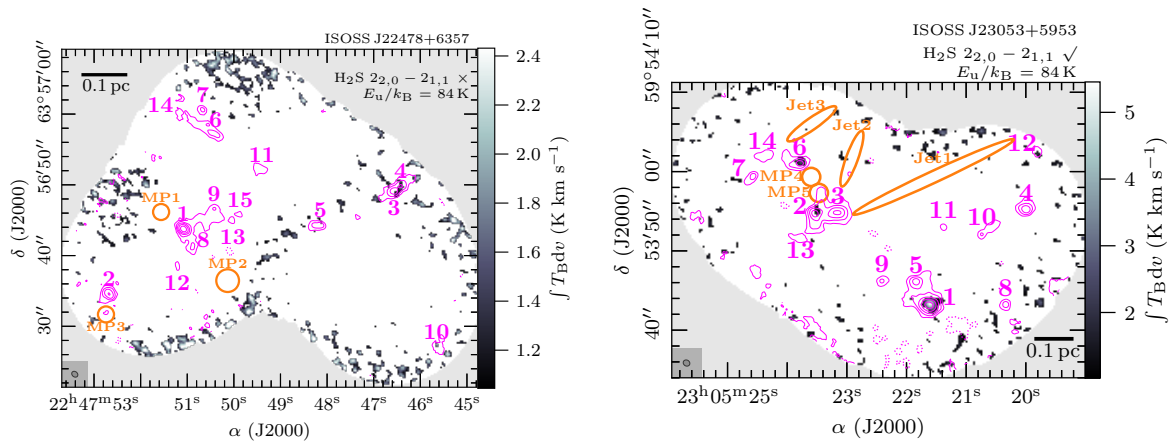
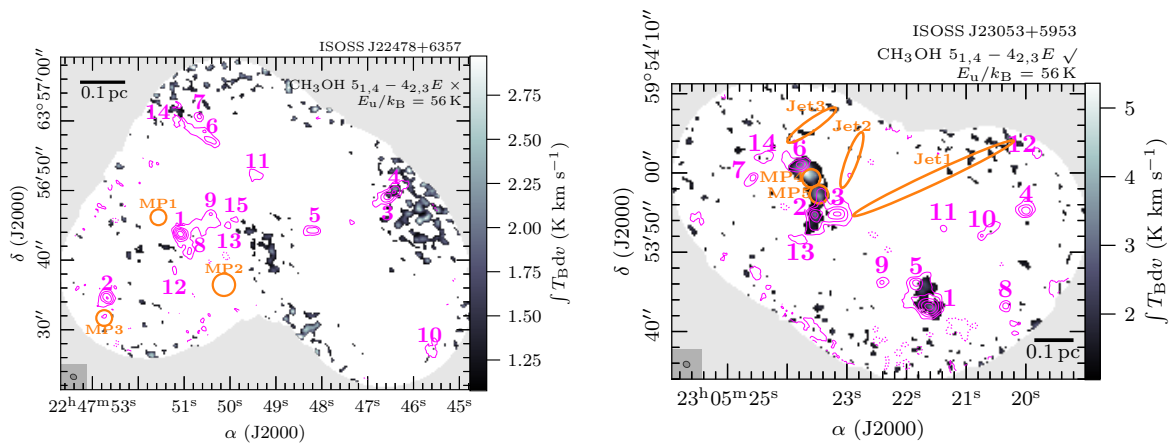


FIGURE B.1: The same as Fig. 3.6, but for $\text{SO } 5_5 - 4_4$. The integrated intensity of the transition with a threshold of $S/N \geq 3$ is presented in color scale. The line intensity is integrated from a velocity of $v_{\text{LSR}} - 3 \text{ km s}^{-1}$ to $v_{\text{LSR}} + 3 \text{ km s}^{-1}$. It is marked if the transition is detected (\checkmark) or not (\times), further explained in Sect. 3.5.2. The NOEMA 1.3 mm continuum data are shown in pink contours. The dotted pink contour marks the $-5\sigma_{\text{cont}}$ level. Solid pink contour levels are 5, 10, 20, 40, and $80\sigma_{\text{cont}}$. All mm cores identified in Beuther et al. (2021) are labeled in pink. Positions with a peak in molecular emission, but no associated continuum (“molecular peaks,” MP) are indicated by orange circles (Sect. 3.5.2). Jet-like structures, seen in $\text{SiO } 5 - 4$ emission, are indicated by orange ellipses (Fig. 3.7). The synthesized beam of the continuum data is shown in the bottom left corner. The synthesized beam of the spectral line data is similar. A linear spatial scale of 0.1 pc is indicated by a black scale bar.

FIGURE B.2: The same as Fig. 3.6, but for DCO⁺ 3-2.FIGURE B.3: The same as Fig. 3.6, but for H₂S 22₀-21₁.FIGURE B.4: The same as Fig. 3.6, but for CH₃OH 5_{1,4}-4_{2,3}E.

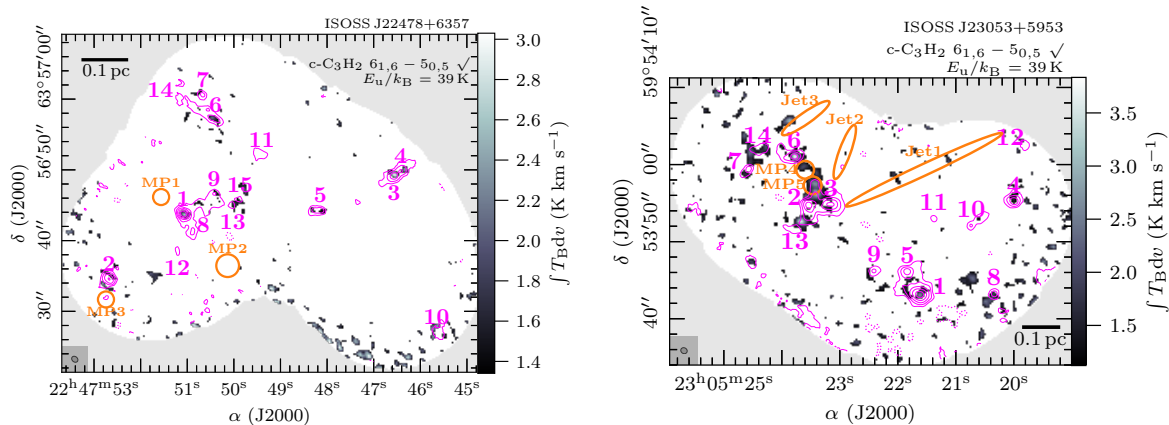


FIGURE B.5: The same as Fig. 3.6, but for $c\text{-C}_3\text{H}_2$ $6_{1,6} - 5_{0,5}$.

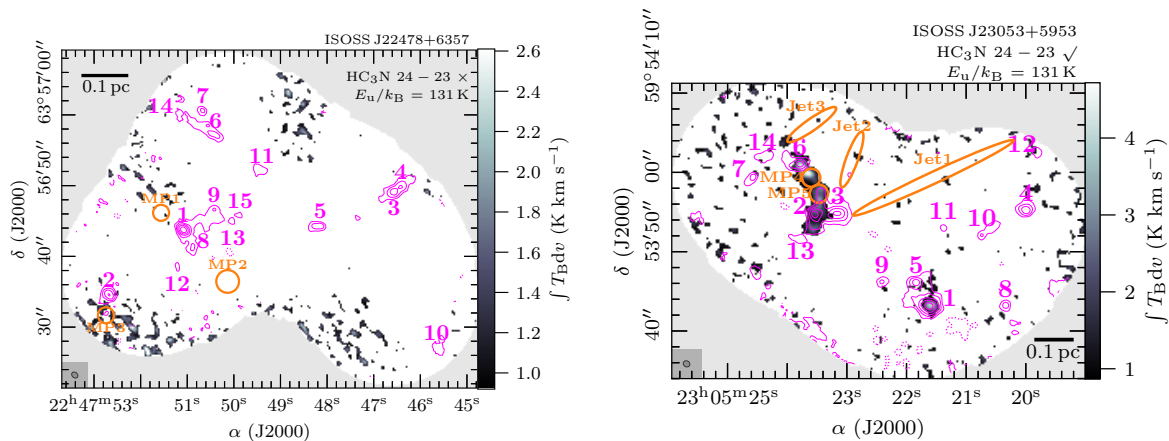


FIGURE B.6: The same as Fig. 3.6, but for HC_3N $24 - 23$.

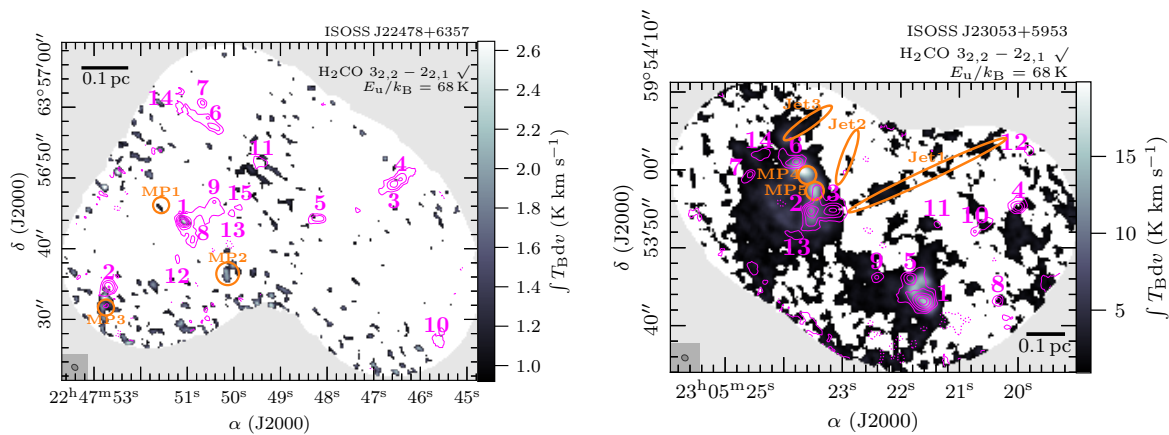
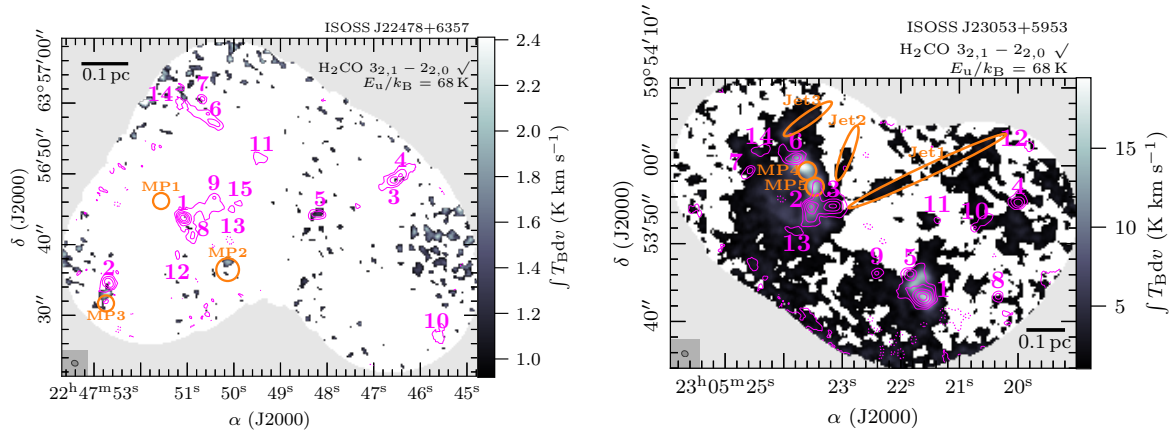
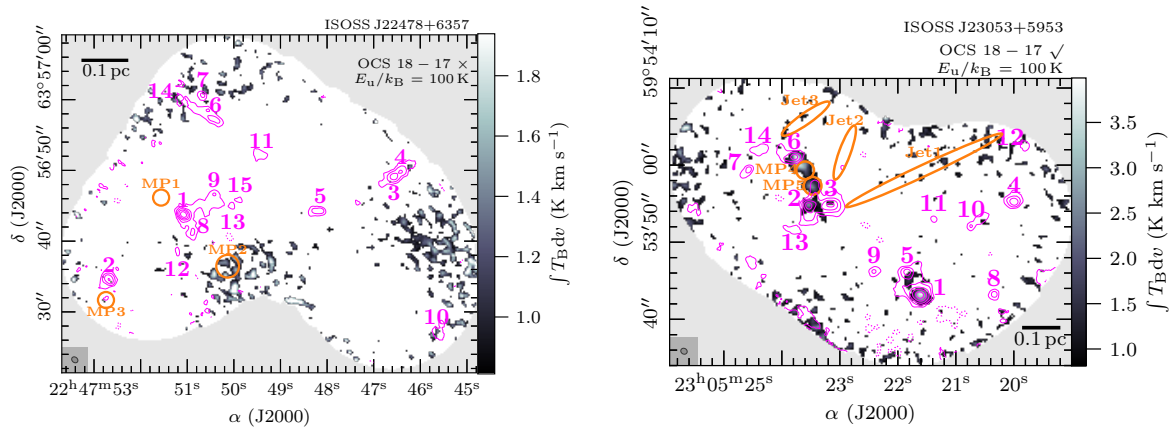
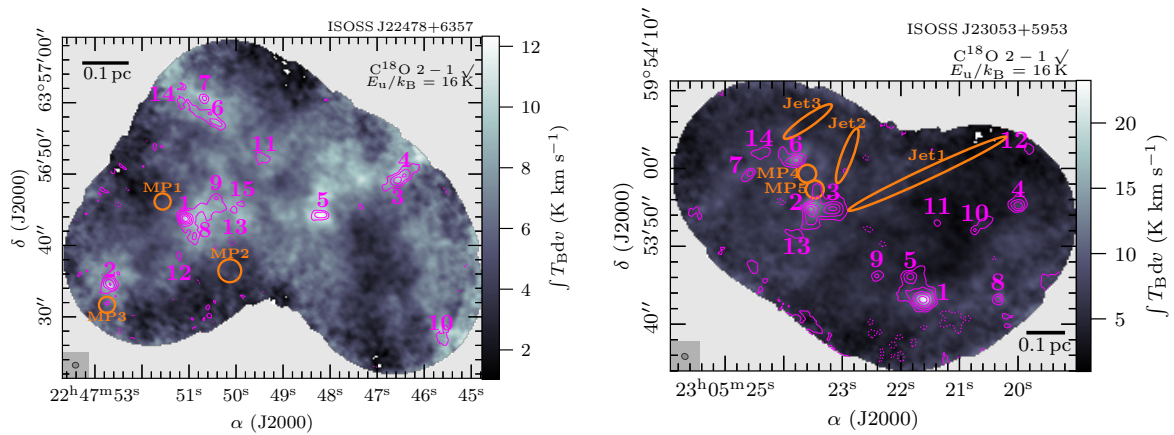


FIGURE B.7: The same as Fig. 3.6, but for H_2CO $3_{2,2} - 2_{2,1}$.

FIGURE B.8: The same as Fig. 3.6, but for $\text{H}_2\text{CO } 3_{2,1} - 2_{2,0}$.FIGURE B.9: The same as Fig. 3.6, but for $\text{OCS } 18 - 17$.FIGURE B.10: The same as Fig. 3.6, but for $\text{C}^{18}\text{O } 2 - 1$.

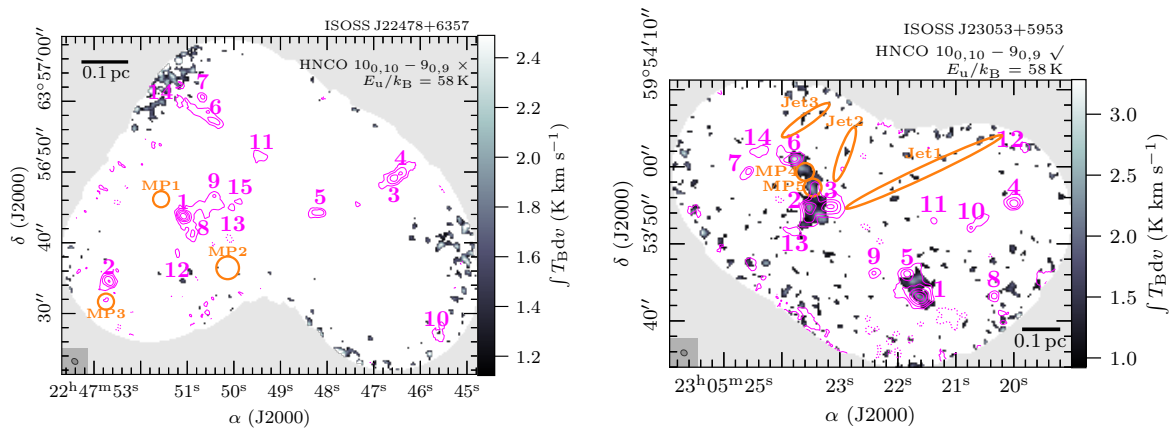


FIGURE B.11: The same as Fig. 3.6, but for $\text{HNC } 10_{0,10} - 9_{0,9}$.

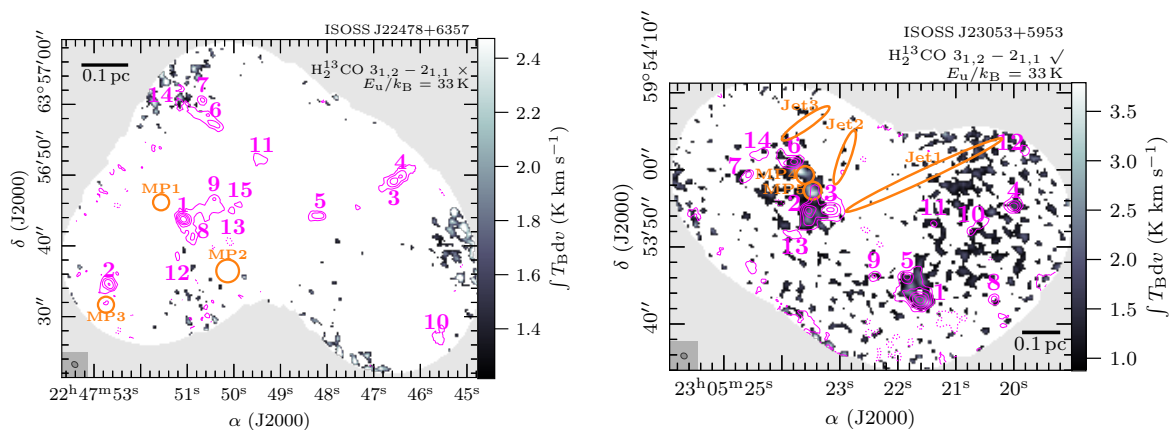


FIGURE B.12: The same as Fig. 3.6, but for $\text{H}_2^{13}\text{CO } 3_{1,2} - 2_{1,1}$.

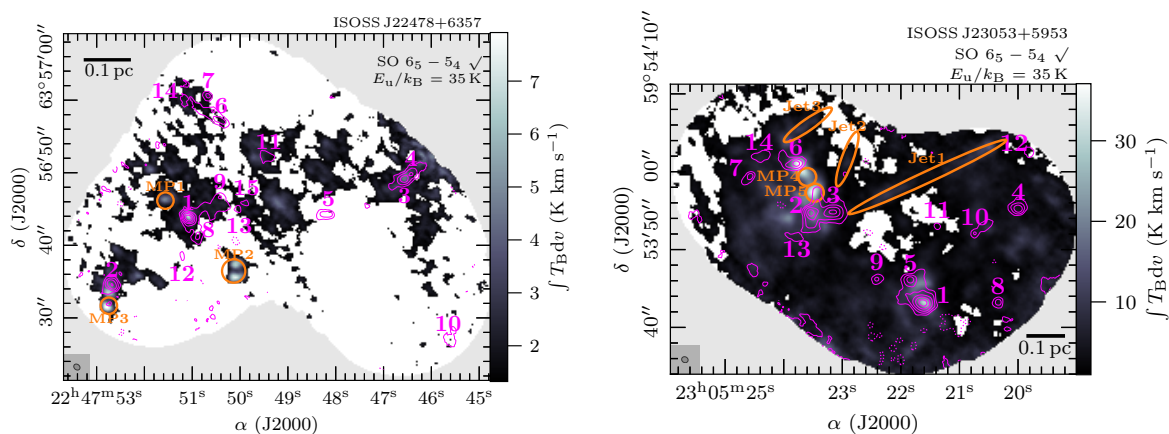
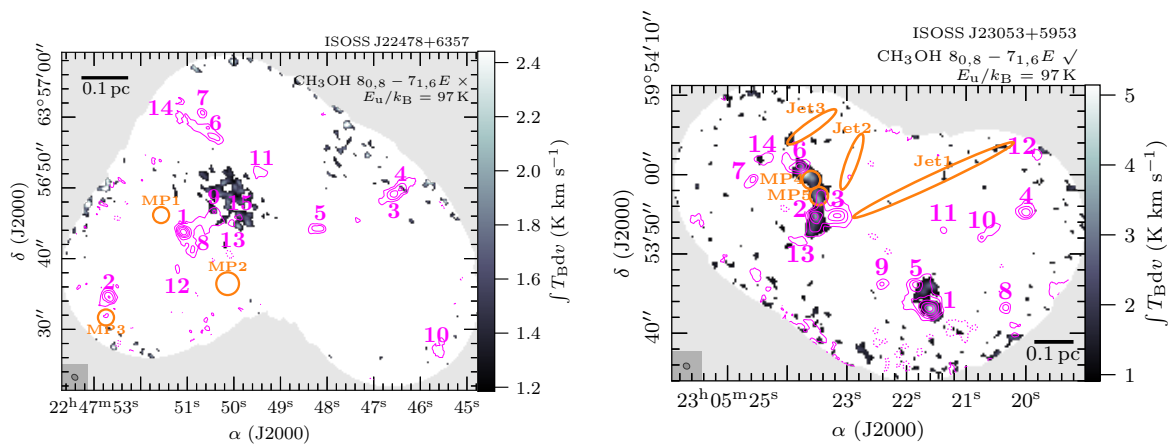
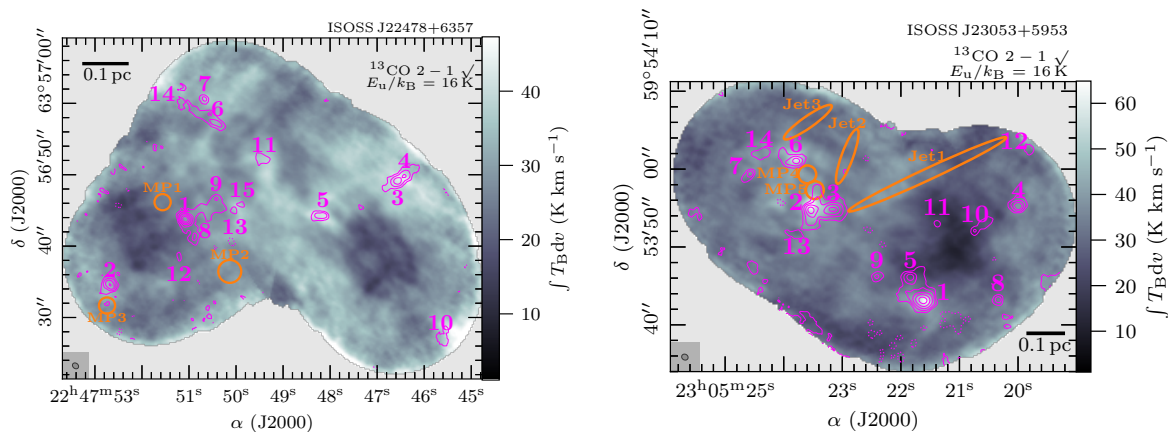
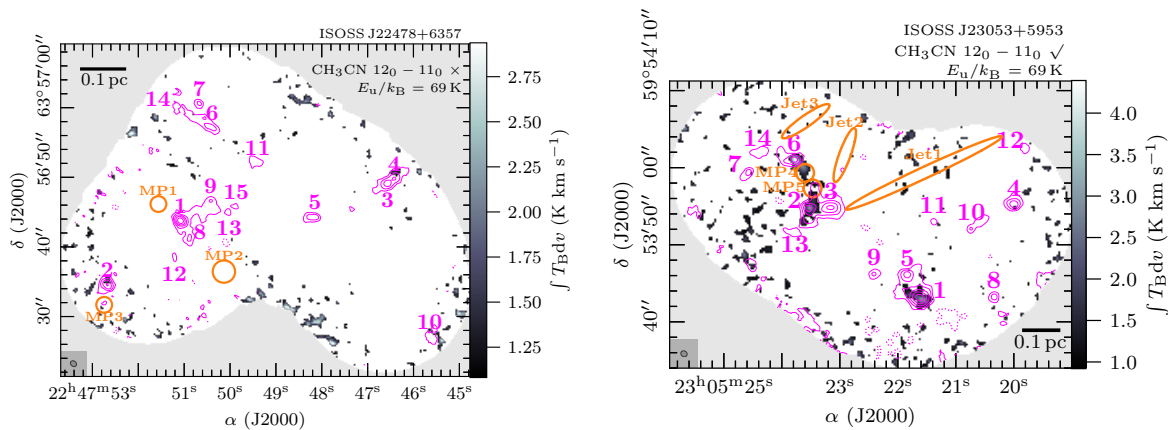


FIGURE B.13: The same as Fig. 3.6, but for $\text{SO } 6_5 - 5_4$.

FIGURE B.14: The same as Fig. 3.6, but for $\text{CH}_3\text{OH } 8_{0,8} - 7_{1,6} E$.FIGURE B.15: The same as Fig. 3.6, but for $^{13}\text{CO } 2 - 1$.FIGURE B.16: The same as Fig. 3.6, but for $\text{CH}_3\text{CN } 12_0 - 11_0$.

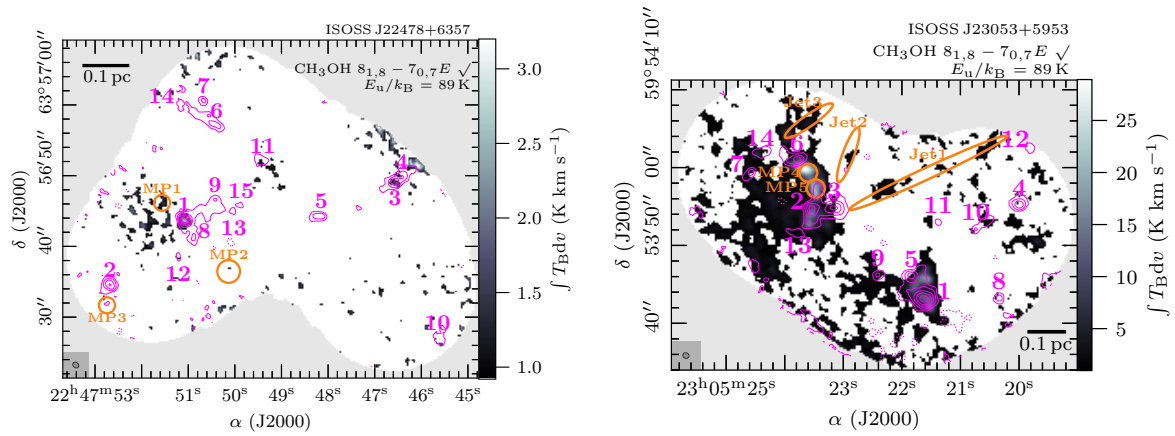


FIGURE B.17: The same as Fig. 3.6, but for $\text{CH}_3\text{OH } 8_{1,8} - 7_{0,7}E$.

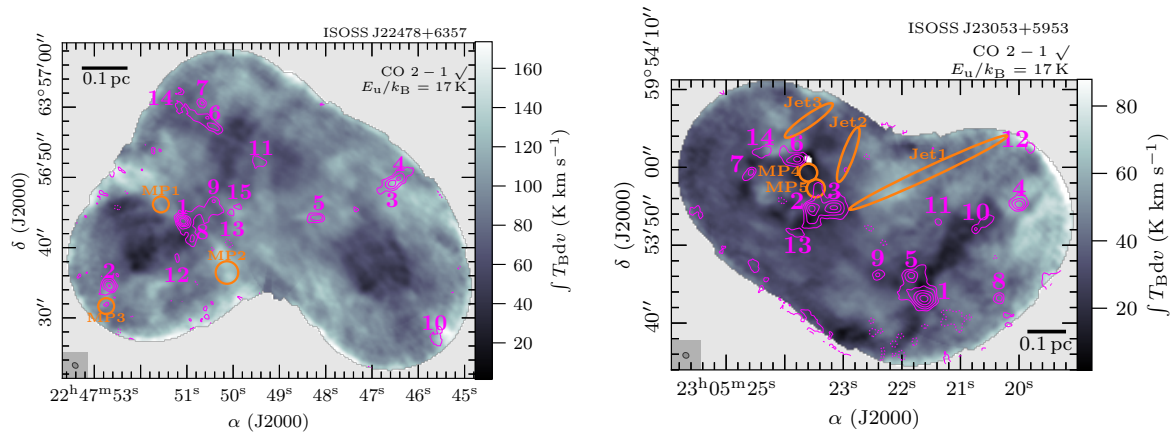


FIGURE B.18: The same as Fig. 3.6, but for $\text{CO } 2 - 1$.

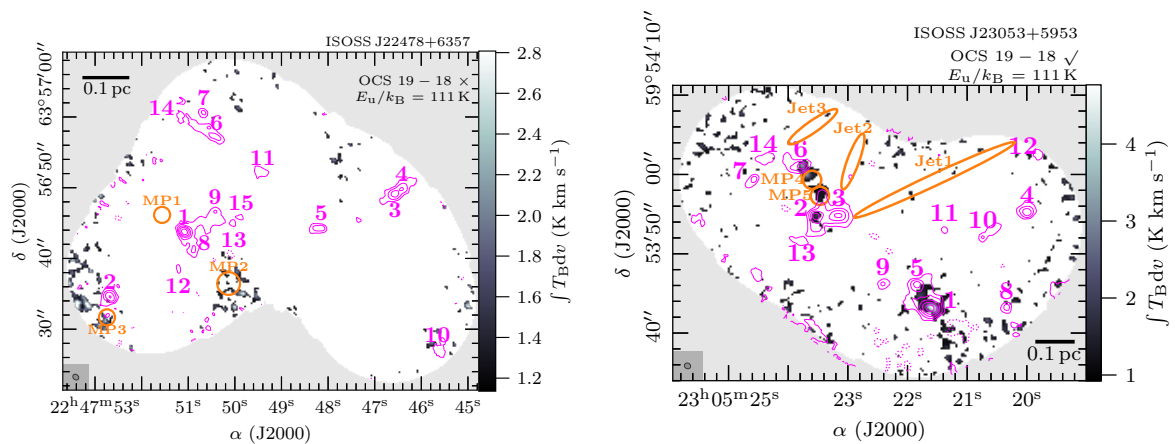
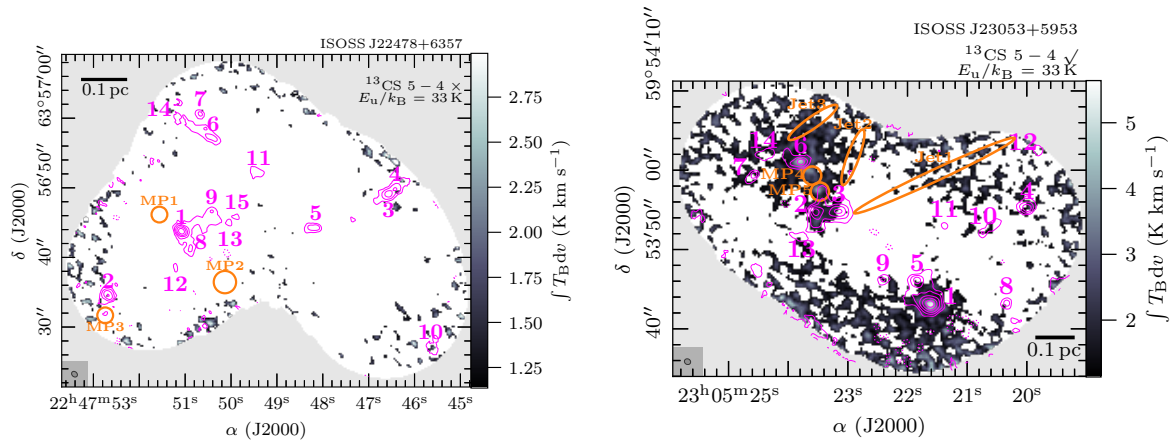
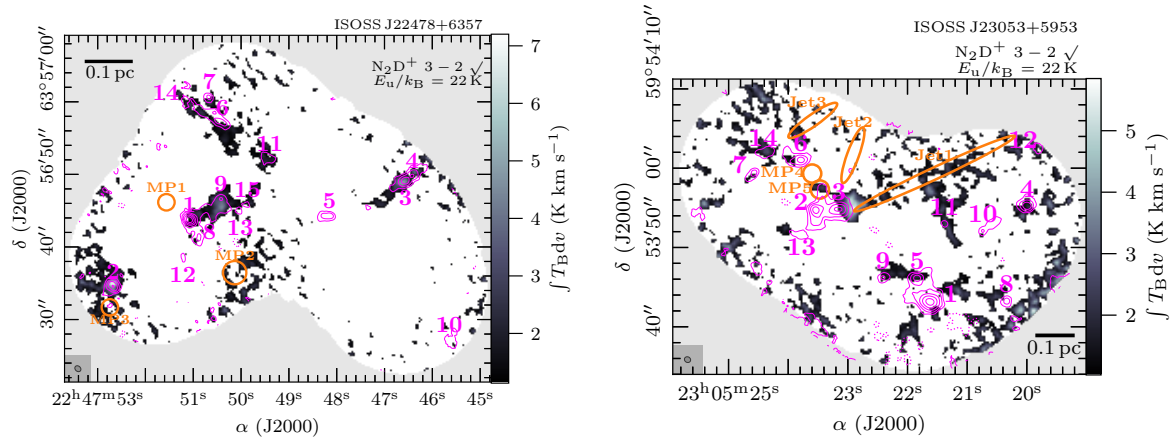
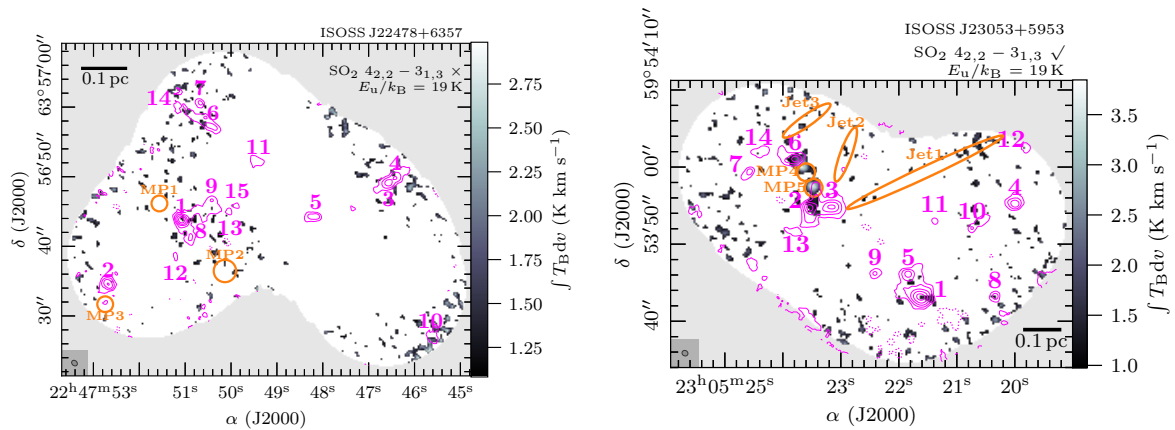


FIGURE B.19: The same as Fig. 3.6, but for $\text{OCS } 19 - 18$.

FIGURE B.20: The same as Fig. 3.6, but for $^{13}\text{CS } 5-4$.FIGURE B.21: The same as Fig. 3.6, but for $\text{N}_2\text{D}^+ 3-2$.FIGURE B.22: The same as Fig. 3.6, but for $\text{SO}_2 4_{2,2} - 3_{1,3}$.

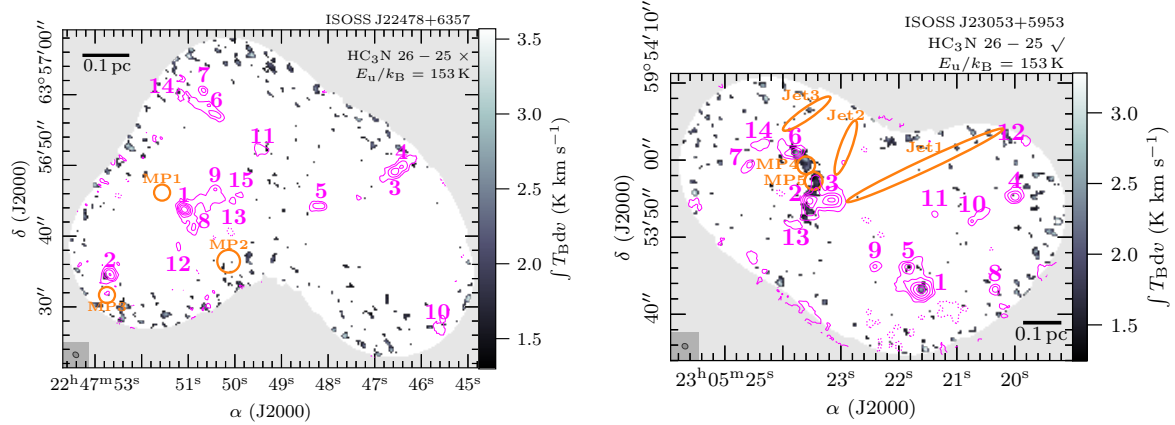


FIGURE B.23: The same as Fig. 3.6, but for $\text{HC}_3\text{N } 26 - 25$.

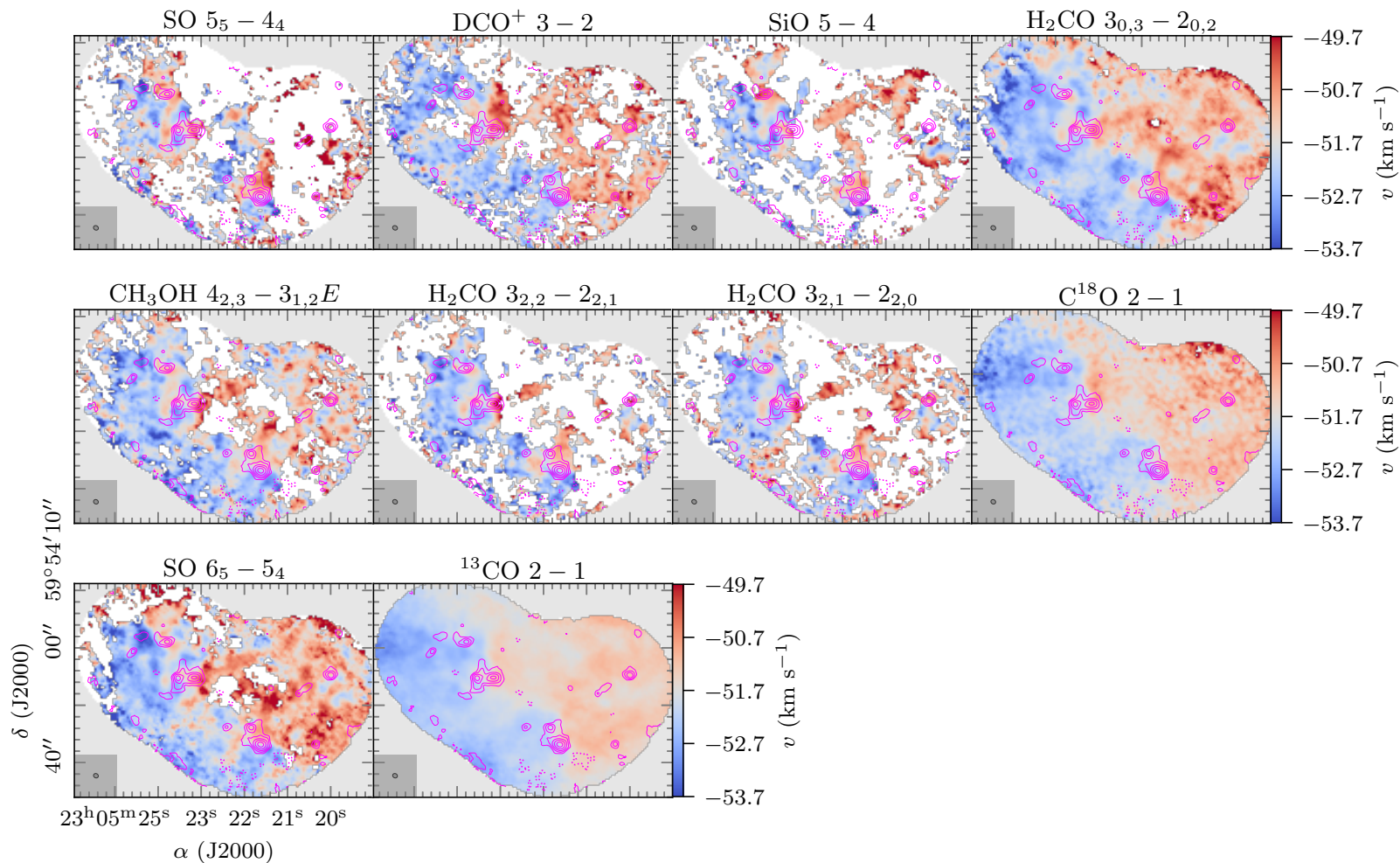


FIGURE B.24: Intensity-weighted peak velocity (moment 1) maps of molecular lines with extended emission in ISOSS J23053+5953. The moment 1 map is presented in color scale (using a threshold of $S/N \geq 3$ of the line integrated intensity). The NOEMA 1.3 mm continuum data are shown in pink contours. The dotted pink contour marks the $-5\sigma_{\text{cont}}$ level. Solid pink contour levels are 5, 10, 20, 40, and $80\sigma_{\text{cont}}$. The synthesized beam of the continuum data is shown in the bottom left corner. The synthesized beam of the spectral line data is similar.

B.2 Molecular column densities derived with XCLASS

In Sect. 3.5.4 we present H₂CO parameter maps derived with XCLASS. The calculation of the modeled spectral lines in XCLASS follows the assumption of LTE and a 1D isothermal source (Sect. 1.5.2). In the dense parts of star-forming regions the LTE conditions are valid. Using the myXCLASSMapFit function, we fitted in each pixel the observed H₂CO spectral line data with one emission component within the full FOV if the peak intensity is >1 K. This threshold corresponds to a minimum S/N of ~ 5 in the high-resolution data (Table 3.3). In both regions, toward the edges of the mosaic the noise increases and therefore the fit results toward the edges of the mosaic are not reliable.

In XCLASS, the best-fit parameters can be obtained using several algorithms with the implemented model optimizer package MAGIX (Möller et al. 2013). We used an algorithm chain utilizing the Genetic algorithm, optimizing global minima, and the Levenberg-Marquart algorithm, optimizing local minima, with 50 iterations each to derive the best-fit parameter set for each species (see also Sect. 2.3.2). The line properties of the three fitted H₂CO transitions are summarized in Table 3.2. We varied each fit parameter within the following ranges: $\theta_{\text{source}} = 0.1 - 2''$, $T_{\text{rot}} = 1 - 200$ K, $N = 10^{12} - 10^{17}$ cm⁻², $\Delta v = 0.5 - 10$ km s⁻¹, and $v_{\text{off}} = -10 - +10$ km s⁻¹. A further input is the beam size of the interferometric observations θ_{beam} and as in XCLASS only a single value can be given as an input, we computed the mean of the major and minor axis of the synthesized beam: $\theta_{\text{beam}} = \frac{\theta_{\text{maj}} + \theta_{\text{min}}}{2}$ (the synthesized beam of each spectral line data product is listed in Table 3.3).

In order to quantify the molecular content of all mm cores (listed in Table 3.4), we fitted the spectral line data with XCLASS in order to derive molecular column densities (Sect. 3.5.6). As we analyze the spectrum at the position of the core and not the full FOV of both regions, minor changes were employed in the XCLASS fitting routine in order to make the fit results as reliable as possible: In order to determine a robust velocity v_{LSR} for each core, we first fitted the C¹⁸O 2 – 1 transition with one emission component. We then corrected all spectra with the obtained velocity offset. The results for the systemic velocity of each core are summarized in Table 3.4. The fit parameter ranges for the source size and rotation temperature were $\theta_{\text{source}} = 0.1 - 10''$, $T_{\text{rot}} = 1 - 200$ K, respectively. Setting 1 K as the lower rotation temperature limit is in no opposition to the fact that the gas temperatures should be higher than the cosmic microwave background (CMB), $T_{\text{CMB}} = 2.73$ K, as toward all species and cores the derived rotation temperature is $T_{\text{rot}} > 3$ K. The fit parameter ranges for the column density N and line width Δv were specified individually for each molecule. The emission of each line was fitted around $\nu_0 \pm 6$ MHz (corresponding to ± 9 km s⁻¹, the rest frequency ν_0 of all transitions is listed in Table 3.2). With both regions being line-poor in general, most of the detected lines do not suffer from line blending, except for CH₃CN. The transition of CH₃CN 12₀ – 11₀ is blended with 12₁ – 11₁. Both transitions were considered when fitting the molecular emission in XCLASS.

The same algorithm chain as used for the H₂CO parameter maps was used for the fitting of individual core spectra. In order to estimate the uncertainties of the fit parameters, the Markov Chain Monte Carlo (MCMC) error estimation algorithm was used afterward with 50 iterations.

The column densities of all fitted species and 29 cores are listed in Tables B.1 and B.2. The uncertainties were estimated using the MCMC error estimation algorithm in XCLASS. Upper limits are listed for fits that were discarded. The constraints are explained in Sect. 3.5.6. An example of the observed and XCLASS modeled spectrum for all fitted lines of core 1 in ISOSS J22478+6357 and ISOSS J23053+5953 is shown in Fig. B.25 and Fig. B.26, respectively.

TABLE B.1: Molecular column densities (C^{18}O , SO , ^{13}CS , OCS , DCO^+ , N_2D^+ , H_2S) derived with XCLASS in the CORE-extension sample (Sect. 3.5.6). Uncertainties are estimated with the MCMC error estimation algorithm. Fits that were discarded are shown as upper limits. The constraints are explained in Sect. 3.5.6.

Core	$N(\text{C}^{18}\text{O})$ (cm^{-2})	$N(\text{SO})$ (cm^{-2})	$N(^{13}\text{CS})$ (cm^{-2})	$N(\text{OCS})$ (cm^{-2})	$N(\text{DCO}^+)$ (cm^{-2})	$N(\text{N}_2\text{D}^+)$ (cm^{-2})	$N(\text{H}_2\text{S})$ (cm^{-2})
ISOSS J22478+6357 1	1.8(16) ^{+2.1(16)} _{-5.0(15)}	1.7(14) ^{+1.4(14)} _{-1.6(14)}	<5.8(12)	<5.6(15)	2.3(13) ^{+3.3(13)} _{-5.9(12)}	2.3(12) ^{+2.1(12)} _{-2.3(12)}	<1.2(14)
ISOSS J22478+6357 2	1.2(16) ^{+4.6(15)} _{-5.4(15)}	<1.3(14)	<5.1(12)	<9.2(15)	1.6(13) ^{+3.5(12)} _{-8.7(12)}	3.0(12) ^{+2.3(12)} _{-9.5(11)}	<7.1(13)
ISOSS J22478+6357 3	2.0(16) ^{+1.7(16)} _{-8.0(15)}	1.7(14) ^{+5.1(14)} _{-1.7(14)}	<1.4(12)	<9.6(15)	3.9(13) ^{+4.8(12)} _{-3.0(13)}	7.9(12) ^{+5.6(12)} _{-3.3(12)}	2.7(14) ^{+5.4(14)} _{-2.2(14)}
ISOSS J22478+6357 4	4.4(16) ^{+2.7(16)} _{-1.4(16)}	<2.2(14)	<1.6(13)	<9.6(15)	3.4(12) ^{+2.7(12)} _{-1.3(12)}	4.0(12) ^{+9.8(12)} _{-3.4(12)}	1.6(14) ^{+2.6(14)} _{-1.3(14)}
ISOSS J22478+6357 5	4.1(16) ^{+1.8(16)} _{-1.7(16)}	4.8(13) ^{+4.7(13)} _{-4.5(13)}	<4.8(12)	<8.3(15)	6.0(12) ^{+9.6(12)} _{-5.4(12)}	<3.6(11)	<3.0(14)
ISOSS J22478+6357 6	9.0(15) ^{+1.0(16)} _{-3.5(14)}	<2.1(14)	<6.6(12)	<2.6(14)	3.3(12) ^{+2.0(12)} _{-3.1(12)}	<2.1(12)	<8.6(13)
ISOSS J22478+6357 7	5.2(16) ^{+3.2(16)} _{-5.9(15)}	<1.7(14)	<1.3(13)	<1.0(16)	4.1(12) ^{+5.9(12)} _{-1.5(12)}	<2.2(12)	<6.1(13)
ISOSS J22478+6357 8	2.4(16) ^{+6.2(15)} _{-8.3(15)}	3.7(14) ^{+1.7(15)} _{-3.4(14)}	<4.6(13)	<3.3(14)	3.9(12) ^{+1.3(13)} _{-2.1(12)}	1.6(12) ^{+9.7(11)} _{-1.6(12)}	<1.0(15)
ISOSS J22478+6357 9	3.0(16) ^{+2.7(16)} _{-1.0(16)}	<3.5(13)	<1.3(12)	<1.0(16)	5.8(12) ^{+3.2(12)} _{-3.7(12)}	7.9(12) ^{+2.1(13)} _{-3.4(12)}	<2.9(13)
ISOSS J22478+6357 10	7.0(15) ^{+2.6(15)} _{-1.9(15)}	<5.3(13)	1.5(13) ^{+1.6(13)} _{-1.2(13)}	<8.8(15)	8.1(13) ^{+5.9(12)} _{-3.8(13)}	<1.7(12)	1.5(14) ^{+2.3(13)} _{-1.4(14)}
ISOSS J22478+6357 11	9.5(15) ^{+1.8(15)} _{-6.0(15)}	<5.6(14)	<5.3(12)	<6.7(14)	2.8(12) ^{+6.1(12)} _{-1.1(12)}	1.1(13) ^{+3.4(12)} _{-1.1(13)}	<5.6(13)
ISOSS J22478+6357 12	1.0(16) ^{+3.5(15)} _{-6.0(15)}	<7.8(13)	<1.7(12)	<1.0(16)	4.3(12) ^{+5.6(12)} _{-3.1(12)}	3.5(12) ^{+5.3(12)} _{-3.3(12)}	<9.2(14)
ISOSS J22478+6357 13	6.9(15) ^{+3.0(15)} _{-1.2(15)}	9.1(14) ^{+1.9(15)} _{-9.0(14)}	<3.2(12)	<9.9(15)	6.7(12) ^{+1.0(13)} _{-5.9(12)}	3.4(12) ^{+4.1(12)} _{-3.3(12)}	<8.9(13)
ISOSS J22478+6357 14	8.4(15) ^{+6.8(15)} _{-2.3(15)}	<8.7(13)	<5.3(12)	<1.0(16)	1.0(13) ^{+1.5(13)} _{-9.7(12)}	<5.0(12)	<2.1(14)
ISOSS J22478+6357 15	1.5(16) ^{+7.1(15)} _{-7.6(15)}	<2.8(14)	<1.8(13)	<1.5(14)	8.3(12) ^{+7.6(12)} _{-5.8(12)}	3.6(12) ^{+3.7(12)} _{-3.5(12)}	<4.2(13)
ISOSS J23053+5953 1	3.1(16) ^{+1.5(15)} _{-1.8(16)}	7.1(14) ^{+4.6(14)} _{-1.4(14)}	3.4(13) ^{+3.8(13)} _{-9.4(12)}	9.1(14) ^{+5.6(14)} _{-3.5(14)}	9.8(12) ^{+6.8(12)} _{-5.4(12)}	<2.6(11)	5.0(14) ^{+7.8(14)} _{-2.7(14)}
ISOSS J23053+5953 2	2.4(16) ^{+4.0(16)} _{-3.8(15)}	4.3(14) ^{+5.6(14)} _{-5.9(13)}	<3.6(13)	<4.9(14)	9.8(12) ^{+7.1(13)} _{-6.7(12)}	<1.0(14)	3.9(14) ^{+1.6(15)} _{-1.3(14)}

Notes. a(b) = $a \times 10^b$.

TABLE B.1: continued.

Core	$N(\text{C}^{18}\text{O})$ (cm^{-2})	$N(\text{SO})$ (cm^{-2})	$N(\text{C}^{13}\text{CS})$ (cm^{-2})	$N(\text{OCS})$ (cm^{-2})	$N(\text{DCO}^+)$ (cm^{-2})	$N(\text{N}_2\text{D}^+)$ (cm^{-2})	$N(\text{H}_2\text{S})$ (cm^{-2})
ISOSS J23053+5953 3	2.2(16) ^{+1.5(16)} _{-1.0(16)}	2.6(14) ^{+1.5(14)} _{-2.6(14)}	6.9(12) ^{+3.9(13)} _{-5.9(12)}	<2.7(14)	7.4(12) ^{+9.0(12)} _{-6.2(12)}	2.4(12) ^{+1.1(13)} _{-1.8(12)}	<6.2(13)
ISOSS J23053+5953 4	1.5(16) ^{+4.0(15)} _{-6.3(15)}	5.6(14) ^{+1.7(15)} _{-5.5(14)}	<2.4(13)	<2.3(14)	6.7(12) ^{+2.1(13)} _{-1.5(12)}	4.2(12) ^{+2.0(13)} _{-3.7(12)}	<1.0(14)
ISOSS J23053+5953 5	1.2(16) ^{+1.9(16)} _{-5.7(15)}	3.6(14) ^{+1.1(15)} _{-3.2(14)}	<4.4(12)	<4.3(14)	1.2(13) ^{+8.4(12)} _{-5.7(12)}	3.8(12) ^{+4.5(12)} _{-3.5(12)}	<7.7(13)
ISOSS J23053+5953 6	6.1(16) ^{+1.2(16)} _{-2.6(16)}	9.1(14) ^{+1.0(15)} _{-1.1(14)}	5.8(13) ^{+4.4(13)} _{-2.5(13)}	5.6(14) ^{+3.5(14)} _{-2.2(14)}	<3.0(12)	<3.9(11)	4.6(14) ^{+3.1(14)} _{-2.8(14)}
ISOSS J23053+5953 7	2.5(16) ^{+1.4(16)} _{-7.7(15)}	2.5(14) ^{+5.2(14)} _{-2.4(14)}	<8.8(12)	<1.3(15)	4.8(12) ^{+1.3(13)} _{-4.1(12)}	<1.0(12)	<1.0(15)
ISOSS J23053+5953 8	3.2(16) ^{+1.9(16)} _{-4.5(15)}	<2.0(14)	<1.1(13)	<1.6(14)	1.1(13) ^{+2.6(13)} _{-4.5(12)}	<6.4(11)	<8.5(13)
ISOSS J23053+5953 9	2.1(16) ^{+9.7(15)} _{-5.7(15)}	<1.7(14)	<1.0(13)	<1.6(15)	1.7(12) ^{+9.5(11)} _{-1.5(12)}	5.0(11) ^{+1.5(12)} _{-4.4(11)}	<8.9(13)
ISOSS J23053+5953 10	1.2(16) ^{+6.6(15)} _{-5.0(15)}	3.6(14) ^{+9.2(13)} _{-3.6(14)}	<8.0(12)	<9.8(15)	6.5(12) ^{+2.5(12)} _{-6.1(12)}	<1.0(12)	<4.8(13)
ISOSS J23053+5953 11	6.6(15) ^{+1.5(16)} _{-2.6(15)}	<5.5(13)	<5.8(12)	<1.0(16)	8.9(12) ^{+3.0(13)} _{-6.2(12)}	7.2(12) ^{+1.9(13)} _{-6.9(12)}	<5.0(13)
ISOSS J23053+5953 12	2.3(16) ^{+3.0(16)} _{-1.3(16)}	1.1(14) ^{+2.4(13)} _{-1.1(14)}	<1.3(13)	<2.1(14)	4.4(12) ^{+2.0(12)} _{-2.8(12)}	1.2(13) ^{+2.6(13)} _{-7.3(12)}	<3.3(13)
ISOSS J23053+5953 13	1.4(16) ^{+1.1(16)} _{-6.9(15)}	2.0(14) ^{+1.8(14)} _{-2.0(14)}	<4.1(12)	<2.7(15)	2.5(12) ^{+1.9(12)} _{-8.9(11)}	<3.7(11)	<1.0(15)
ISOSS J23053+5953 14	4.5(15) ^{+2.7(15)} _{-6.5(14)}	<3.6(14)	<7.8(12)	<2.6(14)	1.1(13) ^{+4.2(13)} _{-7.1(12)}	4.2(12) ^{+3.4(13)} _{-4.0(12)}	<1.0(15)

Notes. a(b) = $a \times 10^b$.

TABLE B.2: Molecular column densities (H_2CO , HNCO , HC_3N , $c\text{-C}_3\text{H}_2$, CH_3OH , CH_3CN) derived with XCLASS in the CORE-extension sample (Sect. 3.5.6). Uncertainties are estimated with the MCMC error estimation algorithm. Fits that were discarded are shown as upper limits. The constraints are explained in Sect. 3.5.6.

Core	$N(\text{H}_2\text{CO})$ (cm^{-2})	$N(\text{HNCO})$ (cm^{-2})	$N(\text{HC}_3\text{N})$ (cm^{-2})	$N(c\text{-C}_3\text{H}_2)$ (cm^{-2})	$N(\text{CH}_3\text{OH})$ (cm^{-2})	$N(\text{CH}_3\text{CN})$ (cm^{-2})
ISOSS J22478+6357 1	1.8(14) ^{+4.9(14)} _{-6.5(13)}	<6.1(13)	<8.6(12)	3.8(13) ^{+1.0(14)} _{-3.3(13)}	2.8(15) ^{+1.7(16)} _{-1.9(15)}	<2.4(14)
ISOSS J22478+6357 2	1.0(14) ^{+1.5(14)} _{-6.1(13)}	<1.0(15)	<3.5(12)	<4.4(13)	<1.1(16)	<3.5(14)
ISOSS J22478+6357 3	9.1(13) ^{+3.8(14)} _{-3.8(13)}	<1.0(15)	<1.1(13)	<3.3(13)	<1.1(15)	<5.0(14)
ISOSS J22478+6357 4	<1.6(14)	<8.0(12)	<7.1(12)	1.5(13) ^{+2.7(12)} _{-1.5(13)}	<1.6(16)	<9.9(12)
ISOSS J22478+6357 5	1.0(14) ^{+8.7(14)} _{-9.3(13)}	<6.3(12)	<7.3(12)	3.5(13) ^{+3.5(13)} _{-3.3(13)}	<3.3(14)	<5.0(14)
ISOSS J22478+6357 6	1.1(14) ^{+1.0(15)} _{-1.1(14)}	<1.7(12)	<5.4(12)	5.1(13) ^{+1.4(14)} _{-4.4(13)}	<2.4(14)	<1.9(13)
ISOSS J22478+6357 7	1.3(14) ^{+5.4(14)} _{-1.3(14)}	<4.3(13)	<1.8(12)	2.4(13) ^{+1.2(13)} _{-2.3(13)}	<1.4(15)	<9.1(12)
ISOSS J22478+6357 8	6.9(13) ^{+1.3(14)} _{-6.9(13)}	<3.4(12)	<1.5(13)	<2.5(13)	<6.7(14)	<6.2(12)
ISOSS J22478+6357 9	<3.0(14)	<9.7(14)	<2.6(12)	3.3(13) ^{+1.6(13)} _{-3.2(13)}	<4.4(15)	<1.5(13)
ISOSS J22478+6357 10	<4.8(13)	5.3(13) ^{+1.1(13)} _{-5.1(13)}	<1.3(13)	<2.2(13)	<5.6(14)	<1.3(14)
ISOSS J22478+6357 11	9.4(14) ^{+4.4(14)} _{-9.4(14)}	<9.8(14)	<6.0(12)	2.7(13) ^{+6.5(13)} _{-2.4(13)}	<1.3(14)	<7.0(12)
ISOSS J22478+6357 12	<9.2(13)	<6.8(13)	<2.4(13)	5.1(13) ^{+9.1(13)} _{-4.9(13)}	<2.4(15)	<4.5(14)
ISOSS J22478+6357 13	<1.8(13)	<1.0(15)	<4.2(13)	7.0(13) ^{+1.0(14)} _{-6.1(13)}	<1.7(14)	<5.0(14)
ISOSS J22478+6357 14	4.3(13) ^{+6.8(13)} _{-4.3(13)}	<5.4(13)	<8.7(12)	<4.7(13)	<1.1(15)	<1.2(13)
ISOSS J22478+6357 15	5.6(13) ^{+9.6(13)} _{-5.6(13)}	<9.7(14)	<1.3(12)	4.3(13) ^{+2.0(14)} _{-3.8(13)}	<1.8(15)	<5.7(13)
ISOSS J23053+5953 1	4.2(15) ^{+4.0(14)} _{-3.7(14)}	1.3(14) ^{+5.7(14)} _{-1.2(14)}	3.6(13) ^{+3.4(13)} _{-1.5(13)}	1.3(14) ^{+9.7(13)} _{-1.2(14)}	5.9(15) ^{+8.5(14)} _{-1.1(15)}	5.9(13) ^{+5.2(13)} _{-4.1(13)}

Notes. a(b) = $a \times 10^b$.

TABLE B.2: continued.

Core	$N(\text{H}_2\text{CO})$ (cm^{-2})	$N(\text{HNCO})$ (cm^{-2})	$N(\text{HC}_3\text{N})$ (cm^{-2})	$N(\text{c-C}_3\text{H}_2)$ (cm^{-2})	$N(\text{CH}_3\text{OH})$ (cm^{-2})	$N(\text{CH}_3\text{CN})$ (cm^{-2})
ISOSS J23053+5953 2	1.1(15) ^{+7.0(14)} _{-9.1(13)}	1.5(14) ^{+2.6(14)} _{-1.4(14)}	<2.2(13)	<3.6(13)	4.8(15) ^{+9.8(14)} _{-5.6(14)}	3.0(13) ^{+8.8(13)} _{-6.4(12)}
ISOSS J23053+5953 3	2.8(14) ^{+3.6(14)} _{-1.0(14)}	<3.9(13)	<3.9(12)	<5.3(13)	8.8(14) ^{+4.3(15)} _{-5.4(14)}	<5.7(12)
ISOSS J23053+5953 4	2.0(14) ^{+1.2(14)} _{-5.3(13)}	<1.8(13)	<3.2(12)	2.0(13) ^{+5.3(13)} _{-1.9(13)}	<6.6(14)	<5.0(14)
ISOSS J23053+5953 5	4.2(14) ^{+5.1(14)} _{-9.9(13)}	<4.1(13)	<1.2(13)	<3.4(13)	1.8(15) ^{+1.3(15)} _{-5.5(14)}	<1.2(13)
ISOSS J23053+5953 6	2.3(15) ^{+8.9(14)} _{-6.4(14)}	9.4(13) ^{+5.9(14)} _{-8.3(13)}	3.0(13) ^{+3.1(13)} _{-2.0(13)}	8.4(13) ^{+1.6(14)} _{-7.3(13)}	4.1(15) ^{+3.1(14)} _{-6.3(14)}	5.2(13) ^{+8.7(13)} _{-2.5(13)}
ISOSS J23053+5953 7	2.1(14) ^{+2.3(14)} _{-5.7(13)}	<2.5(13)	<4.7(12)	<3.1(13)	1.0(15) ^{+3.8(15)} _{-6.5(14)}	<8.9(12)
ISOSS J23053+5953 8	1.5(14) ^{+1.2(14)} _{-4.5(13)}	<9.9(14)	<6.7(12)	3.6(13) ^{+4.8(13)} _{-3.1(13)}	1.4(15) ^{+2.8(15)} _{-1.4(15)}	<5.0(14)
ISOSS J23053+5953 9	3.2(14) ^{+1.4(14)} _{-1.8(14)}	<1.4(14)	<5.7(13)	<1.3(13)	6.7(14) ^{+4.4(14)} _{-3.1(14)}	<9.0(12)
ISOSS J23053+5953 10	1.1(14) ^{+2.8(14)} _{-4.5(13)}	<4.1(13)	<1.8(12)	3.7(13) ^{+1.4(14)} _{-3.4(13)}	7.1(14) ^{+1.0(15)} _{-6.6(14)}	<7.5(12)
ISOSS J23053+5953 11	1.2(14) ^{+2.6(14)} _{-4.7(13)}	<5.0(13)	<1.0(12)	<1.5(13)	<7.4(14)	<6.6(12)
ISOSS J23053+5953 12	1.1(14) ^{+4.2(14)} _{-7.2(13)}	<1.0(14)	<7.9(12)	<7.8(12)	1.5(14) ^{+8.7(14)} _{-8.2(13)}	<4.6(14)
ISOSS J23053+5953 13	4.1(14) ^{+5.3(14)} _{-1.1(14)}	<4.7(13)	<2.5(12)	6.9(13) ^{+2.6(14)} _{-6.0(13)}	8.9(14) ^{+4.9(14)} _{-5.7(14)}	<1.6(13)
ISOSS J23053+5953 14	2.1(15) ^{+2.3(15)} _{-1.1(15)}	<1.2(13)	<3.8(12)	5.8(13) ^{+5.4(14)} _{-4.9(13)}	2.4(15) ^{+1.5(15)} _{-6.6(14)}	<8.8(13)

Notes. a(b) = $a \times 10^b$.

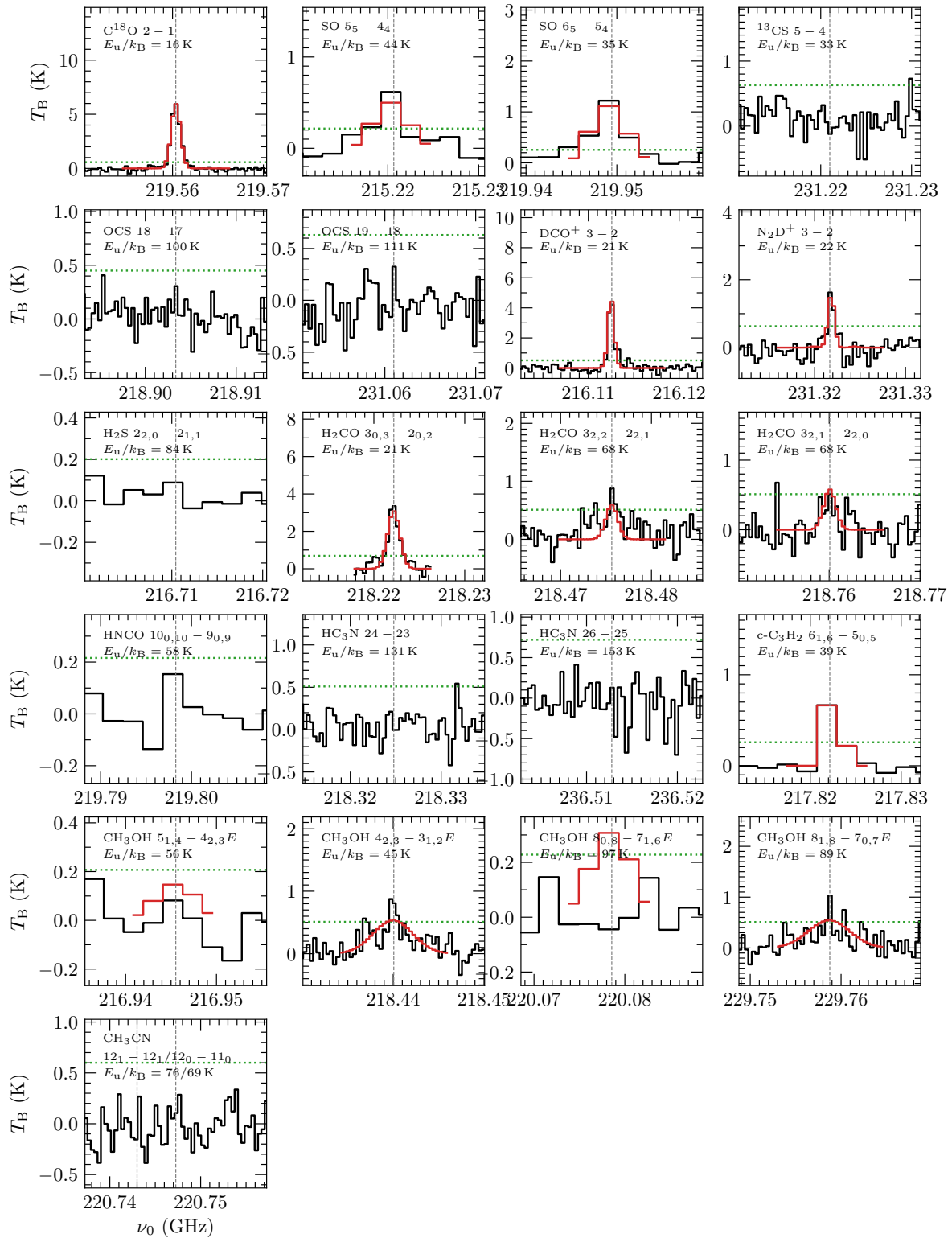


FIGURE B.25: Example spectrum of all molecular transitions fitted with XCLASS toward core 1 in ISOSS J22478+6357. In each panel, the observed spectrum of the emission line and the corresponding XCLASS fit are presented by the black and red lines, respectively. The green dotted line shows the $3\sigma_{\text{line}}$ level of the transition (Table 3.3). The gray dashed line indicates the rest frequency of the transition (Table 3.2). If XCLASS fits were discarded no fit is shown (the constraints are explained in Sect. 3.5.6). An example spectrum of core 1 in ISOSS J23053+5953 is shown in Fig. B.26.

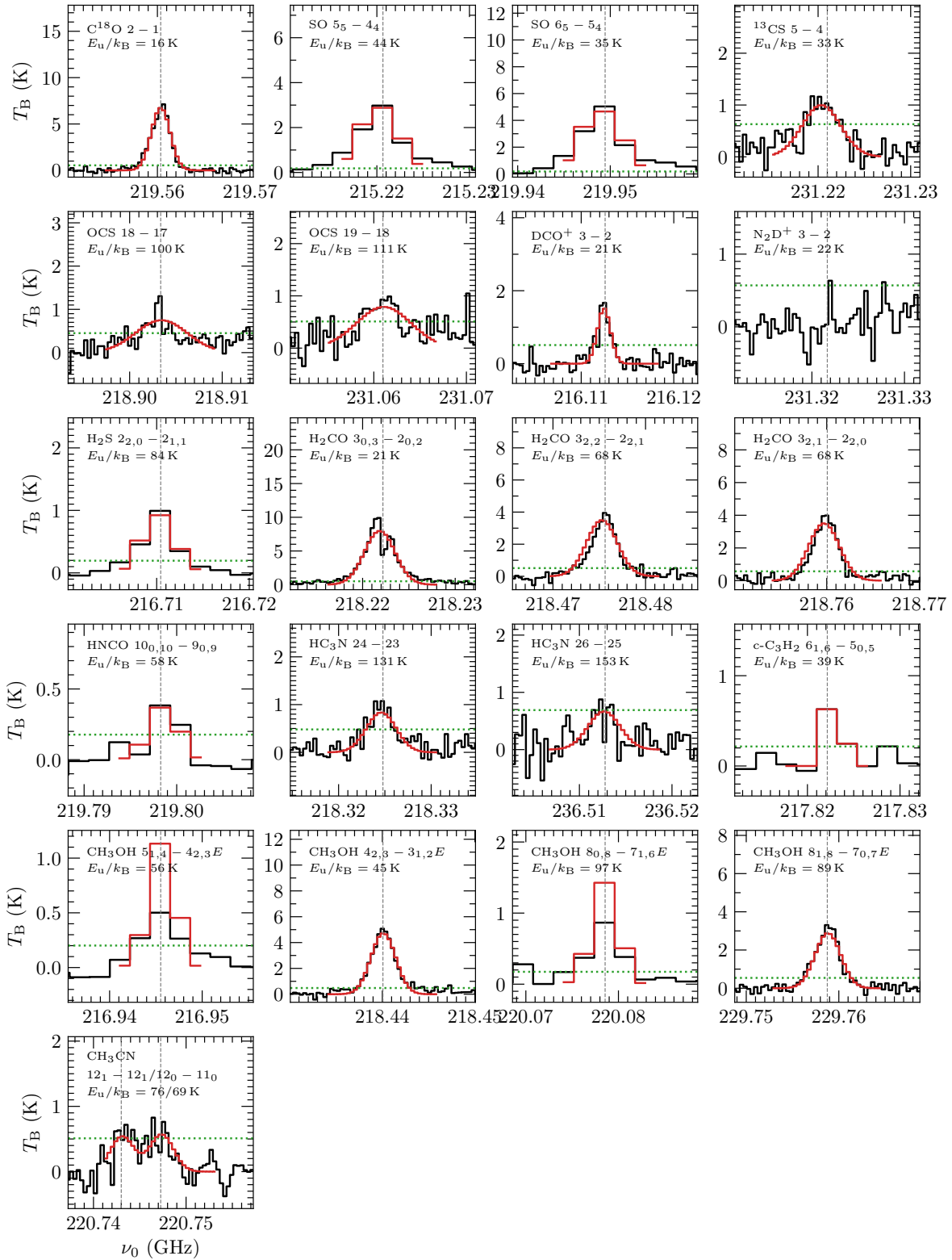


FIGURE B.26: The same as Fig. B.25, but for core 1 in ISOSS J23053+5953.

B.3 MUSCLE results

For four cores in our sample, which have enough species detected in the 1.3 mm setup and for which the density and temperature profiles could be derived, we applied the physical-chemical model MUSCLE in Sect. 3.6 to estimate the chemical timescale τ_{chem} . As the initial chemical

composition of the gas is unknown and the physical structure is static in MUSCLE, we modeled each core with three initial chemical conditions, referred to as the HMPO, HMC, and UCH_{III} model (see also Sect. 2.5). The initial chemical conditions are taken from a study of 59 HMS-FRs by Gerner et al. (2014, 2015).

In each time step, the modeled column densities, computed with ALCHEMIC, are compared to the observed column densities. The time step with the lowest χ^2 is taken as the best fit. Table B.3 shows for each of the four modeled cores and each initial condition model, the best-fit chemical timescale τ_{chem} , the corresponding χ^2 value, and the percentage of well modeled species Y . A molecule is considered as “well modeled” when the modeled and observed column density agree within a factor of ten. A weighted $\bar{\chi}^2$ was computed taking into account the percentage of well modeled species Y : $\bar{\chi}^2 = \frac{\chi^2}{Y^2}$. For each core, the initial condition model with the lowest $\bar{\chi}^2$ was taken as the best-fit model.

TABLE B.3: MUSCLE results for cores in the CORE-extension regions. For each initial condition model, the best-fit chemical timescale τ_{chem} , the χ^2 value obtained from comparing the modeled and observed column densities, the percentage of well-modeled molecules Y , and the weighted $\bar{\chi}^2 = \frac{\chi^2}{Y}$ are shown. Models that have a higher initial temperature as the measured core temperature ($T_{\text{init},500} > T_{500}$) are not considered and indicated by “...”.

Core	HMPO model				HMC model				UCHII model			
	τ_{chem} (10^4 yr)	χ^2	Y (%)	$\bar{\chi}^2$	τ_{chem} (10^4 yr)	χ^2	Y (%)	$\bar{\chi}^2$	τ_{chem} (10^4 yr)	χ^2	Y (%)	$\bar{\chi}^2$
ISOSS J22478+6357 1	3.1	0.293	85.7	0.399	6.0	0.339	78.6	0.548
ISOSS J23053+5953 1	1.9	0.458	71.4	0.898	4.9	0.556	57.1	1.702	8.4	0.457	64.3	1.105
ISOSS J23053+5953 2	1.9	0.365	71.4	0.715	6.0	0.497	64.3	1.203	8.4	0.469	64.3	1.135
ISOSS J23053+5953 6	1.8	0.494	71.4	0.969	6.7	0.500	71.4	0.980	8.4	0.448	64.3	1.084

Appendix C

Supplementary material for Chapter 4

C.1 Summary of the ALMA observations

Tables C.1 and C.2 give an detailed overview of the ALMA 3 mm observations and spectral setup, respectively. The data calibration and imaging are explained in detail in Sect. 4.3.1.

TABLE C.1: Overview of the ALMA 3 mm observation blocks (Cycle 6, project code 2018.1.00424.S). The target regions were grouped into three fields in order to minimize off-source time (Table 4.2).

Field	SPR	Array configuration	Antennae	Date	On-source integration (min)	PWV (mm)	min. baseline (m)	max. baseline (m)
Field 1	SPR1	C43-4	47	2018-10-28 21:06	20.4	1.3	15.1	1 397.8
Field 1	SPR1	ACA	11	2018-12-28 18:08	48.6	6.0	8.9	48.9
Field 1	SPR2	C43-4	41	2018-12-15 19:34	26.6	4.1	15.1	740.4
Field 1	SPR2	ACA	10	2018-12-30 15:27	51.5	5.0	8.9	48.9
Field 1	SPR3	C43-4	48	2018-10-27 21:54	20.6	1.3	15.1	1 397.8
Field 1	SPR3	ACA	11	2018-12-28 17:24	44.2	6.0	8.9	48.9
Field 2	SPR1	C43-4	46	2018-11-20 17:54	47.7	1.4	15.1	1 397.8
Field 2	SPR1	C43-4	46	2018-11-20 18:42	48.6	1.5	15.1	1 397.8
Field 2	SPR1	ACA	11	2019-05-10 09:30	84.2	5.0	8.9	48.0
Field 2	SPR1	ACA	11	2019-05-20 07:12	89.0	2.0	8.9	48.0
Field 2	SPR1	ACA	11	2019-05-23 07:36	83.8	1.0	8.9	48.0
Field 2	SPR2	C43-4	41	2019-05-03 11:22	55.8	1.0	15.1	740.4
Field 2	SPR2	ACA	11	2019-01-26 15:04	76.7	4.0	8.9	48.0
Field 2	SPR2	ACA	11	2019-03-29 08:16	83.2	5.0	8.9	48.0
Field 2	SPR2	ACA	11	2019-03-29 09:39	84.0	5.0	8.9	48.0
Field 2	SPR2	ACA	11	2019-03-29 11:06	54.6	5.0	8.9	48.0
Field 2	SPR3	C43-1	46	2019-01-10 18:20	41.3	2.4	15.1	313.7
Field 2	SPR3	ACA	11	2019-05-20 08:41	83.7	2.0	8.9	48.0
Field 2	SPR3	ACA	11	2019-05-23 08:59	83.4	1.0	8.9	48.0
Field 3	SPR1	C43-4	46	2018-11-16 21:38	43.6	2.0	15.1	1 397.8
Field 3	SPR1	C43-4	46	2018-11-19 20:31	44.3	1.9	15.1	1 397.8
Field 3	SPR1	ACA	11	2019-01-16 13:15	74.8	5.0	8.9	48.9
Field 3	SPR1	ACA	12	2019-01-17 12:35	78.6	5.0	8.9	48.9
Field 3	SPR2	C43-4	41	2019-04-17 11:20	61.8	3.3	15.0	783.5
Field 3	SPR2	ACA	10	2019-04-01 12:04	87.0	4.0	8.9	48.9
Field 3	SPR2	ACA	10	2019-04-17 12:17	86.9	3.0	8.9	44.7
Field 3	SPR3	C43-4	47	2018-10-30 22:39	50.2	1.4	15.1	1 397.8
Field 3	SPR3	ACA	11	2019-01-16 14:43	74.9	5.0	8.9	48.9
Field 3	SPR3	ACA	11	2019-01-19 14:25	74.9	5.0	8.9	48.9

TABLE C.2: Overview of the spectral windows observed with ALMA.

SPR	spw	Central frequency ν_0 (GHz)	Bandwidth (GHz)	number of channels n_{channel}	channel spacing $\delta\nu$ (MHz)	Targeted species
SPR1	0	86.676	0.117	480	0.244	HCO
SPR1	1	86.759	0.117	480	0.244	H ¹³ CO ⁺
SPR1	2	86.852	0.117	480	0.244	SiO, CH ₃ CH ₂ CN
SPR1	3	86.345	0.117	480	0.244	H ¹³ CN
SPR1	4	87.44	0.117	480	0.244	CCH
SPR1	5	88.637	0.117	480	0.244	HCN, CH ₃ OH
SPR1	6	87.93	0.117	480	0.244	HNCO
SPR1	7	87.322	0.117	480	0.244	CCH
SPR1	8	97.721	0.117	480	0.244	³⁴ SO
SPR1	9	97.987	0.117	480	0.244	CS
SPR1	10	96.926	0.117	480	0.244	CH ₃ CH ₂ CN
SPR1	11	96.994	0.117	480	0.244	O ¹³ CS, H ¹³ CCCN
SPR1	12	99.331	0.117	480	0.244	CH ₃ OCH ₃
SPR1	13	100.736	0.117	480	0.244	HC ₃ N, CH ₃ OCHO
SPR1	14	99.305	0.117	480	0.244	SO
SPR1	15	99.872	0.117	480	0.244	CCS
SPR2	0	108.786	0.117	480	0.244	¹³ CN
SPR2	1	110.207	0.117	480	0.244	¹³ CO
SPR2	2	109.469	0.117	480	0.244	OCS, HNCO, HC ₃ N
SPR2	3	109.788	0.117	480	0.244	C ¹⁸ O, NH ₂ CHO
SPR2	4	109.506	1.875	1 920	0.977	C ¹⁵ N, SiS, HC ₃ N, HC ₅ N, CH ₃ OCH ₃
SPR2	5	97.006	1.875	1 920	0.977	C ³³ S, H ₂ ¹³ CS, C ₂ H ₅ OH, CH ₃ NCO
SPR2	6	98.806	1.875	1 920	0.977	H α , CH ₃ CHO, CH ₃ OCHO, CH ₃ COCH ₃
SPR3	0	104.035	0.117	480	0.244	CH ₃ CH ₂ CN, SO ₂ , CH ₃ OH
SPR3	1	102.224	0.117	480	0.244	HSCN, CH ₃ SH
SPR3	2	103.047	0.117	480	0.244	H ₂ CS
SPR3	3	103.223	0.117	480	0.244	NH ₂ CHO
SPR3	4	104.207	0.117	480	0.244	CH ₂ CHCN, SO ₂ , CH ₃ OCH ₃
SPR3	5	104.88	0.117	480	0.244	HOCN
SPR3	6	104.717	0.117	480	0.244	¹³ C ¹⁸ O, CH ₃ OCH ₃
SPR3	7	105.564	0.117	480	0.244	CH ₃ OH, CH ₃ OCH ₃
SPR3	8	90.269	0.117	480	0.244	¹⁵ NNH ⁺ , CH ₃ OCHO
SPR3	9	90.669	0.117	480	0.244	HNC, CCS
SPR3	10	90.985	0.117	480	0.244	¹³ C ³⁴ S, HC ₃ N, CH ₃ OCH ₃
SPR3	11	91.945	0.117	480	0.244	CH ₃ ¹³ CN
SPR3	12	91.64	0.117	480	0.244	CH ₃ COCH ₃
SPR3	13	91.985	0.117	480	0.244	CH ₃ CN
SPR3	14	93.179	0.117	480	0.244	N ₂ H ⁺
SPR3	15	92.415	0.117	480	0.244	CH ₂ CHCN, CH ₃ OH

C.2 Overview of the sample

A multi-wavelength and multi-scale overview of the target regions are presented in Figs. C.1 -C.11 using archival ATLASGAL submm, Herschel FIR and Spitzer MIR data in comparison with the ALMA 3 mm observations.

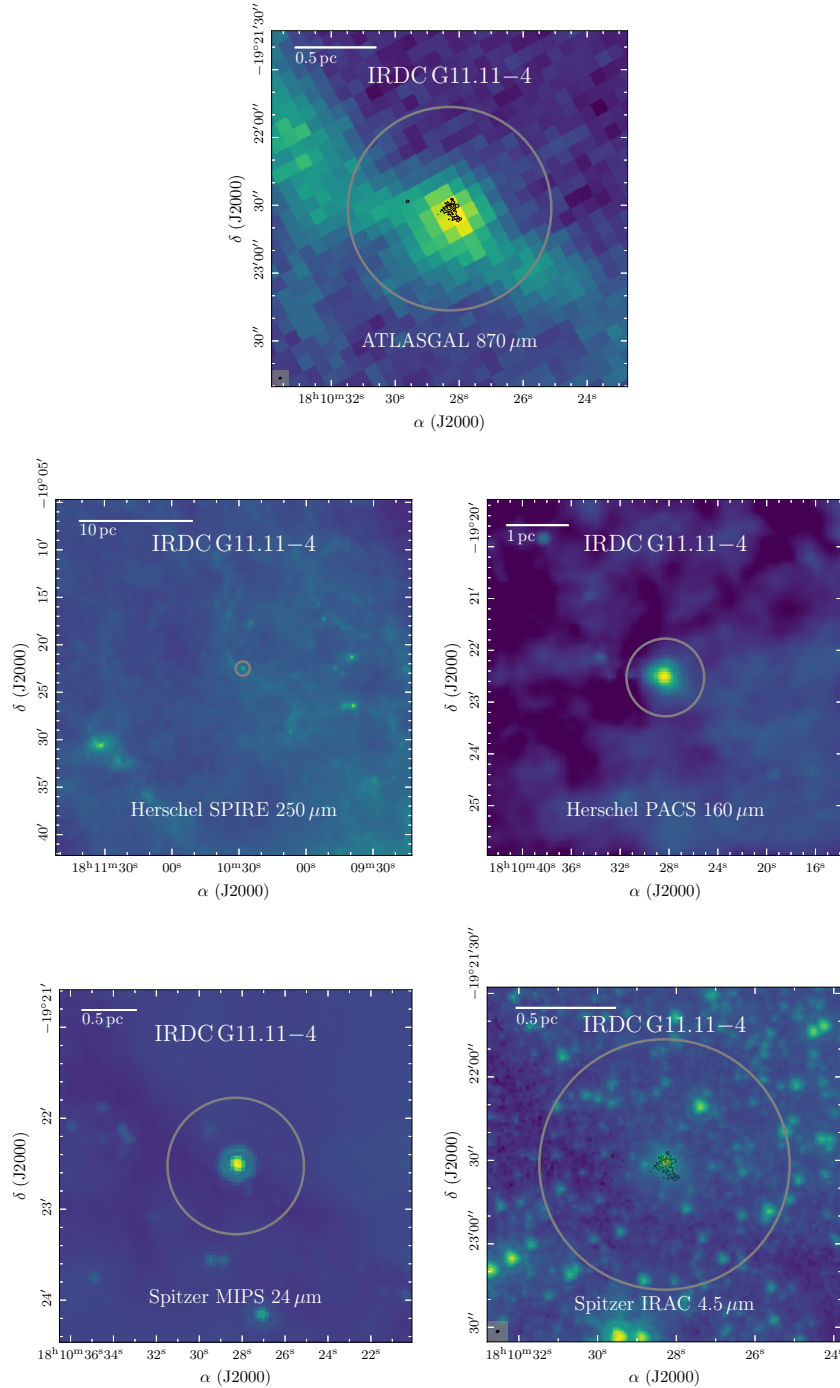


FIGURE C.1: Multi wavelength overview of IRDC G11.11-4. In color, ATLASGAL 870 μ m, Herschel SPIRE 250 μ m, Herschel PACS 70 μ m, Spitzer MIPS 24 μ m, and Spitzer IRAC 4.5 μ m data are presented. In all panels, the ALMA primary beam is indicated by a grey circle. In the top and bottom right panel, the ALMA 3 mm continuum data are shown by black contours. The dotted black contour marks the $-5\sigma_{\text{cont}}$ level. The solid black contours start at $5\sigma_{\text{cont}}$ and contour steps increase by a factor of 2 (e.g., 5, 10, 20, $40\sigma_{\text{cont}}$). The ALMA synthesized beam size is shown in the bottom left corner.

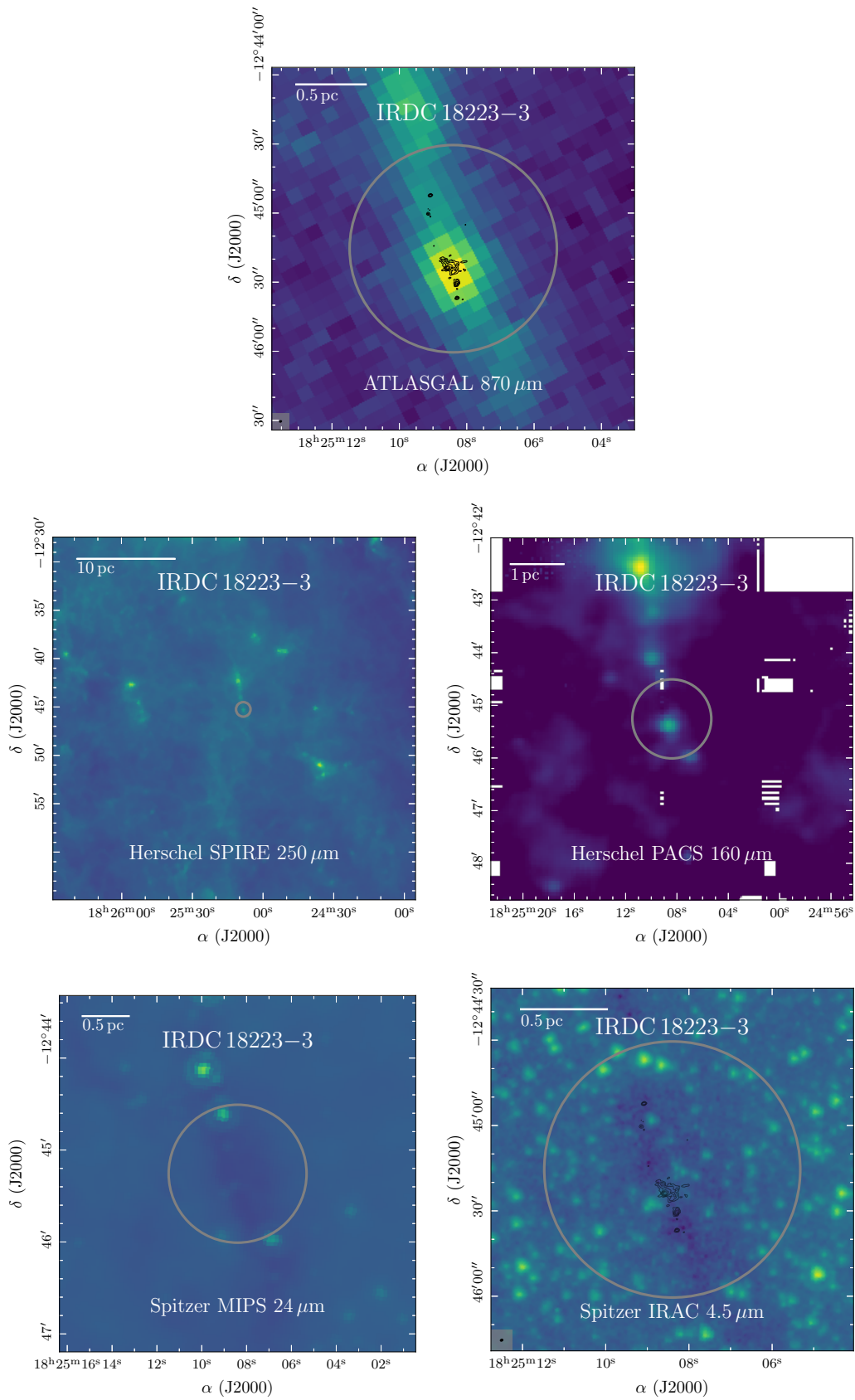


FIGURE C.2: The same as Fig. C.1, but for IRDC 18223-3.

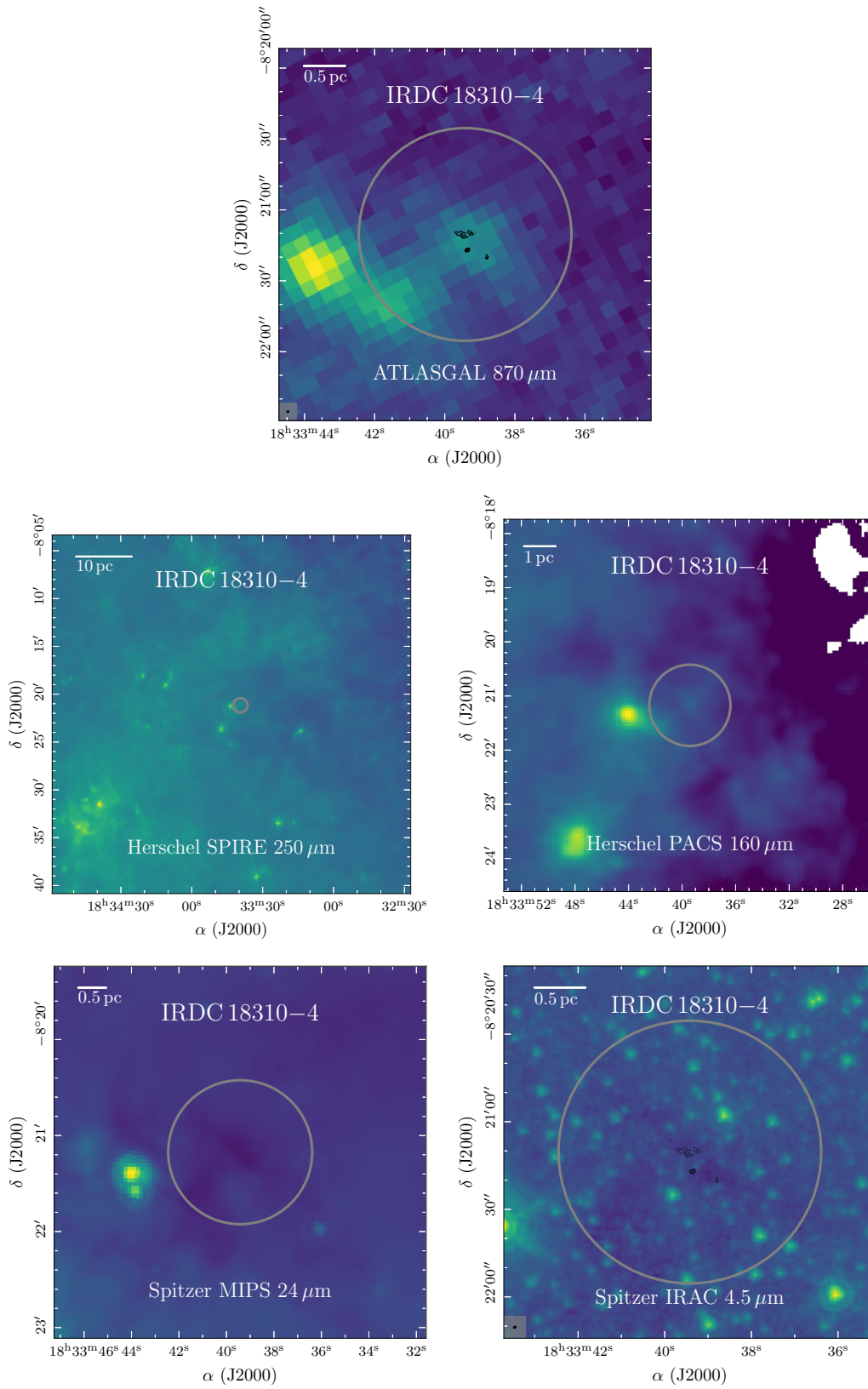


FIGURE C.3: The same as Fig. C.1, but for IRDC 18310-4.

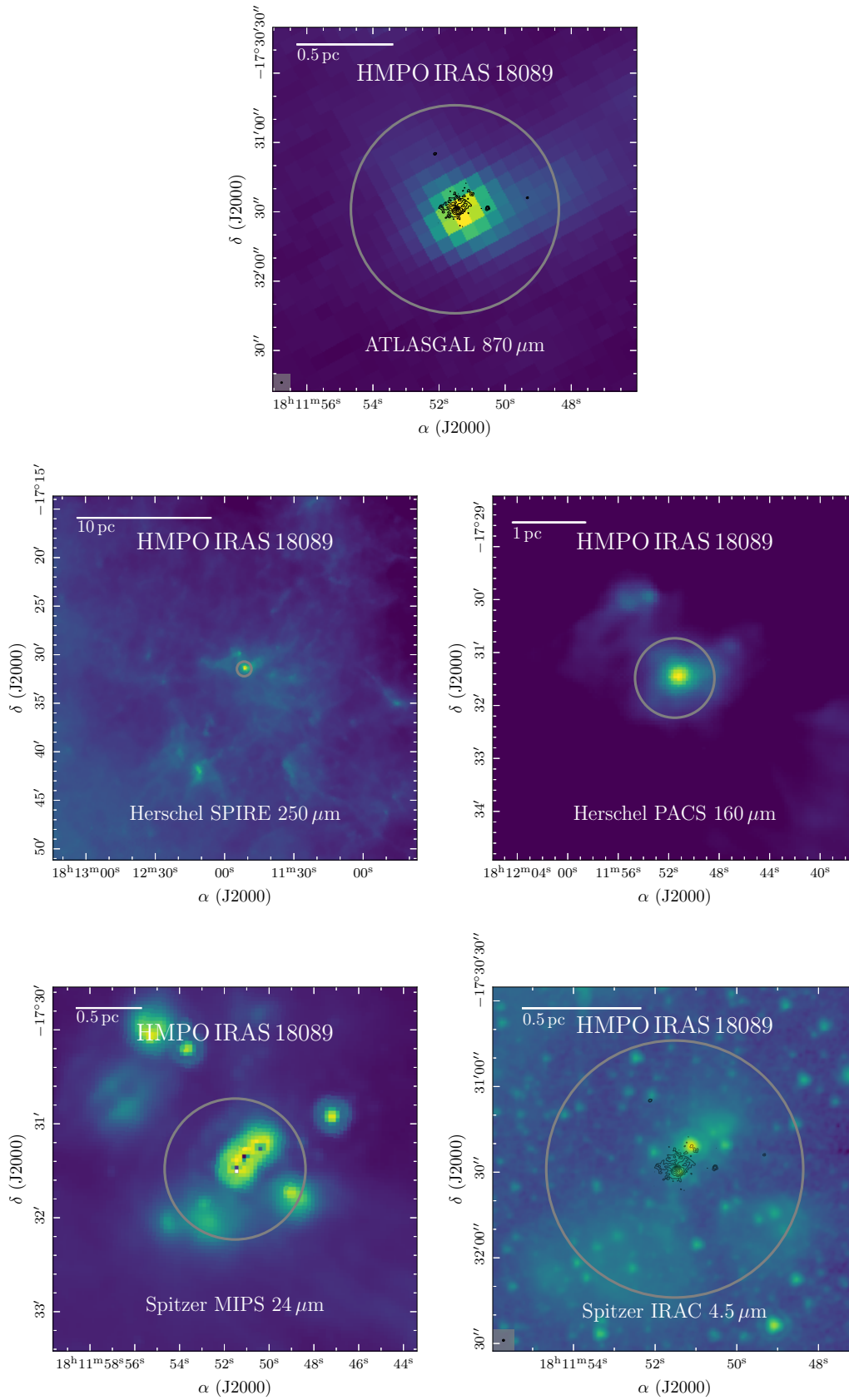


FIGURE C.4: The same as Fig. C.1, but for HMPO IRAS 18089.

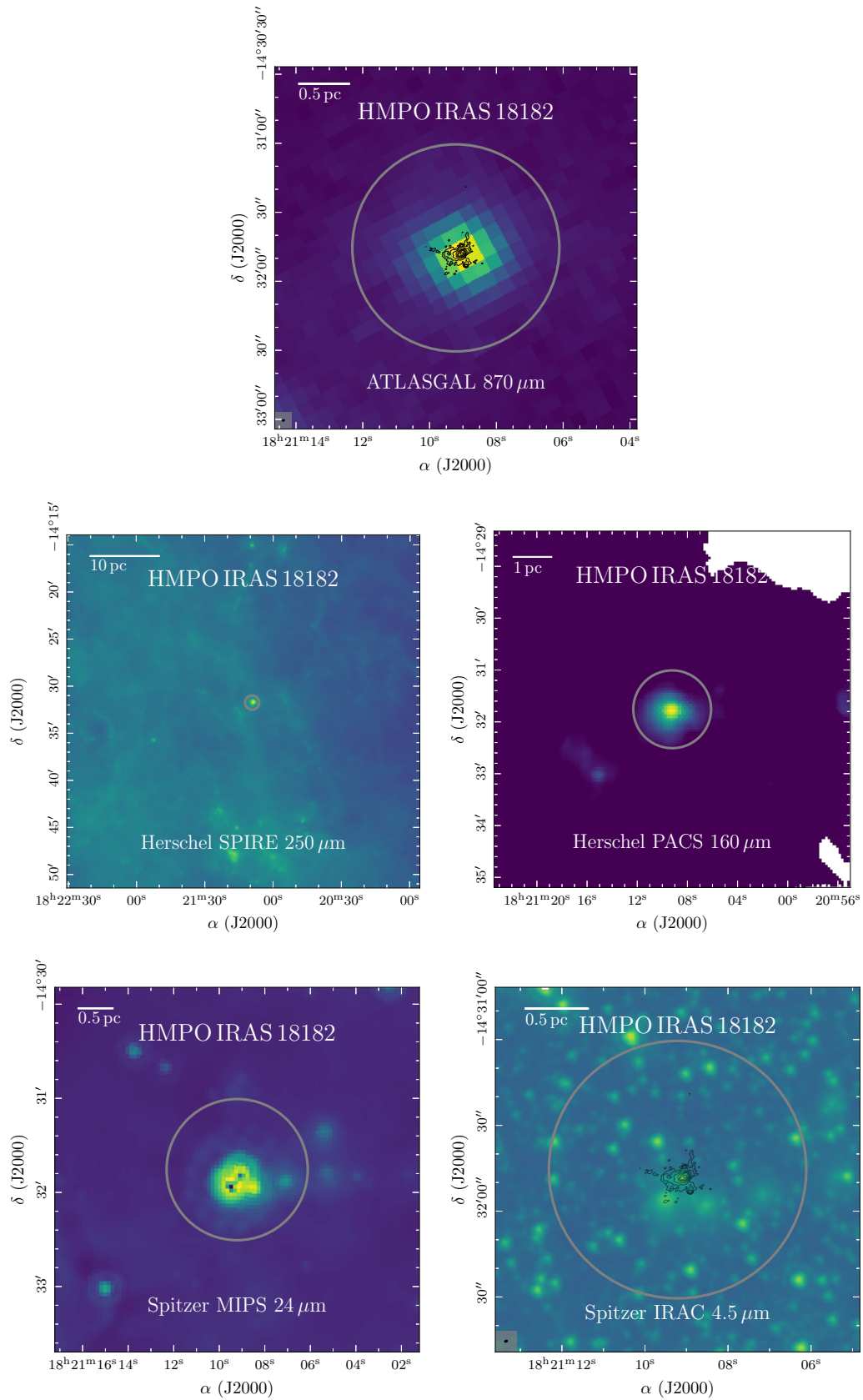


FIGURE C.5: The same as Fig. C.1, but for HMPO IRAS 18182.

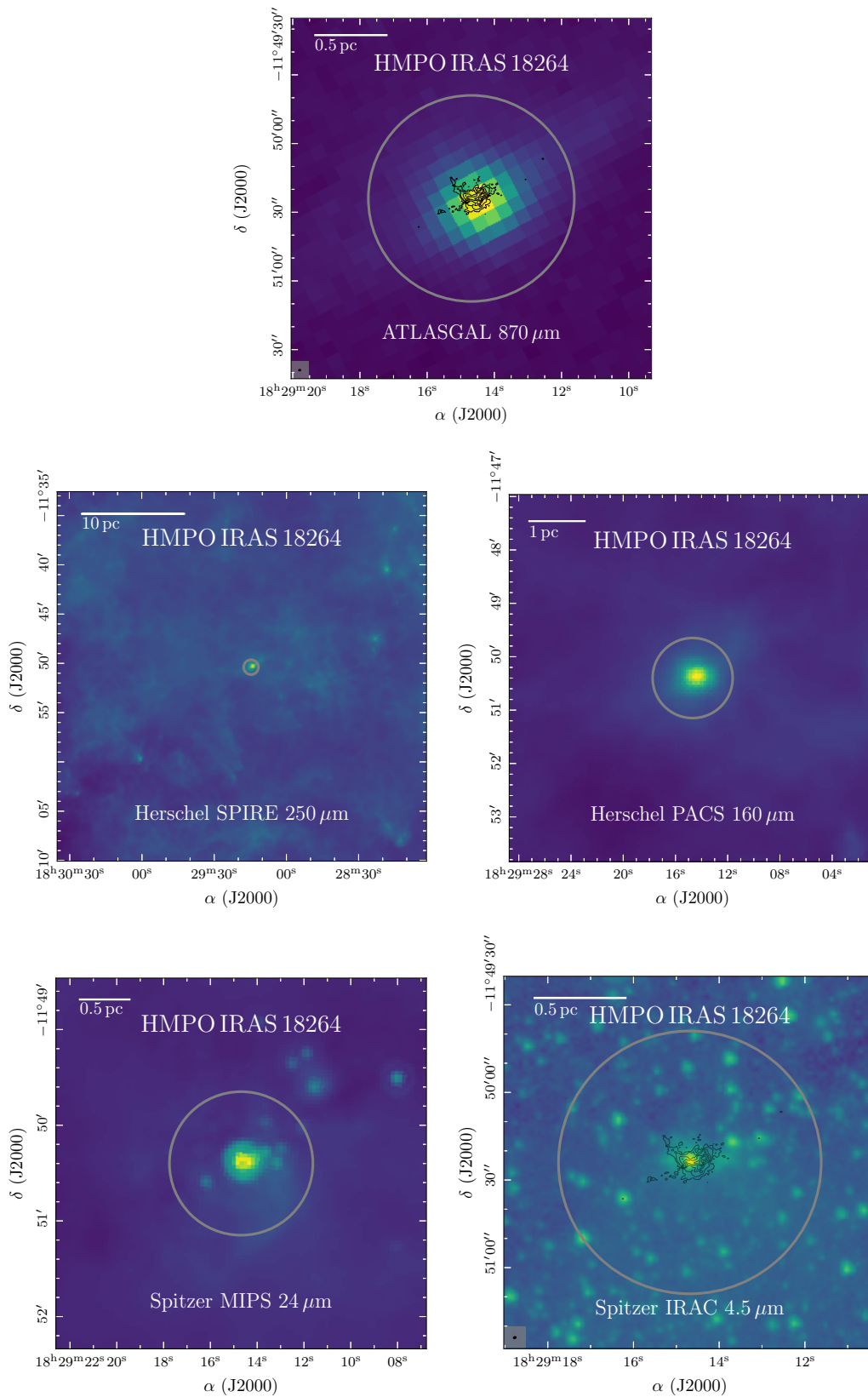


FIGURE C.6: The same as Fig. C.1, but for HMPO IRAS 18264.

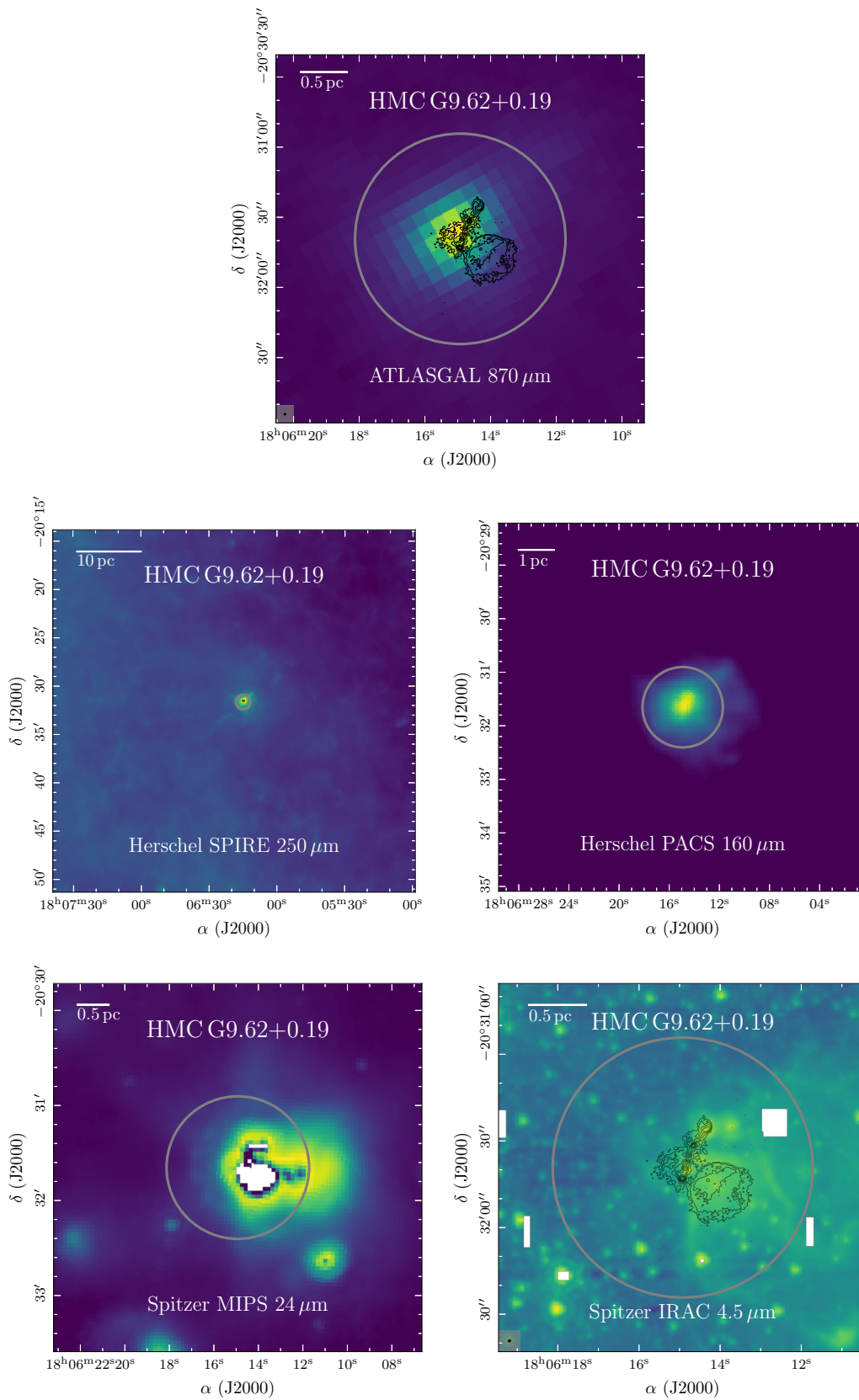


FIGURE C.7: The same as Fig. C.1, but for HMC G9.62+0.19.

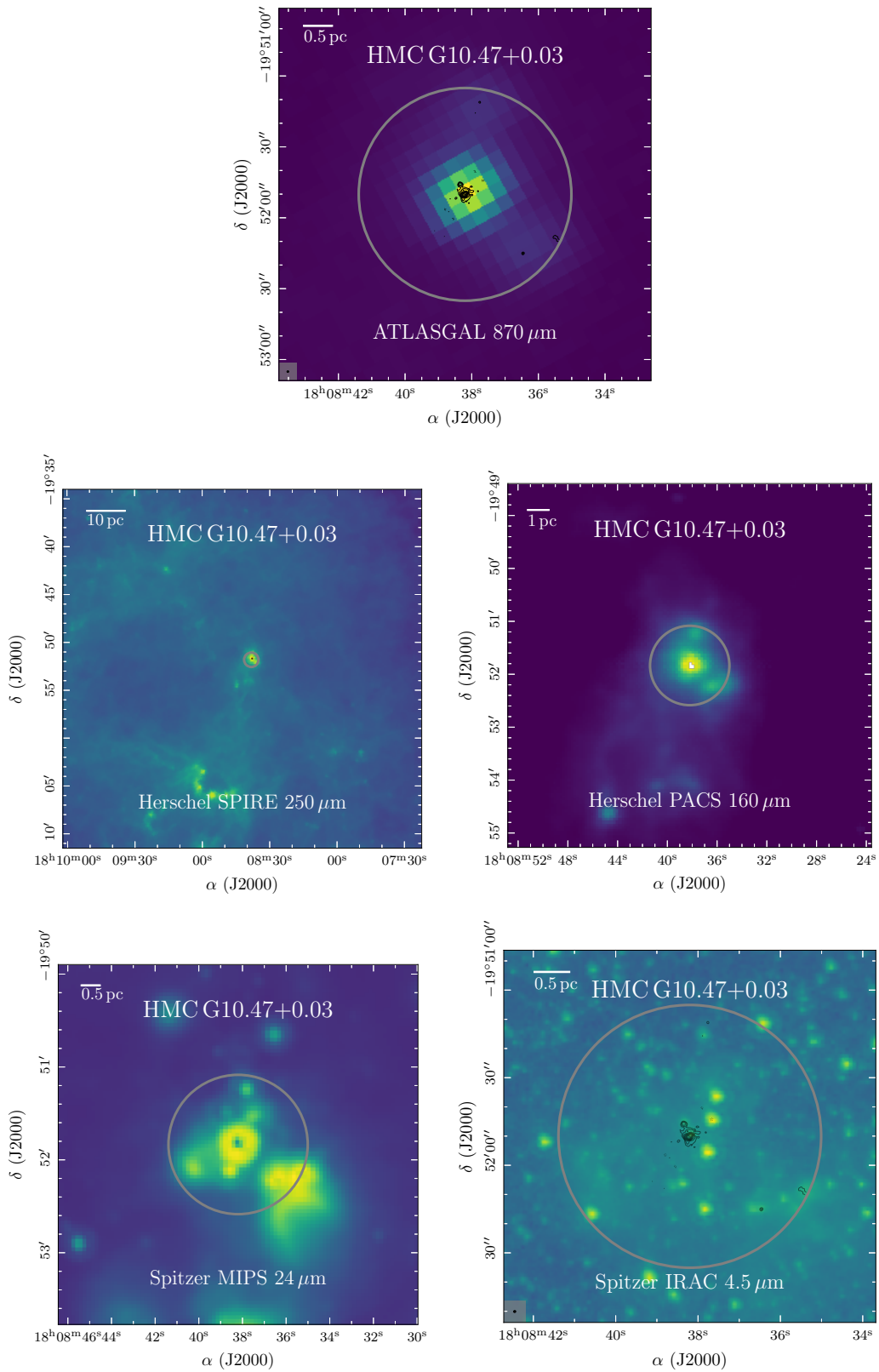


FIGURE C.8: The same as Fig. C.1, but for HMC G10.47+0.03.

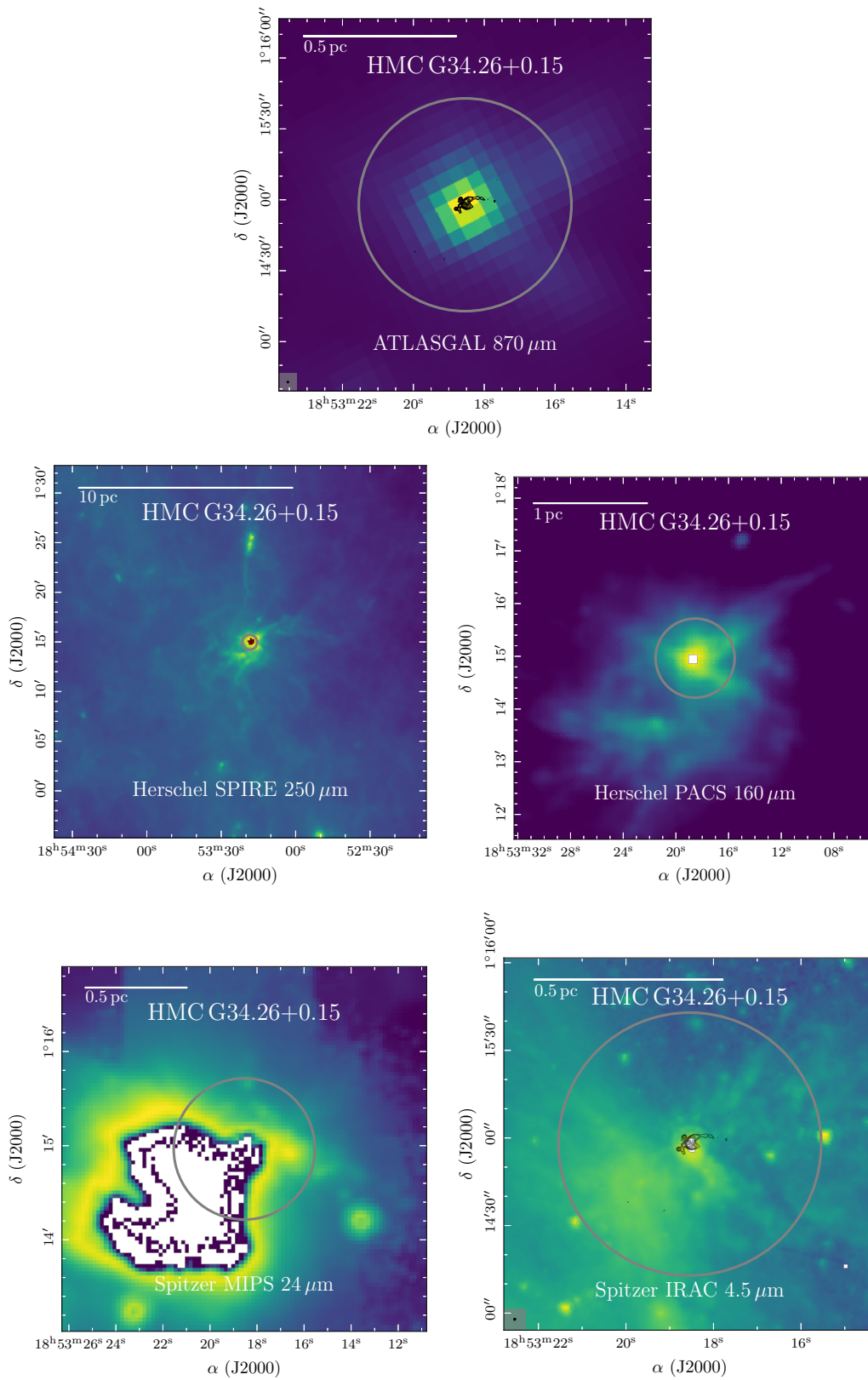


FIGURE C.9: The same as Fig. C.1, but for HMC G34.26+0.15.

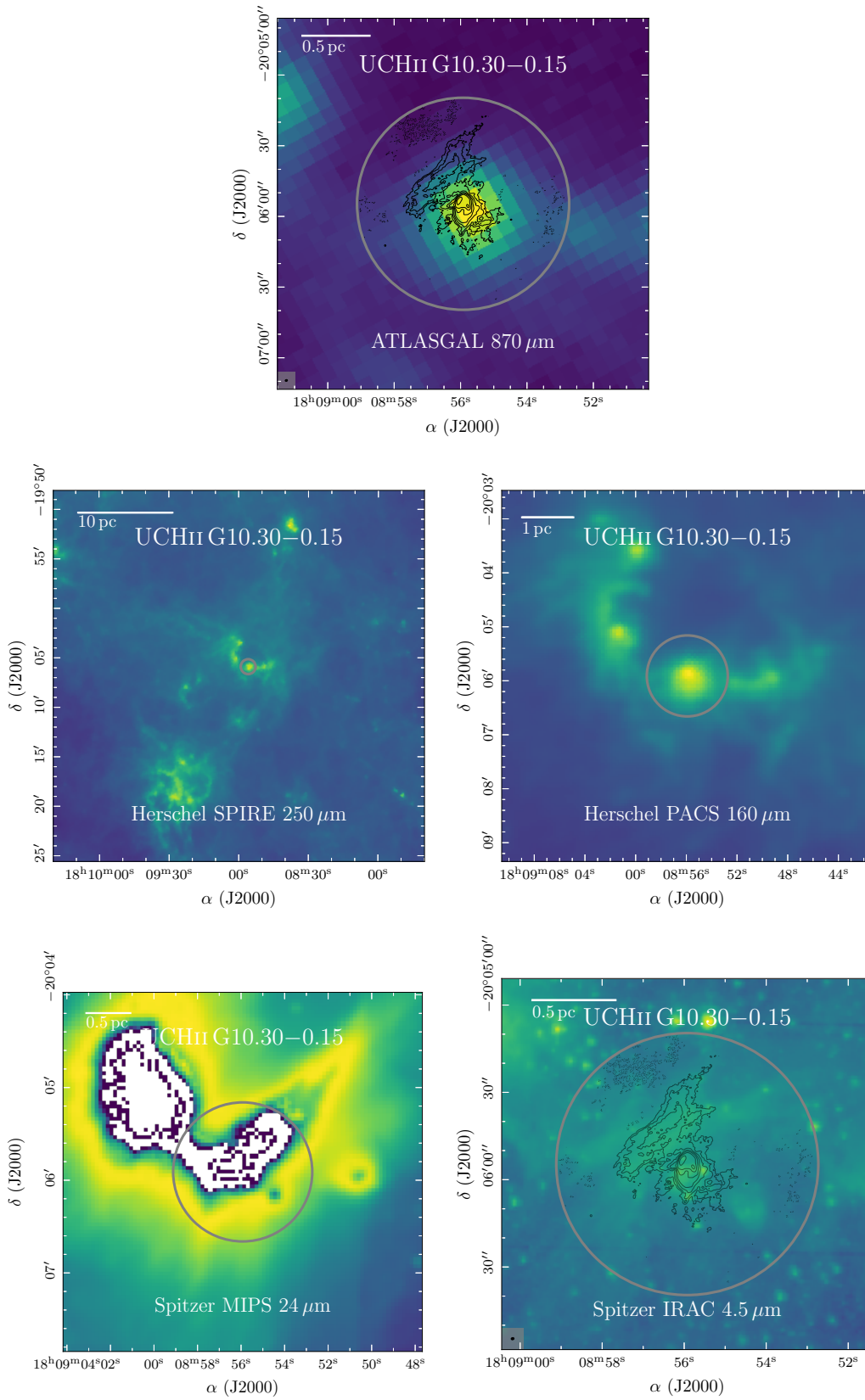


FIGURE C.10: The same as Fig. C.1, but for UCH II G10.30-0.15.

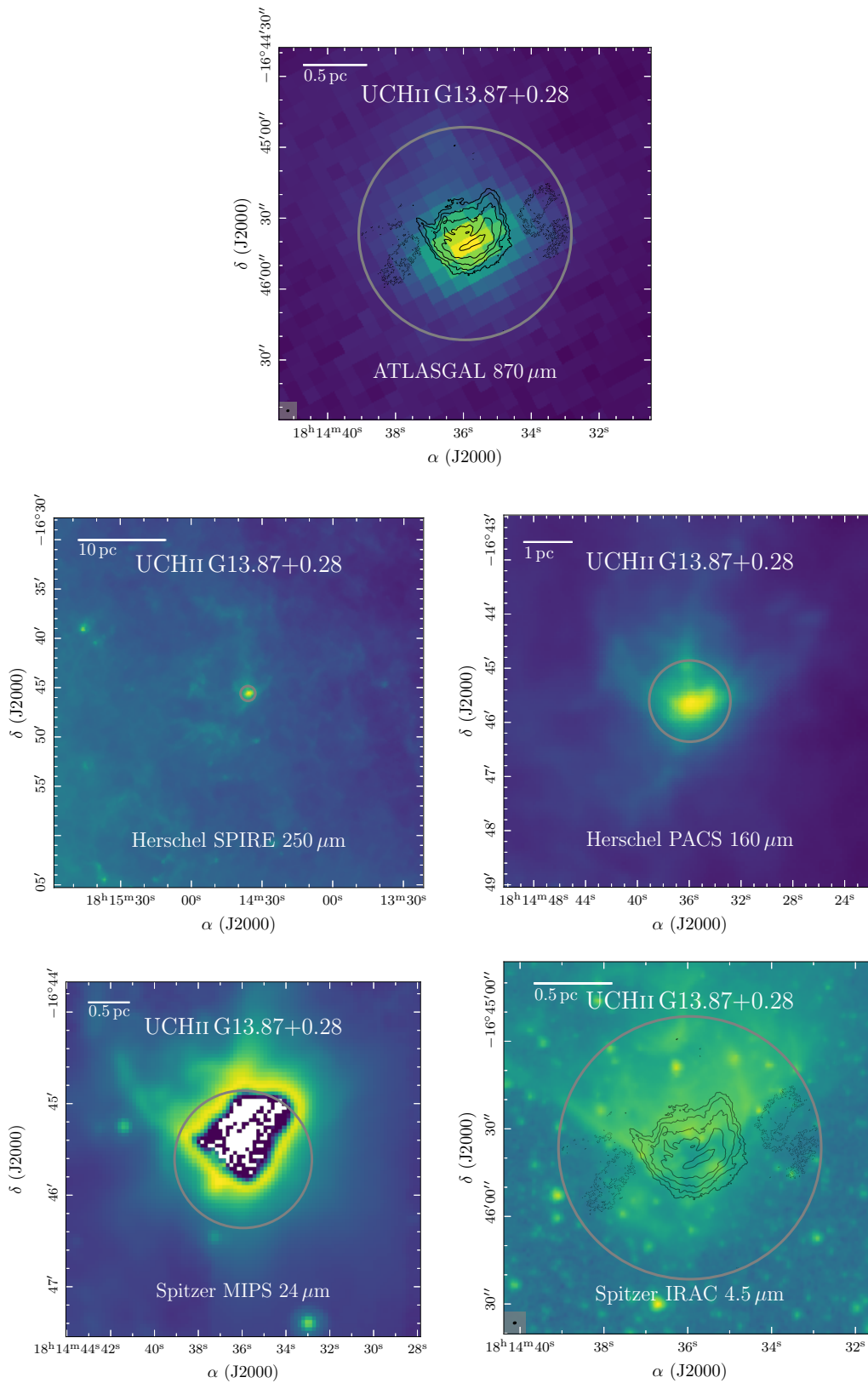


FIGURE C.11: The same as Fig. C.1, but for UCH II G13.87+0.28.

C.3 Source properties

The fragmentation properties of the regions are analyzed in Sect. 4.4.1. Table C.3 summarizes the properties, such as position and peak intensity of all fragments. We classify the fragments into protostellar sources and envelope clumps. The mm cores have compact mm emission, while UCH_{II} regions have in addition H(40) α and cm emission. Cometary UCH_{II} regions have extended, cometary-shaped, mm emission as well as H(40) α and cm emission. Table C.4 summarized the radial temperature fit results derived in Sect. 4.5 for all protostellar sources. The beam-averaged temperature (Sect. 4.5), and H₂ column density and mass (Sect. 4.7) are listed in Table C.5 for all protostellar sources. Table C.6 summarizes the fit results of the visibility profiles and corresponding density profiles for all protostellar sources (Sect. 4.6).

TABLE C.3: Overview of the cores, (cometary) UCH_{II} regions, and envelope positions in the ALMA sample. The properties are determined using the `clumpfind` algorithm, except for the cometary UCH_{II} regions (HMC G9.62+0.19 9, UCH_{II} G10.30–0.15 1, and UCH_{II} G13.87+0.28 1), for which the properties were estimated considering the full extent of the structure. The fragments are classified into mm cores, envelope clumps and (cometary) UCH_{II} regions labeled as type “mm core”, “envelope”, and “(comet.) UCH_{II}”, respectively. The positions are given relative to the phase center of the region (Table 4.1).

Position	α J(2000)	δ J(2000)	$I_{3\text{mm}}$ (mJy beam ⁻¹)	$F_{3\text{mm}}$ (mJy)	r_{out} (au)	type
IRDC G11.11–4 1	–0.45	+0.90	1.4	10	7 700	mm core
IRDC G11.11–4 2	–2.85	–3.90	0.48	2.1	4 400	envelope
IRDC G11.11–4 3	–1.35	–2.55	0.37	0.87	2 900	envelope
IRDC G11.11–4 4	–0.90	–1.80	0.36	0.64	2 400	envelope
IRDC 18223–3 1	+2.55	–8.25	2.9	11	7 900	mm core
IRDC 18223–3 2	–1.50	–15.30	1.1	3.0	4 900	mm core
IRDC 18223–3 3	+9.90	+23.10	0.81	0.89	2 700	mm core
IRDC 18223–3 4	–1.65	–21.45	0.67	0.75	2 700	mm core
IRDC 18223–3 5	–0.45	–8.40	0.57	4.4	7 100	envelope
IRDC 18223–3 6	+3.60	–5.25	0.51	2.4	5 500	mm core
IRDC 18223–3 7	+10.95	+15.15	0.26	0.30	2 200	mm core
IRDC 18310–4 1	–0.90	–6.60	1.2	1.4	5 300	mm core
IRDC 18310–4 2	+0.90	–0.60	0.31	1.7	9 400	mm core
IRDC 18310–4 3	–2.40	+0.45	0.27	0.62	5 800	mm core
IRDC 18310–4 4	–9.30	–9.90	0.25	0.29	4 000	mm core
HMPO IRAS 18089 1	–0.90	+0.15	24	92	8 100	mm core
HMPO IRAS 18089 2	–14.10	+0.45	1.9	3.4	2 400	mm core
HMPO IRAS 18089 3	–3.60	+1.50	1.4	16	5 700	envelope
HMPO IRAS 18089 4	+8.55	+24.00	1.1	1.1	1 500	mm core
HMPO IRAS 18089 5	+6.00	+1.20	0.84	2.2	2 500	envelope
HMPO IRAS 18089 6	–7.35	+6.45	0.67	1.5	2 000	envelope
HMPO IRAS 18089 7	+1.80	+3.90	0.66	2.6	2 700	envelope
HMPO IRAS 18089 8	+0.00	+4.35	0.62	3.2	2 900	envelope
HMPO IRAS 18089 9	–31.35	+4.95	0.61	0.50	1 200	mm core
HMPO IRAS 18089 10	+5.10	–0.00	0.60	1.9	2 400	envelope
HMPO IRAS 18182 1	–2.55	–2.40	13	75	20 000	mm core
HMPO IRAS 18182 2	–2.40	+0.90	2.1	4.9	9 200	mm core
HMPO IRAS 18182 3	–4.35	–7.80	2.1	4.3	7 900	mm core
HMPO IRAS 18182 4	+3.90	–3.45	0.44	3.4	8 800	envelope

TABLE C.3: continued.

Position	α J(2000)	δ J(2000)	$I_{3\text{mm}}$ (mJy beam $^{-1}$)	$F_{3\text{mm}}$ (mJy)	r_{out} (au)	type
HMPO IRAS 18264 1	-4.80	+1.50	9.9	35	6 800	mm core
HMPO IRAS 18264 2	-3.90	-0.45	7.8	35	7 800	mm core
HMPO IRAS 18264 3	+1.80	-1.35	4.0	6.6	4 800	mm core
HMPO IRAS 18264 4	+1.35	-0.15	3.1	11	6 100	mm core
HMPO IRAS 18264 5	-3.15	-1.80	2.4	13	8 800	envelope
HMPO IRAS 18264 6	-0.15	+0.30	1.9	6.2	4 100	envelope
HMPO IRAS 18264 7	-3.00	+1.95	1.7	4.5	4 400	envelope
HMPO IRAS 18264 8	-5.25	+3.75	1.4	5.3	5 600	envelope
HMPO IRAS 18264 9	+2.40	+1.20	1.3	8.3	7 300	envelope
HMPO IRAS 18264 10	-7.20	+3.90	0.49	1.1	3 200	envelope
HMPO IRAS 18264 11	+0.00	-1.95	0.48	1.8	4 200	envelope
HMPO IRAS 18264 12	+5.85	+4.20	0.36	2.6	5 800	envelope
HMPO IRAS 18264 13	-8.70	+3.15	0.32	1.2	4 000	envelope
HMC G9.62+0.19 1	+0.15	-3.75	58	100	11 400	UCHII
HMC G9.62+0.19 2	-3.75	+7.65	24	49	14 100	UCHII
HMC G9.62+0.19 3	-0.75	-0.15	11	37	12 400	mm core
HMC G9.62+0.19 4	-2.10	+4.35	4.5	14	10 500	mm core
HMC G9.62+0.19 5	-1.65	+1.95	4.4	12	9 000	mm core
HMC G9.62+0.19 6	-8.10	+13.05	3.5	34	16 300	UCHII
HMC G9.62+0.19 7	+1.35	-2.10	3.5	15	11 400	mm core
HMC G9.62+0.19 8	-2.25	+9.00	2.1	11	10 700	mm core
HMC G9.62+0.19 9	-12.75	-8.25	2.2	343	62 400	comet. UCHII
HMC G9.62+0.19 10	+3.15	+1.20	0.85	10	13 000	envelope
HMC G9.62+0.19 11	-8.55	+16.05	0.54	1.1	4 500	envelope
HMC G9.62+0.19 12	+1.50	-7.35	0.75	3.7	7 500	envelope
HMC G9.62+0.19 13	+0.00	+5.85	0.54	1.3	4 600	envelope
HMC G9.62+0.19 14	+1.50	+5.40	0.52	2.5	6 700	envelope
HMC G9.62+0.19 15	+1.05	+3.30	0.50	0.73	3 400	envelope
HMC G9.62+0.19 16	+1.50	+4.20	0.49	0.71	3 500	envelope
HMC G9.62+0.19 17	+4.80	-1.50	0.49	3.4	8 300	envelope
HMC G10.47+0.03 1	+0.45	-0.30	336	776	22 800	UCHII
HMC G10.47+0.03 2	+2.10	+4.20	7.2	23	9 700	UCHII
HMC G10.47+0.03 3	+0.75	+1.80	5.4	14	8 800	envelope
HMC G10.47+0.03 4	-24.45	-24.90	3.2	3.4	4 900	UCHII
HMC G34.26+0.15 1	+0.60	+0.30	2502	6636	4 200	UCHII
HMC G34.26+0.15 2	+1.95	+2.40	111	145	1 400	UCHII
HMC G34.26+0.15 3	+3.75	-1.65	81	100	1 200	UCHII
HMC G34.26+0.15 4	+2.25	-0.45	62	89	1 200	envelope
HMC G34.26+0.15 5	+2.55	-2.10	35	46	1 100	envelope
HMC G34.26+0.15 6	+2.10	-3.00	19	14	700	envelope
HMC G34.26+0.15 7	-4.95	+2.85	18	64	1 600	envelope
UCHII G10.30-0.15 1	+0.30	-0.75	18	1006	59 300	comet. UCHII
UCHII G13.87+0.28 1	-2.10	-0.75	7.0	1819	66 100	comet. UCHII

TABLE C.4: continued.

	HCN-to-HNC ratio			CH ₃ CN			type
	r_{in} (au)	T_{in} (K)	q	r_{in} (au)	T_{in} (K)	q	
HMC G9.62+0.19 5	11 700	13.8±1.8	0.38±0.03	11700	130.7±11.8	0.7±0.06	mm core
HMC G9.62+0.19 6	11 700	19.6±1.2	0.66±0.03	UCH _{II}
HMC G9.62+0.19 7	11 700	14.1±1.2	0.4±0.03	11700	114.6±9.9	0.64±0.06	mm core
HMC G9.62+0.19 8	11700	105.6±8.1	0.34±0.08	mm core
HMC G9.62+0.19 9	comet. UCH _{II}
HMC G10.47+0.03 1	19350	210.4±31.9	0.62±0.13	UCH _{II}
HMC G10.47+0.03 2	19 350	19.0±2.6	0.16±0.04	19350	143.2±4.3	0.24±0.06	UCH _{II}
HMC G10.47+0.03 4	19 350	15.6±0.9	0.12±0.05	UCH _{II}
HMC G34.26+0.15 1	1080	245.8±63.2	0.68±0.04	UCH _{II}
HMC G34.26+0.15 2	1080	128.1±5.5	0.16±0.04	UCH _{II}
HMC G34.26+0.15 3	UCH _{II}
UCH _{II} G10.30−0.15 1	8 100	15.4±0.7	0.05±0.01	comet. UCH _{II}
UCH _{II} G13.87+0.28 1	8 775	13.1±0.7	0.35±0.09	2925	36.2±1.4	0.06±0.03	comet. UCH _{II}

TABLE C.5: H₂ column density $N(\text{H}_2)$ and mass M in the ALMA sample. The beam-averaged temperature \bar{T} are computed from the temperature maps (Sect. 4.5). The dust continuum optical depth τ_{ν}^{cont} , H₂ column density $N(\text{H}_2)$, and mass M are calculated according to Eqs. (1.47), (1.48), and (1.49), respectively.

	HCN-to-HNC ratio \bar{T} (K)	CH ₃ CN \bar{T} (K)	CH ₃ ¹³ CN \bar{T} (K)	τ_{ν}^{cont}	$N(\text{H}_2)$ (cm ⁻²)	M (M_{\odot})	type
IRDC G11.11-4 1	6.3±0.0	39.9±0.9	...	5.9(-3)	1.1(24)±2.2(23)	0.82±0.16	mm core
IRDC 18223-3 1	34.0±1.5	42.4±5.2	...	1.3(-2)	2.4(24)±5.8(23)	1.21±0.29	mm core
IRDC 18223-3 2	25.2±0.4	9.0(-3)	1.7(24)±3.4(23)	0.60±0.12	mm core
IRDC 18223-3 3	mm core
IRDC 18223-3 4	13.4±2.0	1.1(-2)	2.0(24)±5.4(23)	0.31±0.08	mm core
IRDC 18223-3 6	33.5±1.2	2.9(-3)	5.5(23)±1.1(23)	0.36±0.07	mm core
IRDC 18223-3 7	mm core
IRDC 18310-4 1	mm core
IRDC 18310-4 2	11.5±0.7	6.1(-3)	1.1(24)±2.4(23)	2.61±0.56	mm core
IRDC 18310-4 3	21.7±0.7	2.5(-3)	4.8(23)±9.7(22)	0.45±0.09	mm core
IRDC 18310-4 4	6.6±0.6	1.0(-2)	1.9(24)±4.5(23)	0.91±0.22	mm core
HMPO IRAS 18089 1	19.6±0.4	179.0±1.0	96.0±1.2	6.0(-2)	1.1(25)±2.2(24)	3.20±0.64	mm core
HMPO IRAS 18089 2	3.5±0.1	3.0(-1)	4.9(25)±1.0(25)	6.71±1.39	mm core
HMPO IRAS 18089 4	mm core
HMPO IRAS 18089 9	mm core
HMPO IRAS 18182 1	29.0±0.5	101.6±2.4	...	2.1(-2)	3.9(24)±7.9(23)	6.08±1.22	mm core
HMPO IRAS 18182 2	22.0±0.7	33.1±2.2	...	1.1(-2)	2.1(24)±4.5(23)	1.28±0.27	mm core
HMPO IRAS 18182 3	26.1±0.2	1.4(-2)	2.6(24)±5.3(23)	1.44±0.29	mm core
HMPO IRAS 18264 1	35.6±0.7	130.0±1.1	...	1.4(-2)	2.6(24)±5.2(23)	1.18±0.24	mm core
HMPO IRAS 18264 2	42.6±0.5	136.7±2.7	...	1.0(-2)	1.9(24)±3.9(23)	1.14±0.23	mm core
HMPO IRAS 18264 3	36.2±0.7	2.1(-2)	4.0(24)±8.1(23)	0.84±0.17	mm core
HMPO IRAS 18264 4	20.8±1.1	3.1(-2)	5.7(24)±1.2(24)	2.48±0.52	mm core
HMC G9.62+0.19 1	14.2±0.1	72.2±1.9	...	4.2(-2)	7.8(24)±1.6(24)	4.29±0.87	UCHII
HMC G9.62+0.19 2	17.6±0.5	195.0±29.7	124.4±3.6	3.7(-2)	6.8(24)±1.4(24)	4.42±0.89	UCHII

Notes. a(b) = a×10^b.

TABLE C.5: continued.

	HCN-to-HNC ratio \bar{T} (K)	CH ₃ CN \bar{T} (K)	CH ₃ ¹³ CN \bar{T} (K)	τ_v^{cont}	$N(\text{H}_2)$ (cm ⁻²)	M (M_\odot)	type
HMC G9.62+0.19 3	14.6±0.1	161.9±6.2	120.8±7.9	1.8(-2)	3.3(24)±7.0(23)	3.55±0.75	mm core
HMC G9.62+0.19 4	13.5±0.2	97.8±6.3	...	8.9(-3)	1.7(24)±3.5(23)	1.72±0.36	mm core
HMC G9.62+0.19 5	14.9±0.2	160.2±36.9	...	5.3(-3)	1.0(24)±3.1(23)	0.90±0.28	mm core
HMC G9.62+0.19 6	24.2±0.7	36.2±1.2	...	3.5(-4)	6.7(22)±1.4(22)	0.21±0.04	UCHII
HMC G9.62+0.19 7	14.8±0.1	109.5±17.7	...	6.2(-3)	1.2(24)±3.0(23)	1.57±0.41	mm core
HMC G9.62+0.19 8	10.9±0.2	108.0±1.6	...	3.8(-3)	7.2(23)±1.5(23)	1.17±0.23	mm core
HMC G9.62+0.19 9	comet. UCHII
HMC G10.47+0.03 1	10.8±0.6	89.0±32.6	148.9±10.2	7.3(-1)	9.8(25)±2.1(25)	197.97±41.92	UCHII
HMC G10.47+0.03 2	21.6±0.5	192.8±21.5	...	4.6(-3)	8.7(23)±2.0(23)	2.41±0.55	UCHII
HMC G10.47+0.03 4	15.6±0.0	184.8±25.9	...	2.5(-3)	4.8(23)±1.2(23)	0.44±0.11	UCHII
HMC G34.26+0.15 1	...	249.8±0.2	153.6±7.1	...	6.3(26)±1.3(26)	50.33±10.34	UCHII
HMC G34.26+0.15 2	...	157.4±21.6	...	1.4(-1)	2.4(25)±5.9(24)	0.97±0.24	UCHII
HMC G34.26+0.15 3	...	112.9±10.3	...	1.3(-1)	2.4(25)±5.3(24)	0.89±0.20	UCHII
UCHII G10.30-0.15 1	16.4±0.2	31.4±1.3	...	5.9(-3)	1.1(24)±2.3(23)	9.81±2.01	comet. UCHII
UCHII G13.87+0.28 1	14.2±0.1	36.2±1.6	...	5.7(-3)	1.1(24)±2.2(23)	49.72±10.22	comet. UCHII

Notes. a(b) = a×10^b.

TABLE C.6: Visibility and density profiles in the ALMA sample. The visibility profiles are shown in Fig. 4.8. In most cases, two power-law profiles were fitted to the observed visibility profile with α_1 and α_2 tracing the clump and core scales, respectively. The corresponding density power-law indices p_1 and p_2 are then estimated according to Eq. (2.3) (Table C.4).

	α_1	p_1	α_2	p_2	type
IRDC G11.11-4 1	-0.37 ± 0.03	2.58 ± 0.03	-0.01 ± 0.02	2.94 ± 0.02	mm core
IRDC 18223-3 1	-0.63 ± 0.09	2.23 ± 0.09	-0.06 ± 0.02	2.80 ± 0.02	mm core
IRDC 18223-3 2	-0.67 ± 0.09	2.15 ± 0.09	-0.03 ± 0.01	2.79 ± 0.02	mm core
IRDC 18223-3 3	-0.67 ± 0.10	...	-0.04 ± 0.01	...	mm core
IRDC 18223-3 4	-0.66 ± 0.10	...	-0.02 ± 0.01	...	mm core
IRDC 18223-3 6	-0.67 ± 0.10	2.07 ± 0.10	-0.02 ± 0.01	2.72 ± 0.02	mm core
IRDC 18223-3 7	-0.67 ± 0.10	...	-0.03 ± 0.01	...	mm core
IRDC 18310-4 1	-0.64 ± 0.11	...	-0.01 ± 0.01	...	mm core
IRDC 18310-4 2	-0.63 ± 0.11	...	-0.01 ± 0.01	...	mm core
IRDC 18310-4 3	-0.64 ± 0.11	2.16 ± 0.17	-0.01 ± 0.01	2.79 ± 0.13	mm core
IRDC 18310-4 4	-0.63 ± 0.11	...	-0.00 ± 0.01	...	mm core
HMPO IRAS 18089 1	-0.52 ± 0.01	1.72 ± 0.10	-0.52 ± 0.01	1.72 ± 0.10	mm core
HMPO IRAS 18089 2	-0.69 ± 0.02	...	-0.11 ± 0.02	...	mm core
HMPO IRAS 18089 4	-0.69 ± 0.02	...	-0.07 ± 0.01	...	mm core
HMPO IRAS 18089 9	-0.72 ± 0.03	...	-0.03 ± 0.02	...	mm core
HMPO IRAS 18182 1	-0.51 ± 0.04	1.81 ± 0.08	-0.19 ± 0.04	2.13 ± 0.08	mm core
HMPO IRAS 18182 2	-0.53 ± 0.04	...	-0.18 ± 0.04	...	mm core
HMPO IRAS 18182 3	-0.53 ± 0.04	2.35 ± 0.05	-0.17 ± 0.04	2.71 ± 0.05	mm core
HMPO IRAS 18264 1	-0.75 ± 0.04	1.87 ± 0.05	-0.24 ± 0.03	2.38 ± 0.04	mm core
HMPO IRAS 18264 2	-0.81 ± 0.04	1.97 ± 0.04	-0.15 ± 0.01	2.63 ± 0.02	mm core
HMPO IRAS 18264 3	-0.87 ± 0.05	2.02 ± 0.05	-0.10 ± 0.01	2.79 ± 0.02	mm core
HMPO IRAS 18264 4	-0.85 ± 0.04	...	-0.10 ± 0.01	...	mm core
HMC G9.62+0.19 1	-0.83 ± 0.15	1.50 ± 0.17	-0.44 ± 0.04	1.89 ± 0.10	UCHII
HMC G9.62+0.19 2	-1.14 ± 0.12	1.13 ± 0.21	-0.24 ± 0.02	2.03 ± 0.17	UCHII
HMC G9.62+0.19 3	-1.23 ± 0.09	1.17 ± 0.13	-0.14 ± 0.05	2.26 ± 0.10	mm core
HMC G9.62+0.19 4	-1.30 ± 0.07	...	-0.09 ± 0.05	...	mm core

TABLE C.6: continued.

	α_1	p_1	α_2	p_2	type
HMC G9.62+0.19 5	-1.30 ± 0.07	1.00 ± 0.09	-0.08 ± 0.05	2.22 ± 0.08	mm core
HMC G9.62+0.19 6	-1.26 ± 0.07	1.08 ± 0.08	-0.18 ± 0.05	2.16 ± 0.06	UCHII
HMC G9.62+0.19 7	-1.27 ± 0.07	1.09 ± 0.09	-0.09 ± 0.06	2.27 ± 0.08	mm core
HMC G9.62+0.19 8	-1.28 ± 0.07	1.38 ± 0.11	-0.10 ± 0.05	2.56 ± 0.09	mm core
HMC G9.62+0.19 9	-1.30 ± 0.06	...	-0.17 ± 0.04	...	comet. UCHII
HMC G10.47+0.03 1	-0.17 ± 0.02	2.21 ± 0.13	-0.61 ± 0.02	1.77 ± 0.13	UCHII
HMC G10.47+0.03 2	-0.20 ± 0.03	2.56 ± 0.07	-0.56 ± 0.04	2.20 ± 0.07	UCHII
HMC G10.47+0.03 4	-0.25 ± 0.05	2.63 ± 0.07	-0.90 ± 0.06	1.98 ± 0.08	UCHII
HMC G34.26+0.15 1	-0.09 ± 0.01	2.23 ± 0.04	-0.75 ± 0.05	1.57 ± 0.06	UCHII
HMC G34.26+0.15 2	-0.19 ± 0.03	2.65 ± 0.05	-0.52 ± 0.06	2.32 ± 0.07	UCHII
HMC G34.26+0.15 3	-0.19 ± 0.03	...	-0.52 ± 0.06	...	UCHII
UCHII G10.30-0.15 1	-1.17 ± 0.10	1.78 ± 0.10	-0.21 ± 0.04	2.74 ± 0.04	comet. UCHII
UCHII G13.87+0.28 1	-1.67 ± 0.08	1.27 ± 0.09	-0.12 ± 0.04	2.82 ± 0.05	comet. UCHII

C.4 Integrated intensity maps

Figure C.12 show the H(40) α recombination line integrated intensity map of all regions. In Sect. 4.4.2 we then estimate the contribution of free-free emission at 3 mm wavelengths based on 5 GHz continuum observations.

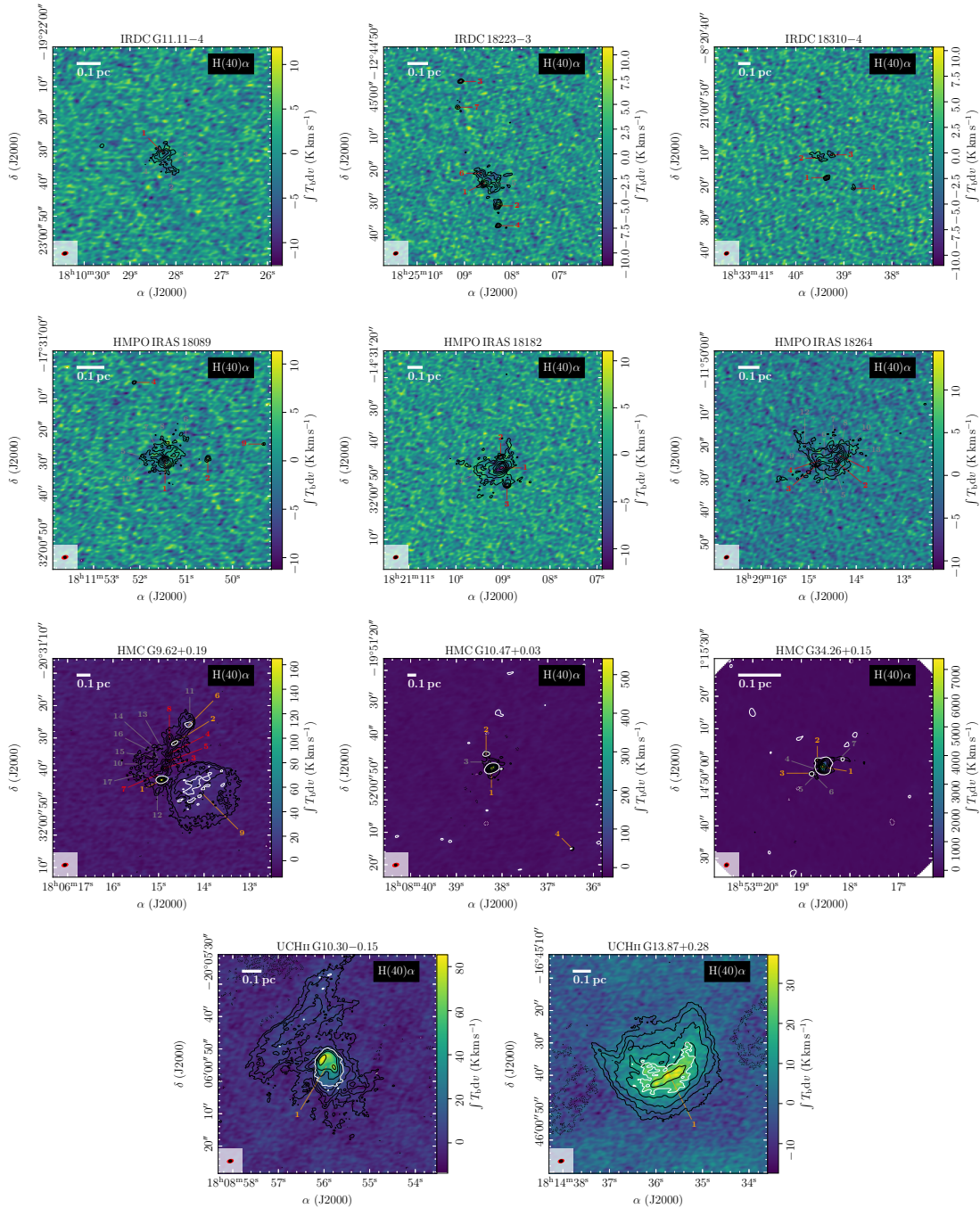


FIGURE C.12: Integrated intensity maps of H(40) α . In each panel, the H(40) α integrated intensity of the region is shown in color and white contours (dotted: -5σ and solid: $+5\sigma$). The 3 mm continuum data is shown by black contours. The dotted black contour marks the $-5\sigma_{\text{cont}}$ level. The solid black contours start at $5\sigma_{\text{cont}}$ and contour steps increase by a factor of 2 (e.g., 5, 10, 20, $40\sigma_{\text{cont}}$). The synthesized beam sizes of the continuum (black) and line (red) data is shown in the bottom left corner. The continuum fragments are classified into mm cores (red), (cometary) UCHn regions (orange), and envelope clumps (grey), further explained in Sect. 4.4.1.

Acknowledgements

In 2016 I had to give a presentation about “The most complex molecules detected in the interstellar medium” as part of a Master seminar. To prepare for this talk, I was reading the famous review paper “Complex Organic Interstellar Molecules” by Eric Herbst and Ewine van Dishoeck (Herbst & van Dishoeck 2009) and this was the moment I found my scientific passion: astrochemistry and star formation. I can still not fully grasp right now that I am about to submit my PhD thesis having worked on these topics for five years. Throughout this time I grew a lot as a researcher, met fantastic people, and learned a lot about so many topics in astrophysics. This would have definitely not been possible without my co-workers, family, and friends, that always believed in me.

First of all, my biggest gratitude goes to my supervisor Henrik Beuther, who always supported, helped, and encouraged me throughout all of my PhD. I am deeply grateful for all the opportunities you made possible during my PhD, for everything you taught me, and for always backing me up. I would also like to thank Dmitry Semenov for teaching me so much about astrochemistry and chemical modeling. I am very thankful to Thomas Henning for all your fruitful science ideas for my PhD projects, but also for the support and advice you gave me for my future career. Being part of the “CORE” collaboration was very rewarding and I would like to thank everyone in the team for their help and discussions regarding the CORE projects.

During my PhD, I received a lot of help and support from so many people at MPIA and I would like to thank them all. I am especially grateful to all former and current members of the star formation group for their continuous support even when things did not seem work out. I am very thankful to my former and current office mates and IMPRS fellows for the fun times. I am very grateful for all the support I received at IRAM Grenoble for all of the NOEMA data calibration and imaging. I also appreciate a lot the support from IRAM Granada at the IRAM 30m telescope and from the CfA/SAO at the SMA during my stays at the observatories.

I am very grateful for my family, especially my parents Anja and Peter and my brother Marc, for their unconditional love and support throughout my life. I promise I will not become a crazy physics professor (maybe a little). I would also like to give thanks to our family dogs Emily, Dana, and Ella, that always made/make me smile and were a huge emotional support throughout my life. Studying physics was always challenging, but I also had the best time of my life and I would like to thank especially Eva, Katja, Falk, Mattis, and Paddy, because without you I would have never made it to this point. Many thanks go to Cosima, Fiona, and Sophia that you are a part of my life since our high-school years. During a pandemic including several lock downs, one really appreciates having a friend next door: I am so grateful to Kristina that you were always there for me. I already miss long summer nights on the terrace and our hikes through the forest!

I want to thank Cornelis Dullemond for being the second referee of this thesis and Holger Kreckel and Joachim Wambsgansß for being examiners in the thesis defense. Special thanks go to Katja, Molly, Dima, and Marten for proof-reading this thesis! And at last, I want to thank everyone I forgot to mention.

These last words were written at Ringberg Castle and I believe there is no better place to finish such a chapter in life. And now while JWST is finally in space commissioning its instruments, I am excited for the future of astrochemistry and star formation!